UNIVERSITY OF SOUTHAMPTON

FACULTY OF ENGINEERING, SCIENCE AND MATHEMATICS

AEROSPACE ENGINEERING

DEVELOPMENT OF DESIGN TECHNIQUES FOR THE AVOIDANCE OF ACOUSTIC FATIGUE IN AIRCRAFT BOX-TYPE STRUCTURES

by

Ying XIAO

MAY 2004

DEVELOPMENT OF DESIGN TECHNIQUES FOR THE AVOIDANCE OF ACOUSTIC FATIGUE IN AIRCRAFT BOX-TYPE STRUCTURES

by

Ying Xiao

of the

School of Engineering Sciences
Aerospace Engineering
Faculty of Engineering, Science and Mathematics
University of Southampton
England

A thesis submitted for the degree of

Doctor of Philosophy

UNIVERSITY OF SOUTHAMPTON

ABSTRACT

FACULTY OF ENGINEERING, SCIENCE AND MATHEMATICS

SCHOOL OF ENGINEERING SCIENCES
AEROSPACE ENGINEERING

Doctor of Philosophy

DEVELOPMENT OF DESIGN TECHNIQUES FOR THE AVOIDANCE OF ACOUSTIC FATIGUE IN AIRCRAFT BOX-TYPE STRUCTURES

by Ying Xiao

This thesis describes a programme of work carried out on the acoustic fatigue of aluminium alloy, carbon fibre reinforced plastic (CFRP) and GLARE box-type structures representative of aircraft flaps. GLARE is a hybrid material made of aluminium alloy and glass reinforced plastic. "Tee-coupon" specimens were also used to obtain fatigue data for the composite materials. A brief introduction is given concerning CFRP and GLARE composites used to build the test coupons and box structures. A review of the state-of-the-art in the research on the acoustic fatigue of aircraft structures is also presented.

The characteristics of the sound pressure field at the test section of the progressive wave tube (PWT) used in the acoustic fatigue testing were investigated. The highest overall sound pressure level measured was 162dB. Non-Gaussian distribution behaviour in measured sound pressure signals was observed. Results showed that sound pressure field was uniformly distributed in amplitude around the test section but spatial phase change occurred in the direction along the axis of the PWT.

Damping measurements for coupon specimens revealed that the CFRP coupons had higher loss factors than the GLARE coupons. Fatigue tests were carried out to generate fatigue data for CFRP and GLARE coupons. It has been found that the fatigue damage patterns for the CFRP coupons were cracks in the joint region of the skin and stiffener and delamination of the skin plate. For the GLARE coupons, the 'fibre bridging effect' was not as effective as expected.

Mode shapes, resonance frequencies and modal damping ratios of the box structures were obtained by the means of forced vibration tests. Results showed that stiffeners behaved differently at low and high frequencies. The CFRP box had the highest damping compared with the GLARE and aluminium alloy boxes. The acoustic excitation tests of three box-type structures showed that the strain responses of the two skin panels were coupled at high excitation levels. Non-linear behaviour in the forms of resonance peak broadening, peak frequency shifting and strain energy redistribution as the excitation level increased were observed. Fatigue damage in the form of cracks in the metallic and hybrid structures was induced and propagation rates noted. Damage to rivets occurred in the CFRP box, but this was the most acoustic fatigue resistant structure followed by the GLARE and aluminium alloy constructions. Formulae based on the fatigue data of coupon tests and Miner's accumulation theory were derived for the fatigue life predication of the CFRP and GLARE structures. Estimated fatigue life gave good indication of the fatigue resistance of the composite structures.

FE analysis was carried out for both coupon specimens and box structures. A good agreement was achieved for RMS strain response and spectral densities at various locations on the test boxes and coupon specimens.

ACKNOWLEDGEMENTS

I wish to express my deepest gratitude to Professor R. G. White, who offered me the opportunity to work on this project and has given me patient guidance and encouragement during the course of the project and the writing of the thesis.

I would also like to gratefully thank Professor R. S. Langley, Dr. G. Aglietti for their encouragement and much valuable help and advice.

I wish to extend my thanks to the Department of Aeronautics and Astronautics and ISVR for their fine technical assistance and co-operation, which was vital for the completion of this study. My appreciation to everyone, especially to Mr. J. Baker, Mr. D. Edwards and Mr. R. Stansbridge, for their support in many aspects of experimental studies.

My thanks to British Airbus and EPSRC for proving test specimens and funding for this project.

My thanks also to Lloyds Register of Shipping, my employer, for providing time and facilities for final completion of this thesis, especially to Mr. C Badger and Mr. S Yiannakis.

Finally, my thanks are also to my husband and daughter, for all support and the tolerance shown to me whilst I have been engaged in this endeavour.

CONTENTS

LIST OF SYMBOLS

C	damping coefficient
C_0	critical damping coefficient
E(D)	expected probability value of damage
F	force
G_p	spectral density of acoustic pressure
$H(i\omega)$	complex frequency response function
K	stiffness
L	wavelength
M_k	central moment of the distribution
N_i	fatigue failure life (cycles)
N_p	total number of peaks to failure
N(s)	number of cycles to failure for a random amplitude stress
P(s)	peak probability density
T	time period
T_{60}	time for vibration amplitude to decay to 60dB of its original value
V_x	wave velocity

a	acceleration
f	frequency, Hz
$f_{1,2}$	frequency at half power points
f_l	lower frequency limit
f_n	resonance frequency of the nth mode
f_u	upper frequency limit
m	mass
n_i	number of load cycles
n(s)	cycles number of random stress in the range s to s+ds
p(x)	probability density distribution function
t	time
x_0	initial vibration amplitude

x_N	vibration amplitude after N cycles
γ	kurtosis
η	damping loss factor
λ	skewness
μ	mean value
ν	Poisson's ratio
σ	stress
σ_0	static stress
ε	RMS strain
ζ	viscous damping ratio
Δf	narrow band frequency range
ω	frequency, radians
$\mu\varepsilon$	micro strain

ARALL	Aramide Reinforced ALuminium Laminate
ASTM	American Society of Testing and Materials
BAe	British Aerospace
CFRP	Carbon Fibre Reinforced Plastics
ESDU	Engineering Sciences Data Unit
FEA	Finite Element Analysis
FRF	Frequency Response Function
GLARE	GLAssfibre REinforced aluminium laminates
MAC	Modal Assurance Criterion
OASPL	OverAll Sound Pressure Level
PSD	Power Spectral Density
PWT	Progressive Wave Tube
RAE	Royal Aircraft Establishment
RMS	Root-Mean-Square
SACMA	Suppliers of Advanced Composite Materials Association

CHAPTER 1

GENERAL INTRODUCTION

1.1 BACKGROUND

The various operational loads, with different magnitudes and durations, experienced by an aircraft in its service life form a very complicated fatigue environment[1, 2]. In the design of aircraft structures, one of the major concerns is their ability to withstand the high levels of random pressure loading, which can cause acoustic fatigue failure.

Acoustic fatigue of aircraft structure is defined as "the structural failure caused by intensive acoustic loading, which forces structural components to vibrate". In aircraft structures, regions which are close to, or in the path of the engine efflux, such as flaps, are more likely to suffer acoustic fatigue failure. In general, the stress and strain in aircraft structures induced by acoustic loading are smaller than those caused by aircraft manoeuvres, as shown in Figure 1.1. However, they are far more numerous and usually in a high frequency band, around 100 Hz to 1 kHz. Because of this, and also because there are always inevitable defects which exist in aircraft structural components, acoustic fatigue can occur in a short time due to the growth of old defects and formation of new cracks[3].

Acoustic fatigue failures had been reported in the late 1950s following the introduction of powerful gas turbine engines. Extensive theoretical and experimental studies have been carried out since then. However due to the complexity of acoustic fatigue, it being difficult to find a precise theoretical solution as a design tool, semi-empirical analysis techniques were developed based on Miles' single-degree-freedom approach in combination with experimental data from full-scale aeroplane tests and laboratory acoustic fatigue tests[4]. These semi-

empirical analysis techniques were developed further into practical design rules and guides, such as ESDU data sheets and AGARDograph, etc, which have been used extensively in the design of metallic components of aircraft structures[5, 6]. It is fair to say that acoustic fatigue is under control to some extent for aircraft built predominately from metallic materials.

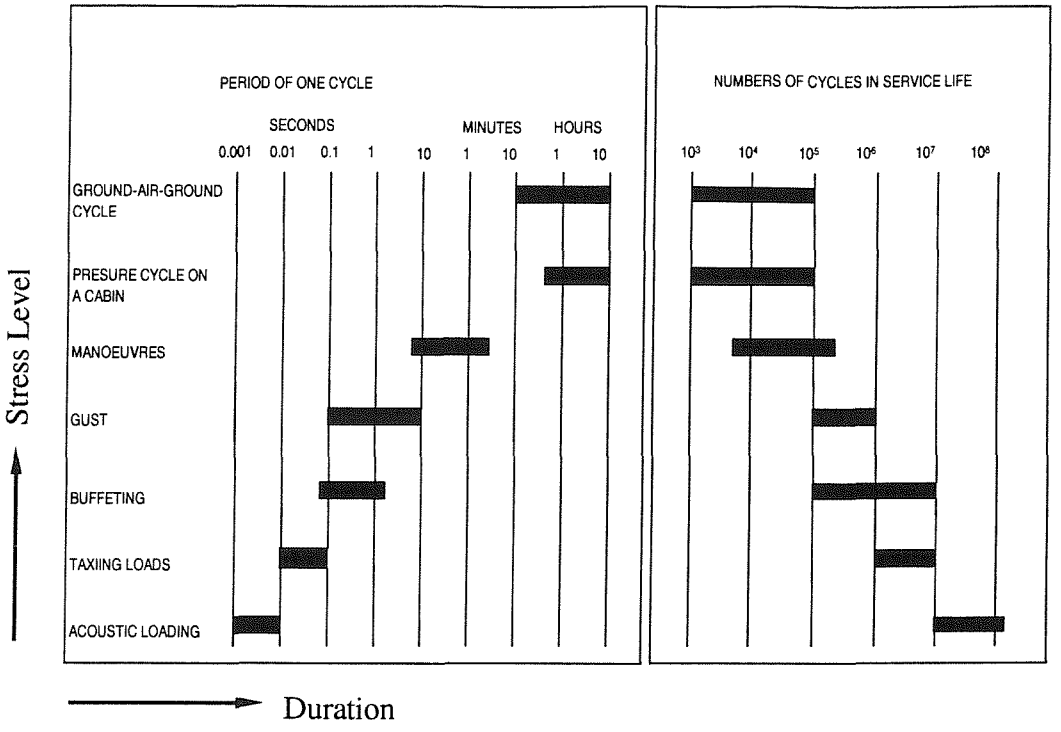

Figure1.1 Loads occurring in the service life of aircraft [Ref.2]

In order to improve aircraft load carrying capacity, more and more composite materials are employed in the structure to reduce the weight and increase the strength/weight ratio. At the same time, larger and more complex aircraft structures as well as supersonic/hypersonic vehicles are being developed. This has resulted in high intensity acoustic loading over 180 dB with temperatures as high as 1650°c, which could cause acoustic fatigue, thermal buckling and non-linear response[7, 8, 9]. Therefore the acoustic fatigue of aircraft structures has become of considerable interest again since the 1980s. The need for new design guides to cover acoustic fatigue failures in composite structures under the high level random acoustic loading has become inevitable. Clarkson[8] has made a comprehensive review of the state of acoustic fatigue research, which showed that although much higher efforts have been made, there is still a gap between the understanding of acoustic fatigue and the increased demand for practical design guidance.

1.2 BRIEF REVIEW OF ACOUSTIC FATIGUE

There are three aspects which affect prediction of the acoustic fatigue performance of aircraft components under acoustic loading, these are:

* The nature of the acoustic loading that leads to the possible acoustic fatigue failure of structures.
* Estimation of the response stress/strain level of a structure to acoustic loading.
* Prediction of fatigue life under the acoustically induced strains/stresses.

1.2.1 Acoustic Loading

The sources of acoustic pressure fields acting on the surfaces of an aircraft component can be divided into the following categories[7]: boundary layer loads; jet and plume loads and separated aerodynamic flow. These loads are random in nature with broadband frequency range and vary with time and space. The levels of acoustic loads from engines and aerodynamic sources depend on aircraft flight conditions. There are still difficulties in accurate prediction of the loading data, and semi-empirical methods, such as the ESDU data sheets, are used. In theoretical analyses of aircraft structures subjected to acoustic loading, the uniform pressure field is usually used to predict the response of structures. This may not be adequately representative of in-service loading and there is the need to use pressure excitation with spatially varying amplitude and phase characteristics.

Efforts have been made to establish the characteristics of acoustic loading by estimation from historical data measured by a small number of microphones in a test rig or in flight conditions, or by theoretical analysis[5, 7, 10, 11]. However much still needs to be done to predict the distributions of surface pressure with reasonable accuracy.

1.2.2 Structural Response

The main problem in acoustic fatigue analysis is the calculation of the vibration stress levels in structural panels subjected to random acoustic excitation, and then to predict the fatigue life of the structures. In the early stage of the research on acoustic fatigue, estimation of structural response was based on a single degree of freedom theory, which is still used in the design of aircraft structures. Powerful computer based, numerical methods have been developed and the

accuracy of estimation has been improving, but no existing method is fully capable of giving satisfactory results for structural design. Experimental study is therefore still necessary.

1.2.2.1 Theoretical approach

The major characteristics of acoustic loading and the structural response are random in nature. These cause the problem to be very complicated, and it is difficult to develop a precise theoretical model[4]. Therefore, some simplified approximate methods of analysis were developed by three earlier researchers, Miles[12], Powell[13] and Clarkson[14], who have made significant contributions to the estimation of acoustic fatigue life for aircraft structures. Existing acoustic fatigue design guides used extensively for metallic structures are based on their work.

Miles' single degree-of-freedom theory was based on the assumption that the structure is simplified as a single panel; the acoustic load is a uniform pressure field with spectral density $G(f_n)$ at the fundamental resonance frequency of the panel. Then the mean square response and the mean square stress are calculated. Miles' theory means that the designer only needs to be concerned with estimation of the fundamental mode resonance frequency and to determine the static stress response. Powell developed a general method for analysing structures excited by acoustic loads, but it is too complicated to be used in practice and requires input data that are not generally available[4]. To make Powell's theory useful in practical design, Clarkson made some suggestions to simplify the problem. His assumptions were: the panel is vibrating predominantly in its fundamental mode; the vibration mode is identical with the mode of deflection of the panel when subjected to a uniform static pressure, and the panel is usually fully fixed at its edges; the pressure is in phase over the whole panel; and finally, the power spectral density of the pressure is constant over the frequency range near the natural frequency of the panel, which is lightly damped. Then the mean square bending stress at the point of interest is given by[14]

$$\overline{\sigma^2(t)} = \frac{\pi}{4\zeta} f_n G_p(f_n) \sigma_0^2 \qquad (1.1)$$

Where f_n = the fundamental mode natural frequency

$G_p(f_n)$ = spectral density of the acoustic pressure at frequency f_n

σ_0 = static stress at the point of interest due to uniform static pressure

ζ = damping ratio of the fundamental mode, typically 0.01 - 0.02, and taken as 0.017 for an aluminium alloy panel as recommended in the ESDU design guides[5]

The assumption of a single mode response is not realistic in general and should result in an under-estimate of the actual stress, and the assumption of fully fixed edges should yield an over-estimate of the stresses. However, this simple formula has been well established and proven, and is used as the basis of most design methods. This method is validated for aircraft structures, and extension of the procedure to composite panels is still based on Clarkson's method[15 to 18].

In recent years, with the development of aircraft construction, configuration and propulsion systems, aircraft structures have to withstand much higher levels of acoustic and thermal loads, and for longer periods. It is therefore necessary to re-evaluate the existing design methods. Also with the increasing use of composite materials and increase of pressure level, the non-linear response of structures is becoming a major issue. It is required to develop an improved design method, which can accurately predict the structural response to severe acoustic environments, cover more complex structures and also non-linear effects. Efforts have been made recently to develop theoretical methods for predicting strain and modal response characteristics and to understand the effects of high temperature on structural response behaviour and performance of fibre-reinforced composite material structures.

Developments in the Finite Element Analysis method and the increase of computer capability show promise of more accurate numerical response predictions. Most theoretical methods developed for aircraft panels concern rectangularly shaped panels with simply supported or clamped boundary conditions. One of the advantages of the finite element method is that it enables more complex structural shapes and boundary conditions with detailed acoustic loading characteristics to be analysed. The accuracy of the method depends on the precision of the elements adopted and the number of elements used. The sources of error are well understood and there are guidelines available to ensure accurate results[19]. However, the choice of correct element types, and proper modelling of the real boundary conditions and loading spectrum will affect the results. By use of the FE method, not only the fundamental mode, but also the higher order modes can be determined. From knowledge of the excitation

spectrum, the power spectral density of the stress can be predicted.

Use of the FE method to analyse stiffened structures began in the late 1960s. The early work was to use the FE method to determine the mode shapes and natural frequencies of stiffened plates[20]. With development of the FE method and increased computer power, more complicated analysis can now be carried out. There are several factors that affect the accuracy of FE modelling of the acoustically induced response of stiffened panels: the acoustic loading; modelling of reinforcements; modelling of boundary conditions; damping; the element mesh size; large non-linear deflection, etc. and the effect of panel curvature.

Theoretically, any variations of the amplitude and phase of acoustic pressure in any frequency range can be simulated in FE modelling. Due to the lack of a database in relation to the acoustic loading, in most FE modelling and other prediction methods, the assumption of a uniformly distributed pressure field is used, and pressures are assumed to be in phase across the structure[5, 21]. When the wave length of acoustic pressure variation in the frequency range of interest is long compared with the characteristic length given by the overall structure dimension, this assumption is acceptable. Random loading can be simulated by means of the Power Spectral Density (PSD) in the frequency domain[21]. The alternative way to consider random vibration reported recently[22], is that in which the loads are simulated in the time domain using the Monte-Carlo approach. The advantage of the time-domain approach is the possibility of considering non-linear structural behaviour. To accurately model the response of a structure, knowledge of the spatial distribution of the pressure field is necessary. In the BRITE-EURAM Program ACOUFAT[23], based on wind-tunnel tests, a semi-empirical model of the spatial-temporal characteristics of the aero-acoustic loads on a flat panel has been developed and utilised as "load data input" for FE calculations. In the FE modelling, the test panel was divided into a number of elements. At each element, the pressure spectral density is considered to be uniform over each element and the pressure to be spatially in-phase. The correlations between elements are defined by the Cross-Spectra. The entire load is input to the FE model as a multiple-pressure input system.

Aircraft structures are mainly composed of stiffened panels. The reinforcements, i.e. stiffeners or stringers have made the problem more complicated rather than the overall size of panels. Experiments have shown that high stress/strain gradients occur close to joint lines of panels

and reinforcements and fatigue cracks normally appear along rivet lines. The proper modelling of stiffeners is of importance in response prediction. Generally, the stiffeners can be modelled by either beam elements, or shell (plate) elements which completely simulate the shapes of stiffeners and can give better results but produce more degrees-of-freedom (DOF) which results in a longer computation time. Lindberg[20] conducted a FE analysis of a stiffened panel with different modelling techniques for the stringers. The results showed that mode shapes and natural frequencies were significantly affected by the modelling method used for the stringers. How to model the connection of skin panels with the flanges of stringers is another concern. Koenig[24] used a method to represent the rivet lines. First, each rivet line was modelled by seven vertical rigid bars which connect the flange of the stringer to the skin at each relevant rigid point. Second, the skin is connected with flanges of stringers at all the grid points by rigid bars, which makes the modelled structure stiffer than in the first case. In the use of the FE method for predicting failure of cracked stiffened panels[25], the rivet connection was modelled by an elastic-perfectly plastic shear spring.

Boundary conditions can significantly affect the response of aircraft panels. The easiest way to model boundary conditions is to assume that the edges of the panels are simply supported or clamped. But such ideal conditions do not exist in practical structures. Typical aircraft structures can also have some in-plane motion. Elastic constraints can be used to model the actual boundary conditions. An artificial boundary stiffness method has been used by Gordon[26]. The approach is to apply translational or rotational stiffness elements at the boundary of a local area for the finite element model to approximate the dynamic effects of the surrounding structures. Modal updating methods are then used to tune the stiffness to minimize the error between selected natural frequencies or mode shapes of the model and experimental modal data. The advantage of this method is that it can accurately model a local area of stiffened structures without the need to build up a large FE model.

Damping plays an important role in the dynamic behaviour of structures. In FE analysis, either material damping or modal damping may be used. In the absence of measured modal damping or a good estimation, the ESDU data sheets recommend use of a damping ratio ζ of 0.005 to 0.030 for typical metallic aircraft skin and stringer panels vibrating in their fundamental mode, and 0.003 to 0.012 for a typical integrally-machined panel. Due to the complexity of damping mechanisms, it is difficult to have accurate damping value for every type of structure

modelled in FE analyses. Assumed values of viscous damping ratio are therefore commonly used.

The size of mesh in FE modelling depends on the number of elements and the size of the structure to be analysed. A general rule is to use a minimum of four elements per half wavelength. This means that the higher the frequencies of interest, the larger the problem size. This is one of the limitations in FE modelling, although powerful computers permit large jobs to be performed. In practice, we can start with a coarse mesh and then check the result with a finer mesh.

Some work has been done to consider the effects of a large deflection and non-linearity of a panel when subjected to high intensity acoustic loads[27, 28]. A finite element formulation is presented for the analysis of beams and rectangular plates undergoing large deflections[28]. Single mode response is assumed in the analysis.

The FE method is a powerful structural analysis tool and has been widely used in the study of structural behaviour under the action of acoustic loading and the design of structures. Some examples are given below. The design techniques developed by Holehouse for diffusion-bonded titanium sandwich structures[18] and advanced composite materials, CFRP[15, 16], utilized the finite element method to predict the natural frequencies of in-phase stringer bending modes and static stress/strain response of an aircraft panel. These theoretical results, together with experimental data, were used to develop a semi-empirical design nomograph and formulae. However, in that work, single-degree-freedom theory was used. Climent and Casalengua's[21] work on acoustic fatigue stress calculation in complex substructures, i.e., a part of the keel beam separating the two engine tunnels between two fuselage frames, predicted resonance frequencies close to those measured during testing apart from two frequency peaks which appeared in test data and were not predicted in the analysis. Predicted stresses and accelerations were in a good agreement with those obtained in acoustic testing. In the work of Wolfe[29], the FE method was also used to calculate the modal frequencies and their results were compared with experimental results. Koenig[24] used FE modelling to study CFRP coupons for acoustic testing, with the objective of establishing how reliable were S-N curves which could be used in acoustic fatigue design. The FE approach also has been used to investigate plates undergoing large deflection subjected to acoustic

loading[27, 28]. In the investigation on acoustic fatigue problems in aircraft with ultra high bypass engines[30], a FE model of the fuselage panels which were tested in a progressive wave tube (PWT) was constructed prior to testing. The results were used to define the panel response characteristics and most favourable mounting locations for accelerometers and strain gauges.

Apart from the FE estimation, a number of linear theories have been developed to calculate the modal frequencies of the panels, such as, Lin's equation[31], AGARD nomograph, Blevins` formula[32] and the formulae given in ESDU data sheets[Ref.5]. These theories are mainly for plates or beams with simply supported or clamped boundary conditions. Mei[33] has pointed out that the average value of the clamped and the simple supported plate theories yield fundamental modal frequencies close to test values obtained with typical aircraft structures at low levels of excitation. A method for the direct identification of vibration parameters from the free response in the time domain is proposed by Ibrahim[34], where the free response of a structure was used directly in a computational procedure which yields the required data. Either the acceleration, velocity or displacement response may be used. The advantage of this method is that the direct use of time response information is possible without transformation to the frequency domain and without the necessity to make assumptions about the interference of modes due to heavy damping or the effects of closely spaced natural frequencies.

Large deflections can affect the natural frequency and mode shape of thin, panel-like structures. White[35] studied the effects of non-linearity due to large deflections in the resonance testing of structures. He indicated that if the membrane strains become significant and contribute to the restoring force then the force-deflection relationship becomes non-linear. As the non-linearity increased, the steady-state frequency response function, both modulus and phase curves showed the "hardening" spring effect, and the frequency "jump" effect occurred. These phenomena have been also observed by Wolfe[29] in his experiments. The effects of large vibration amplitudes on mode shapes and natural frequencies of structures were studied by Benamar al et[36, 37].

Many analytical and experimental researches on acoustic fatigue have repeatedly shown a poor comparison between measured and calculated root-mean-square (RMS) response[7, 10]. One of the major reasons suspected for the discrepancy was that the panel response was based

on small deflection linear structural theory, whereas the test panels responded with large deflections at high sound pressure levels (over 120 dB)[29]. Also, test results[6, 9, 38, 39] have shown that the higher order modes contribute significantly to the response of a panel when excited under high sound pressures. So the single mode theory for response prediction is not adequate. The linear analysis often predicts RMS deflections and RMS strains/stresses well above those obtained in experiments, and resonance frequencies well below those obtained in experiments, which will lead to a poor estimation of the fatigue life of panels. There is a number of approaches to the problems reported in Ref.[33, 40 to 43], which are mainly based on some ideal boundary conditions and beams or rectangular plates and are far too simple to represent aircraft structures. Some of the methods are still based on the assumption of a single degree of freedom though large deflections were included. But experiments have shown the existence of multi-modal response in the acoustically induced vibration of plates. To accurately predict random response, it is necessary to use multiple modes in the analysis.

Another way to solve the nonlinear structural response and acoustic fatigue problem is to use the time domain approach. The time domain Monte Carlo approach has been used to construct practical solutions[9, 19]. The time domain Monte Carlo method consists of three basic steps: first, realizations of random inputs, second, solving the equations of motion by a numerical method, and last, computing the quantities of the response processes from ensemble averages. The time domain approach requires a very large memory storage capacity and extensive computation time. In Ref.[19], numerical results are presented for a typical, discretely stiffened titanium panel. Uniformly distributed Gaussian white noise was taken as the excitation. The results showed that the response of the panel reaches a transition point between linear and non-linear behaviour. It is also observed that for high pressure inputs, the response is no longer Gaussian and the peak distribution does not follow the Rayleigh distribution. The analysis of CFRP composite panels has also shown the existence of non-linear response and non-Gaussian characteristics[9, 44].

1.2.2.2 Experimental approach

From the above discussion, it can be seen that efforts have been made to produce satisfactory, improved theoretical methods and experimental data have shown some agreement with theoretical results. The comparisons are improving, but the situation is still not satisfactory. Experimental research still continues to be important.

For design purposes, fatigue testing is performed for two reasons. The coupon test is used to provide basic material data which are used to generate design curves, and the complete components or assembly subjected to an acoustic fatigue test for confirmation of the design. The coupons used in fatigue testing are normally in the form of a beam, a Tee-coupon or a panel, which are excited under sinusoidal or random loading at constant input RMS acceleration levels using vibration exciters or shakers. The coupons were designed to establish S-N curves valid for random excitations of materials used in aircraft construction. Normally, the design data/curves obtained from beam and Tee coupons testing tend to be conservative compared with panel or component tests[45]. For research purposes, the most popular methods of acoustic fatigue testing are reverberation chamber and progressive wave tube (PWT). The reverberation chamber test is a classic approach for high frequency testing, by which relatively large samples can be tested in a clean environment. Due to concern that the conventional test method using large reverberation chambers may underestimate the fatigue problems in certain situations, and the need to increase temperature, the progressive wave tube method has been developed. The advantages of the PWT method are that the excitation is well defined, high temperature tests can be performed, high sound pressure level can be reached at lower frequencies and the cost of the test facility is reasonable. There is a disadvantage, however, that tunnels of small cross-section can greatly influence the modal damping of panels mounted in their walls. The PWT facilities available in Europe are listed in Ref.[46].

Koenig[45] suggests that the test specimen should have a box-type design to avoid nonrepresentative spar and frame movement; modal testing must be carried out to reveal the natural frequencies and mode shapes involved in predicting maximum strain; it is necessary to measure the pressure field of the PWT. Clarkson[8] summarised some work which has been done on the standardization of test specimens for acoustic fatigue testing and concluded that suitable test structure would be one having four or more frames and eight or more stringers. The acoustic loading spectrum should be wide enough to cover the dominant modal responses of the panels, typically 100-1000 Hz.

In an attempt to understand the over estimation of acoustic fatigue stresses by the use of the simple formula or the design nomographs, NASA set up a carefully controlled experiment on several flat aluminium alloy and composite panels[7]. The measured and predicted panel

accelerations agreed well, but the dynamic strains were over predicted by theory. A similar situation was encountered in the study on the effects of boundary conditions on dynamic strain response of rectangular panels[47]. It was found that predicted acceleration response spectra agreed well with those measured, but the predicted strain spectra were consistently higher than those measured. There could be several reasons which affect the results. The errors in strain measurements: normally, the strain gauge response is proportional to the deflection and dominates by the low frequency components which is the acceleration divided by the $(2\pi f)^2$. This indicates a lower levels in the higher frequencies and might caused more measured errors for the high frequency by the strain transducers. Damping values applied in predictions would also affect the accuracy of the prediction. Under the high intensity acoustic loading, the test panel shown nonlinear behaviours as discussed below.

One of the first studies of the response of composite plates to random acoustic loads in comparison with the response of aluminium alloy plates was made by White[38]. The experimental results for an aluminium alloy plate showed that the modal responses of the plate could be clearly seen at the lower excitation levels. At the highest level, broadening of the resonance peaks was seen to be owing to non-linear behaviour. The response strain spectral density at 154 dB OASPL was very different in nature from those at the lower excitation levels. The resonance frequencies shifted upwards with increasing excitation level. For the CFRP plates, relatively flat strain spectra were observed, which showed evidence of considerable non-linear behaviour. These non-linear effects were much greater for the CFRP plate than for the aluminium alloy panel. The peak broadening and modal frequency increase phenomenon also was observed by others[29, 44].

Holehouse[17] carried out series of experiments to investigate the random response and acoustic fatigue life characteristics of CFRP and aluminium alloy stiffened skin panels subjected to random acoustic loading. The multi-bay panels were subjected to high intensity random acoustic loading up to 160 dB in a PWT, and shaker tests were also performed on sections of skin laminates in order to provide additional random fatigue data. Non-linear response characteristics, such as peak broadening and increasing resonant frequency, were also observed at higher response level. However, the difference between the non-linear response characteristics of CFRP and Al alloy panels appeared to be less pronounced than that reported by White[38]. Holehouse pointed out that a panel can show an extreme, non-linear

behaviour which may be due to the non-visible laminate damage. He concluded that the non-linearity of panels is significant but not dominant. A paper by White[15] reviewed the development of acoustic fatigue research and the work done by him and his colleagues. He concluded that at response levels lower than those which produce pronounced non-linearity, the response of single plates is dominated by the response in one or two of the lower modes, and the overall level is close to that predicted by the simple, single mode formula; when in-plane loads or higher excitation levels produce marked non-linear response the estimations are higher than the measured overall levels. In the work[48] on a clamped-clamped beam, a considerable decrease in fatigue life was found in the non-linear response induced by random loading compared to a cantilever undergoing linear vibration at the same RMS strain. The main reason for the non-linear behaviour of the total strain was the axial strain contribution, the bending strain was linear in nature.

In order to improve the understanding of the non-linear behaviour of beams and plates excited from low to high levels of excitation, Wolfe[29, 39] conducted a series of tests on beams and plates made of both aluminium alloy and CFRP composites. Shaker table and PWT excitation were used to excite the beams and plates sinusoidally and randomly. The linear and non-linear responses were investigated. Linear mode shapes and non-linear deflection shapes were analysed. Frequency shifts and peak broadening in the resonant response were observed for both beams and plates made of both materials and the plates exhibited greater frequency shift and peak broadening than the beams. The contribution of the fundamental mode to the total strain decreased as the excitation level increased. At the highest excitation level, the resonant phenomenon almost disappeared and the modal contributions were not very distinguishable. Axial strain associated with stretching of the beam was observed, which was very low compared to the bending strains, but it lowered the overall strain and moved the neutral axis. Based on the experimental results, Wolfe developed a fatigue model to give reasonable estimates of the fatigue life of structures with multi-modal response.

1.2.3 Estimation of Fatigue Life under Acoustically Induced Strains/Stresses

In general, acoustic fatigue life estimation of aircraft structures is based on knowledge of RMS stress/strain and dominant response frequency of the structure, to estimate the time to failure using fatigue results from coupon tests. The earliest and most widely used fatigue damage accumulation theory is the Palmgren-Miner linear cumulative damage rule[2]. It is

assumed that the damage in a constant amplitude test is a linear function of the number of cycles. At a stress level S_i, load cycles n_i will consume a portion of fatigue life equal to n_i/N_i, where N_i is the number of cycles to failure in a constant amplitude fatigue test. Failure will occur when

$$\sum_i \frac{n_i}{N_i} = 1 \tag{1.2}$$

Miner's rule has also been extended to random loading by assuming that the fatigue damage caused by each stress peak is equal to the damage caused by one cycle in a sinusoidal fatigue test with the same stress amplitude. If N_p is the total number of peaks to failure, the expected probability value of the damage is[2]

$$E(D) = N_p \int_{-\infty}^{\infty} \frac{P(s)}{N(s)} ds \tag{1.3}$$

where P(s) is the peak-probability density function.

The expected probable damage resulting from stress peaks in the range (S to S+dS) with a frequency f_n (rate of stress/strain repetition) for a time period T is

$$\frac{n(s)}{N(s)} = f_n T \frac{P(s)}{N(s)} ds \tag{1.4}$$

where n(s) is the probable number of cycles of random stress having an amplitude in the range (S to S+dS) at a time T.

The total expected damage for all stress amplitudes is

$$E[D_M(T)] = f_n T \int_0^{\infty} \frac{P(s)}{N(s)} ds \tag{1.5}$$

So the time at which $E[2D_M(T)]$ is equal to 1, i.e, failure occur, is

$$T = [f_n \int_0^{\infty} \frac{P(s)}{N(s)} ds]^{-1} \quad \text{seconds} \tag{1.6}$$

Miner's rule has been used to predict fatigue life under random loading and been proven in practice to yield conservative fatigue life estimates[49].

To improve upon the conservative fatigue life estimates, a modified Miner's rule was used in design[2]. The expected damage is:

$$E[D_M(s)] = N_f(\bar{\sigma}) \int_0^\infty \frac{P(s)}{N(s)} ds \tag{1.7}$$

where N(s) the number of cycles to failure at a constant amplitude stress level σ determined from sinusoidal test data, N_f is the number to failure for a random amplitude stress, σ. So the number of cycles to failure is

$$N_f(\bar{\sigma}) = [\int_0^\infty \frac{P(s)}{N(s)} ds]^{-1} \tag{1.8}$$

By considering the interaction effects, sequence effects, favourable effects of positive peak loads, etc, all of which can lead to $\Sigma n/dN \neq 1$, some theoretical advances have been made, but the improvement in obtaining analytical fatigue life estimates has not general warranted use of the methods[5, 50].

Clarkson's theory (Equation 1.1) and Miner's rule were originally developed for metallic structures, and stress is used as the parameter estimated. For application of the theories to composite studies, most experimental and theoretical work involves strain prediction rather than stress and fatigue work is usually based on surface strain criteria. However, it is the combination of internal stresses/strains at some critical point or within some small critical volume inside the structure which will cause fatigue damage to initiate and propagate[15]. For composites, fatigue life prediction procedures are still based on the RMS surface strain in Equation (1.1) and Equation (1.8). For structures exhibiting random vibration, failure may be estimated by using the strain response peak probability distribution. RMS strain has been used in the past, for example, to predict the fatigue life of an aluminium alloy beam undergoing large deflections when subjected to random loading. The formula used in Ref.[48] was

$$N_T(\text{hours}) = \frac{1}{\Sigma P(s) / N} \frac{1}{f} \frac{1}{3600} \tag{1.9}$$

where f is the rate of strain repetition in sinusoidal tests.

Fatigue life estimates based on negative peak and positive peak probability distributions were

compared in Ref.[48], and the contribution of negative peaks was very small. It was concluded that the estimated time to failure based on a one sided peak probability distribution should be double the time based on a symmetrical strain peak probability distribution. The comparison of predicted and experimental results showed that Miner's rule gave a conservative estimation of fatigue life. Holehouse[16] developed a semi-empirical formula for predicting the fatigue life of CFRP structures, where the random fatigue curves for CFRP test specimens (RMS strain vs. cycles to failure) were used to estimate the number of cycles to failure for a given RMS strain level. The most commonly used method for fatigue life estimation is based upon the assumption that one resonant mode contributes to the fatigue damage. The approach is to assume that damage results only from the mode having the lowest resonant frequency. The responses due to all other modes are neglected. The amplitude of response in the first mode is therefore assumed to determine the amount of damage during each cycle. As mentioned before, with increase of excitation level, the contributions of higher modes become significant. So in this case, the single mode response is still used, but the effects of the higher frequency modes are included. The response amplitude is defined by mean square value of the overall response due to all of the contributing modes.

When subject to high intensity acoustic loading, the response of an aircraft structure is non-linear, which leads to a non-Gaussian distribution of stress amplitudes. This has been demonstrated in experimental results[38]. Some papers[52 to 54] have given analytical results on fatigue damage prediction when the response is non-Gaussian. Apart from the stress-type cumulative damage theories, another approach to fatigue damage prediction is the use of fracture mechanics, which is nonlinear in determining the cumulative damage and addresses to some extent, the problem of the correct stress measurement in structural elements by dealing with the stress intensity at the crack tip rather than the continuum-type stress state. It should be point out although for the metallic materials, fracture mechanics is well developed, there are some problems with this method when composite materials are concerned because of the complexity of structure and damage mechanisms of composites, and more work needs to be done[9, 54].

1.2.4 Summary

Research on acoustic fatigue started as early as the late 1950s, led to the development of semi-empirical analysis techniques based on Miles's single-degree-freedom approach. From the 1980s, with the increasing use of composite materials in aircraft structures, and the development of new super/hyper sonic vehicles, the acoustic environments of aircraft became more severe and have caused more problems. There are three factors which generally influence fatigue life estimation of panel-type aircraft structures. These are acoustic loading, structural response analysis and the methods used for fatigue life estimation. The acoustic loading data, which are suitable for use in structural response analyses, are still very poor at present. So the uniform loading distribution is used in most analyses. Due to the random characteristics of acoustic loading, estimation of the structural response is very complicated. In the theoretical analysis, some assumptions are used to simplify the problem, which has resulted in methods used in the ESDU Data Sheets. To cope with new problems created by composites and high pressure/temperature loading, new developments in theoretical and experimental research have been made. The improvement of computer power has permitted the development of numerical methods. One of the most often used numerical methods is the Finite Element Method. The factors which affect the accuracy of use of the FEM are the modelling of acoustic loading, modelling of reinforcements, proper application of boundary conditions, damping effects, mesh size, large deflection effects, etc. By the proper use of the method and consideration of these factors, the FEM can model structures with any shape and boundary conditions and acoustic loading, in theory.

On another hand, experimental work plays an important role in aircraft structure research and development. Coupon testing provides fatigue data for design and research purposes. Also, reverberation chamber and progressive wave tube (PWT) facilities are used for acoustic fatigue testing. The PWT is a very useful facility in which high sound pressure levels can be generated and specimen heating facilities can be incorporated. So structures can be tested in an environment similar to actual flight conditions.

Experimental research has shown that both Aluminium alloy and CFRP plates exhibit multi-mode contributions in strain/stress response under sound high pressure levels. Peak broadening and frequency jump effects have been observed. Heating can cause buckling of

structural panels, and a decrease in natural frequencies.

Although much work has been done to increase understanding of acoustic fatigue behaviour, more research is needed to develop improved design techniques which will be based upon improved knowledge of the behaviour of complicated structures composed of new materials. This is vital if full advantage is to be taken of new forms of construction in the aerospace industries.

1.3 BRIEF INTRODUCTION TO CFRP AND GLARE COMPOSITES

The use of composite materials in aircraft structures has been said to be the one of most significant revolutions in the aircraft industry. The demand for composites in the aircraft industry has increased rapidly in the last 15 to 20 years[56]. Composites are gradually replacing aluminium alloy and their use is extending from secondary structures to primary structures. Taking the Airbus as an example, the proportion of composites content in the Airbus A300 was only 4% but is 17% in the A340[57]. Figure 1.2 shows some uses of composites in the Airbus A320[58]. Comparing with aluminium alloy conventionally used as aircraft material, the main attraction of composites is that they have low weight, high strength and stiffness, which are of importance in the development of large and high speed aircraft.

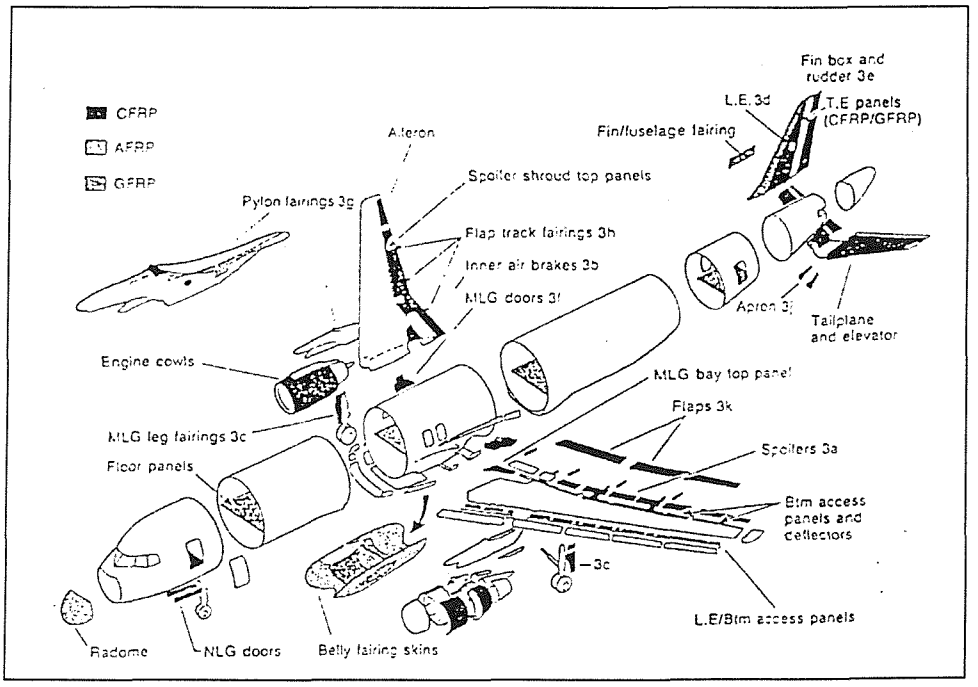

Figure1.2 Airbus A320 composite structures [Ref. 58]

The composite materials available at present have different forms with difference functions and uses. In this study, interest is focused on Carbon Fibre Reinforced Plastics (CFRP) and GLAssfibre REinforced aluminium laminates (GLARE). CFRP has been used in aircraft structures for many years and GLARE is relatively new form of composite. In this project, box-type structures made of both CFRP and GLARE were investigated.

1.3.1 Advanced Carbon Fibre Reinforced Plastics (CFRP)

CFRP composites consist of carbon fibres, called the reinforcement, and a resin, or matrix material. The principal difference between conventional metals and composites is that composites are anisotropic and inhomogeneous. The stiffness and strength of the fibres are normally much higher than for matrix materials, so the fibres carry most of the loads. The main factors which decide the mechanical properties are fibre type, volume fraction of the fibre and fibre direction relative to load direction, which are explained in details in Ref. [58]. CFRP has excellent specific stiffness (i.e., the ratio of elastic modulus to density). The basic mechanical properties of CFRP, such as elastic modulus, damping and Poission's ratio can be determined by calculation according to the properties of fibre and matrix, or by tests. Modulus of elasticity and Possion's ratio are normally calculated by the rule-of-mixtures[58, 59], and damping is usually determined by testing. The best way to determine the properties of CFRP is by experimental methods. Some standards have been established concerning this matter by the American Society for Testing and Materials (ASTM), the Suppliers of Advanced Composite Materials Association (SACMA), and The Royal Aircraft Establishment (RAE) in the UK[60]. A free vibration method to measure the dynamic modulus, damping loss factor and Possion's ratio of CFRP beams and plates was introduced in Ref. [61]. A theoretical prediction method has been introduced in Ref. [92] to predict the effect of fibre orientation and laminate geometry on the flexural and torsional damping and modulus of fibre reinforced composites. Further work was carried out on vibrational damping parameters of composite beams and plates by theoretical prediction and experimental measurements [93, 94].

As for metallic materials, CFRP also exhibits fatigue behaviour. Degradation of the material can occur with repeated stresses below those needed for static failure, but the failure mechanisms are different from those in metals[62, 63]. The damage phenomena of fibre reinforced composites generally fall in to several categories, such as, matrix cracking, matrix

yielding, interfacial debonding and delamination and fibre breakage or fibre pull out, etc. (Figure1.3)[64, 65]. One or several of these damage modes could be present in CFRP before failure. The fatigue of composites is defined as the progression of the damage rather than the initiation of a crack as in metals. The presence of the damage in composites has a great influence on their dynamic properties, such as stiffness, damping and natural frequency[63, 65, 66]. Stiffness, and hence natural frequency, are reduced as the damage develops, which are parameters associated with fatigue and are used as criteria to define fatigue failure in the composites, particularly in coupon testing. as a result of the damage, the damping can increase during fatigue or friction at delamination interfaces. Also CFRP is sensitive to environmental changes, such as temperature and moisture, which affect the stiffness of the material. It has been proved that hot and wet combined conditions are worst case for CFRP[67, 68].

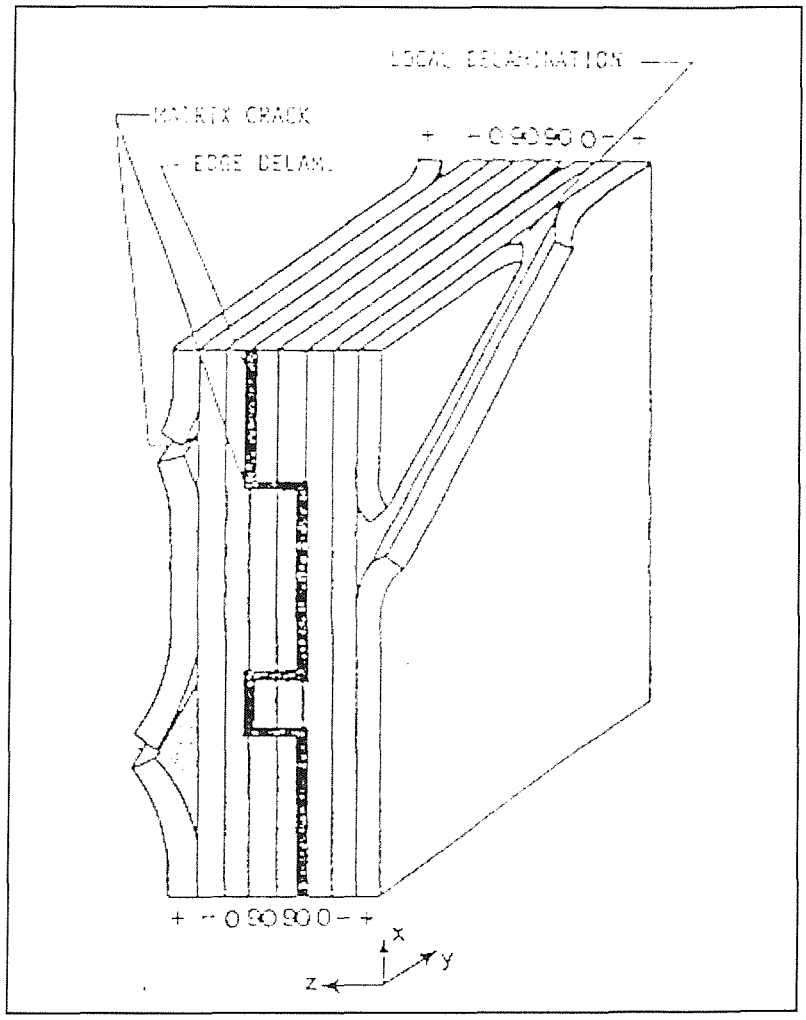

Figure 1.3 Typical types of damage in composite laminates [Ref. 64]

The fatigue performance of composites is very good compared with metallic materials. Figure 1.4 illustrates the comparative "fatigue strength" of various aircraft materials. It can be seen that CFRP has superior fatigue strength over other aircraft materials[69].

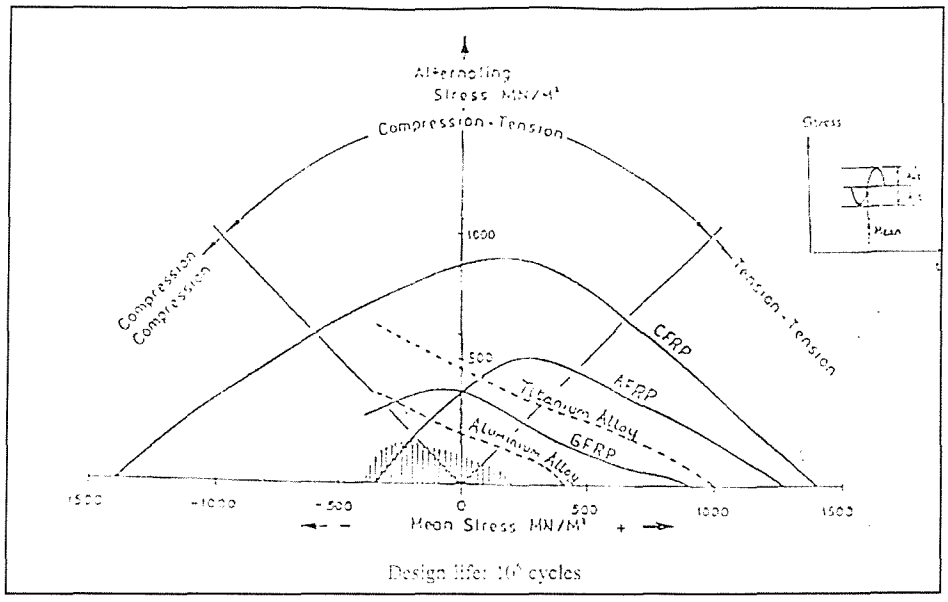

Figure 1.4 Fatigue strength of various aircraft materials [Ref. 69]

1.3.2 Fibre Metal Laminates

Fibre Metal Laminates consist of alternating thin metal alloy sheets and unidirectional or cross-ply layers of fibre composites as shown in Figure 1.5[70]. The first generation of these laminates was ARALL which uses aramid fibres, and the second one is GLARE with high strength glass fibres. The laminates were developed as an alternative to monolithic aluminium alloys for fatigue prone areas in primary aircraft structures. In certain conditions, the fatigue crack initiation behaviour and fatigue crack growth behaviour are superior to those of aluminium alloys. The laminates also have low density compared with aluminium alloy. Table 1.1 lists the advantages of fibre-laminates compared with aluminium alloy[71] and Table 1.2 gives the laminates which are currently commercially available[71, 72]. Table 1.3 lists the mechanical properties of commercially available FML material[73].

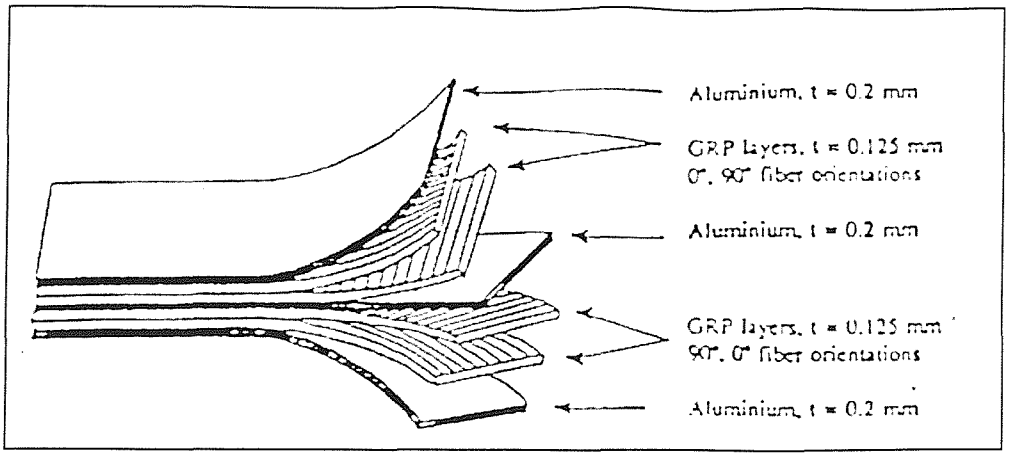

Figure 1.5 Fibre Laminates Lay-up [Ref. 70]

Table 1.1 Advantage of fibre metal laminates over aluminium alloys [Ref. 71]

Improved material behaviour	+ fatigue
	+ fracture toughness
	+ impact
	+ corrosion
Increased safety	+ improved material behaviour
	+ fire resistance
Possibilities for cost saving	- material price
	+ operating cost
	+ maintenance and inspection
	+ production simplification

Fibre-metal laminates are constructed by stacking thin (0.2 mm to 0.4 mm) aluminium alloy sheets alternately with fibre reinforced composite layers and curing in an autoclave where the epoxy resin of the fibre composites acts as the adhesive. Due to the existence of residual stress in the laminate after the curing process, the laminates are divided into two groups: 'as-cured' or 'post stretched'. The residual stresses are induced by different thermal expansion coefficients between the metal sheets and the composite layers. In the 'as-cured' state, a tensile residual stress is carried by the metal sheets whilst a compressive one exists in the composites. This is not a preferred state in relation to fatigue performance. So the 'post-stretch' process is used to reverse the residual stress distributions, which postpones fatigue crack initiation and lowers the overall stress level in the aluminium sheets during fatigue cycling[74]. Because aramid fibre is extremely sensitive to compressive loading which damages the fibre, ARALL

performs better in the post-stretch state compared with the as-cured. While GLARE is normally used in the 'as-cured' state. Also GLARE has cross-ply composite layers to give reinforcements in both directions[75, 76].

Table 1.2 Commercially available fibre-metal laminates [Ref. 71,72]

FML GRADE		Metal Type	Metal Thickness (mm)	Composites		Post cure stretch
				Thickness (mm)	Grade	
GLARE	1	7475-T76	0.3-0.4	0.25	UD glass	5%
	2	2024-T3	0.2-0.3-0.4	0.25	UD glass	non
	3	2024-T3	0.2-0.3-0.4	0.25	CP glass 50/50	non
	4	2024-T3	0.2-0.3-0.4	0.375	CP glass 67/33	non
ARALL	2	2024-T3	0.3	0.2	UD aramid	4% or non
	3	7475-T76	0.3-0.4	0.2	UD aramid	4%

UD - Unidirectional CP - Cross ply

50/50 - 50% of fibres in long. and 50% in trans. direction

67/33 - 67% of fibres in long. and 33% in trans. Direction

Table 1.3 Mechanical properties of GLARE and ARALL [73]

			GLARE				ARALL		Aluminum
			1	2	3	4	2	3	2024-T3
Tensile ultimate strength	MPa	L	1282	1074	717	930	717	765	455
		LT	352	317	700	592	317	352	448
Tensile yield strength	MPa	L	545	360	305	352	365	565	359
		LT	338	228	283	255	228	296	324
Tensile modulus	GPa	L	64	65	58	57	66	68	72
		LT	49	50	58	50	53	49	72
Ultimate strain	%	L	4.1	4.5	4.5	4.5	2.5	1.8	19
		LT	7.7	10.8	4.5	4.5	12.7	6.4	19
Compression yield strength	MPa	L		415	310	365	255	317	303
		LT		236	310	285	234	331	345
Compression modulus	GPa	L		67	59	60	65	66	74
		LT		52	59	54	53	50	74
Shear yield	MPa	L					110	159	207
		LT					110	159	207
Bearing ultimate strength (e/D = 1.5)	MPa	L		566	644		545	579	758
		LT		619	644		593	634	758
Bearing ultimate strength (e/D = 2.0)	MPa	L	834	727	819	662	634	669	945
		LT		757	819		621	655	945
Bearing yield strength (e/D = 1.5)	MPa	L		440	445		393	476	538
		LT		410	445		393	483	538
Bearing yield strength (e/D = 2.0)	MPa	L	710	574	573	517	469	552	648
		LT		493	573		455	531	648
Blunt notch strength (1)	MPa	L	793	765	496	593	441	545	414
		LT	352	283	496	414	276	352	414
Sharp notch strength (2)	MPa	L	669	558	393	476	331	331	372
		LT	228	228	393	331	248	248	372
Density	g/cm^3		2.49	2.48	2.48	2.40	2.31	2.33	2.77

(1) Net residual strength, Open hole specimen: w=100 mm, D=25 mm
(2) Net residual strength, Center crack specimen: w=100 mm, 2a(0)=25 mm

Research has shown that the fibre-metal hybrid material has fatigue resistance superior to that of aluminium alloy. Crack growth rates in the fibre-metal material are much lower than those in aluminium alloys. Figure 1.6 shows a comparison of crack growth rates in aluminium alloy and fibre-metal laminate plates with central cracks under tensile-tensile loading[71]. The reason why ARALL and GLARE have high fatigue resistance is based on a mechanism called '**the fibre bridging' effect**', i.e., a crack initiated in a metal layer is bridged by the fibres as shown in Figure 1.7. When a crack is initiated in a metal layer, the fibres in the composite layers impose restraint on further opening at the crack tip. At the same time, unbroken fibres in the cracked area still carry the load through the crack. In Ref. [77], the bridge effect was studied in detail and it was concluded that there were two mechanisms affecting the behaviour of the laminates: crack growth in the metal layers and delamination growth along the fibre-resin interface in the composite layer. The presence of the fatigue crack at the fibre-resin interface leads to initial debonding of fibre and resin. During crack growth a small area delamination occurred around the fatigue crack, which resulted in the fibres to carrying extra loading from

the cracked metal layer and reduction of stress intensity factor at the crack tip. The development of the delamination zone helped to prevent failure of the fibres in the crack region by increasing the length of fibres which carry the extra loading, thereby facilitating bridging.

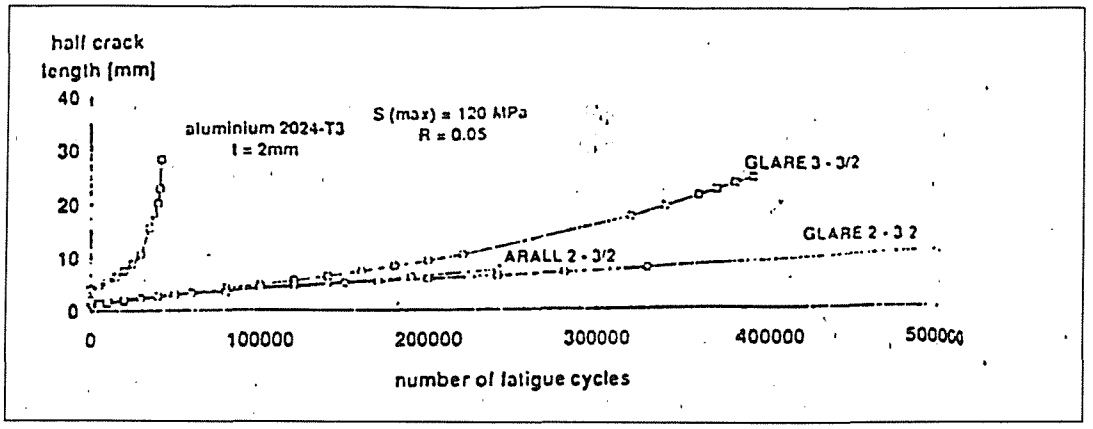

Figure 1.6 Comparison of fatigue crack growth rates of fibre-metal laminates and aluminium plates with a central crack under tensile-tensile loading [Ref.71]

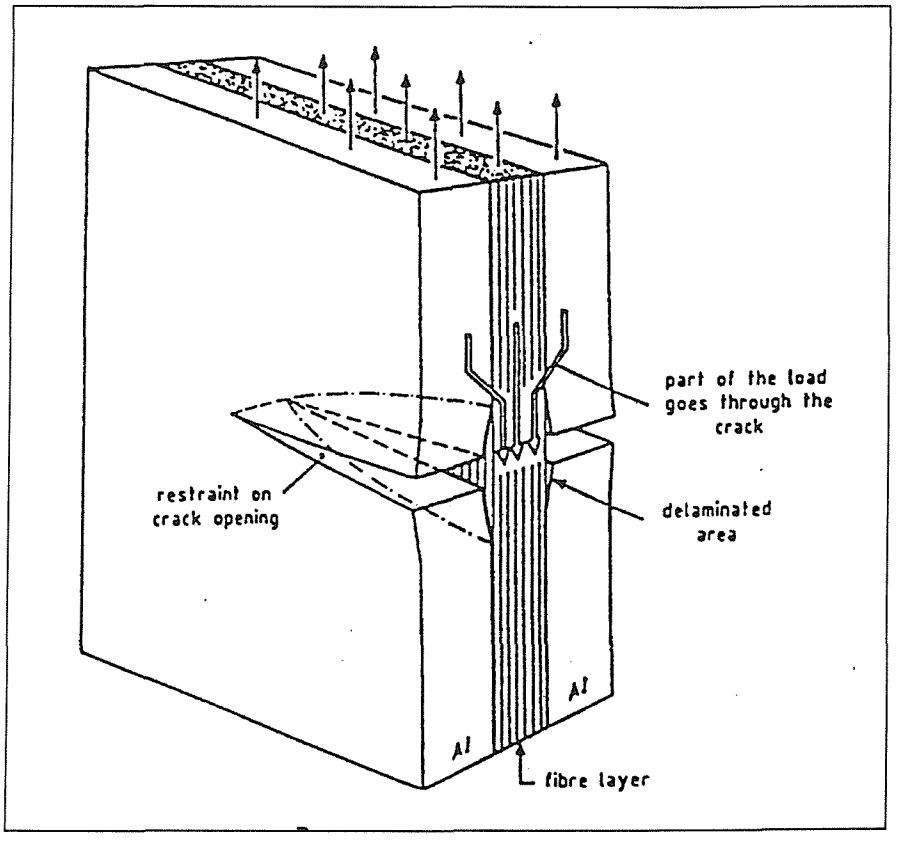

Figure 1.7 Fibre bridging effect in fibre-metal laminates [Ref.74]

Among the fibre-metal laminates, it has been proved that GLARE has very high toughness compared to ARALL and aluminium alloy, which makes it a very damage tolerant material[78, 79].

Although ARALL and GLARE both have excellent performance in relation to fatigue loading, GLARE has some advantages over ARALL, aluminium alloy and conventional composites:

* As shown in Table 1.3, the tensile strength of GLARE is remarkably high and largely outperforms aramid ARALL and aluminium alloys.
* Normally, the damage resistance of composites, such as impact resistance, is relatively low compared to monolithic aluminium alloys. But for GLARE, due to the high failure strain of the glass fibres, a considerably higher energy absorption before failure of these fibre layers occurs. The impact behaviour of GLARE is superior to CFRP and comparable to that of aluminium alloy[78].
* GLARE can be used in the "as cured" condition because the glass fibre is less sensitive to compressive loading than aramid fibre, which also permits the use of cross-ply composites.
* Because of the sensitivity of aramid fibre to compressive loading, ARALL is preferably used in tension-tension loading conditions[78]. GLARE can be used in any loading conditions due to the high compressive strength of the glass fibres.
* A definite advantage of GLARE over CFRP is its ease of formability and machinability. In many ways GLARE can be handled in the same manner as monolithic aluminium. The laminates can be bent, cut, drilled and joined using traditional methods.
* Due to the inclusion of polymer-based composites, the damping of FML is improved compared with aluminium alloy, which is very important in influencing of response of FML structures to dynamic loading.

According to the results from some published experimental studies, fibre-metal laminates are said to have superior fatigue performance. However, research carried out on the acoustic fatigue behaviour of FML (i.e., predominately in bending) is very limited. Most studies on the fatigue of GLARE are limited to in-plane loading. So it is very important to investigate the dynamic behaviour of GLARE if it is to be used to structural parts prone to acoustic fatigue.

Some of the shaker tests on GLARE coupons and PWT tests carried out on two typical panels were reported in Ref. [70]. For this particular set of tests, the results showed that GLARE panels can withstand high acoustic loads, if support structures (such as ribs and frames) are properly designed. The rib design seems to be the most critical area for a wing-like structure subjected to acoustic loads.

To completely understand the behaviour of GLARE panels under the action of acoustic loading, more research is required.

1.4 THE PURPOSE AND THE OBJECTIVE OF THIS STUDY

The main motivation to start this project was based on two major objectives: to provide detailed information on the dynamic behaviour of general ***box-type*** structures, such as flaps, under acoustic loading and to make suggestions for good design practice; and to identify possible advantages of composite materials, such as Carbon Fibre Reinforced Plastic (CFRP) and GLAssfibre REinforced aluminium alloy laminates, over conventional aluminium alloys (GLARE), in this situation.

Box-type structures are those constructed of relatively thin, stringer-stiffened skins on a skeletal structure comprising of a number of span-wise spars and fairly regularly spaced chordwise ribs. Besides flaps, there are other components of an aircraft structure which are also of the box-type, such as wings, ailerons, fins and rudders. Although the direct subject of this study was flap structures, the findings are applicable to all box-type structures.

As a major partner in the multinational Airbus programme, British Aerospace (BAe) has an outstanding reputation for advanced commercial aircraft wing design. In the modern wing design, leading and trailing edge devices are used to change the lift capacity of aircraft. One of the trailing edge devices is take-off and landing flaps, which are used to supply high lift at relatively low speed when they are deployed. Because all Airbus aircraft have wing mounted engines, the flaps experience very high sound pressure loading when they are deployed. The highest sound pressure level measured on the flaps of an Airbus aircraft was 155 dB[80]. This level of excitation could result in acoustic fatigue damage of the flaps, unless they are

sufficiently robust to resist high intensity pressure loading.

In the ESDU data sheets on acoustic fatigue of aircraft structures, the response of stiffened panels is considered but the items provide only an approximation for the overall response of a continuous box-type structure, which is not applicable to flaps for two reasons. First the skin panels of the flap can not be treated as panels isolated from each other and the remainder of the structure. Tests carried out by BAe have shown that acoustic excitation on the lower surface of the flaps leads to significant vibration of the upper surface. This means that the two surfaces are strongly coupled. Second, the surface of the flaps has variable curvature, which is not sufficiently represented in existing design guides.

As the first manufacturer of large commercial aircraft to use composite materials for the series production of primary structures, the Airbus consortium has seen a number of advantages in cost and weight saving including the elimination of corrosion. Because of the lack of appropriate S-N data and appropriate design guides, many Airbus composite components were certified by acoustic endurance testing in the laboratory, rather than by calculation or analysis techniques. This process is time consuming and expensive. To obtain detailed information on the response behaviour of composite box-type structures to acoustic loading, not only flap structures made of aluminium alloy must be considered but also those made of advanced composite materials.

Overall, this whole project was carried out in two phases, 1). Theoretical modelling and analysis of box-type structures, and 2). Experimental and supporting Finite Element Analysis. The work presented in this thesis concerns the second part only. The experimental work involved three simplified flap-like box-type structures made of three different materials, and a number of test coupons in different forms and materials. Two major types of tests were carried out on the box-type structures. First, the test structures were subjected to modal testing in order to identify basic structural properties, such as resonance frequencies, mode shapes and structural damping which is especially of importance in theoretical modelling. Secondly, the box structures were excited by high intensity acoustic loading by means of a Progressive Wave Tube (PWT), which it was hoped would reveal the dynamic response of the structure to acoustic loading and serve to guide the theoretical modelling.

In the acoustic fatigue study of aircraft structures, the estimation of the fatigue life of a component under acoustic loading is one of the important tasks. In the present programme, a number of composite coupons was tested under simulated acoustic loading to generate S-N (strain verse number of cycles to failure). The combination of the results from acoustic excitation tests and S-N data enable the prediction of the fatigue life of the test structures.

Finite Element Analyses (FEA) of the test box structures and coupons was also performed. The results were used initially as a guide in setting up the test procedures and could be finally modified according to experimental results. The experimental results together with that of FEA will provide a basis for validation of the theoretical studies by another Researcher and assessment of the accuracy of the theoretical modelling for strain/stress estimation.

This part of study will also characterise the composite materials to be used in box-type structures by comparison of test results from box structures composed by different materials. This will enable assessment of the use of new materials in flaps and similar structures and other regions of potential acoustic fatigue on an aircraft.

1.5 OUTLINE OF THIS THESIS

The study presented in this thesis includes experimental research and Finite Element Analysis (FEA) of coupon and box-type structure specimens consisting of different materials with the aim of understanding their dynamic behaviour and to reveal possible advantages of the use of composites. In an attempt to summarise the state-of-art and developments in the study of acoustic fatigue in the aircraft industry, a brief review was presented in Chapter 1 based on the literature published on the topic. An introduction to the composite materials used in this study was also included in this chapter. Experimental data for coupon specimens are given in Chapter 2 in two parts. First, the damping values measured on the coupon specimens are presented. Second, the S-N curves have been obtained for CFRP and GLARE Tee-coupons under simulated acoustic excitation. As an important factor which affects the accuracy of estimation of the response of test structures to acoustic loading, the pressure field characteristics at the test section of the Progressive Wave Tube (PWT), where the test specimens were mounted, were investigated in Chapter 3. The Modal testing of the box-type structures was carried out and reported in Chapter 4, which showed the mode shapes,

resonance frequencies and damping of the test structures. The RMS strain response and dynamic characteristics of the three box-type structures under high intensity acoustic loading are discussed in Chapter 5. The fatigue resistances of the test structures are also described in this chapter. Finite element analysis of the coupon specimens and box structures are discussed in Chapter 6. Finally, Chapter 7 concludes this thesis and indicates further work which should be carried out.

CHAPTER 2

COUPON SPECIMEN INVESTIGATION

The box structures studied in this thesis were made of three different materials, aluminium alloy, CFRP and GLARE composites. Of the three materials, the mechanical properties and dynamic characteristics of the aluminium are well understood and documented. But for the composites, especially the GLARE, relatively limited information is available.

To obtain the basic dynamic properties and fatigue data of composite materials, namely, CFRP and GLARE, an investigation was carried out using coupon specimens.

2.1 TEST COUPON SPECIMENS

In research on the acoustic fatigue of aircraft skin panels, it was found that fatigue damage is usually located at joint lines of skin and stiffeners as shown in Figure 2.1. For this reason, Tee-shaped coupons are used to represent the skin panel and stiffener joints. Besides the CFRP and GLARE Tee-coupons, CFRP Tee-beam coupons and GLARE plain beam coupons were also used in the damping measurements to be compared with the damping values of Tee-coupons.

The CFRP coupons with an integral stiffener consisted of two 8-layer unidirectional tapes T300/924 with a thickness of 0.125 mm for each layer, which gives the total thickness of 2mm for both skin panel and stiffener. The top 8-layers and bottom 8-layers were bonded together to form the skin panel. The stringer was formed by the two bottom 8-layers joining together at 90 degrees. The void between the tapes was filled with the same unidirectional tape, rolled with fibres along the stringer length. Figure 2.2 shows the CFRP coupon and its dimensions, and the lay-up is given in Figure 2.3.

The GLARE Tee-coupons were in riveted skin form and built-up using GLARE 2 and GLARE 3 with a configuration of 3/2, i.e., three layers of aluminium alloy and two layers of glass fibre composite. The skin part was made of GLARE 3 with 0°/90° cross ply glass fibre reinforced plastic (GRP), and the stringer was of GLARE 2 with unidirectional GRP, in which the fibres are along the stringer length. The thickness of the metallic layer was 0.3 mm and 0.25 mm for the GRP, which resulted in a total thickness of 1.4 mm for both skin and stringer. The coupon dimensions and composite lay-ups are shown in Figure 2.4 and Table 2.1 respectively.

The CFRP Tee-beam was made of the same material as the Tee-coupon and is shown in Figure 2.5. GLARE plain beam coupons were made of GLARE 1, GLARE 2 and GLARE 3 respectively, the details are shown in Figure 2.6.

2.2 DAMPING LOSS FACTOR MEASUREMENTS

The damping of a type of engineering material or structure indicates its ability to dissipate vibration energy. The higher the damping, the lower the vibration response of a structure to sinusoidal excitation at resonance or to random excitation. There are two ways to represent damping, the viscous damping ratio ζ and structural or hysteretic damping loss factor η. For light damping in a linear system, the loss factor is twice the viscous damping ratio, i.e., $\eta=2\zeta$[82].

The viscous damping ratio* is defined as:

$$\zeta = \frac{C}{C_0} \tag{2.1}$$

where C is the viscous damping coefficient and C_0 is the critical damping coefficient.

The damping force under this definition is proportional to the vibration velocity.

* Viscous damping does not exists in reality, this is engeer's approximation

The hysteretic damping loss factor η is the ratio of dissipated energy to stored energy of a vibrating system. In this form, the loss factor can be presented as the imaginary part of the complex stiffness, $K = k(1+i\eta)$, where k is the stiffness of the vibrating system. Here the damping force has an amplitude proportional to displacement of vibration but in counter-phase with the velocity.

In this chapter, damping loss factors of coupons were determined mainly by the frequency response method. The free vibration method was also employed for comparison for one of the CFRP Tee-coupons. Loss factors of the CFRP Tee-coupons being subjected to endurance testing were also estimated.

2.2.1 Testing Procedures and Measurement Methods

Each specimen was suspended by a fishing line to form a freely supported condition. The coupon could move freely when subjected to dynamic loading and there would be no introduction of additional damping due to supports. The schematic diagram of the experimental apparatus is illustrated in Figure 2.7. Coupons were excited by a loudspeaker and the responses were measured by a laser vibrometer. The excitation and response signals were input to a Solartron 2000 Signal Analyser to obtain the transfer function.

One coupon of each type was first excited by a broadband (up to 1 kHz) noise to identify its first few resonance frequencies f_n. Then each coupon was excited over a narrow band (100 Hz bandwidth with central frequency f_c close to f_n) noise to obtain the transfer function. The loss factor was calculated using the half power point method. A total of 16 CFRP Tee-coupons, 8 CFRP beam-coupons, 35 GLARE Tee-coupons and 6 GLARE plain beams was tested.

For the CFRP Tee-coupons, another set of damping tests was carried out for a few coupons with tip masses attached when mounted on the shaker for fatigue testing. The purpose of these tests was to obtain the damping value when coupons were subjected to shaker excitation and to compare with the loss factor measured when 'freely' supported. The instrumentation arrangement is shown in Figure 2.8.

The damping measurement methods used are briefly outlined below:

2.2.1.1 Half power point method – free supported condition

This is a frequency domain analysis method which uses the frequency response function of a vibrating structure to determine the loss factor at a certain resonance.

The modulus of a transfer function at a resonance frequency is shown in Figure 2.9. If f_n is the resonant frequency, and f_1 and f_2 are the frequencies where the amplitude of the transfer function is equal to 70% of its peak value or 3dB reduction of amplitude, i.e., $A_{1,2}=A_{max}/2^{1/2}$. The loss factor is given by:

$$\eta = \frac{f_2 - f_1}{f_n} \tag{2.2}$$

2.2.1.2 Free vibration method – clamped on shaker

This is a time domain method, which uses the time history of the response signal of a vibrating structure at known natural frequency to determine its damping ratio. When a structure is disturbed it starts to vibrate. Once the disturbance stops, the vibration of the structure decreases and eventually decays to an immeasurable level due to the existence of damping as shown in Figure 2.10. The higher the damping, the faster the decay of vibration amplitude. According to Figure 2.10, damping ratio ζ is usually estimated by formulas below:

$$\zeta = \frac{1}{2\pi N}\ln\left(\frac{x_0}{x_N}\right) \tag{2.3a}$$

or $$\zeta = \frac{1.1}{T_{60} \times f_n} \tag{2.3b}$$

where x_0 - the initial vibration amplitude of a structure at resonance frequency $f_d = f_n\sqrt{(1-\zeta^2)}$

x_N - the vibration amplitude after N cycles

T_{60} - the time for the vibration amplitude to decay to 60 dB of its original value

The loss factor can then be determined by $\eta = 2\zeta$.

2.2.2 Damping Measurement Results

2.2.2.1 Damping values of CFRP Tee-coupons

A. Free supported condition

Sixteen CFRP Tee-coupons with fibre orientation shown in Figure 2.3 were subjected to damping tests. Three out of the 16 coupons had damage or defects.

One of the coupons was first subjected to broadband (40 Hz - 1040 Hz) random noise excitation, which showed that the CFRP coupon had one response peak in this frequency band, which was at 411.8 Hz for Coupon No. 11, for example. Damping loss factor tests were then carried out using narrow band random excitation with a bandwidth of 100 Hz and central frequency of 400 Hz. Frequency resolution was 0.2 Hz. The loss factor was estimated by the half power point method.

Figure 2.11 is a typical transfer function plot for the CFRP Tee-coupons. The damping loss factor values and resonance frequencies of coupons tested are plotted in Figures 2.12 and 2.13 respectively and test data are also listed in Table 2.2. The average loss factor of the CFRP Tee-coupons was 0.7% with standard deviation of 0.001.

For those specimens with damage or defects, such as coupon Nos. 2, 3 and 5, the damping values measured are above the average value. Figure 2.14 gives ultrasonic C-scan results of these three specimens. It can be seen that the defects in coupon No. 2 were located on both sides of the skin panel. The scan images of the CFRP coupons Nos. 3 & 5 show widening of the white central region which indicates that the damage is progressed from the joint towards the skin panel. Damage in coupons No. 3 and No. 5 was induced by the fatigue tests and the defects in No. 2 were original. Although the measured loss factor of coupons Nos. 9 and 10 are well above the average value, ultrasonic C-scans showed no damage or defects in these two coupons. There was no explanation why those two coupons had much higher damping than other ones.

The average measured resonance frequency was 419.6 Hz, with standard deviation of 4.97 Hz, which is the frequency of the first bending mode of the coupons in this test condition. This

has been confirmed by Finite Element predictions which estimated the natural frequency to be 419.1 Hz, details are given in Chapter 6.

For coupons (Nos. 5 and 3) with fatigue damage at their joint region of skin and stiffener, resonance frequencies were below average as shown in Table 2.2. This is because of the nature of the mode shape. Joint stiffness has a dominant effect on the coupon behaviour. For coupon No. 2, damage was found in the skin away from the joint, which has no great effect on the resonance frequency of this mode.

These results indicate that development of damage in the CFRP coupon caused a decrease of resonant frequency and an increase of damping. Results also show that measured loss factor values are more scattered than measured resonance frequency values by comparing their standard deviations. For resonance frequency, the standard deviation is 1.2% of its average value, but for loss factor, it is 15.9%. This type of behaviour has been observed in all test results.

B. Clamped by stringer on a shaker

To investigate the influence of the fatigue test set-up on the damping of the CFRP coupons, damping tests were also carried out on coupon No. 4 when it was mounted on a shaker as it would be during fatigue testing (Figure 2.22). The coupon was excited by a hammer with aluminium or nylon tip and response was recorded via a strain gauge installed on the top surface of the skin panel. Because the decay time was very short, signals were sampled at a very high rate of f_s = 40 kHz with 20k sample points to obtain a good time signal (0.5 seconds). Figures. 2.15 and 2.16 show two of the decaying response signals.

Test data are listed in Table 2.3. It shows that the average damping loss factor is 0.0163 which is much higher than that measured in the freely supported condition. The extra damping is introduced by the constraint, strain gauge cables and the shaker, etc. Whilst the coupons were fatigue tested, their damping was also estimated from the transfer function between the shaker excitation and strain response which gave average loss factor of approximately 0.02 (see section 2.3).

2.2.2.2 Damping values of CFRP Tee-beam coupons

As for the Tee-coupons in the 'freely' supported condition, a CFRP Tee-beam was first excited by broadband (20 Hz - 1020 Hz) random noise and there was one resonance peak at a frequency of 846 Hz for beam No. 2 for example. Further narrow band tests were carried out on all of the 8 beams in a 100 Hz bandwidth with a central frequency of 846 Hz. Table 2.4 lists the test data.

Results show that the average damping loss factor for the CFRP beams was 0.0044 with standard deviation of 0.0005. The loss factor is about 36% lower than that of the Tee-coupons. The measured average resonance frequency was 833.2 Hz with a standard deviation of 10.9 Hz.

2.2.2.3 Damping values of GLARE Tee-coupons

All 35 coupons were tested using the same method as for the CFRP coupons in the freely supported condition. Broadband excitation showed that there were actually three resonance frequencies in the 40 Hz - 1040 Hz band, they were 300 Hz, 480 Hz and 1016 Hz for coupon No. 1. Two narrow bands (100 Hz bandwidth) of random noise with central frequencies of 300 Hz and 480 Hz respectively were used to excite the coupons. Figures 2.17 and 2.18 are the response transfer functions of coupon No. 1 at the first and second resonance frequencies respectively.

Test results for loss factors and resonance frequencies of the GLARE Tee-coupons are shown in Figures 2.19 and 2.20. Data are also listed in Tables 2.5 and 2.6 for the first and second resonance frequencies respectively. The average damping loss factor is 0.0037 for the first mode with standard deviation of 0.00086 and 0.0038 with standard deviation of 0.001 for the second. The overall average loss factor of the GLARE Tee-coupons was 0.0038. These values are similar to the results in Ref. [75] which gives the damping ratio values of GLARE coupons with various lay-ups as 0.00152-0.00171, i.e., 0.00302-0.00342 loss factor. Compared with the CFRP Tee-coupons, the typical loss factor of the GLARE Tee-coupons was about 46% lower. From Tables 2.5 and 2.6, it can be seen that Coupon No. 35 had a much higher loss factor compared with the other specimens and well above the average. However, no obvious reason was found for this characteristic.

2.2.2.4 Damping values of GLARE plain beams

A total of six GLARE plain beam coupons were subjected to damping measurements in the freely supported condition. Coupon No. 1 was made of GLARE 1 of smaller size compared with the others. Coupons No. 2 & No. 3 were made of GLARE 2 and the remainder were made of GLARE 3. The coupons were first excited by broadband noise with bandwidth of 10 Hz to 510 Hz to identify the first two modes and were then excited using narrow band noise with 50 Hz bandwidth and central frequency around their resonance frequencies. The test results are listed in Table 2.7. Results show that the average loss factor for the GLARE plain beam-coupons was 0.0016. The loss factor of the GLARE beams was about 43% lower than that of the Tee-coupons.

From Table 2.7, it can be seen that the resonance frequencies of the GLARE 2 Beams (coupon Nos. 2 & 3) were higher than those of the GLARE 3 beams (coupon Nos. 4, 5 & 6). The reason is that the longitudinal modulus of the elasticity of GLARE 2 is higher than that of GLARE 3 due to the difference between their glass fibre composite layers as shown in Figure 2.6. Frequency differences also occurred between the three GLARE 3 beams. This was caused by the fact that beams Nos. 4 & 5 were from the same batch of material and No. 6 from another.

Although the loss factors of the GLARE coupons are generally lower than those of the CFRP coupons, the results are still of encouragement if compared with aluminium alloy for which loss factor is normally in the range of 10^{-4} to 10^{-3} [95, 96].

2.2.3 Summary of Damping Measurements

Damping loss factor measurements have been carried out for CFRP Tee-coupons, CFRP Tee-beam coupons, GLARE Tee-coupons and GLARE plain beams. Results have shown that the CFRP Tee-coupons had the highest average loss factor of 0.0070 among those coupons tested. Damage in the CFRP coupons would increase damping value and reduce the resonance frequency.

The average loss factor of the GLARE Tee-coupons was 0.0038 which was 46% lower than that of the CFRP Tee-coupons.

The results show that the beam specimens tended to have lower damping values than Tee-coupons. The loss factor of the CFRP Tee-beams was 0.0044 and was 36% of that of the CFRP Tee-coupons. For the GLARE, the beams had a loss factor of 0.0016, which is 43% lower than that of GLARE Tee-coupons.

Though the GLARE coupons had a lower loss factor compared with CFRP, it is still higher than that of aluminium alloy due to the presence of glass fibre composite layers.

The standard deviation values show that measured damping values are more scattered than measured resonance frequencies. This suggests that in the theoretical estimation of the response of a structure to dynamic loads, it is always a good practice to employ a damping value in certain range rather than a single value if computation cost permits.

The CFRP coupon which was clamped on a shaker had a much higher loss factor. This was not only due to material damping but also includes contributions from the measurement set-up. So much higher damping values for box structures can be expected when subjected to dynamic loading, compared with data from freely supported material specimens.

2.3 ENDURANCE OF COUPON SPECIMENS SUBJECT TO SIMULATED RANDOM ACOUSTIC LOADING

In research on the acoustic fatigue of aircraft components, one of the main test methods is the endurance testing of structural coupons subjected to simulated random loading. In the tests, specimens are excited using narrow band acceleration excitation to produce random response as a simulation of the response of an aircraft structural panel to acoustic loading in a resonant mode. The purpose of the test is to establish fatigue data, i.e., RMS strain/stress (S) versus number of cycles to failure (N) curves, i.e., S-N curve, valid for random excitations of materials used in aircraft components. In practice, 2% decrease of the resonance frequency of a test coupon, or if damage is visible or detectable, are used as criteria for coupon failure.

In aerospace industry specimens used in acoustic fatigue testing are normally in the form of Tee-coupons, Tee-beams and panels to represent the joint of the skin panel and stringers. The

response of the test item is monitored by means of reference strain gauges which are installed on the outer surface of the skin panel. For Tee-coupons, the strain gauge is aligned with the spanwise direction of the skin plate to measure the bending strains. In the presentation of the fatigue data, the RMS strain rather than RMS stress is used for composite coupons.

In this section, it is described how the endurance tests of the CFRP and GLARE Tee-coupons were carried out to obtain the S-N curves of these two composites.

2.3.1 Test Set-up and Procedures

The objectives of the programme of fatigue tests on the CFRP and GLARE coupon specimens were:

* To establish fatigue data (RMS strain via number of cycles to failure);
* To identify possible fatigue failure mechanisms.

For the type of coupons used in the tests, fatigue failure was expected to occur at the joint between skin and stiffener. Preliminary test data and finite element analysis were combined to determine the location of the maximum strain where strain gauges were installed and approximate acceleration excitation levels required for the tests. Because acoustic loading of aircraft structures behind engines has the characteristic of random noise, the excitation and response are represented overall by their RMS value, i.e., RMS strain and RMS acceleration, and fatigue data are noted in terms of RMS strain versus N (number of cycles to failure).

The coupon was attached to an electrodynamic shaker by clamping its stiffener on a fixture. The test set-up and instrumentation are illustrated in Figure 2.21. This arrangement ensured that the skin panel experienced a pure bending vibration (butterfly mode) under narrow band random loading. Excitation was a one third octave bandwidth random signal with central frequency close to that of the first pure bending mode of the coupon. Coupon fixture is shown in Figures 2.22 and 2.23.

Excitation level was defined as the RMS acceleration of the shaker and measured by an accelerometer on the coupon fixture. Response of the coupon was quantified as RMS strain and measured by the means of strain gauges installed on the upper surface of the skin panel.

An optical vibrometer was used to monitor the resonance frequency of the coupon during the endurance test. This was achieved by using a PC based data acquisition system, which is described in Appendix G.

During the endurance test, resonance frequency was monitored and the CFRP coupon was inspected by ultrasonic C-scan to identify initiation of damage and show the shape, position and extent of the damage. For the GLARE coupons, change in resonance frequency and visual inspection were the only way to detect the occurrence of the fatigue damage.

The following test procedures were followed:

* Initial C-scanning was conducted on all CFRP coupons, and visual inspection on GLARE coupons to find any original damage and defects.
* Finite Element prediction, static tensile and compressive bending tests were used to determine the location of maximum strain. Static tests were also carried out on each coupon before beginning the fatigue tests. Results of the static tests are given in Appendix A.
* Preliminary dynamic loading tests were carried out to determine excitation levels and relative response levels.
* Tip mass loading was used to increase the dynamic response strain level of the coupons.
* Fatigue tests were performed at five different RMS levels of acceleration excitation.
* Together with strain gauges, an optical vibration detector was used to monitor the response of the coupons.
* Coupons were inspected in intervals to identify any possible damage during fatigue tests.
* The resonance frequency of the test specimen was monitored.

2.3.2 Preliminary Tests

2.3.2.1 Inspection of test coupons

Before carrying out the endurance tests, all the coupons were inspected for any existing defects and damage which could affect the accuracy of S-N data.

A. CFRP coupons

The ultrasonic C-scan is an effective method to identify defects and damage in CFRP composite specimens. Any defect or damage existing in the specimen will be shown in the scan pictures as a white patch while would otherwise be black. Figure 2.14 shows some examples.

Due to the existence of the stiffener on the coupon and the radius at the joint, which caused acoustic scattering in the C-scan probe, results in the whole of the unidirectional filling part between the top 8 layers and bottom 8 layers is shown as a white stripe in the central region. Therefore the scan picture cannot yield any useful information on the status of the joint. This region was visually inspected. 22 specimens were scanned and it was found that 21 out of 22 coupons were in good condition and only one had original defects (CFRP Tee-coupon No. 2).

B. GLARE coupons

Attempts were also made to check the GLARE Tee-coupons using ultrasonic C-scanning without success. The reason is that the ultrasonic C-scan system used cannot work effectively on laminates built up of different material types, such as GLARE with aluminium alloy and glass fibre composites. Therefore, all the specimens were visually inspected and no visible defect was found.

2.3.2.2 Static test – determine the strain gauge location

Preliminary finite element analyses of the coupons were carried out to give some indications where the maximum bending strain would be. Based on the findings of the FE predictions, static tests were carried out to determine the monitoring strain gauge location for the fatigue tests and to check the linearity. Detailed testing results are given in Appendix A.

Static test results indicated that the maximum strain occurred in the region where the joint radius ended for the CFRP Tee-coupons. For the GLARE coupons, maximum strain was found to be in the region where skin and stringer met. For each coupon, two strain gauges were attached as shown in Figures 2.24 and 2.25. The static test results show that to the maximum strain level investigated, strain/load characteristics of the coupons followed a linear relationship (See Figure A.2 of Appendix A for example).

2.3.2.3 Dynamic evaluation test – determine the excitation levels of endurance tests

Two parameters that affect the endurance tests are response strain level in the skin panel and the shaker excitation level. Because of the low density of CFRP and GLARE materials, test specimens had very low self weight of 29.5 gram and 47.3 gram respectively. For the mode shape expected for the coupons, this would not permit introduction of a high enough strain response in the skin panel to cause fatigue damage. Therefore, the tip mass loading method was used to increase the strain level.

A series of tip mass weights and excitation levels were tried to determine the desired range of strain level in the skin panel. Appendix A.2 gives the detailed test results. According to the dynamic evaluation results and by consulting the fatigue data illustrated in ESDU data sheets[5] for similar materials, a tip mass of 24 grams was used at each end of the skin panel of coupons, and five shaker excitation levels of RMS acceleration: 3.0, 5.0, 6.7, 7.50 and 8.75 g (1 g = 9.81 ms^{-2}) were chosen. This resulted in the reduction of coupon resonance frequencies to around 108 and 85 Hz, and the creation of response strain at levels in the range of 1000 to 3000μ strain and 500 to 2000μ strain for CFRP and GLARE coupons respectively.

To ensured that the responses to the shaker excitation were in the skin bending mode (butterfly mode), coupons were excited by narrow band random acceleration with 1/3 octave bandwidth and central frequency of 100 Hz for CFRP coupons and 80 Hz for GLARE ones. The bandwidth at the 3 dB points was 23 Hz and 18.3 Hz respectively which gave adequate excitation of the coupons after resonance frequency had decreased due to the development of damage.

2.3.2.4 Data processing

During the endurance testing of coupons, resonance frequency was monitored and recorded by means of an optical vibrometer. Any change in the response frequency would be an indication of the change of coupon status. The excitation and response strain time histories were also recorded by tape recorder in order to extract the relevant information. A data processing program based on MATLAB was used which enabled power spectral density (PSD), transfer function, damping loss factor, RMS value, mean value, standard deviation and probability distribution curves to be derived. Figures 2.26 and 2.27 give examples of processed data.

Fatigue data are presented by reference to RMS strain and RMS acceleration excitation respectively. The number of cycles was calculated by multiplication of time (second) of fatigue testing and resonance frequency (Hz). The latter engineering assumption concerning the average frequency of oscillation is justified in Newland's book[89].

2.3.3 Definition of Failure

By monitoring the response frequency of the specimens and inspecting them by means of ultrasonic C-scan and visual observation at intervals, it is possible to establish damage initiation and final failure of the coupons during the test. The 'settlement phase' was observed during the test and it was more obvious in the GLARE coupons than in CFRP ones. This behaviour was also observed by other researchers when carrying out this type of tests[70]. What this means is that a decrease of the resonance frequency of the test specimen occurred in an initial small number of cycles at the commencement of the endurance process. Then the resonance frequency remained at a constant value or decreased at a very low rate until the initiation of the fatigue damage. The settlement frequency is used as the initial frequency f_0 (Hz). Once damage is formed, a rapid decrease of response frequency is observed and failure status is reached when resonance frequency is **2%** less than the initial frequency f_0. This process is illustrated in Figure 2.28. The time taken between the initial frequency to the point when frequency decreased by 2% is used as the endurance period t (second). Therefore the number of cycles N to failure is define as $t \times f_0$. As mentioned above, this assumption is acceptable as discussed in Ref. [89].

2.3.4 Test Results

A total of 21 CFRP and 34 GLARE Tee-coupons was tested at several excitation levels. Different damage patterns and behaviours were observed for these two kinds of coupons. For each specimen, initial and final resonance frequencies, RMS excitation acceleration, RMS response strain, damping loss factor and number of cycles were recorded and derived. Results are summarised in Tables 2.8 and 2.9 respectively for CFRP and GLARE coupons.

2.3.4.1 CFRP Coupons

For this type of coupon, damage patterns observed were mainly joint cracking and delamination of the skin plate. Once damage became visible or detectable, response frequency decreased rapidly leading to the fatigue failure of the specimen.

Coupon No. 5 was the first specimen tested and was excited with an RMS acceleration of 8.75g which produced an RMS surface strain of 2642μ strain. The recorded initial response frequency was 103.8 Hz. After just a very short endurance period of 28026 cycles, a C-scan revealed that fatigue damage had already started in the skin panel and no information could be revealed on the status of the joint. Visual inspection found no sign of damage at all on the outer surfaces. At this point, the measured resonance frequency was 96 Hz. Further endurance testing was carried out until damage became visible. Figure 2.29 shows the C-scan results of CFRP Tee-coupon No. 5 in three stages: before testing started, at N = 28026 and when damage in the central joint became visible. It can be seen that the damage propagated into the skin plate as the endurance testing continued. For the central unidirectional insert, fatigue cracks were seen on both sides of the joint and are shown in Figure 2.30. The resonance frequency at this stage had reduced to 84 Hz. This is well below the failure frequency of 101.7 Hz. Figure 2.30A shows a fatigue crack parallel to the top surface across the central region and joined to the delamination line which separates the bottom 8-layer with the central unidirectional insert along the curves. At the opposite side (Side B) a vertical crack across the joint was visible and also connected to the delamination line of the lower 8 layers. Because of limitations in the C-scan facility, it is difficult to have a full picture of how the crack in the central part initiated and developed. However, from the evidences shown in Figures 2.29 and 2.30, it can therefore concluded that delamination occurred first at where the top and bottom 8-layers joined together to form the skin panel, due to the stress concentration. As the endurance testing continued, delamination propagated in both directions into skin panel and central joint. The rate of progression of the delamination into the curvature of joint filling area was much higher than to the skin and eventually caused the central region to fracture as shown in Figure 2.30.

Coupon No. 6 was excited at an RMS acceleration level of 7.5g and visible damage was found after about 35000 cycles. Its damage pattern was the same as that of No. 5 and is shown in Figure 2.31. The C-scan picture of this coupon in Figure 2.32 indicates that delamination was

just starting to propagate into the skin plate. Coupon No. 4 was tested at a lower excitation level of RMS acceleration of 4.47g. This resulted in a surface strain of 987μ strain. The C-scan picture of No. 4 coupon is given in Figure 2.33, it has similar feature to those shown in Figures 2.29 and 2.32. The fatigue crack at the central joint region of No. 4 coupon is shown in Figure 2.34.

Fatigue damage of the central joint region has been observed in all other coupons with one exception, the case of coupon No. 3. Only delamination in the skin plate was observed during the test on this coupon when it was excited at an RMS acceleration level of 6.7g. Figure 2.35 is the C-scan results of coupon No. 3. Observation under a microscope revealed that there was no damage in the central region and delamination was not between layers 8 and 9 but between layers 1 and 8. Fatigue crack in the central joint region was one of damage mechanisms found in the tee-coupon tests. Further work can be carried out to reveal detailed information on how the cracks started and propagated, which will benefit the design of stringer and skin joints.

During the endurance testing, the displacement of the skin plate of the CFRP Tee-coupon was also monitored via an optical vibrometer to provide continuous information on the change of the resonance frequency of the coupon. When fatigue damage occurred, the resonance frequency of the coupon decreased rapidly. Figure 2.36 shows plots of resonance frequency change versus number of cycles for coupons Nos. 3, 4 and 7. Coupon No. 3 had skin delamination damage only but the other two had damage in the joint region together with skin delamination. It shows that central joint region damage appears to have more influence on resonance frequency than did skin plate delamination. Results show that once damage occurred, the stiffness of the CFRP coupons deteriorated which led to a rapid decrease of the resonance frequencies.

Table 2.8 is a summary of the fatigue test results. Because the specimens were tested under random excitation, the excitation acceleration of the shaker and response strain of the coupons are presented in the form of square root of the mean square of recorded excitation signals. The damping loss factors were obtained by the half power point method. It can be seen that from Table 2.8, fatigue failure did not occur for the coupons with strain response level below 1000μ strain. The damping loss factor estimates are in the range of 0.0093 to 0.028 with an average of 0.019, which is 2.7 times the value measured in the freely supported condition (Table 2.2). For coupon No. 4, measured response frequency was 104 Hz and damping loss factor was

0.016 which are comparable with the values obtained using the free decay method (103 Hz and 0.016 respectively as shown in Table 2.3).

Table 2.8 shows that coupons Nos. 6, 8, 10 and 21 did not have valid strain values owing to premature failure of the strain gauges. Therefore, the final RMS strain versus number of cycles to failure (S - N) curve was produced based on data from 17 coupons. Figure 2.37 gives the final S-N curve for the CFRP Tee-coupons. Logarithmic scales are used and the data are presented as a straight line. To obtain the fatigue data in the strain range other than shown in Figure 2.37, following regression formula can be used to represent the fatigue data in Figure 2.37:

$$\varepsilon = 1.50E4\, N^{-0.143} \qquad (2.4)$$

Where ε - RMS Strain (μ)

N - Number of cycles to failure.

The fatigue strength of CFRP materials and a CFRP composite structure depends on material composition, lay-up and manufacturing process, etc., so it is difficult to compare the results with each other. However, ESDU data sheets do have a collection of fatigue data of coupon specimens subjected to simulated random acoustic loading. The fatigue data for a similar CFRP Tee-coupon are given in ESDU data sheet No. 84027[5] and the fatigue data are reproduced** in Figure 3.38 for the purpose of comparison. Comparing Figure 3.37 with Figure 3.38, it is found that they show similar trends and the fatigue data are compatible. However, the data shown in Figure 3.38 are more scattered and do not show a definite trend.

** Permission has been granted by ESDU to use figures in their data sheets No.84027 (Appendix H)

2.3.4.2 GLARE Tee-Coupons

A total of 34 GLARE Tee-coupons was tested at several excitation levels, which produced response strain levels at the skin surface in the range between 300μ to 2000μ strain. The fatigue damage in the GLARE Tee-coupons was in the form of cracks initiated from rivets and propagating along the rivet line. Once these cracks became visible, the propagation rate was high, and consequently the resonance frequency decreased rapidly. Figure 2.39 shows the

fatigue crack of coupon No. 6, and its resonance frequency f and crack length d versus the number of cycles N curves for the coupon are given in Figure 2.40. A rapid frequency drop occurred during the first 7000 cycles, i.e., 73.8 Hz to 72.8 Hz, which was then followed by a short settlement period. When N reached 27,000, the frequency started to decline again until reaching a relatively slow change stage. This frequency reduction was caused by the initiation of a fatigue crack, because a 2 mm crack started from the rivet No. 2 was seen when the number of cycles reached around 41,000. As the endurance testing continued, a crack at No. 2 rivet grew at a steady rate and more cracks formed at the other two rivets. The final crack length was just under 5 mm as shown in Figure 2.39.

For all the specimens tested, the damage patterns were similar although the length of the fatigue cracks may be different, as shown in Figures 2.39 and 2.41 for coupons No. 6 and No.41 respectively. The relationship between resonance frequency and number of cycles follows the pattern shown in Figure 2.28. There is always a clear settlement period followed by a constant frequency range till the coupon failed with rapid frequency drop, and the results for a few more of the coupons are illustrated in Figures 2.42 to 2.45.

The fatigue cracks on the skin panel were seen on both surfaces, but no damage was found on the stringer surface. Figures 2.46 and 2.47 show the fatigue cracks of coupons No. 1 and No. 11. Both have the same damage pattern, i.e., the cracks on the upper surface were always almost along the rivet line, but offset to the side on the lower surface.

As a general statement based on previously published work, one of the most important advantages of GLARE materials is said to be that it has a very low fatigue crack growth rate because of the 'fibre bridging effect' provided by the composite layer as discussed in Chapter 1. However, experimental results obtained in this study have shown a different picture. During the endurance test, coupons were inspected at intervals under the microscope in an attempt to identify the fatigue crack at an early stage. Failure always followed very quickly after cracks started to form. To investigate the damage mechanism further, it is necessary to find out what happened to the glass fibre layer under the surface aluminium alloy layers.

By removing the surface aluminium alloy layers of the skin panel, it is possible to inspect the glass fibre reinforced plastic layers, which should be a 0° / 90° cross ply with 0° fibre direction along the skin span, i.e., perpendicular to the stringer. To ensure that the status of the GRP

layer was maintained, a chemical method was employed to remove the outside metallic layers, i.e., skin panels of a few coupons were treated with sodium hydroxide solution. Figures 2.48 to 2.50 show the composite layers under the surface aluminium alloy layers. It was found that the composite layer consisted of two unidirectional layers with fibres perpendicular to each other. The fibre direction of the unidirectional layers immediately under surface aluminium alloy layers was along the stringer instead of in the skin span direction. There were fatigue cracks similar to those in the aluminium alloy on the outer layers and delamination between these two unidirectional layers. Both upper and lower layers showed the same pattern. This finding explains why 'fibre bridging' was not as effective as expected. For this effect to work, it is necessary that the fibre direction in the layers immediately under the surface metal layers is perpendicular to the crack growth path, i.e., the rivet line, in order to carry the extra load after the metal layers lost their strength due to the presence of fatigue damage.

For the coupons tested, when the cracks formed in the aluminium alloy layers, load redistribution resulted in the extra load being carried by the resin rather than glass fibres, and this explains the reason why fatigue cracks also formed in the outer composite layers. Because of failure of the outer composite layer, the second composite layer now had to take more load. Because of high strength of the glass fibre, the result is delamination between two unidirectional layers as shown in Figures 2.48 to 2.50. It is worth mentioning that in most published work, the test results were based on the GLARE plates subjected to in-plane loading. In this work, the skin panel is under the action of bending loads.

All of the 34 coupons showed the same damage and response patterns. Table 2.9 is a summary of the GLARE Tee-coupon endurance testing results. Apart from the fatigue data, the damping loss factors of these specimens were also obtained by the half power point method. The average loss factor was 0.030, which is much higher than that measured in the freely supported condition (Tables 2.5 and 2.6) and even higher than the damping value (0.019) of CFRP Tee-coupons in the endurance test condition (Table 2.8). The average resonance frequency was 84.7 Hz. For the GLARE coupons, two strain gauges were installed at different locations, so the fatigue data given in Figure 2.51 includes two sets of data. The regression formulae were also obtained as follows:

For the maximum strain: $\varepsilon = 8014.4\,N - 0.1659$ (2.5)

For the reference strain: $\varepsilon = 4833.1\,N - 0.1816$ (2.6)

A similar set of test results is presented in ESDU data sheet No. 84027. The coupon was made of GLARE material as shown in Figure 2.52. There are two major differences between this specimen and coupons used in this study. First, although the skin panel arrangement was the same, the lay up was different. The composite layers immediately under the metal surfaces of the ESDU coupon were in the skin panel span direction, which is a favourable lay up. Second, there is a composite doubler between the skin panel and the stringer. Fatigue data for this type of coupon are given in Figure 2.52. Comparing Figures 2.51 and 2.52, the latter indicates better fatigue resistance. This is probably due to the ESDU specimens having a favourable lay up in the skin panel. Because the fatigue data depend on many factors, this comparison is not decisive and could not be used as a general conclusion. But it is useful in the process of understanding the fatigue resistance of GLARE material.

2.3.4.3 Post-fatigue test of GLARE Tee-Coupons

To examine the effect of fatigue cracking on the residual strength of GLARE coupons, four coupons were subjected to post-fatigue tensile testing. They were No. 13 (original untested), No. 5 (tested but no damage found at N = 8.61E6) and Nos. 6 & 34 (tested and damaged with number of cycles to failure as $N_{2\%}$ = 6.40E4 and 7.79E5 respectively). Figures 2.39 and 2.41 show the crack lengths of coupons No. 6 and No. 34 before undergoing post-fatigue tensile testing. Tests were carried out using a testing machine. Each coupon was clamped by the edges of the skin plate, and subjected to the tension. Due to the difficulty in measuring the extension of coupons in the test arrangement, the strain was measured during tensile tests (Gauge location same as Gauge 1 in Figure 2.25).

The stress-strain and tensile force-strain curves measured are plotted in Figures 2.53 to 2.56 and summarised in Table 2.10. The residual strength of coupon No. 13 is 318.5 MPa, which is much lower than the ultimate strength of perfect GLARE material (717 MPa, see Appendix F). This is caused by stress raisers, i.e., the rivets. For the other three coupons, the lowest residual strength is 285.7 Mpa. The residual strength of untested original coupon No. 13 is 7% higher than that of No. 5 and 11% higher than those of No. 6 and No. 34. The surface tensile strain of the damaged coupon was about 45% lower than that of undamaged coupons.

Figures 2.53 to 2.55 indicate that the stress and strain relationships of coupons become non-linear when the maximum surface strain goes beyond 2800μ strain. Comparing the stress-strain data in Figure 2.56, the apparent modulus of coupons No. 5 and No. 13 are almost the same, but that of No. 34 is higher than that of the other two. This is because the fibre layers shared more loading in No. 34, due to the introduction of surface fatigue cracks, than that in the un-cracked specimens.

During post-fatigue tests, the coupons failed along the rivet line (Figures 2.57 to 2.60). Coupons No. 6 and No. 34 have cracks through the whole thickness along the rivet line and the surface plates became two pieces. For coupons No. 5 and No. 13, cracks occurred on one side of the rivet line but did not propagate into the full length of the rivet line.

2.4 SUMMARY OF ENDURANCE TEST OF THE TEE-COUPONS

Endurance testing of the CFRP and GLARE Tee-coupons under simulated random acoustic loading has been carried out. Damage mechanisms have been observed and fatigue data are established. Failure is defined as 2% drop of fundamental resonance frequency as illustrated in Figure 2.28.

The damage pattern of the CFRP coupons was cracking in the central joint region and delamination between the upper and lower 8-layers. Cracking along the rivet line is the damage form of the GLARE specimens, and a fatigue crack not only appeared in the outer metal layer but developed into the first glass fibre reinforced plastic layer. The 'fibre bridging effect' reported in other research work was not as effective as expected. This is probably owing to the lay up of composite layers in the GLARE material used in the tests which were not the most favourable where fatigue is concerned. The presence of damage in the specimens lead to a rapid decrease of resonance frequency. When the maximum surface strain was less than 1000μ strain, no fatigue damage occurred to the CFRP specimens up to the maximum 5.1E7 cycles which could be investigated in this study. For GLARE coupons this limit lowered to 500μ strain.

The average damping loss factors obtained were 0.021 and 0.030 for CFRP and GLARE coupons respectively. These values are much higher than those obtained in the freely

supported condition, which are the combination of material damping, the damping due to acoustic radiation and joint friction, etc.

Table 2.1 Lay-up of GLARE materials

Lay-up	Materials	Layer Thickness (mm)	Fibre Orientation	
			GLARE 2	GLARE 3
1	2423-T3	0.30		
2	Glass composite	0.25	UD* 0°	CP** 0°/90°
3	2423-T3	0.30		
4	Glass composite	0.25	UD 0°	CP 0°/90°
5	2324-T3	0.30		

* UD - unidirectional ** CP - cross-ply

Table 2.2 Damping test data for the CFRP Tee-coupons measured in the 'freely' supported condition

Coupon No.	f_n(Hz)	f_1(Hz)	f_2(Hz)	Loss factor
9	409.6	407.6	411.6	0.00960
10	423.6	423.5	425.7	0.00924
11	411.8	410.5	413.1	0.00642
12	414.0	412.6	415.2	0.00646
13	425.2	423.8	426.3	0.00611
14	424.2	422.9	425.8	0.00670
15	422.8	421.2	424.1	0.00670
16	422.8	421.5	424.2	0.00639
17	424.2	422.9	425.3	0.00637
18	419.0	417.7	420.4	0.00632
19	418.8	417.4	420.4	0.00613
20	422.0	420.6	423.4	0.00664
21	416.2	414.6	417.8	0.00769

Statistical parameter	Resonance Frequency (Hz)	Loss Factor
Maximum	419.6	0.0096
Minimum	409.6	0.0061
Average	425.2	0.0070
Standard Deviation	4.967	0.0011

2*	434.8	433.0	436.6	0.00824
5**	402.0	400.3	403.5	0.00816
3**	382.0	379.4	383.8	0.0115

* Coupon with defect

** Coupon with fatigue induced damage

Table 2.3 CFRP Tee-coupon damping measurement results by hammer excitation

(clamped by the stiffener on a shaker)

Aluminium tip			Nylon tip		
f_n (Hz)	η_1^*	η_2^*	f_n (Hz)	η^*_1	η_2^*
103.9	0.0190	0.0190	104.9	0.0167	0.0167
103.9	0.0173	0.0173	101.9	0.0174	0.0174
102.9	0.0173	0.0172	103.9	0.0185	0.0185
102.0	0.0165	0.0165	103.9	0.0178	0.0178
103.6	0.0171	0.0171	103.9	0.0176	0.0176
104.9	0.0190	0.0190	104.9	0.0167	0.0176
103.9	0.0190	0.0190	103.9	0.0181	0.0189
104.9	0.0163	0.0163	102.9	0.0176	0.0176
101.9	0.0178	0.0178	103.9	0.0158	0.0159
102.9	0.0167	0.0168	102.9	0.0168	0.0168
102.9	0.0168	0.0167	101.9	0.0148	0.0148
101.9	0.0182	0.0168	103.9	0.0149	0.0149
101.9	0.0162	0.0183	103.9	0.0172	0.0173
103.9	0.0162	0.0164	103.9	0.0166	0.0166
103.9	0.0158	0.0162	102.9	0.0157	0.0157
102.9	0.0175	0.0158	102.9	0.0159	0.0159
103.9	0.0156	0.0175	102.9	0.0180	0.0180
104.9	0.0164	0.0156	103.9	0.0146	0.0146
Average resonance frequency: 103.3 Hz			**Average loss factor: 0.016**		

* η_1 - Calculated by equation (2-3a)
η_2 - Calculated by equation (2-3b)

Table 2.4 Damping test data of CFRP beam-coupons measured in the 'freely' supported condition

Coupon No.	f_n(Hz)	f_1(Hz)	f_2(Hz)	Loss factor
1	834.4	832.6	836.5	0.00479
2	845.4	843.7	847.4	0.00447
3	829.8	828.3	831.3	0.00363
4	824.8	822.2	826.3	0.00504
5	844.4	843.0	846.1	0.00371
6	821.8	819.6	823.4	0.00445
7	817.2	815.6	819.6	0.00479
8	847.8	845.7	849.3	0.00427

Statistical Parameter	Resonance Frequency (Hz)	Loss Factor
Maximum	847.8	0.00363
Minimum	817.2	0.00504
Average	833.2	0.00440
Standard Deviation	10.94	0.000475

Table 2.5 Damping test data of GLARE Tee-coupon measured in the 'freely'supported condition (first mode)

Coupon No.	f_n(Hz)	f_1(Hz)	f_2(Hz)	Loss factor η
1	300.6	300.1	301.0	0.00285
2	307.4	306.6	308.0	0.00457
3	311.2	310.5	311.7	0.00387
4	300.2	299.8	301.0	0.00397
5	298.4	297.9	298.8	0.00302
6	312.2	311.6	313.0	0.00456
7	304.2	303.7	305.0	0.00404
8	305.8	305.2	306.5	0.00414
9	310.4	309.8	311.0	0.00414
10	307.0	306.4	307.9	0.00470
11	309.2	308.6	310.0	0.00386
12	306.4	306.0	306.9	0.00288
13	299.2	298.7	299.9	0.00375
14	292.2	291.9	292.6	0.00229
15	306.6	306.0	307.2	0.00383
16	305.4	304.8	305.8	0.00317
17	308.2	307.7	308.7	0.00307
18	306.0	305.6	306.6	0.00332
19	311.0	310.6	311.5	0.00312
20	301.4	300.9	301.9	0.00318
21	299.2	298.7	299.6	0.00310
22	309.6	309.1	310.2	0.00334
23	309.2	308.7	309.8	0.00353
24	305.2	304.8	305.8	0.00330
25	307.8	307.3	308.3	0.00304
26	306.6	306.0	307.2	0.00395
27	307.8	307.3	308.3	0.00336
28	289.2	288.8	289.6	0.00280
29	303.6	303.1	304.1	0.00331
30	298.6	298.0	299.1	0.00364
31	297.0	296.5	297.6	0.00370
32	309.6	309.1	310.4	0.00440
33	302.8	302.4	303.6	0.00386
34	308.0	307.4	308.8	0.00481
35	301.2	300.3	302.5	0.00735

Statistical Parameter	Resonance Frequency (Hz)	Loss Factor
Maximum	312.2	0.00735
Minimum	289.2	0.00229
Average	304.5	0.00371
Standard Deviation	5.306	0.000858

Table 2.6 Damping test data of GLARE Tee-coupon measured in the 'freely' supported condition (second mode)

Coupon No.	f_n (Hz)	f_1 (Hz)	f_2 (Hz)	Loss factor η
1	479.2	478.8	480.1	0.00270
2	488.8	488.0	489.6	0.00332
3	493.4	492.5	494.0	0.00315
4	485.0	484.0	486.3	0.00476
5	476.6	475.9	477.3	0.00310
6	492.8	491.4	492.9	0.00314
7	489.6	485.8	487.6	0.00382
8	487.8	486.9	488.7	0.00381
9	498.2	497.4	499.1	0.00342
10	492.6	491.6	493.4	0.00375
11	493.6	493.0	494.6	0.00392
12	493.9	493.0	494.6	0.00333
13	478.6	477.6	479.7	0.00444
14	479.2	478.2	480.0	0.00373
15	489.4	488.4	490.1	0.00333
16	491.4	490.6	492.2	0.00319
17	492.0	491.0	492.8	0.00361
18	488.4	487.6	489.4	0.00357
19	492.2	491.4	493.0	0.00312
20	486.6	483.8	485.4	0.00331
21	476.6	475.8	477.6	0.00388
22	496.6	495.8	497.6	0.00372
23	497.4	496.5	498.3	0.00349
24	494.6	493.6	495.5	0.00389
25	496.4	495.6	497.1	0.00311
26	498.6	497.8	499.6	0.00354
27	491.8	491.0	492.9	0.00397
28	470.6	469.6	471.8	0.00460
29	487.2	486.3	488.3	0.00418
30	485.6	484.3	486.6	0.00476
31	477.2	476.3	478.1	0.00381
32	489.0	488.3	489.9	0.00335
33	492.4	491.3	493.5	0.00437
34	497.6	496.7	498.4	0.00351
35	485.4	483.2	487.6	0.00911

Statistical Parameter	Resonance Frequency (Hz)	Loss Factor
Maximum	498.6	0.00911
Minimum	470.6	0.00270
Average	488.7	0.00380
Standard Deviation	7.044	0.00103

Table 2.7 GLARE plain beam-coupons damping measurement results in 'freely' supported condition

Coupon No.	f_n (Hz)	f_1 (Hz)	f_2 (Hz)	η
FIRST MODE				
1	190.4	190.32	190.74	0.00221
2	138.3	138.15	138.38	0.00166
3	138.2	138.03	138.27	0.00174
4	135.6	135.43	135.74	0.00229
5	135.7	135.61	135.78	0.00140
6	128.4	128.33	128.54	0.00164
SECOND MODE				
1	527.3	526.94	527.65	0.00135
2	271.5	271.38	271.74	0.00133
3	272.2	272.08	272.52	0.00162
4	266.4	266.27	266.55	0.00105
5	266.5	266.26	266.58	0.00120
6	253.0	252.69	253.17	0.00190
Average Loss Factor = 0.0016				

Table 2.8 Summary of endurance test results of CFRP Tee-coupons

Coupon No.	Initial frequency	Failure frequency	Excitation acceleration	RMS strain S	Damping loss factor	Number of cycles to failure
	f_0 (Hz)	$2\%f_0$ (Hz)	RMS (g)	μ strain		N
1	108.0	105.8	2.78	650	0.0163	51274296(u)
3	103.8	101.7	6.75	1791	0.0119	1371320
4	104.2	102.1	4.47	987	0.0164	5283720
5	103.8	101.7	8.75	2642	0.0196	46710
6	106.2	104.1	7.07		0.0093	35244
7	103.8	101.7	5.00	1639	0.0094	15159363
8	104.8	102.7	7.65			140582
9	103.2	101.1	6.75	3214	0.0203	496186
10	105.5	103.4	8.75			25853
11	103.7	101.6	5.21	2180	0.0103	1485100
12	103.5	101.4	5.32	1948	0.0233	6427710
13	107.4	105.3	3.19	1006	0.0255	30775830(u)
14	105.5	103.4	5.45	2212	0.0251	10115340(u)
15	107.4	105.3	7.13	3410	0.0232	232958
16	106.4	104.3	8.16	3343	0.0278	56948
17	105.5	103.4	6.96	2384	0.0229	614925
18	106.4	104.3	8.68	3067	0.0274	181407
19	104.5	102.4	8.21	3299	0.0239	98431
20	107.4	105.3	6.61	2610	0.0256	35234
21	103.5	101.4	8.18		0.025	259371
22	103.5	101.4	5.41	1398	0.0285	954780
Average	**105.1**				**0.021**	

u - no fatigue damage found

Table 2.9 Summary of endurance test results of GLARE Tee-coupons

Coupon No.	Initial frequency	Failure frequency	Excitation acceleration	RMS strain S	RMS strain S	Damping loss factor	Number of cycles to failure
	f_0 (Hz)	$2\%f_0$ (Hz)	RMS (g)	Max (μ)	Ref. (μ)		N
1	83.0	81.3	5.17	1288	707	0.0326	20626
2	72.5	71.1	3.10	1136	525	0.0279	853981
3	76.5	75.0	1.40	609	301	0.0364	17848916 (u)
4*	215.8	211.5	6.37	369	159	0.0316	19032734 (u)
5	88.9	87.1	2.21	659	268	0.0284	8606425 (u)
6	73.4	71.9	4.46	1412	666	0.0248	63950
7	88.8	87.0	2.30	580	260	0.0267	8806747 (u)
8	87.3	85.6	3.4	906	422	0.0277	999037
9	86.9	85.2	3.49	703	329	0.0322	3435220
10	87.3	85.6	3.55	755	381	0.0264	998197
11	86.7	85.0	4.32	833	380	0.0326	2469108
12	85.7	84.0	6.06	1680	919	0.0324	16243
14	87.1	85.4	1.90	746	373	0.0303	341260
15	87.1	85.4	3.91	1207	601	0.0280	144000
16	85.2	83.5	6.31	1825	913	0.0359	13236
17	88.3	86.5	3.75	620	330	0.0298	867596
18	87.2	85.5	4.11	964	463	0.0229	246425
19	87.7	85.9	4.45	775	353	0.0223	1609000
20	85.9	84.2	6.54	1843	917	0.0339	13750
21	86.6	84.9	3.68	810	406	0.0266	406000
22	87.3	85.6	3.29	705	331	0.0243	276000
23	86.9	85.2	5.20	1212	617	0.0272	56000
24	88.0	86.2	2.81	519	246	0.0299	15245000
25	85.5	83.8	4.98	1087	598	0.0331	91000
26	85.9	84.2	3.85	1045	539	0.0294	101000
27	86.6	84.9	4.56	989	499	0.0329	107500
28	84.6	82.9	4.08	1795	909	0.0228	33500
29	86.2	84.5	4.67	1188	578	0.0274	61500
30	85.7	84.0	3.93	1111	558	0.0315	396996
31	85.8	84.1	4.82	1582	797	0.0308	29000
32	85.9	84.2	4.44	1030	538	0.0238	87767
33	72.1	70.7	5.46	1765	882	0.0354	54300
34	73.8	72.3	2.49	991	521	0.0373	779100
35	85.5	83.8	5.43	1261	634	0.0385	77000
Average	**88.5**					**0.030**	

u - no fatigue damage found * - coupon tested without tip mass

Table 2.10 Post-fatigue tensile tests results

Coupon No.	13	5	6	34
Status	Original untested	Tested un-damaged	damaged	damaged
Number of cycles to failure ($N_{2\%}$)		8.61E6	6.40E4	7.79E5
Ultimate tensile force (kN)	26.8	25.1	23.2	24.0
Residual stress (MPa)	318.5	298.9	276.2	285.7
Residual strain (μ)	9829	9013		5452

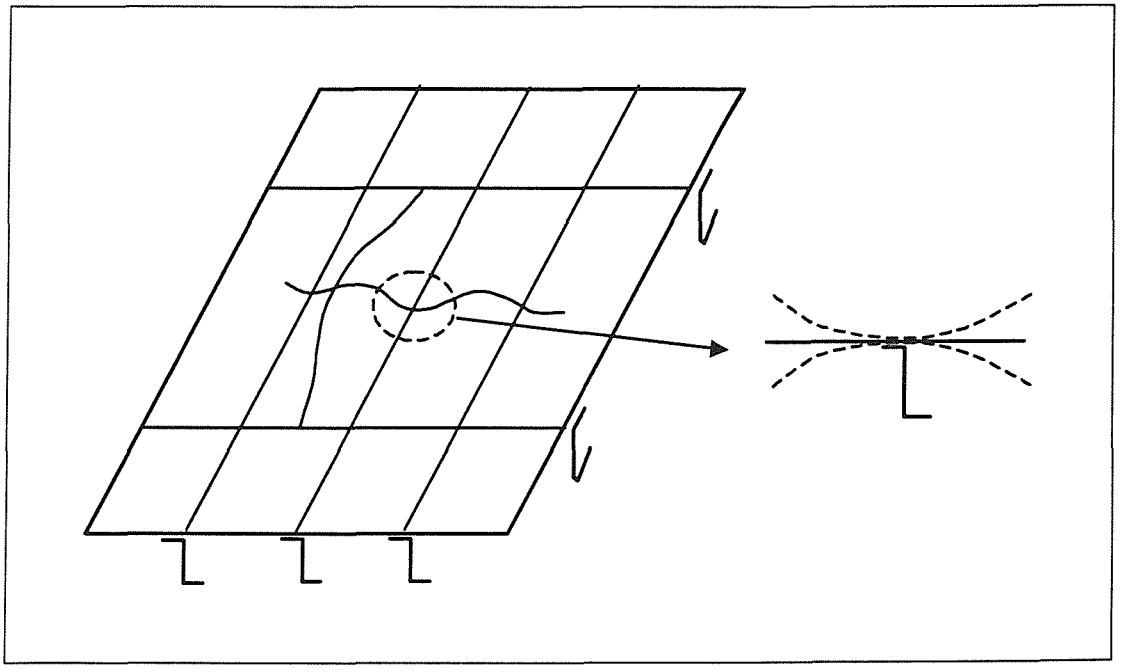

Figure 2.1 Critical location in a stiffened panel under acoustic pressure loading

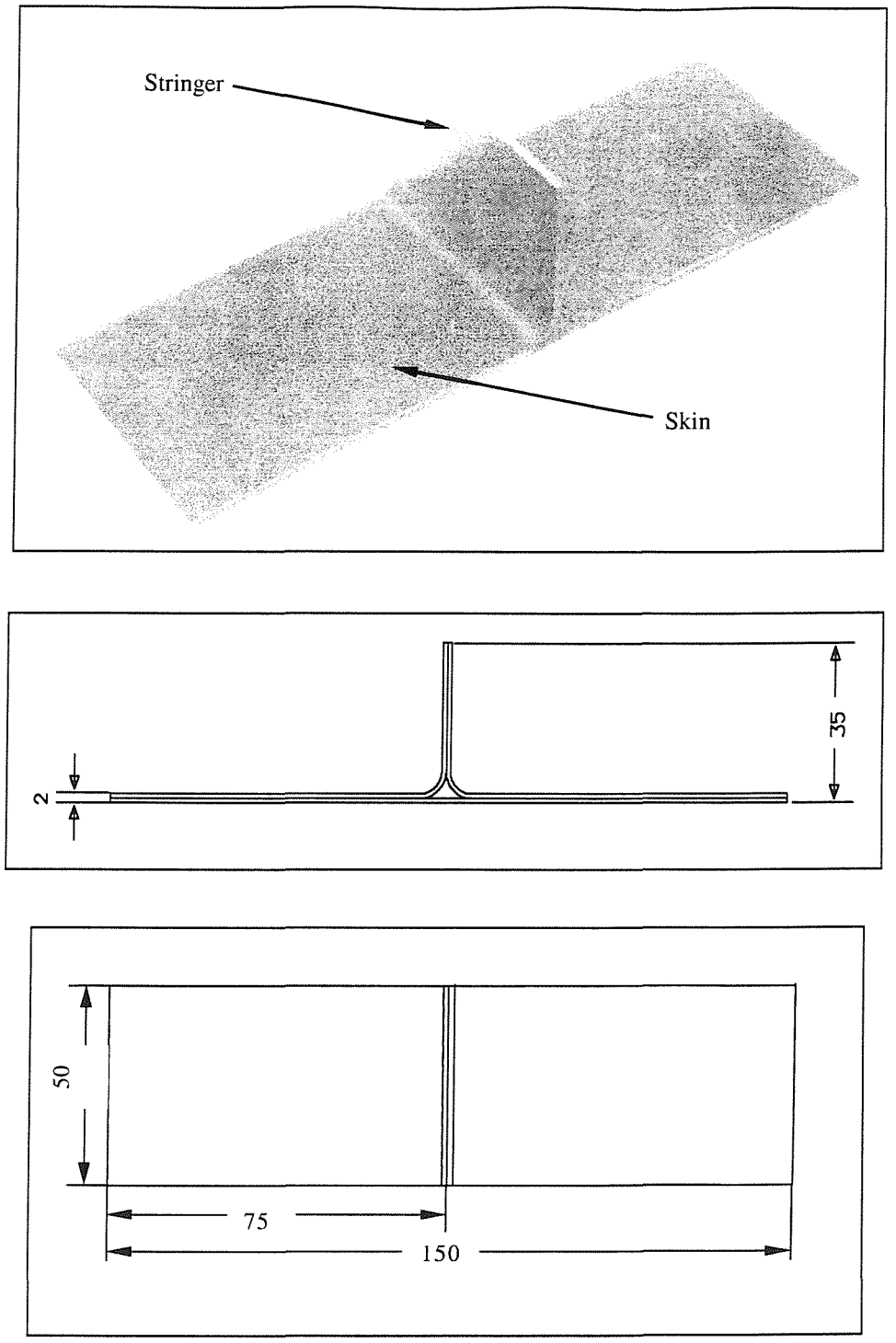

Figure 2.2 CFRP T-coupons

LAYER No.	FIBRE DIRECTION	MATERIAL
1	0	CFRP UD TAPE T300/924
2	-45	CFRP UD TAPE T300/924
3	+45	CFRP UD TAPE T300/924
4	90	CFRP UD TAPE T300/924
5	0	CFRP UD TAPE T300/924
6	-45	CFRP UD TAPE T300/924
7	+45	CFRP UD TAPE T300/924
8	90	CFRP UD TAPE T300/924
9	90	CFRP UD TAPE T300/924
10	+45	CFRP UD TAPE T300/924
11	-45	CFRP UD TAPE T300/924
12	0	CFRP UD TAPE T300/924
13	90	CFRP UD TAPE T300/924
14	-45	CFRP UD TAPE T300/924
15	+45	CFRP UD TAPE T300/924
16	0	CFRP UD TAPE T300/924

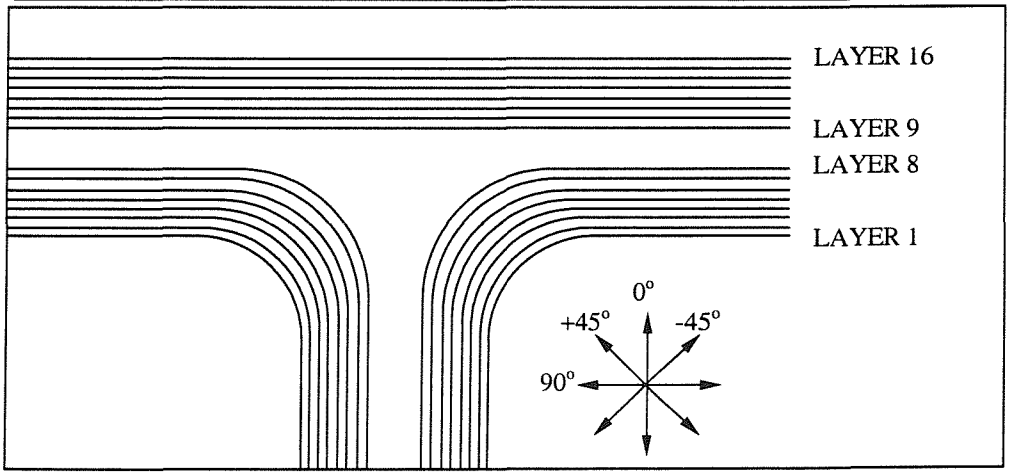

Figure 2.3 Lay-up of the CFRP material

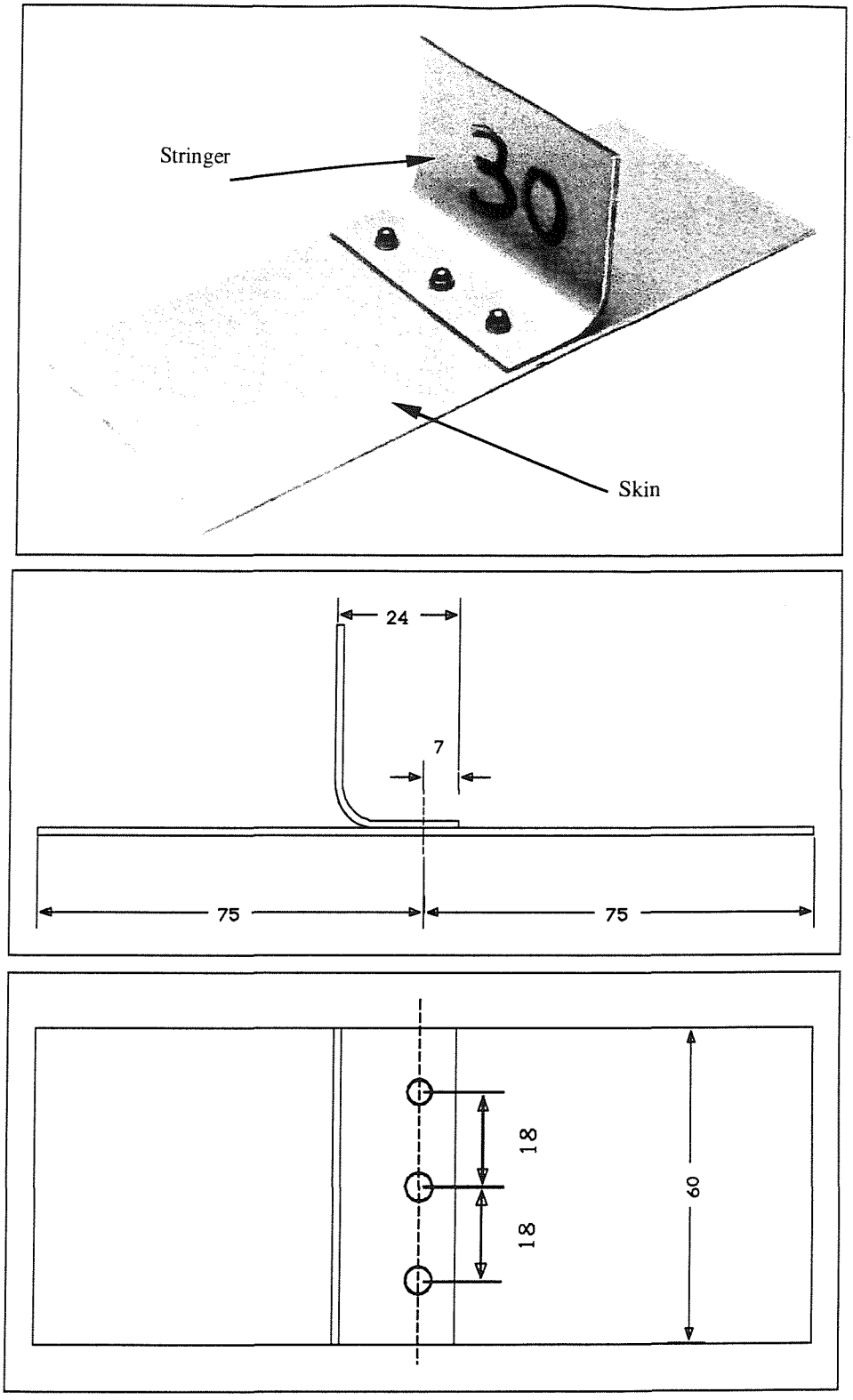

Figure 2.4 Dimensions of the GLARE Tee-coupons (Appendix D.2)

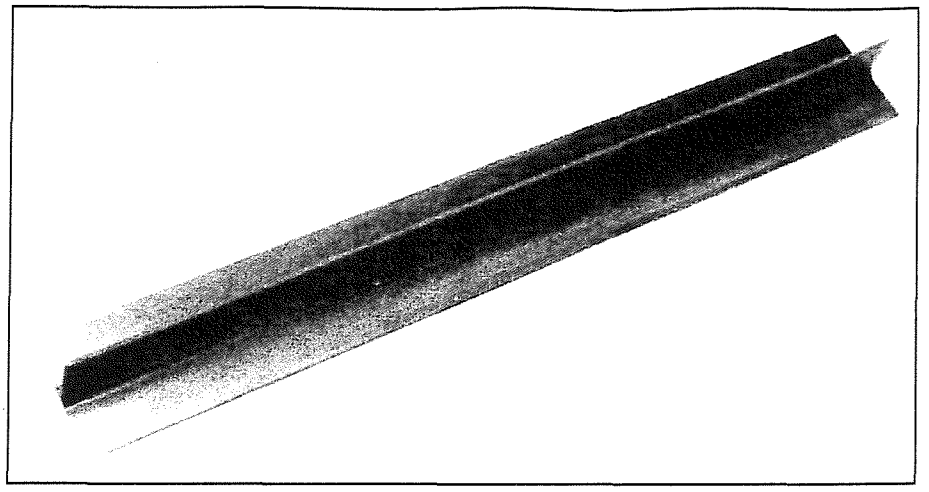

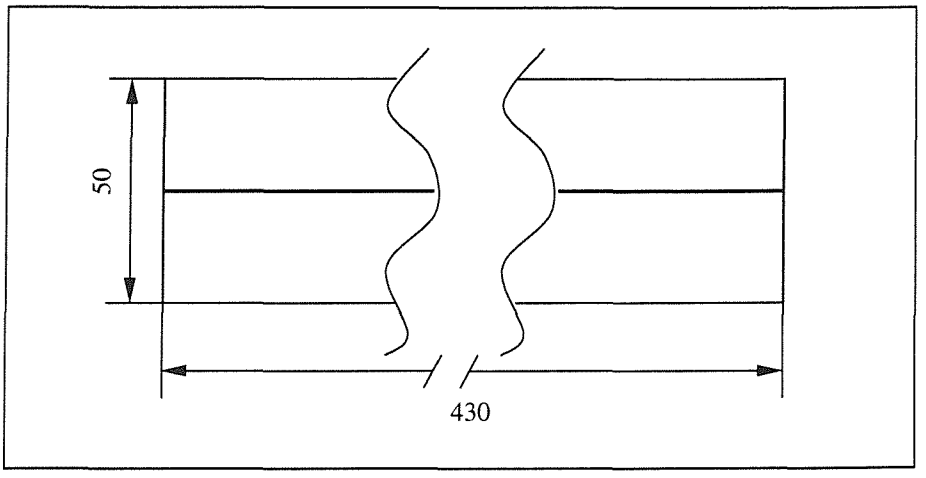

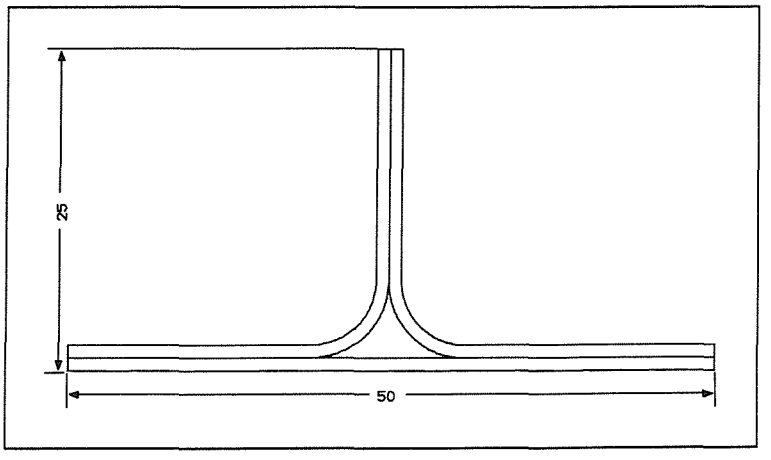

Figure 2.5 CFRP Tee-beams

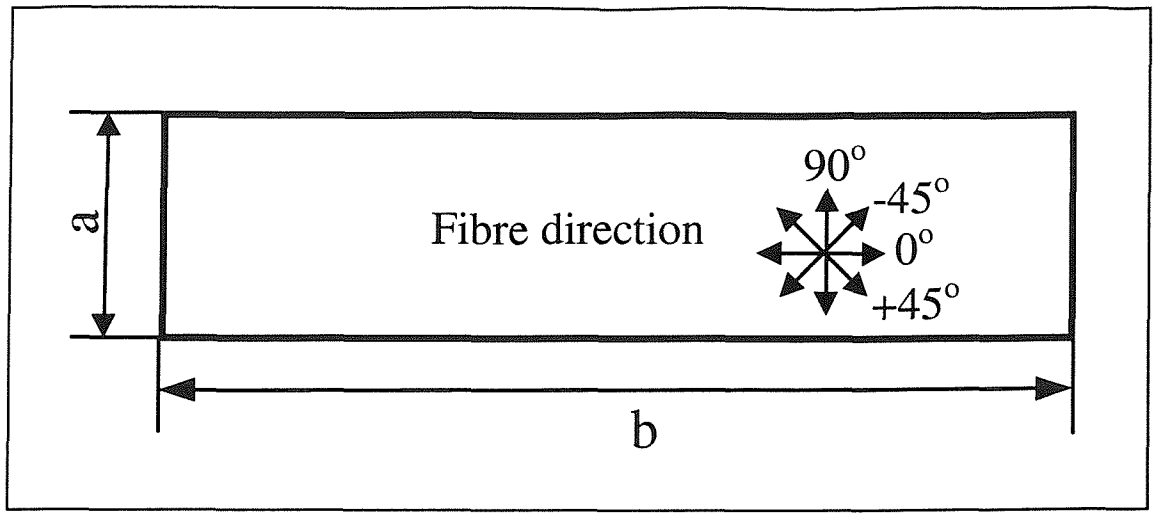

No.	Dimension (mm)		Material	Fibre direction
	a	b		
1	35	200	GLARE 1	0^0
2	50	400	GLARE 2	0^0
3	50	400	GLARE 2	0^0
4	50	400	GLARE 3	$\pm 45^0$
5	50	400	GLARE 3	$\pm 45^0$
6	50	400	GLARE 3	$0^0/90^0$

Figure 2.6 The shape and dimensions of plain GLARE Beams

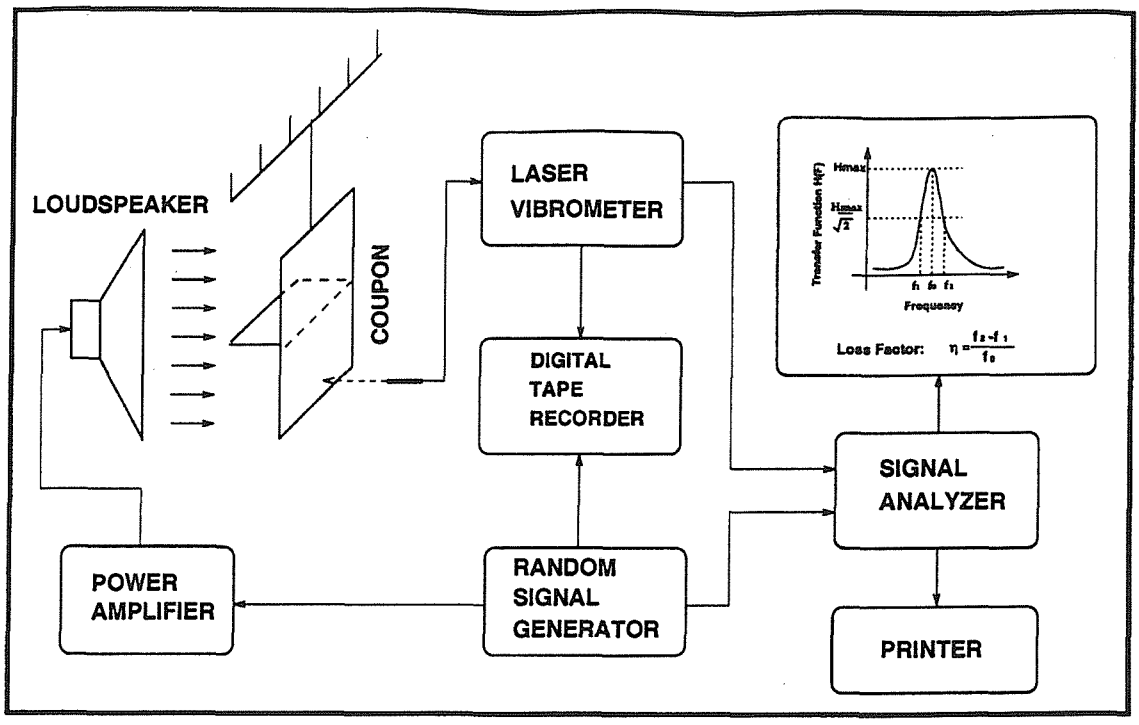

Figure 2.7 Schematic diagram of the experimental apparatus for the measurement of loss factor of the coupon specimens Freely supported condition

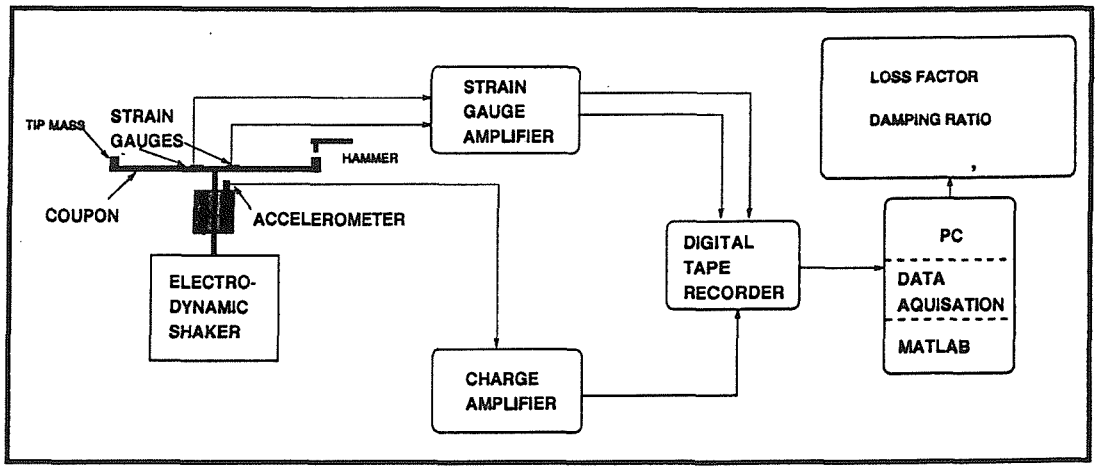

Figure 2.8 Schematic diagram of the experimental apparatus for the measurement of loss factor of the coupon specimens Clamped at stringer condition

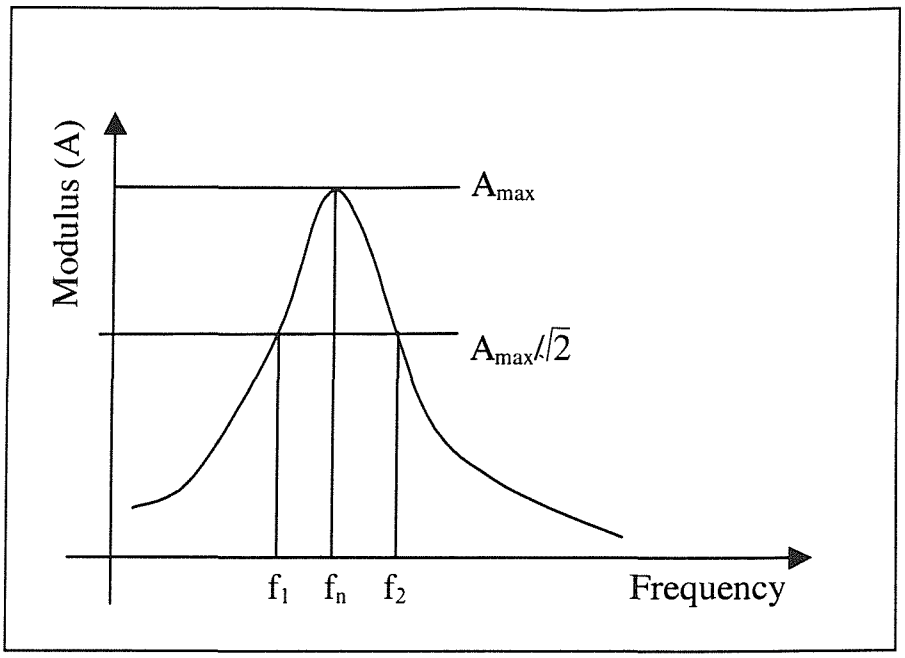

Figure 2.9 Damping measurement method - Half power point

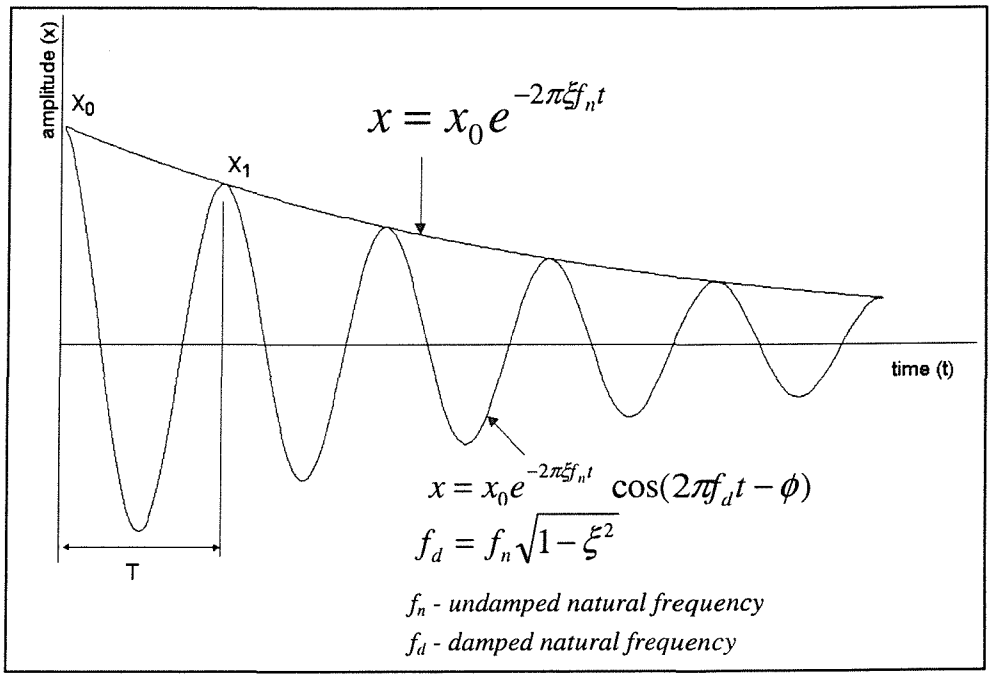

Figure 2.10 Damping measurement methods – Free vibration

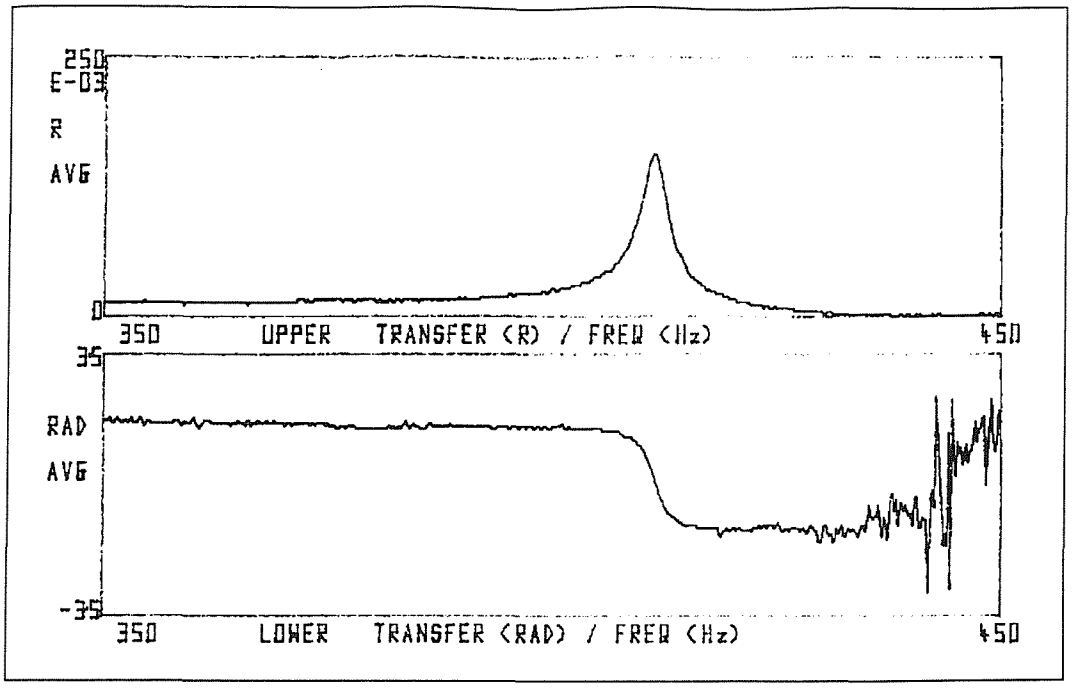

Figure 2.11 Typical transfer function plot of CFRP coupon for the damping measurement – freely supported condition

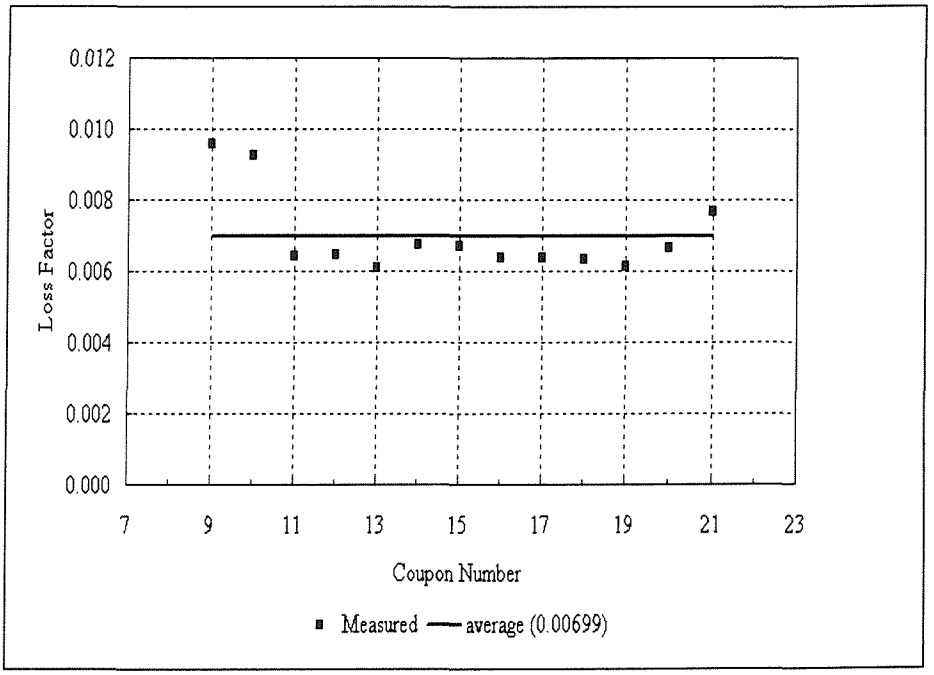

Maximum 0.0096 Minimum 0.00611 Standard Deviation 0.00111

Figure 2.12 Measured loss factors of the CFRP Tee-coupons in the freely supported condition

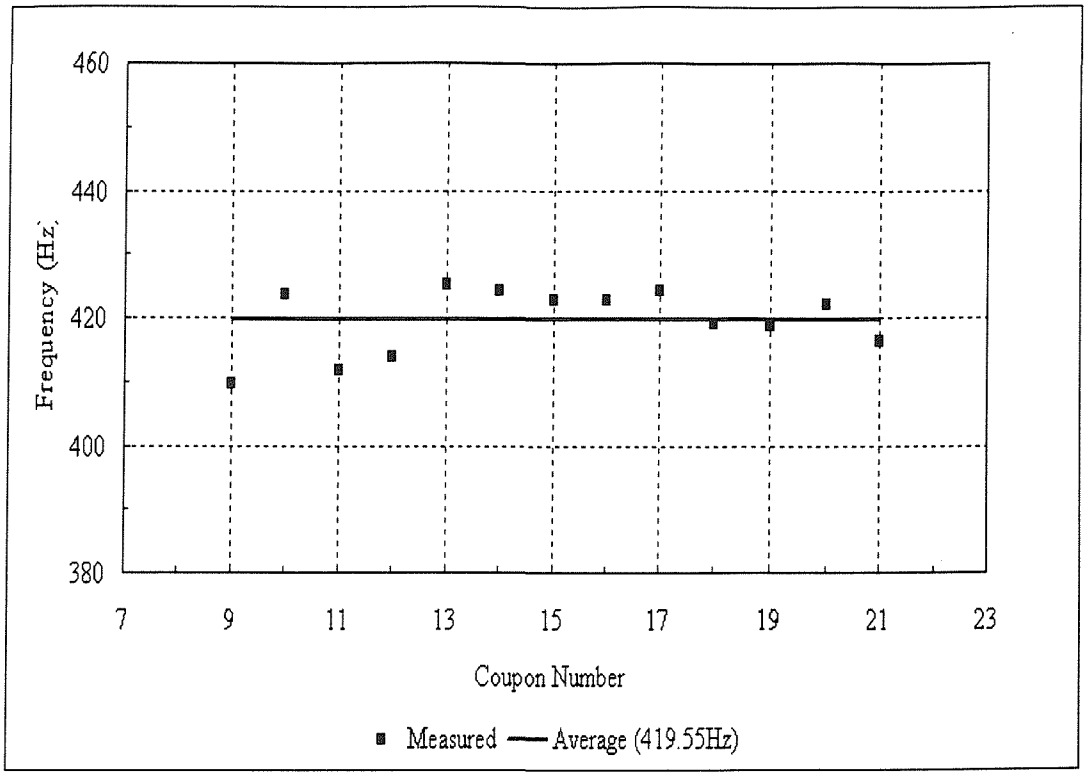

Maximum 425.Hz Minimum 409.6Hz Standard Deviation 4.966Hz

Figure 2.13 Measured resonance frequencies of the CFRP Tee-coupons in the freely supported condition

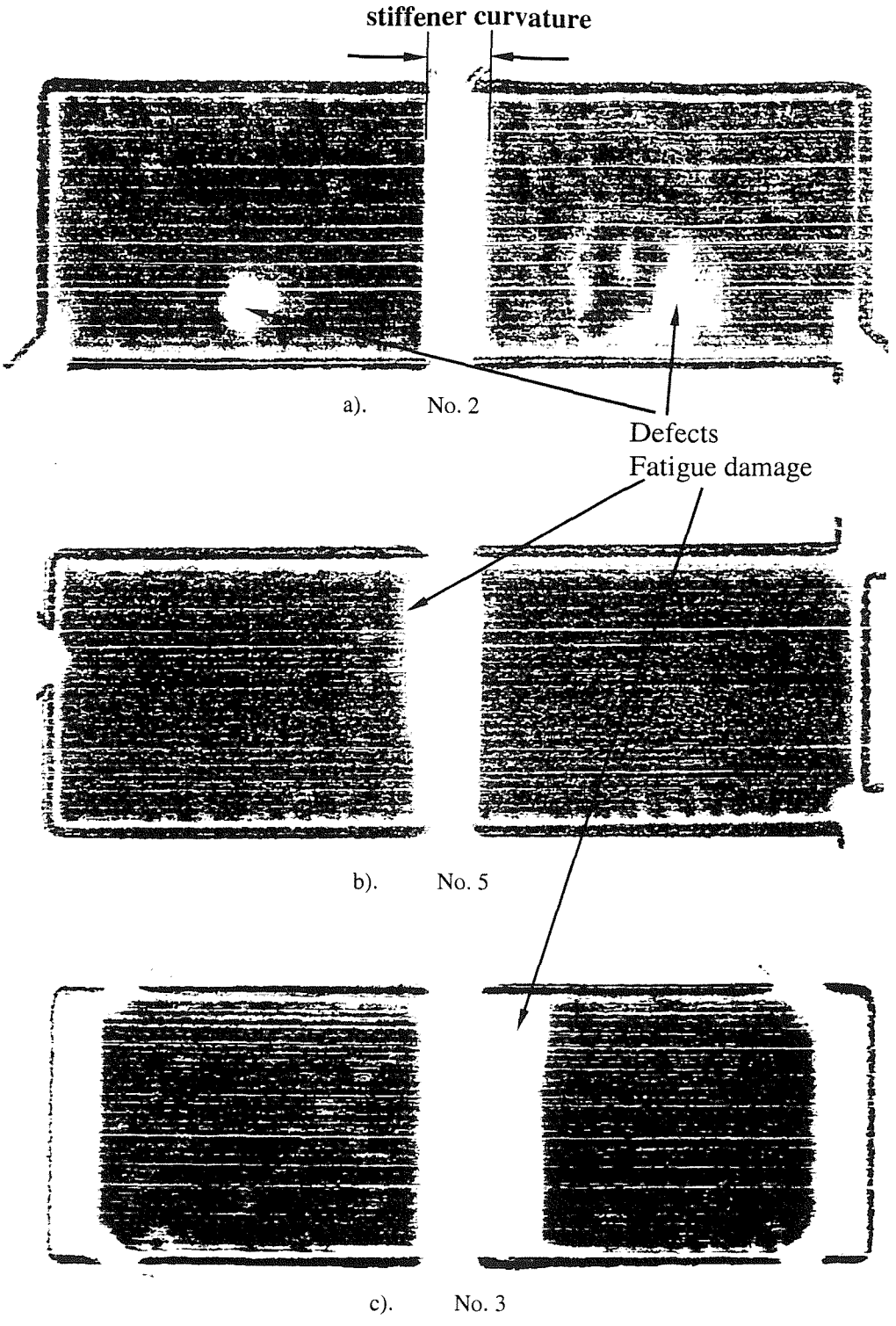

Figure 2.14 Ultrasonic C-scan results of CFRP Tee-coupons

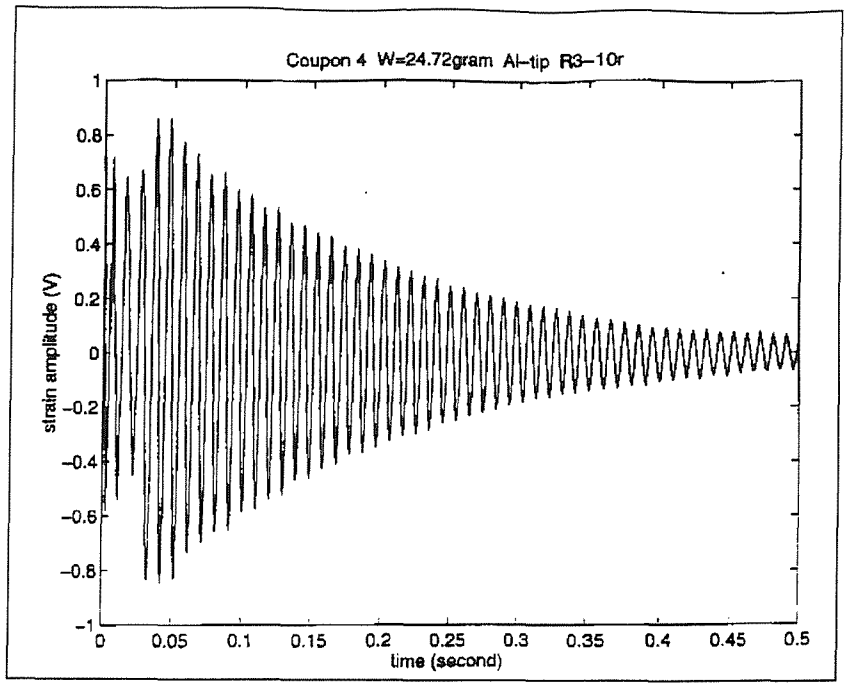

Figure 2.15 Free vibration decay signal of CFRP Tee-coupon excited by a transient force (Coupon No. 4, Hammer with aluminium tip)

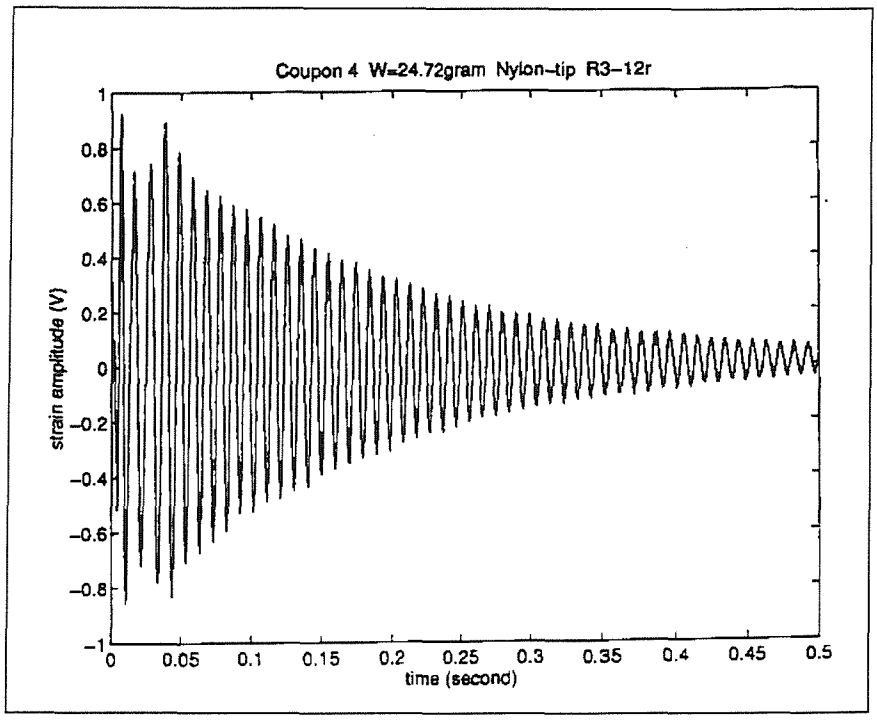

Figure 2.16 Free vibration decay signal of CFRP Tee-coupon excited by a transient force (Coupon No. 4 Hammer with Nylon tip)

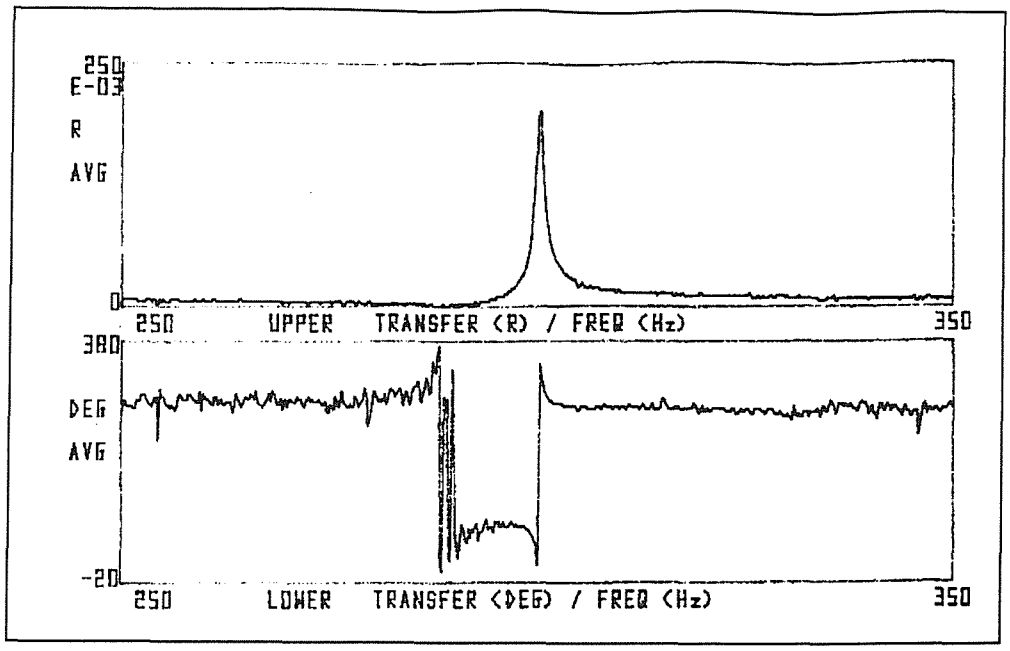

Figure 2.17 Transfer function of GLARE Tee-coupon (No. 1) under narrow band random noise excitation - mode 1 (Bandwidth 100Hz Centre frequency 300Hz)

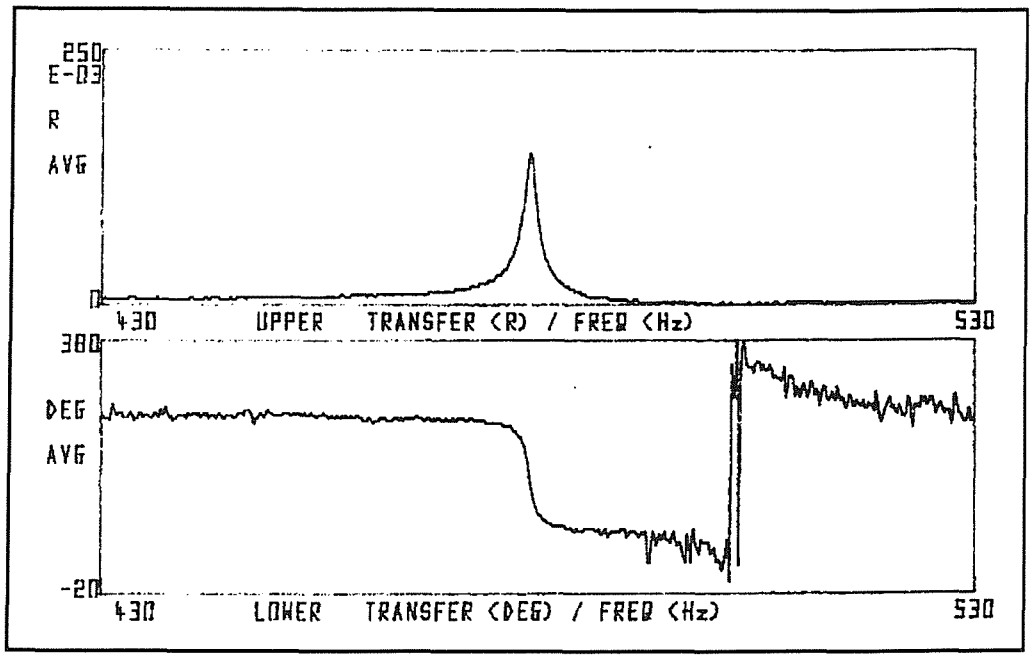

Figure 2.18 Transfer function of GLARE Tee-coupon (No. 1) under narrow random noise excitation - mode 2 (Bandwidth 1000Hz Centre frequency 540Hz)

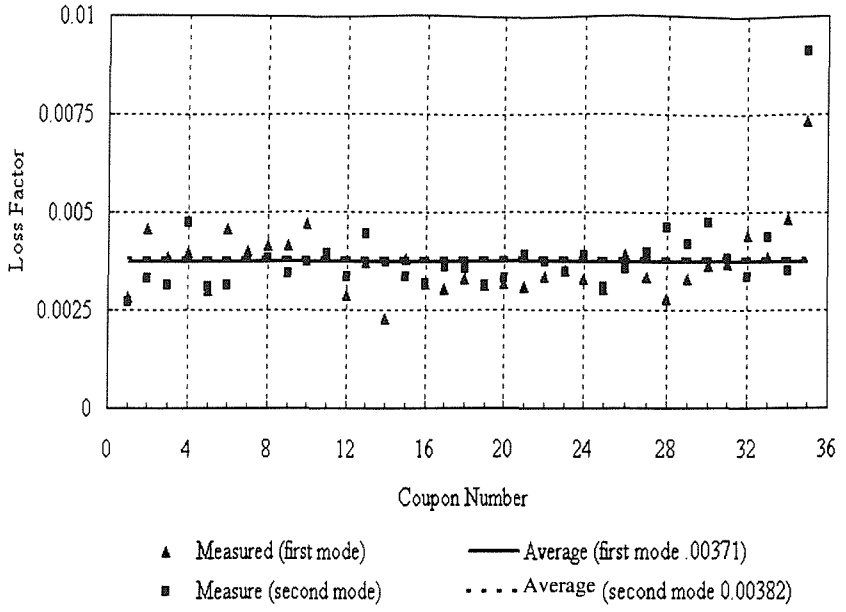

Maximum 0.00911 Minimum 0.00229 Standard Deviation 0.000949

Figure 2.19 Measured loss factors of the GLARE Tee-coupons in the freely supported condition

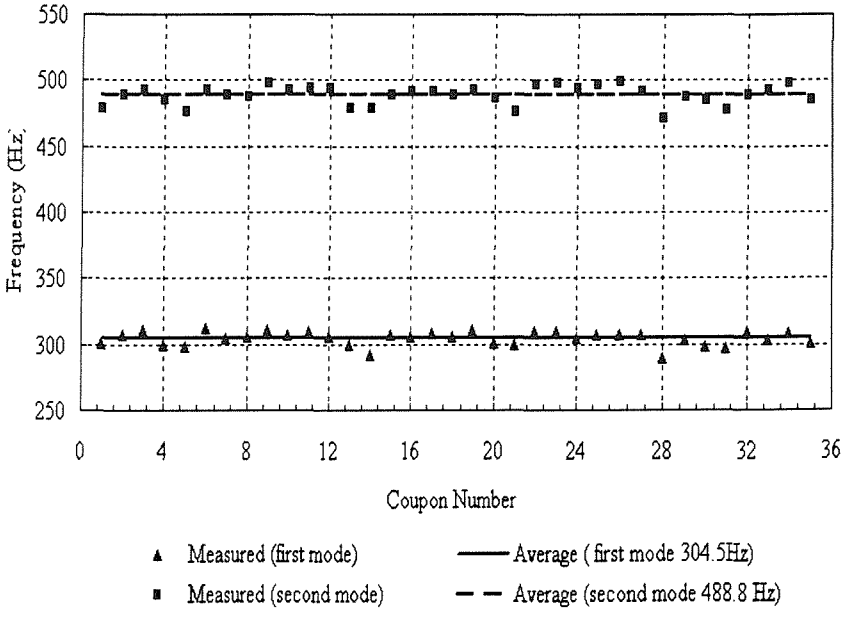

mode 1 - Maximum 312.2Hz Minimum 289.2Hz Standard Deviation 5.306Hz
mode 2 - Maximum 498.6Hz Minimum 470.6Hz Standard Deviation 7.044Hz

Figure 2.20 Measured resonance frequencies of the GLARE Tee-coupons in the freely supported condition

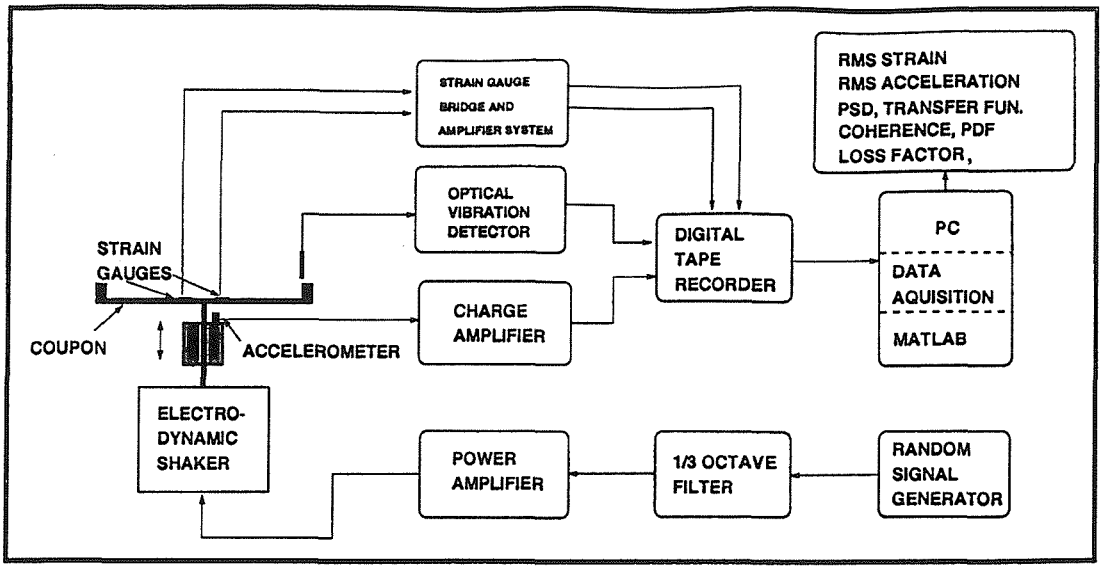

Figure 2.21 Schematic diagram of the test rig for endurance test of Tee-coupons

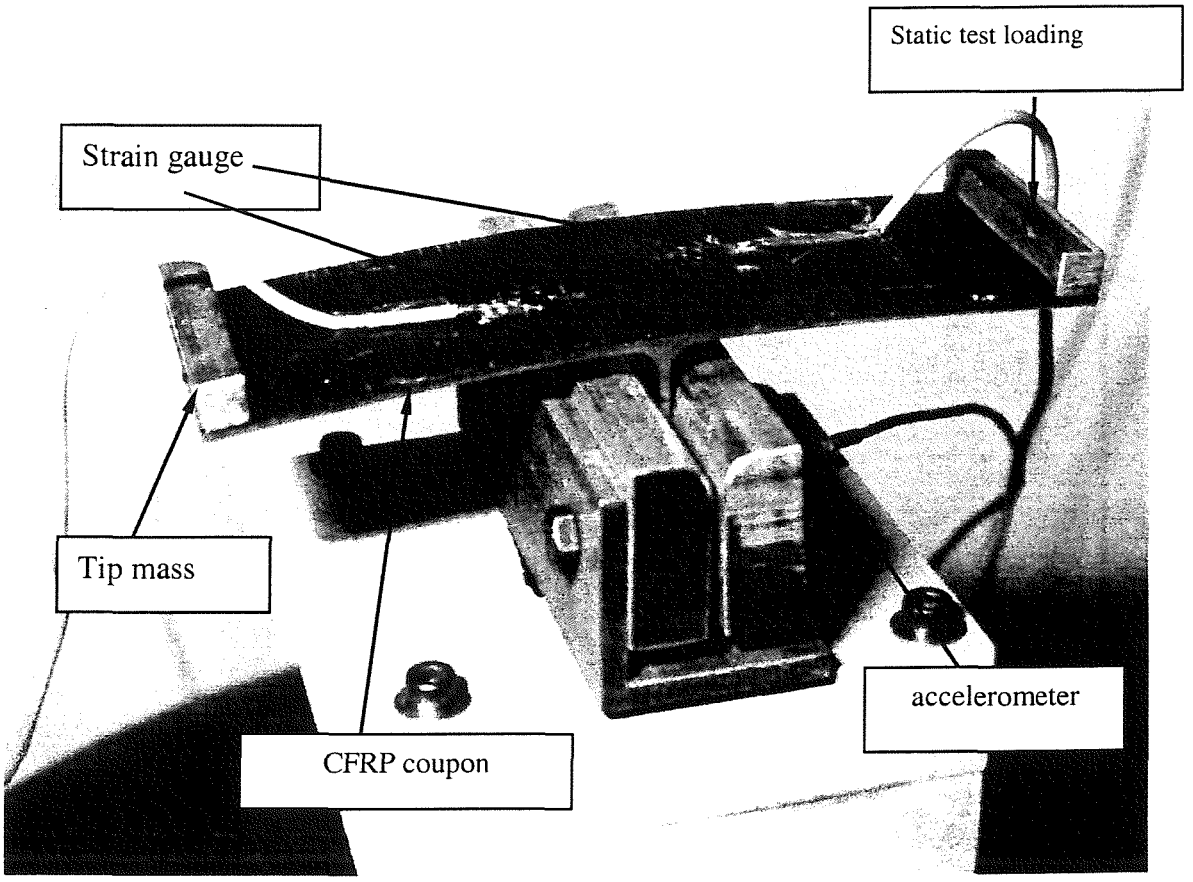

Figure 2.22 CFRP Tee-coupon mounted on the shaker

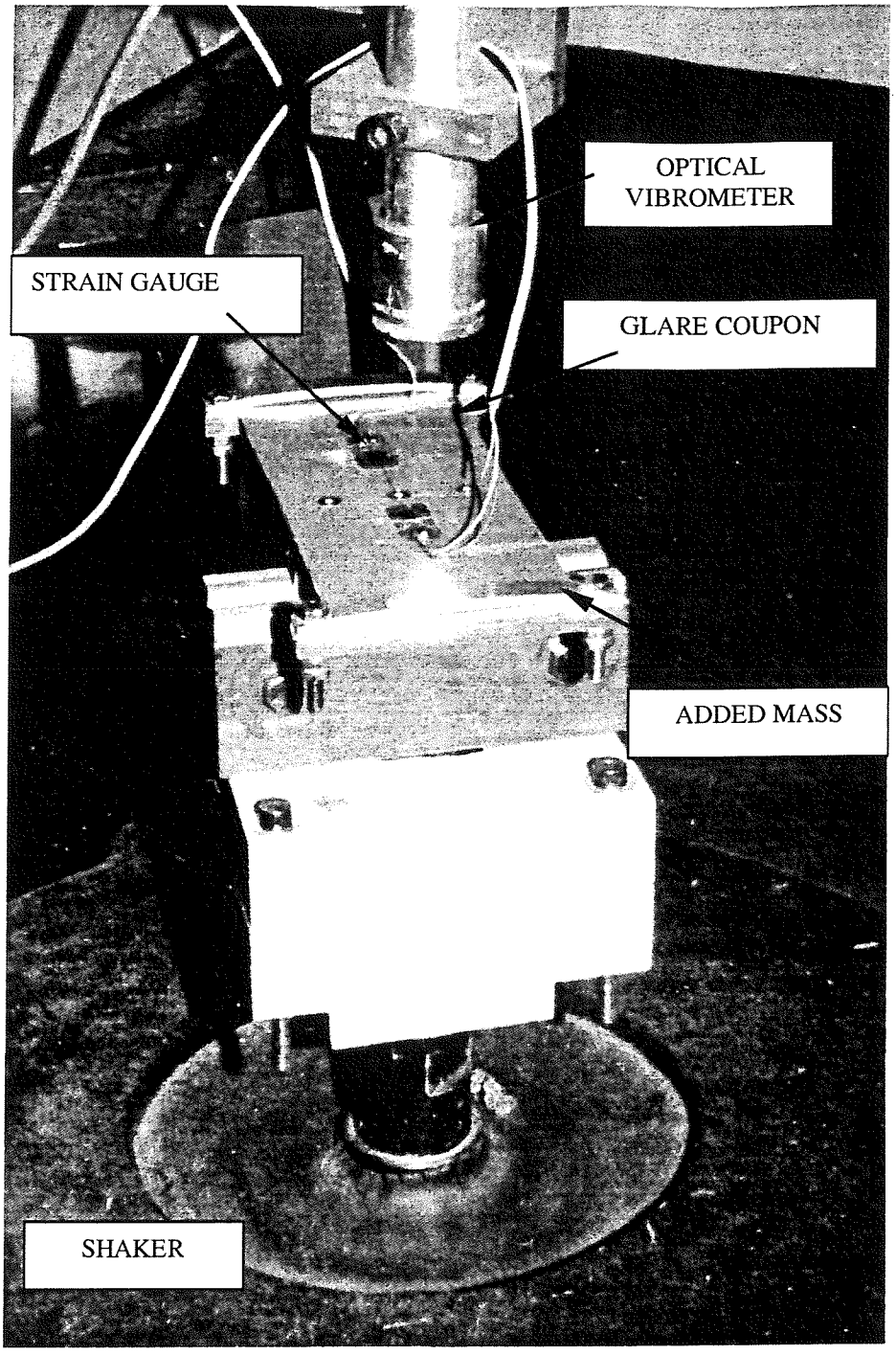

Figure 2.23 GLARE coupon mounted on the shaker for the endurance test

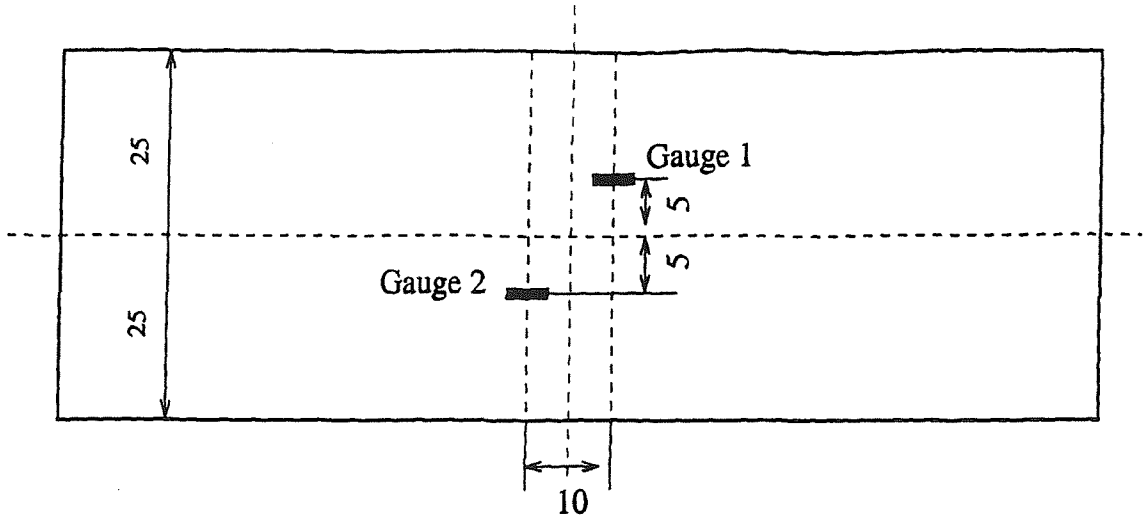

Figure 2.24 Strain gauge location for fatigue test of CFRP Tee-coupons

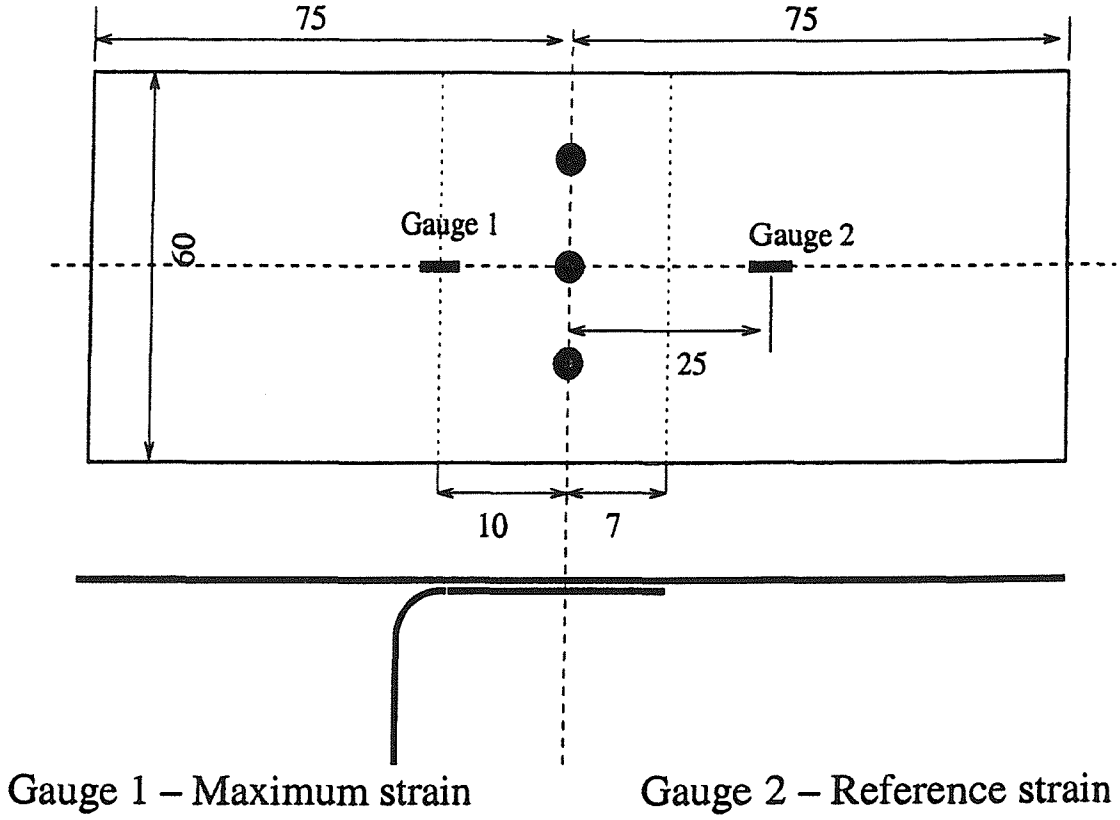

Figure 2.25 Strain gauge location for fatigue test of GLARE Tee-coupons

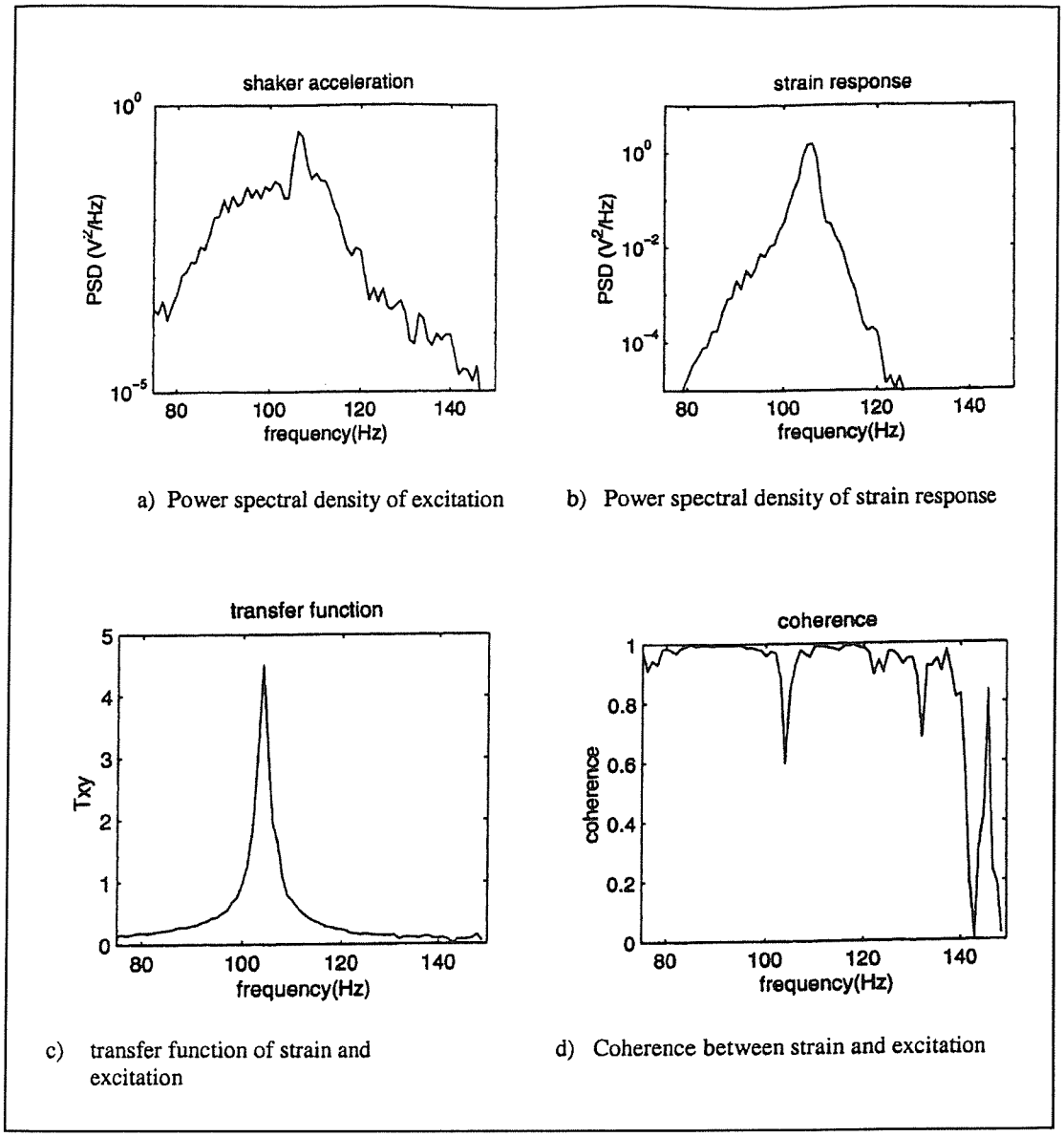

a) Power spectral density of excitation

b) Power spectral density of strain response

c) transfer function of strain and excitation

d) Coherence between strain and excitation

Figure 2.26 Fatigue test results of CFRP Tee-coupon No. 5

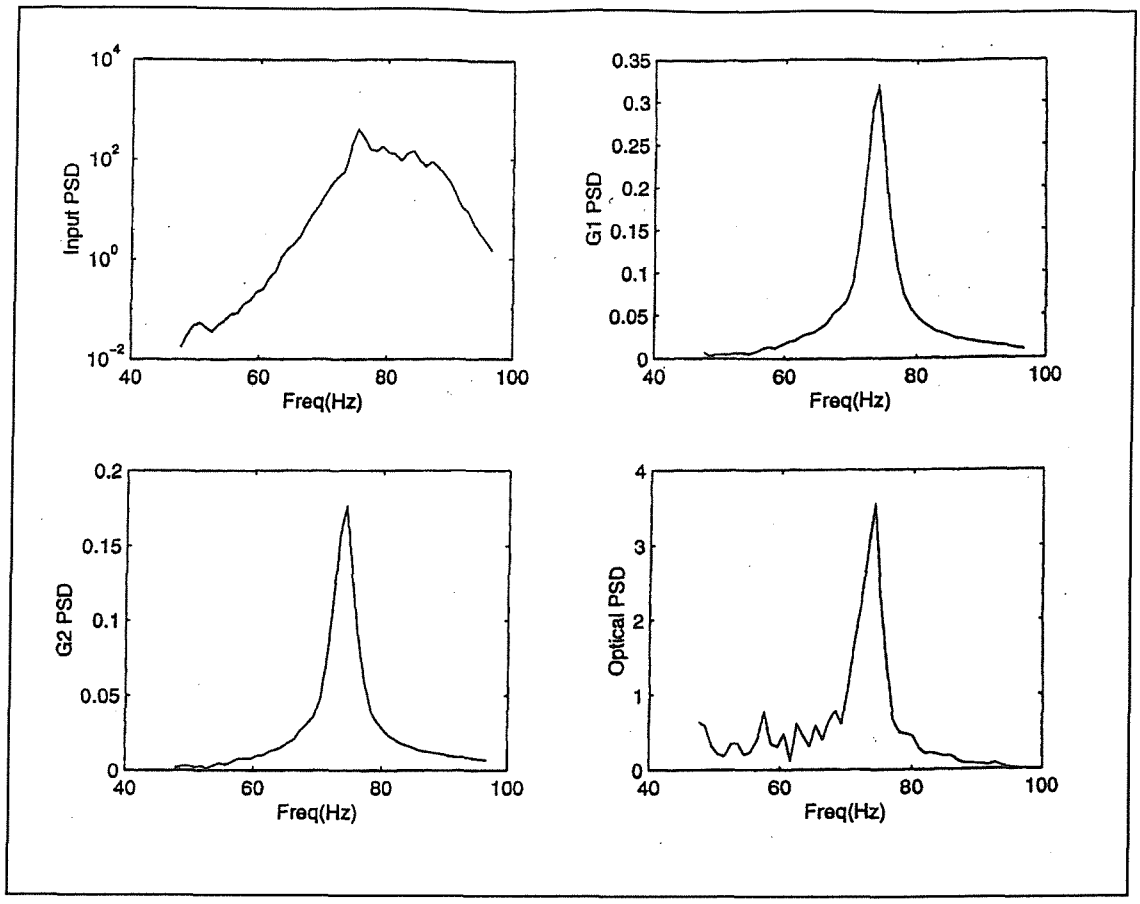

Figure 2.27 Fatigue test results of GLARE Tee-coupon No. 34

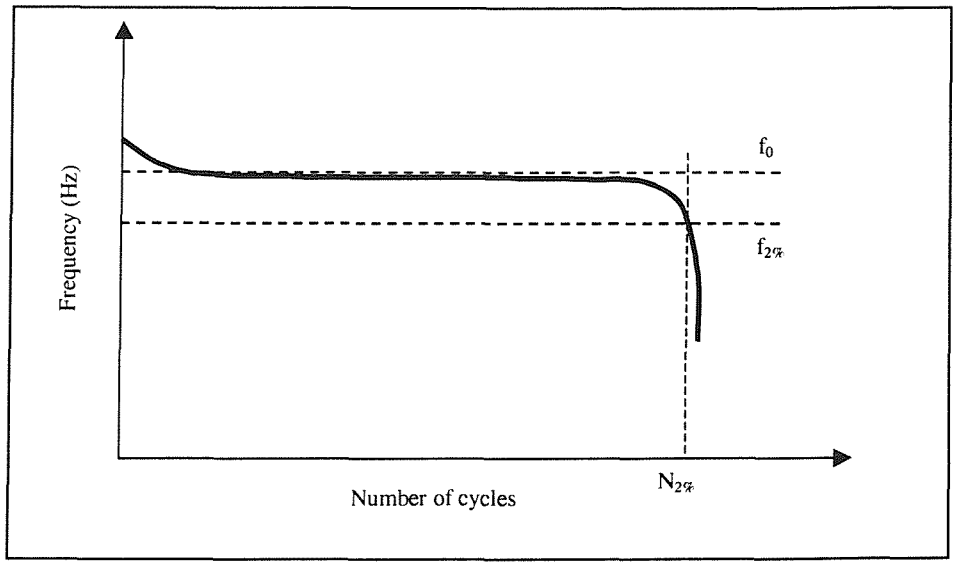

Figure 2.28 Definition of frequency terms

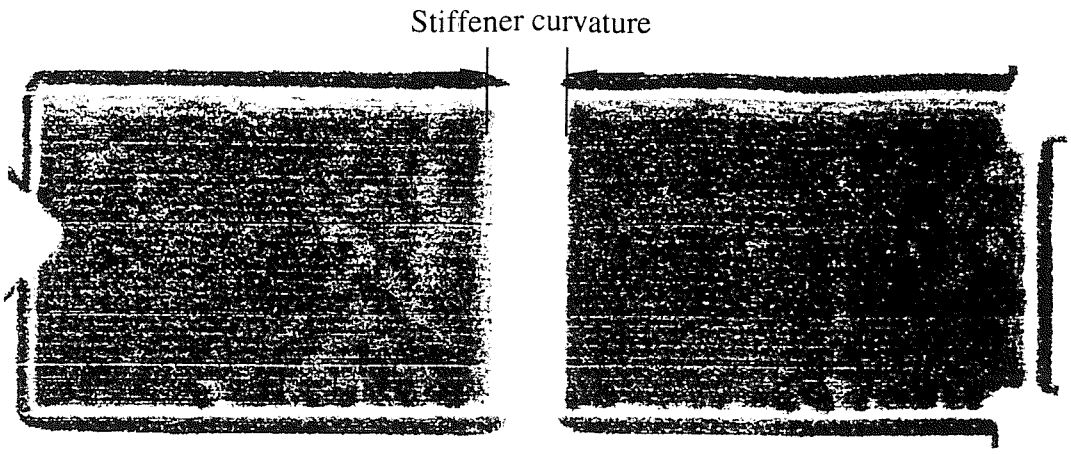

a) Before endurance testing

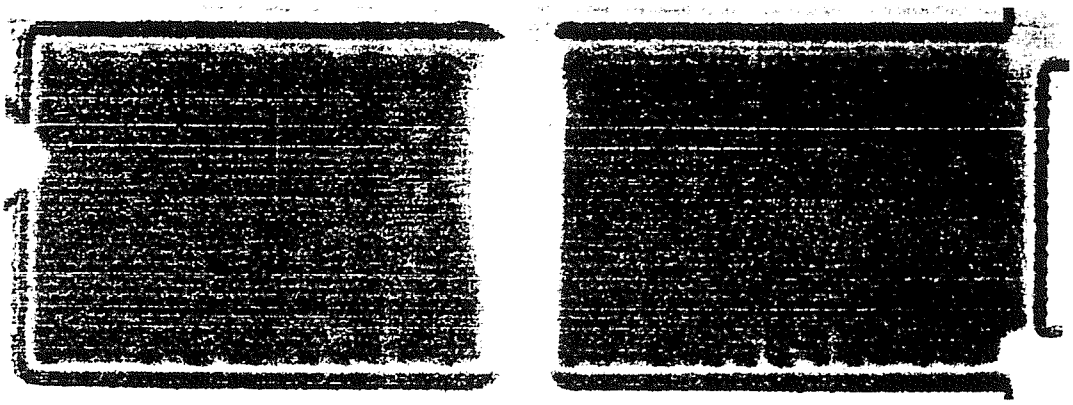

b) N=28026

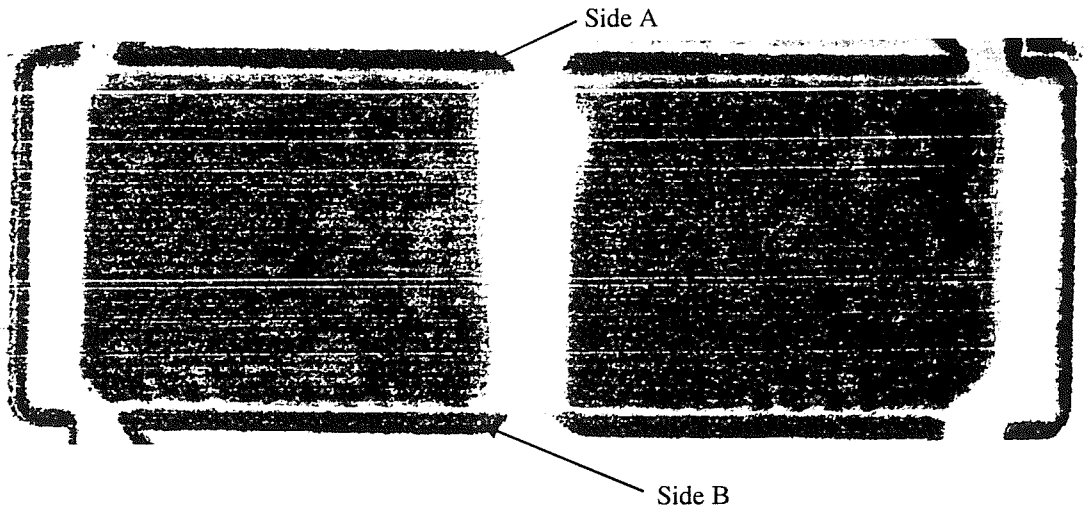

c) Damage became visible

Figure 2.29 Ultrasonic C-scan pictures of CFRP Tee-coupon No. 5 (excited at RMS surface strain of 2642.4μ strain)

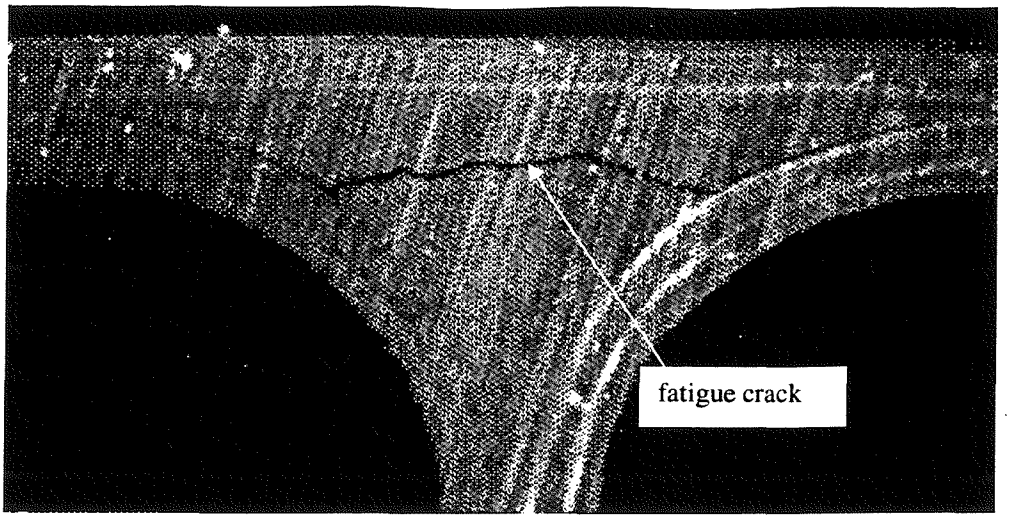

a) side A

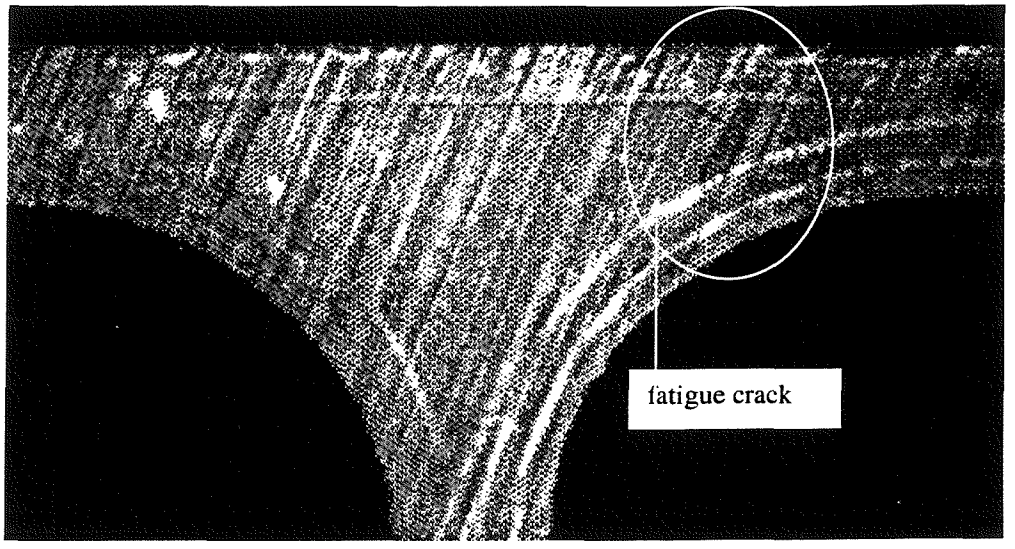

b) side B

Figure 2.30 Fatigue cracks in CFRP Tee-coupon No. 5

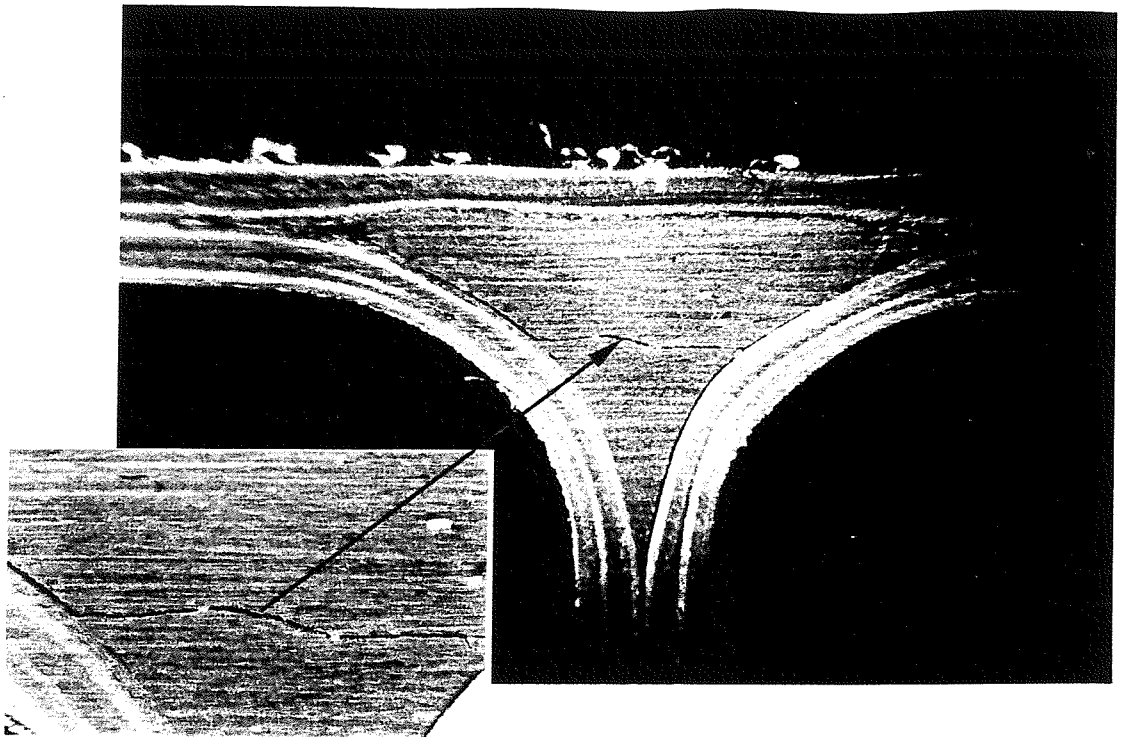

a) Side A

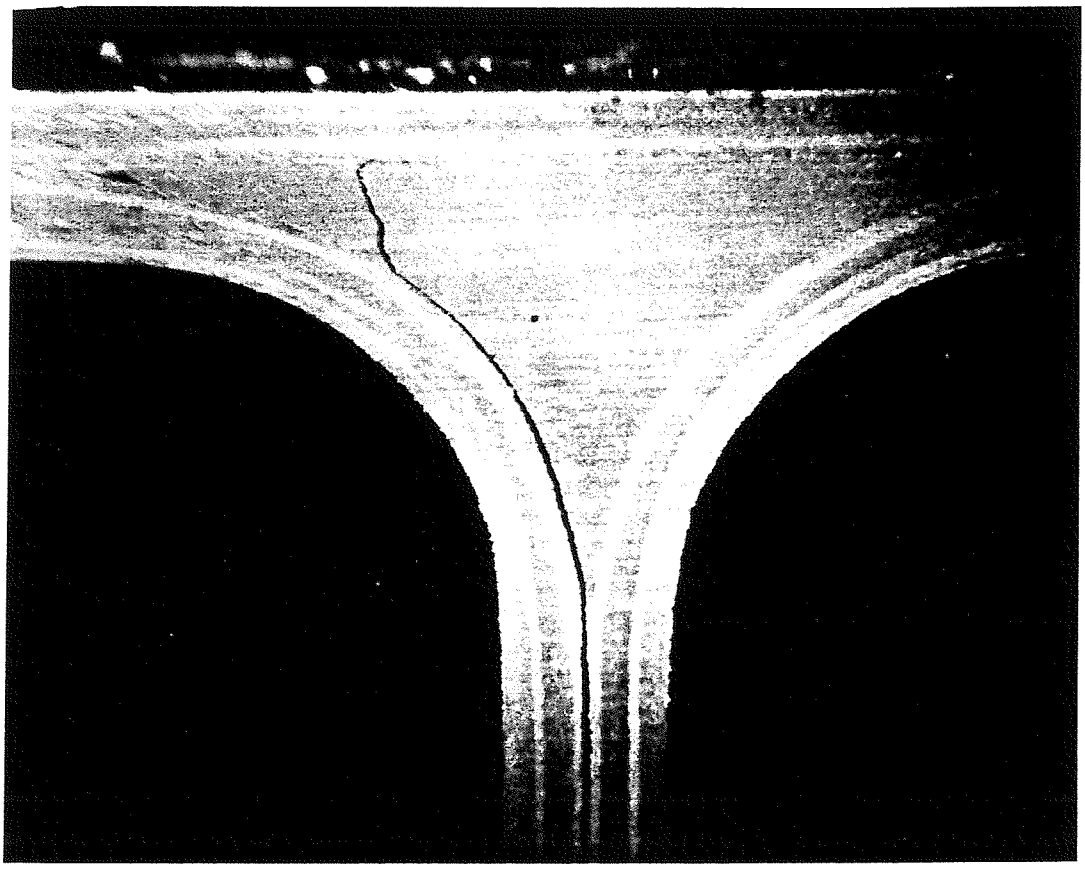

c) Side B

Figure 2.31 Fatigue cracks in CFRP Tee-coupon No. 6

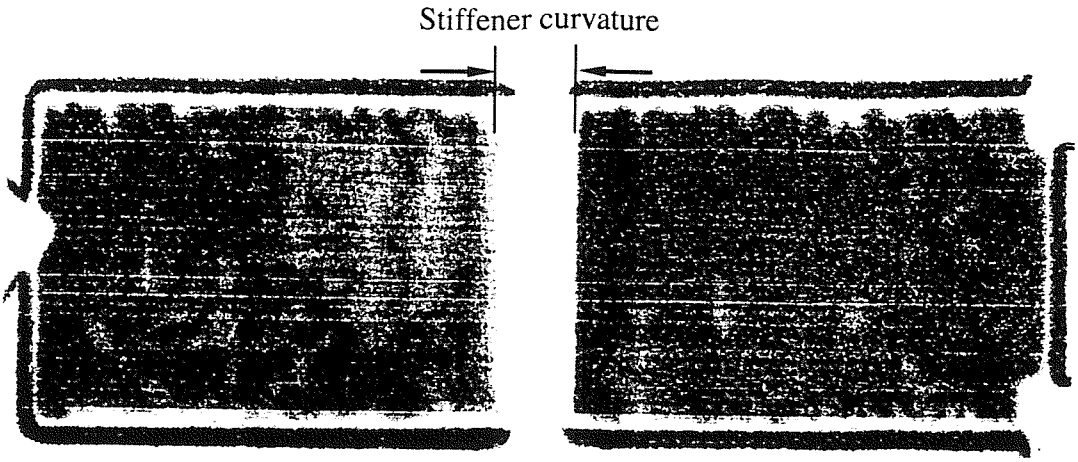

a) Before test

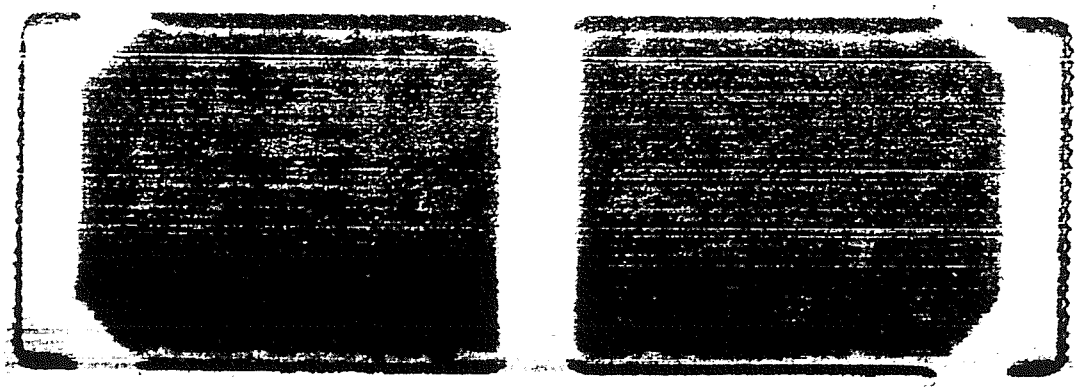

b) Damage became visible

Figure 2.32 Ultrasonic C-scan pictures of CFRP Tee-coupon No. 6

Stiffener curvature

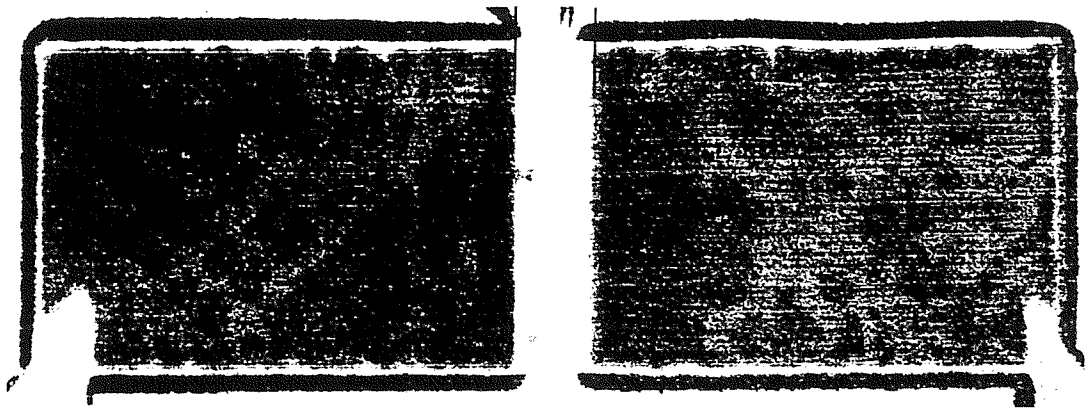

a) Before test

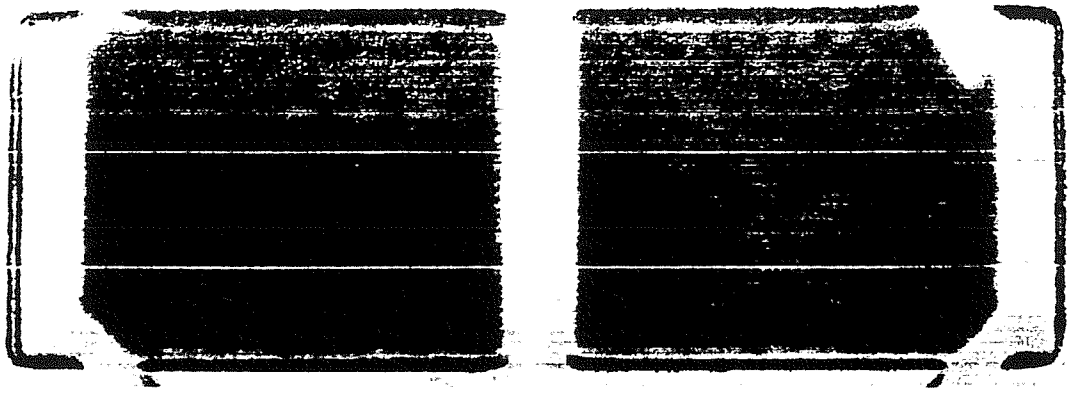

b) N=1512192

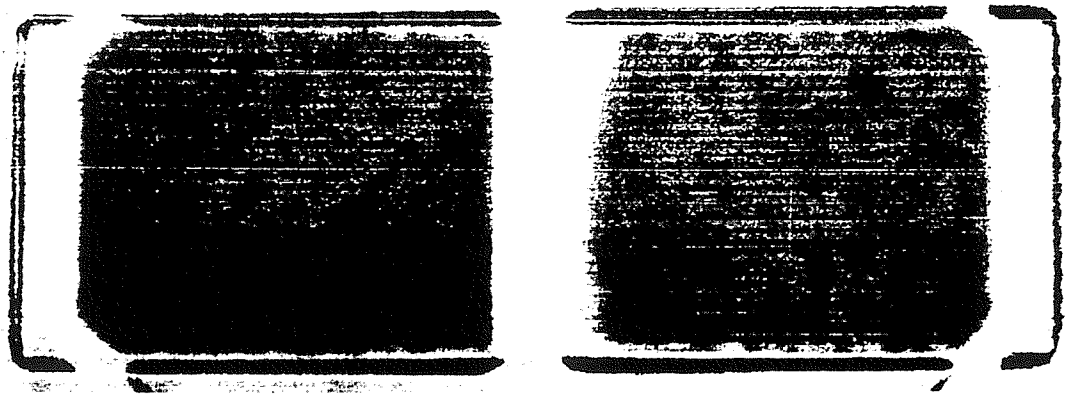

c) Damage became visible

Figure 2.33 Ultrasonic C-scan pictures of CFRP Tee-coupon No. 4 (N – number of cycles) (excited at RMS surface strain of 986.6μ strain)

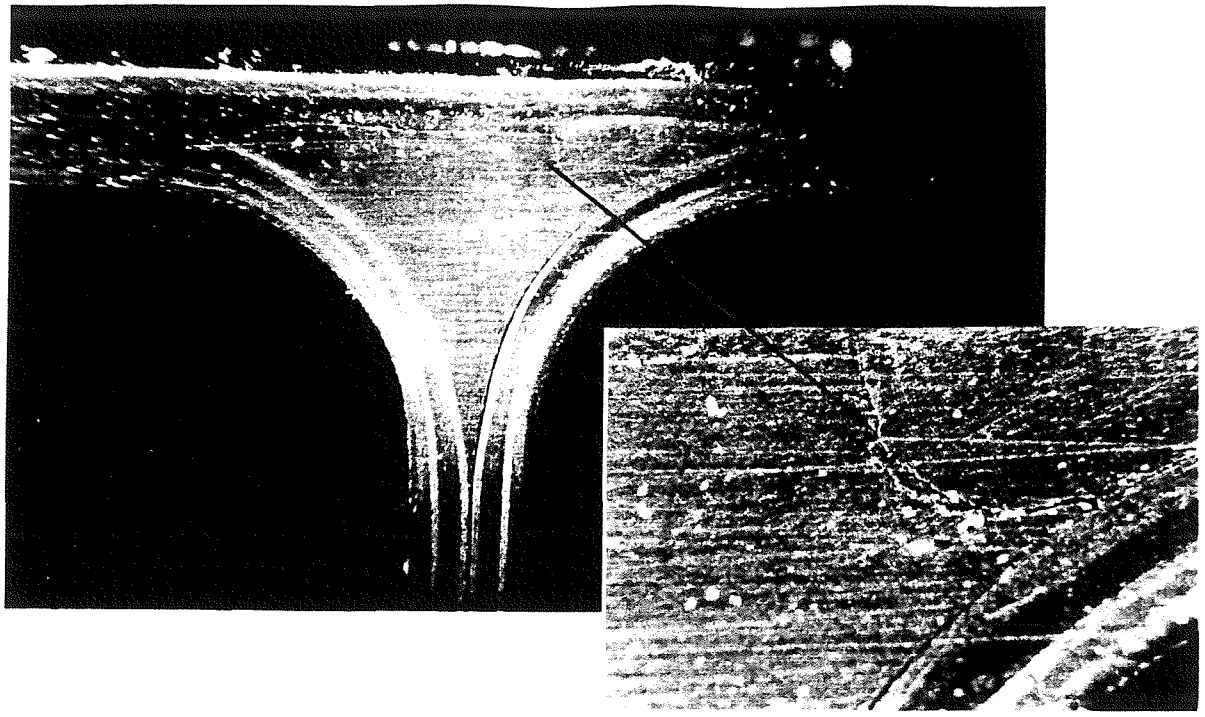

a). Side A

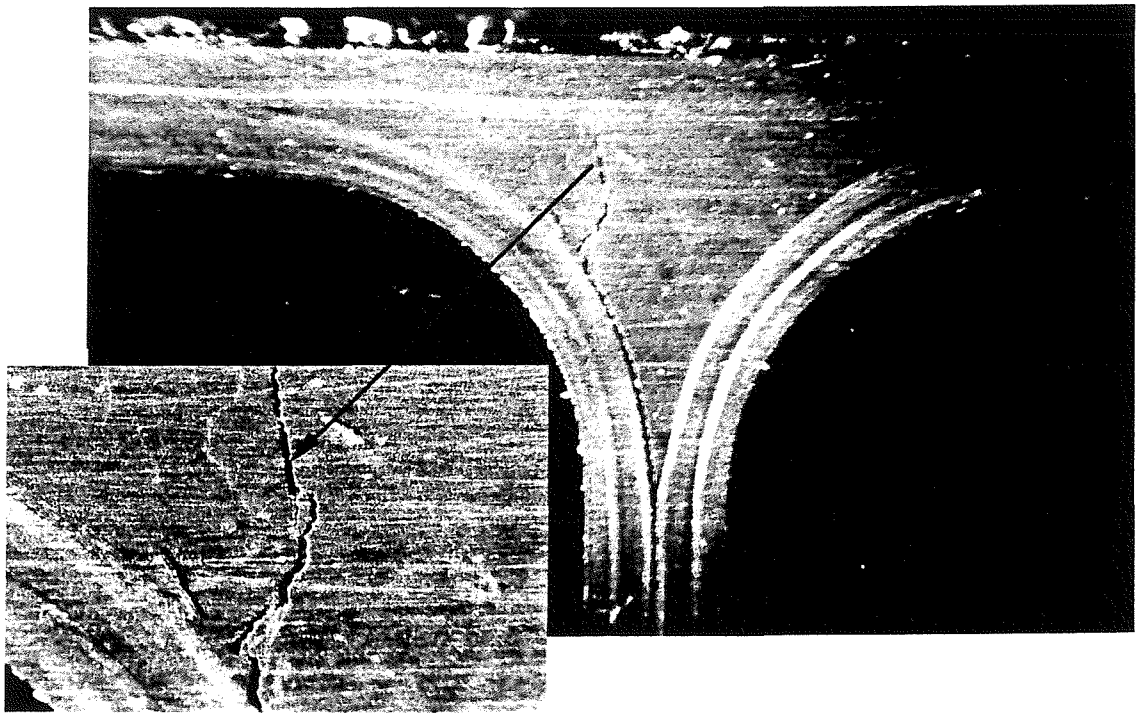

b). Side B

Figure 2.34 Fatigue cracks in CFRP Tee-coupon No. 4

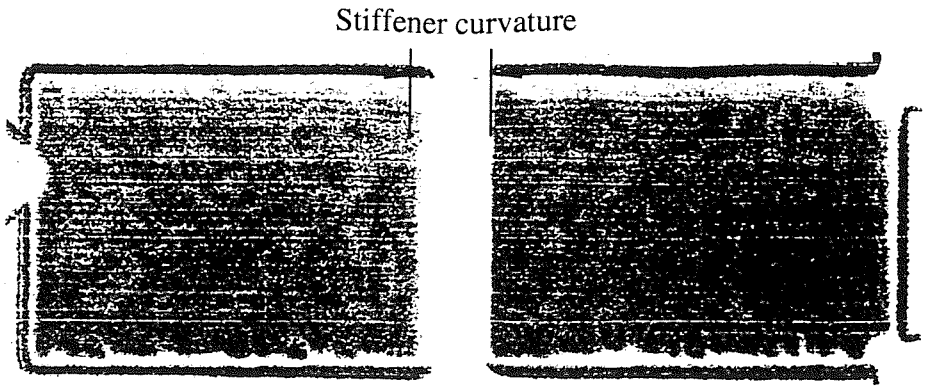

a) N=0

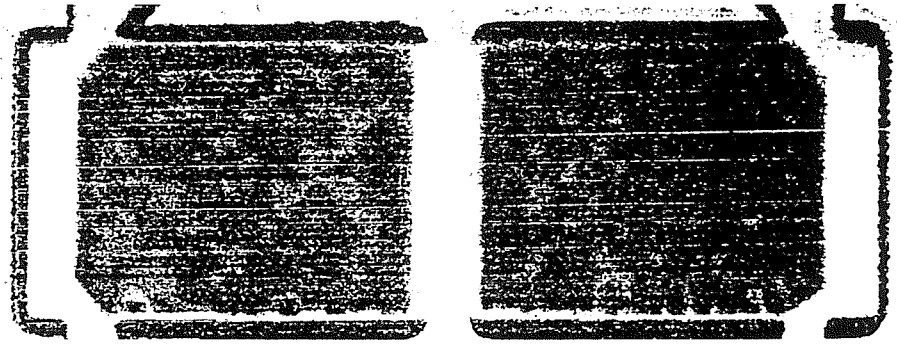

b) N=448520

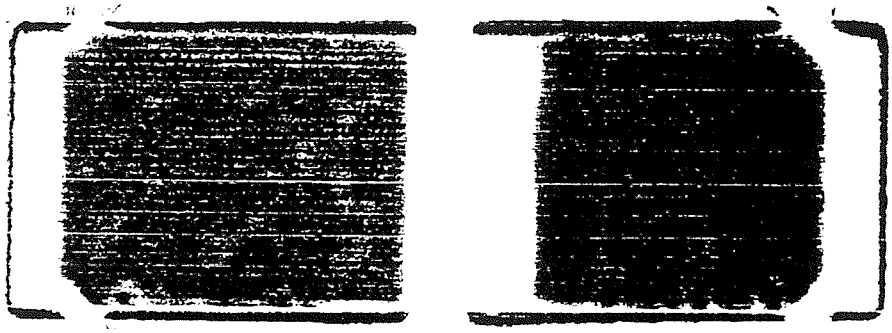

c) N=1371328

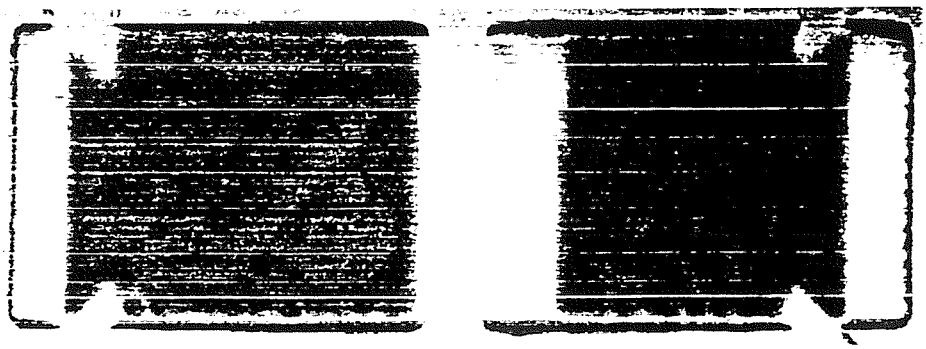

d) Complete failure

Figure 2.35 Ultrasonic C-scan pictures of CFRP Tee-coupon No. 3 (N – number of cycles) (excited at RMS surface strain of 1791με)

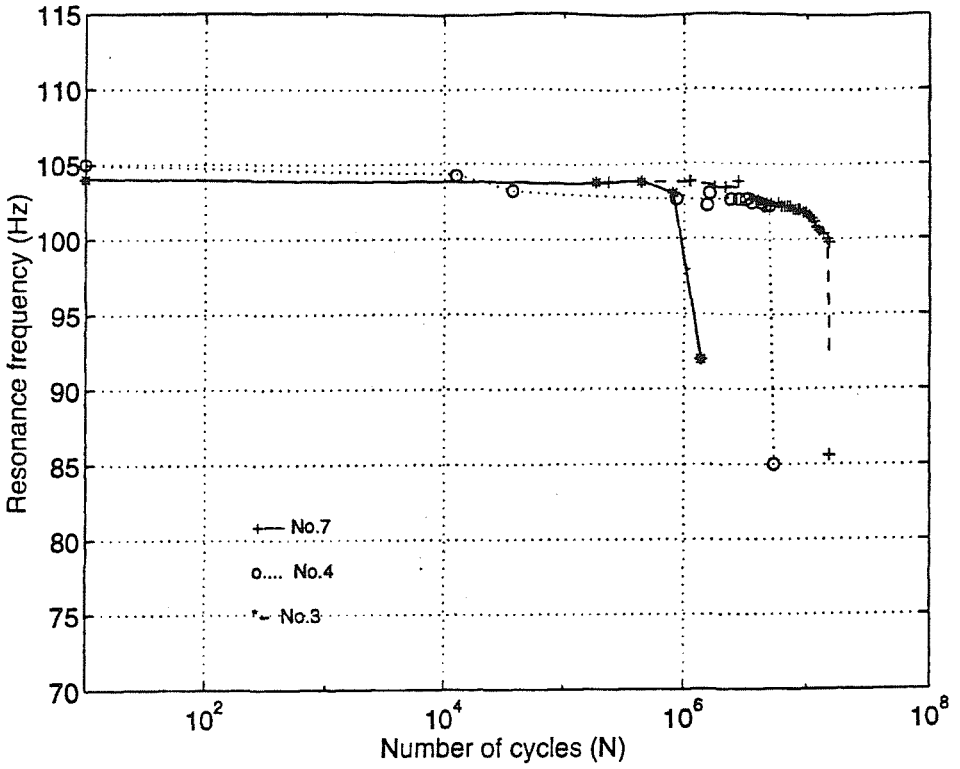

Figure 2.36 Resonance frequency change of the CFRP coupons with number of cycles

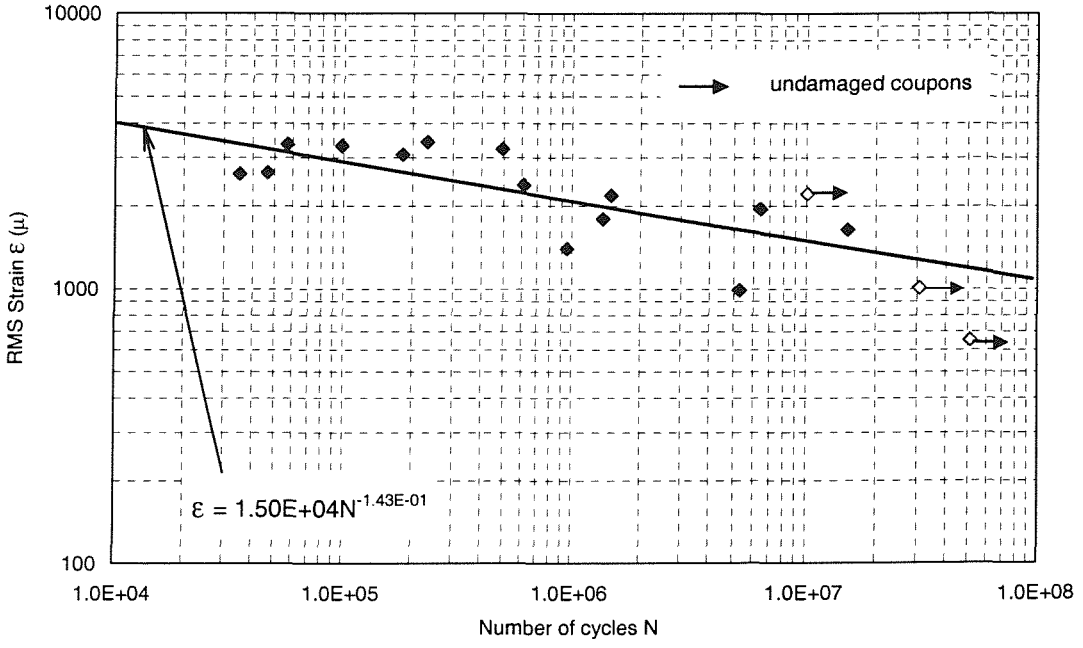

Figure 2.37 Fatigue data of the CFRP Tee-coupons

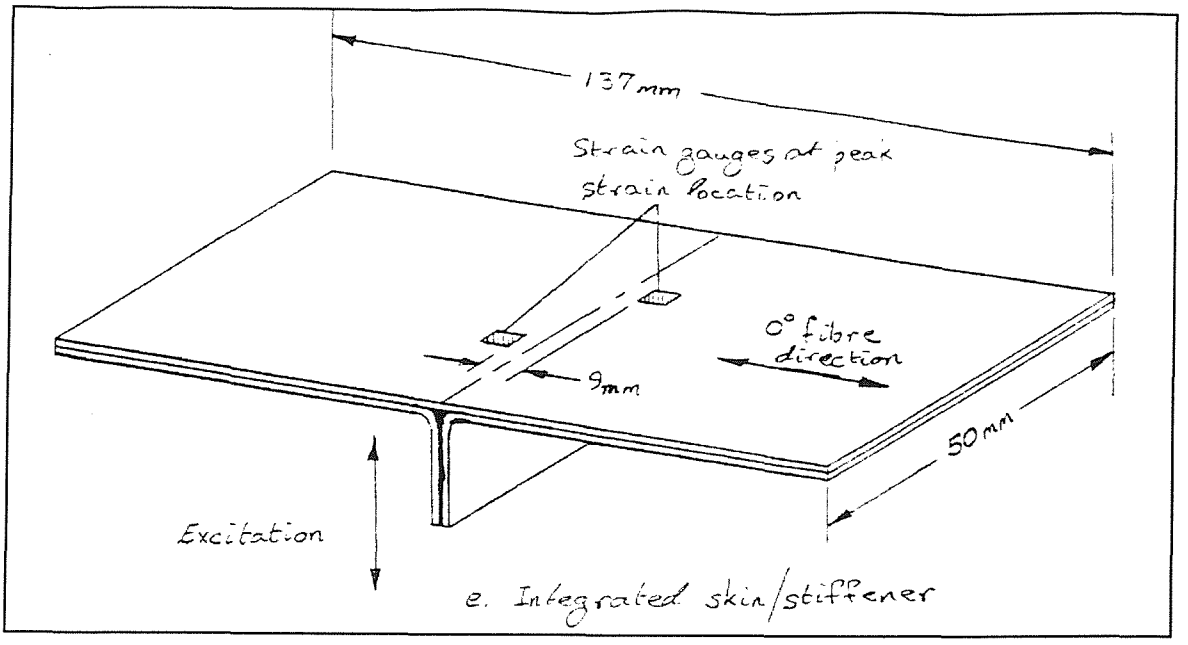

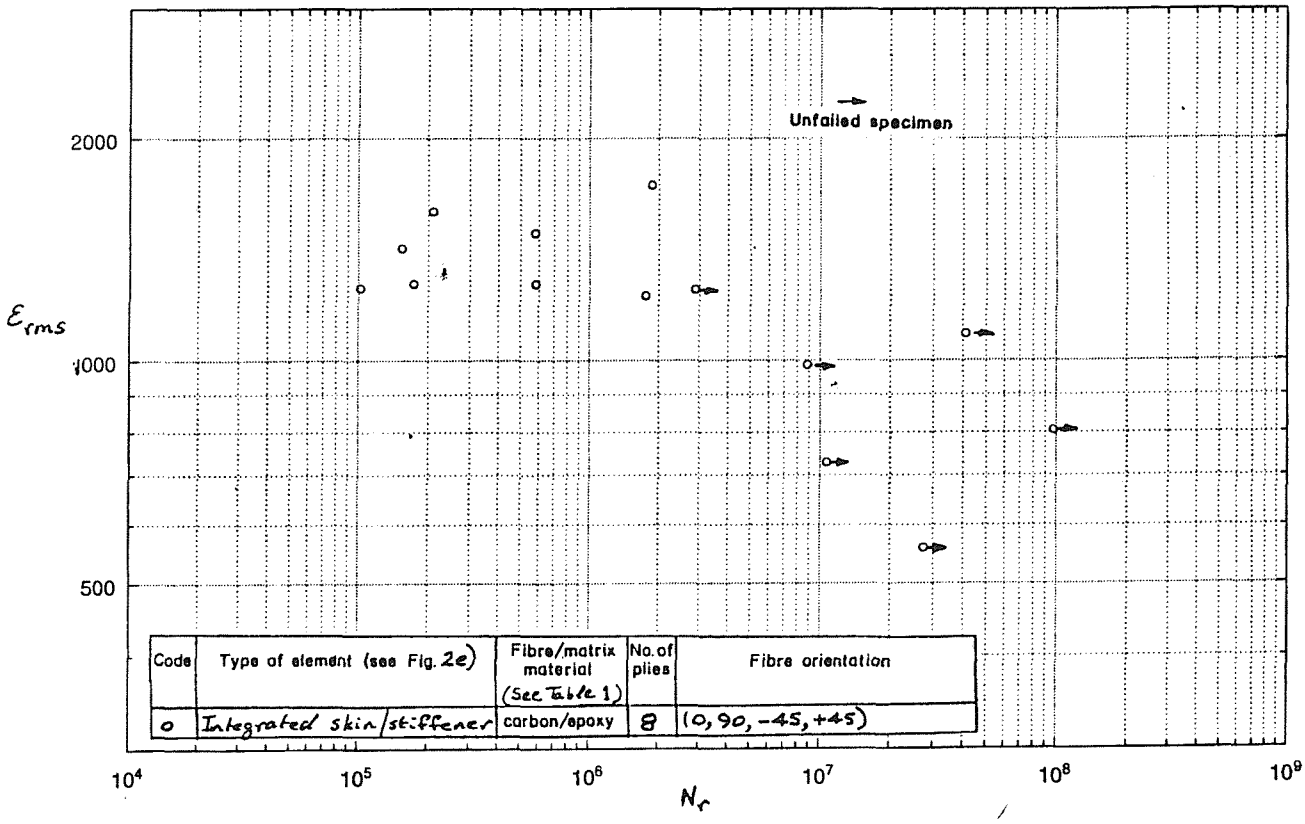

Figure 3.38 Reference fatigue data of CFRP Tee-coupons - ESDU Data sheet 84027

(A permission has been granted by ESDU to use these figures , Appendix H)

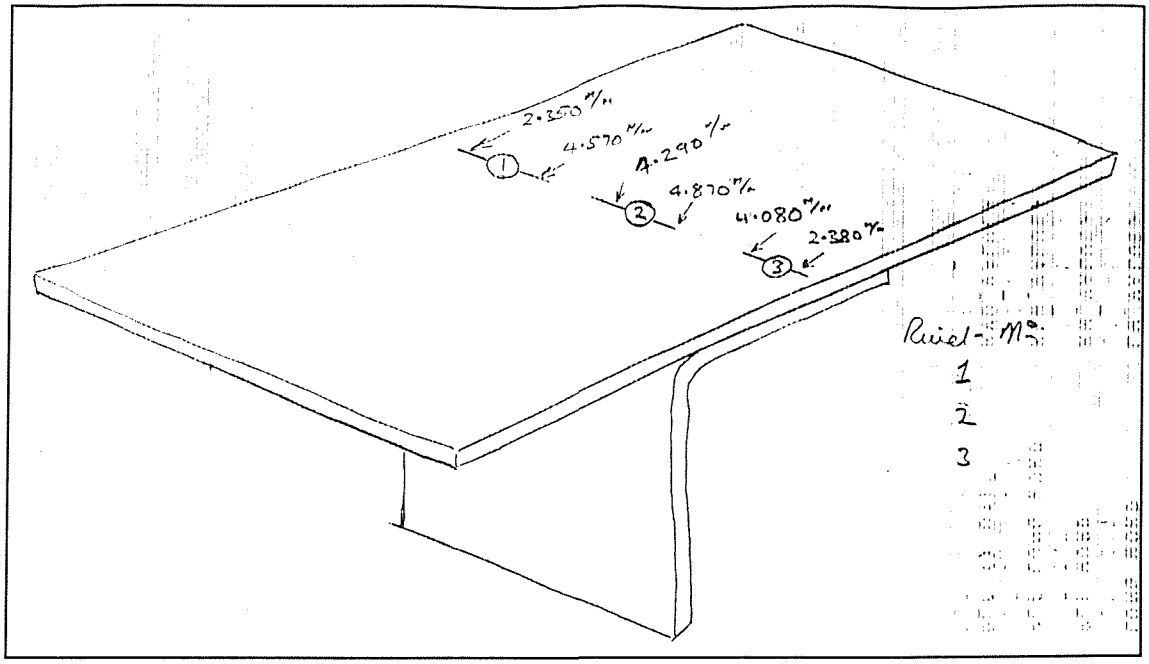

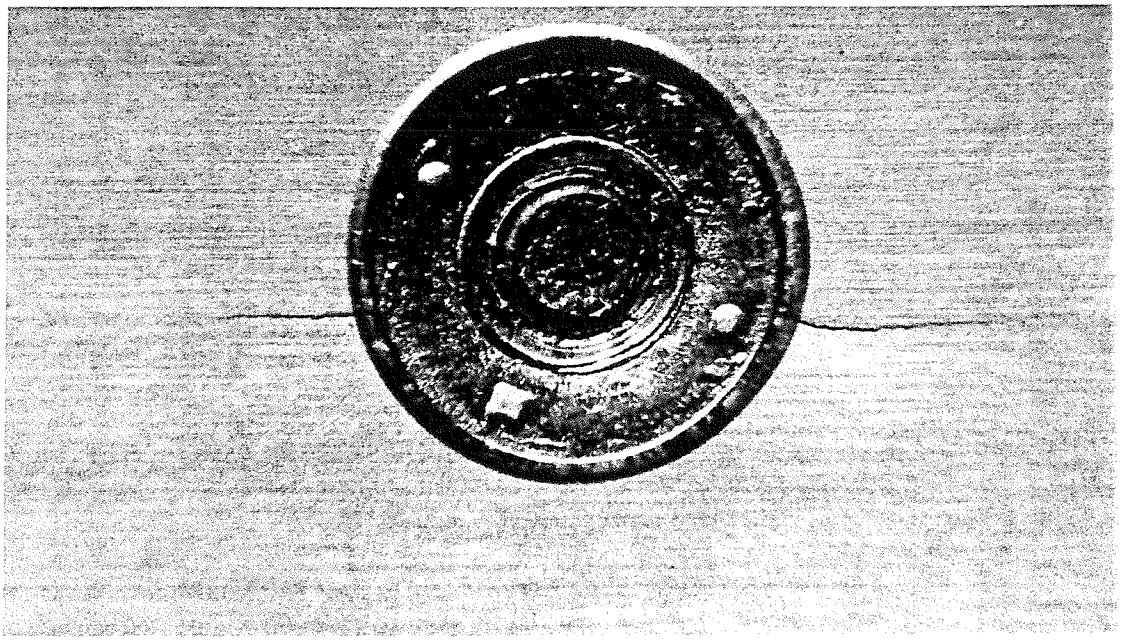

close look of crack at rivet No. 3

Figure 2.39 Fatigue cracks of GLARE No. 6

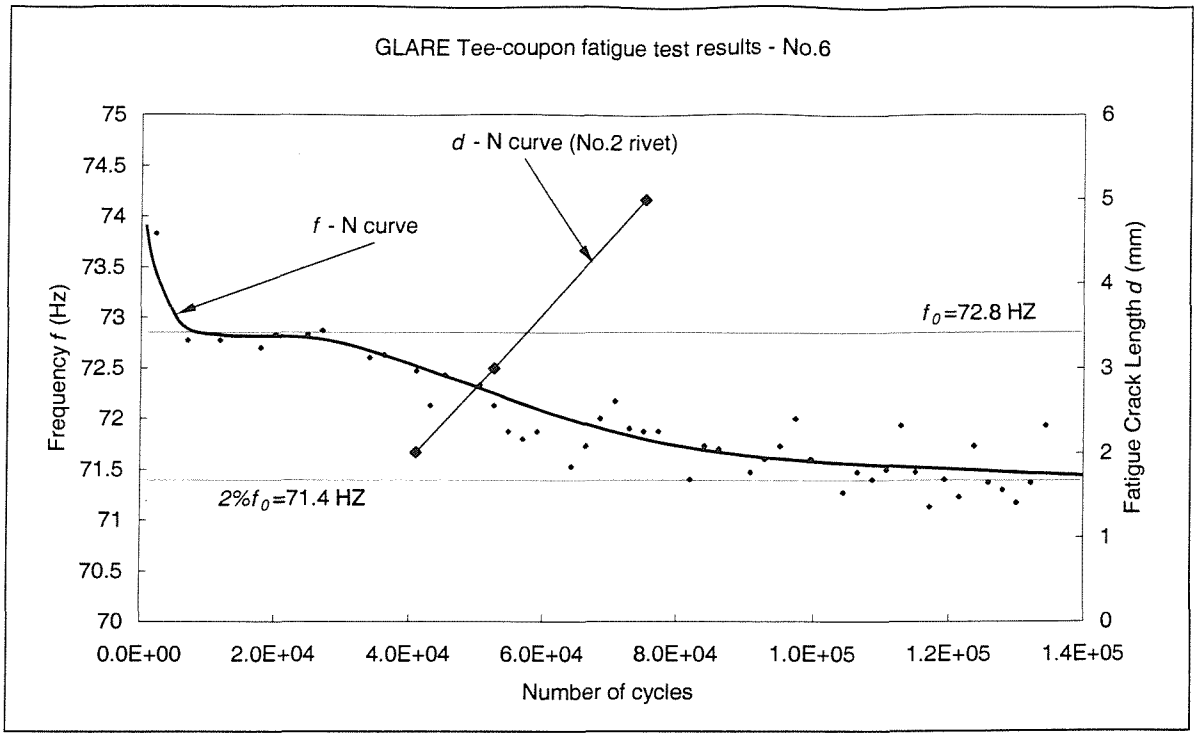

Figure 2.40 Resonance frequency and fatigue crack length verse number of cycles (GLARE Tee-coupon No. 6)

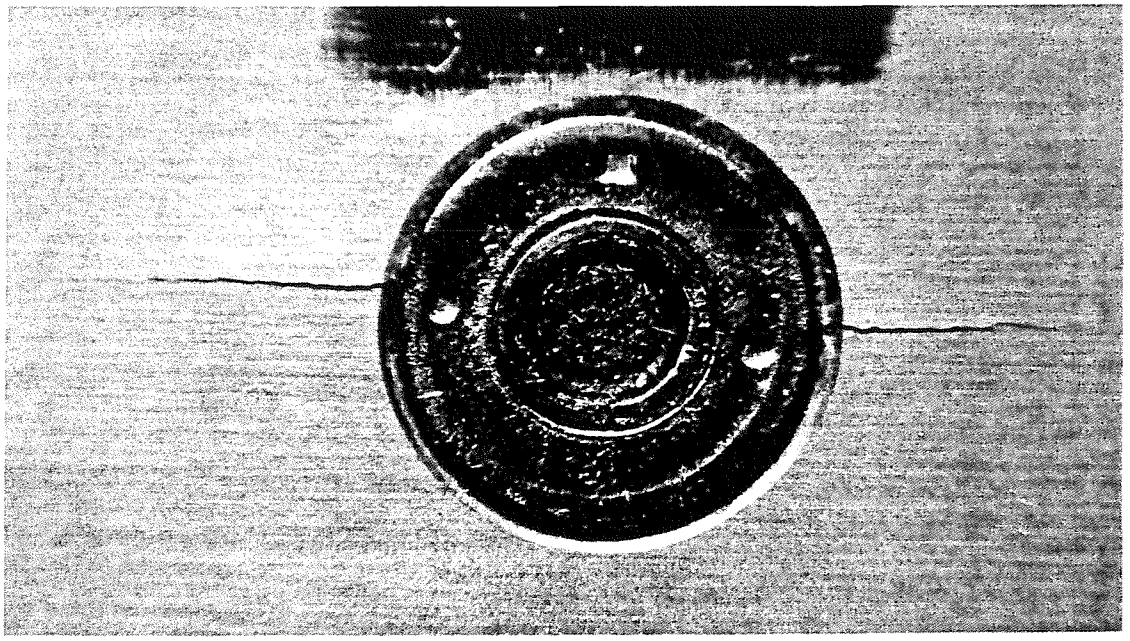

close look of crack at rivet No. 2

Figure 2.41 Fatigue cracks of GLARE No. 34

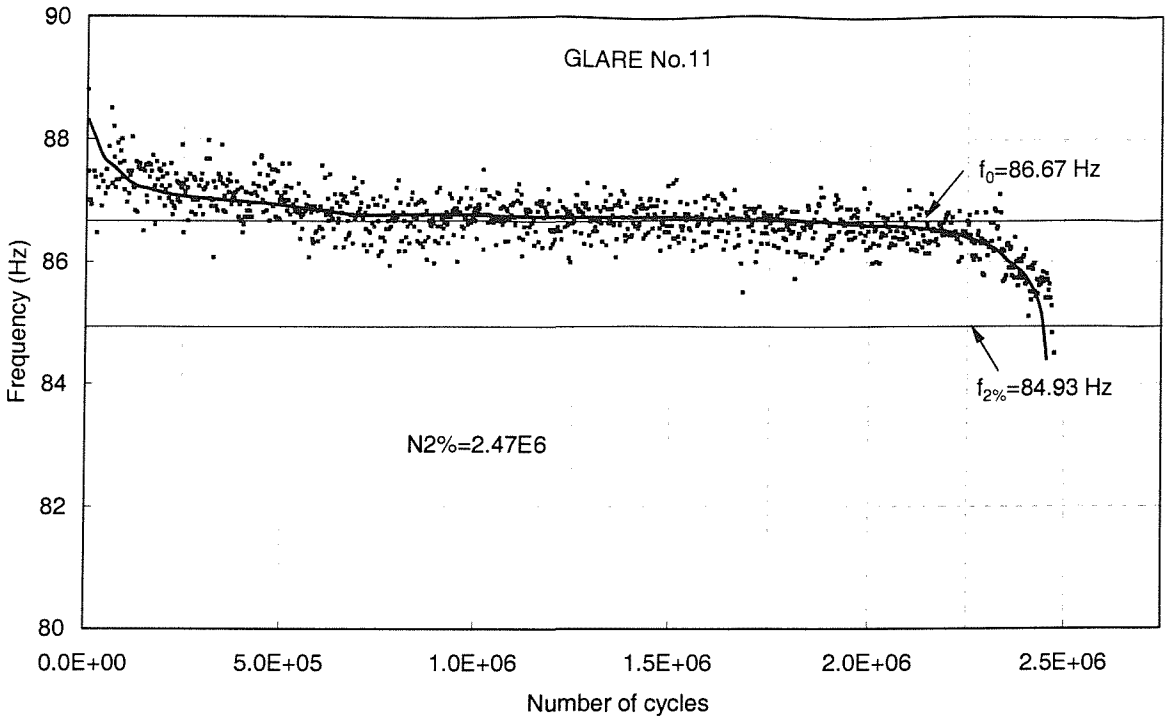

Figure 2.42 Resonance frequency versus number of cycles (GLARE Tee-coupon No. 11)

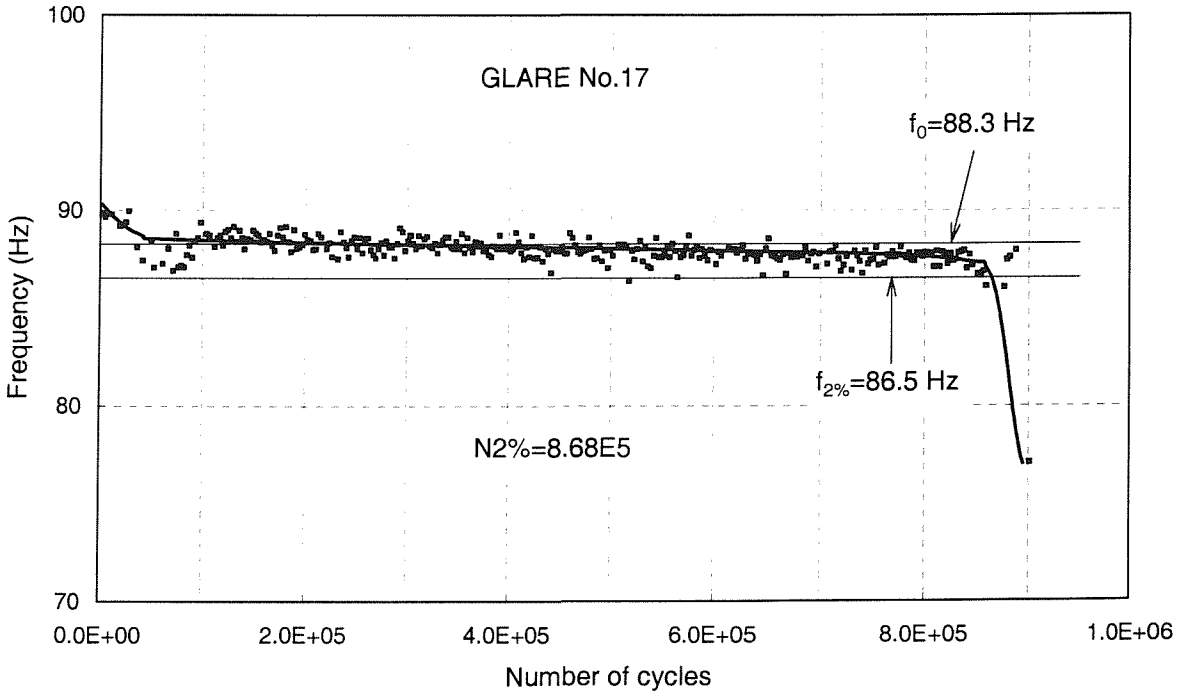

Figure 2.43 Resonance requency versus number of cycles (GLARE Tee-coupon No. 17)

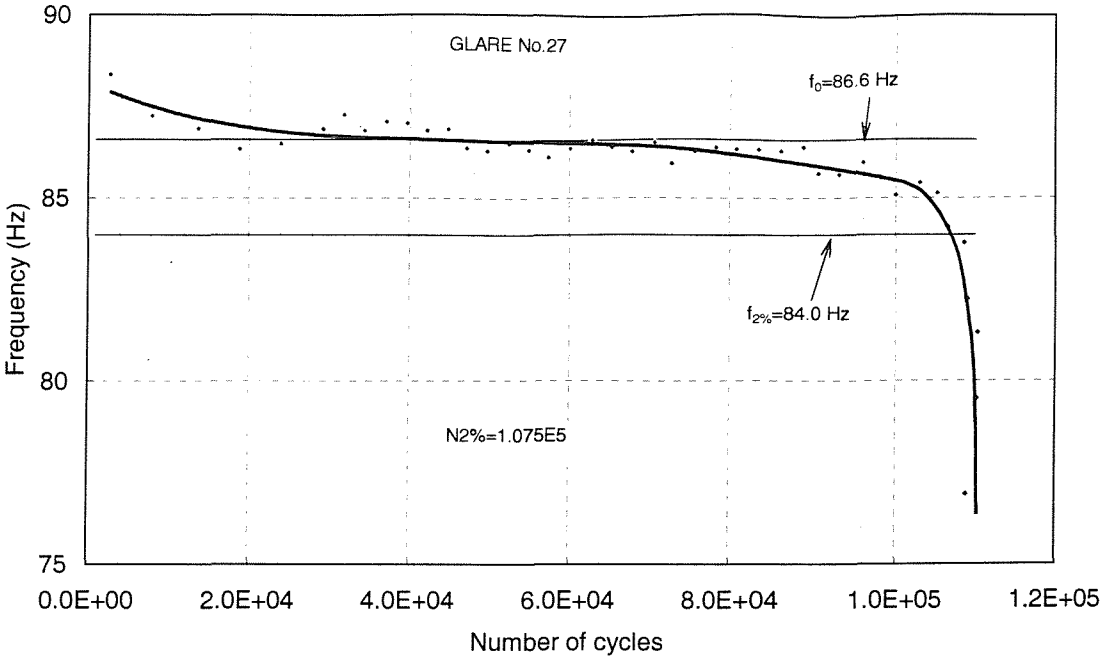

Figure 2.44 Resonance frequency versus number of cycles (GLARE Tee-coupon No. 27)

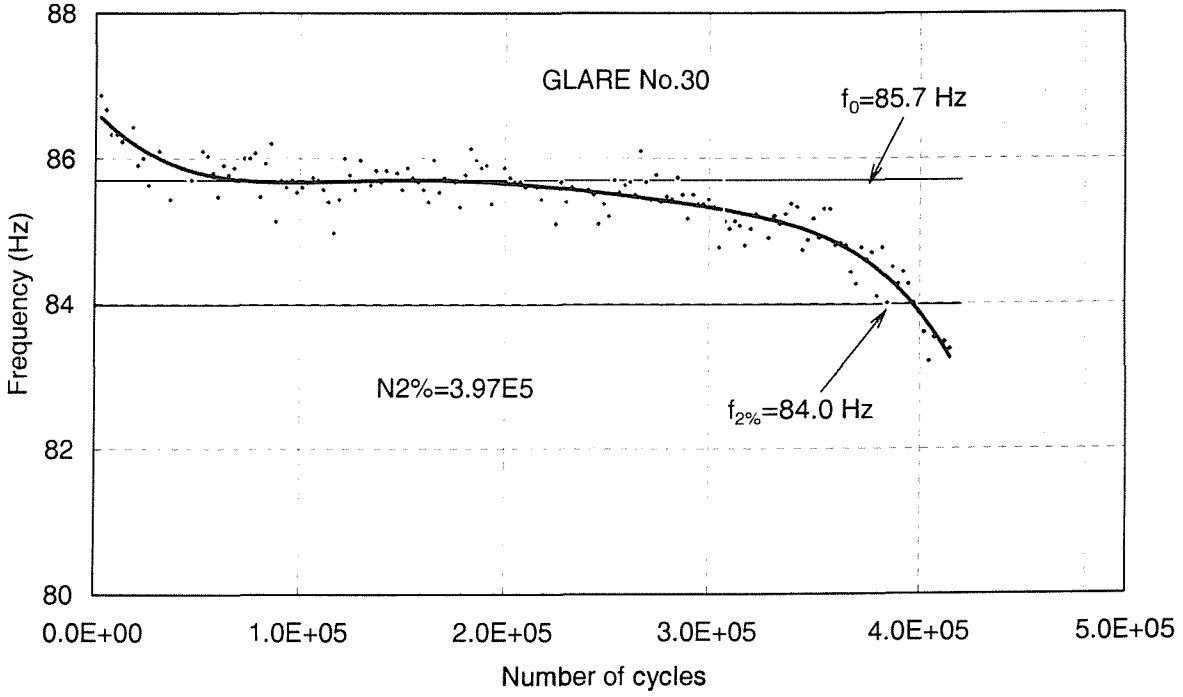

Figure 2.45 Resonance frequency versus number of cycles (GLARE Tee-coupon No. 30)

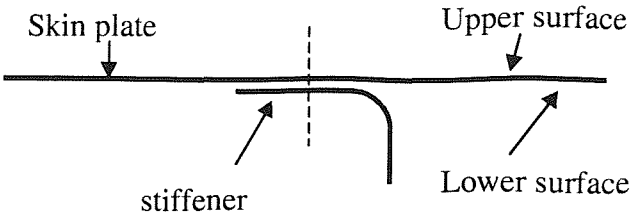

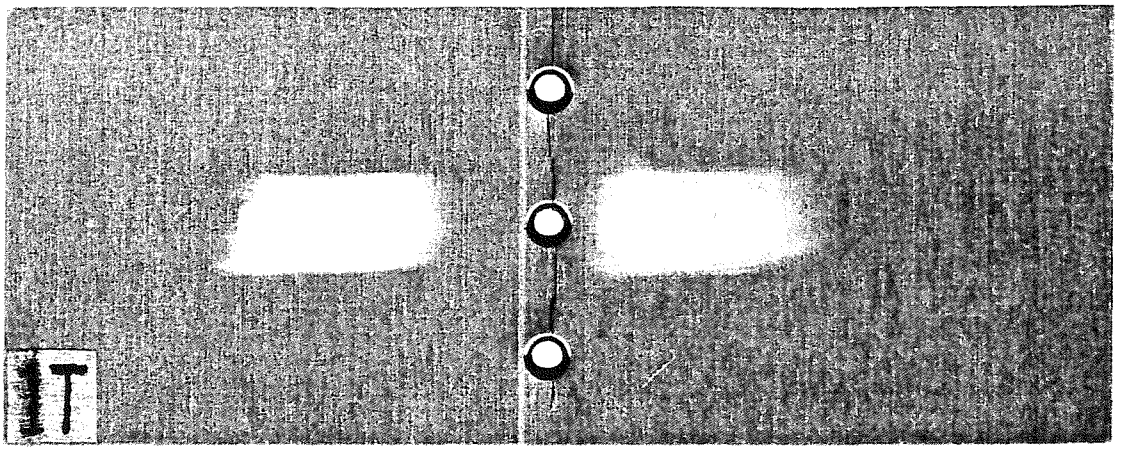

a) upper surface

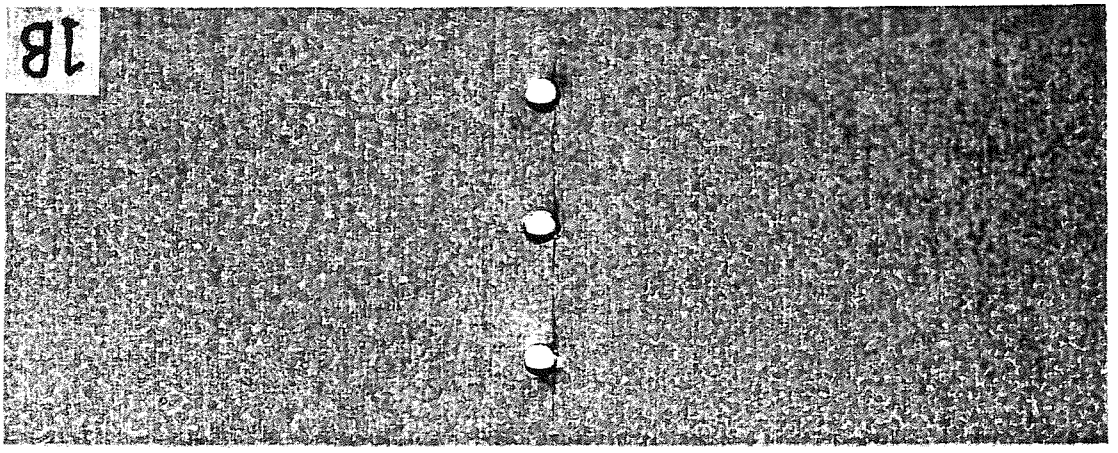

b) lower surface

Figure 2.46 Fatigue cracks on the surfaces of skin panel (GLARE Tee-coupon No. 1)

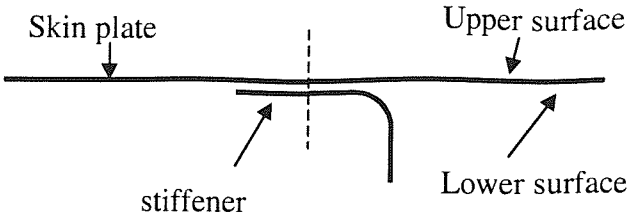

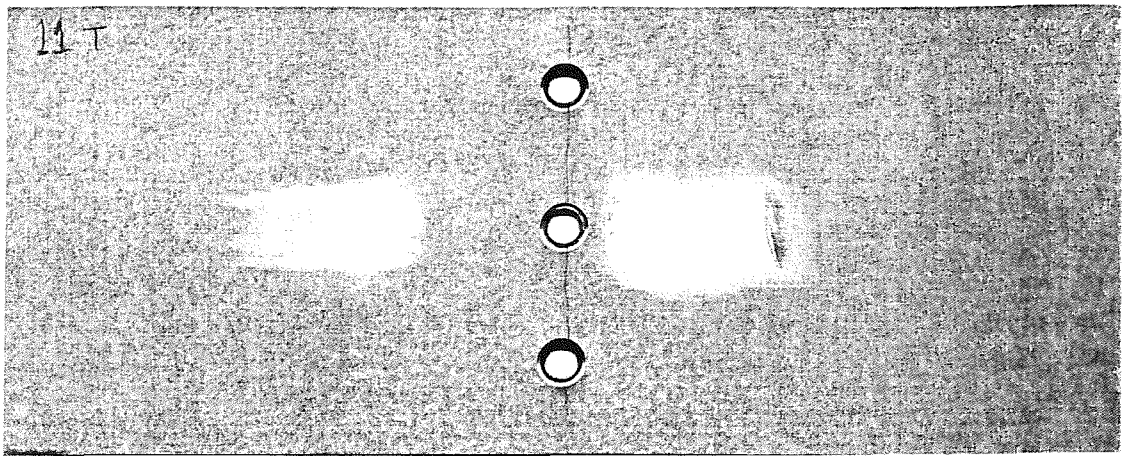

a) Upper surface

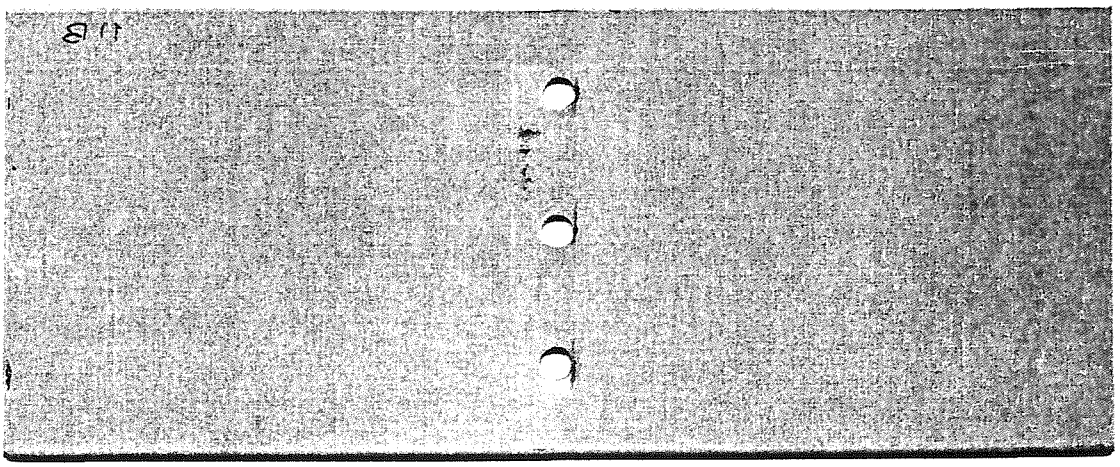

b) Lower surface

Figure 2.47 Fatigue cracks on surfaces of skin panel (GLARE Tee-coupon No. 11)

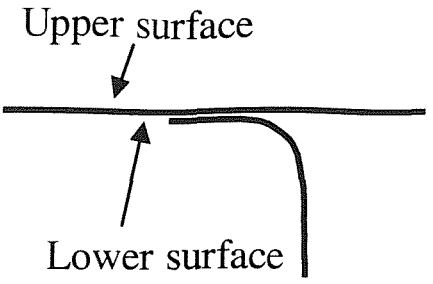

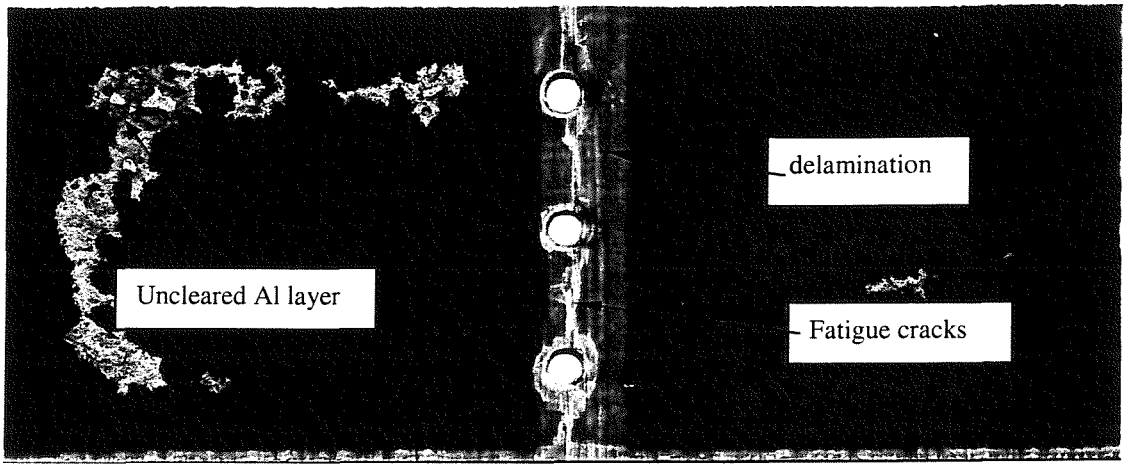

a) upper surface

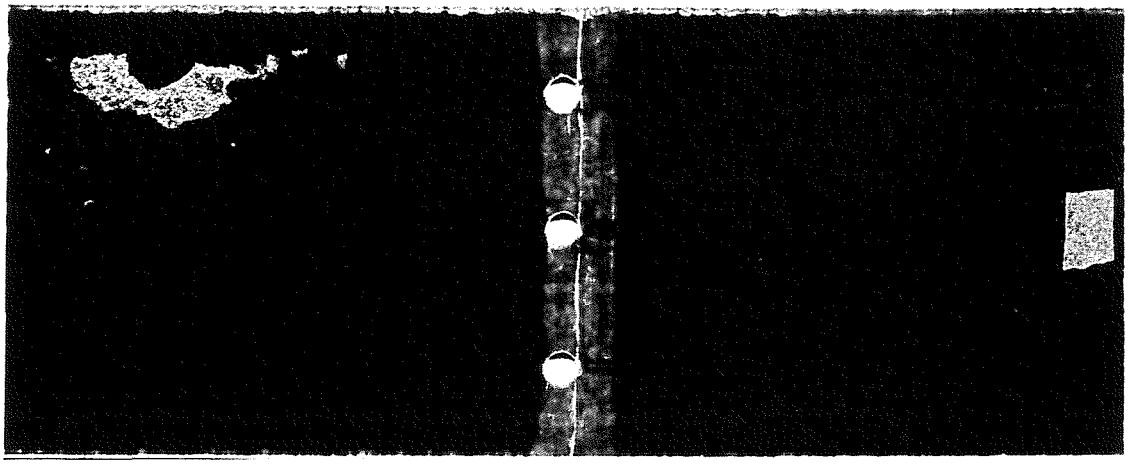

b) Lower surface

Figure 2.48 Fatigue cracks in glass fibre layers of the skin plate (GLARE Tee-coupon No. 17)

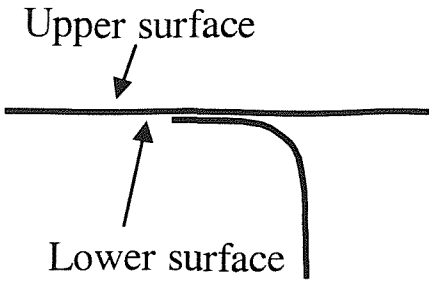

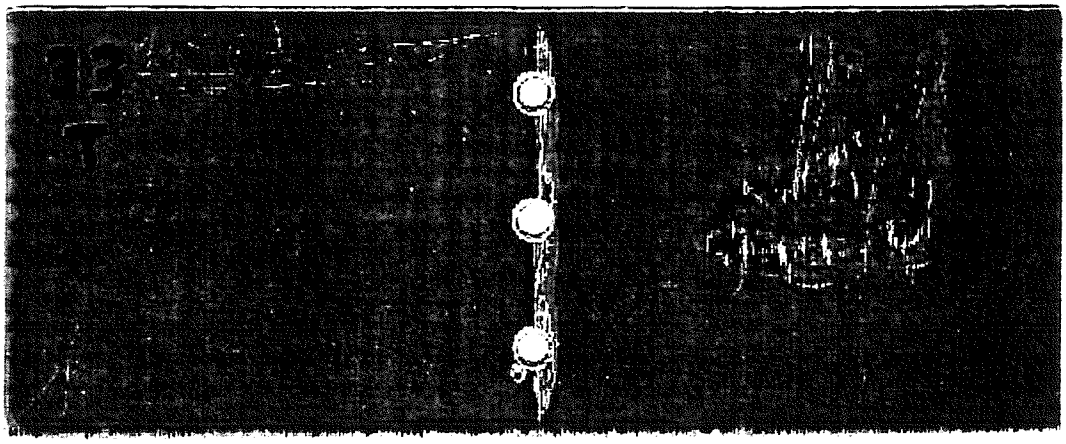

a) upper surface

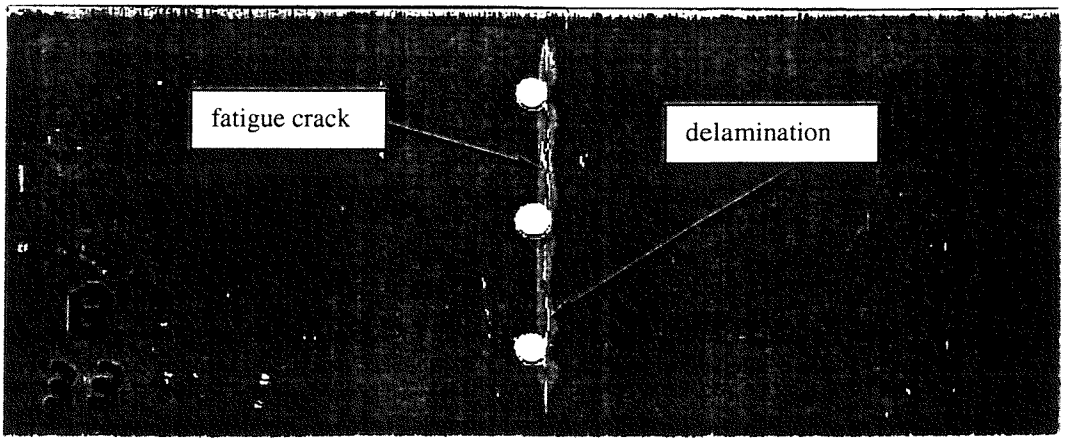

b) lower surface

Figure 2.49 Fatigue cracks in glass fibre layers of the skin plate (GLARE Tee-coupon No. 33)

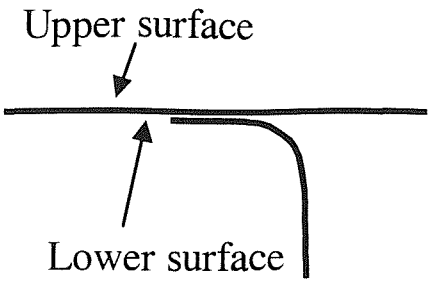

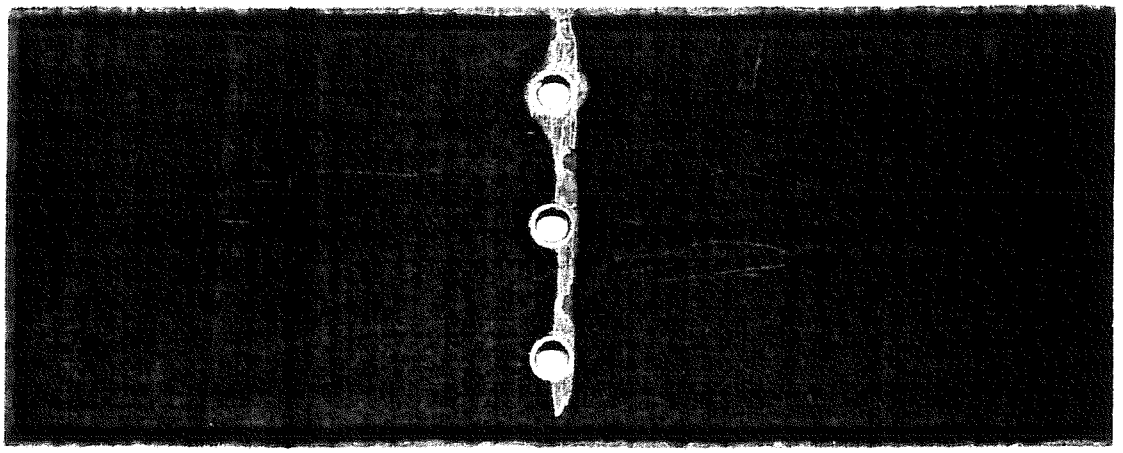

a) upper surface

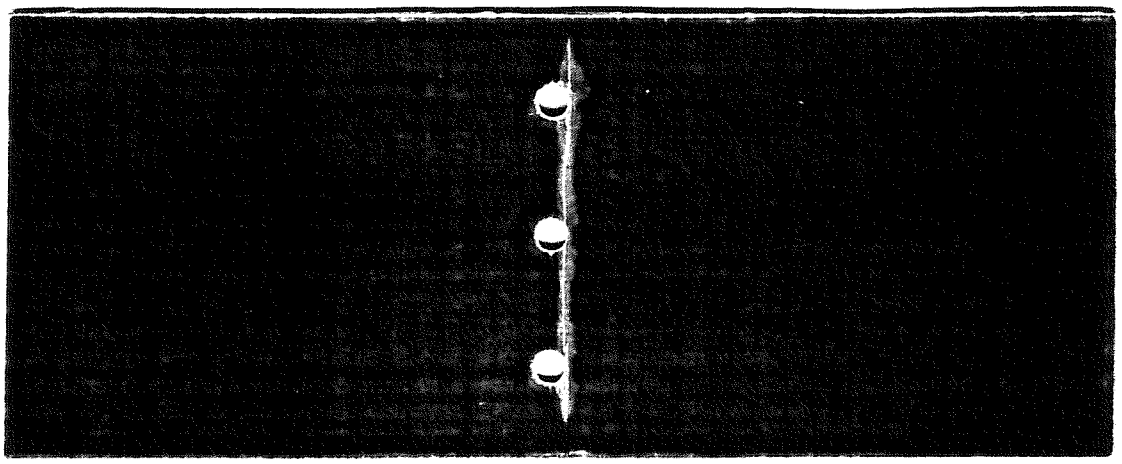

b) lower surface

Figure 2.50 Fatigue cracks in glass fibre layers of the skin plate (GLARE Tee-coupon No. 1)

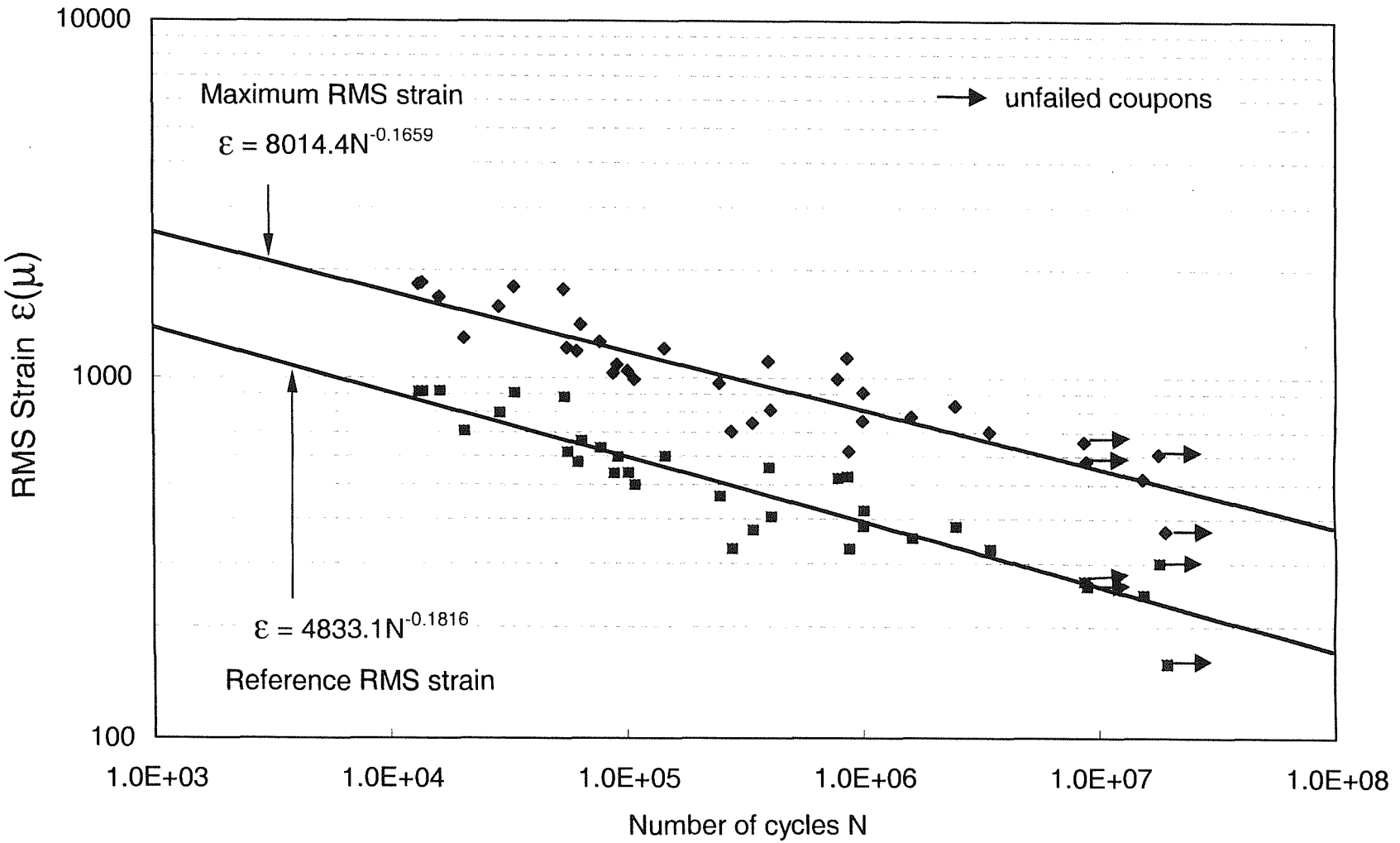

Maximum RMS strain – measured by gauge No. 1 Reference RMS strain – measured by gauge No. 2
For gauge position please see Figure 4B.6

Figure 2.51 Fatigue data of the GLARE Tee-coupons

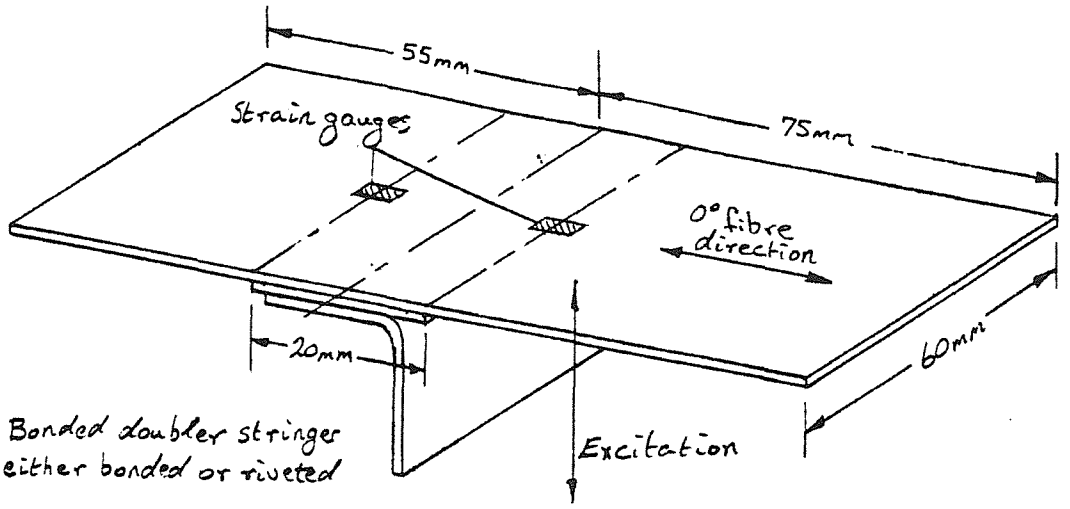

FIBRE METAL LAMINATED SKIN/STIFFENER JOINTS

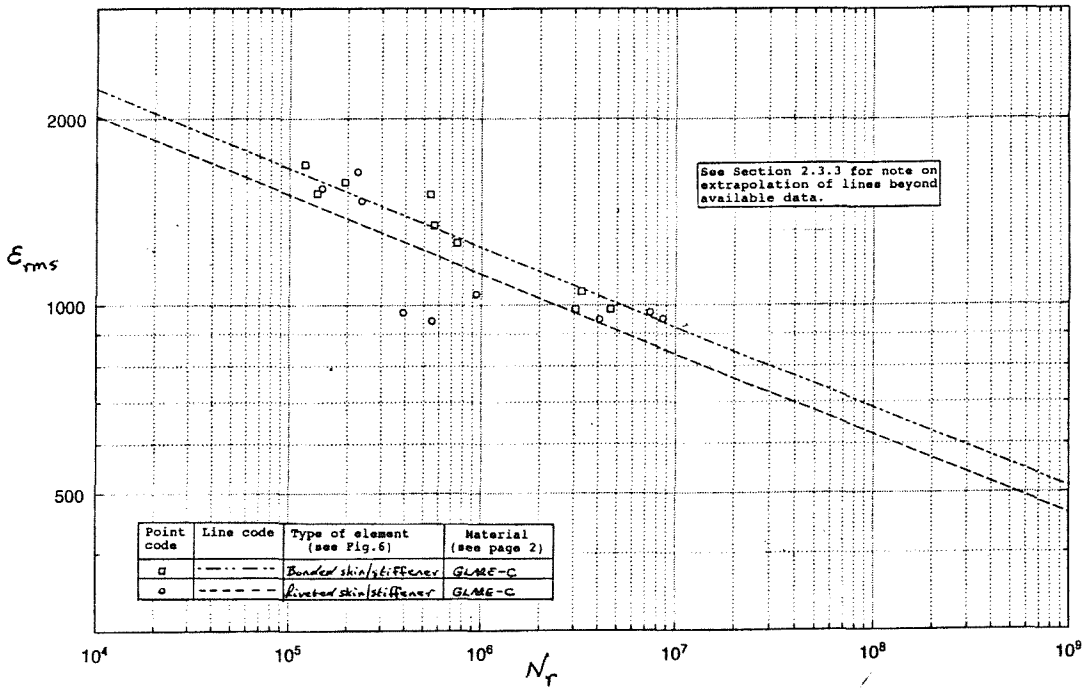

Figure 2.52 Fatigue data of GLARE-C Tee-coupon (ESDU data sheet No. 84027)

(A permission has been granted by ESDU to use these figures , Appendix H)

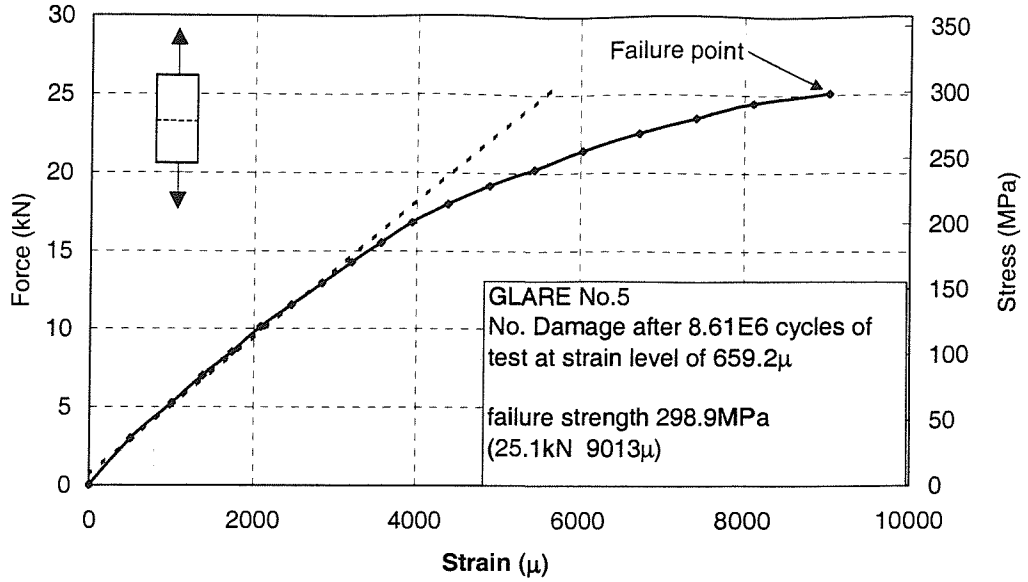

Figure 2.53 Stress (force) and strain relationship of GLARE coupon No. 5 in the post-fatigue tests

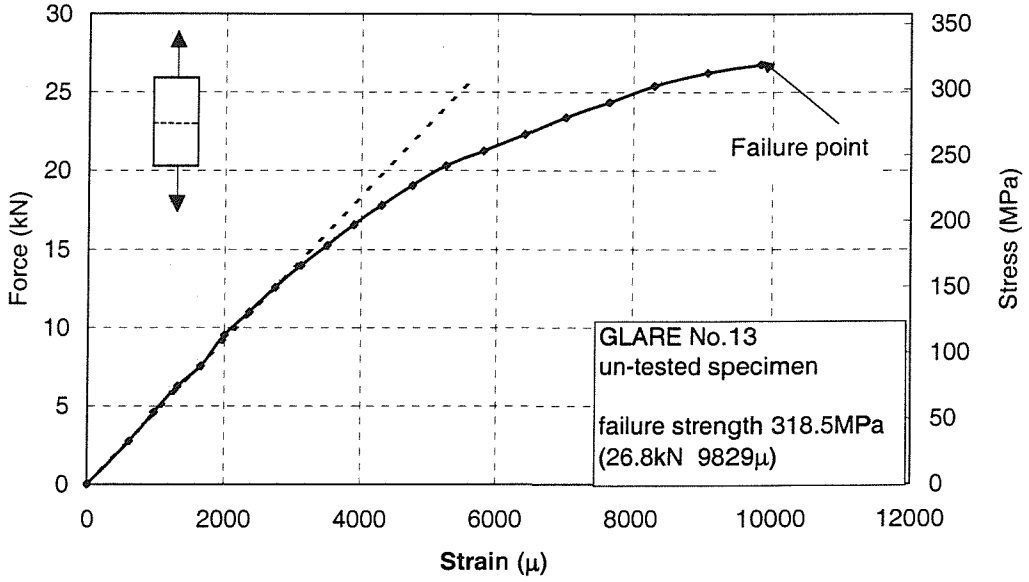

Figure 2.54 Stress (force) and strain relationship of GLARE coupon No. 13 in the post-fatigue tests

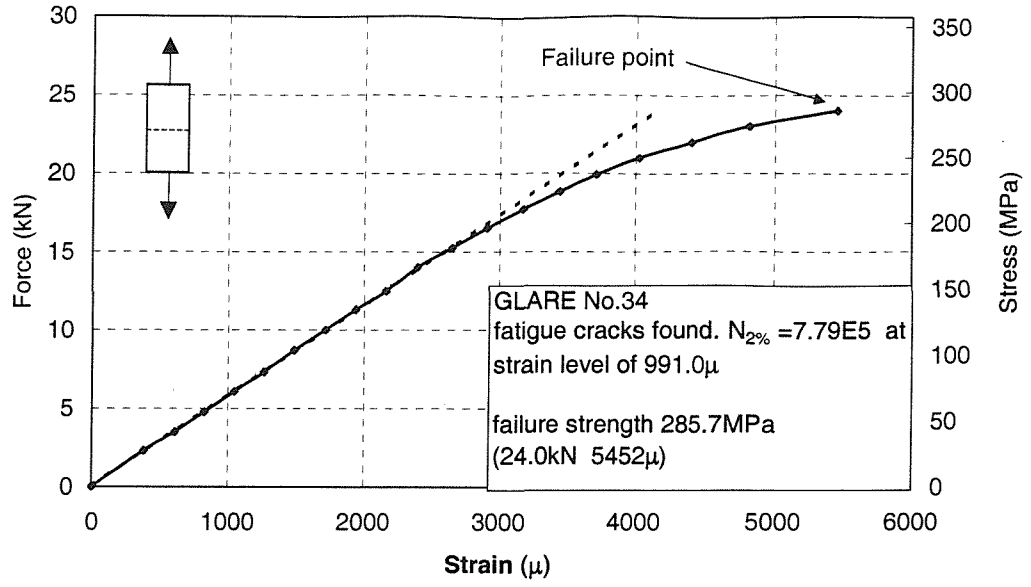

Figure 2.55 Stress (force) and strain relationship of GLARE coupon No. 34 in the post-fatigue tests

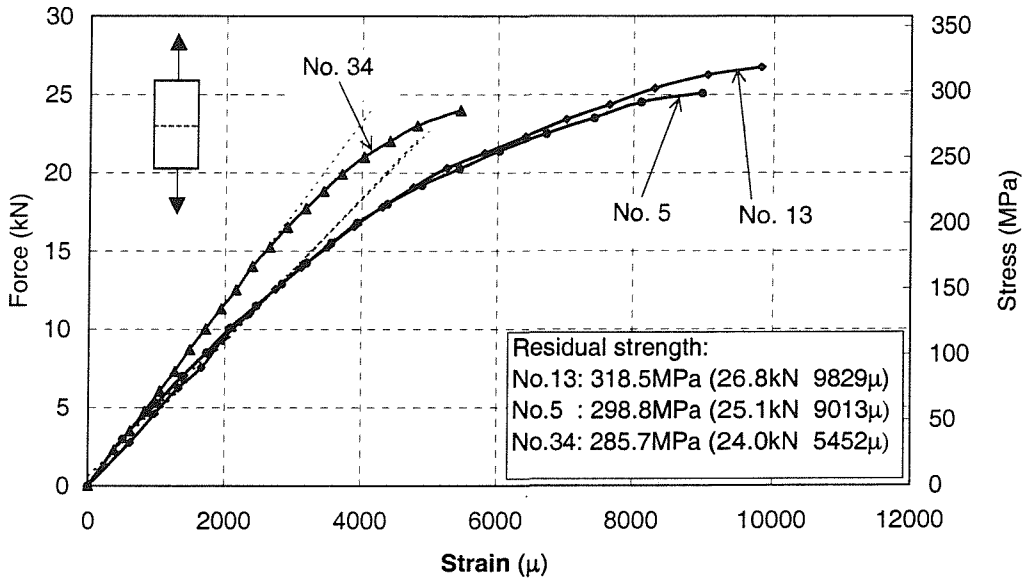

Figure 2.56 Comparison of the stress (force) and strain relationship of GLARE coupons No. 5, No. 13 and No. 34 in the post-fatigue tests

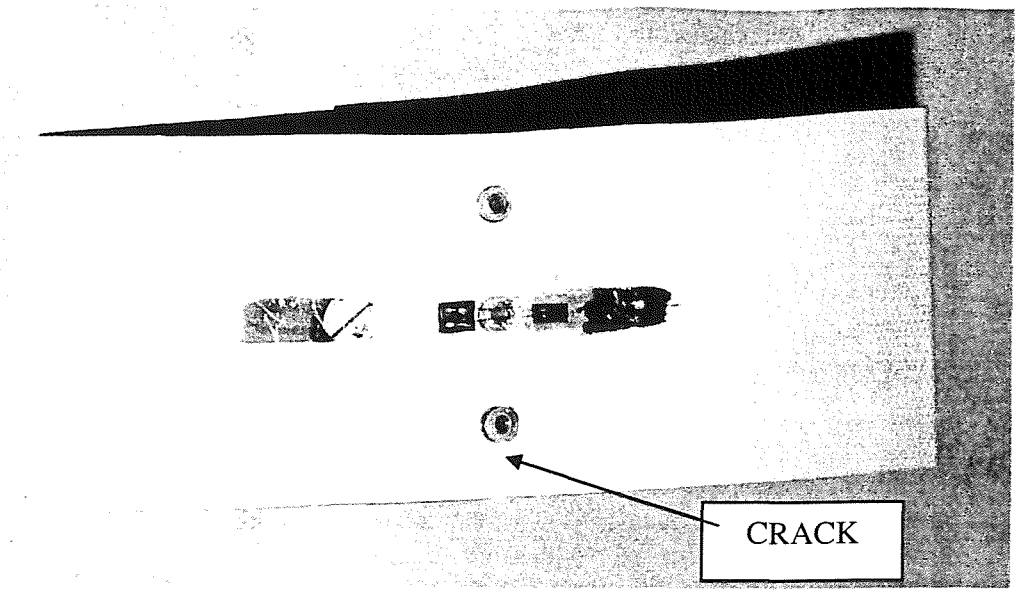

Figure 2.57 GLARE coupon after post-fatigue tensile test (No. 5)

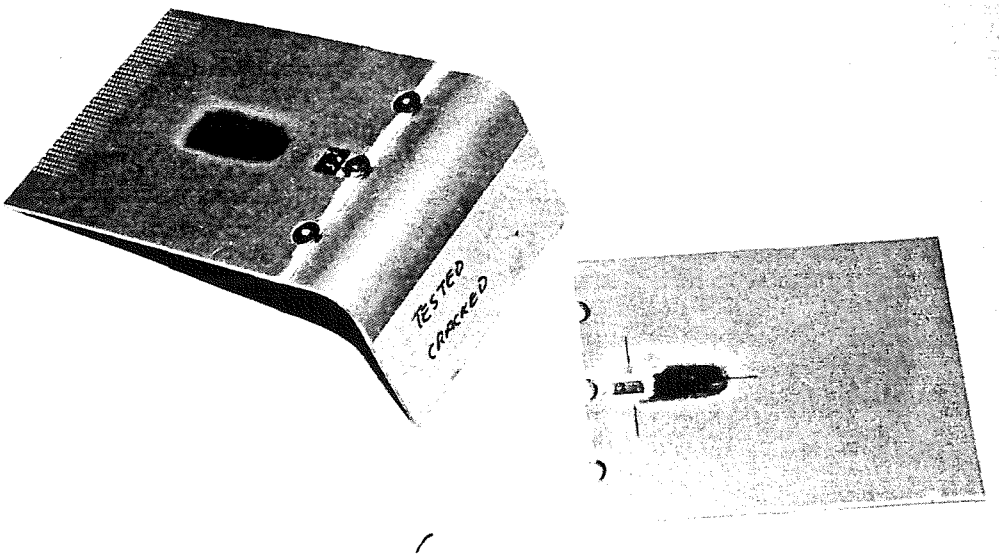

Figure 2.58 GLARE coupon after post-fatigue tensile test (No. 6)

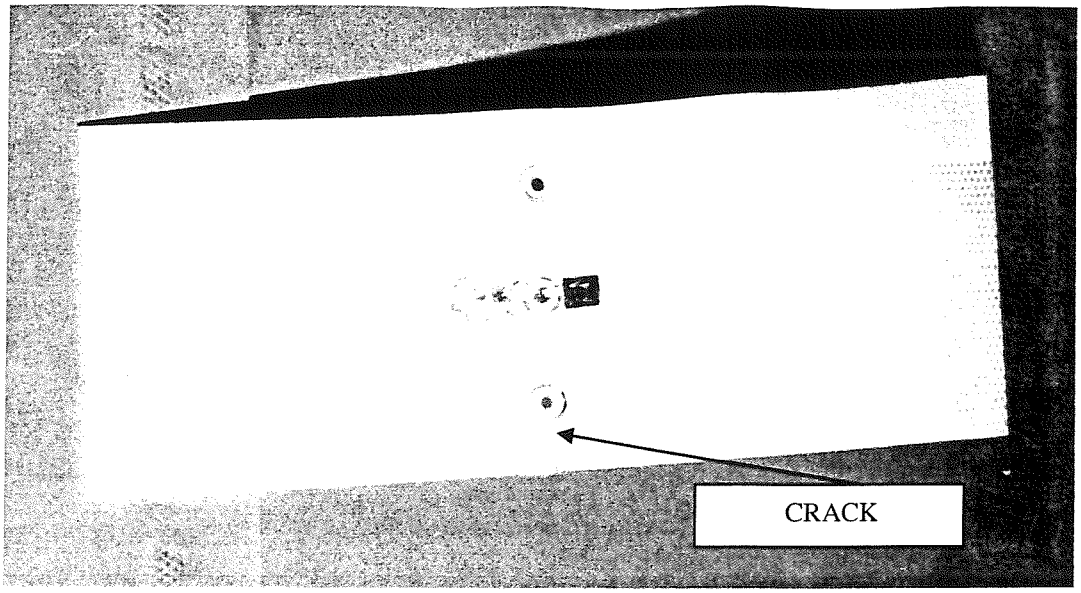

Figure 2.59 GLARE coupon after post-fatigue tensile test (No. 13)

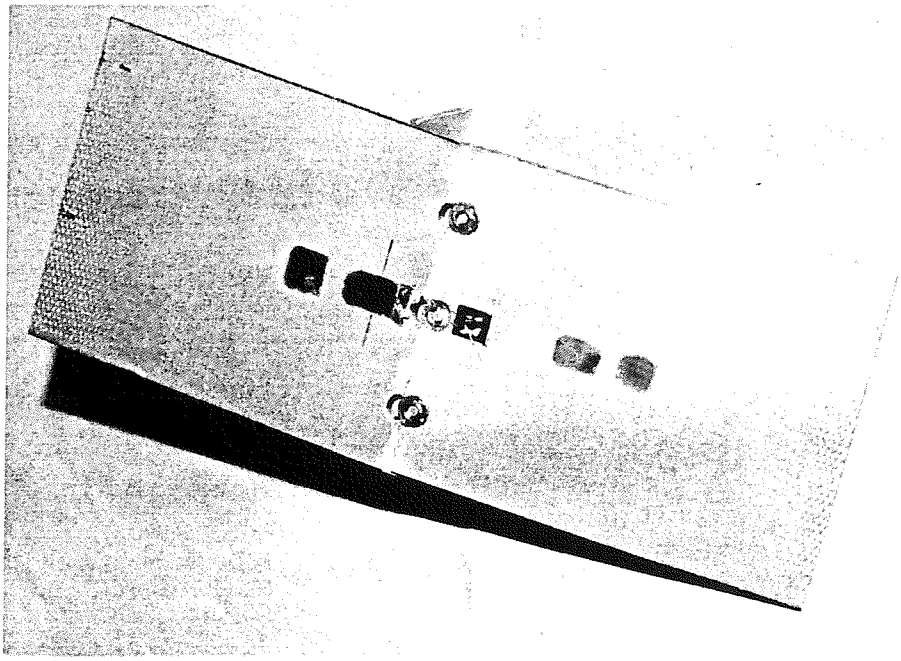

Figure 2.60 GLARE coupon after post-fatigue tensile test (No. 34)

CHAPTER 3

SOUND PRESSURE FIELD MEASUREMENT AT THE TEST SECTION OF THE PWT FACILITY

3.1 THE PURPOSE OF THE MEASUREMENT

Acoustic fatigue failures of aircraft structures, which are located close to/or in the path of the jet efflux, are caused by high intensity pressure loading. Although the design guides for dynamic stress prediction have been developed on a good structural dynamics basis, little information exists concerning the spatial distribution of sound pressure fields. In structural response analysis, a uniform random pressure field is often used as the acoustic loading input for theoretical estimation of structural response.

In the present project, box-type structures, representing aircraft flaps, were designed to be tested in the Progressive Wave Tube (PWT) facility. In the previous use of the PWT, a reference microphone has been used to monitor overall sound pressure levels at the test section and also to provide input data for theoretical estimation of structural response strain and stress.

The objective of this experimental work was to measure the sound pressure field distribution (overall sound pressure level - SPL and spectral density) and to identify the random characteristics of acoustic excitation over the test section. The conclusion drawn from this experimental work will be used for the theoretical estimation of structural responses to acoustic loading of the test structures.

3.2 TEST SET-UP

To simulate acoustic loading on aircraft components, the PWT facility was designed to produce a high intensity sound pressure field in the test section where a test structure is mounted in an opening in the wall. The tube is driven by a siren via a horn and can produce an overall Sound Pressure Level up to163 dB. The test section of the PWT is 1.2 m long, 0.6 m high and 0.3 m deep. The test panel, which is mounted at the test section, is excited by high intensity sound propagating along the tube. A good description of the apparatus is given in Ref. [91].

Two sets of measuring microphones were used. One was located at the centre of the test section of the PWT tunnel and was used as the reference to monitor the overall sound pressure levels for this experiment and all other tests in this thesis. The position of the reference microphone and the size of the test section of PWT are shown in Figure 3.1.

Another set of microphones was used to measure the sound pressure levels and signals at several points across the test section. A plywood panel with thickness of 25mm was used to close the test section of the PWT. The pressure loading on this panel represents what the acoustic loading would be on the surface of test structures. The panel was divided into six sub-sections. At the centre of this panel and each sub-section, seven access holes were drilled to accommodate the panel microphone. Figure 3.2 shows the position of panel measuring points. Because there were only two sets of microphone systems available, measurements were repeated seven times by moving the panel microphone from point 1 to point 7 while the microphone at the reference point monitored the sound pressure level during each measurement. Figure 3.3 is the instrumentation set-up. B&K Type 4136 1/4 inch microphones and B&K Type 2615 Preamplifiers were used, which are specially designed to be used to measure random incidence signals, sound pressure level, boundary layer pressure fluctuations and pulses, etc.[83]. Microphone sensitivities were 1.24 mV/Pa and 1.17 mV/Pa respectively for reference microphone and panel microphone.

3.3 TEST PROCEDURES

3.3.1 Calibration

The measurement system was calibrated using a B&K Type 4220 PistonPhone which produces a signal with sound pressure level of 124 dB (ref. 20E-6 Pa) at frequency of 250 Hz . The calibration also was carried out at each time the measurement point was changed.

3.3.2 Overall Sound Pressure level Measurement

During each run of the PWT, the overall sound pressure signals from the two microphones were measured, so the relationship between pressures in each sub-section could be determined. Measurements were taken at six overall sound pressure levels based on the level indicated by the reference microphone. These were 135, 140, 145, 150, 155 and 160 dB. An overall sound pressure level of 135 dB was the basic sound pressure level in the PWT before any driving signal was input into the siren, i.e., this represents the contribution of the flow of compressed air through the siren to the acoustic field in the PWT. During the measurements, four signals were recorded, which were the driving signal generated by the random voltage generator coupled to the power amplifier (noted as 'Generator' in this thesis); the signal fed into the siren ('Siren') which is used to examine whether there was any change induced by the power amplifier to the driving signal; the reference microphone ('ref.') and panel microphone ('panel') outputs.

3.4 TEST RESULTS

3.4.1 Characteristic of Pressure Spectrum

To be able to excite as many modes of the box structures as possible and also reach as high as possible sound pressure level, three different spectrum shapes of driving signals were tested. These three driving signals produced different sound spectral shapes at the test section of the PWT.

3.4.1.1 Random signal with bandwidth of 60Hz-1kHz

A random signal with bandwidth of 60 Hz - 1 kHz was used as the input to the siren. Power spectral density distributions and coherence curves between generator and siren input and output of the microphones are shown in Figures 3.4 and Figure 3.5. Measured overall SPL for Figure 3.4 is 140 dB and 160 dB for Figure 3.5. It can be seen that the highest sound pressure is in the frequency range around 100 Hz with a rapid decay towards the higher frequency. Coherence functions are presented in Figures.3.4(d)/3.5(d) and 3.4(e)/3.5(e) which show the coherence between the driving signal and those measured by microphones. These plots indicate that coherence functions reduce rapidly at frequencies above 500 Hz. This is due to the non-linear response characteristics of the siren; it has very low response sensitivity at high frequency. The high frequency components in the pressure field are mainly caused by distortion in the response of the siren to low frequency components in the input.

3.4.1.2 Shaped random signal with bandwidth of 60Hz –1kHz

The spectrum shapes shown in Figures.3.4(b)-3.6(b) are not ideal for producing random acoustic loading at the surface of the test structures, because in practice, acoustic loading of aircraft structures is broadband in nature (normally 80 Hz to 800 Hz), and also the fundamental frequency of the box-structures under investigation is greater than 100 Hz. A pressure field with a flat spectrum shape in the 80 Hz - 800 Hz band was sought. The approach was to reduce the low frequency components in the driving signal and increase the contributions of high frequencies. The shaped driving signal is shown in Figure 3.7(a), and Figure 3.7(b) shows the pressure spectrum at the test section. The spectral density distributions with an overall SPL of 135 dB measured by reference microphone and panel microphone at point 2 are shown in Figure 3.8. There is a sharp peak in the spectrum of the signal from the reference microphone. This was caused by the compressed air flowing through the siren as indicated in the spectrum of air flow given in Figure 3.8. Comparing Figures 3.7(b) & 3.8 there are some similar characteristics between them, which means the pressure field is the combination of that due to the compressed air and the driving signal. This is also clearly shown in coherence functions (Figures 3.7(d)-3.7(f)).

In these measurements, although the required pressure spectrum shape at the test section was achieved, the highest sound pressure level only reached 150 dB or 151 dB due to the loss of low frequency components in the driving signal.

3.4.1.3 Shaped random signal with bandwidth of 80-600Hz

Because the sound pressure level at the test section was mainly caused by low frequency components and their "harmonics" due to distortion caused by the siren, the bandwidth of the driving signal was reduced to have an upper frequency limit of 630 Hz. In this case, a reasonably flat spectrum in the 100Hz - 500 Hz band with maximum sound pressure level of 160 dB was achieved. Figures 3.9 & 3.10 give spectra at 155 dB and 160 dB. The spectrum shape in Figure 3.9(a) is that of the driving signal. It can be seen that as the sound pressure level increased, the coherence became worse especially in the high frequency region. The best coherence is in the region around 250 Hz. This driving signal was used for all the PWT excitations.

Although Figures 3.4 to 3.10 only shown results for measurement point 2, all other points had similar spectral characteristics.

3.4.2 Sound Pressure Level Distribution

Test results show that the sound pressure levels measured by both microphones are very close for all of the seven measuring points. This means that sound pressure levels are uniform in the axial direction along the test section. Table 3.1 shows the recorded overall SPL for a random signal input with bandwidth of 80 Hz – 600 Hz (as described in section 3.4.1.3).

To summarise the characteristics of the Power Spectral Densities of the acoustic loading at the test section, the spectra at seven testing points have been averaged. The overall spectral shapes for six overall SPLs are shown in Figure 3.11. It can be seen that the changes of sound pressure level in the frequency band of 100 Hz to 500 Hz are in the 5 dB range.

3.4.3 Spatial Phase Distribution at the Test Section of PWT

In section 3.4.2, it was concluded that sound pressure level at the test section is uniformly distributed. This section examines how the sound pressure signals measured at different points would be correlated, which will reveal the spatial phase distribution of sound pressure signals at the test section. The relative phase spectra of sound pressure signals at each measurement point related to the reference microphone are shown in Figures 3.12-3.14. It can be seen that the phase spectra are the same at the section perpendicular to the air flow direction, such as points 2 & 5 of the down stream section (Figure 3.13); Points 1, 3 & 6 of the middle section (Figure 3.12); and points 4 & 7 of the up stream section (Figure 3.14) respectively. But each of these sections has different spatial phase relative to the reference point. The phase spectra have shown a linear change over the frequency band, which means that the phase difference at each cross section of the PWT tube is due to time delay.

Comparing the relative phase spectrum between the each test point on the test section, the phase spectra referring to point 2 are shown in Figure 3.15. It shows the linear relationship between phase and frequency. The higher the frequency, the larger the phase difference. Figure 3.15(c) is the phase difference between points 2 & 5 which are in the same cross section, and therefore there is no phase difference between them. These facts indicate that the sound pressure wave is travelling in the tube at a constant velocity along the axial direction on the surface of the test panel. This velocity can be determined from phase spectra as follow.

The distance between points 2 & 4 (0.8 m) is twice of that between points 2 & 3 (0.4 m), which is reflected in the phase difference by comparing Figures 3.15(a) and 3.15(b). The phase difference at frequency of 425 Hz is 360 degrees in the middle of frequency band 50 Hz to 800 Hz as shown in Figure 3.15(a), this means the wavelength at frequency 425 Hz is equal to the distance between points 2 & 4, i.e., 0.8m. Therefore the wave velocity along the air flow direction is given as following:

$$V_x = L \times f = 0.8 \times 425 = 340 \ (m/s)$$

Where L – wave length (metres)

f – Wave frequency (Hz)

It shows that V_x is the speed of sound in air at normal ambient conditions.

From these results, it can be concluded that the acoustic loading, on the surface of a test structure which is mounted at the test section of the PWT, is a sound wave travelling at a constant velocity V_x of 340.8 ms^{-1} along the axial direction of the tube. The sound pressure magnitude is uniformly distributed on the surface of a test structure but with a spatial phase distribution of $2\pi fx/V_x$, where x is the distance along the PWT in the air flow direction.

3.4.4 Statistical Characteristics of Acoustic Loading

Statistical analyses of the acoustic loading in the test section of PWT were performed to examine whether non-Gaussian behaviour was present in the signals. The probability density distribution was determined, and skewness and kurtosis values were also calculated using 30,000 data points for each signal.

For a normal distribution random signal, its instantaneous value should follow the Gaussian distribution, i.e. its probability density distribution function $p(x)$ can be described by

$$p(x) = \frac{1}{\sigma\sqrt{2\pi}} e^{\frac{-(x-\mu)^2}{2\sigma^2}} \tag{3.1}$$

where x is the instantaneous value of a random signal

Mean value:

$$\mu = \frac{1}{n}\sum_{i=1}^{n} x_i \tag{3.2}$$

Standard deviation from the mean value

$$\sigma = \sqrt{\frac{1}{n}\sum_{i=1}^{n}(x_i - \mu)^2} \tag{3.3}$$

Equation (3.1) is normalised in the terms of standard deviation σ, so that the integration of $p(x)$ should equal to 1.

The root mean square (RMS) value of a random signal is also used frequently as a measure of the level of certain physical parameter, such as RMS strain or stress, etc., which is defined as,

$$RMS = \sqrt{\frac{1}{n}\sum_{i=1}^{n}(x_i)^2} \tag{3.4}$$

It can be seen that the RMS value of random signal is equal to its standard deviation σ if the mean value μ is zero.

Two parameters are used to examine the non-Gaussian feature in a random signal, which are the skewness λ and the kurtosis γ. Skewness is measure of the bias of distribution from the central distribution and kurtosis indicates sharpness of distribution around the mean value compared with the Gaussian distribution.

$$\lambda = \frac{M_3}{(M_2)^{\frac{3}{2}}} \tag{3.5}$$

$$\gamma = \frac{M_4}{(M_2)^2} \tag{3.6}$$

where M_k (k=2, 3 and 4) is called the central moments of the distribution:

$$M_k = \frac{1}{n}\sum_{i=1}^{n}(x_i - \mu)^k \tag{3.7}$$

It can be seen that standard deviation σ is the square root of the second central moment M_2.

The skewness and kurtosis should have values of 0 and 3 respectively for a random signal which follows the Gaussian distribution.

As described above, a random signal from the random noise generator ('Generator') was used as input to control the spectrum shape of acoustic excitation in the test section. The signal fed

into the siren ('Siren') was also recorded to be compared with the input signal to examine if any distortion is introduced by the power amplifier. The probability density distributions of signals from the random noise generator and input to siren are shown in Figure 3.16.

Table 3.2 shows that the average RMS value of the signal from the random noise generator was 0.335 V with a deviation of 0.0015, which means that input signal was in a steady condition during the test. The skewness and kurtosis values for both signals are very close to the values of 0 and 3. These indicate that the signals follow a Gaussian distribution law but as expected there were some disturbances in the signals. These are shown in Figures 3.16.

The signals measured by two microphones were also analysed to be compared with the Gaussian distribution. Table 3.3 lists the statistical parameters of signals from the reference microphone and the panel microphone at measurement point 2, and the probability density distributions are shown Figures 3.17 and 3.18. The statistical parameters for sound pressure measured at the remainder of the 6 points are listed in Appendix B.

From Table 3.3 and Figures 3.17 and 3.18, it can be seen that both pressure signals followed the Gaussian distribution at overall sound pressure level of 135 dB, i.e., in the situation that sound pressure was induced only by compressed air. The skewness and kurtosis values of signals from both measuring microphones are very close to zero (-0.00676 & -0.00834) and three (2.99 & 3.04). But when the siren started to generate the noise signal at the test section, the pressure signals measured by both microphones showed non-Gaussian features. The kurtosis values of both signals were greater than 3, their probability density distributions became sharper than for a Gaussian distribution. The signals measured by the panel microphone had greater kurtosis values than those measured by the reference microphone, i.e., the probability density distribution curves of the former signals are sharper than those of the latter. The greater the kurtosis values, the more high peaks there are in the signals. Figures 3.19 and 3.25 show the time history of signals at 140dB, which shows that the signal measured by panel microphone had more high peaks away from its RMS value than that of the signal measured by reference microphone. The ratios of the maximum value to RMS value of both signals are 4.59 (= 12.6/2.75) and 6.03 (= 4.19/0.694) respectively.

The results in Table 3.4 and Figures 3.17 and 3.18 also show that with the increase of sound pressure level at the test section, the signals become more skewed but less sharp, especially the

signal measured by reference microphone. The time histories of both signals at a sound pressure level of 160 dB are shown in Figure 3.27. The reference signal was offset from its mean value towards to the positive side and the panel signal to the negative side. Also, there are more high peaks in the panel signal, which produce a greater kurtosis value as shown in Figure 3.18.

3.5 SUMMARY

To investigate the spatial and statistical characteristics of sound pressure field at the test section of PWT, a series of sound measurements were carried out. A plywood panel with seven microphone access holes was used to close the test section. The sound signals at these seven points and a reference point in the centre of the test section were measured at five OASPLs from 135 dB to 160 dB in 5 dB steps.

The measurement results at seven measuring points shown that the spatial distributions of the overall sound pressure level at the test section were almost constant, which indicates that a uniformly distributed sound pressure amplitude was present in the test section. However, relative spatial phase differences between measuring points in airflow, i.e., axial, direction were observed. It was found that this phase difference was dependent on the frequency and axial distance between measuring points. Further investigation found that spatial phase difference could be expressed as:

$$\Phi(f, x)=2\pi fx/V \tag{3.8}$$

This concludes that the acoustic loading on the surface of a test structure, which is mounted in the test section of the PWT, is caused by sound waves travelling at the speed of sound in an axial direction in the PWT. It was also found that a fairly constant spectral level could be achieved for sound spectral density distribution in the frequency band of 80 Hz to 600 Hz by controlling the spectral shape of the driving signal to the siren.

The statistical characteristics of sound signals measured by both microphones were investigated. At OASPL of 135 dB, pressure load at the test section was induced only by the compressed air, which followed the Gaussian distribution law. When overall sound pressure levels were greater than 135 dB, the sound signals measured showed non-Gaussian distribution behaviour mainly in the deviation of distribution sharpness from the normal

distribution law. Signals tend to become more skewed with the increasing sound pressure level but sharpness reduced.

Table 3.1 Overall sound pressure levels measured by reference and panel microphones (dB ref. 20E-6 Pa)

Reference Microphone SPL (dB)		135	140	145	150	155	160
Panel Microphone (dB)	Point 1	135	140	145	150	154	160
	Point 2	137	140	145	151	157	163
	Point 3	132	139	143	149	154	160
	Point 4	135	139	145	150	155	160
	Point 5	134	139	146	151	157	163
	Point 6	136	142	147	151	155	161
	Point 7	135	140	145	149	154	161
	Average	135	140	145	150	155	161

Table 3.2. Statistical parameters of input signals

(Unit: voltage)

Reference Microphone (dB)	Signal from random noise generator				
	μ	RMS	σ	λ	γ
135	0.00	0.33	0.33	-0.02	2.97
140	0.00	0.33	0.33	-0.02	2.94
145	0.00	0.34	0.34	-0.01	2.89
150	0.00	0.33	0.33	0.04	3.05
155	0.00	0.34	0.34	-0.01	2.97
160	0.00	0.34	0.34	0.00	3.01
	Signal to siren				
135	N/A				
140	0.00	0.09	0.09	0.02	2.98
145	0.00	0.13	0.13	0.00	2.94
150	0.00	0.21	0.21	-0.05	3.13
155	0.00	0.38	0.38	0.01	2.98
160	0.00	0.60	0.60	0.01	2.89

where μ - mean value
σ - standard deviation
λ - skewness
γ - kurtosis

Table 3.3 Statistical parameters of sound pressure signals at point 2 of the test section (data were not scaled to their physical values)

(Unit: voltage)

Reference Microphone SPL (dB)	Reference Microphone				
	μ	RMS	σ	λ	γ
135	-0.01	0.63	0.63	-0.01	2.99
140	-0.01	2.75	2.75	0.03	4.22
145	-0.01	1.57	1.57	0.07	4.23
150	-0.01	2.89	2.89	0.19	4.06
155	-0.01	1.71	1.71	0.41	3.40
160	-0.01	2.82	2.82	0.42	3.09
	Panel Microphone at Point 2				
135	0.00	0.16	0.16	-0.01	3.04
140	0.00	0.69	0.69	0.02	5.33
145	0.00	0.41	0.41	-0.02	4.30
150	0.00	0.80	0.80	-0.01	4.39
155	0.00	0.52	0.52	-0.12	3.83
160	0.00	0.98	0.98	-0.41	3.80

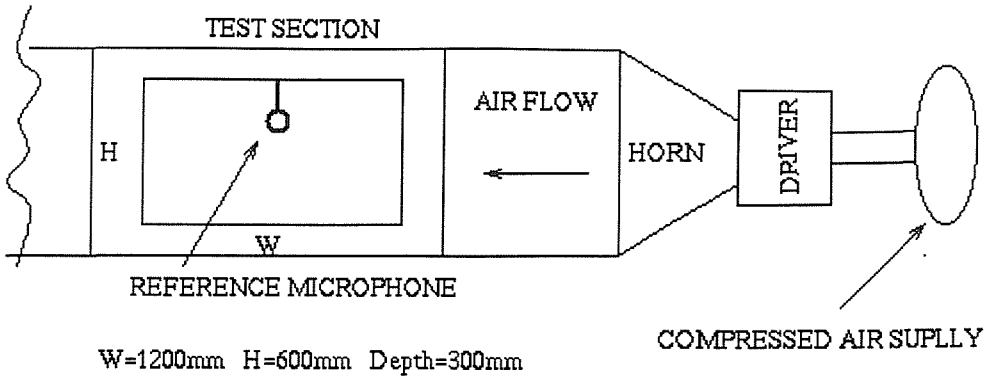

Figure 3.1 Dimensions of test section and position of reference microphone

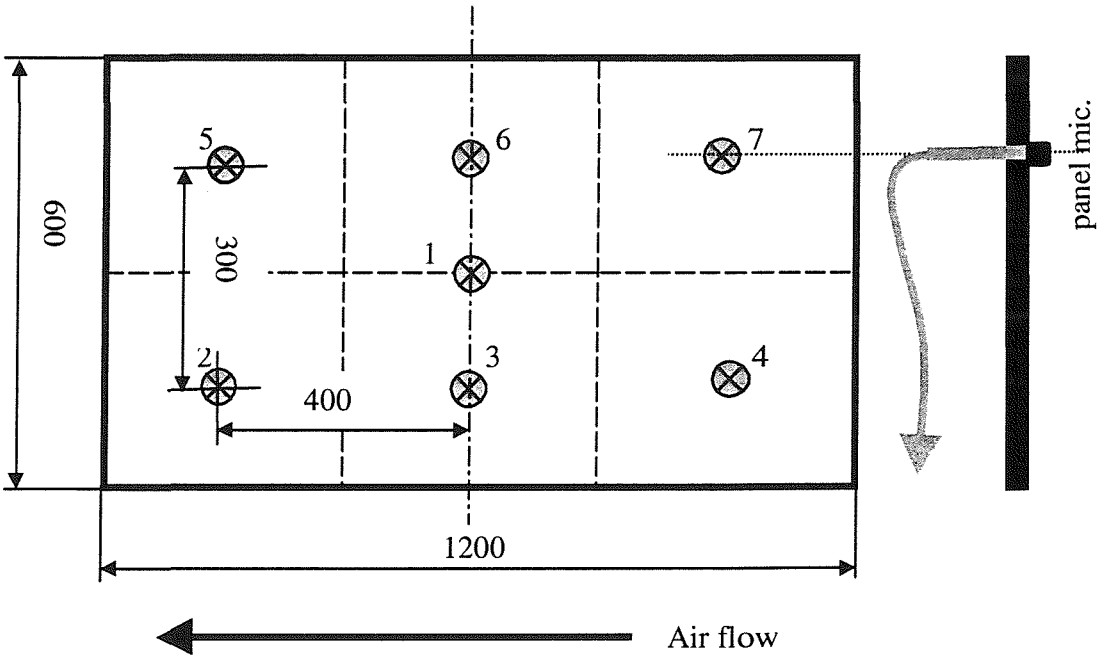

Figure 3.2 Position of panel measuring points

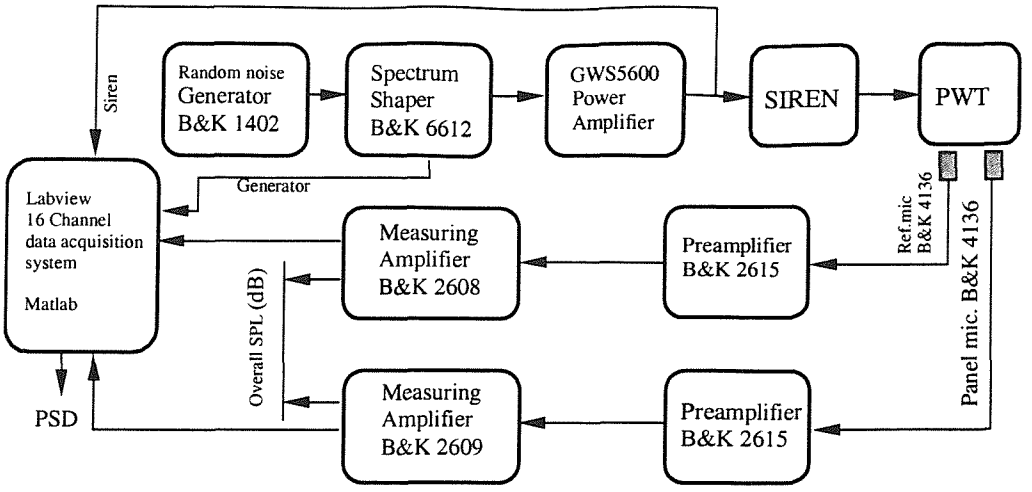

Figure 3.3 Instrumentation set-up for sound pressure measurements

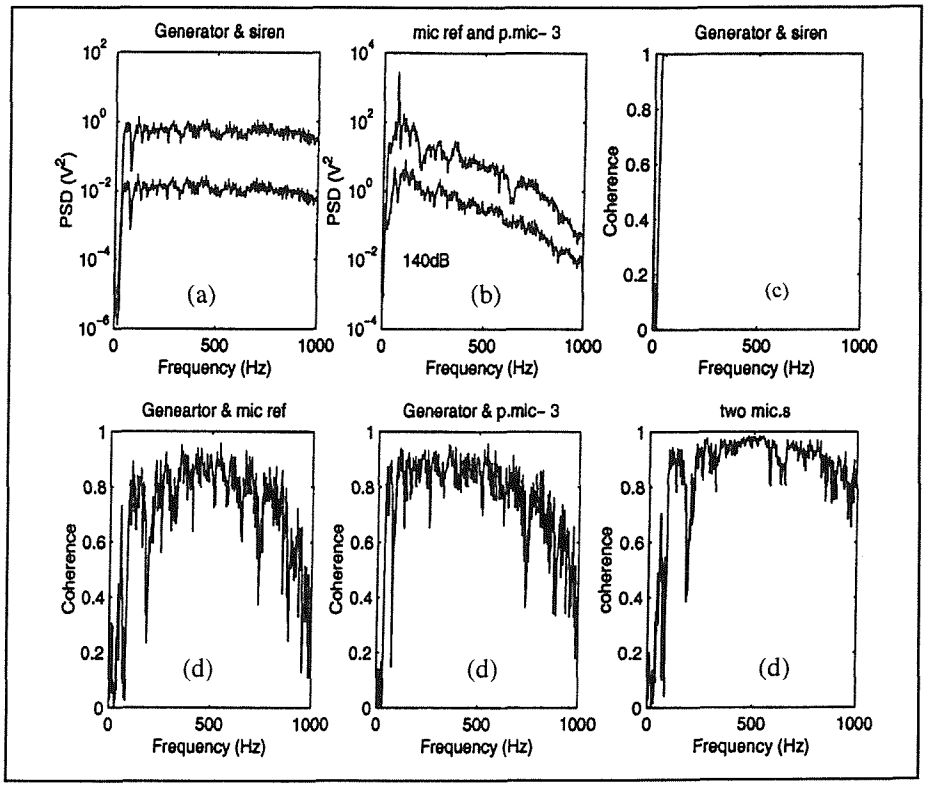

Figure 3.4 Test results at test section of the PWT with a driving signal of bandwidth 60 Hz – 1 kHz at overall sound pressure of 140 dB at measuring point 3

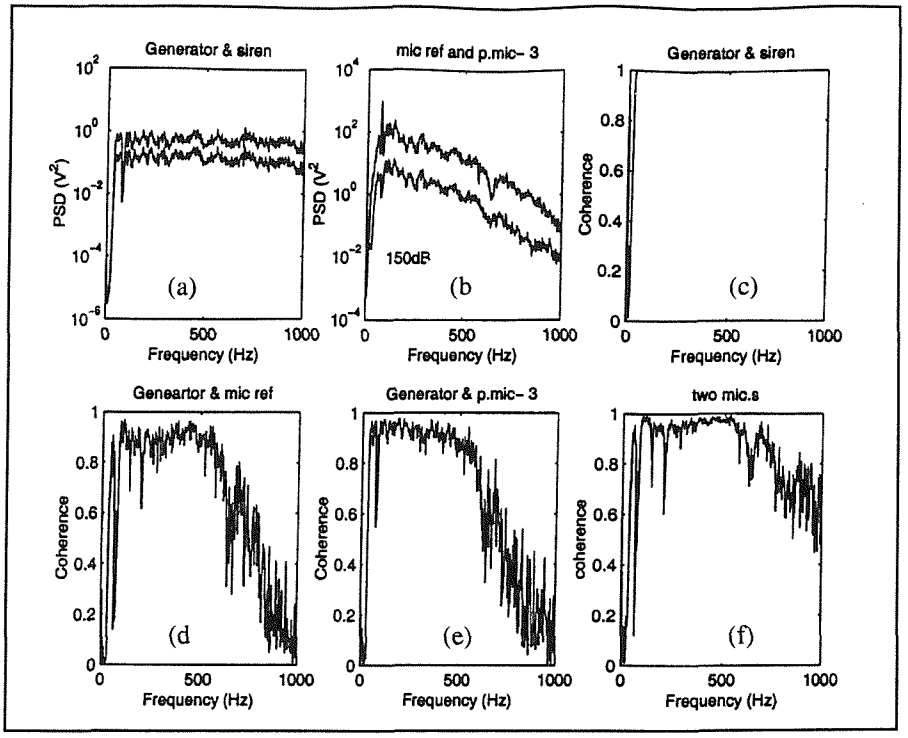

Figure 3.5 Test results at test section of the PWT with a driving signal of bandwidth 60 Hz – 1 kHz at overall sound pressure of 150 dB at measuring point 3

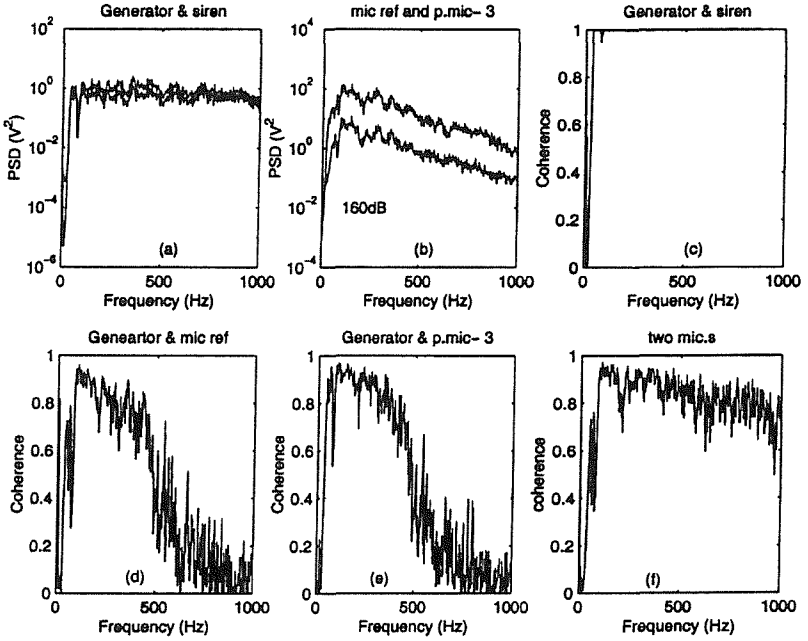

Figure 3.6 Test results at test section of the PWT with a driving signal of bandwidth 60 Hz – 1 kHz at overall sound pressure of 160 dB at measuring point 3

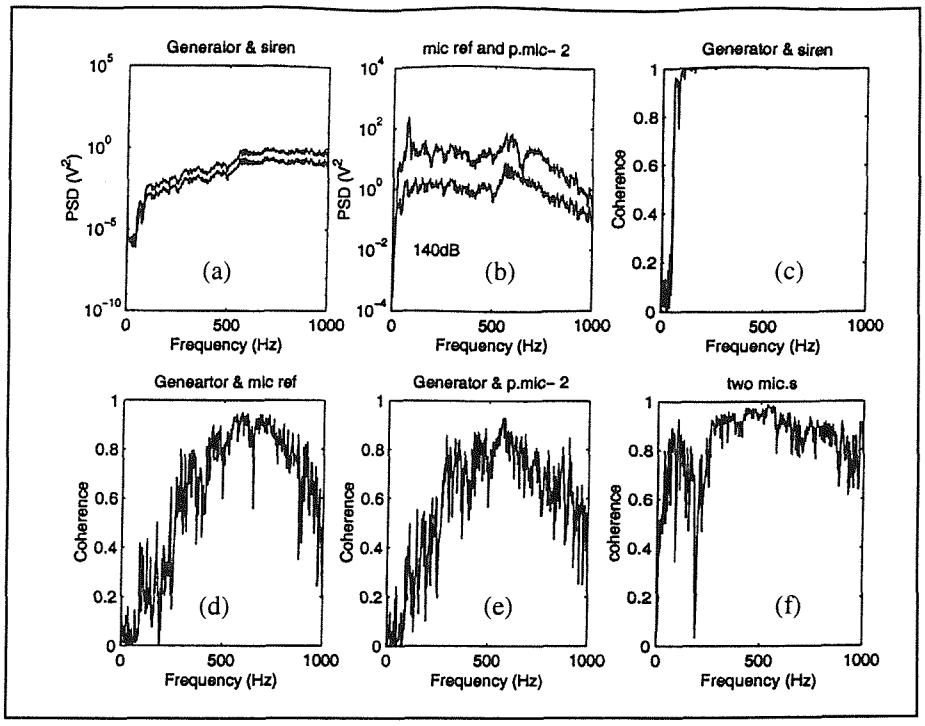

Figure 3.7 Test results at test section of the PWT with a shaped driving signal of bandwidth 60 Hz – 1 kHz at overall sound pressure of 140 dB at measuring point 2

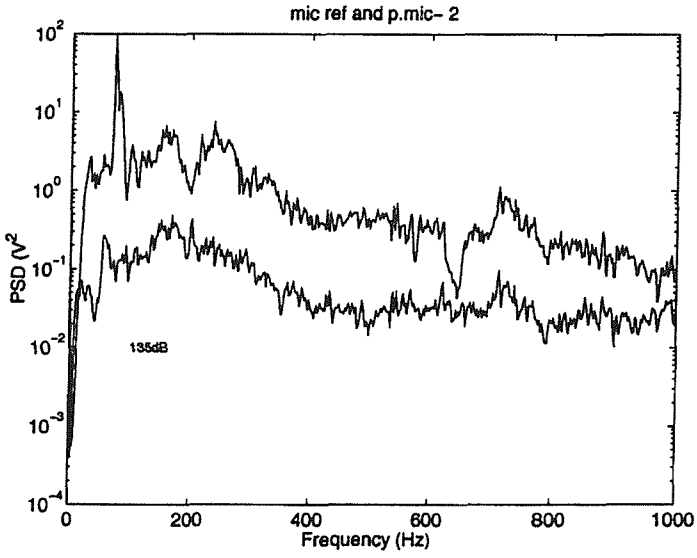

Figure 3.8 Sound spectral density distribution of the signal caused by compressed air flow at test section of PWT at point 2 (135 dB)

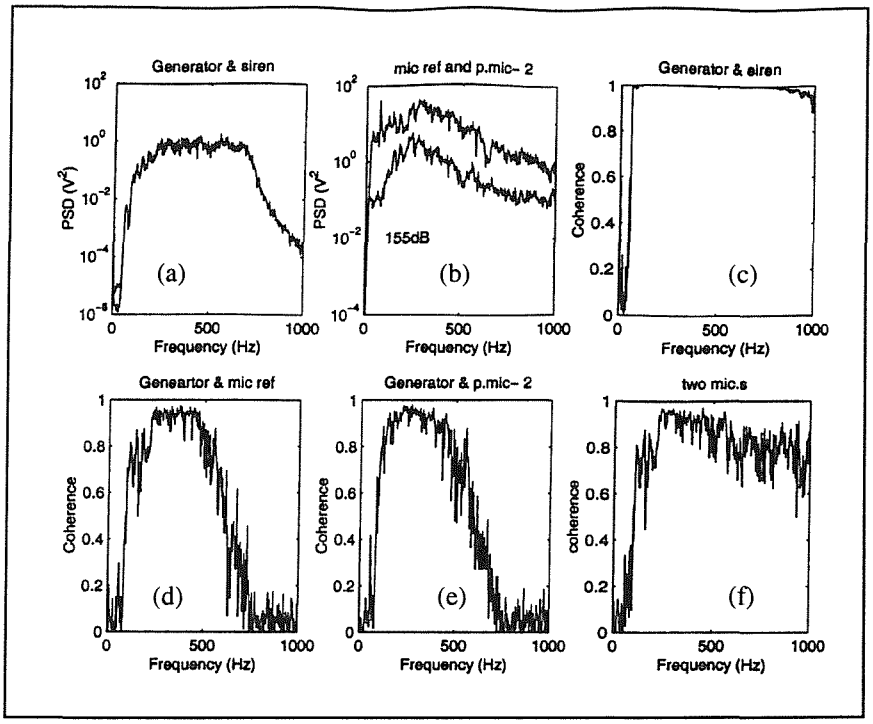

Figure 3.9 Test results at test section of the PWT with a shaped driving signal of bandwidth 80 Hz – 600 Hz at overall sound pressure of 155 dB at measuring point 2

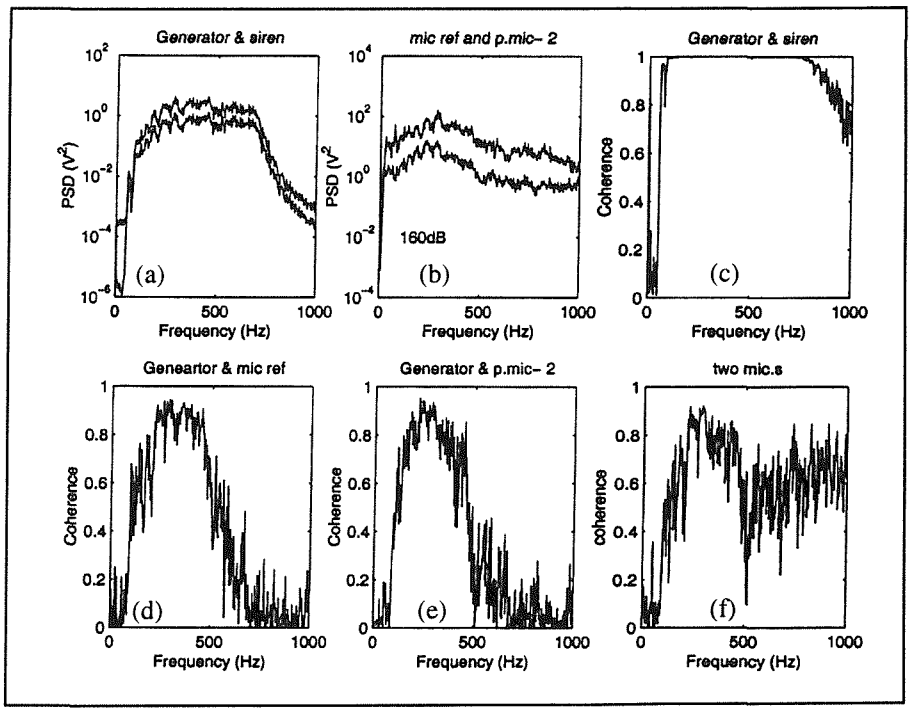

Figure 3.10 Test results at test section of the PWT with a shaped driving signal of bandwidth 80 Hz – 600 Hz at overall sound pressure of 160 dB at measuring point 2

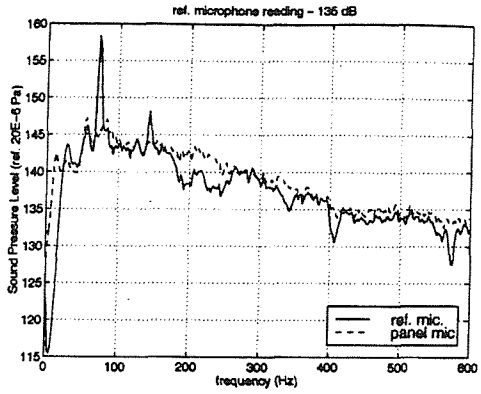

a). 135dB

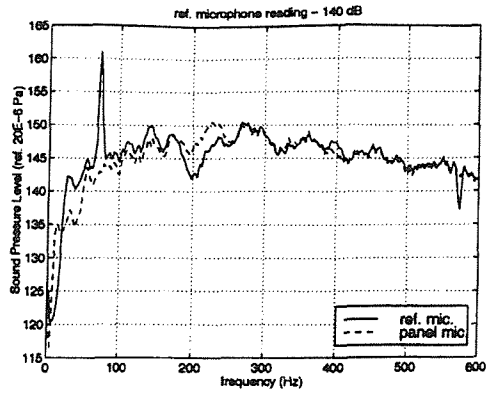

b). 140dB

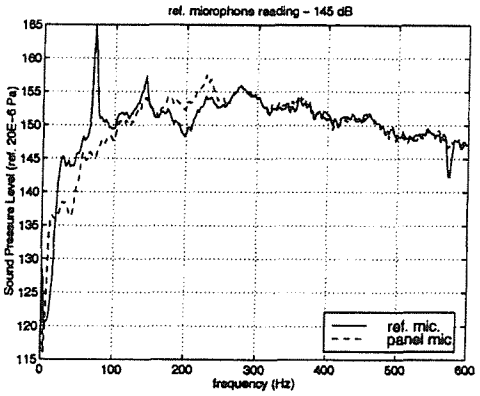

c). 145dB

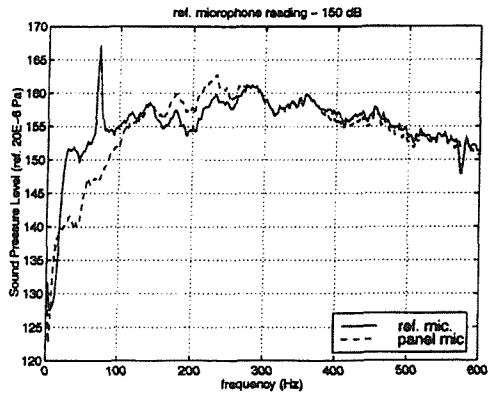

d). 150dB

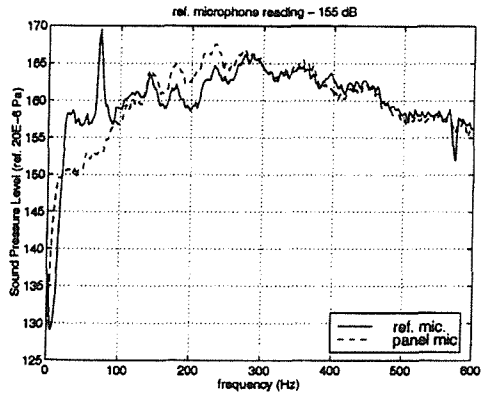

e). 155dB

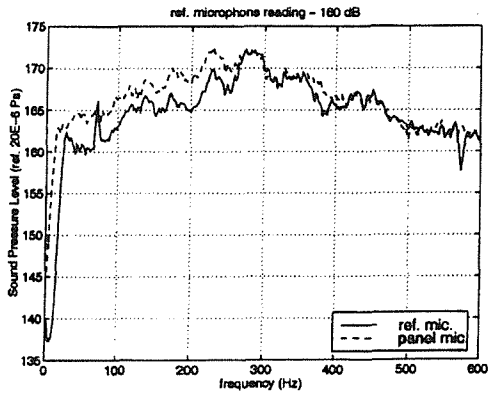

f). 160dB

Figure 3.11 Power Spectral Density of acoustic pressure in the PWT

——— Reference microphone

– – – – Panel microphone

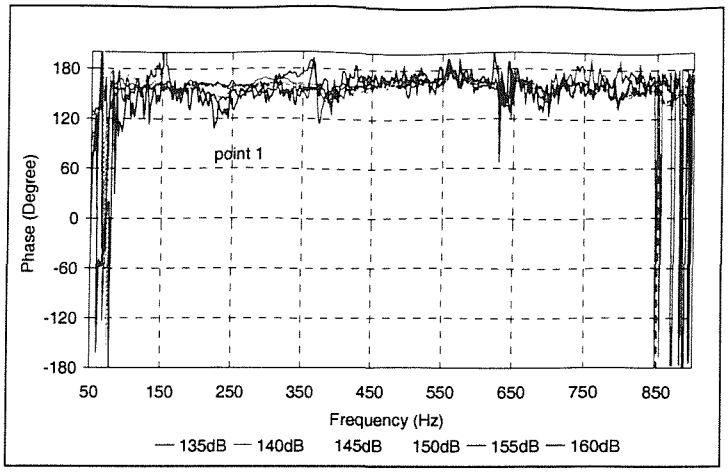

a). Point 1

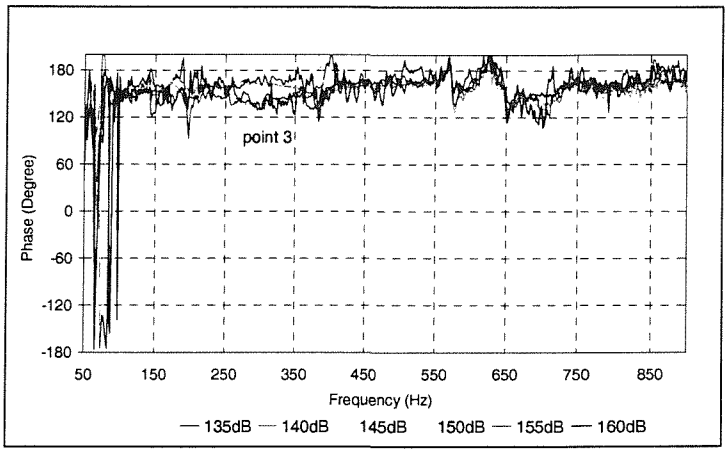

b). Point 3

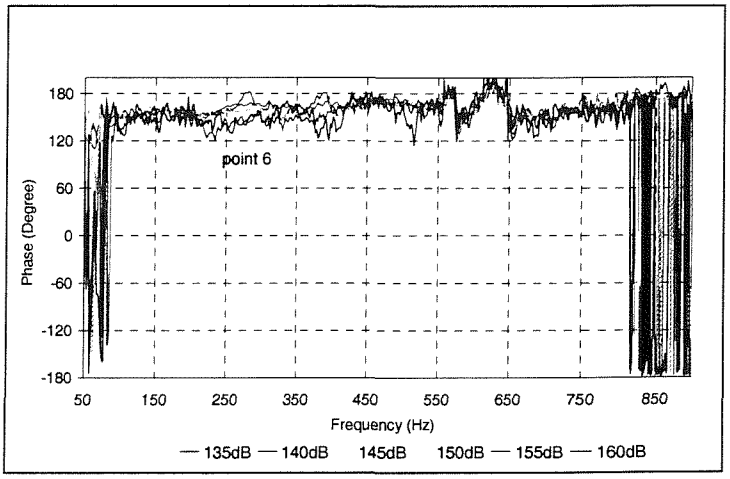

c). Point 6

Figure 3.12 Phase spectra of measuring points 1, 3 & 6 referring to reference microphone

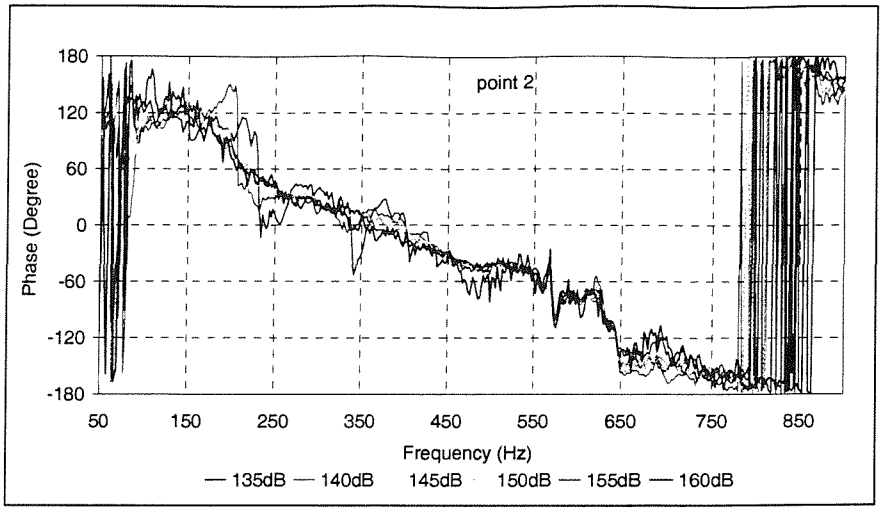

a). Point 2

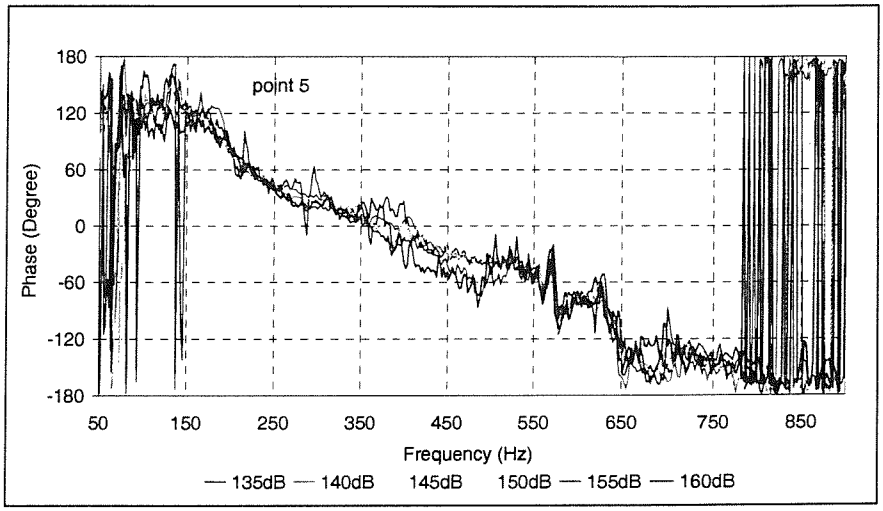

b). Point 5

Figure 3.13 Phase spectra of measuring points 2 & 5 referring to reference microphone

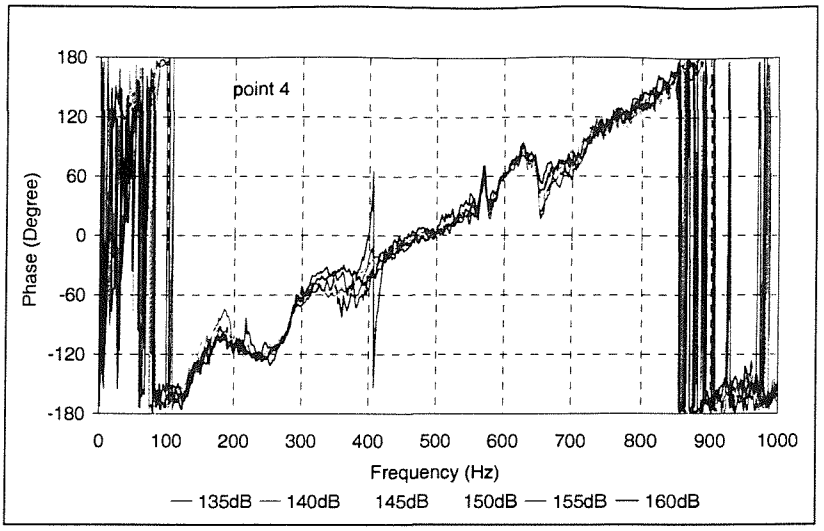

a). Point 4

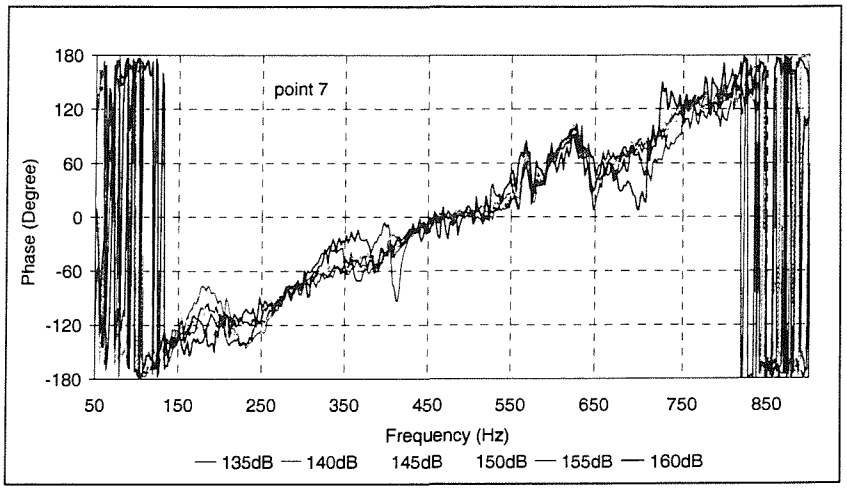

b). Point 7

Figure 3.14 Phase spectra of measuring points 4 & 7 referring to reference microphone

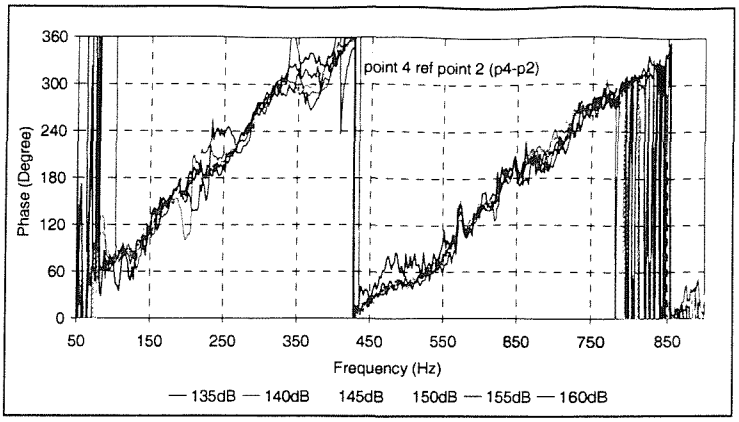

a). Point 4 referring to point 2

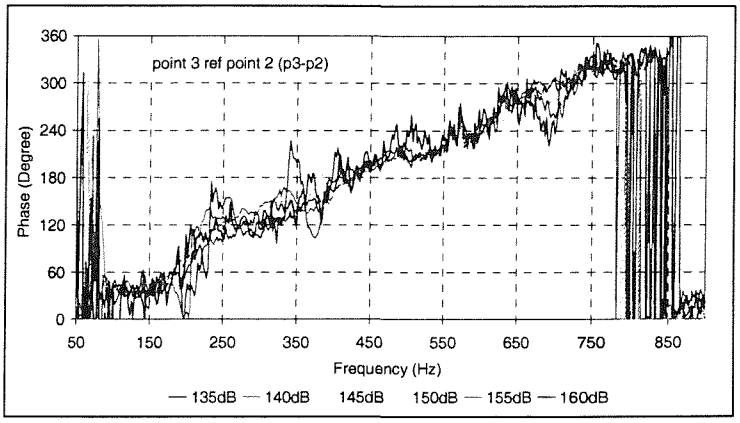

b). Point 3 referring to point 2

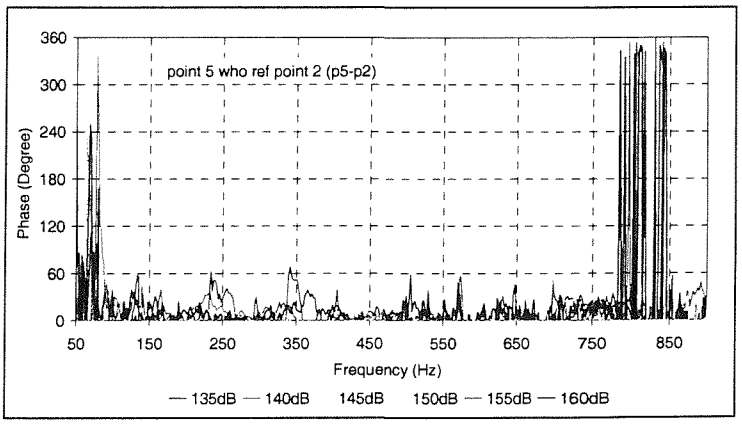

c). Point 5 referring to point 2

Figure 3.15 Phase spectra referring to point 2 at test section of PWT

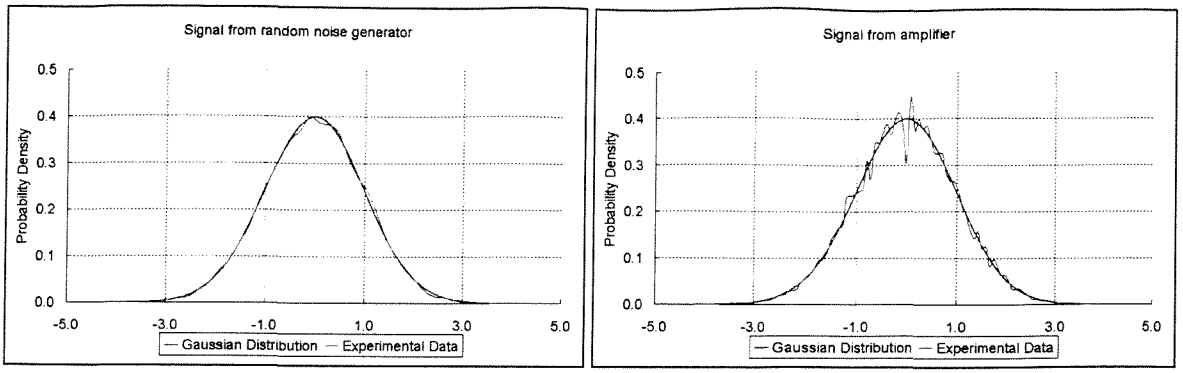

a). Reference microphone reading 140 dB

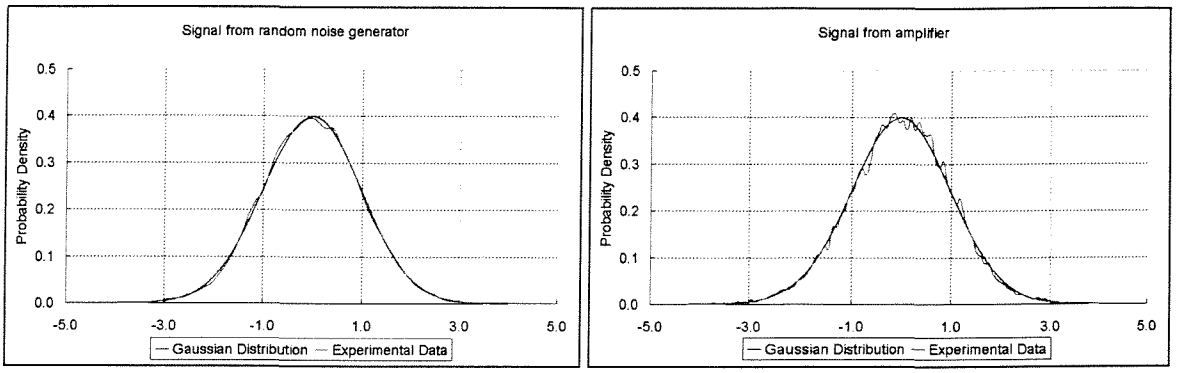

b). Reference microphone reading 150 dB

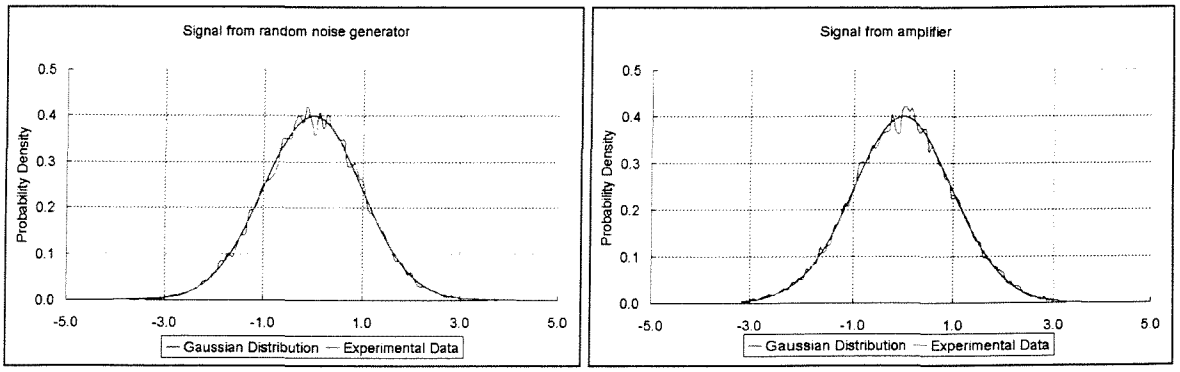

c). Reference microphone reading 160 dB

Figure 3.16 Probability density distribution of input signals

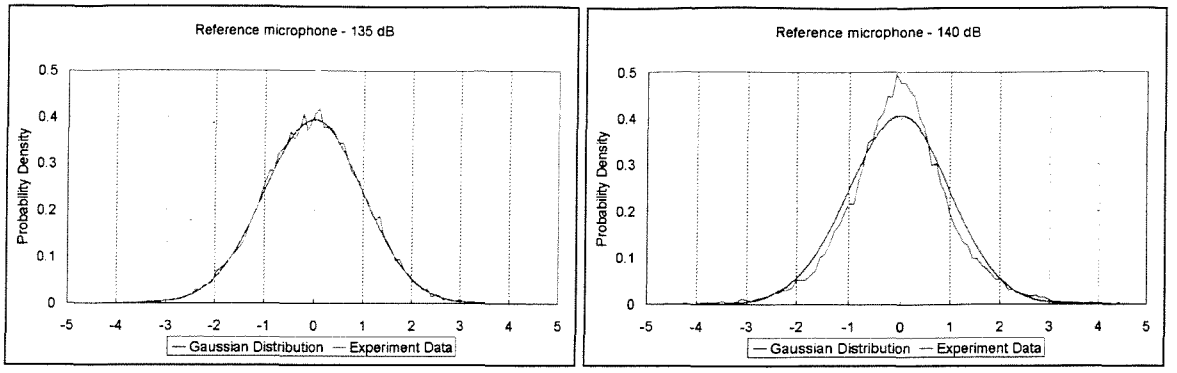

a). 135 dB b). 140 dB

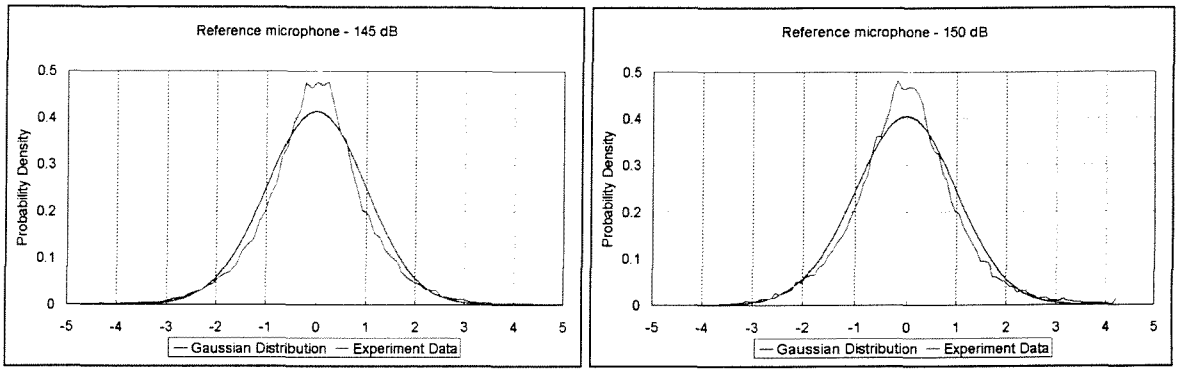

c). 145 dB d). 150 dB

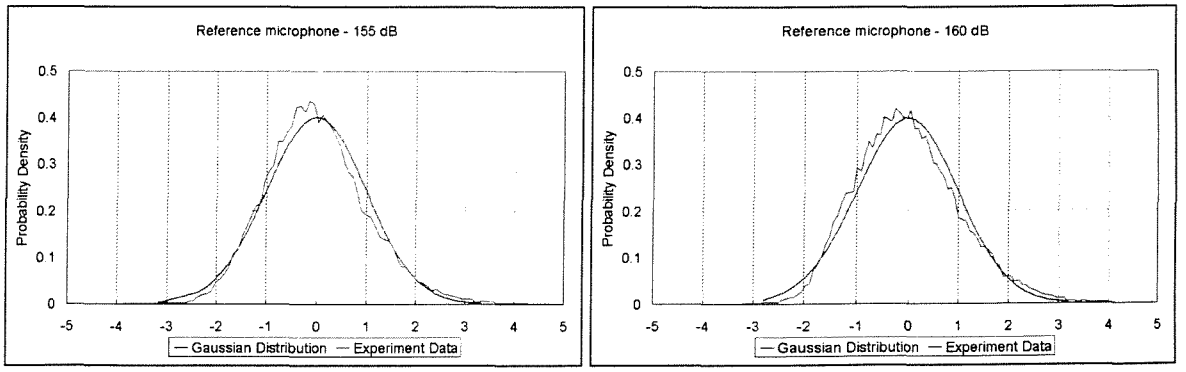

e). 155 dB e). 160 dB

Figure 3.17 Probability density distribution of signals measured by reference microphone

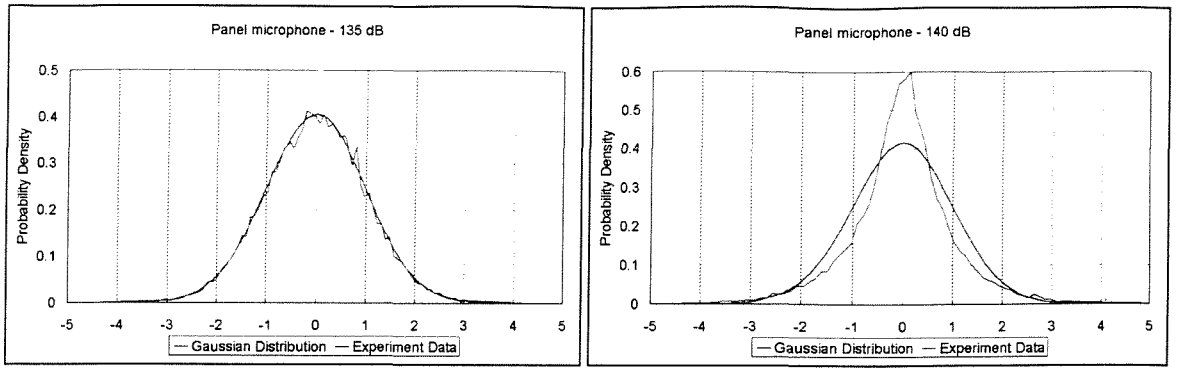

a). 135 dB b). 140 dB

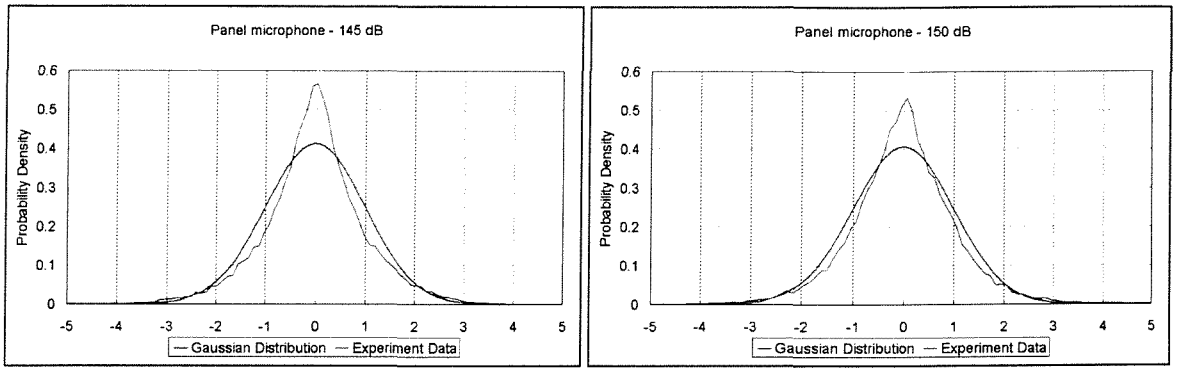

c). 145 dB d). 150 dB

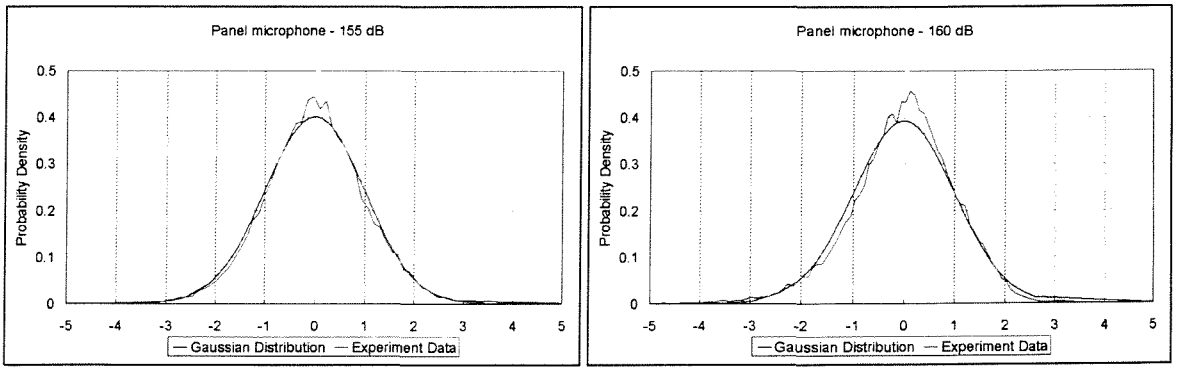

e). 155 dB e). 160 dB

Figure 3.18 Probability density distribution of signals measured by panel microphone at point 2

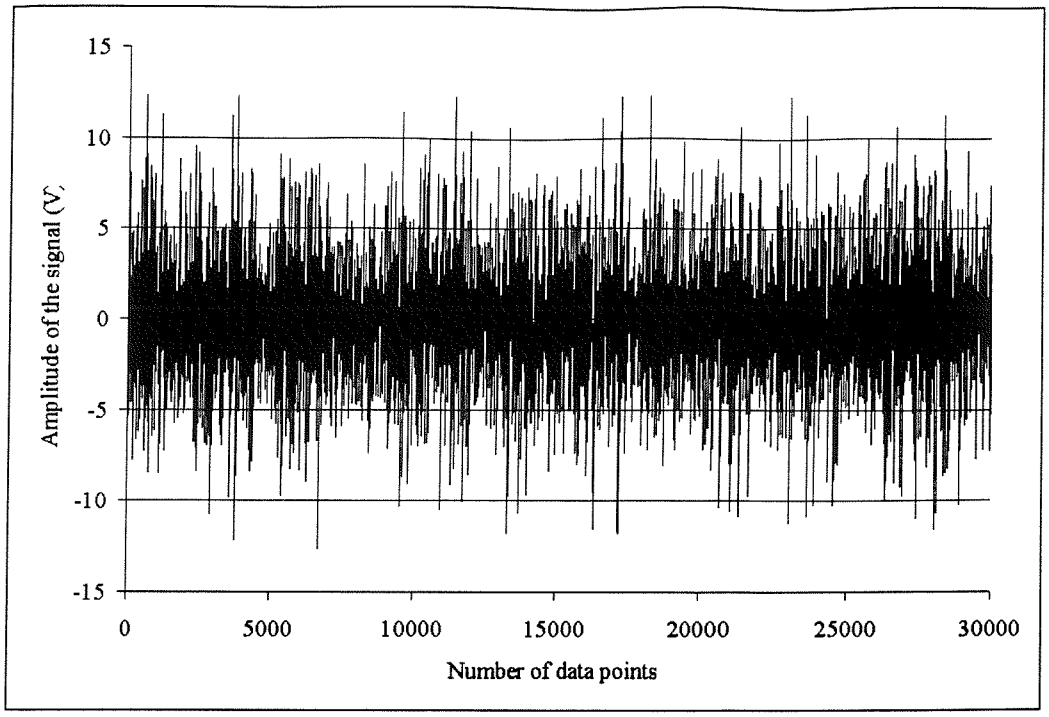

Figure 3.19 Time history of sound pressure signal measured by reference microphone (140 dB – point 2)

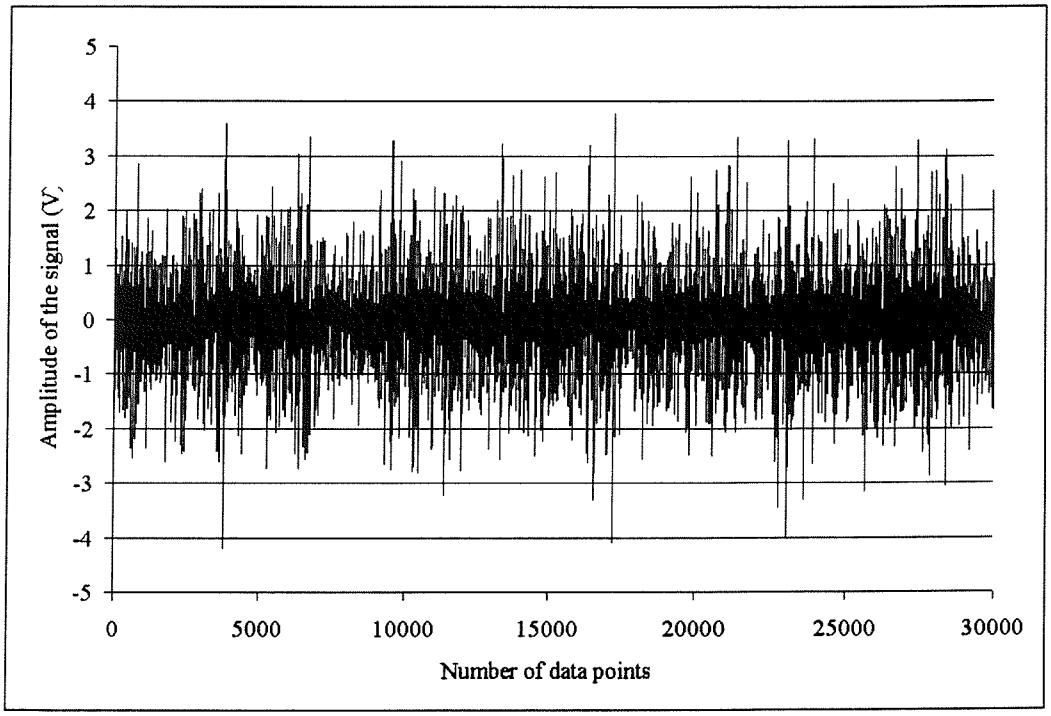

Figure 3.20 Time history of sound pressure signal measured by panel microphone (140 dB – point 2)

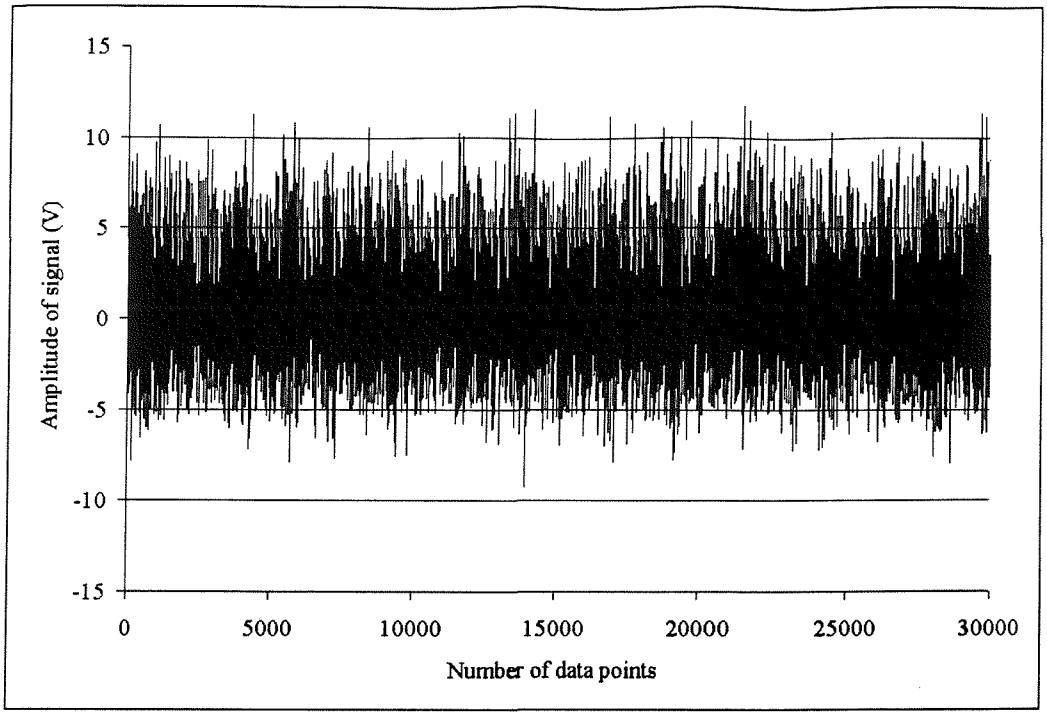

Figure 3.21 Time history of sound pressure signal measured by reference microphone (160 dB – point 2)

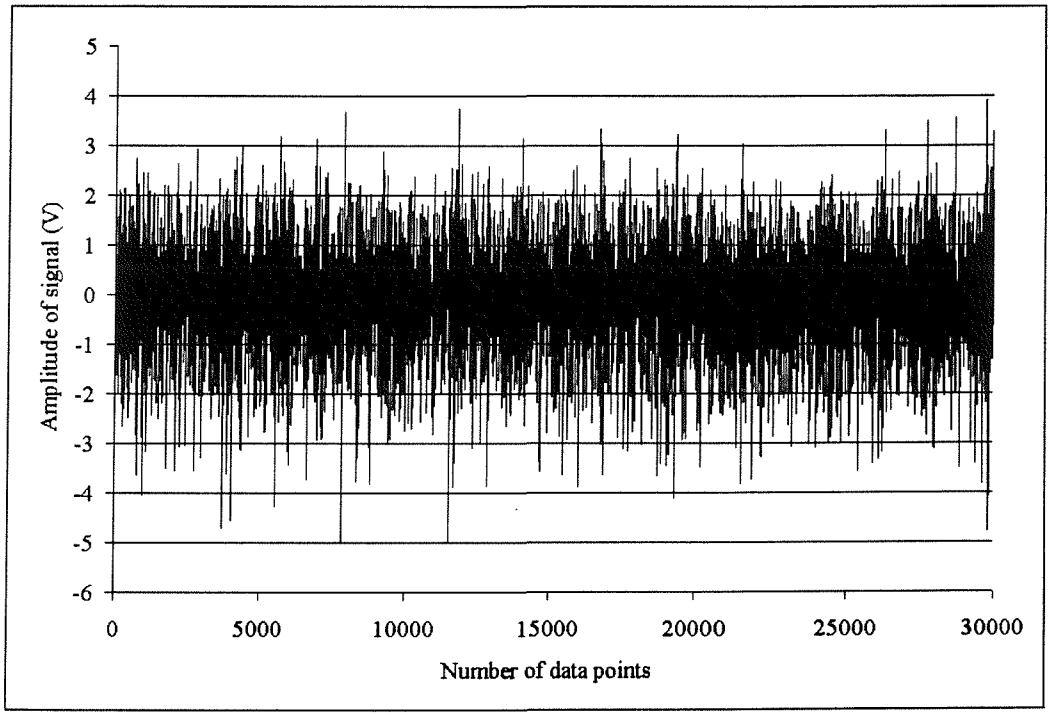

Figure 3.22 Time history of sound pressure signal measured by panel microphone (160 dB – point 2)

CHAPTER 4

EXPERIMENTAL MODAL ANALYSIS OF THE FLAP-LIKE BOX STRUCTURES

This chapter describes experimental modal analysis of the three flap-like box-type structures. The experiments were carried out on box-type structures to identify basic structural properties, such as mode shapes, resonance frequencies and damping values. The objective was to provide modal data which could be used to verify the theoretical and finite element predictions of response to random acoustic loading, incorporating measured damping data.

Modal analysis is a method for identifying the linear dynamic properties of a mechanical structure. The analysis is based on the theory that the vibration of a mechanical structure can be represented by a series of vibration modes, which are defined by their mode shapes and associated natural frequencies. The mode shape, natural frequency and damping ratio are the modal parameters, which are of importance in dynamic structural analysis. In experimental modal analysis, a dynamic force excites the test structure, and response is measured so that frequency response functions (FRFs) can be obtained. From measured FRFs modal parameters are then determined[85]. The theory and practice are well developed and some computer based commercial packages are available for this purpose. In this thesis, the **STAR** structural measurement system was used[86].

4.1 THE TEST STRUCTURES – FLAP LIKE BOX STRUCTURES

The test specimens used were the three flap-like box-type structures designed and manufactured by British Aerospace Airbus Ltd. These are representatives of aircraft flaps and were constructed from three different materials: aluminium alloy, CFRP composite and

GLARE laminates. These boxes consisted of one flat (bottom) and one curved (top) stringer stiffened skin panel together with front and rear spars and ribs which divided the structures into three bays. The end ribs were relatively rigid compared with other parts of the structures to provide mounting points during the various tests. The three boxes were built in the same way with same external dimensions, which were 1140 mm (stiffener wise) × 600 mm (rib-wise) × 80 mm to170 mm (between two skin panels). The aluminium alloy and GLARE structures were of almost exactly the same dimensions with Z-shaped stiffeners (see Appendix D), which were connected to the skins by rivets. The CFRP structure was slightly different in the dimensions of the three bays from the other two structures and had integral stiffeners (flat bar). The skin panels, ribs and spars were all connected by riveting. Figures 4.1 and 4.2 show the box structures without one of the skin panels to reveal the internal structure. It can be seen that there were access holes on the front spars and two sets of pre-made bolt holes in the end ribs for supporting the structures during the various tests.

The aluminium alloy parts in the three structures were made of different grades of BS2024 metal. All three structures had the same aluminium alloy end ribs. The skin panels of the CFRP box with integral stiffeners were made of 16 layers of CFRP unidirectional tape T300/924 with fibre volume fraction of 66%. The lay-up was same as that of the CFRP Tee-coupons with 0° fibre direction along the stiffeners as shown in Figure 2.3 of Chapter 2. The front and rear spars of the CFRP box were built of the same CFRP unidirectional tape but had 24 layers, and the inner ribs had 20 layers. For the GLARE structure, the skin panels were made of GLARE 3 with 0°/90° cross-ply glass fibre reinforced plastic and stiffeners GLARE 2 with fibre along the stringer length. The lay-up and material information of GLARE 2 and GLARE 3 are given in table 2.1 of Chapter 2 and Appendix D.2. The remainder of the components of the CFRP and GLARE boxes were the same as for the aluminium alloy structure. Construction details of the three boxes are given in Appendix D, and the material properties for the test structures are given in Appendix F.

4.2 THE EXPERIMENTAL SET-UP AND PROCEDURES

Modal tests were intended to characterise the linear dynamic properties of the box structures by extracting a number of mode shapes at specific natural frequencies. The

results are presented in the terms of modes and each includes the mode shape, resonance frequency and modal damping ratio.

4.2.1 Measurement System

During the experiments, each of the structures was mounted on a test bed by supporting brackets through 4 sets of holes on the end ribs as shown in Figure 4.3. The structure was driven by random excitation by means of a coil & magnet shaker in the frequency range from 40 Hz to 700 Hz. The response of the structure at various measuring points across the surface of the structure and the excitation force signal were measured by accelerometers and force transducer respectively to produce a series of transfer functions between the excitation and responses. The modal parameters were then extracted using the modal analysis software **STAR.**

The measurement points were mainly on both of the skin panels but measurements were also made at a few points on the spars and end ribs. The measurement grids for the skin panels are shown in Figure 4.4. There were a total of 10×25 = 250 measurement points on the middle bay of the curved skin panel and 10×21 = 210 points on the middle bay of the flat skin panel. Although the measurements were concentrated in the middle bays, measurements were also made in two side bays and on ribs and spars for the purpose of comparison. Figure 4.5 shows the instrumentation arrangements.

4.2.2 Calibration of the Measurement System

To check the instruments and experimental set-up, the necessary calibrations were undertaken based on the following concepts:

1). For a linear system, the excitation and the response of the structure have a linear relationship, so the response increases proportionally with excitation level increase, but the transfer function, which is the ratio between input and output, would remain the same. To ensure that the modal tests were carried out in their linear range, the box structures were excited at three different levels and the response at the point closest to the driving point was measured. Figure 4.6 shows the measured transfer and coherence functions at three different driving force levels (RMS) for the GLARE and CFRP structures. It can be seen

that the structures responded in a linear fashion in the driving force range used. For the modal tests, the driving force was chosen to be in this range. These tests were carried out for all three box structures to ensure that all the modal tests were performed in the linear response range of the structures.

2). To be able to obtain accurate results during the measurement of the transfer functions, it is important to know the sensitivities of the transducers used. Each transducer had the sensitivity value supplied. However, it is always a good practice to calibrate the accelerometers and force transducer before beginning any measurements due to the fact that the sensitivity of a transducer might change after being used for some time and instruments might also induce errors. Because it is difficult to measure the sensitivity of each individual transducer, the following indirect calibration method was used.

A mass was suspended on a fishing line with an exciter and force transducer at one end and an accelerometer at the other as illustrated in Figure 4.7. The relationship between the excitation force F and the response acceleration a of the mass (m) should follow Newton's Law: $F = ma$. The transfer function therefore can be expressed as $a/F = 1/m$, which means that measured transfer function should be a straight line with a constant amplitude of $1/m$ in the frequency range concerned. The ratio between a/F and $1/m$ represents an overall sensitivity S (ms^{-2}/N). This means that the actual transfer function (accelerance) is $a/F = (a/F)_m/S$, where $(a/F)_m$ is the measured transfer function. For the modal tests, only the transfer functions are of interest and this calibration method is satisfactory. Force transducer and all the accelerometers used in the measurements were calibrated in this way. Figures 4.8 shows one example of the calibration results for the transducers in the conditions of the measurement set-ups. More calibration results can be found in Appendix C.

4.3 MODAL TEST RESULTS

This section shows some of the modal test results when the skin panels of each structure were driven at the points shown in Figures 4.4(a) and 4.4(b) respectively. Measurements were made at a total of 250 points on the middle bay of the curved skin panel and 210 points on the middle bay of the flat skin panel plus a few points on two side bays and on the

spars and end ribs. Both excitation force and response acceleration signals were digitally sampled at a rate of 6,000 samples per second with record length of 5 seconds (30,000 data points) using a PC based National Instruments VXI acquisition system. Measured signals were filtered at 1kHz using a multi-channel anti-liasing filter before they were sampled. The data were then processed using the mathematical signal processing toolbox of **MATLAB** to produce the transfer and coherence functions. A random signal with frequency bandwidth of 40 Hz to 700 Hz was used as the driving signal. Typical measured spectra of the excitation forces on the three test structures are shown in Figure 4.9.

4.3.1 Frequency Response Functions

For each measurement point on the test structures, a frequency response function (FRF), i.e. transfer function, was generated. Figures 4.10 to 4.15 show some of the transfer and coherence functions of the three box structures when driven on the top panel. More results are given in Appendix C. These FRFs indicate that the highest response level was at the driving point and the lowest at a point on the inner rib line (T3) for the top skin. The two side bays also showed high response at higher frequency. When driving on the top skin panel, the responses of the bottom panel, front and rear spars and end ribs were also measured. The results can be seen in Appendix C. The responses of the end ribs were very low compared with other points on the structure. So the end ribs can be treated as rigid (clamped) boundaries. The front spar showed a relatively high response level but the response of the rear spar was much less. For the aluminium alloy structure at around 400Hz, the ratios of accelerances between driving point and other parts of the test structure were 6.4 (T3 on inner rib joint line), 1.5 (T7 side bay A), 5.4 (B1 on the bottom), 4.8 (front spar) and 90 (rear spar) and 130 (end rib). These ratios showed that response of the bottom skin was about of 20% of the top skin when driving on top skin. The response of the side bay was of about the same level as that of the middle bay; and rear spar and end rib could be treated as rigid boundaries (clamped) but not the front spar.

Due to the fact that the GLARE structure had almost the same construction as the aluminium structure, its frequency response functions showed some similarity. Comparing Figures 4.10 and 4.11 with Figures 4.12 and 4.13, it can be seen that the GLARE structure had a lower fundamental resonance frequency and higher modal density. The resonance peaks overlapped which indicates that the GLARE structure had higher damping than the

aluminium alloy structure. There were greater differences between the response levels at the driving point and other measurement points. For the most of the points given in this chapter and Appendix C, the response ratio between driving point and other points was great than 5. Both front and rear spars showed very low responses, and the response of the end rib was negligible. This means that it is less easy for driving energy to be transferred to other parts of the structure because of the higher damping and lower stiffness of a GLARE panel compared with an aluminium alloy panel.

For the CFRP structure the response levels at various measurement points had higher ratios compared with that at the driving point. The accelerance at the bottom skin (B2) was about 60% of that at the driving point. The front spar showed high response with peak accelerance value of around 35 (ms^{-2}/N) compared with 80 (ms^{-2}/N) at the driving point at the same frequency (320Hz). Compared with frequency response functions of the aluminium alloy and GLARE boxes, the differences between response levels at various measuring points were lower, which indicated the vibrational energy could be more easily transferred to other parts of the structure due to the high stiffness of CFRP skin panels. The frequency peaks of the transfer function were wider and resonance peak overlap was more evident, which indicates it had higher damping than the other two structures

4.3.2 Modal Parameters

To extract the modal parameters, the **STAR** Modal Analysis System was used which employs measured transfer functions to estimate the mode shapes and modal damping at specified resonance frequencies.

The modal analysis system STAR identifies model parameters using single degree of freedom or multi-degree of freedom curve fitting methods based on the measured frequency response functions at various points on the structure. Strictly speaking, only the deflection shapes rather than true mode shapes at resonance peaks are generated. But for lightly damped structures, deflected shapes can give a good approximation of mode shapes. Therefore, the term mode shape is used.

The mode shapes of the middle bays of the three box structures are shown in Figures 4.16 to 4.19. Mode shape plots for higher resonance frequencies are plotted in Appendix C. It

can be seen that the three structures showed very similar mode shapes and have some common characteristics. First, the natural frequencies of the curved skin panel were higher than those of the flat panels due to the existence of curvature. Secondly, in the low frequency range, the skin panels tended to vibrate as an un-stiffened panel and stiffeners deformed mainly in bending. With increasing frequency, each panel between the stiffeners behaved like a single plate and the stiffener motion became torsion dominated. From the mode shape plots, it is also observed that some modes have very similar mode shapes but different modal frequencies, such as the modes with frequencies of 298.8 Hz and 301.2 Hz for the aluminium curved panel. This could be due to that the fact although the middle bay showed similar mode shapes at different frequencies the two side bays might have deformed differently.

The modal damping ratios for three structures have also been obtained and are listed in Tables 4.1 to 4.5. The results show that the CFRP box had the highest damping ratios and the aluminium alloy structure had the lowest values among the test structures. The overall average damping ratios across the modal frequencies measured for the CFRP, GLARE and aluminium alloy structures were 1.14%, 0.71% and 0.55% respectively.

To evaluate the degree of correlation between modes, The Modal Assurance Criterion (MAC) data were also obtained, which checks the orthogonality between the modes. If two modes are identical or the difference between them is only a matter of a scalar factor, the MAC = 1; and if two modes are unrelated the MAC = 0.0. This implies that the MAC table should have the value of 1 along the diagonal line and 0.0 for the remainder of the data. For good experimental data, values close to 1 or 0.0 are expected.

The MAC tables for the middle bays of the flat skin panels for the three boxes are listed in Tables 4.6 to 4.8. For the most of modes, the results are satisfactory. The MAC tables also show a certain degree of correlation between a few modes, this could be due to the fact that the data presented are only for part of the structure. If all of the three bays were considered together, improvement of the MAC value of certain modes could be expected.

4.4 SUMMARY

Experimental modal tests had been carried out on the three box-type structures. When driving on the middle bay of the top skin, other parts such as the bottom skin, side bays and front spars all showed various levels of response, and not the rear spar and end ribs, for all three structures. The GLARE structure exhibited a similar frequency response function to the aluminium alloy box but with lower fundamental frequency and higher modal density. Due to the high damping value of The CFRP material, measured transfer functions of the CFRP structure showed wide peaks and strong modal overlap. It was found that response levels at various measuring points were more evenly distributed for the CFRP box than for the other two boxes due to the high stiffness of the CFRP skin panels. The mode shape results showed that stiffened skin panels behave like an un-stiffened panel at low frequency where the stiffeners are mainly subjected to bending deformation. At high frequency, each bay between stiffeners vibrates like a simply supported plate and the stiffeners are mainly in torsion.

The modal damping ratios were obtained, which showed that the CFRP box structure had the highest damping ratios and the aluminium alloy structure had the lowest damping values among the three box structures. Typical damping ratios for the CFRP, GLARE and aluminium alloy structures are 1.14%, 0.71% and 0.55% respectively.

The Modal Assurance Criterion (MAC) data were obtained. Results showed that most of the modal results are satisfactory.

Table 4.1 Modal frequency and modal damping ratio of curved skin panel of the aluminium alloy box structure

Mode No.	Modal Frequency (Hz)	Modal Damping Ratio (%)
1	184.8	1.73
2	237.6	0.94
3	266.4	0.92
4	285.6	1.05
5	298.8	0.59
6	301.2	0.44
7	321.6	0.39
8	340.8	0.44
9	395.4	0.33
10	457.2	0.89
11	498.0	0.41
12	520.8	0.52
13	546.0	0.54
14	573.6	0.42
15	633.6	0.20
16	657.6	0.21
17	681.6	0.85
18	694.8	0.64
19	807.6	0.35
20	819.6	0.28
Average Damping Ratio (%)		0.62

Table 4.2 Modal frequency and modal damping ratio of flat skin panel of the aluminium alloy box structure

Mode No.	Modal Frequency (Hz)	Modal Damping Ratio (%)
1	173.0	1.31
2	259.5	0.50
3	269.5	0.63
4	399.5	0.51
5	402.0	0.38
6	444.0	0.43
7	472.8	0.44
8	500.4	0.40
9	518.4	0.48
10	530.4	0.40
11	562.2	0.32
12	584.4	0.51
13	628.8	0.67
14	661.2	0.52
15	676.8	0.30
16	694.8	0.41
17	728.4	0.80
18	756.0	0.26
19	769.2	0.66
20	814.7	0.20
21	818.4	0.32
22	865.2	0.33
23	894.0	0.48
Average Damping Ratio (%)		0.49

Table 4.3 Modal frequency and modal damping ratio of curved skin panel of the CFRP box structure

Mode No.	Modal Frequency (Hz)	Modal Damping Ratio (%)
1	218.4	2.59
2	241.8	2.14
3	264.0	1.26
4	282.0	1.02
5	320.4	1.08
6	361.2	0.21
7	388.8	0.82
8	399.6	0.83
9	433.2	1.17
10	459.6	1.25
11	477.2	1.22
12	493.2	1.48
13	540.0	1.79
14	568.8	0.80
15	579.6	1.71
16	616.8	1.04
17	658.8	0.46
18	724.8	1.18
19	788.4	1.03
20	849.6	0.80
21	877.2	0.70
22	930.0	0.90
Average Damping Ratio (%)		1.16

Table 4.4 Modal frequency and modal damping ratio of flat skin panel of the CFRP box structure

Mode No.	Modal Frequency (Hz)	Modal Damping Ratio (%)
1	185.7	1.00
2	216.9	1.87
3	259.2	1.22
4	285.5	1.02
5	320.8	1.32
6	359.1	1.50
7	406.5	1.23
8	492.6	1.00
9	557.7	1.01
10	602.7	1.34
11	637.4	0.70
12	658.3	0.91
13	712.3	0.64
14	734.1	1.11
15	811.6	1.29
16	878.0	0.68
Average Damping Ratio (%)		1.11

Table 4.5 Modal frequency and modal damping ratio of flat skin panel of the GLARE box structure

Mode No.	Modal Frequency (Hz)	Modal Damping Ratio (%)
1	181.2	2.07
2	229.2	0.93
3	237.6	0.68
4	251.3	0.80
5	259.1	0.78
6	277.2	0.70
7	282.2	0.73
8	303.6	0.69
9	318.1	1.01
10	348.0	0.38
11	368.4	0.83
12	383.3	0.83
13	410.4	0.90
14	412.8	0.89
15	442.8	0.67
16	462.0	1.26
17	541.2	0.43
18	567.6	0.56
19	596.4	0.37
20	637.2	0.61
21	678.0	0.47
22	686.4	0.38
23	727.2	0.56
24	740.4	0.55
25	776.4	0.38
26	802.8	0.83
27	843.6	0.25
28	871.2	0.69
29	931.2	0.42
Average Damping Ratio (%)		0.71

Table 4.6 Modal Assurance Criterion of the flat (bottom) skin panel of the aluminium alloy structure

	1	2	3	4	5	5	6	7	8	9	10	11	12	13	14	15	16	17	19	20	21	22	23
1	1	0.02	0.05	0.14	0.01	0.01	0	0.01	0	0	0.03	0.02	0.01	0.02	0.01	0	0.02	0.02	0.02	0	0	0	0.01
2	0.02	1	0.39	0.04	0.06	0	0.01	0.01	0	0.01	0.02	0	0.02	0	0	0.01	0	0	0	0	0	0	0
3	0.05	0.39	1	0	0.17	0	0.01	0.07	0.02	0.02	0	0	0.01	0.01	0	0.01	0.01	0	0.02	0	0	0	0
4	0.14	0.04	0	1	0.01	0.01	0.07	0.04	0.1	0.03	0.06	0.02	0.03	0.03	0.02	0	0	0.03	0	0.02	0.02	0	0
5	0.01	0.06	0.17	0.01	1	0.01	0.01	0	0	0.01	0.04	0	0.02	0	0	0	0.02	0.01	0	0.01	0.01	0.01	0
6	0.01	0	0	0.01	0.01	1	0.38	0	0.23	0.09	0.1	0.07	0	0.01	0.02	0	0	0.01	0.01	0	0	0.01	0.02
7	0	0.01	0.01	0.07	0.01	0.38	1	0.3	0.19	0.02	0.12	0	0.01	0.01	0	0	0.02	0.01	0.02	0	0	0	0.06
8	0.01	0.01	0.07	0.04	0	0	0.3	1	0.11	0.45	0.21	0.01	0.02	0.01	0.01	0	0.04	0.02	0.01	0	0	0	0.02
9	0	0	0.02	0.1	0	0.23	0.19	0.11	1	0.05	0.07	0.12	0	0.01	0.02	0	0.06	0.06	0.01	0.01	0.01	0	0.01
10	0	0.01	0.02	0.03	0.01	0.09	0.02	0.45	0.05	1	0.03	0.04	0.06	0	0.01	0	0.06	0.01	0	0	0	0	0.01
11	0.03	0.02	0	0.06	0.04	0.1	0.12	0.21	0.07	0.03	1	0.42	0.21	0.1	0.16	0.03	0	0.04	0.05	0	0.01	0	0
12	0.02	0	0	0.02	0	0.07	0	0.01	0.12	0.04	0.42	1	0.12	0.04	0.13	0.03	0	0.02	0.05	0.01	0.01	0	0
13	0.01	0.02	0.01	0.03	0.02	0	0.01	0.02	0	0.06	0.21	0.12	1	0.02	0.02	0.05	0	0	0.06	0.02	0.03	0	0
14	0.02	0	0.01	0.03	0	0.01	0.01	0.01	0.01	0	0.1	0.04	0.02	1	0.73	0.02	0	0.12	0.06	0.01	0.01	0	0
15	0.01	0	0	0.02	0	0.02	0	0.01	0.02	0.01	0.16	0.13	0.02	0.73	1	0.16	0.03	0.02	0.18	0	0.01	0.02	0
16	0	0.01	0.01	0	0	0	0	0	0	0	0.03	0.03	0.05	0.02	0.16	1	0.06	0.09	0.01	0.02	0.03	0.01	0
17	0.02	0	0.01	0	0.02	0	0.02	0.04	0.06	0.06	0	0	0	0	0.03	0.06	1	0.47	0.01	0.09	0.09	0.18	0.03
18	0.02	0	0	0.03	0.01	0.01	0.01	0.02	0.06	0.01	0.04	0.02	0	0.12	0.02	0.09	0.47	1	0.01	0.16	0.16	0.15	0.05
19	0.02	0	0.02	0	0	0.01	0.02	0.01	0.01	0	0.05	0.05	0.06	0.06	0.18	0.01	0.01	0.01	1	0.29	0.26	0.05	0.05
20	0	0	0	0.02	0.01	0	0	0	0.01	0	0	0.01	0.02	0.01	0	0.02	0.09	0.16	0.29	1	0.92	0.1	0.04
21	0	0	0	0.02	0.01	0	0	0	0.01	0	0.01	0.01	0.03	0.01	0.01	0.03	0.09	0.16	0.26	0.92	1	0.05	0.04
22	0	0	0	0	0.01	0.01	0	0	0	0	0	0	0	0	0.02	0.01	0.18	0.15	0.05	0.1	0.05	1	0
23	0.01	0	0	0	0	0.02	0.06	0.02	0.01	0.01	0	0	0	0	0	0	0.03	0.05	0.05	0.04	0.04	0	1

Table 4.7 Modal Assurance Criterion of the flat (bottom) skin panel of the CFRP structure

modes	1	2	3	4	5	6	7	8	9	10	11	12	13	14	15	16
1	1	0.4	0.12	0	0	0.01	0	0	0	0	0	0	0	0	0	0
2	0.4	1	0.07	0.02	0.04	0.05	0.03	0	0.04	0	0	0.02	0	0	0.01	0.02
3	0.12	0.07	1	0.25	0.01	0	0	0.01	0	0	0	0.02	0	0	0	0.01
4	0	0.02	0.25	1	0	0	0	0.01	0	0	0.02	0.01	0	0	0.01	0
5	0	0.04	0.01	0	1	0.01	0.05	0	0.05	0	0.01	0	0	0.01	0	0.02
6	0.01	0.05	0	0	0.01	1	0.07	0	0	0	0	0.01	0.01	0	0.01	0
7	0	0.03	0	0	0.05	0.07	1	0.15	0.17	0	0.02	0.06	0.01	0.03	0.03	0.04
8	0	0	0.01	0.01	0	0	0.15	1	0.15	0.01	0.1	0.07	0	0	0	0.01
9	0	0.04	0	0	0.05	0	0.17	0.15	1	0.02	0.03	0.03	0	0.02	0.01	0.01
10	0	0	0	0	0	0	0	0.01	0.02	1	0.15	0.1	0.05	0.11	0.05	0.07
11	0	0	0	0.02	0.01	0	0.02	0.1	0.03	0.15	1	0.11	0.03	0	0.05	0.03
12	0	0.02	0.02	0.01	0	0.01	0.06	0.07	0.03	0.1	0.11	1	0	0	0.16	0
13	0	0	0	0	0	0.01	0.01	0	0	0.05	0.03	0	1	0.11	0	0.03
14	0	0	0	0	0.01	0	0.03	0	0.02	0.11	0	0	0.11	1	0	0.07
15	0	0.01	0	0.01	0	0.01	0.03	0	0.01	0.05	0.05	0.16	0	0	1	0.07
16	0	0.02	0.01	0	0.02	0	0.04	0.01	0.01	0.07	0.03	0	0.03	0.07	0.07	1

Table 4.8 Modal Assurance Criterion of the flat (bottom) skin panel of the GLARE structure

mode	1	2	3	4	5	6	7	8	9	10	11	12	13	14	15	16	17	18	19	20	21	22	23	24	25	26	27	28	29
1	1	0.44	0.11	0.01	0.04	0.16	0.02	0.02	0.01	0.06	0.05	0.09	0	0.01	0.02	0	0	0.01	0	0.01	0	0.04	0	0	0	0	0	0	0
2	0.44	1	0.46	0.1	0.08	0.12	0	0.06	0.02	0.01	0.13	0.01	0.01	0	0	0	0	0.01	0	0	0	0.01	0	0.01	0.01	0.01	0	0	0
3	0.11	0.46	1	0.06	0.01	0.13	0.08	0.05	0.01	0.03	0.06	0.05	0.03	0.01	0.01	0.01	0	0.01	0	0.02	0.01	0.01	0	0.03	0.01	0	0.01	0	0
4	0.01	0.1	0.06	1	0.17	0.05	0.16	0	0	0.02	0.02	0.03	0.01	0.03	0	0.01	0	0.01	0.05	0	0	0.02	0	0	0	0.01	0	0	0
5	0.04	0.08	0.01	0.17	1	0.08	0.14	0.02	0.01	0.01	0.01	0.03	0.08	0.01	0.01	0	0.01	0.01	0.14	0.02	0.01	0.01	0	0.05	0.01	0.01	0	0	0
6	0.16	0.12	0.13	0.05	0.08	1	0.48	0.22	0.15	0.13	0.05	0.05	0.01	0.01	0.01	0	0	0	0.05	0.01	0	0.02	0	0.01	0	0.01	0	0	0
7	0.02	0	0.08	0.16	0.14	0.48	1	0.05	0.32	0.11	0.04	0.04	0.01	0.05	0	0.01	0	0	0.03	0.02	0	0.02	0	0.02	0	0.02	0	0	0
8	0.02	0.06	0.05	0	0.02	0.22	0.05	1	0.05	0.12	0.06	0.03	0.05	0.01	0.01	0.01	0	0.01	0	0	0	0	0	0	0.01	0.01	0	0	0
9	0.01	0.02	0.01	0	0.01	0.15	0.32	0.05	1	0.39	0.04	0.34	0	0	0.01	0.01	0.01	0.01	0.02	0.02	0	0	0	0.01	0	0.01	0.01	0	0
10	0.06	0.01	0.03	0.02	0.01	0.13	0.11	0.12	0.39	1	0.21	0.48	0.02	0.02	0	0.07	0	0	0.01	0.03	0	0	0	0	0.02	0.01	0.01	0	0
11	0.05	0.13	0.06	0.02	0.01	0.05	0.04	0.06	0.04	0.21	1	0.03	0.01	0	0.02	0.01	0	0	0.01	0.01	0	0	0	0	0	0.01	0.01	0	0.01
12	0.09	0.01	0.05	0.03	0.03	0.05	0.04	0.03	0.34	0.48	0.03	1	0.08	0.05	0	0.05	0	0	0	0.05	0	0.02	0	0	0.01	0.01	0.02	0	0
13	0	0.01	0.03	0.01	0.08	0.01	0.01	0.05	0	0.02	0.01	0.08	1	0.37	0.06	0.01	0	0	0	0.02	0.01	0	0.01	0.01	0.01	0.01	0.01	0.02	0
14	0.01	0	0.01	0.03	0.01	0.01	0.05	0.01	0	0.02	0	0.05	0.37	1	0.28	0.01	0.01	0	0.07	0	0.01	0	0	0.02	0	0	0.01	0.02	0
15	0.02	0	0.01	0	0.01	0.01	0	0.01	0.01	0	0.02	0	0.06	0.28	1	0.07	0.03	0	0.01	0	0.01	0.02	0	0	0	0	0.01	0.03	0
16	0	0	0.01	0.01	0	0	0.01	0.01	0.01	0.07	0.01	0.05	0.01	0.01	0.07	1	0.05	0.02	0	0	0.01	0	0	0	0.01	0	0	0.01	0
17	0	0	0	0	0.01	0	0	0	0.01	0	0	0	0	0.01	0.03	0.05	1	0	0.16	0	0	0.01	0.01	0	0	0	0.01	0	0
18	0.01	0.01	0.01	0.01	0.01	0	0	0.01	0.01	0	0	0	0	0	0	0.02	0	1	0	0	0.01	0	0.02	0	0.01	0.01	0	0	0
19	0	0	0	0.05	0.14	0.05	0.03	0	0.02	0.01	0.01	0	0	0.07	0.01	0	0.16	0	1	0.03	0.06	0.01	0	0.01	0	0	0.01	0	0
20	0.01	0	0.02	0	0.02	0.01	0.02	0	0.02	0.03	0.01	0.05	0.02	0	0	0	0	0	0.03	1	0.1	0.01	0	0.01	0	0.02	0.01	0	0
21	0	0	0.01	0	0.01	0	0	0	0	0	0	0	0.01	0.01	0.01	0.01	0	0.01	0.06	0.1	1	0.19	0.14	0.01	0.02	0.01	0.02	0.01	0
22	0.04	0.01	0.01	0.02	0.01	0.02	0.02	0	0	0	0	0.02	0	0	0.02	0	0.01	0	0.01	0.01	0.19	1	0.21	0.04	0	0	0.05	0	0
23	0	0	0	0	0	0	0	0	0	0	0	0	0.01	0	0	0	0.01	0.02	0	0	0.14	0.21	1	0.04	0.06	0.01	0	0	0.01
24	0	0.01	0.03	0	0.05	0.01	0.02	0	0.01	0	0	0	0.01	0.02	0	0	0	0	0.01	0.01	0.01	0.04	0.04	1	0.19	0.01	0	0.01	0.02
25	0	0.01	0.01	0	0.01	0	0	0.01	0	0.02	0	0.01	0.01	0	0	0.01	0	0.01	0	0	0.02	0	0.06	0.19	1	0.14	0.03	0.01	0.01
26	0	0.01	0	0.01	0.01	0.01	0.02	0.01	0.01	0.01	0.01	0.01	0.01	0	0	0	0	0.01	0	0.02	0.01	0	0.01	0.01	0.14	1	0.01	0	0
27	0	0	0.01	0	0	0	0	0	0.01	0.01	0.01	0.02	0.01	0.01	0.01	0	0.01	0	0.01	0.01	0.02	0.05	0	0	0.03	0.01	1	0.01	0.02
28	0	0	0	0	0	0	0	0	0	0	0	0	0.02	0.02	0.03	0.01	0	0	0	0	0.01	0	0	0.01	0.01	0	0.01	1	0
29	0	0	0	0	0	0	0	0	0	0	0.01	0	0	0	0	0	0	0	0	0	0	0	0.01	0.02	0.01	0	0.02	0	1

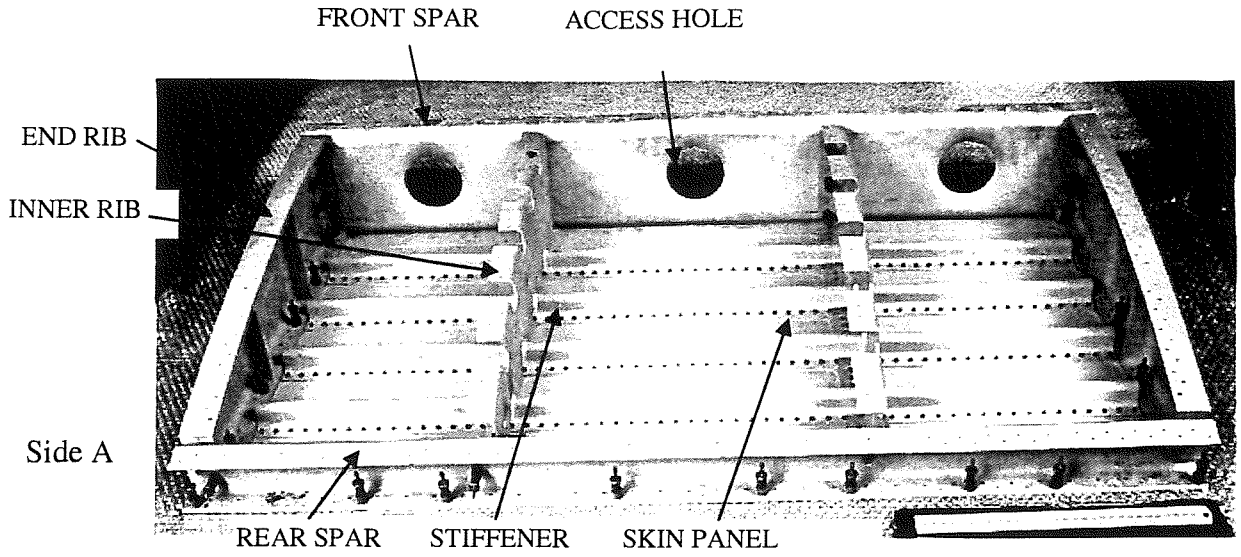

Figure 4.1 Aluminium alloy and GLARE flap-like box without curved panel to show the inside structure

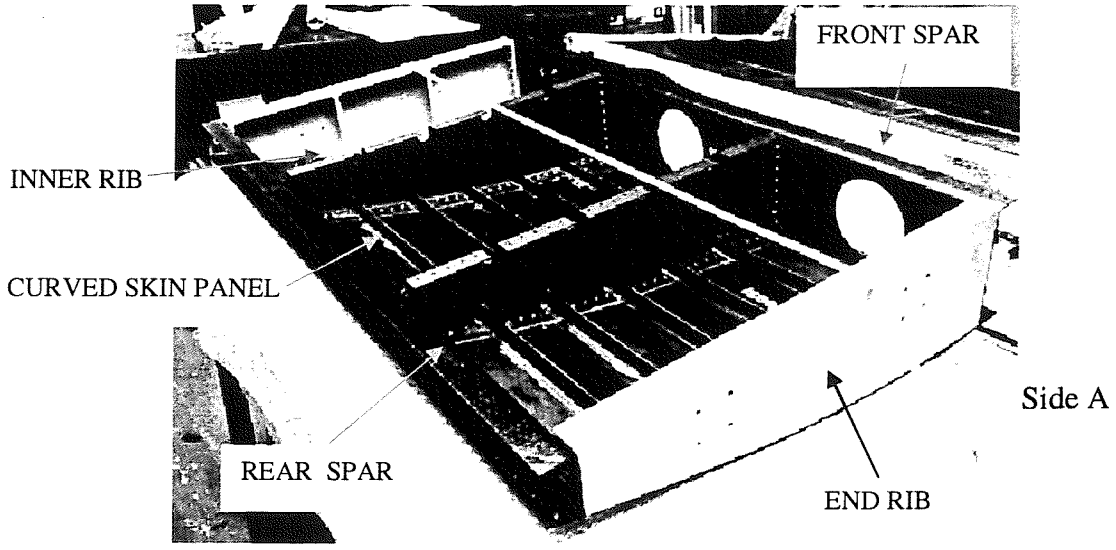

Figure 4.2 CFRP flap-like box without flat panel to show the inside structure

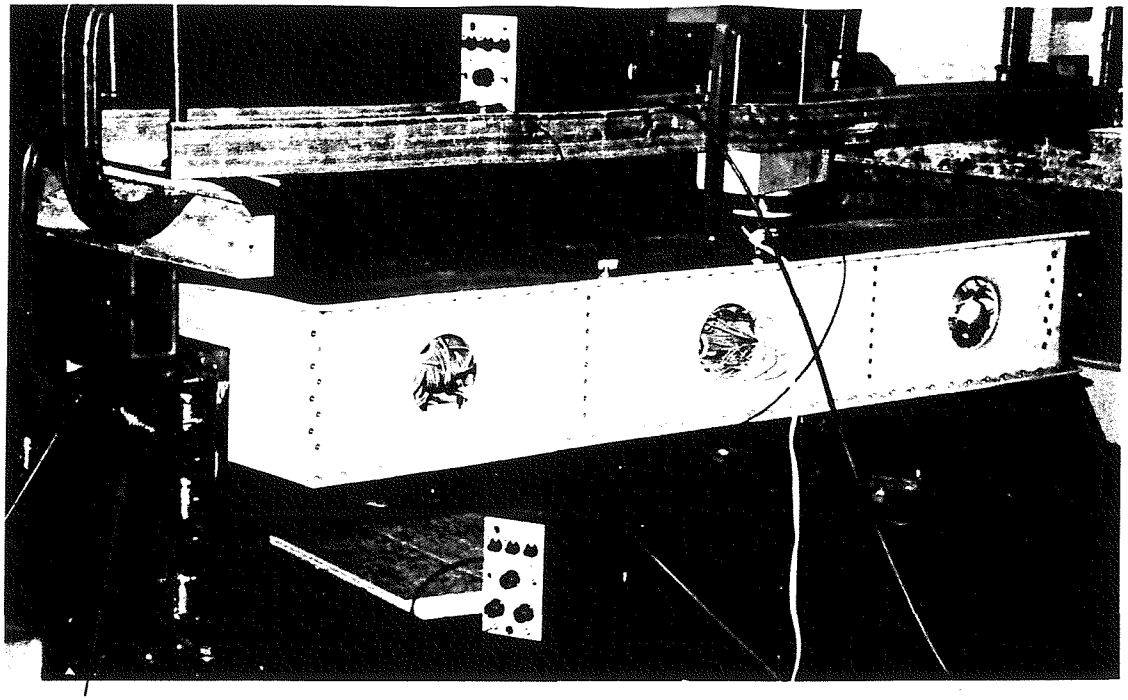

a) Test set-up

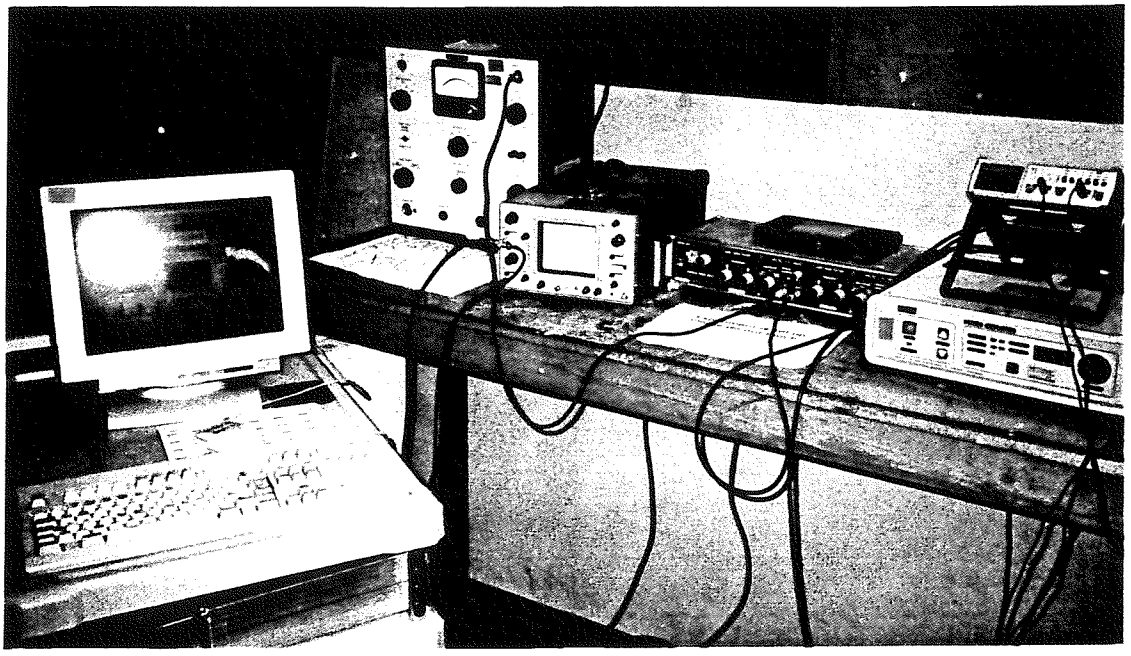

b) Instrumentation

Figure 4.3 Box structure mounted on the test bed for modal testing

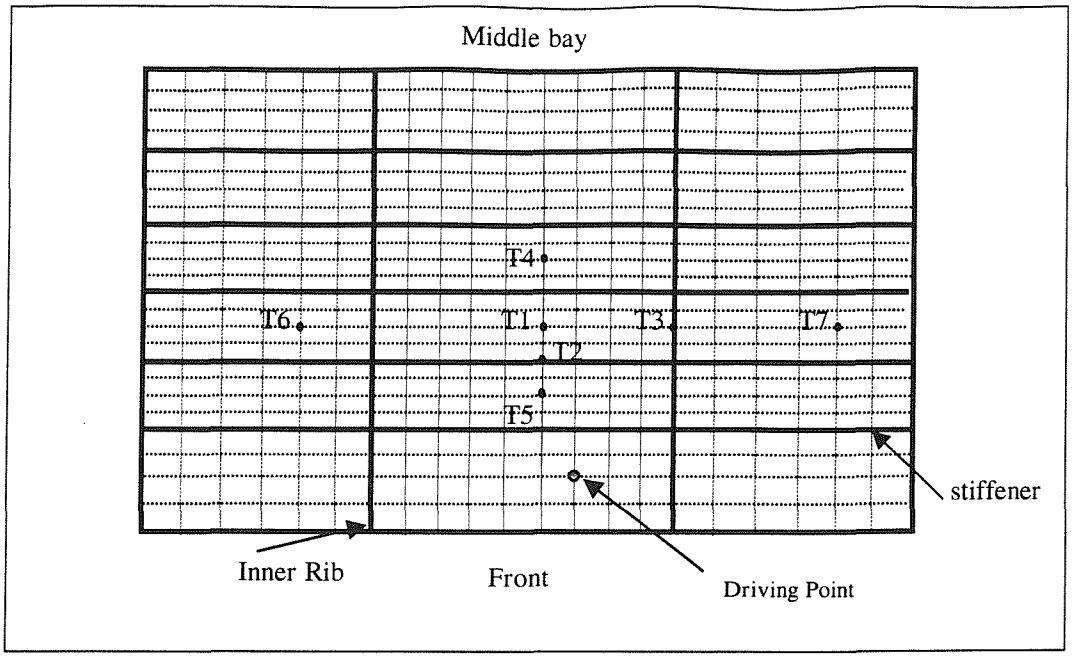

a) Curved skin panel (10×25=250 measuring points)

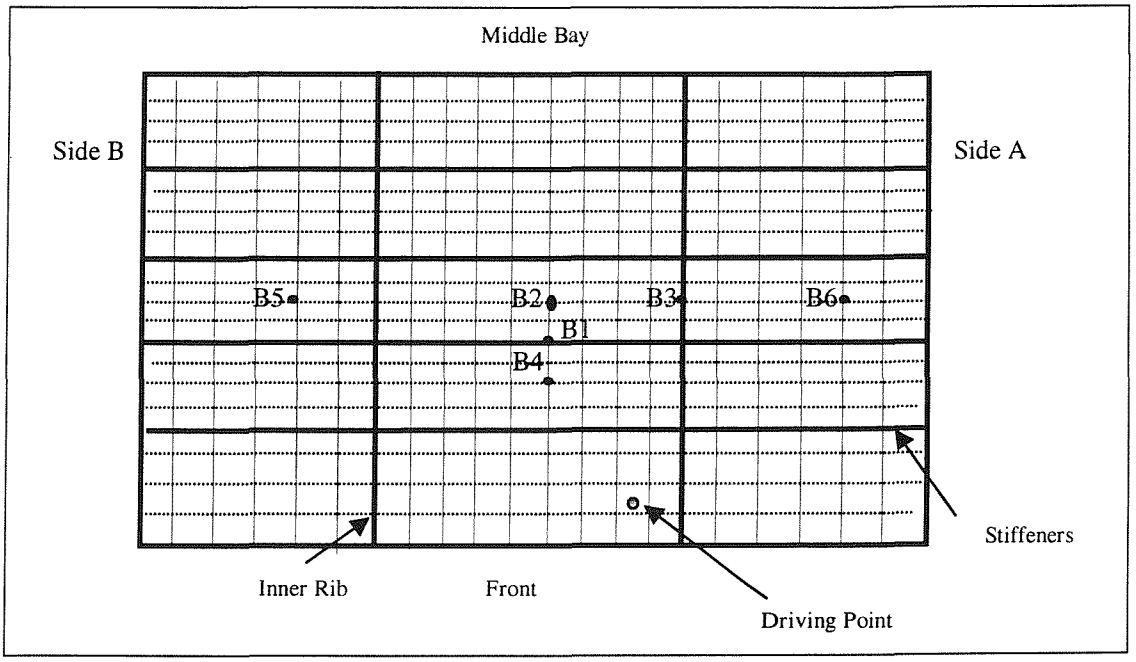

b) Flat skin panel (10×21=210 measuring points)

Figure 4.4 Modal test measurement points on the box structures (at intersections of grid)

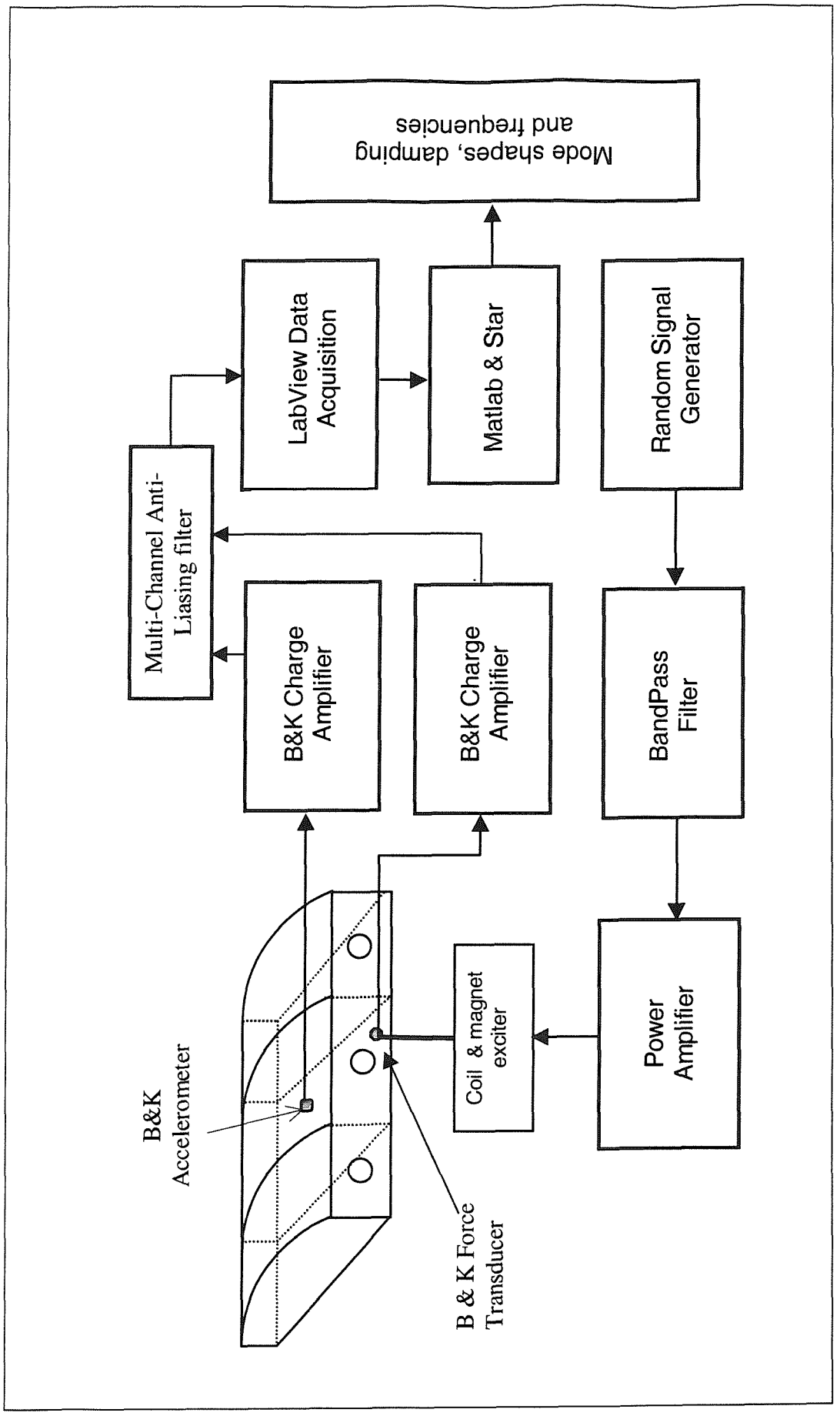

Figure 4.5 Instrument arrangement for the modal tests of the box structure

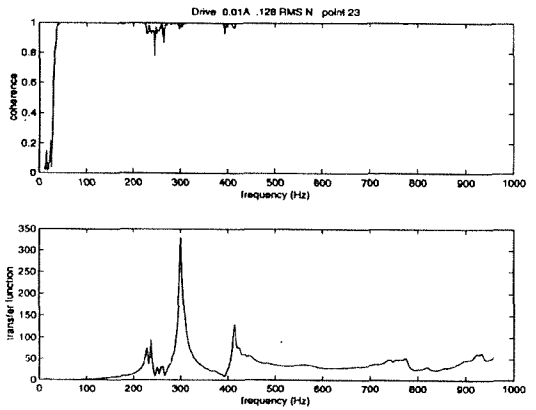

Driving force 0.231N (RMS)

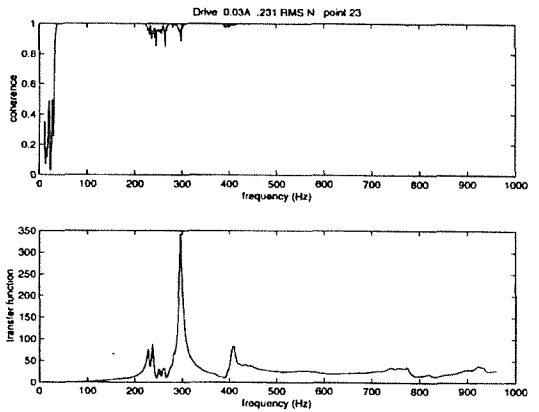

Driving force 0.128N (RMS)
GLARE structure

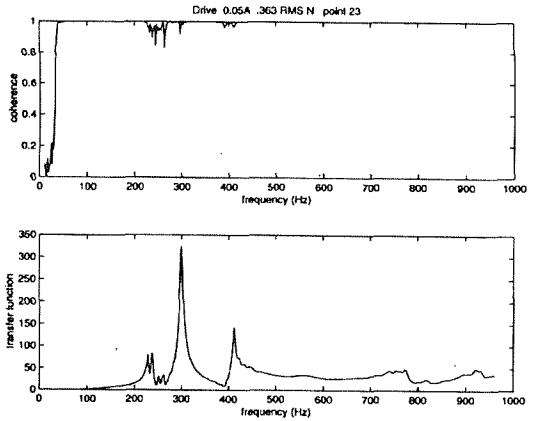

Driving force 0.363N (RMS)

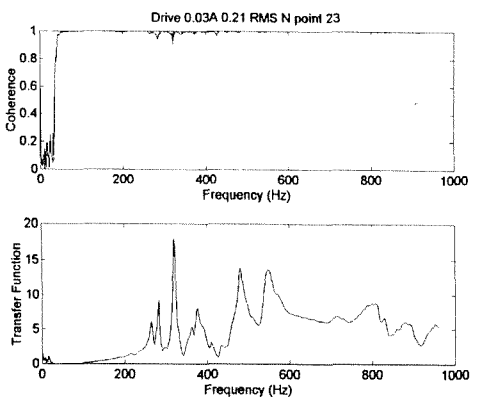

Driving force 0.21N (RMS)

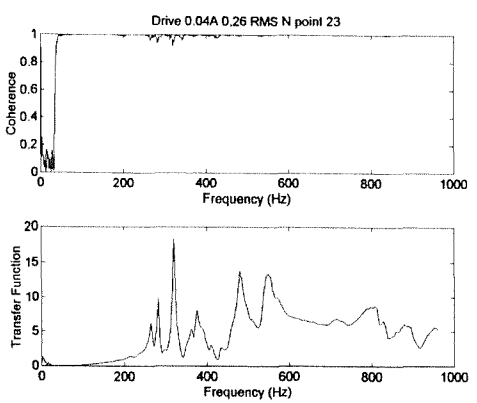

Driving force 0.26N (RMS)
CFRP structure

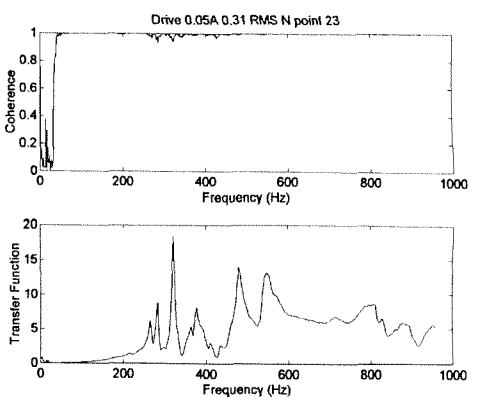

Driving force 0.31N (RMS)

(Upper – Coherence Lower – Transfer Function)

Figure 4.6 Modal test linearity check of CFRP box structure (Top excitation, measured at the point next to driving point)

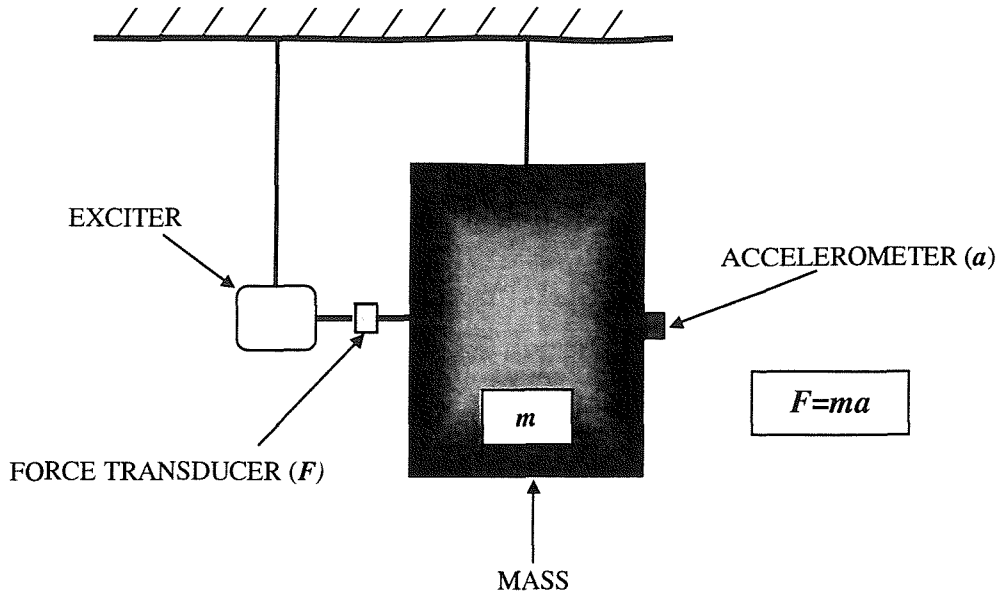

Figure 4.7 Accelerometer and force transducer calibration

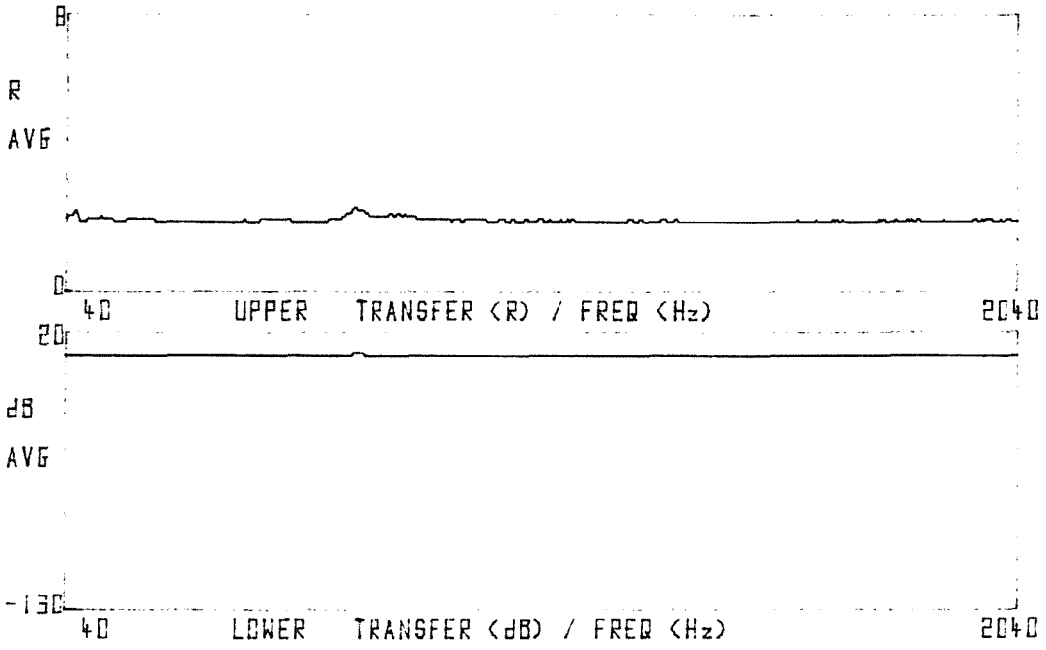

(Upper – Linear scale Lower – Logarithmic scale)

overall sensitivity was 0.77 (ms^{-2}/N)

B&K force transducer Type 8200 (No.673465)
B&K accelerometer Type 4344 (No.225380)

Figure 4.8 Calibration result of transducers for the modal tests of the box structures

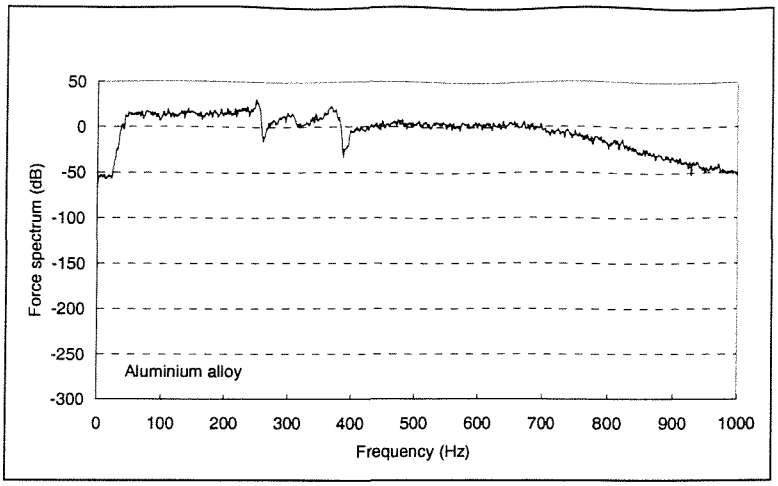

a) Aluminium alloy structure

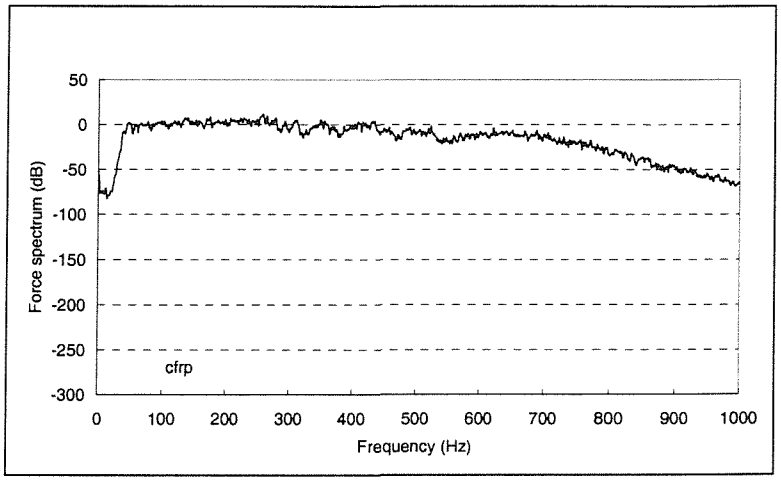

b) CFRP structure

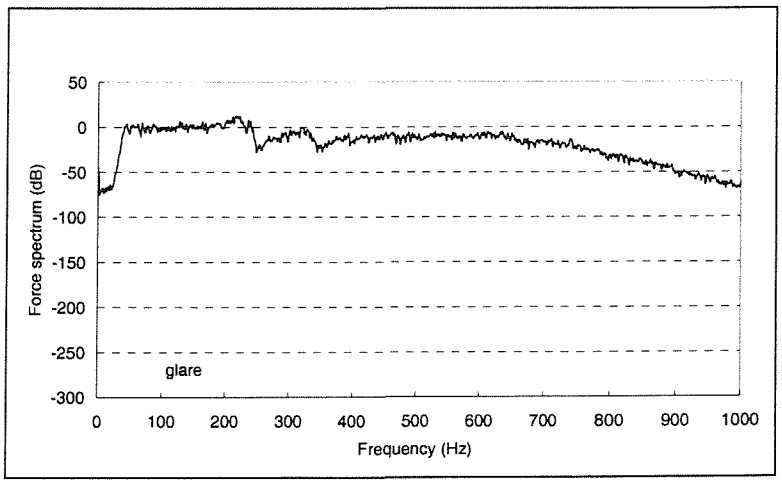

c) GLARE structure

Figure 4.9 Spectra of the excitation force measured in the modal tests of the box structures (driven on the top panel)

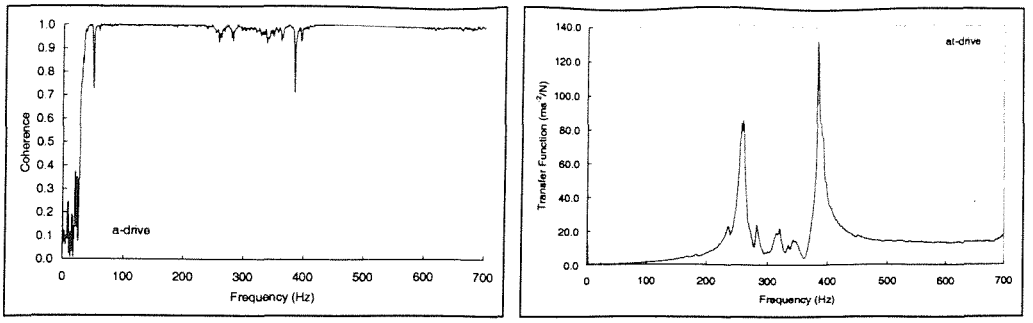

a) Coherence b) Transfer function

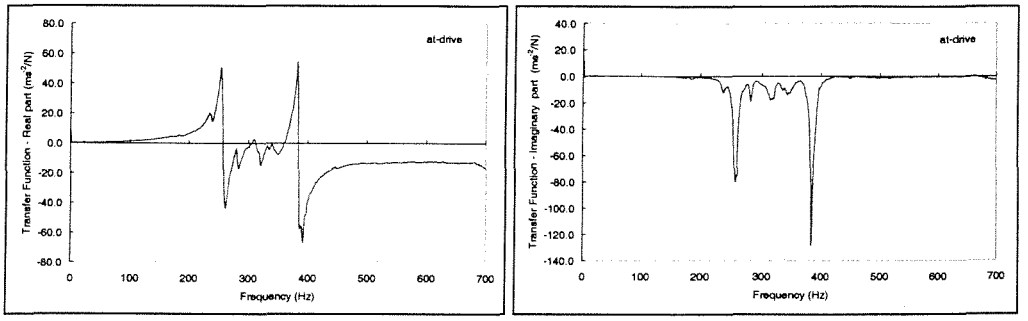

c) Real part d) Imaginary part

Figure 4.10 Measured coherence and transfer functions of driving point on the curved panel of aluminium box

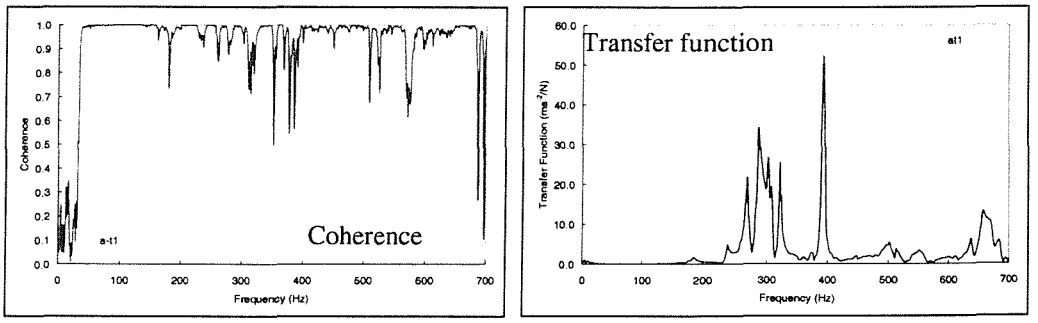

a) top skin panel - point T1

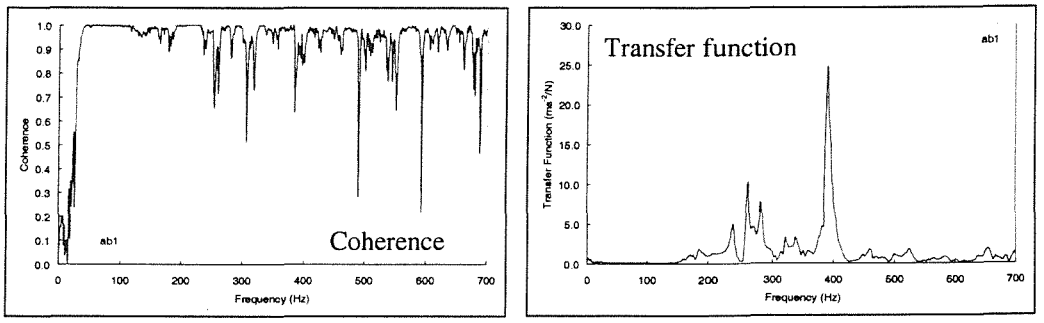

b) bottom skin panel - point B1

Figure 4.11 Measured coherence and transfer functions of aluminium box

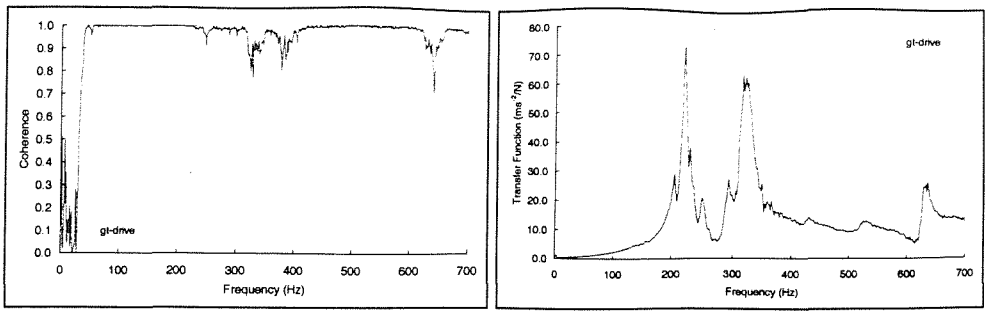

a) Coherence b) Transfer function

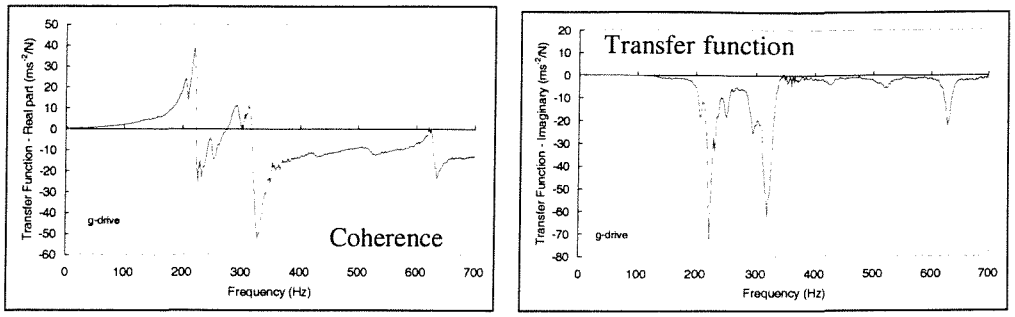

c) Real part d) Imaginary part

Figure 4.12 Measured coherence and transfer functions of driving point on the curved panel of GLARE box

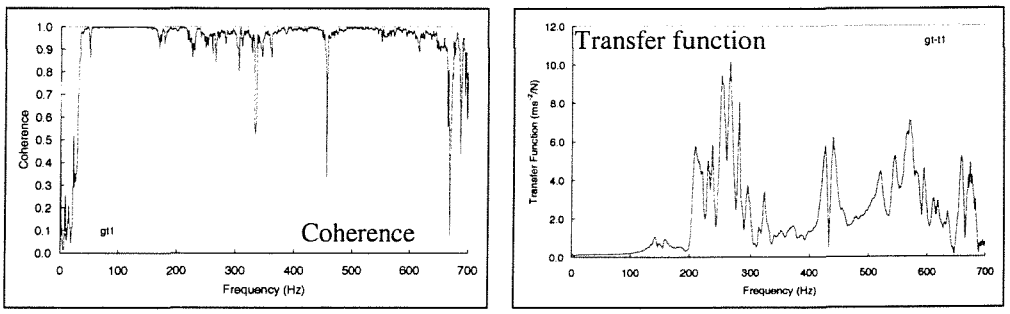

a) top skin panel - point T1

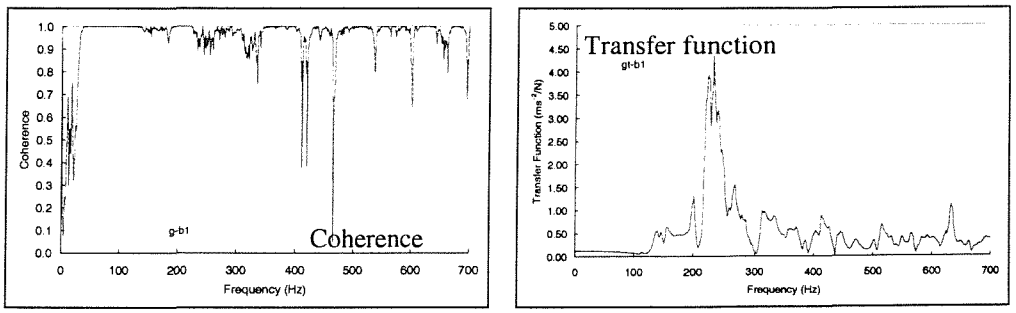

b) bottom skin panel - point B1

Figure 4.13 Measured coherence and transfer functions of GLARE box

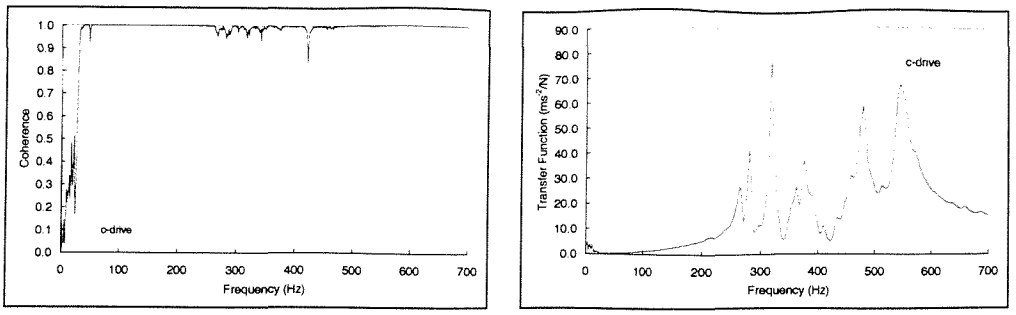

a) Coherence b) Transfer function

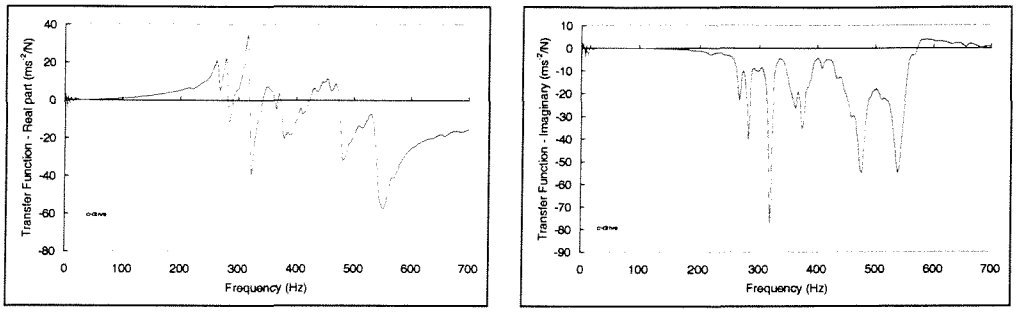

c) Real part d) Imaginary part

Figure 4.14 Measured coherence and transfer functions of driving point on the curved panel of CFRP box

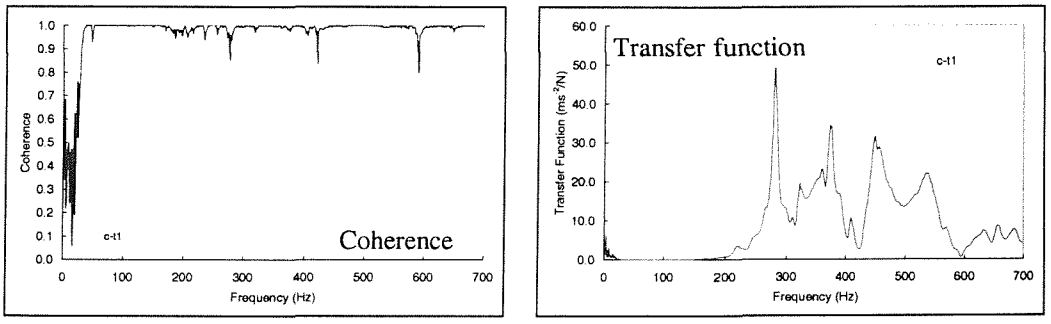

c) top skin panel - point T1

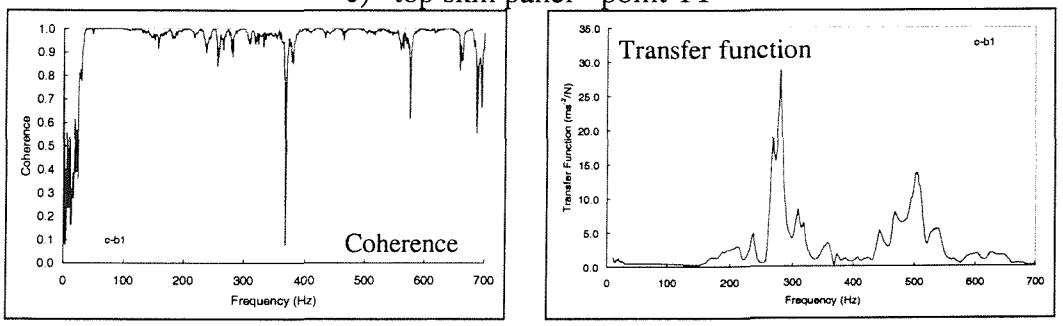

d) bottom skin panel - point B1

Figure 4.15 Measured coherence and transfer functions of CFRP box

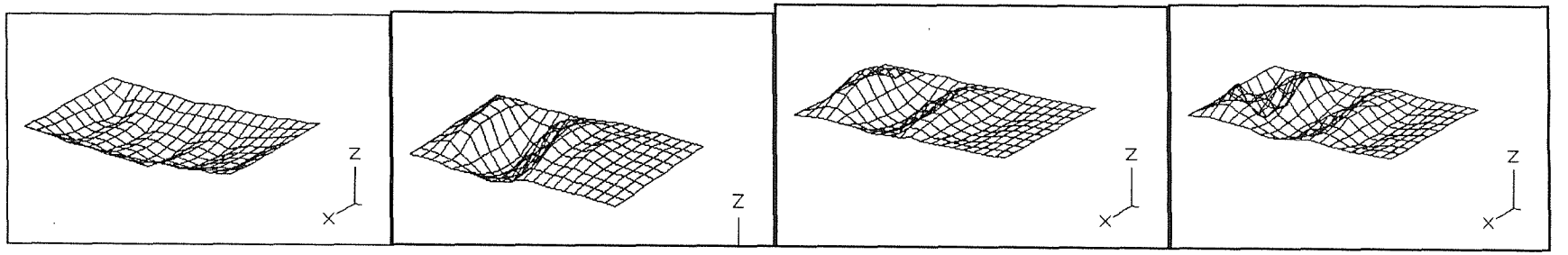

f_1=173.0 Hz f_2=259.5 Hz f_3=269.5 Hz f_4=399.5 Hz

a) Aluminium box

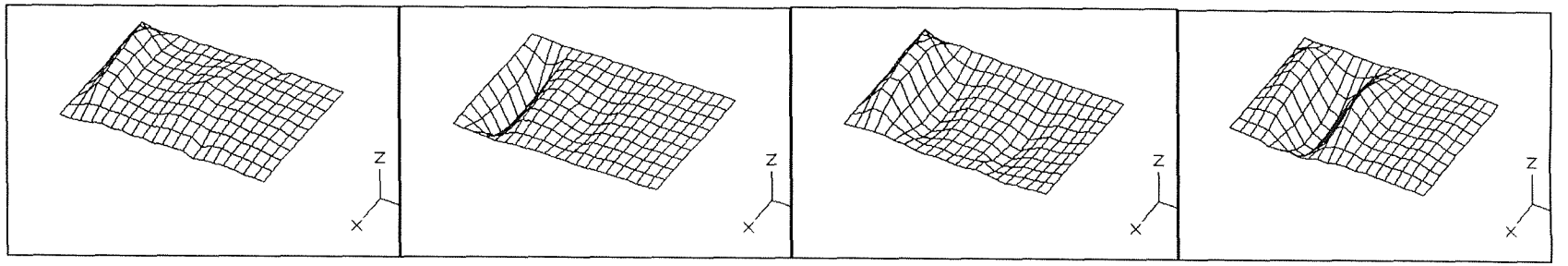

f_1=181.2 Hz f_2=229.2 Hz f_3=237.7 Hz f_4=251.3 Hz

b) GLARE box

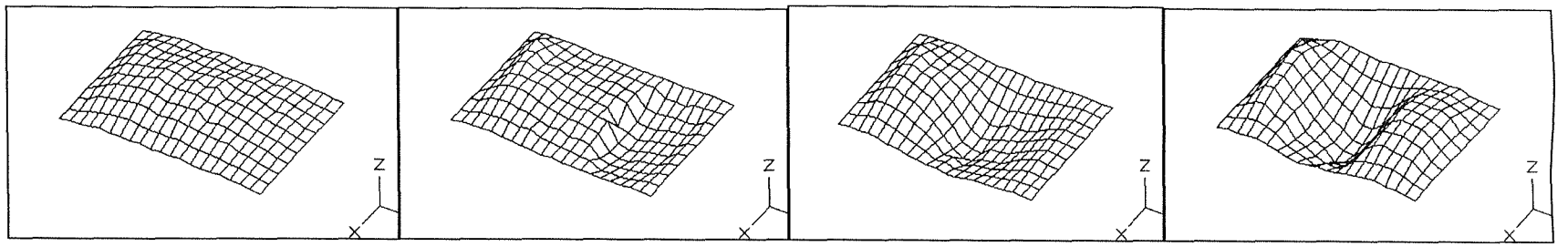

f_1=189.6 Hz f_2=219.6 Hz f_3=319.2 Hz f_4=360.0 Hz

c) CFRP box

Figure 4.16 The first 4 mode shapes of the middle bay of flat skin panel

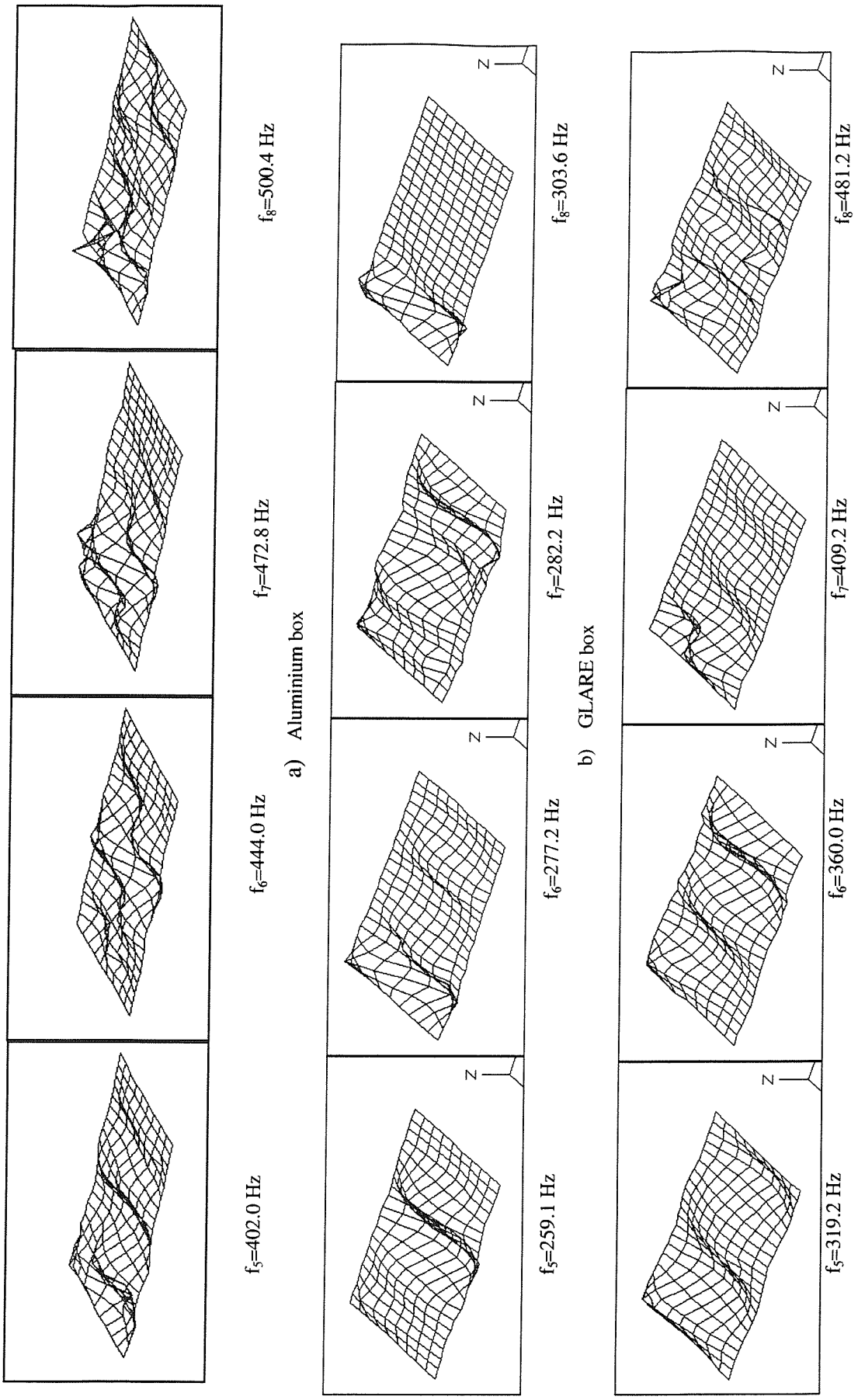

Figure 4.17 Mode shapes of modal nos. 5 to 8 of the middle bay of flat skin panel

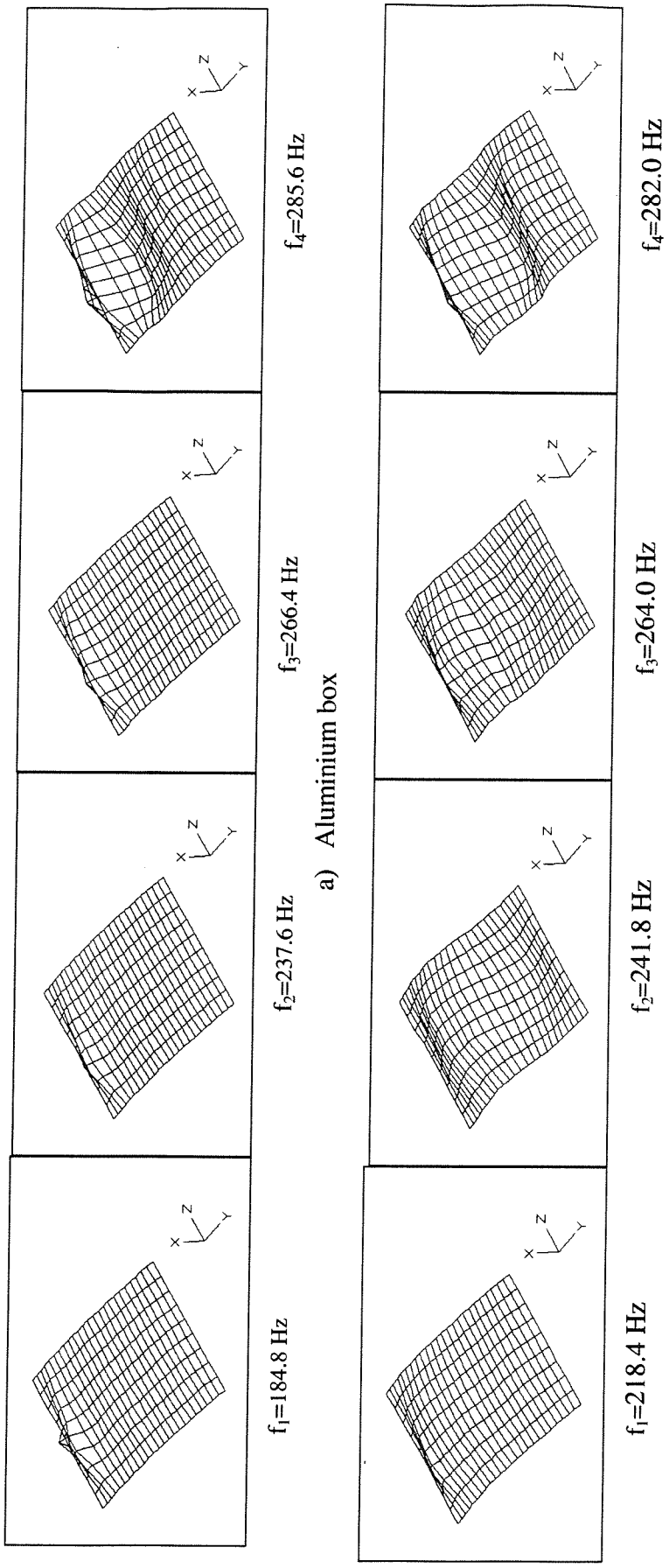

Figure 4.18 Mode shapes of modal nos. 1 to 4 of the middle bay of curved skin panel

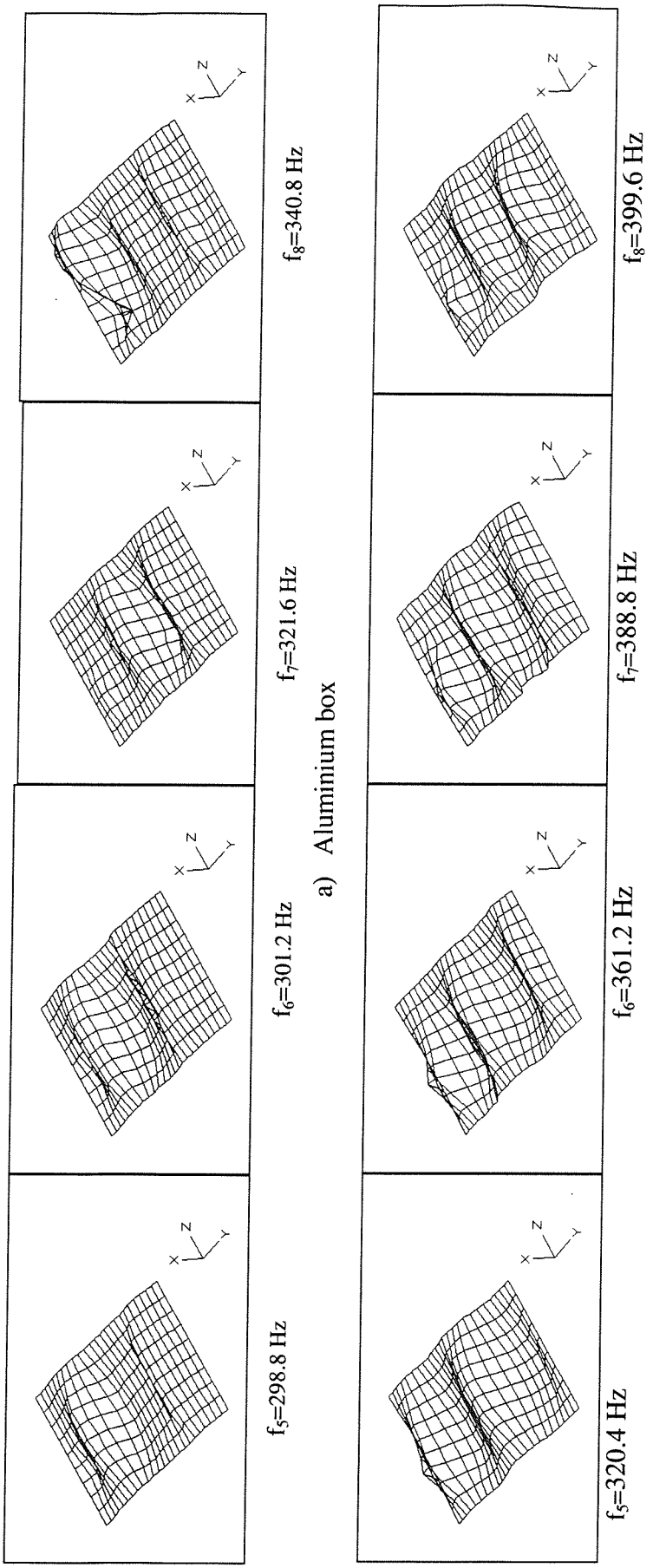

Figure 4.19 Mode shapes of modes Nos. 5 to 8 of the middle bay of the curved skin panel

CHAPTER 5

ACOUSTIC FATIGUE ENDURANCE OF THE FLAP-LIKE BOX STRUCTURES

For Airbus aircraft with wing mounted engines, the highest sound pressure level measured on the flaps was 155 dB, which could cause fatigue damage [3, 80]. This chapter describes experimental investigations into the dynamic behaviour of the three box-type structures under high intensity acoustic loading. Acoustic endurance tests were carried out in two stages by means of a Progressive Wave Tube (PWT). The structures were first excited by high pressure loading from 140 dB to 161 dB or 162 dB with bandwidth from 100 Hz to 600 Hz to obtain the strain responses at various measuring points. The structures were then subjected to fatigue tests to study the initiation and propagation of fatigue damage caused by high intensity acoustic loading.

5.1 EXPERIMENTAL SETUPS

Acoustic testing of the box structures was carried out using the Progressive Wave Tube (PWT) at the University of Southampton. The PWT is a facility that was specially designed to simulate the acoustic loading on aircraft components. Detailed discussion concerning the sound pressure field at the test section of the PWT can be found in Chapter 3, which gives the characteristics of acoustic loading provided by the PWT at its test section in both spectral and statistical aspects.

The box structures for the acoustic endurance tests are described in Chapter 4 and shown in Figures 4.1 and 4.2. Construction details of the box structures can be found in Appendix D. To easily locate a particular position on the box structures, the side A is defined as the left hand side when the box lies on its flat skin panel with rear spar facing the observer, and side B is the opposite side. The stiffener closest to the rear spar is defined as stiffener No. 1. The number increases in the direction towards the front spar. The stiffeners next to the front spar are numbered as No. 4 or No. 5 respectively for bottom and top skin panels. Longitudinal direction is defined as along the stringer length, and transverse direction as perpendicular to stringer length.

The test structure was mounted in the opening of the test section of the PWT on a wooden supporting frame, which was suitable for all three structures. Figure 5.1 shows the structure of the supporting frame. During the tests, one of three boxes was fixed on to the frame, which was then bolted to the test section of the PWT. For each measurement run, one of the top and bottom skin panels was placed facing the inside of the PWT so it was directly excited by acoustic pressure loading. For each box structure, at least two sets of measurements were taken to record the responses. Overall sound pressure level (OASPL) of acoustic excitation at the test section of the PWT was measured by the reference microphone, which was fixed in the middle of the test section (Figure 5.2). The responses of the structures to the acoustic loading were measured by a number of strain gauges. These gauges were installed inside the structures at the various locations of interest, and the leads from the gauges brought out of the access holes. The advantages of installing the gauges inside the boxes were to minimise the disturbance to the pressure field during the tests and to protect the gauges during transport and various other tests.

The locations of the strain gauges were chosen based on the intention to obtain as much information as possible during the tests. The middle bay of the skin panel was heavily gauged to supply the information required. The gauges were attached at both the middle (a little off centre) and edges of the sub-bay (surrounded by inner ribs and stiffeners). Strain gauges were attached to both curved and flat skin panels to establish the relationship of the responses of the two panels to acoustic loading. Gauges were also attached to the other two bays to investigate the response relationships between three bays. There were seven 3-gauge rosettes on the curved skin panels plus another two on one of the five stiffeners and six on the flat panel with two on one of four stiffeners. Another two strain gauges were also

installed on one of the inner ribs. Strain gauges of 5 mm length were used to give good strain resolution. Figures 5.3 and 5.4 show an inside view of the boxes with strain gauges installed and Figure 5.5 shows the locations and numbering of the gauges.

As the pressure loading applied to flaps in service is random and broadband in nature, a shaped broadband random signal was fed into to the siren of the PWT in order to generate a simulated acoustic field in the test section (detailed in Chapter 3). Thirty strain amplifier channels were used to take the strain measurements. The LABVIEW, which is a PC based 16-channel data acquisition system, was used to acquire data. Data analysis was carried out using the MATLAB signal processing toolbox. The instrumentation set up for the PWT excitation tests is given in Figure 5.6.

Because the data acquisition system and low pass filter had only 16 channels, 30 strain gauges were divided into two groups of 15 gauges and measurements were taken in two batches for each excitation level. For each batch, the sound signal from the B&K Type 4136 microphone and signals from one of the 15 strain gauge groups were measured. A 16-channel antiliasing low pass filter was employed to filter signals at 1kHz before they were digitally sampled at sampling rate of 6000 Hz. The frequency resolution of spectral distributions was 1.2 Hz.

During the PWT excitation tests, all the measurements were carried out in the control room due to the high sound pressure level produced by PWT in the laboratory. Hence, 15 m long extension wires were necessary to the leading wires (2 meters) of the strain gauges. To ensure the accuracy of strain response measurements, gauge factors of strain gauges were corrected accordingly. For the strain gauge connections, a three instead of a two wire system was used to eliminate any error induced by leads and to ensure an accurate balance of the Wheatstone bridges even with long extension cables.

5.2 MEASUREMENT PROCEDOURES

Experiments were carried out in three phases. First, calibration of microphone and strain amplifiers was carried out. The second part was strain data collection when the structures were driven on each skin panel at OASPL levels of 140 dB to 161 dB (or 162 dB). Finally,

the boxes were excited at their flat skin panels at sound pressure level of 161 dB over a period of time to observe the possible initiation and propagation of fatigue damage. The bottom skin panel was chosen to carry out the endurance tests because it is the side actually facing the loading in operation conditions.

5.2.1 Measurement System Calibration

The reference microphone was calibrated using a B&K Type 4220 PistonPhone which produces a signal with a SPL of 124 dB at a frequency of 250 Hz. This calibration was performed as many times as possible to ensure accurate sound pressure level measurement.

For the strain measurements, although the amplifiers have an internal calibration system that is reasonably accurate, external calibrations were still carried out to ensure accuracy of strain measurement. A cantilevered aluminium alloy beam was used to calibrate the measurement system, the details are given in Appendix E.1. All 30 channels were checked and the relationship between output voltage and strain value for each channel was established. Results are listed in Table E.1.

5.2.2 Acoustic Excitation

The acoustic pressure loading tests were carried out using the PWT facility. The Overall Sound Pressure Level (OASPL) of the excitation was increased from 135 dB to 161 dB (or 162 dB) in steps of 5 dB. As already discussed in Chapter 3, a sound pressure level of 135 dB was purely caused by the airflow. At this level, the sound energy of the excitation was concentrated around the 100 Hz region, so that the test structure showed no sign of response due to its first mode, the resonance frequency of which, was well above 100 Hz. A shaped driving signal in the frequency range of 80 Hz to 600 Hz was used (details can be seen in Chapter 3), and overall sound pressure levels (OASPLs) were measured by reference microphone which was located at the middle of the test section. Power spectral densities of the acoustic excitation measured by reference microphone are shown in Figure 5.7. Note that the sound energy is mainly in the frequency range of 100 Hz to 600 Hz.

The responses of the test structures to the acoustic excitation were measured by 30 strain

gauges, including strain gauges on both skin panels, stiffeners and inner ribs. By this arrangement, it was possible to obtain extensive information on the structural response to acoustic loading. Note that not all of the strain gauges in a rosette were used due to only a limited number of amplifier channels being available. Strain response levels of the test structures are presented as their root-mean-square (RMS) values, the Power Spectral Densities (PSDs) are used to show the frequency contents.

Following the collection of satisfactory strain data in the first set of tests, the box structures were subjected to acoustic fatigue tests. For each structure, the excitation lasted more than 500 minutes. During this period, an endoscope was used to inspect the inside of the structures, and the outside was examined by visual inspection, at several time intervals.

5.3 STRAIN MEASUREMENT RESULTS

Each box structure was excited first on the flat skin panel and then on the curved panel. Measured strain results for each strain gauge are identified by the gauge number. Gauges on top (curved) skin panels are numbered with prefix T, on bottom (flat) skin panels with B, on inner ribs with R, and on stiffeners of the top and bottom panels with TS & BS respectively. By referring to Figure 5.5, one can easily connect strain results with their location on the structures. Apart from the RMS strain and the strain spectral density, normalised integrals across strain spectral densities are also given to demonstrate how the strain energy is distributed through the frequency range of interest.

Overall sound pressure levels (OASPLs) of the acoustic excitations recorded were 140 dB, 145 dB, 150 dB, 155 dB and 160 dB. For certain sets of the measurements, higher excitation level over 160 dB was also achieved, the strain results at this level are also presented for the purpose of comparison. In following discussions, all the RMS strain values quoted are for an excitation level of 160 dB, unless stated otherwise.

5.3.1 Aluminium Alloy Box Structure

The skin panels of the aluminium alloy structure were subjected to acoustic loading from 140 dB to 160 dB in steps of 5 dB. When it was excited on the bottom skin, an extra set of

data was also collected for an excitation level of 161 dB. The RMS strain results for 30 strain gauges on the skin panels are listed in Table 5.1 when excited on the top skin panel, and Table 5.2 when driven on the bottom skin panel. The variations of the RMS strain with increase of excitation level are given in Figures 5.8 to 5.13. At excitation levels below 155 dB, the relationships between sound pressure and RMS strain are linear, but show the tendency to non-linear form when the excitation level was over 155 dB as shown in Figures 5.8 to 5.13, especially at those locations with higher strain levels.

Excitation on top skin panel: the RMS strain responses were, in general, below 100μ strain for both top and bottom skin panels, except for T1-2 with strain level of 138μ strain at 160 dB in the longitudinal direction (wing span) (see Table 5.1). The highest strain responses were found on stiffeners in directions perpendicular to the stringer. At excitation level of 160 dB, measured strain level by strain gauge TS1-1 in the side bay A was 145μ strain, and a strain level of 122μ strain for gauge TS2-1 was found in the middle bay. Although the box was excited on its curved panel, the strain responses of the flat panel were comparable with those of the curved panel at high excitation levels of 155 dB and 160 dB, especially for gauge B1-2, a transverse strain level of 85με was found. The response of the inner rib was 59με measured by gauge R1-1, which was relatively low but not negligible compared with the responses of the skin panels.

The spectral density of each strain response signal was obtained. To evaluate the modal contributions to the overall strain, normalised integrals across the spectral densities in the frequency band up to 1000 Hz were also generated for each strain gauge. Figures 5.14 to 5.16 give the strain spectral densities and their normalised integrals for strain gauge T1-2, TS2-1 and T7-1.

For gauge T1-2, a multi-peaked power spectral density distribution is shown in Figure 5.14(a) with the highest peak around 290 Hz, where several modal responses coalesced to form a wide peak, which is more obvious at excitation levels over 150 dB and 160 dB. This peak contributes more than 50% of total RMS strain response as shown in Figure 5.14(b). With increase of excitation level, it can be seen from Figure 5.14(b) that the contribution of high frequency modes to the total RMS strain value was increased. In the frequency range above 500 Hz, it was also shown that some resonance peaks disappeared

and the spectra became smoother.

The stringer response is dominated by resonance peaks between 340 Hz to 480 Hz as shown in Figure 5.15(a), which accounts for 90% of the strain value (Figure 5.15(b)). In this frequency band, the stringer is mainly in torsional deformation as shown in Figure 4.19(a) and Appendix C.2.4.2 for the modal test results. The strain response of the side bay is shown in Figure 5.16, where the dominant peak is around 360 Hz. The response spectrum of the bottom panel B1-2 is given in Figure 5.17. At excitation level of 160 dB, both Figures 5.16(b) and 5.17(b) show increase of high frequency modes, especially for the strain spectral density of gauge B1-2.

Excitation on the flat panel: As when excited on the top skin panel, RMS strains at various locations on the skin panels, stringers and inner rib were measured and listed in Table 5.2. The maximum strain was also found on the stiffeners in the transverse direction. At excitation level of 160 dB, RMS strain value at strain gauge location BS1-2 was 267με and 186με at BS2-2. These values were higher than those at corresponding positions on the top panel when excited on the top skin. For the bottom skin panel, the highest strain was found to be 157με at locations B32 in the transverse direction and B42 in the longitudinal direction. For the top skin panel, maximum strain was 79με measured by gauge T6-2 in side bay B. In the middle bay of the top skin, lower strain values were found. Responses of inner rib measured by R1-1 was 51με which was similar to that measured when excited on the top skin, but a higher value of 117με was found in the vertical direction measured by gauge R1-2. Figures 5.11 to 5.13 show the changes of RMS strain with increasing excitation level. Non-linear relationships between the RMS strain and sound pressure of excitation are shown at higher excitation levels.

Compared with those obtained when excited on the top panel, strain spectral densities of the bottom skin panel (Figures 5.18(a) to Figure 5.21(a)) have lower fundamental resonance frequency and the multi-peak distribution became more evident especially at the higher excitation levels. This is clearly reflected by the normalised integrals across strain spectral densities shown in Figures 5.18(b) to 5.21(b). As the excitation level increased, the contribution from the modes with higher frequencies increased, which results in the re-distribution of strain energy in the structure. This effect is more obvious in the flat panel

than in the curved panel.

By comparing Figures 5.17 and 5.18 of strain responses measured by strain gauge B1-2, it can be seen that the strain PSDs have similar frequency peaks but the strain energy distributions are not exactly the same. This is due to the fact that the response of the skin panel shown in Figure 5.17 is induced mainly through the joint structures, such as ribs, and the air enclosed in the structure. It is also found that the response peak has shifted up when the panel is directly excited by acoustic loading. This means that the directly driven panel, having higher response level than the non-driven panel, exhibited greater non-linear behaviour. This effect can also be seen in by comparing Figures 5.15 and 5.21 of power spectral density plots of gauge T1-2. Another phenomenon is the 'smearing' effect. This means that the well separated frequency peaks joined together to form a wide peak with the increase of excitation level. This phenomenon was seen in the spectral densities of both skin panels.

The maximum strain responses in the strain gauge rosettes on the stiffeners of both skin panels were always in the transverse direction to the stiffeners (such as TS1-1, TS2-1, BS1-2 and BS2-2), which indicates that the stiffeners responded mainly in torsion during acoustic excitation.

5.3.2 GLARE Box Structure

As for the aluminium alloy structure, each skin panel of the GLARE box was subjected to acoustic loading from 140 dB to 160 dB in steps of 5 dB for the purpose of strain data collection. Measured RMS strains for 30 strain gauges when excited on top and bottom skin panels are listed in Tables 5.3 and 5.4 respectively, and illustrated in Figures 5.22 to 5.27. Extra sets of data were also listed for an excitation level of 162 dB It can be seen that the relationships between excitation levels and structural response RMS strain values became non-linear with increase of sound pressure level of acoustic loading.

As for the aluminium alloy structure, high strains were found on the stringers of both skin panels in transverse direction. When it was excited on the top skin, for strain gauge TS1-1, the measured RMS strain was 173με, which was 20% higher than that of the aluminium alloy box. Strain values measured in the middle bay of top skin were similar in magnitudes

to those of the aluminium alloy box. But strain responses in side bays of the Glare box were higher than those of aluminium alloy structure. Strain value at strain gauge location B2-2 was 128με, which showed strong coupling of the top and bottom skins.

When the GLARE box was excited on the bottom skin, the strain level measured by BS1-2 was 152με, which was much less than that of the aluminium alloy structure. The highest strain of 165με was found at gauge B2-2 location in the transverse direction. Two side bays also showed higher strain response as for the aluminium alloy box. The responses of the top skin panel were relatively low and similar in amplitudes to those of the Al alloy box. Responses of the inner rib measured by strain gauges R1-1 and R1-2 were similar to those of the Al alloy structure.

The strain power spectral densities and their normalised integrals for the GLARE structure are given in Figures 5.28 to 5.35, which have similar characteristics to those of the aluminium alloy box. The fundamental resonance frequency of the GLARE structure was lower than that of the metallic box because the ratio between effective modulus and density of the GLARE 3 (58GPa, 2480kg/m^3) is lower than that of aluminium alloy (72GPa, 2.77kg/m^3) (see Appendix F.2.4) . Those findings discussed in the last section for the metallic structure, such as peak frequency shifting up when excited directly, multi-peak response, strain energy redistribution as excitation level increases, etc., were also evident in the GLARE structure. As for the aluminium alloy structure, the higher strain values were found in the stiffeners in the transverse direction. By comparing the strain spectral densities measured by strain gauge B6-2 shown in Figures 5.31 (top excitation) and Figures 5.32 (bottom excitation), the resonance peaks at 280 Hz and 400 Hz of the bottom skin panel in Figure 5.31 have moved up to 300 Hz and 430 Hz in Figure 5.32 respectively when the panel was acoustically excited directly. Resonance peaks for directly excited panels were wider than those for indirectly excited panels.

5.3.3 CFRP Box Structure

The CFRP box structure was first subjected to acoustic loading on its bottom skin panel in order to collect the strain data. The excitation levels were 140 dB, 145 dB, 150 dB, 155 dB, 160 dB and 162 dB, measured RMS strain results are listed in Table 5.5 and plotted in Figures 5.36 to 5.38. Much higher strain levels occurred than in the aluminium alloy and

GLARE structures, especially on the stiffeners.

The measurements were carried out twice and each test lasted around 9 minutes. After these tests, damage was found on the rivets which connected the bottom skin panel and the inner rib (side B). A total of eight rivets were found to be snapped (Figure 5.39), which was the reason why very high strain results were found. From Figure 5.39(b) it can be seen that the original countersunk rivets used were hollow in the centre. No other forms of damage were found, so the CFRP structure was returned to Airbus and repaired before further tests were carried out. It was found that the wrong type of rivets (Aluminium Alloy instead of Monel rivets) had been fitted. Inspection found no damage to the rivet holes. All of the original rivets, except those connecting spars and ribs, were replaced. Details of the repair report can be found in Appendix E.2.

The repaired CFRP box was then subjected to acoustic excitation using the same procedures as for the aluminium alloy and GLARE structures. Excitation levels were 140 dB, 145 dB, 150 dB, 155 dB, 160 dB and 161 dB. RMS strain responses are listed in Tables 5.6 and 5.7 for excitation on top and bottom skin panels respectively, and are plotted in Figures 5.40 to 5.45. Comparing results listed in Table 5.7 with those in Table 5.5, the repaired structure showed lower strain levels. The maximum strain on the stringers was reduced by about 21% (BS1-1), and 50% reduction of strain value at gauge location B4-2 was found. The damage to the rivets had effect not only on the responses of the bottom skin, also on the responses of the inner rib and top skin. The vertical strain measured by gauge R1-2 reduced from 257με to 196με, and 121με to 59με for the transverse strain measured by gauge T1-1.

The relationships between the sound pressure and RMS strain (Figures 5.40 to 5.45) show less tendency of non-linear behaviour compared with the aluminium and GLARE structures. Non-linear behaviour of strain responses was more apparent when direct excitation was on the bottom skin than on the top skin. The maximum strains were found on the stringers but in the longitudinal direction rather than in the transverse direction as for the aluminium alloy and GLARE structures. This indicated that bending dominated the deformation of the stiffeners. The maximum RMS strain value at strain gauge location BS1-1 was 385με for bottom excitation, and 252με for top excitation at TS1-2. These values are higher than the maximum values on the stringers of the aluminium alloy and

GLARE structures. For the skin panels, the maximum strain responses were 111με (T1-1) for the top skin and 184με (B2-2) for the bottom skin. When excitation was on the top skin, responses on the bottom skin were also high, strain values of 139με were found at gauge locations B2-2 and B6-2. The responses of the top skin were relatively low when excitation was on the bottom skin. Vertical strain of inner rib (R1-2) was 196με for bottom excitation, which was quite high compared with responses at other locations.

Strain spectral densities and normalised integrals across the strain PSD of the CFRP box are given in Figures. 5.46 to 5.53. Compared with the other two structures, multi-modal contributions dominate the spectra; individual peaks are less distinguishable than for the aluminium alloy box; peak smearing is also evident. Strain energy redistribution was more apparent for the responses of the bottom skin (Figure 5.53) than for those of the top skin with increase of excitation level for the top skin panel, but, in general, this type of behaviour was less significant compared with the other two boxes. The response spectra of the the CFRP structure have broad peaks compared with the other two boxes, which indicates the high damping of the CFRP structure. When it was directly excited by acoustic loading, more resonance peaks appeared in strain spectra than in the situation of indirect excitation. This can be seen in the spectra measured by gauge B2-2 on the bottom skin as shown in Figures 5.50 and 5.49. When directly excited, a group of resonance peaks in the frequency range of 200 Hz to 450 Hz accounted for 90% of the strain energy (Figure 5.50); This happened in a narrow frequency band from 200 Hz to 340 Hz for the indirectly excited case(Figure 5.49).

5.3.4 Characteristics of Strain Response of the Box Structures

Among the three box structures, the CFRP structure had the highest RMS strain response reflecting the difference in material, construction and spectra of strain modal responses between it and the other two test boxes. The strain response levels of Aluminium alloy and GLARE structures were similar but with some differences. The highest strain level was found on the stiffeners of all three structures. For the stiffeners of the aluminium alloy and GLARE structures, maximum strain was in the transverse direction to the length of the stiffeners, which indicates that the stiffeners responded mainly in torsion during acoustic excitation. For the CFRP structure, the maximum strain on a stiffener was in the

longitudinal direction along the length of the stiffener, which means that stiffeners were mainly undergoing bending deformation during acoustic excitation.

The relationship between excitation levels and RMS response strains at various locations of the test structures showed non-linear behaviour, especially for the aluminium alloy and GLARE boxes. When the structures were excited on one skin panel, the other skin panel and inner ribs all showed a relatively high strain response, which indicates the coupling of the top and bottom skins. When excitation was on the top skin panels of the three boxes, the maximum responses of the bottom skin panels were 61% (aluminium alloy, B1-2), 122% (GLARE, B2-2) and 125% (CFRP, B6-2) of the maximum strain values found on the top skin panels. For excitation on the bottom skin panels, the ratio of the highest strains between top and bottom skin panels were 50% (Al alloy box, T6-2), 28% (GLARE, T6-1) and 32% (CFRP, T1-1), which were lower compared with those for bottom excitation cases, but still were not negligible. Therefore, for a box-type structure, the skin panels should not be simply treated as isolated items.

As the excitation level increased, the strain energy redistributed in the frequency band of interest, i.e., the response of the higher frequency modes was enhanced, and their contribution to the total strain therefore became more significant. This is shown by the normalised integrals across the strain spectral densities. As shown in Figure 5.18(b) for the aluminium alloy box with acoustic excitation in the bottom skin, the contribution to total RMS value of the first two peaks between 200 Hz to 300 Hz was around 58% at excitation level of 140dB, but was reduced to about 45% at 160 dB. At 600 Hz, the normalised integral was 0.91 for excitation level of 155dB, but decreased to 0.85 for 160 dB. In this case the single mode approach is no longer suitable. The same type of behaviour can also be found in the response results of the CFRP box as shown in Figure 5.53. It shows the multi-mode distribution of strain spectra. The first mode at a frequency around 240 Hz only accounted for 50% of the total response. This phenomenon was more evident for the GLARE and aluminium alloy structures, especially when the boxes were excited on their flat skin panels. At the higher excitation levels, adjacent individual frequency peaks tended to coalesce to form broad peaks. Results for the CFRP box showed less peaky resonance peaks owing to its high damping.

The characteristics of RMS strain responses of the three box-type structures are indicative

of non-linear behaviour at high excitation levels. The dynamic behaviour observed was very similar to that occurring in acoustically excited, plate-type structures with constrained boundaries at high response levels[41]. In this Chapter, only strain spectral densities at four strain gauge locations for each skin panel are given. The strain spectral densities for other locations can be found in Ref. [90].

5.3.5 Statistical Characteristics of Strain Response

In Chapter 3 it was found that the sound pressure excitation showed non-Gaussian distribution behaviour. To investigate whether strain response has similar behaviour, the statistical properties of the strain responses were calculated. Examples of the probability distributions of the responses of the three box structures are shown in Figures 5.54 to 5.56. It can be seen that three structures showed very similar behaviour and low levels of non-Gaussian behaviour. The skewness values of the strain responses were close to zero, The kurtosis values calculated showed slight deviation from that of the Gaussian distribution (=3). It can also be seen that there were more disturbances caused by compressed air in the strain signals at lower excitation levels, which was reflected by slightly higher kurtosis values. At higher excitation levels, probability distributions tend to be less peaky. These behaviours were similar to statistical behaviours of excitations discussed in Chapter 3.

5.4 ACOUSTIC FATIGUE ENDURANCE OF BOX STRUCTURES

After all the strain measurements had been completed, the three structures were subjected to acoustic endurance tests. The excitation was applied to the flat skin panel at an overall sound pressure level of 161 dB with the spectrum shape shown in Figure 5.7. The structures were inspected at regular intervals during endurance tests using an endoscope to trace the propagation of fatigue cracks.

In the following discussions, each structure is considered in three parts: middle bay, bay side A and bay side B (for definition of side A & B see Figures 4.1 and 4.2). In each bay, rivets along stiffeners were numbered. No. 1 was that closest to the end and the identification number increased towards the middle bay. Crack length has been estimated according to the position of the crack tip. Because of the lack of suitable measurement

equipment, it was difficult to establish the precise location of the crack tip. Therefore, if a crack tip was between two rivets, it was assumed that the tip was midway between two rivets.

5.4.1 Aluminium Alloy Structure

This structure was excited on the bottom skin at 161 dB for a total of 521 minutes. Most of the fatigue damage was found on the stiffeners in two side bays on the bottom skin panel.

After the first 50 minutes of the endurance test, the end part of stiffener 3 on the bottom panel at side B broke off from the structure. Figure 5.57 shows photographs of the detached part, which show that the crack started at the end of the stiffener and propagated along the rivet line towards the inside of the structure. After the crack went through four rivets (distance between two rivets was 18mm) it propagated into the web of the stiffener and eventually towards the stiffener edge causing the part to detach. The endoscope inspection also revealed that there were cracks on every stiffener on both side bays (A & B) along rivet lines. The longest crack went through eight rivet holes. As the testing continued, the cracks grew quickly and two more end parts of the stiffeners on side A detached from the box at 156 minutes and 200 minutes respectively as shown in Figure 5.58. In the total 521 minutes of endurance testing, no fatigue cracks were found in the top panel and ribs. A fatigue crack was found in stiffener No. 3 of the bottom middle bay at 372 minutes. Tables 5.8 and 5.9 summarise the inspection results. The longest crack was 296 mm across 17 rivets on stiffener No. 2 of bay side B, which is almost across the whole length of bay side B. Figures 5.59 and 5.60 illustrate the crack propagation path. In these two Figures, crosses show the position of crack tips, and test times (minutes) are shown in numbers next to crosses. The crack on stiffener No. 3 of the middle bay is also shown in Figure 5.60.

Crack length versus test time curves are plotted in Figures 5.61 and 5.62, which show the crack growth rates. Bay side B, which was at the "down stream" end of the test tunnel in the PWT, had longer fatigue cracks than bay side A. As the test time increased, crack propagation rate decreased especially after 280 minutes exposure to the acoustic loading. But rivets connecting inner ribs and the bottom panel started to loosen and some finally snapped. Figure 5.63(a) shows an outside view of the bottom skin panel after acoustic endurance testing and closer view at two inspection times of 320 and 437 minutes are given

in Figures 5.64 and 5.65. Figure 5.63(b) indicates when rivets in the rivet line on side A were broken. From Figures 5.63 to 5.65, it can be seen that there was black powder around some of the rivets, which indicated that those rivets were loose and experienced substantial movements.

To examine the effect of damage on resonance frequencies, Figures 5.66 to 5.68 show the strain spectral densities for the middle bay and side bays. Strain gauge B3-2 was on the middle bay, strain gauge B5-2 on the bay side B and gauge B6-2 on the bay side A. It is very clear that the damage in the side bays had an effect on the dynamic response in not only the side bays but also in the middle bay.

5.4.2 GLARE Structure

Acoustic endurance testing of the GLARE box was continued for 588 minutes at an overall sound pressure level of 161 dB. The structure was excited on its bottom skin panel. The structure was inspected internally using an endoscope. Fatigue cracks were seen in the stiffeners of the bottom skin panel of both side bays and in the inner rib at side B.

Tables 5.10 and 5.11 summarise the endurance testing results. It can be seen that the first visible cracks in the bay on side A were seen after 92 minutes of testing. But for side bay B, fatigue cracks were present before the endurance testing started. These cracks were induced during the strain measurement tests, which were carried out twice and each took about a total of 9 minutes from excitation level of 140 dB to 162 dB (about 3 to 4 minutes at levels of 160 dB and 162 dB). Fatigue crack propagation paths for both side bays are illustrated in Figures 5.69 and 5.70. Compared with the aluminium alloy structure, the GLARE structure had shorter crack lengths at the end of the testing. For the aluminium alloy structure, when a crack initiated, it propagated rapidly through the thickness of the stiffener. But, for the GLARE structure, cracks initiated in the outer metal layer and were arrested by the glass fibre composite layer, which delayed propagation. For stiffener No. 3 on bay side B, it took 362 minutes to see the crack through the thickness. Similar to the aluminium alloy structure, the longest fatigue crack was seen in the "down stream" side of the GLARE structure. Figures 5.71 and 5.72 are the curves of crack length against time, which show lower crack growth rates compared with Figures 5.61 and 5.62.

From Figures 5.69 and 5.70, it can be observed that there are two types of cracks, one mainly along the rivet line and other at the lower curvatures of the stiffeners.

No rivet failures were found on the rib lines. But one of the rivets that connected the rear spar and inner rib (side B) snapped at a test time of 233 minutes. Cracks were also seen in the inner rib at side B (Figure 5.73).

Figures 5.74 and 5.75 are strain spectral densities for the GLARE structure after prolonged acoustic excitation. As for the aluminium alloy structure, its resonance frequencies decreased due to the existence of fatigue cracks in both side bays.

5.4.3 CFRP Structure

The CFRP structure was subjected to acoustic loading of 161 dB for a total of 536 minutes. Excitation was on the bottom skin. No visible structural failure was found except that three of the four rivets connecting the rear spar and inner ribs were found to be snapped at endurance times of 60, 77 and 120 minutes respectively. In fact, the snapped rivets were the original rivets (with hollow centres) which were not replaced when the CFRP structure was returned for repair after initial acoustic excitation.

To examine whether there was any undetected damage which could affect the resonance frequencies of the CFRP structure, the strain spectral densities at the four inspection times were checked in Figure 5.76. No significant changes of the resonance frequency and strain spectral shape were found.

5.5 FATIGUE LIFE ESTIMATION OF BOX STRUCTRUES

Use of the RMS strain responses of three box structures discussed above and the S (RMS strain) - N (number of cycles to failure) curves given in Chapter 2, would be a logical method to estimate the fatigue life of the test structures using the information available. To estimate the acoustic fatigue life of a structure with a broadband response, Miner's cumulative damage theory can be used.

In the discussions given in Section 5.3, it was concluded that the contribution of the high frequency components of strain spectral densities to the total RMS strain was not negligible, therefore the single mode approach was no longer suitable. In the estimation of the fatigue life of box structures, the multi-mode response needs to be taken into account. i.e., the distribution of both amplitudes and frequencies of RMS strain in a broad frequency band should be included in the calculation of fatigue life. In the following discussion, an attempt has been made to derive formulae for the estimation of fatigue life based on the experimental results obtained in Chapters 2 and 5 using Miner's cumulative damage theory. The basic idea is to divide the frequency band of interest into a number of narrow bands. For each of these narrow bands, the fatigue damage can be estimated, and the total damage will be the summation of the fatigue damage from each of these narrow bands.

The RMS strain response value can be calculated using either the time domain signal or its spectral density distribution in the frequency domain as follows:

$$RMS^2 = \int_{f_l}^{f_u} p(f)df \tag{5.1}$$

Where f_l and f_u are the lower and upper frequency bounds of the frequency range of interest

$p(f)$ is the power spectral density distribution of random response

If dividing the frequency range into a number of narrow bands, the above formula can be expressed as below:

$$RMS^2 = \sum_{i=1}^{m} p(f_{ni})\Delta f_i \tag{5.2}$$

where Δf is a narrow band frequency range with central frequency f_{ni}

m is the number of narrow bands

According to the Miner's rule, each of these narrow bands will take a portion of fatigue life equal to n_i/N_i, where N_i is the fatigue life corresponding to RMS value $\Delta\varepsilon$ in this narrow band, which can be obtained from the S-N curves given in the Chapter 2, and n_i is the number of strain response cycles equal to $T \times f_{ni}$. T is the fatigue life. Fatigue will occur when

$$\sum_{i=1}^{m}\frac{n_i}{N_i}=\sum_{i=1}^{m}\frac{Tf_{ni}}{N_i}=1 \tag{5.3}$$

Therefore the total fatigue life in hours will be

$$T_{hour}=\frac{1}{3600(\sum_{i=1}^{m}\frac{f_{ni}}{N_i})} \tag{5.4}$$

From Chapter 2, the regression equations for the CFRP and GLARE coupons are given as following:

$$\text{CFRP}\qquad \varepsilon = 15000N^{-0.143} \tag{5.5}$$

$$\text{GLARE}\qquad \varepsilon = 8014.4N^{-0.1659} \tag{5.6}$$

For each narrow band zone with central frequency of f_{ni} , $\Delta\varepsilon^2=p(f)\Delta f$, therefore, the number of cycles to failure N_i for the RMS strain in the frequency range Δf can be written as following:

$$\text{CFRP}\qquad N_i=(\frac{2.25e8}{p(f_{ni})\Delta f_i})^{\frac{1}{0.286}} \tag{5.7}$$

$$\text{GLARE}\qquad N_i=(\frac{6.423e7}{p(f_{ni})\Delta f_i})^{\frac{1}{0.3318}} \tag{5.8}$$

Substituting Equations (5-7) and (5-8) into Equation (5-4) respectively, the fatigue life for CFRP and GLARE structures can be expressed as follows:

$$\text{CFRP}\qquad T_{hour}=\left[3600\sum\frac{f_{ni}}{(\frac{2.25e8}{p(f_{ni})\Delta f_i})^{\frac{1}{0.286}}}\right]^{-1} \tag{5.9}$$

$$\text{GLARE}\qquad T_{hour}=\left[3600\sum\frac{f_{ni}}{(\frac{6.423e7}{p(f_{ni})\Delta f_i})^{\frac{1}{0.3318}}}\right]^{-1} \tag{5.10}$$

Formulae (5-9) and (5-10) were derived based on the fatigue data from Tee-coupon tests described in Chapter 2, which simulated the dynamic behaviour of joint lines of skin and stiffeners. Therefore, these two formulae should only be suitable to predict the fatigue life at those regions.

For the CFRP and GLARE structures, the location of strain gauge B1-2 was similar to that of the gauges used in the fatigue tests of Tee-coupons, hence the fatigue life at the joint lines of the skin and stiffeners next to strain gauges B1-2 could be predicted using Formulae (5.9) and (5.10). The highest RMS strain values measured, when excitation was on the bottom skin, by gauge B1-2 were 102με at excitation level of 161 dB and 144με at 162 dB for the CFRP and GLARE structures respectively. These values were much lower than the fatigue damage data given by S-N curves of the CFRP and GLARE coupons. For these RMS strain values, formulae (5.9) and (5.10) gave the estimated fatigue life of 1.0E10 years and 10,000 years at the joint lines next to strain gauges B1-2 for the CFRP and GLARE structures respectively. The reason for such unrealistic estimates was that S-N curve data were only established for minimum strain levels of 500με and 1000με and up to 10E8 cycles for the GLARE and CFRP coupons respectively. For strain level as low as 100με, number of cycles to failure was estimated using the regression formulae, which could lead to unrealistic results. By increasing the strain level, a meaningful prediction can be obtained using these two formulae. For the same spectra of strain responses, different strain levels were used to calculate the fatigue life. Figures 5.77 and 5.78 show the relationships between RMS strain levels and predicted fatigue life for the joint lines near the strain gauges B1-2 of the CFRP and GLARE structures. It can be seen that estimated fatigue life is very sensitive to the change of response level, the fatigue life decrease dramatically with increase of response level. For CFRP structure, at RMS strain level of 1600με, estimated fatigue life of a joint line close to strain gauge B1-2 location decreased to 49 years, and for GLARE, to only 64 hours at 1500με. The reason for choosing these apparently high strain levels will be clear later in this section. It should also be noted that strain gauges yield average measurements over their length and measurement of highly concentrated strain is not possible.

The fatigue life at other locations of the box structures were also estimated using formulae (5.9) and (5.10). Strictly speaking, fatigue data used in these two formulae are not

suitable for other locations. Even for the joint region of the skin panel and stringers, the fatigue data from the simple tee-coupons tests cannot represent the complex structures. However in the situation where other fatigue data are absent, they can be used to give some indications to the fatigue life at other locations. When excited on the bottom skin at excitation level of 162 dB, RMS strain measured at locations B2-2 (Figure 5.34a) and BS1-2 (Figure 5.33a) of the GLARE box were both 210με. At this level, predicted fatigue life was 1865 years for B2-2 and 4702 years for BS1-2. If strain levels were to be increased to 1500με, the fatigue life decreased to 117 and 296 hours for these two locations as shown in Figure 5.78. Although the RMS strain levels were the same for both strain gauges B2-2 and BS1-2, because there were more high frequency peaks in the strain spectral density of B2-2 than there were in that of BS1-2, the estimated fatigue life for B2-2 was only about 40% of that for BS1-2. This indicates that frequency has strong influence on fatigue life estimation. The estimated fatigue life with the change of response strain levels for locations covered by strain gauges B2-2 and BS1-1 of the CFRP structures excited on bottom skin are also given in Figure 5.77.

In the acoustic endurance tests of the box structures, fatigue damage was found on stringers on the bottom skins of both GLARE and aluminium alloy boxes in the very early stage of tests. Fatigue cracks started and propagated along the rivet lines of the stringers. FE analysis results of the aluminium alloy box given in Chapter 6 showed very high strain (1357με and 1346με) at the lower end of the stiffener web at both ends of the stringers (see Figure 6.25). Because the GLARE box has the same construction and similar response level to the acoustic loading as the aluminium alloy box, a similar level of strain response should be expected at the same locations. The strain levels around the rivet holes may be even higher, therefore, the early fatigue damage found in the stringers of the aluminium alloy and GLARE structures are not unreasonable according to the fatigue life predictions given in Figure 5.78.

5.6 SUMMARY

Two types of acoustic tests were performed on three box structures. First, strain response data at a number of locations on the boxes were recorded under high intensity acoustic loading at various levels. Results showed that CFRP structure had the highest strain response among the three box structures. The strain response levels of the Aluminium alloy and GLARE structures were similar but with some differences. The highest strain level was found on the stiffeners of all three structures. For the stiffeners of the aluminium alloy and GLARE structures, the maximum strain was in the transverse direction to the length of the stiffeners, which indicates that the stiffeners responded mainly in torsion during acoustic excitation. For the CFRP structure, the maximum strain on a stiffener was in the longitudinal direction along the length of the stiffener, which means that stiffeners were mainly undergoing bending deformation during acoustic excitation.

Non-linear relationships were found between excitation levels and RMS response strains at various locations of the test structures, especially for the aluminium alloy and GLARE boxes. When the structures were excited on one skin panel, the other skin panel and inner ribs all showed a relatively high strain response, which indicates the coupling of top and bottom skins. When the top skins of the boxes were under direct acoustic loading, the bottom skin panels showed high response levels. The maximum responses of the bottom skin panels were 61% (aluminium alloy, B1-2), 122% (GLARE, B2-2) and 125% (CFRP, B6-2) of the maximum strain values found on the top skin panels. Relatively low response levels were found on top skins when excitation was on the bottom skins. The ratio of the highest strains between top and bottom skin panels were 50% (Al alloy box, T6-2), 28% (GLARE, T6-1) and 32% (CFRP, T1-1). These values were relatively low compared with those for bottom excitation cases, but still were not negligible. The inner ribs of the three structures also exhibited high responses in the vertical direction. These proved that components, such as skins and ribs, of a box-type structure should not be treated as isolated items in the analysis.

Spectral densities of the strain responses have shown strain energy redistribution with increase of excitation level. As the excitation level increased, the responses of higher frequency modes enhanced, and their contribution the total strain therefore is more

significant. This is shown by the normalised integration of the strain spectral densities. As shown in Figure 5.18(b) for the aluminium alloy box with bottom excitation, the contribution to total RMS value of the first two peaks between 200 Hz to 300 Hz was around 58% at excitation level of 140dB, but was reduced to 45% at 160 dB. At 600 Hz, the normalised integral was 0.91 for excitation level of 155dB, but decreased to 0.85 for 160 dB. In this case the single mode approach is no longer suitable. This phenomenon was seen for all three box structures. At the higher excitation levels, adjacent individual frequency peaks tended to coalesce to form broad peaks. These behaviours indicate non-linear response of the test structures at high excitation levels.

Acoustic fatigue endurance tests had shown that CFRP has superior fatigue resistance compared with GLARE and aluminium alloy structures. There was no visible fatigue damage found in the CFRP structure apart from the fact of that a few original rivets snapped during the endurance tests. For the aluminium alloy and GLARE structures, fatigue cracks located in the stiffeners of the both side bays and started at the early stage of the endurance tests. Due to the existence of glass fibre composites, the growth rate of the fatigue crack in the GLARE structure was lower than that of the aluminium alloy structure. Some of rivets connecting the inner ribs and bottom skin panel of the aluminium alloy structure also failed. This behaviour did not occur in the GLARE structure. For both aluminium alloy and GLARE structures, longer fatigue cracks were seen in the "down stream" bay (side B).

Types of acoustic fatigue failures in the aluminium alloy and GLARE structures have been recorded. Crack propagation rate data are also presented. From the endurance testing carried out, it appears that for the box-type structures of the form used in this project, the CFRP structure was the most acoustic fatigue resistant followed by the GLARE structure, the aluminium alloy structure being the least fatigue resistant. It must be noted, however, that only visual inspections were carried out during the tests, no NDT examinations were made for the CFRP structure.

It should also be pointed out that the ends of the stringers of the aluminium alloy and GLARE structures were not constrained, therefore, large deflections were induced during the acoustic excitation. This explains why the ends of the stringers detached from the structure at an early stage during the endurance tests. This type of design would not occur

in a full scale, large aircraft structure.

Miner's accumulation theory has been used to predict the fatigue life based on the RMS strain response data of the box structures and the S-N curves from the Tee-coupon tests. Two formulae were derived for fatigue life prediction of the GLARE and CFRP structures, which used a broadband approach and took into account the frequency distribution of the strain responses. These were used to predict the fatigue life at some locations of the composite box structures. It was found that fatigue life of the boxes was very sensitive to the change of response level, and frequency distribution of strain spectral density has strong influence on the fatigue life. Depending on the strain response level, these formulae could give a good indication of the fatigue life of structures in a certain strain range. When these formulae are used to estimate the fatigue life of a structure with very low response levels, an unrealistic fatigue life could be predicted owing to the lack of valid fatigue limit data in the S-N curves.

It may be questionable whether coupon specimens can truly represent the stiffened aircraft panels; the fatigue life prediction method discussed in this chapter can still be a useful tool to give an indication on the fatigue life of the type of the structure investigated in this thesis when there is no better method available. Compared with the panel or component tests, the coupon test is less expensive and easier to conduct. If there are enough testing data available, careful analysis and calibrations are carried, coupon tests can be a useful design tool.

Table 5.1 RMS strain response of the aluminium alloy box structure to acoustic pressure loading when excited on the curved skin panel (με)

STRAIN GAUGE	ACOUSTIC EXCITATION LEVEL					
	140dB	145dB	150dB	155dB	160dB	
T1-1	7.8	15.0	23.8	49.5	83.2	RMS STRAIN RESPONSE (με)
T1-2	8.0	21.5	49.1	105.1	138.6	
T1-3	4.2	8.0	13.0	27.2	46.4	
T2-1	3.1	5.1	8.3	15.0	24.3	
T2-2	5.9	10.2	16.0	30.7	54.1	
T2-3	4.4	7.3	11.6	22.0	38.3	
T3-1	8.8	18.3	30.5	58.4	94.8	
T3-2	2.2	3.2	5.1	9.2	15.2	
T3-3	4.5	8.4	14.5	27.7	45.8	
T4-1	9.9	17.9	27.3	52.6	87.8	
T4-2	1.8	3.5	6.1	11.7	20.4	
T5-1	6.4	13.9	22.5	45.9	76.4	
T5-2	2.5	5.0	8.7	16.0	26.4	
T6-1	6.2	12.0	19.7	32.1	47.2	
T6-2	1.8	3.0	4.7	8.3	12.7	
T7-1	7.6	17.3	27.0	47.3	71.8	
T7-2	4.6	5.6	8.1	12.4	19.0	
TS2-1	23.7	29.1	46.8	73.7	121.9	
TS2-2	8.7	18.0	33.9	54.1	85.2	
TS2-3	12.7	12.1	13.0	15.2	21.4	
B1-1	7.6	8.1	9.2	12.4	23.4	
B1-2	10.5	18.7	33.5	56.9	84.5	
B5-1	10.1	10.1	10.6	12.5	18.2	
B5-2	10.6	15.7	25.5	42.4	69.2	
B6-1	6.9	7.3	8.6	11.5	25.8	
B6-2	6.4	12.0	21.8	36.6	56.6	
TS1-1	8.3	24.9	54.1	95.3	144.7	
TS1-2	10.1	18.4	37.0	62.6	98.8	
TS1-3	9.6	17.6	28.4	47.8	81.1	
R1-1	10.4	12.8	18.4	30.5	58.6	

Table 5.2 RMS strain response of the aluminium alloy box structure to acoustic pressure loading when excited on the flat skin panel (με)

STRAIN GAUGE	ACOUSTIC EXCITATION LEVEL						RMS STRAIN RESPONSE (με)
	140dB	145dB	150dB	155dB	160dB	161dB	
B1-1	5.4	7.5	12.0	20.5	33.7	36.6	
B1-2	13.8	24.7	43.9	77.6	131.2	140.1	
B2-1	3.7	6.3	10.8	19.2	34.0	36.8	
B2-2	7.6	12.9	23.5	47.1	94.9	104.0	
B3-1	3.8	5.0	7.8	13.3	24.0	26.2	
B3-2	15.1	29.7	53.7	93.7	156.8	169.3	
B4-1	3.8	6.5	11.4	19.8	33.7	36.2	
B4-2	20.2	33.4	60.8	104.1	157.0	152.1	
B5-1	3.5	5.2	8.8	15.3	26.6	28.4	
B5-2	13.1	23.3	42.0	68.8	120.1	131.3	
B6-1	2.1	3.8	6.9	12.4	23.1	25.9	
B6-2	12.7	25.4	44.4	70.4	109.4	120.1	
BS1-1	18.4	34.6	63.5	111.2	175.7	187.8	
BS1-2	26.8	51.1	93.5	164.8	266.5	288.8	
BS1-3	6.2	12.0	21.3	37.1	64.2	70.7	
BS2-1	11.5	24.5	39.3	66.1	107.9		
BS2-2	20.5	43.1	70.0	115.9	185.8		
BS2-3	8.7	17.2	27.4	45.2	76.8		
R1-1	5.8	11.9	18.7	31.6	50.5		
R1-2	13.1	27.5	43.6	71.6	116.6		
T1-1	6.7	11.0	15.7	25.5	41.4		
T1-2	4.9	9.7	16.8	37.8	56.5		
T2-1	8.2	8.4	8.9	10.4	13.7		
T2-2	6.4	10.7	15.7	22.4	37.6		
T6-1	7.4	14.2	21.6	29.9	41.2		
T6-2	7.9	9.0	12.5	38.2	78.7		
T7-1	5.7	8.2	12.1	19.4	31.6		
T7-2	5.4	5.5	6.2	9.3	14.7		
TS2-1	10.9	18.9	29.1	42.3	63.0		
TS2-2	6.6	10.3	15.7	22.3	33.4		

Table 5.3 RMS strain response of the GLARE box structure to acoustic pressure loading when excited on the curved skin panel (με)

STRAIN GAUGE	ACOUSTIC EXCITATION LEVEL						RMS STRAIN RESPONSE (με)
	140dB	145dB	150dB	155dB	160dB	162dB	
T1-1	11.5	22.2	32.3	55.4	75.5	90.6	
T1-2	4.0	7.0	10.0	18.4	28.0	39.7	
T2-1	3.8	7.5	10.8	19.4	28.9	39.1	
T2-2	9.0	19.3	29.4	52.2	75.8	100.3	
T3-1	3.8	6.5	9.5	18.5	29.7	45.1	
T3-2	4.6	9.5	14.3	25.7	37.8	51.8	
T4-1	8.4	18.6	28.2	48.6	67.6	96.8	
T4-2	3.1	6.1	9.3	17.6	27.1	39.3	
T5-1	7.9	14.3	20.4	37.7	54.9	73.3	
T5-2	5.7	8.5	11.5	19.7	29.3	40.6	
T6-1	10.3	18.9	27.3	46.6	72.2	103.4	
T6-2	2.0	3.9	6.0	11.8	18.2	25.4	
T7-1	13.9	26.5	41.3	78.5	104.5	128.9	
T7-2	2.1	4.8	7.4	13.1	21.1	31.3	
TS1-1	13.3	36.0	55.5	112.1	172.8	220.6	
TS1-2	5.9	11.7	21.8	40.7	72.5	99.1	
TS1-3	11.8	22.9	45.6	79.0	125.8	160.1	
BS1-1	6.1	10.1	17.1	28.1	46.4	63.5	
BS1-2	7.6	13.7	24.4	40.8	68.9	96.3	
BS1-3	2.6	4.6	8.2	13.0	20.7	27.4	
B3-1	7.3	8.7	12.0	17.9	33.0	44.7	
B3-2	7.0	9.5	15.3	24.7	42.5	59.9	
B2-1	27.9	28.0	29.3	32.9	51.9	67.6	
B2-2	13.7	22.0	40.5	68.8	128.3	185.6	
B5-1	6.1	6.6	8.6	14.1	29.0	40.1	
B5-2	9.8	15.1	25.2	41.4	68.9	92.6	
B6-1	7.6	8.8	13.9	24.2	55.3	71.2	
B6-2	15.0	26.7	46.6	74.7	137.8	178.0	
R1-1	8.2	9.6	14.8	23.5	49.3	63.8	
R1-2	11.5	17.9	31.9	50.7	94.4	129.1	

Table 5.4 RMS strain response of the GLARE structure to acoustic pressure loading when excited on the flat skin panel (με)

STRAIN GAUGE	ACOUSTIC EXCITATION LEVEL						
	140dB	145dB	150dB	155dB	160dB	162dB	
B1-1	4.9	7.3	10.3	15.8	30.8	43.9	RMS STRAIN RESPONSE (με)
B1-2	15.4	29.1	43.6	65.6	120.5	143.8	
B2-1	3.6	6.4	9.2	14.7	31.5	47.5	
B2-2	21.8	39.9	58.5	87.0	165.0	210.2	
B3-1	5.3	8.4	12.2	18.7	38.4	46.7	
B3-2	6.2	10.6	16.0	24.6	50.2	69.8	
B4-1	4.4	8.2	12.1	19.5	38.5	56.4	
B4-2	16.2	31.2	45.6	67.3	135.1	188.0	
B5-1	3.8	5.6	8.1	13.0	32.5	41.0	
B5-2	27.4	45.9	62.8	83.5	137.4	214.0	
B6-1	2.6	4.8	7.5	12.5	29.4	43.4	
B6-2	18.3	34.0	50.2	76.0	149.4	200.3	
BS1-1	12.7	24.9	39.0	59.6	119.0	160.2	
BS1-2	16.4	32.7	50.8	78.1	151.7	210.2	
BS1-3	4.6	9.2	14.0	22.7	44.7	61.0	
BS2-1	7.1	18.2	27.4	43.6	85.0	108.1	
BS2-2	12.9	32.3	47.0	74.1	143.3	185.1	
BS2-3	7.0	18.1	27.4	44.9	89.0	113.9	
R1-1	2.2	5.0	7.4	11.4	23.6	31.1	
R1-2	8.6	22.5	34.9	55.2	118.0	155.3	
T1-2	3.9	5.3	6.9	9.7	16.3	19.7	
T2-1	25.9	26.0	26.3	27.0	31.4	33.6	
T2-2	5.4	10.8	15.6	22.7	37.6	43.6	
T6-1	5.7	11.3	16.3	23.5	46.3	67.3	
T6-2	4.2	4.9	5.8	7.7	15.3	20.8	
T7-1	6.4	12.8	17.2	21.8	37.7	44.8	
T7-2	4.4	4.7	5.4	7.0	19.0	24.2	
TS2-1	9.5	19.3	26.6	39.4	65.0	71.9	
TS2-2	6.5	14.1	20.9	31.1	52.8	60.0	

Table 5.5 RMS strain response of the CFRP structure to acoustic pressure loading when excited on the flat skin panel (με) (initial excitaiton)

STRAIN GAUGE	ACOUSTIC EXCITAITON LEVEL						RMS STRAIN RESPONSE (με)
	140dB	145dB	150dB	155dB	160dB	162dB	
B1-1	3.9	5.7	6.6	9.1	16.8	21.1	
B1-2	10.7	29.5	38.0	60.2	116.6	140.6	
B2-1	2.5	5.5	6.8	10.1	21.2	24.0	
B2-2	23.3	61.2	76.9	103.6	192.9	213.5	
B3-1	4.6	11.0	14.4	21.3	40.9	49.8	
B3-2	10.1	25.4	31.7	43.9	77.7	89.0	
B4-1	2.7	5.7	7.1	11.2	22.6	27.8	
B4-2	19.1	54.9	70.6	114.4	206.0	241.1	
B5-1	2.9	6.9	8.5	11.9	25.9	29.8	
B5-2	16.9	47.8	59.4	82.6	164.4	184.8	
B6-1	2.1	5.4	7.0	10.7	23.8	28.6	
B6-2	14.0	37.9	49.3	71.8	149.9	182.3	
BS1-1	44.0	124.9	162.0	237.3	464.6	558.0	
BS1-2	6.7	34.6	44.9	66.1	130.0	155.7	
BS1-3	16.5	47.1	61.0	89.9	175.5	209.0	
BS2-1	27.5	72.6	136.0	196.9	371.0	471.1	
BS2-2	7.7	20.1	37.6	54.5	102.8	130.6	
BS2-3	9.2	24.1	45.3	65.9	123.1	155.8	
R1-1	4.3	10.3	18.8	26.3	50.2	65.1	
R1-2	18.8	49.6	91.8	134.1	256.5	327.7	
T1-1	10.7	27.0	49.1	69.9	120.5	137.9	
T1-2	4.7	5.9	8.3	10.7	18.6	23.3	
T2-1	0.1	0.5	1.5	3.0	8.5	12.4	
T2-2	6.1	10.9	18.7	28.3	57.7	69.2	
T6-1	4.6	4.6	8.3	13.6	29.9	38.8	
T6-2	5.8	5.9	6.9	8.1	13.0	15.9	
T7-1	5.2	5.6	6.7	8.3	11.8	14.0	
T7-2	8.3	16.8	29.6	41.5	72.3	85.4	
TS2-1	7.9	13.9	21.4	28.2	45.4	53.3	
TS2-2	19.8	47.8	81.3	110.8	184.9	221.1	

Table 5.6 RMS strain response of the CFRP structure to acoustic pressure loading when excited on the curved skin panel (με) (after repair)

STRAIN GAUGE	ACOUSTIC EXCITATION LEVEL						
	140dB	145dB	150dB	155dB	160dB	161dB	
T1-1	9.8	21.4	38.0	65.7	111.3	127.0	RMS STRAIN RESPONSE (με)
T1-2	2.5	3.9	6.3	11.4	21.0	25.2	
T2-1	2.0	3.9	6.6	12.3	22.7	26.6	
T2-2	7.8	16.3	30.6	52.3	96.6	110.2	
T3-1	5.7	11.8	21.2	40.1	75.3	89.1	
T3-2	3.4	6.2	11.1	20.4	37.8	44.7	
T4-1	5.8	12.4	22.1	39.6	70.0	82.3	
T4-2	1.9	3.4	5.8	10.1	17.4	21.1	
T5-1	7.1	15.0	26.8	50.2	84.9	98.5	
T5-2	4.5	5.2	6.6	10.6	19.0	22.1	
T6-1	8.8	18.8	35.4	54.3	88.9	103.4	
T6-2	1.3	2.0	3.5	5.7	9.4	10.9	
T7-1	1.1	2.0	3.7	6.7	12.9	15.1	
T7-2	9.4	19.4	34.5	61.2	104.8	119.4	
TS1-1	4.9	10.5	19.6	35.8	57.8	66.8	
TS1-2	18.3	38.0	77.5	143.5	251.7	290.8	
TS1-3	7.1	14.3	28.7	54.4	98.6	118.0	
TS2-1	3.7	7.5	15.5	29.1	52.1	60.1	
TS2-2	14.5	29.8	61.3	116.2	210.4	243.2	
TS2-3	5.3	10.5	21.3	40.1	72.8	83.4	
B1-1	2.8	3.1	4.3	7.7	13.8	17.8	
B1-2	10.2	12.5	19.6	34.3	63.7	74.4	
B2-1	22.6	22.8	23.1	24.2	28.4	30.8	
B2-2	15.8	18.2	36.3	71.9	138.7	163.7	
B5-1	5.7	4.5	5.5	10.0	15.6	18.0	
B5-2	4.4	7.6	14.5	28.2	50.9	61.4	
B6-1	3.6	4.3	6.5	12.2	22.4	26.3	
B6-2	20.9	28.2	43.7	78.6	138.9	162.0	
R1-1	21.4	20.5	21.5	26.9	39.8	47.0	
R1-2	9.4	18.0	36.1	69.3	132.2	155.7	

Table 5.7 RMS strain response of the CFRP structure to acoustic pressure loading when excited on the flat skin panel (με) (after repair)

STRAIN GAUGE	ACOUSTIC EXCITATION LEVEL						RMS STRAIN RESPONSE (με)
	140dB	140dB	150dB	155dB	160dB	161dB	
B1-1	3.8	4.9	6.7	10.2	18.7	20.7	
B1-2	8.5	17.3	28.7	47.3	90.6	101.2	
B2-1	2.0	3.4	5.4	8.8	17.2	19.3	
B2-2	18.2	37.3	60.5	101.4	184.0	203.5	
B3-1	4.0	7.6	12.8	21.3	40.8	46.9	
B3-2	10.3	22.9	39.1	65.9	121.5	137.7	
B4-1	2.3	3.7	6.4	9.4	18.1	20.9	
B4-2	13.2	27.1	44.8	72.7	137.0	150.6	
B5-1	2.5	4.6	7.8	12.7	24.5	27.0	
B5-2	13.5	29.4	51.1	82.3	156.8	170.8	
B6-1	1.9	3.8	5.9	9.2	19.7	21.8	
B6-2	12.3	27.7	42.9	68.1	140.6	153.1	
BS1-1	33.6	70.9	120.7	201.6	384.9	431.3	
BS1-2	9.4	19.9	33.9	56.3	106.7	119.7	
BS1-3	12.3	25.8	43.9	73.2	140.2	157.8	
BS2-1	32.6	59.2	101.8	163.3	296.4	328.7	
BS2-2	9.1	16.4	28.1	45.1	81.7	90.6	
BS2-3	10.7	19.6	33.3	54.1	106.9	120.1	
R1-1	4.7	8.2	14.5	23.9	43.7	48.7	
R1-2	23.9	37.9	67.3	106.8	196.0	213.3	
T1-1	8.7	13.7	22.0	34.5	58.6	65.7	
T1-2	6.4	7.0	8.3	11.1	17.7	20.3	
T2-1	0.3	0.6	1.4	2.8	7.6	9.6	
T2-2	7.8	10.8	16.1	24.1	40.4	46.3	
T6-1	2.4	1.4	2.3	3.7	5.5	8.7	
T6-2	5.6	5.7	5.7	6.2	8.2	9.1	
T7-1	6.1	6.2	6.5	7.2	9.9	10.4	
T7-2	8.6	11.7	17.3	25.7	45.5	51.6	
TS2-1	8.7	10.9	14.4	19.8	29.6	31.0	
TS2-2	17.1	30.3	49.6	74.9	127.2	135.1	

Table 5.8 Acoustic endurance tests results – Aluminium alloy structure (bay side A)

<table>
<tr><th colspan="9">ALUMINIUM ALLOY STRUCTURE - bay side A</th></tr>
<tr><th rowspan="2">ENDURANCE TIME (minutes)</th><th colspan="2">STIFFENER No.1</th><th colspan="2">STIFFENER No.2</th><th colspan="2">STIFFENER No.3</th><th colspan="2">STIFFENER No.4</th></tr>
<tr><th>Crack length (mm)</th><th>Rivet No.</th><th>Crack length (mm)</th><th>Rivet No.</th><th>Crack length (mm)</th><th>Rivet No.</th><th>Crack length (mm)</th><th>Rivet No.</th></tr>
<tr><td>0</td><td>0</td><td>0</td><td>0</td><td>0</td><td>0</td><td>0</td><td>0</td><td>0</td></tr>
<tr><td>50</td><td>26</td><td>2</td><td>35</td><td>2.5</td><td>17</td><td>1.5</td><td>17</td><td>1.5</td></tr>
<tr><td>80</td><td>116</td><td>7</td><td>89</td><td>5.5</td><td>17</td><td>1.5</td><td>116</td><td>7</td></tr>
<tr><td>110</td><td>143</td><td>8.5</td><td>116</td><td>7</td><td>35</td><td>2.5</td><td>179</td><td>10.5</td></tr>
<tr><td>146</td><td rowspan="10">end part detached from the structure at 156 minutes (see Figure 7.200)</td><td rowspan="10"></td><td>134</td><td>8</td><td>62</td><td>4</td><td>206</td><td>12</td></tr>
<tr><td>190</td><td>170</td><td>10</td><td>152</td><td>9</td><td>206</td><td>12</td></tr>
<tr><td>230</td><td>215</td><td>12.5</td><td colspan="2" rowspan="2">end part detached at 200 minutes (Figure 7.200)</td><td>233</td><td>13.5</td></tr>
<tr><td>280</td><td>224</td><td>13</td><td>179</td><td>10.5</td><td>251</td><td>14.5</td></tr>
<tr><td>320</td><td>233</td><td>13.5</td><td>197</td><td>11.5</td><td colspan="2" rowspan="3">crack stopped growing</td></tr>
<tr><td>372</td><td colspan="2" rowspan="5">crack stopped growing</td><td>197</td><td>11.5</td></tr>
<tr><td>437</td><td>224</td><td>13</td></tr>
<tr><td>486</td><td colspan="4" rowspan="2"></td></tr>
<tr><td>521</td></tr>
</table>

Table 5.9 Acoustic endurance test results – Aluminium alloy structure (bay side B and middle bay)

ALUMINIUM ALLOY STRUCTURE - bay side B								
ENDURANCE TIME (minutes)	STIFFENER No.1		STIFFENER No.2		STIFFENER No.3		STIFFENER No.4	
	Crack length (mm)	Rivet No.	Crack length (mm)	Rivet No.	Crack length (mm)	Rivet No.	Crack length (mm)	Rivet No.
0	0	0	0	0	0	0	0	0
50	143	8.5	125	7.5	98	6	116	7
80	161	9.5	152	9	end part detached from the structure at 50 minutes (Figure 7.201)		116	7
110	161	9.5	215	12.5			116	7
146	179	10.5	233	13.5			125	7.5
190	197	11.5	251	14.5			125	7.5
230	215	12.5	251	14.5			125	7.5
280	224	13.5	269	15.5	107	6.5	152	9
320	269	15.5	269	15.5	107	6.5	152	9
372	crack stopped growing		287	16.5	116	7	161	9.5
437			296	17	134	8	161	9.5
486			crack stopped growing		crack stopped growing		161	9.5
521							206	12

AIUMINIUM ALLOY STRUCTURE - Stiffener No.3 - Middle bay					
ENDURANCE TIME (minutes)	320	372	437	486	521
CRACK LENGTH (mm)	0	35	53	53	62
RIVET No.	0	2.5	3.5	3.5	4

Table 5.10 Acoustic endurance test results – GLARE structure (bay side A)

GLARE STRUCTURE - bay side A								
ENDURANCE TIME (minutes)	STIFFENER No.1		STIFFENER No.2		STIFFENER No.3		STIFFENER No.4	
	Crack length (mm)	Rivet No.	Crack length (mm)	Rivet No.	Crack length (mm)	Rivet No.	Crack length (mm)	Rivet No.
0	0	0	0	0	0	0	0	0
38	0	0	0	0	0	0	0	0
92	8	1	53	3.5	8	1	17	1.5
145	62	4	53	3.5	17	1.5	35	2.5
181	89	5.5	107	6.5	17	1.5	53	3.5
233	98	6	125	7.5	17	1.5	53	3.5
296	107	6.5	125	7.5	44	3	80	5
362	134	8	143	8.5	53	3.5	80	5
439	143	8.5	crack stopped growing				89	5.5
511	152	9					98	6
588								

Table 5.11 Acoustic endurance test results – GLARE structure (bay side B)

GLARE STRUCTURE - bay side B								
ENDURANCE TIME (minutes)	STIFFENER No.1		STIFFENER No.2		STIFFENER No.3		STIFFENER No.4	
	Crack length (mm)	Rivet No.	Crack length (mm)	Rivet No.	Crack length (mm)	Rivet No.	Crack length (mm)	Rivet No.
0	26	2	17	1.5	0	0	0	0
38	44	3	35	2.5	35	2.5	35	2.5
92	62	4	53	3.5	35	2.5	53	3.5
145	71	4.5	53	3.5	80	5	53	3.5
181	106	6.5	53	3.5	116	7	71	4.5
233	161	9.5	62	4	134	8	71	4.5
296	179	10.5	143	8.5	170	10	89	5.5
362	179	10.5	161	9.5	170	10	107	6.5
439	188	11	179	10.5	170	10	116	7
511	188	11	179	10.5	170	10	116	7
588	197	11.5	197	11.5	188	11	134	8

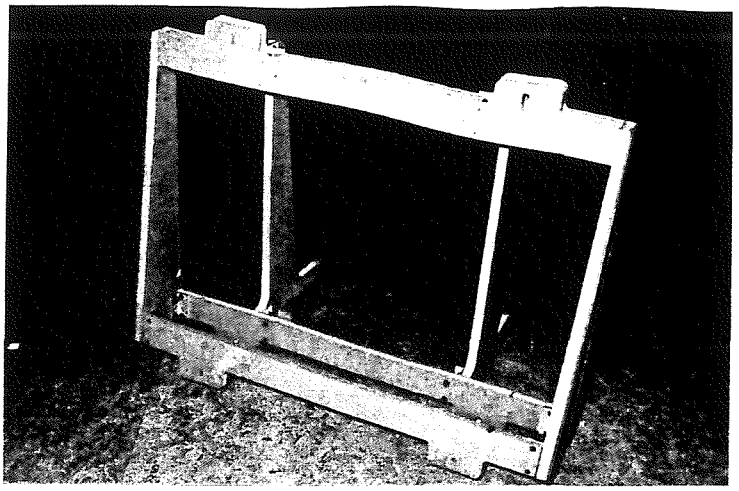

a) Supporting frame

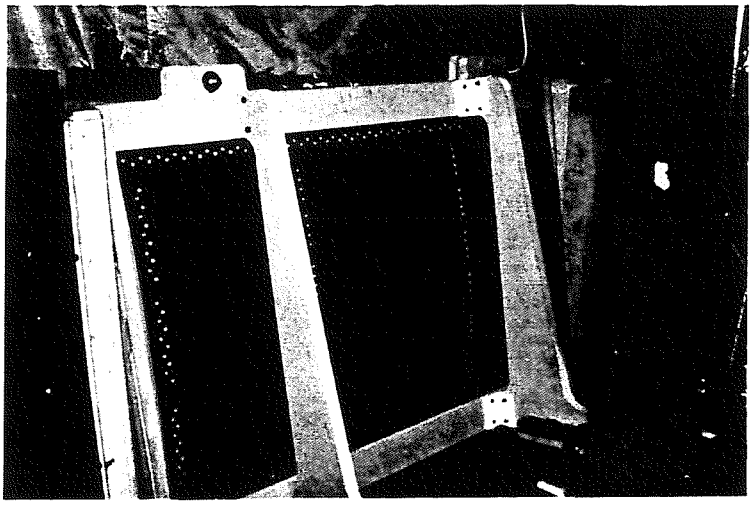

b) CFRP box in the supporting frame during the acoustic endurance testing

Figure 5.1 Supporting structure for the acoustic endurance testing of box structures

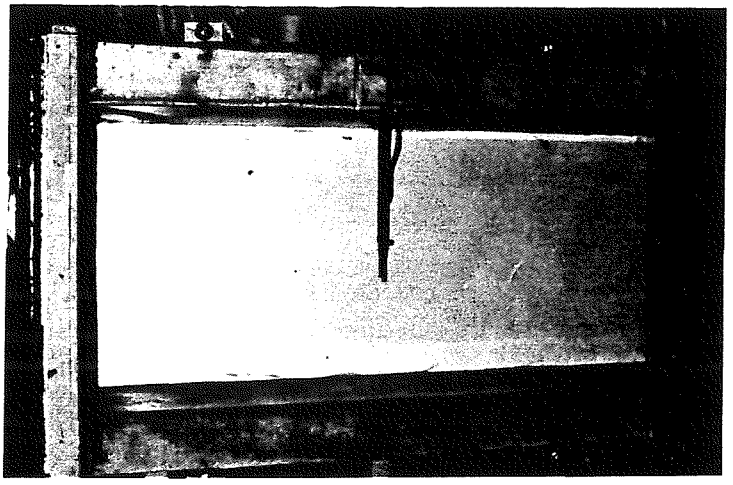

Figure 5.2 Reference microphone fixed in the test section of the PWT

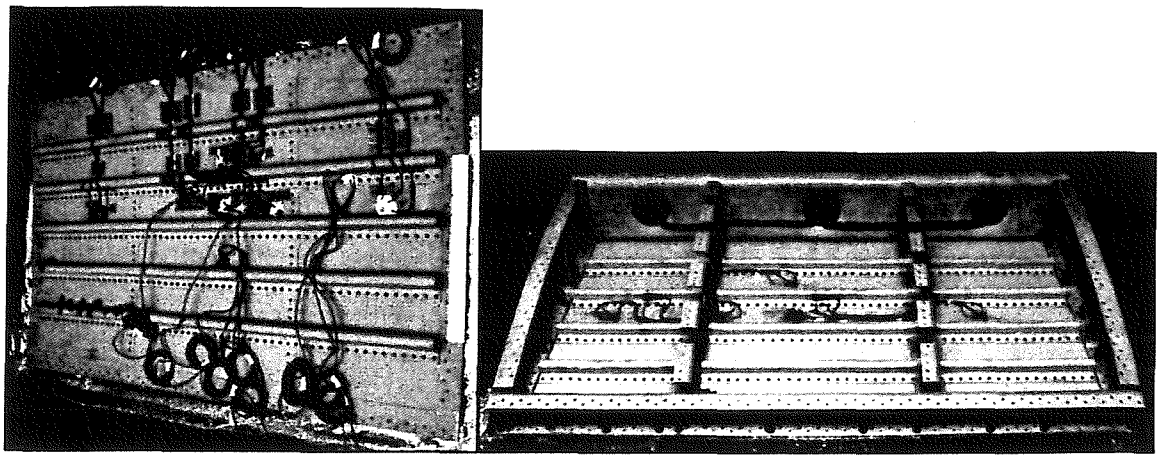

a) Curved skin panel b) Flat skin panel, ribs and stiffeners

Figure 5.3 Strain gauge installation on the Aluminium alloy and GLARE structures

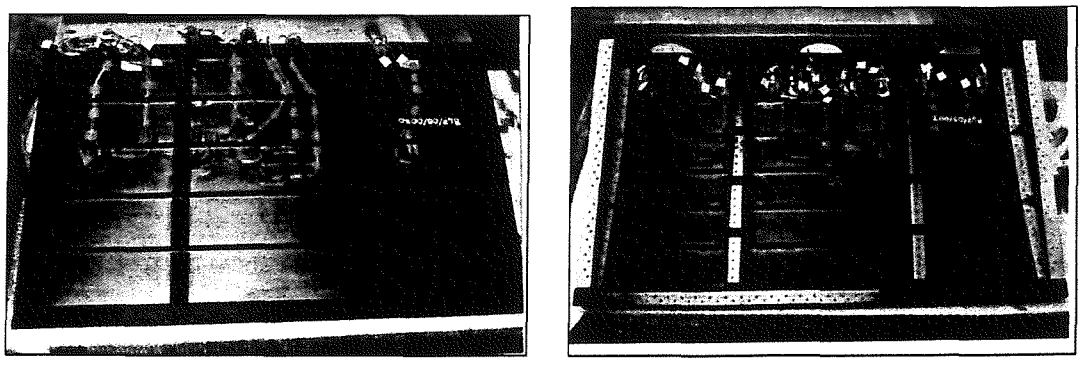

a) Flat skin panel b) Curved skin panel

Figure 5.4 Strain gauge installations on the CFRP structure

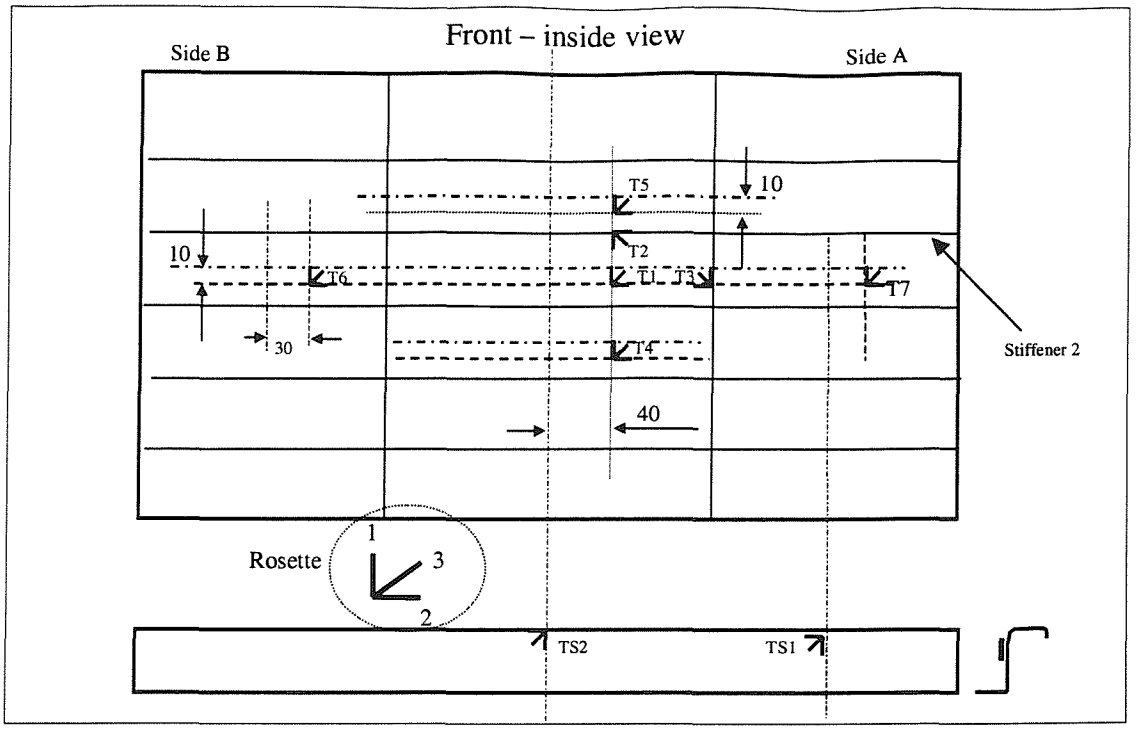

a) Curved skin panel

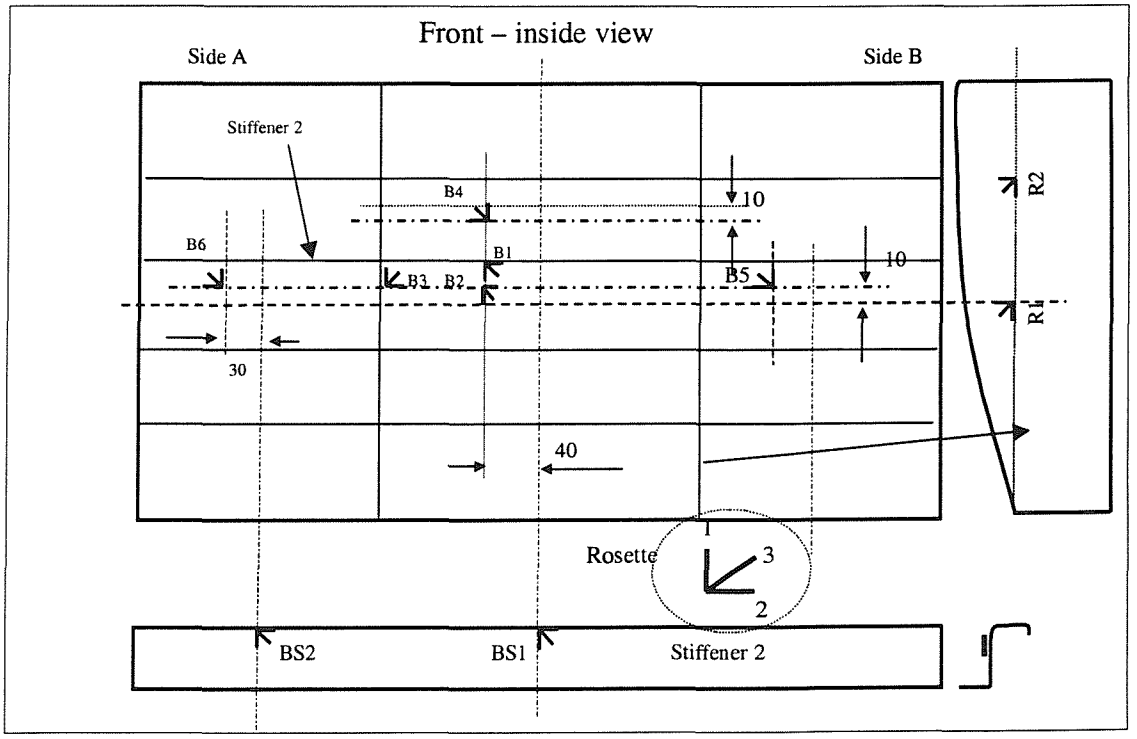

a) Flat skin panel and inner rib

Figure 5.5 Locations and numbering of the strain gauges for acoustic excitation of the box structures

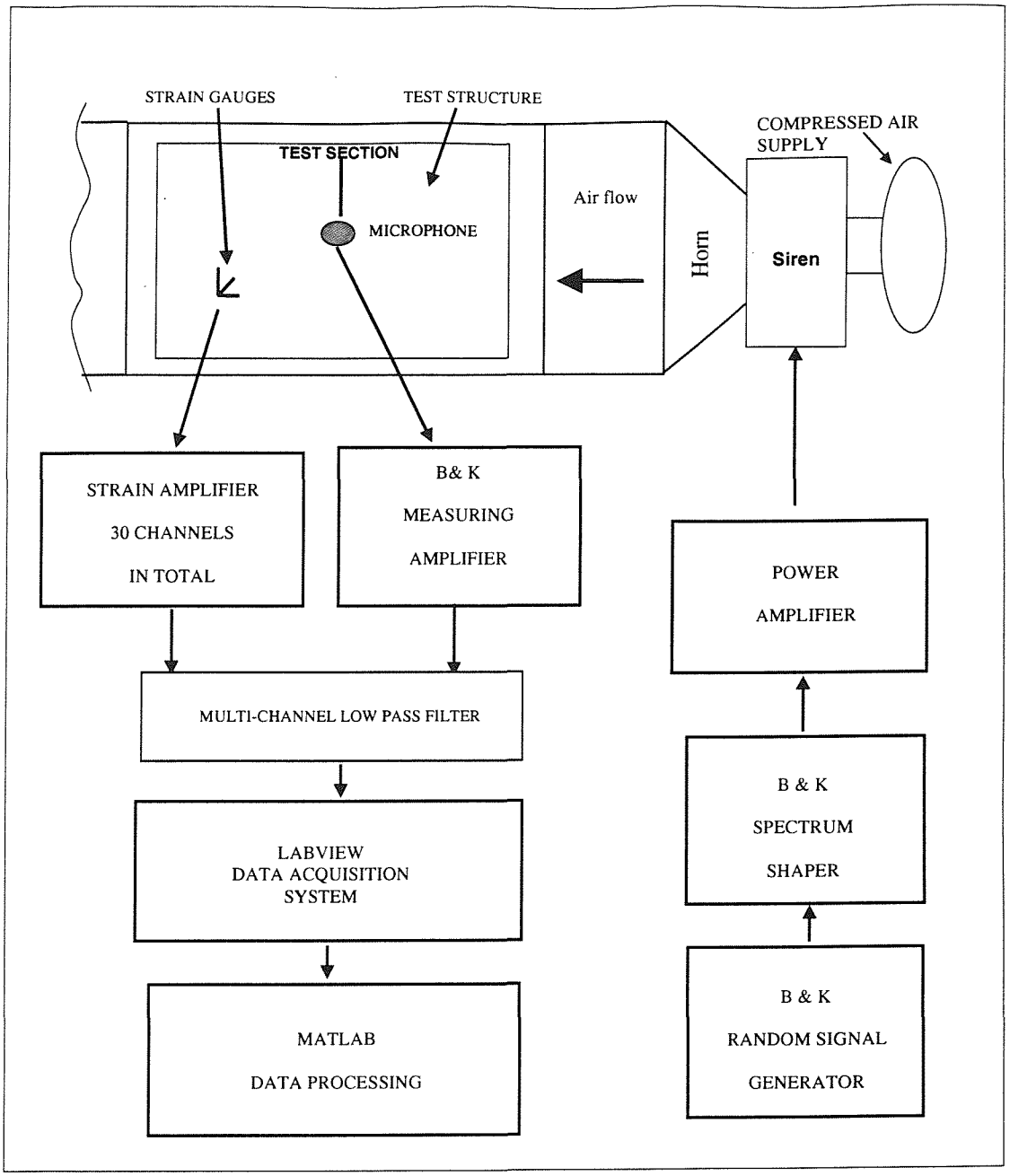

Figure 5.6 Instrumentation set-up for acoustic excitation of a box structure by the PWT

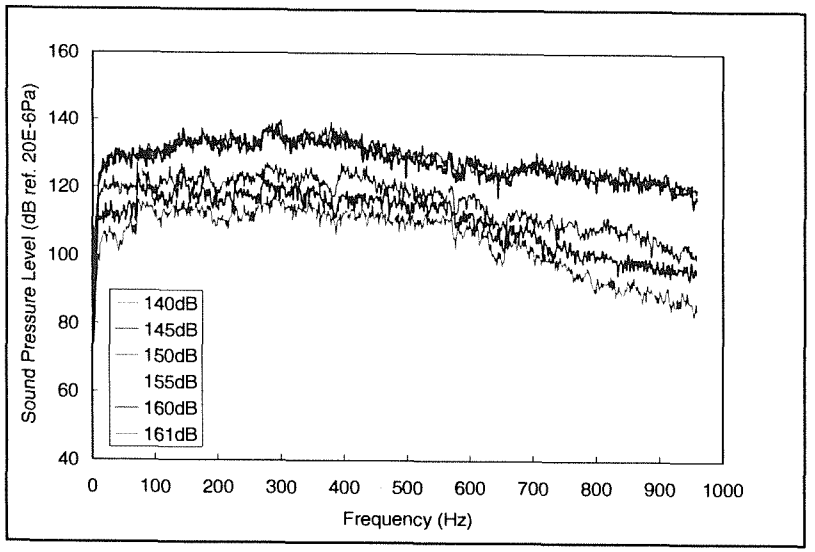

Figure 5.7 Spectra of the acoustic pressure loading measured by reference microphone

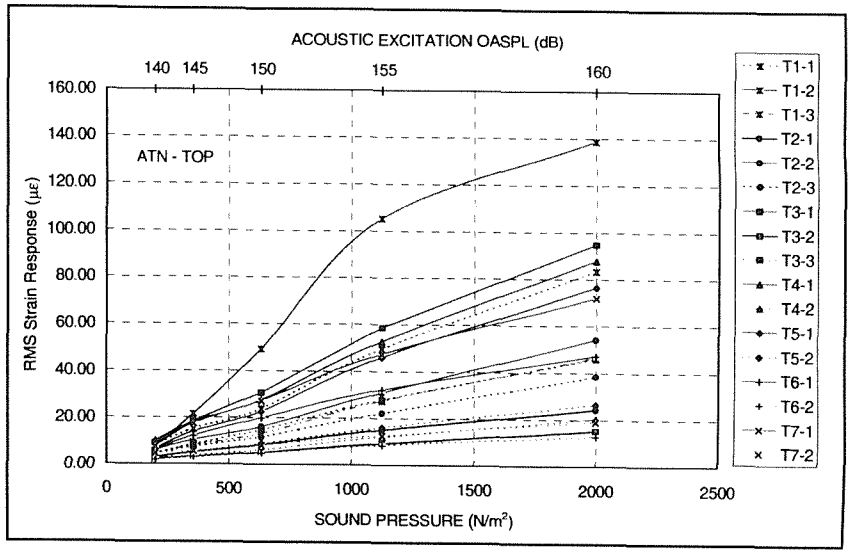

Figure 5.8 RMS strain response of the top skin panel of aluminium alloy structure excited on top skin

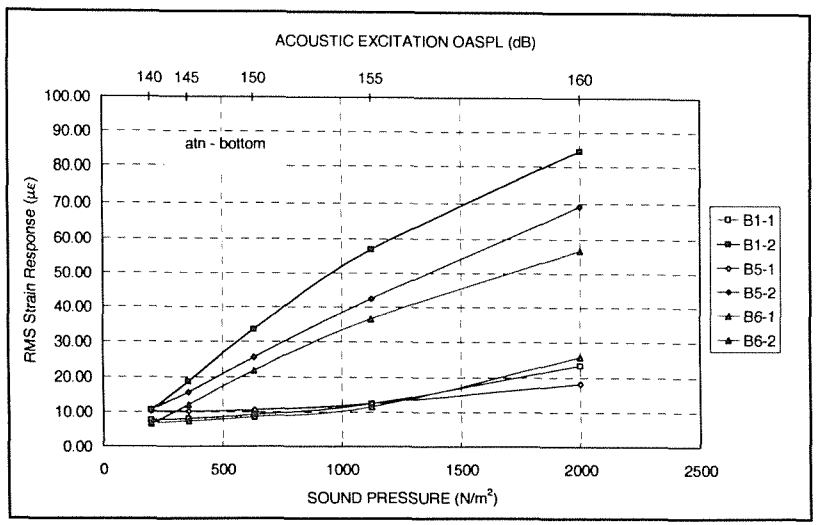

Figure 5.9 RMS strain response of the bottom skin panel of aluminium alloy structure excited on top skin

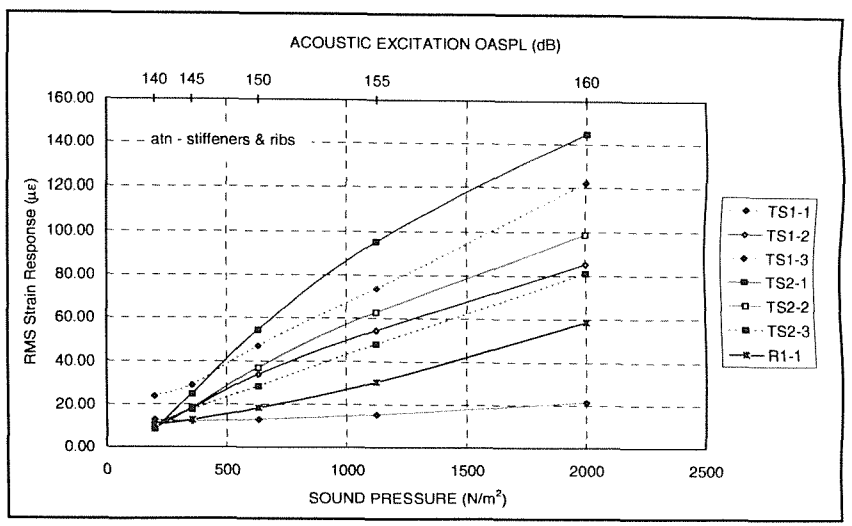

Figure 5.10 RMS strain response of the inner rib and stiffeners of aluminium alloy structure excited on top skin

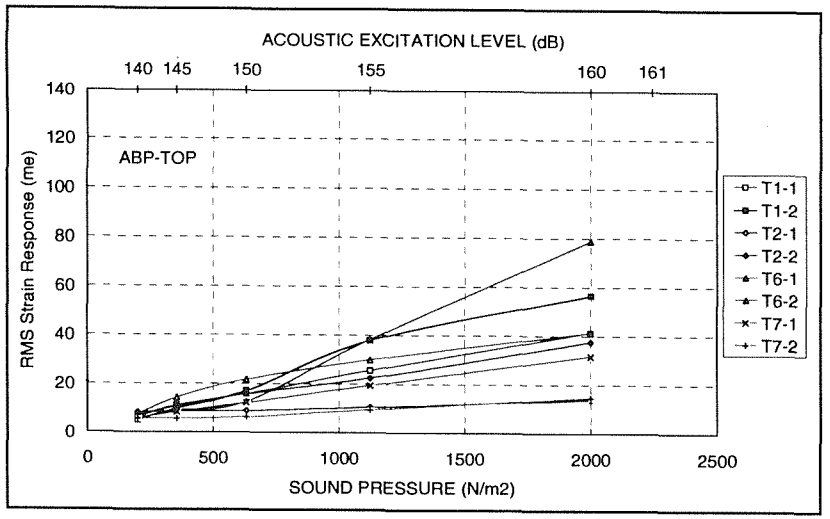

Figure 5.11 RMS strain response of the top skin panel of aluminium alloy structure excited on bottom skin

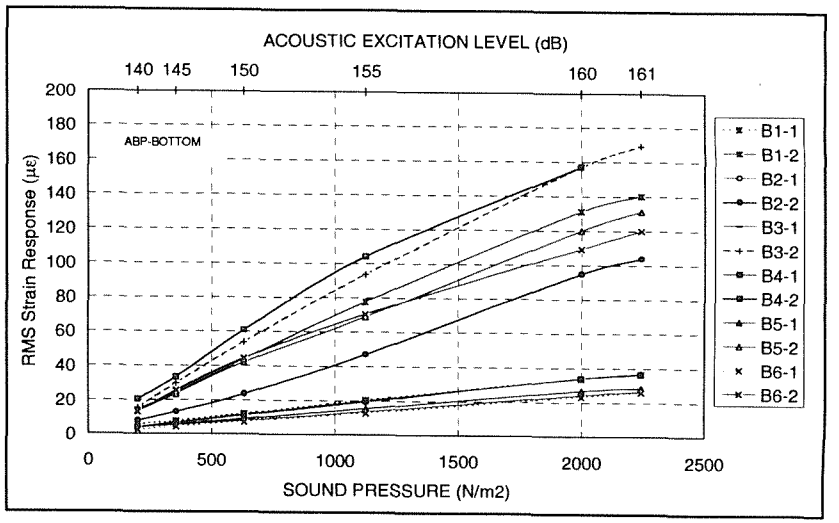

Figure 5.12 RMS strain response of the bottom skin panel of aluminium alloy structure excited on bottom skin

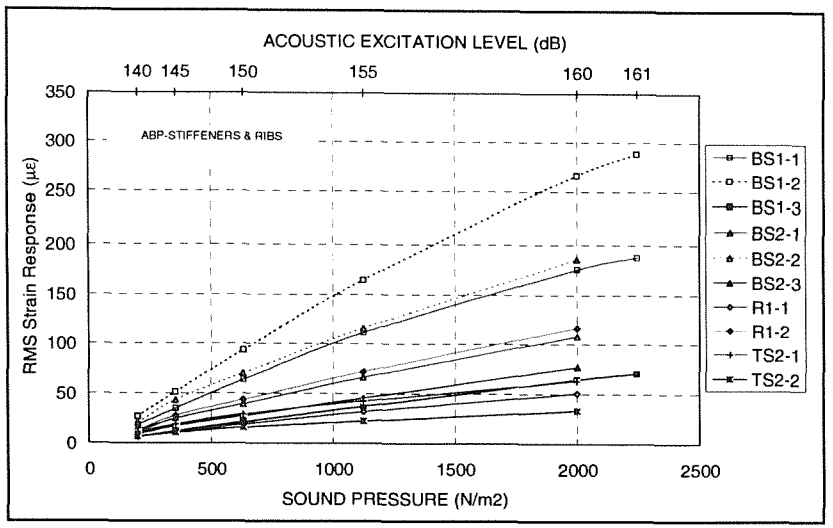

Figure 5.13 RMS strain response of the stiffeners and rib of aluminium alloy structure excited on bottom skin

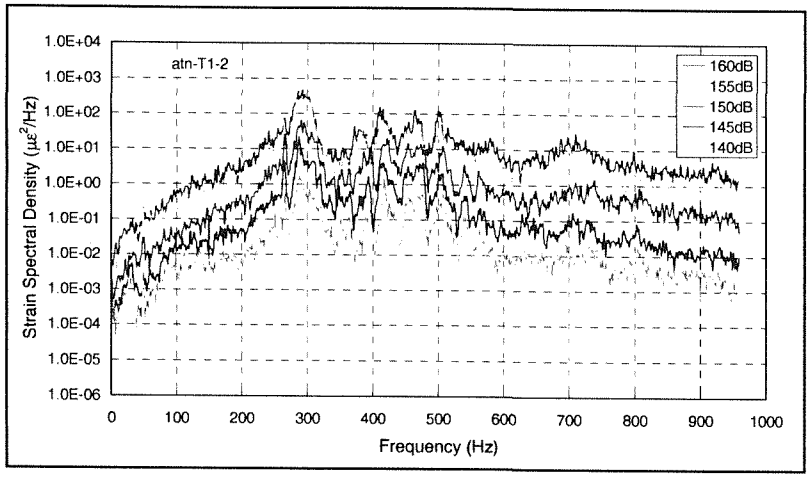

a). **Strain spectral density**

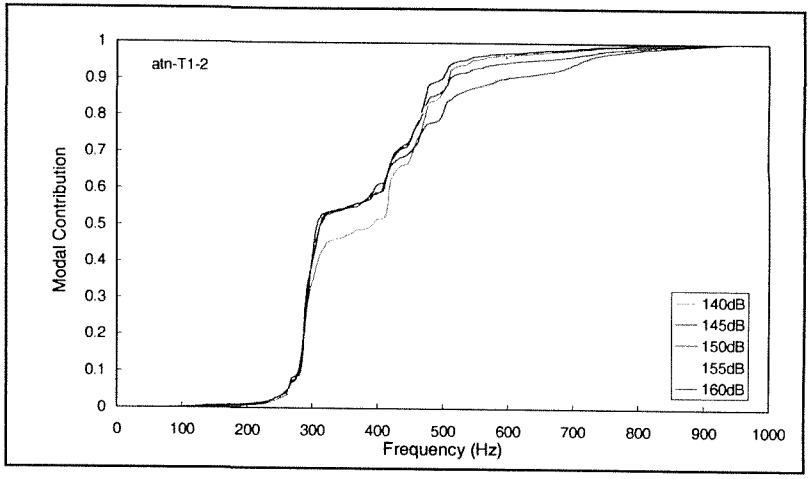

b). **Normalised integral across strain spectral density**

Figure 5.14 Al Alloy box - top excitation - Gauge T1-2

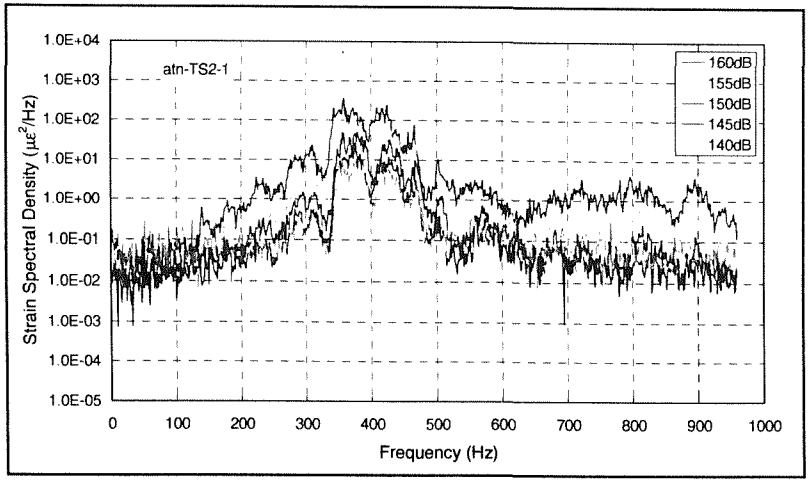

a). Strain spectral density

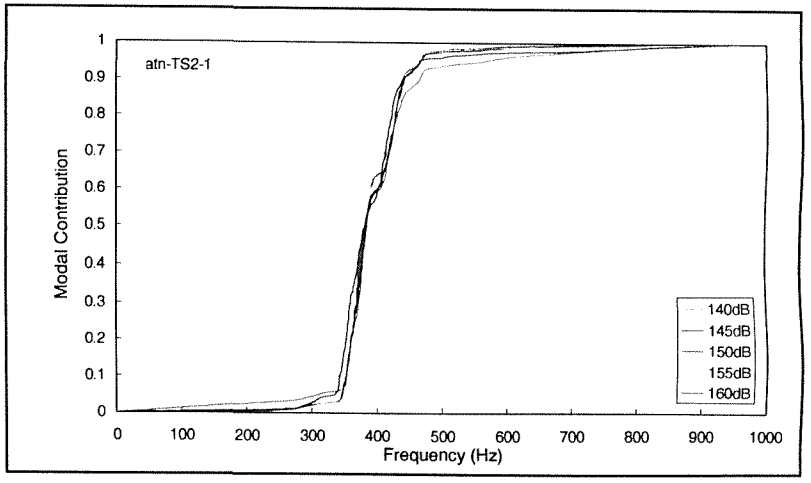

b). Normalised integral across strain spectral density

Figure 5.15 Al Alloy box - top excitation - Gauge TS2-1

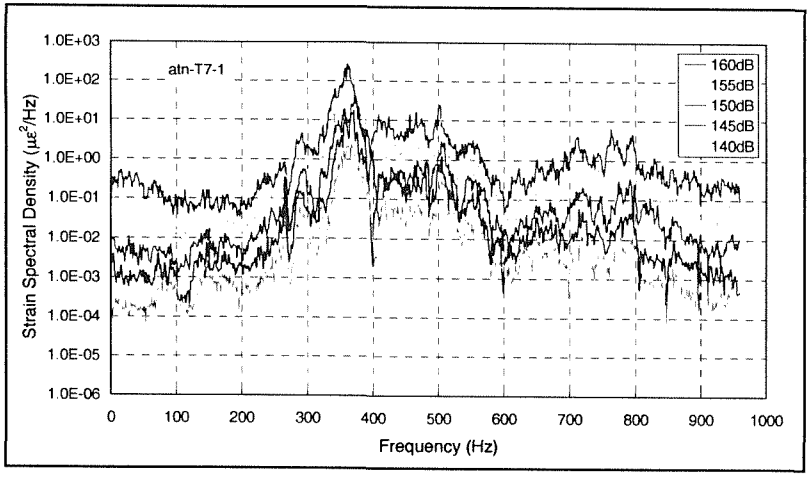

a). Strain spectral density

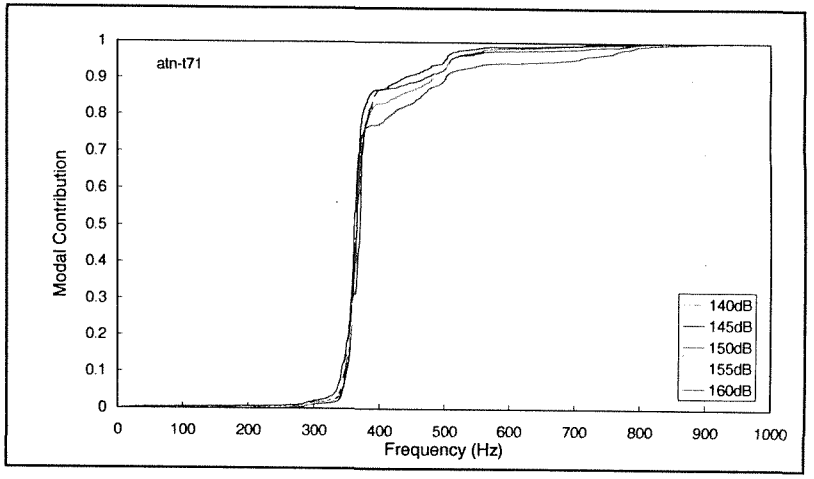

b). Normalised integral across strain spectral density

Figure 5.16 Al Alloy box - top excitation - Gauge T7-1

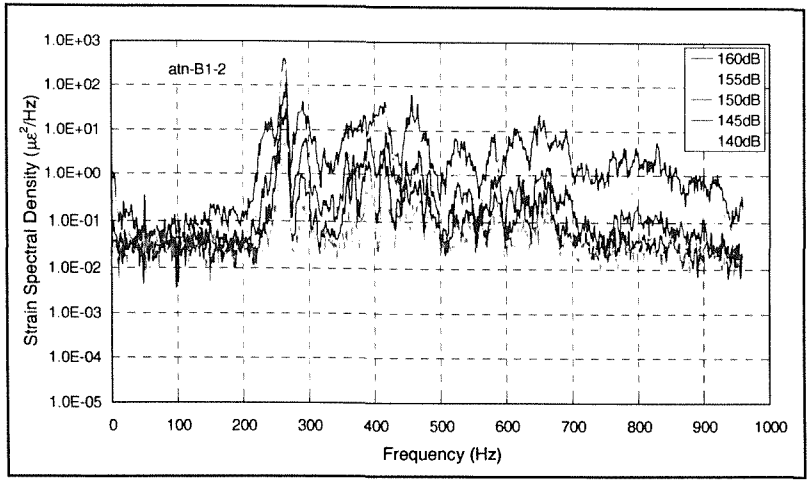

a). Strain spectral density

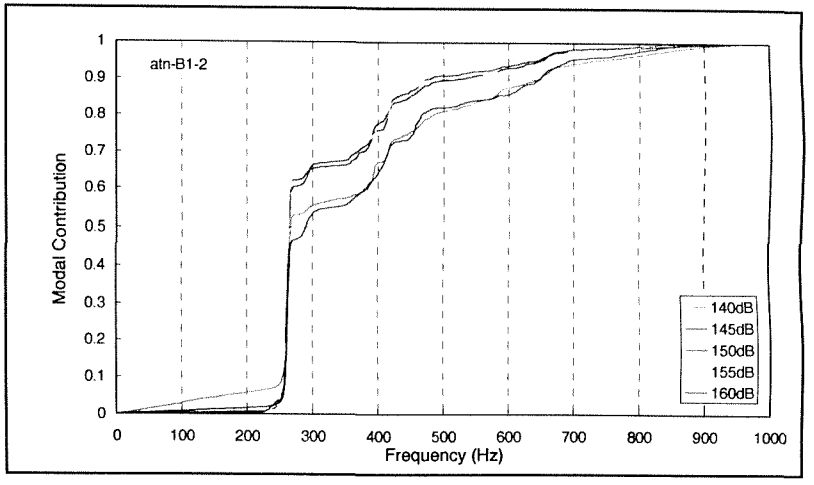

b). Normalised integral across strain spectral density

Figure 5.17 Al Alloy box - top excitation - Gauge B1-2

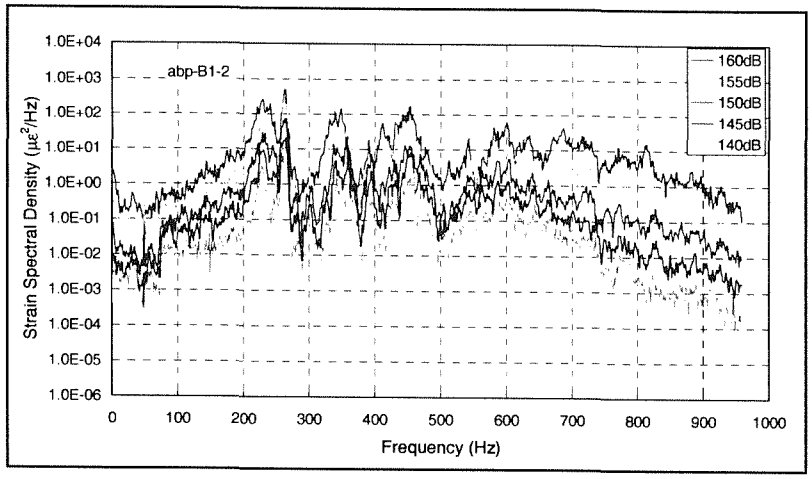

a). Strain spectral density

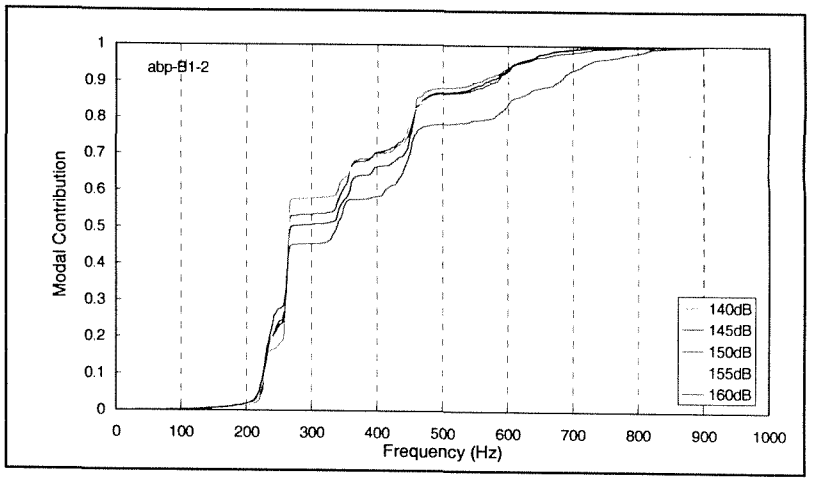

b). Normalised integral across strain spectral density

Figure 5.18 Al Alloy box - bottom excitation - Gauge B1-2

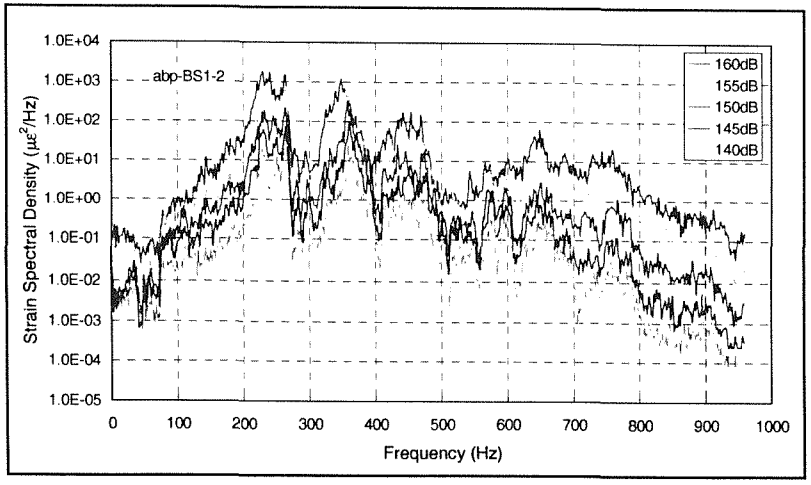

a). Strain spectral density

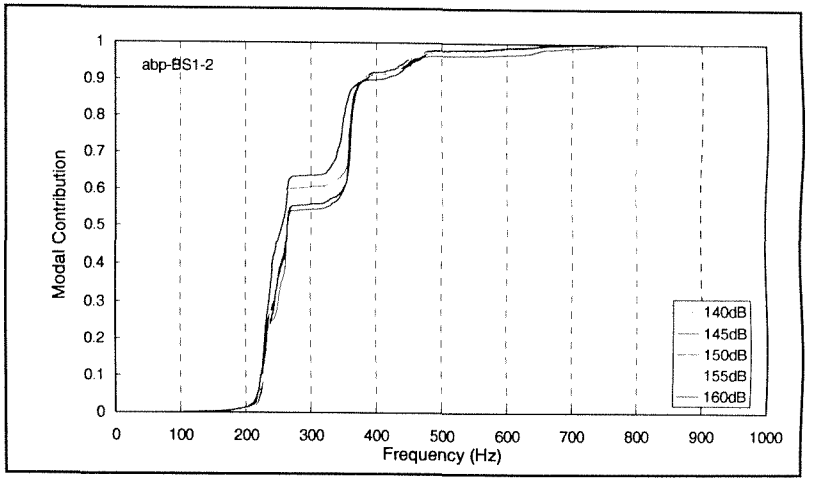

b). Normalised integral across strain spectral density

Figure 5.19 Al Alloy box - bottom excitation - Gauge BS1-2

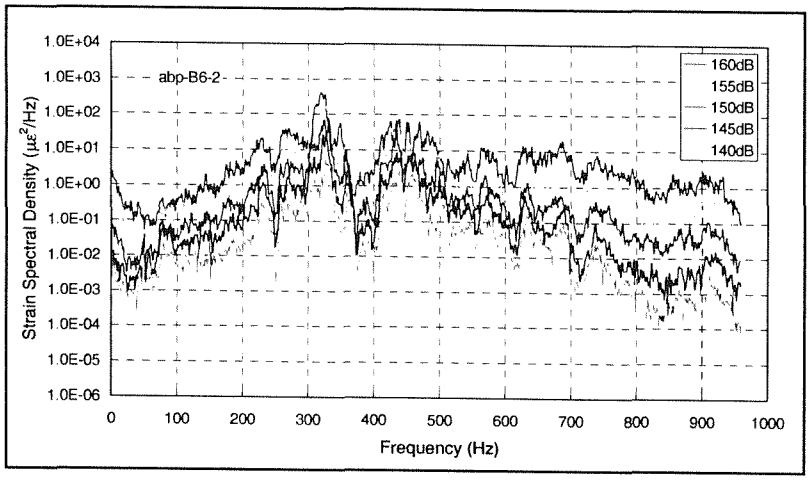

a). Strain spectral density

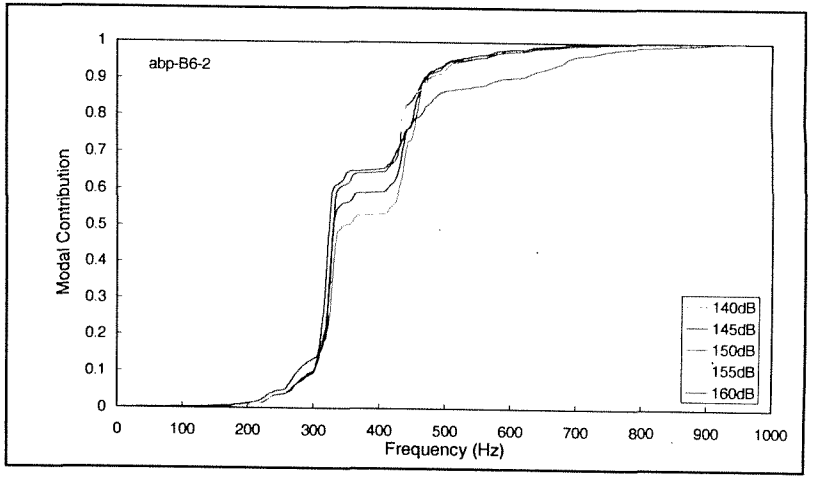

b). Normalised integral across strain spectral density

Figure 5.20 Al Alloy box - bottom excitation - Gauge B6-2

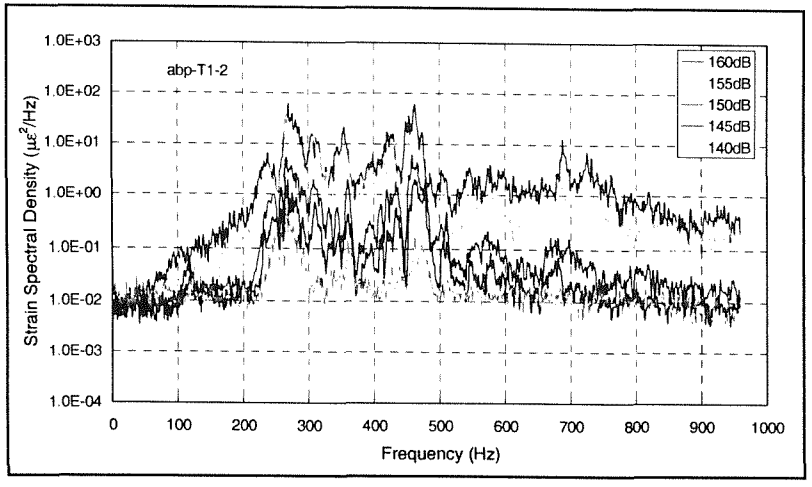

a). Strain spectral density

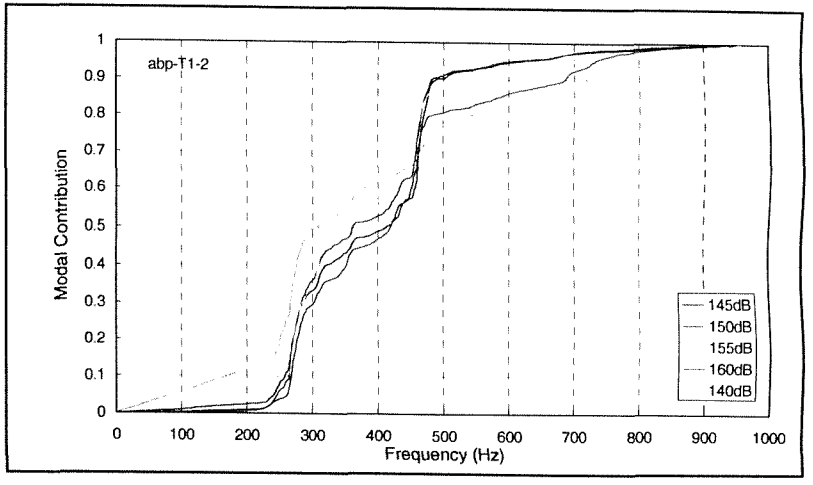

b). Normalised integral across strain spectral density

Figure 5.21 Al Alloy box - bottom excitation - Gauge T1-2

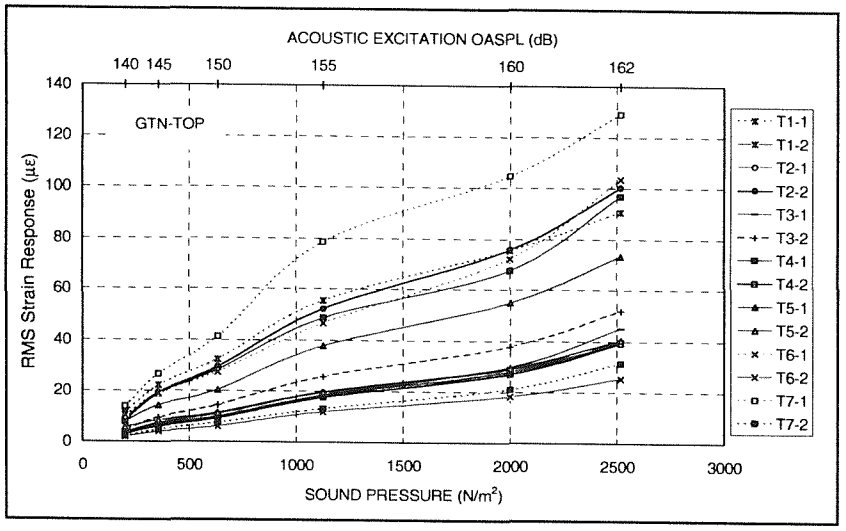

Figure 5.22 RMS strain response of the top skin panel of GLARE structure excited on top skin

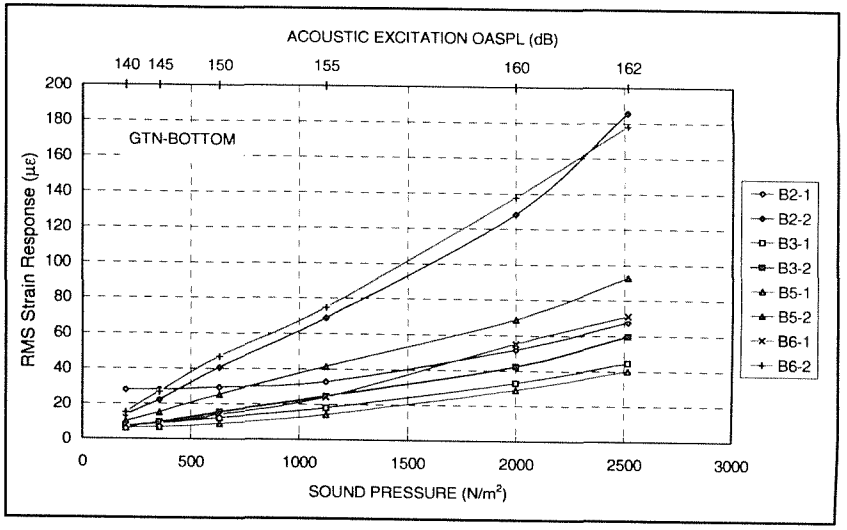

Figure 5.23 RMS strain response of the bottom skin panel of GLARE structure excited on top skin

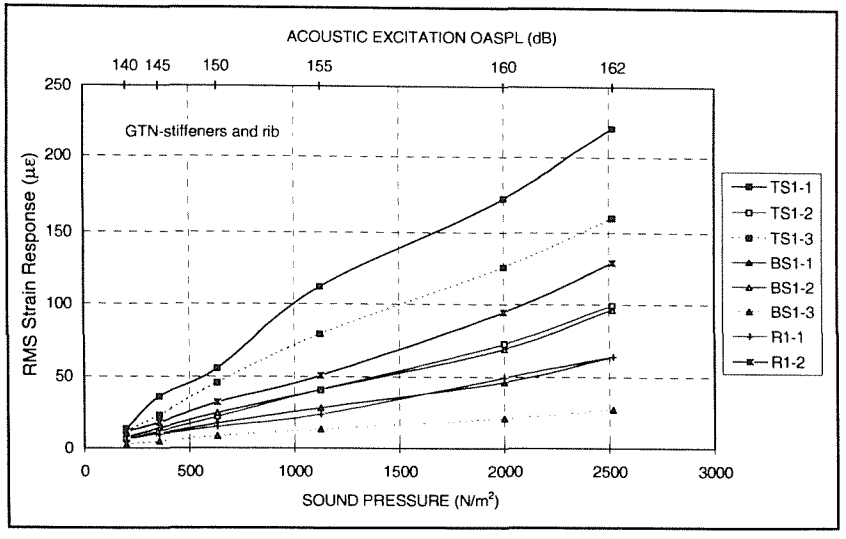

Figure 5.24 RMS strain response of the stiffeners and inner rib of GLARE structure excited on top skin

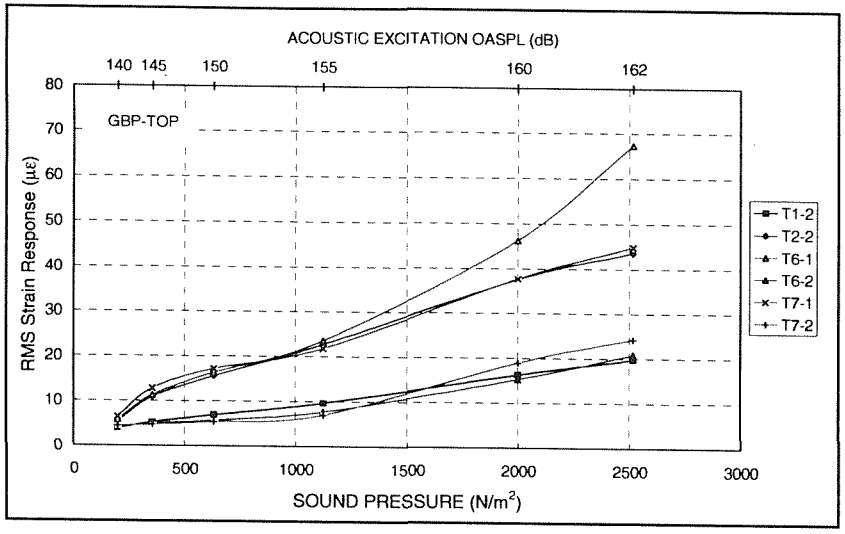

Figure 5.25 RMS strain response of the top skin panel of GLARE structure excited on bottom skin

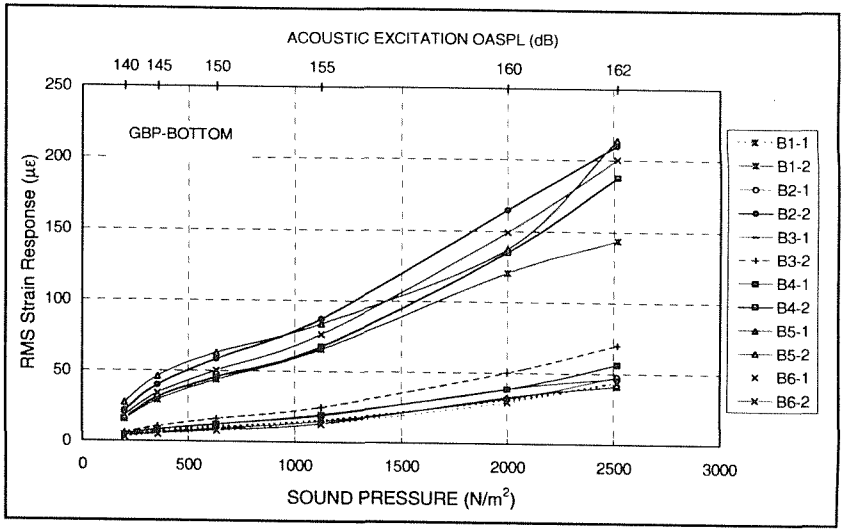

Figure 5.26 RMS strain response of the bottom skin panel of GLARE structure excited on bottom skin

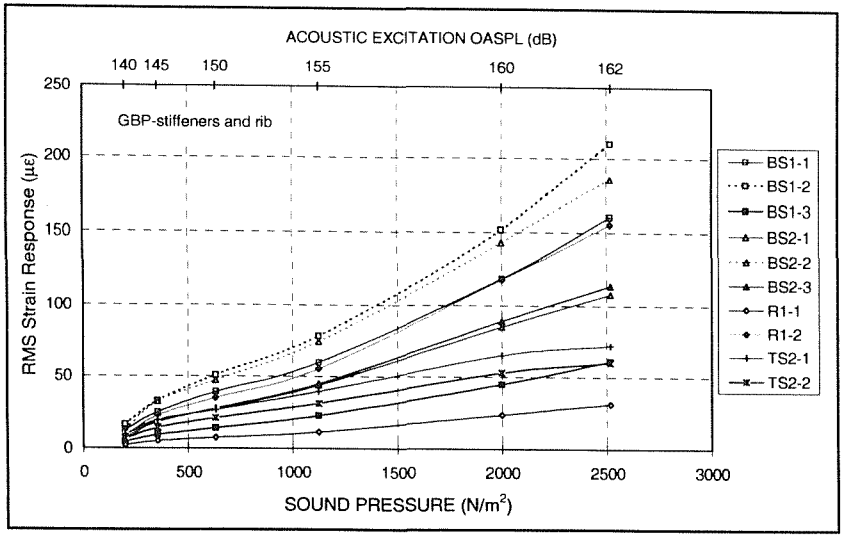

Figure 5.27 RMS strain response of the stiffeners and inner rib of GLARE structure excited on bottom

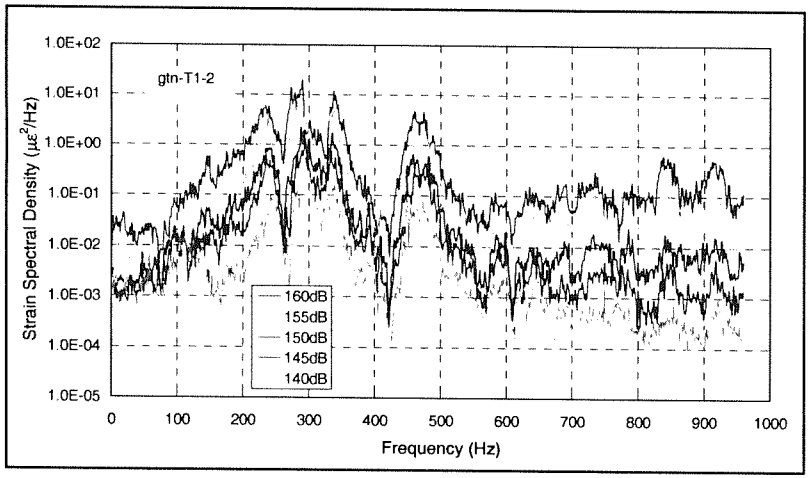

a). Strain spectral density

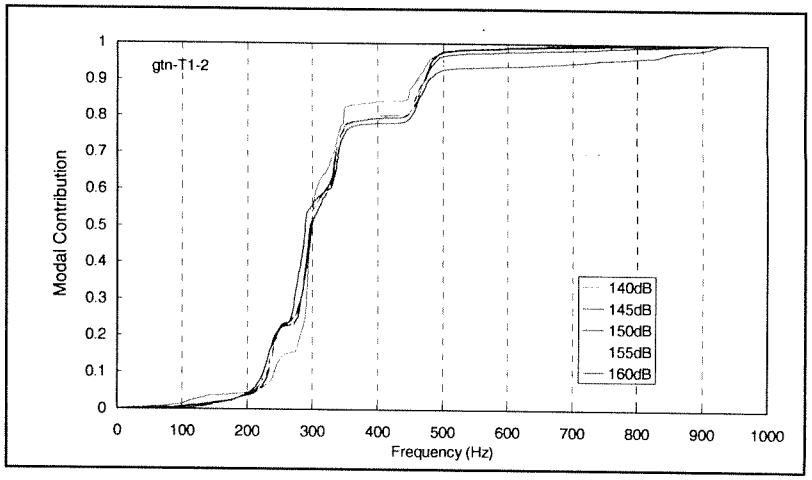

b). Normalised integral across strain spectral density

Figure 5.28 GLARE box - top excitation - Gauge T1-2

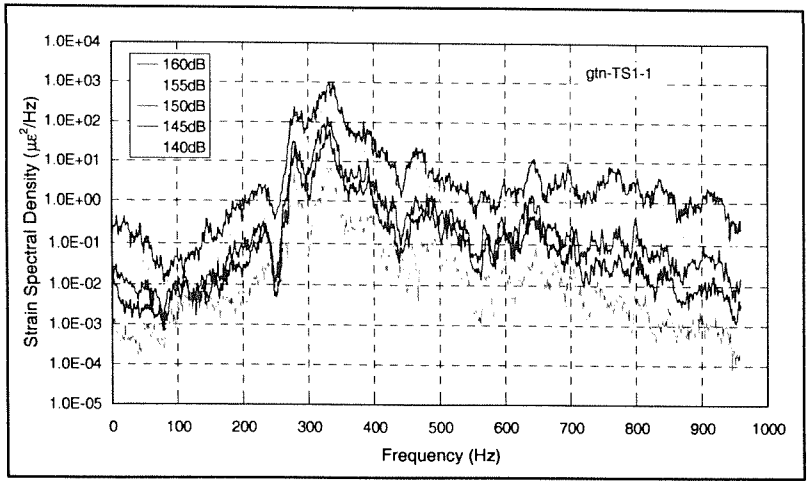

a). Strain spectral density

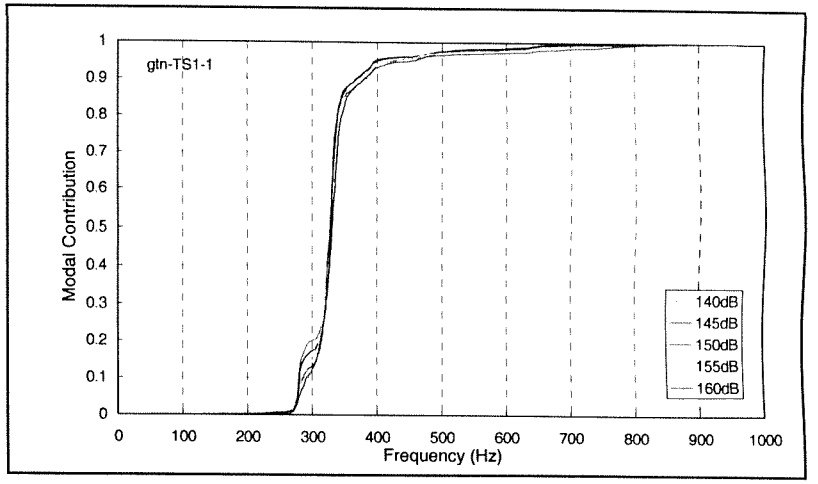

b). Normalised integral across strain spectral density

Figure 5.29 GLARE box - top excitation - Gauge TS1-1

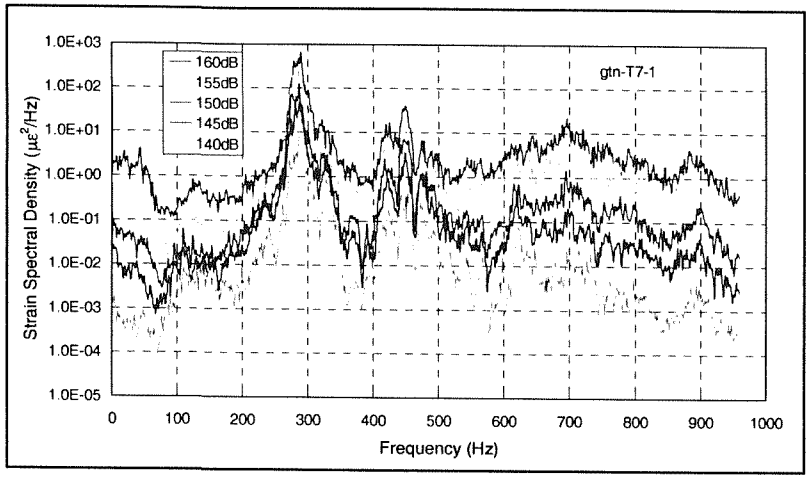

a). **Strain spectral density**

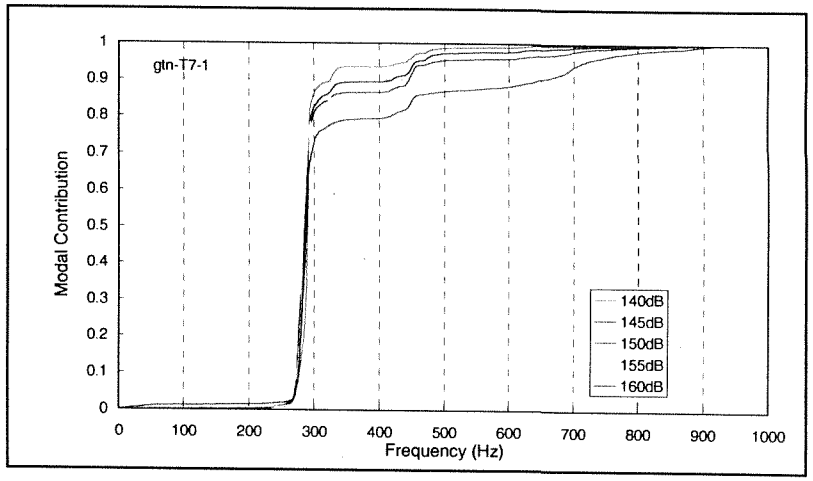

b). **Normalised integral across strain spectral density**

Figure 5.30 GLARE box - top excitation - Gauge T7-1

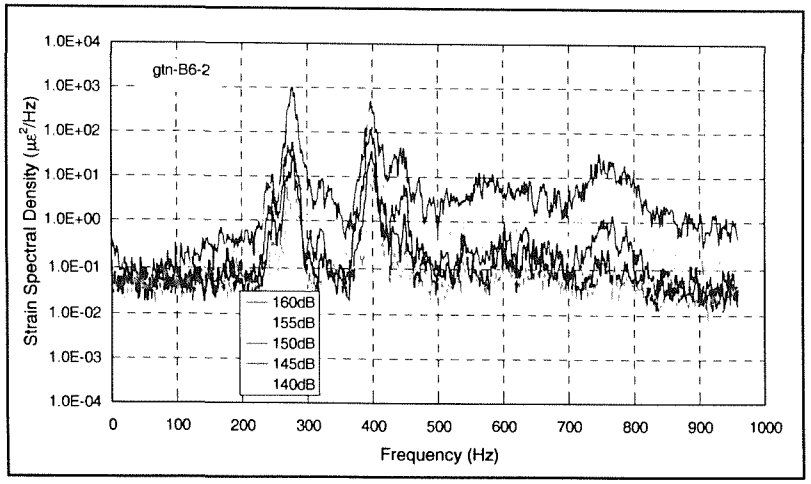

a). Strain spectral density

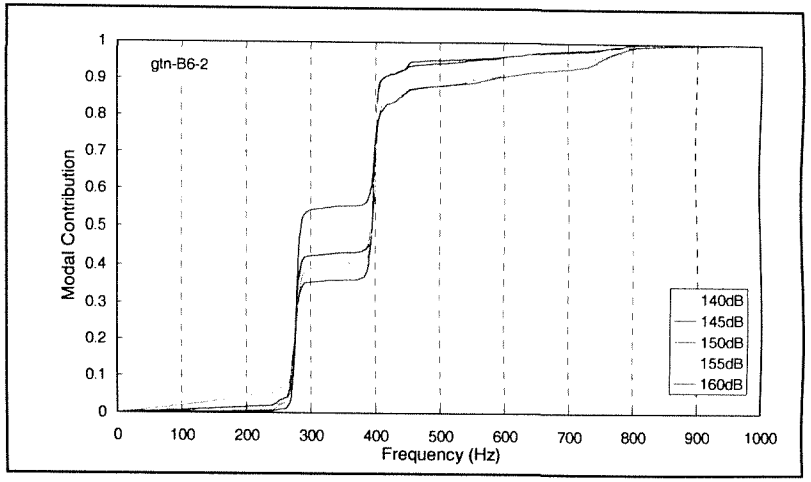

b). Normalised integral across strain spectral density

Figure 5.31 GLARE box - top excitation - Gauge B6-2

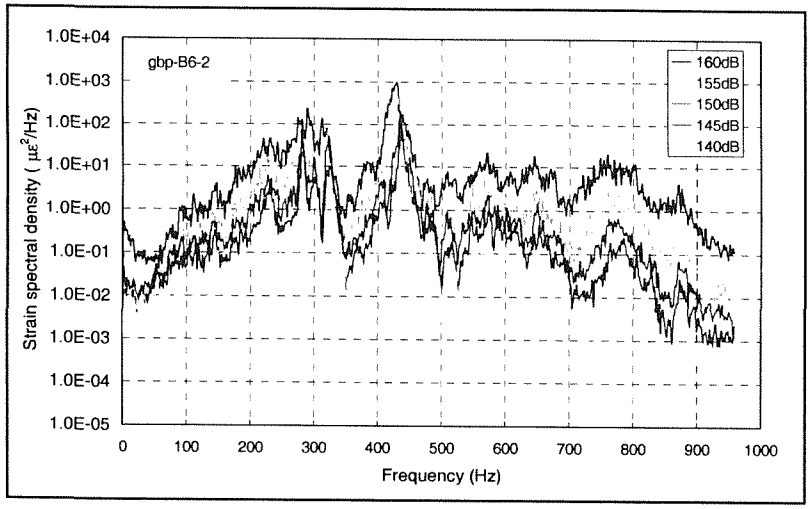

a). **Strain spectral density**

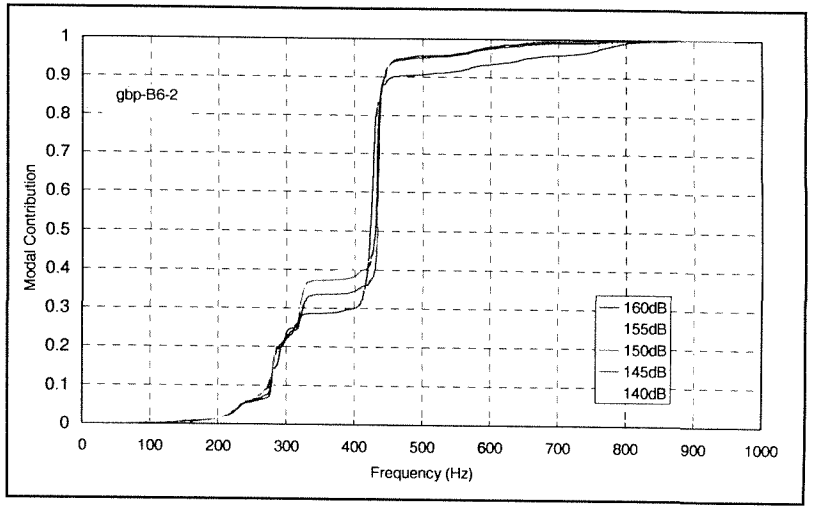

b). **Normalised integral across strain spectral density**

Figure 5.32 GLARE box - bottom excitation - Gauge B6-2

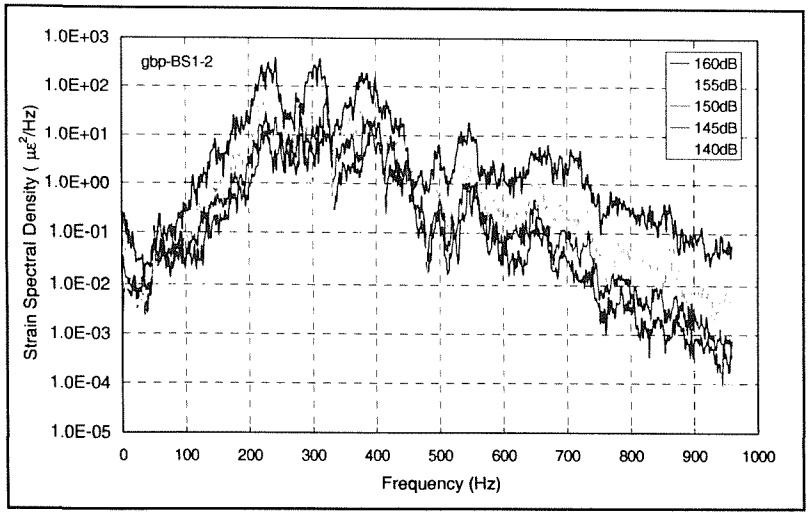

a). Strain spectral density

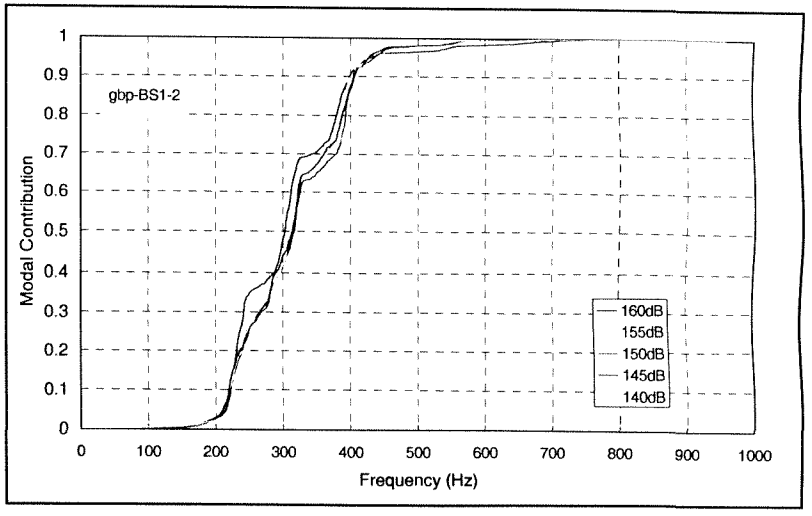

b). Normalised integral across strain spectral density

Figure 5.33 GLARE box - bottom excitation - Gauge BS1-2

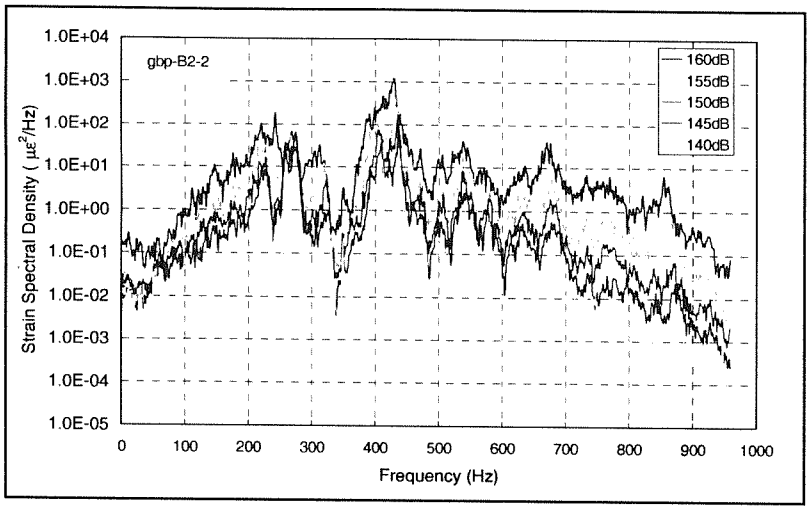

a). Strain spectral density

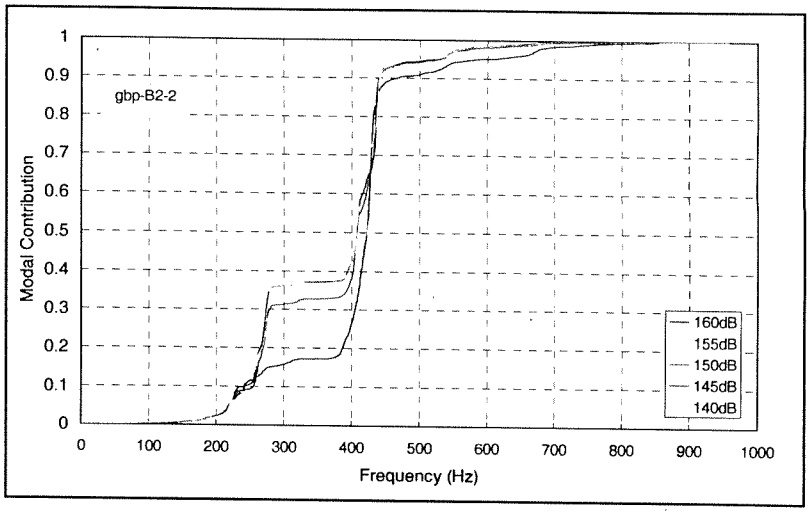

b). Normalised integral across strain spectral density

Figure 5.34 GLARE box - bottom excitation - Gauge B2-2

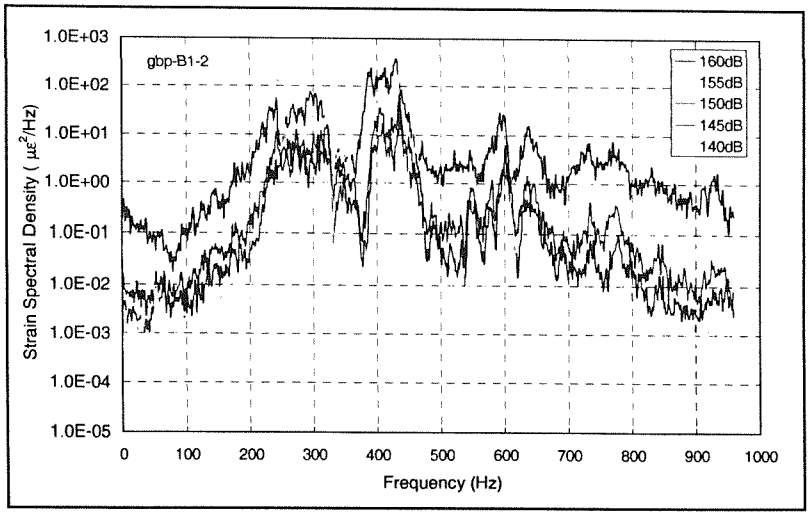

a). Strain spectral density

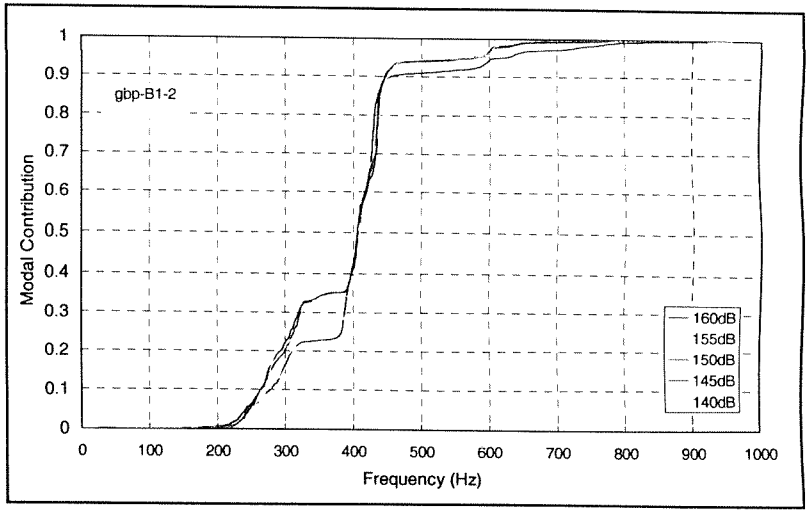

b). Normalised integral across strain spectral density

Figure 5.35 GLARE box - bottom excitation - Gauge B1-2

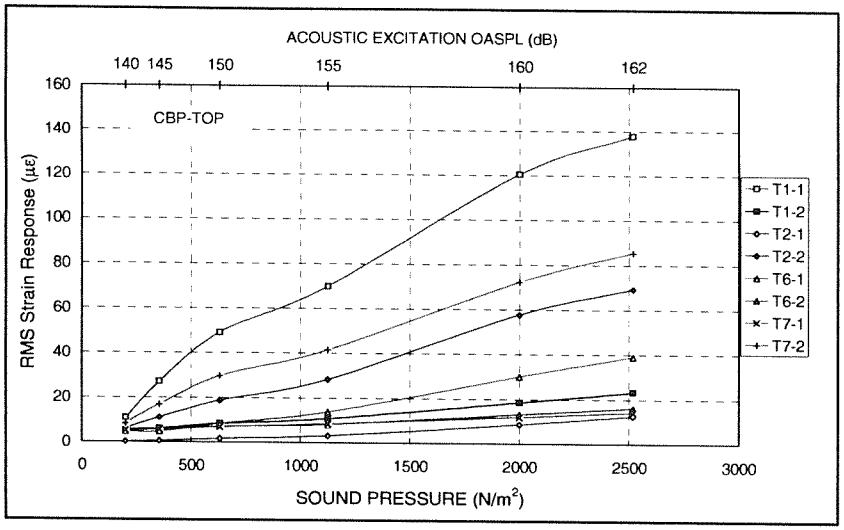

Figure 5.36 RMS strain response of the top skin panel of the CFRP structure excited on bottom skin (initial excitation)

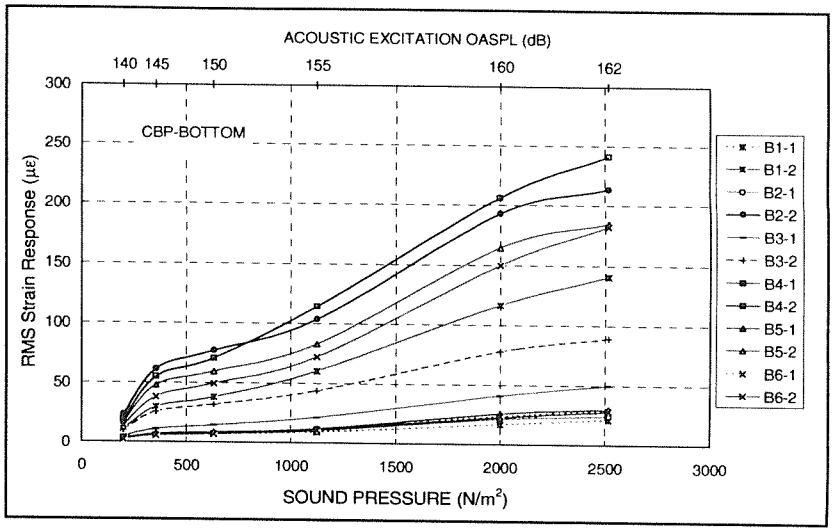

Figure 5.37 RMS strain response of the bottom skin panel of the CFRP structure excited on bottom skin (initial excitation)

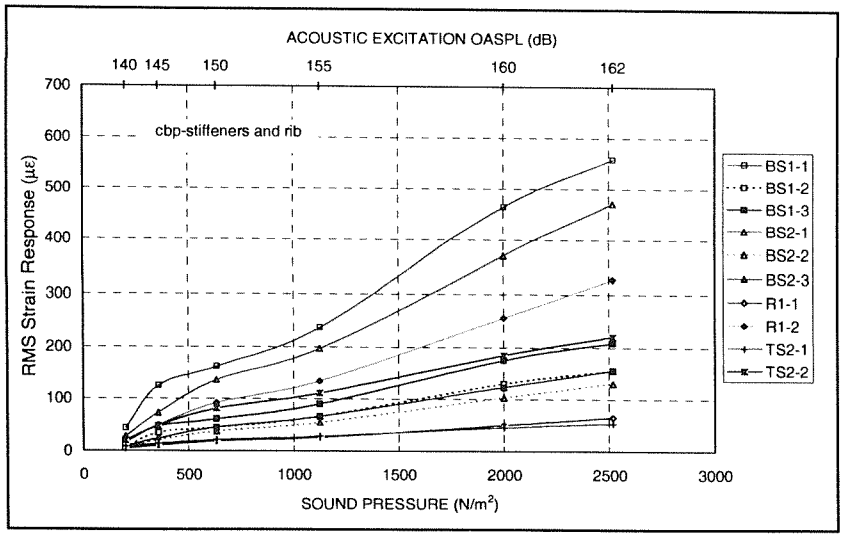

Figure 5.38 RMS strain response of the stiffeners and inner rib of CFRP structure excited on bottom skin (initial excitation)

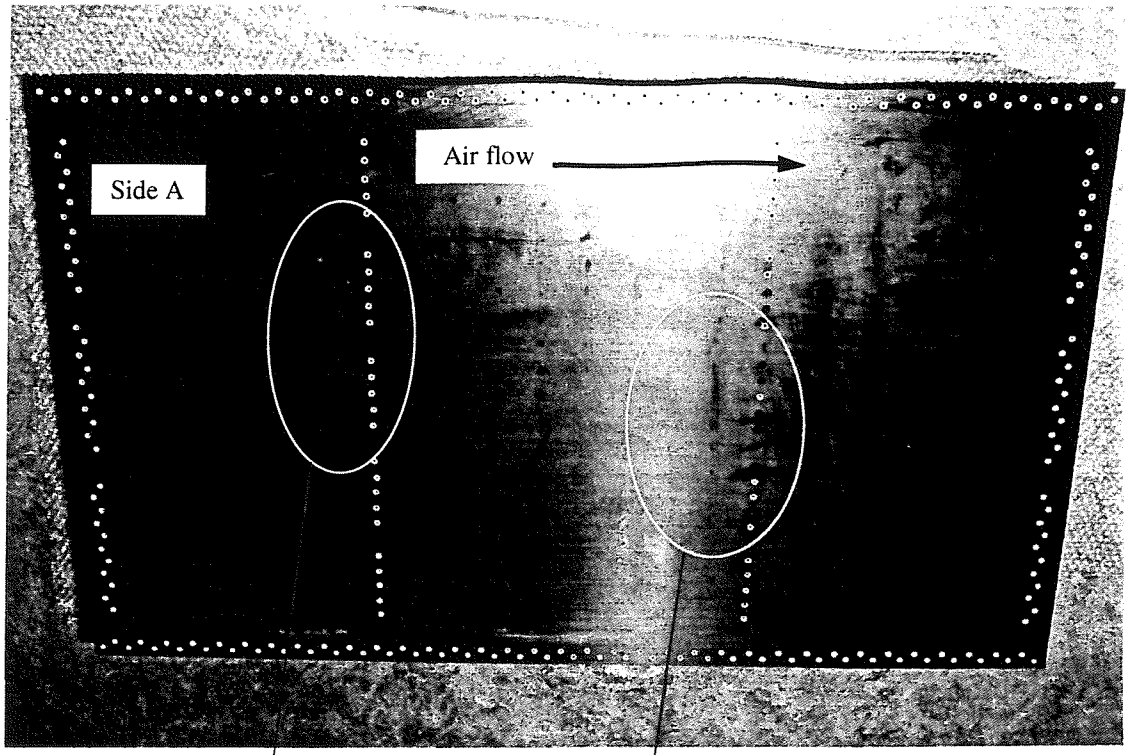

a) CFRP bottom skin panel

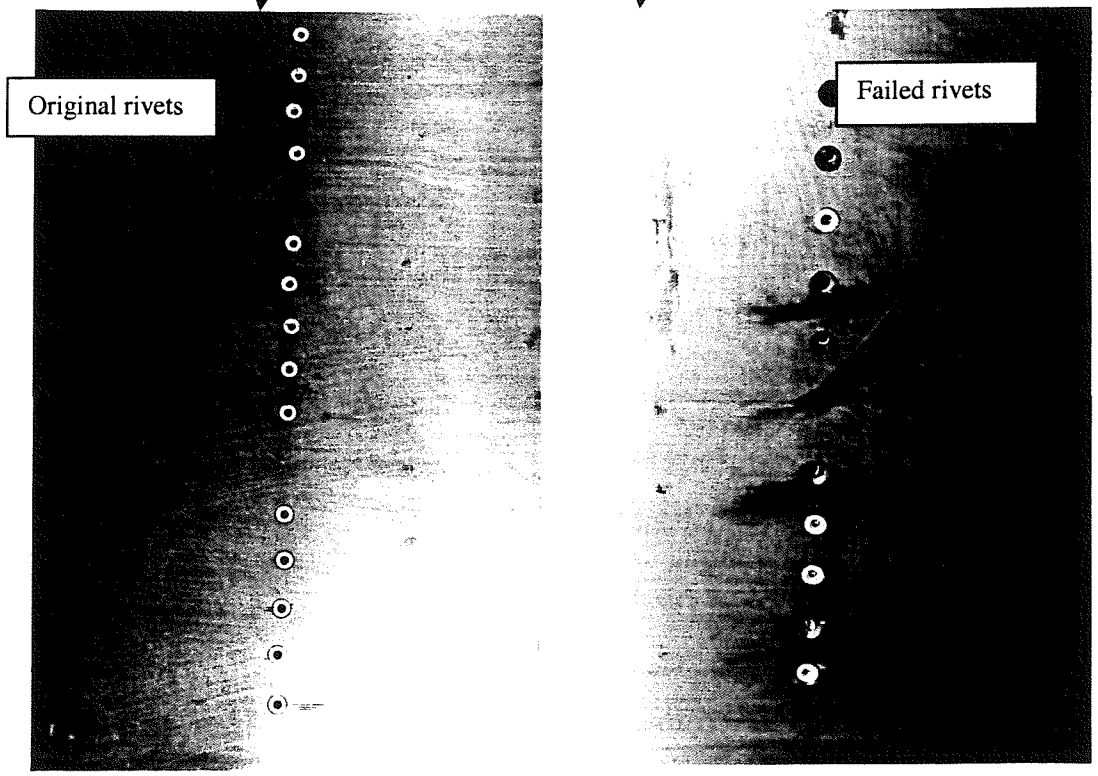

b) original rivets c) snapped rivets

Figure 5.39 Failure at rivets connecting bottom skin panel and inner rib

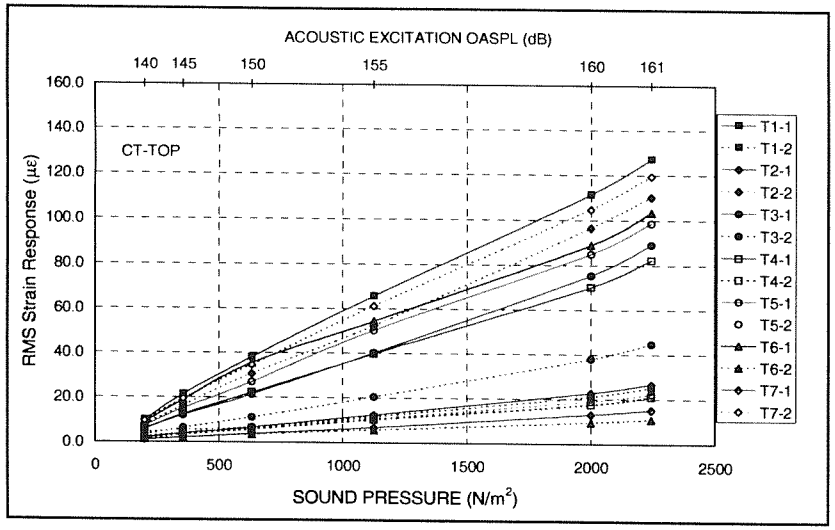

Figure 5.40 RMS strain response of the top skin panel of the CFRP structure excited on top skin (after repair)

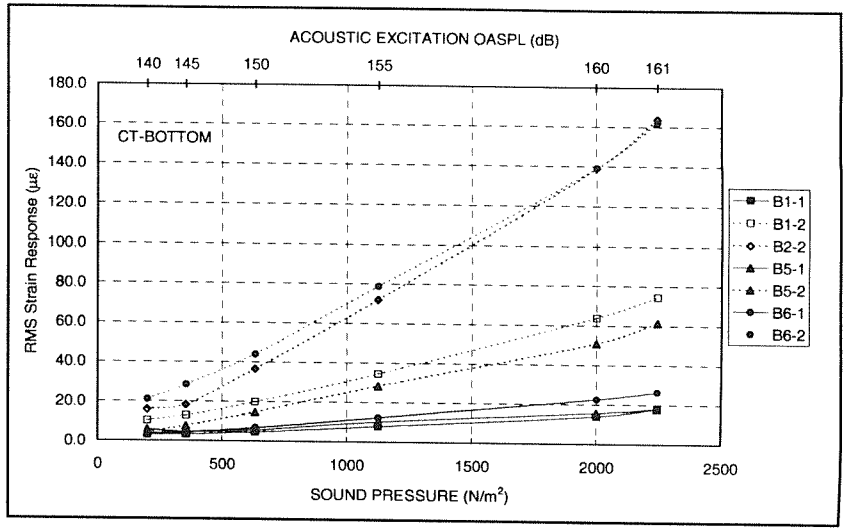

Figure 5.41 RMS strain response of the bottom skin panel of the CFRP structure excited on top skin (after repair)

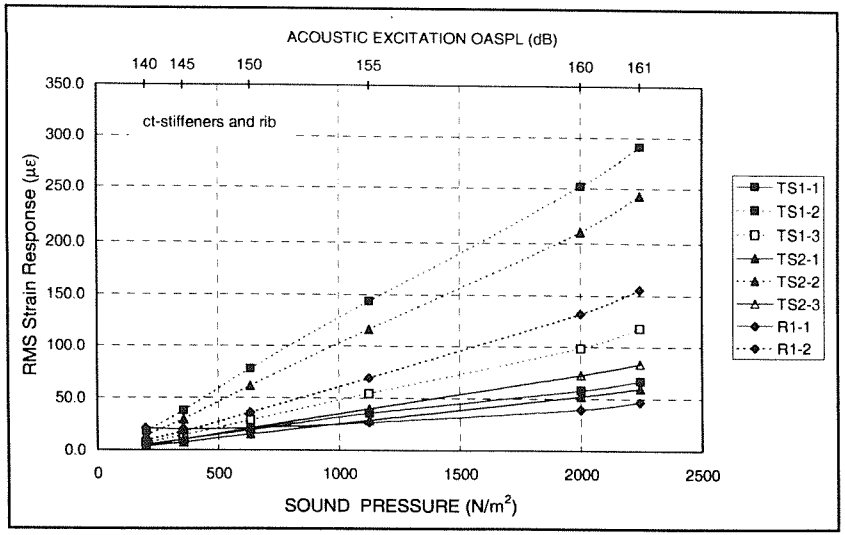

Figure 5.42 RMS strain response of the stiffeners and inner rib of the CFRP structure excited on top skin (after repair)

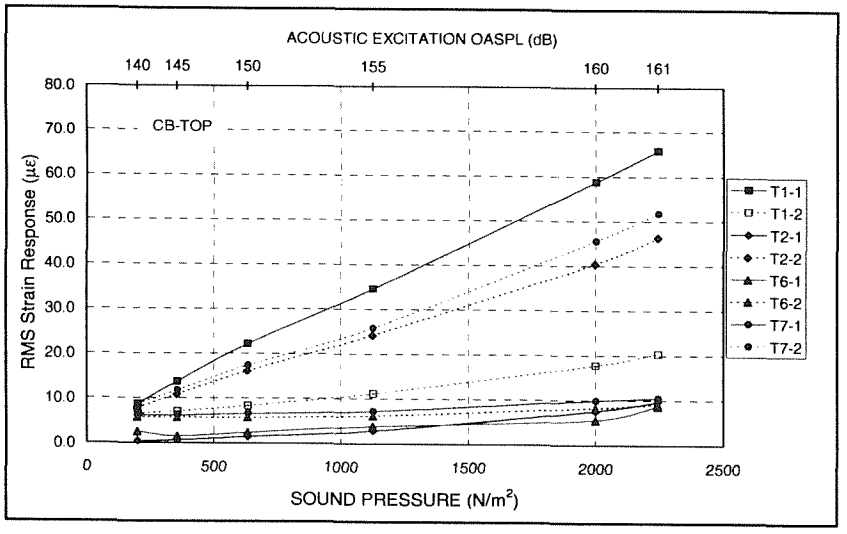

Figure 5.43 RMS strain response of the top skin panel of the CFRP structure excited on bottom skin (after repair)

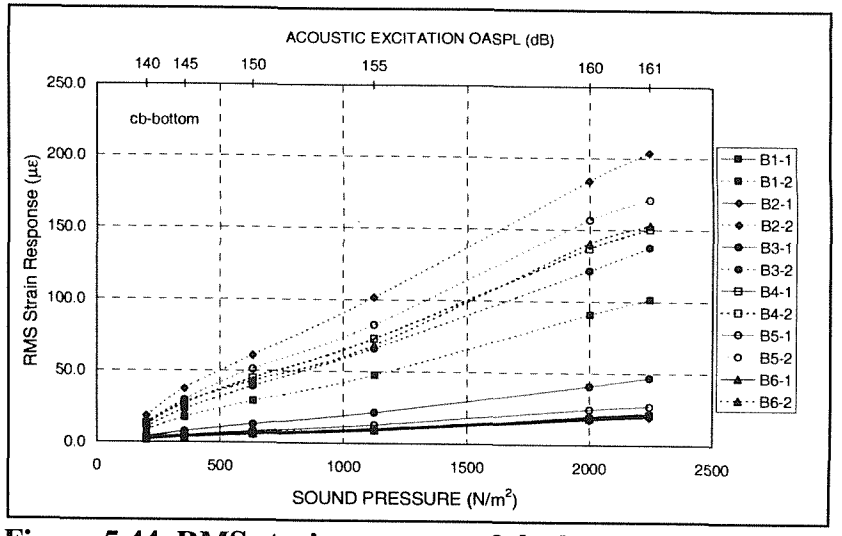

Figure 5.44 RMS strain response of the bottom skin panel of the CFRP structure excited on bottom skin (after repair)

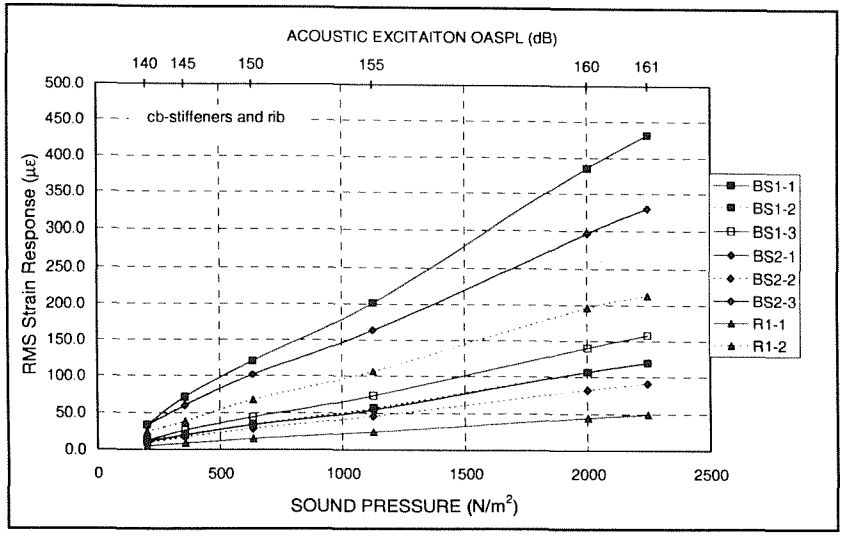

Figure 5.45 RMS strain response of the stiffeners and inner rib of CFRP structure excited on bottom skin (after repair)

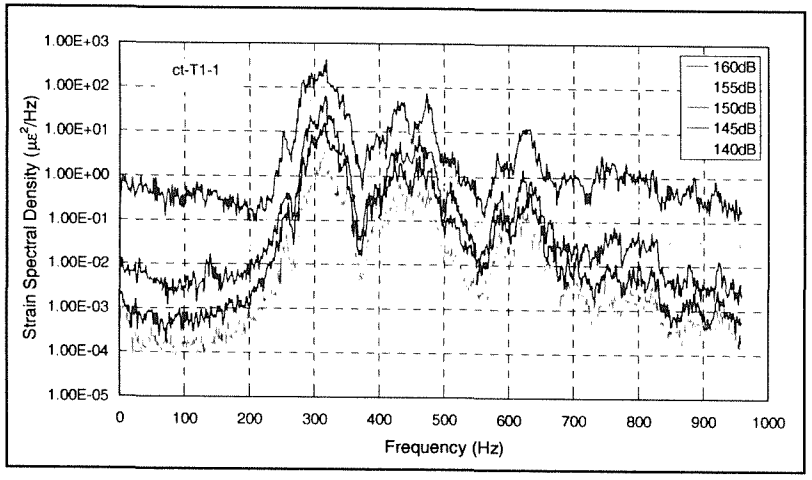

a) Strain spectral density

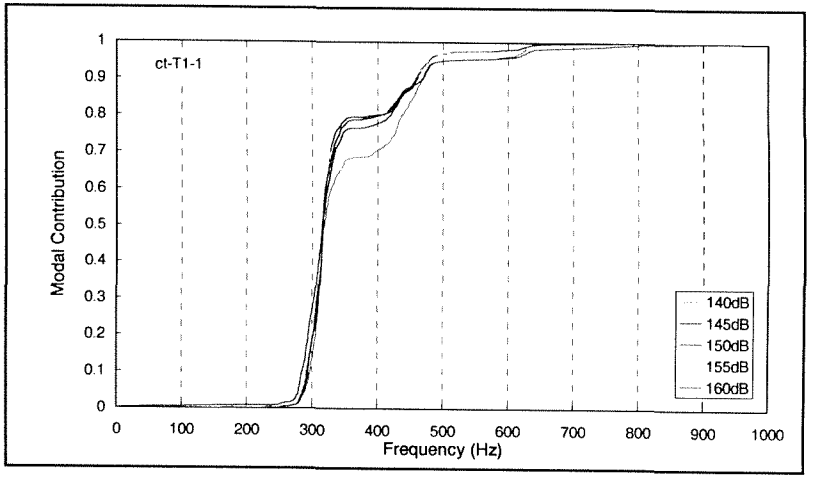

b) Normalised integral across the strain spectral density

Figure 5.46 CFRP box - top excitation - gauge T1-1

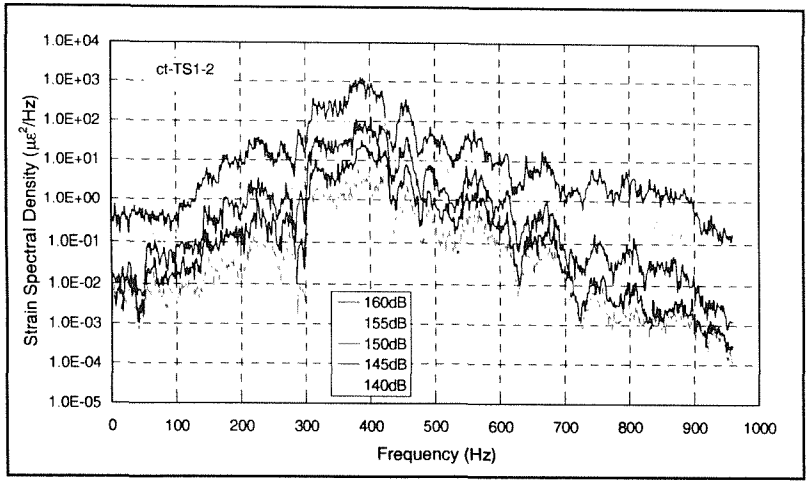

a) Strain spectral density

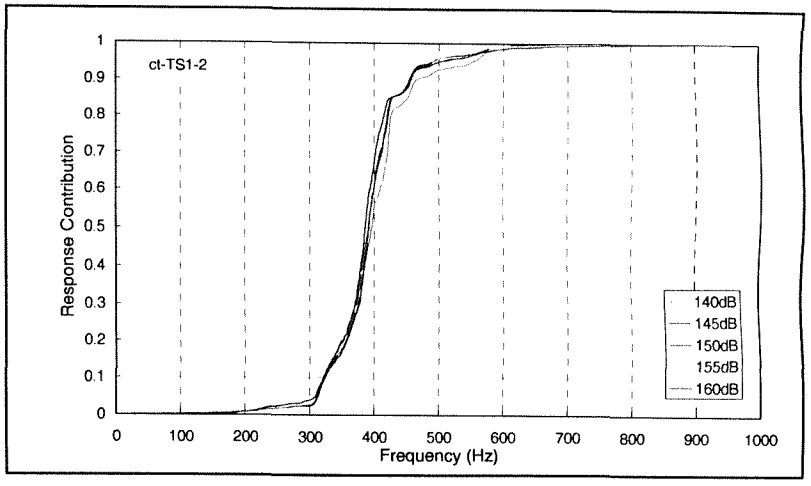

b) Normalised integral across the strain spectral density

Figure 5.47 CFRP box - top excitation - gauge TS1-2

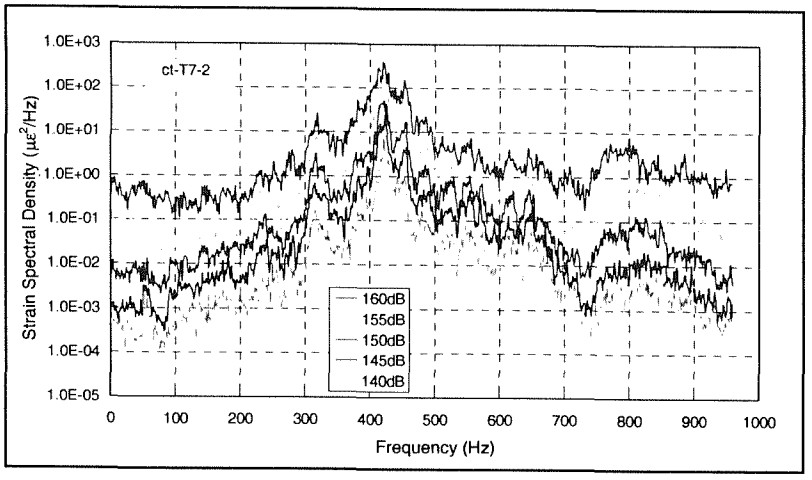

a) Strain spectral density

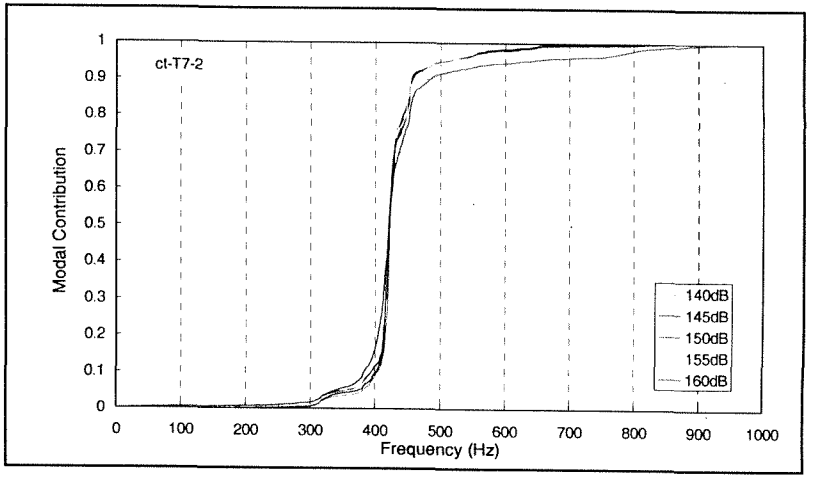

b) Normalised integral across the strain spectral density

Figure 5.48 CFRP box - top excitation - gauge T7-2

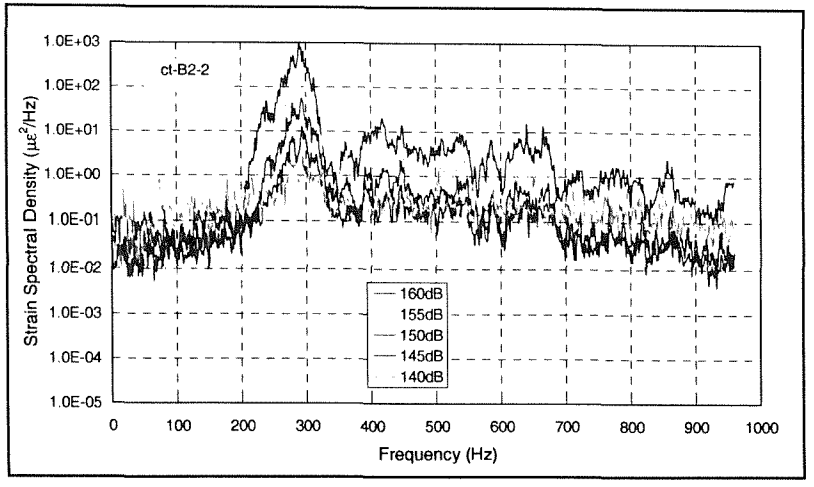

a) Strain spectral density

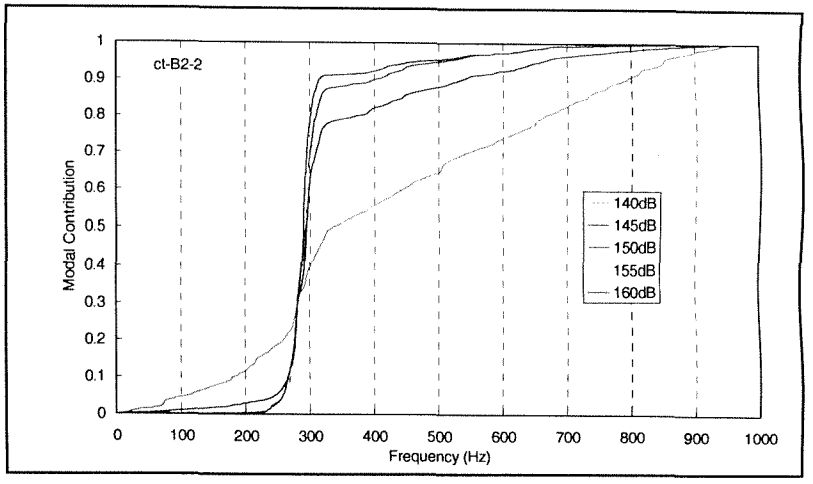

b) Normalised integral across the strain spectral density

Figure 5.49 CFRP box - top excitation - gauge B2-2

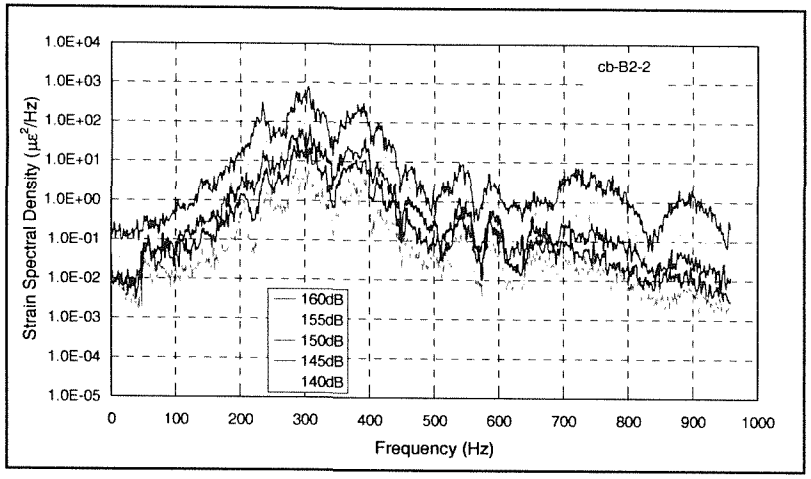

a) Strain spectral density

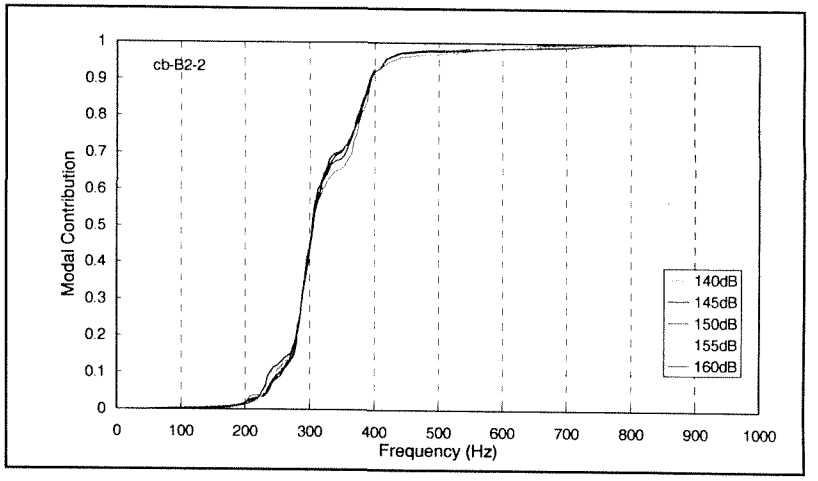

b) Normalised integral across the strain spectral density

Figure 5.50 CFRP box - bottom excitation - gauge B2-2

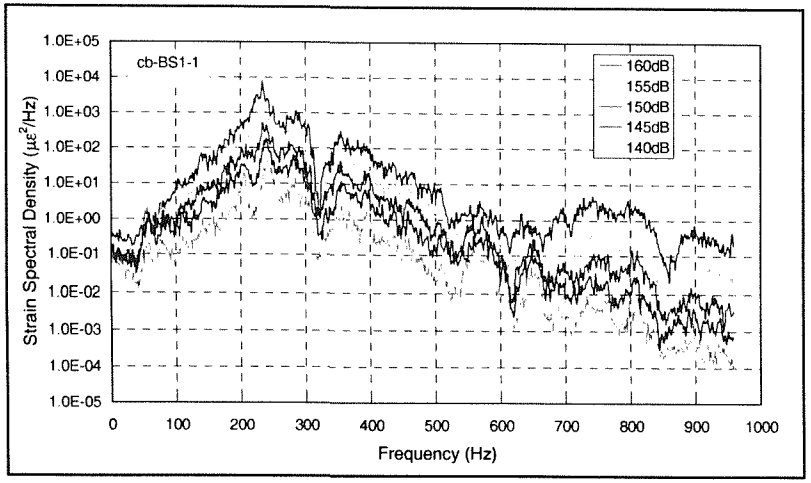

a) Strain spectral density

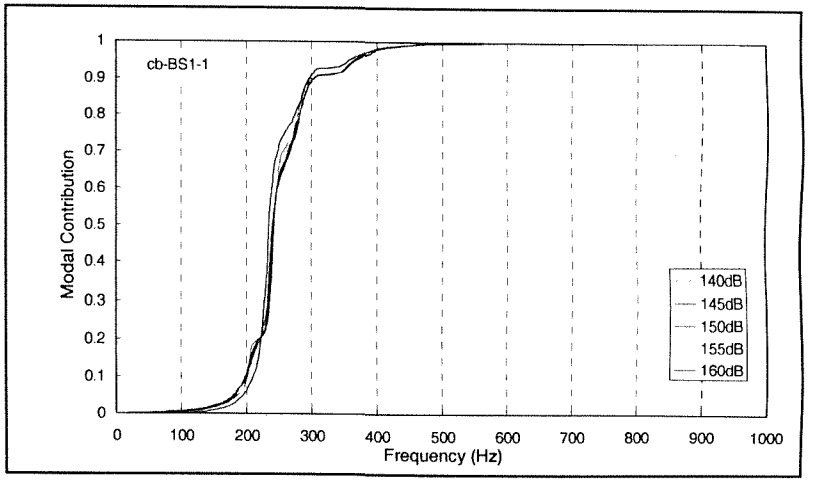

b) Normalised integral across the strain spectral density

Figure 5.51 CFRP box - bottom excitation - gauge BS1-1

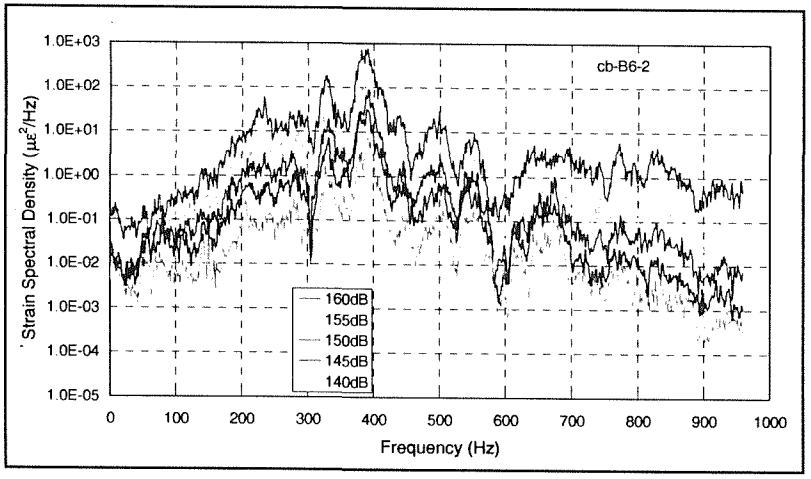

a) Strain spectral density

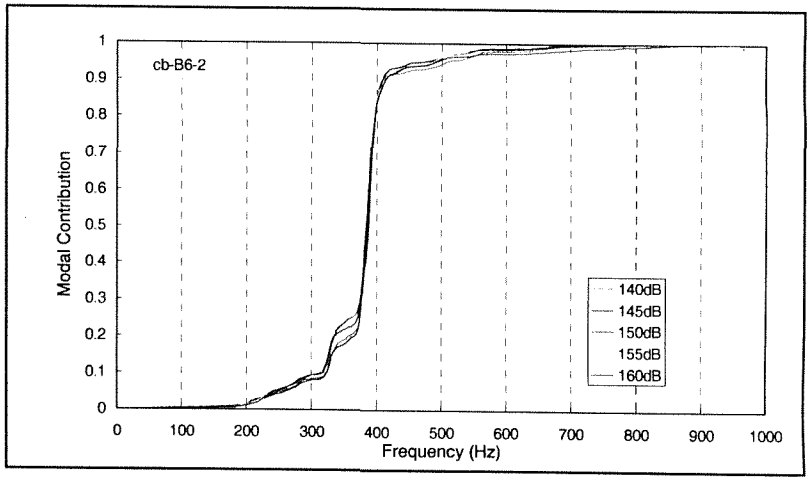

b) Normalised integral across the strain spectral density

Figure 5.52 CFRP box - bottom excitation - gauge B6-2

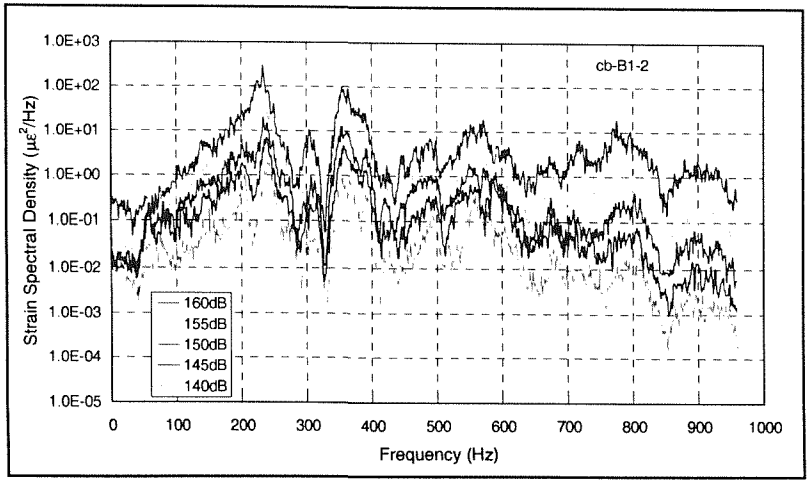

a) Strain spectral density

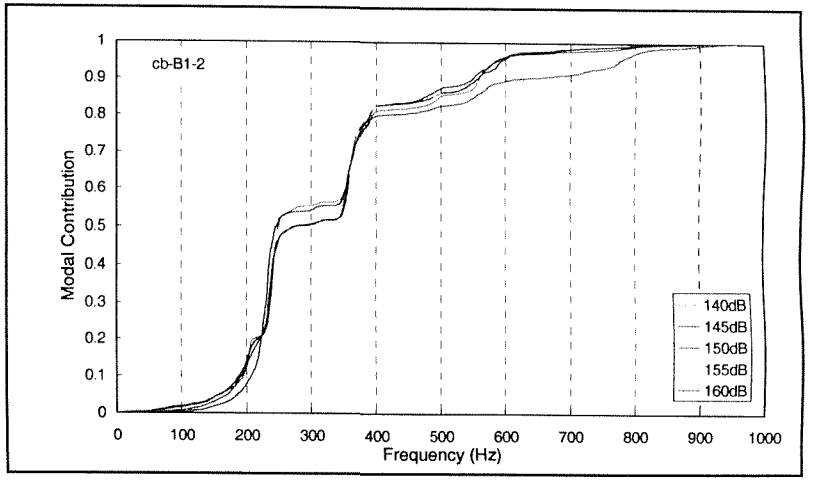

b) Normalised integral across the strain spectral density

Figure 5.53 CFRP box - bottom excitation - gauge B1-2

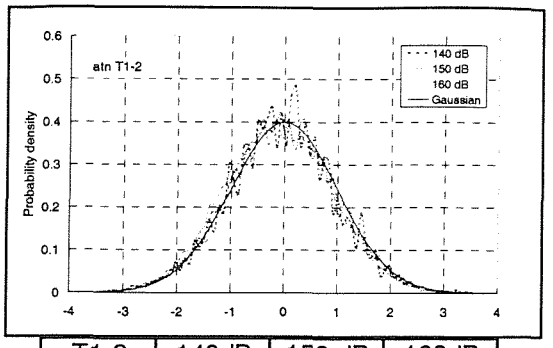

T1-2	140dB	150 dB	160dB
γ	3.3	3.0	2.9
λ	0.0	0.0	0.0

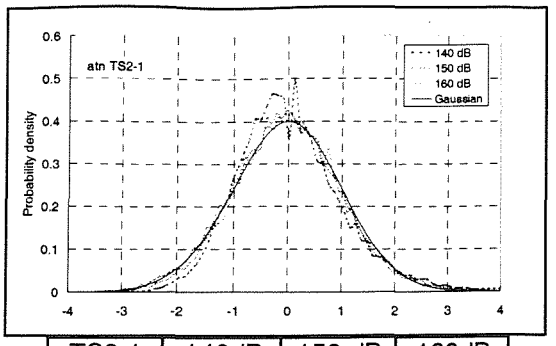

TS2-1	140dB	150 dB	160dB
γ	4.7	3.4	3.1
λ	0.8	0.2	0.1

a) Top excitation

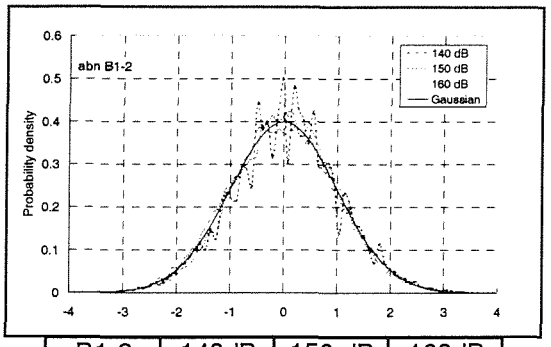

B1-2	140dB	150 dB	160dB
γ	3.3	3.4	2.9
λ	0.0	0.0	0.0

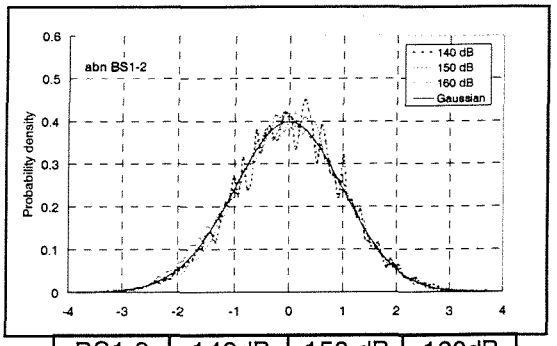

BS1-2	140dB	150 dB	160dB
γ	3.1	3.5	2.8
λ	0.0	0.0	0.0

b) Bottom excitation

γ - Kurtosis λ - Skewness

Figure 5.54 Probability density distribution of strain response - Aluminium box

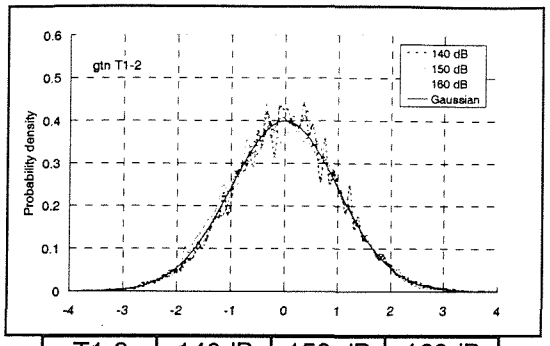

T1-2	140dB	150 dB	160dB
γ	3.2	3.2	2.7
λ	0.0	0.0	0.0

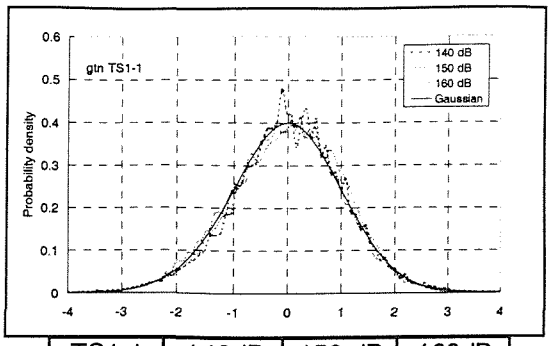

TS1-1	140dB	150 dB	160dB
γ	3.4	3.0	3.0
λ	-0.1	-0.2	-0.1

a) Top excitation

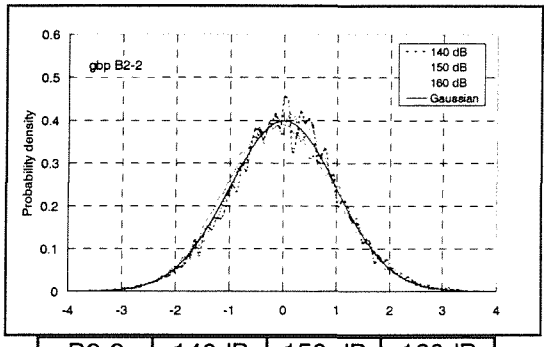

B2-2	140dB	150 dB	160dB
γ	3.2	3.0	2.9
λ	0.0	0.0	0.1

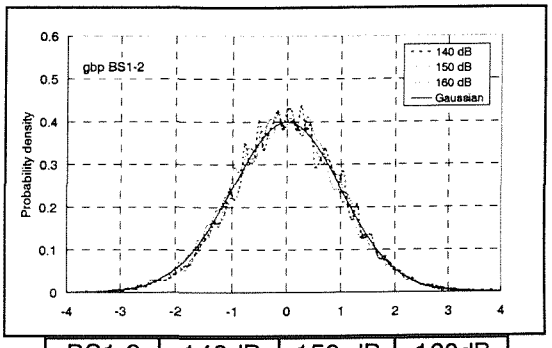

BS1-2	140dB	150 dB	160dB
γ	3.3	3.3	3.0
λ	0.0	0.0	0.0

b) Bottom excitation

γ - Kurtosis λ - Skewness

Figure 5.55 Probability density distribution of strain response - GLARE box

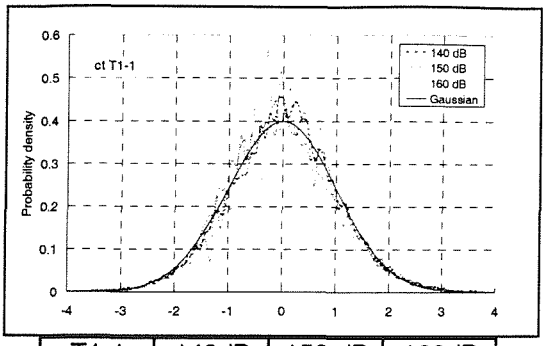

T1-1	140dB	150 dB	160dB
γ	3.4	3.6	3.3
λ	0.0	0.1	0.3

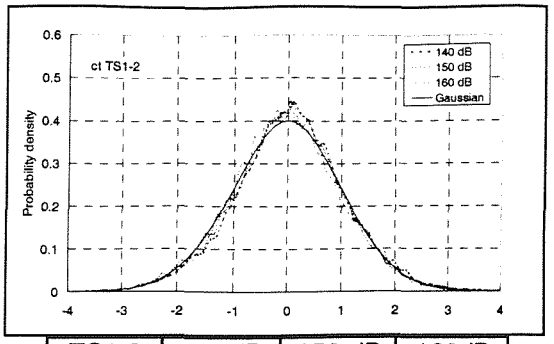

TS1-2	140dB	150 dB	160dB
γ	3.6	3.4	3.2
λ	0.0	0.0	0.0

a). Top excitation

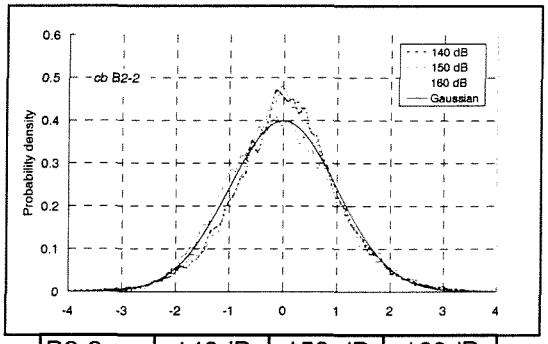

B2-2	140dB	150 dB	160dB
γ	4.1	3.8	2.9
λ	0.0	0.1	0.1

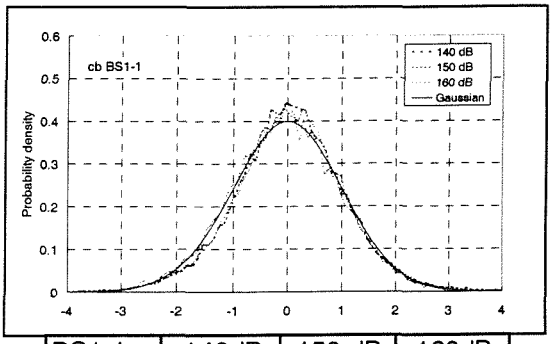

BS1-1	140dB	150 dB	160dB
γ	3.8	3.7	3.1
λ	0.0	0.0	0.0

b) Bottom excitation

γ - Kurtosis λ - Skewness

Figure 5.56 Probability density distribution of strain response- CFRP box

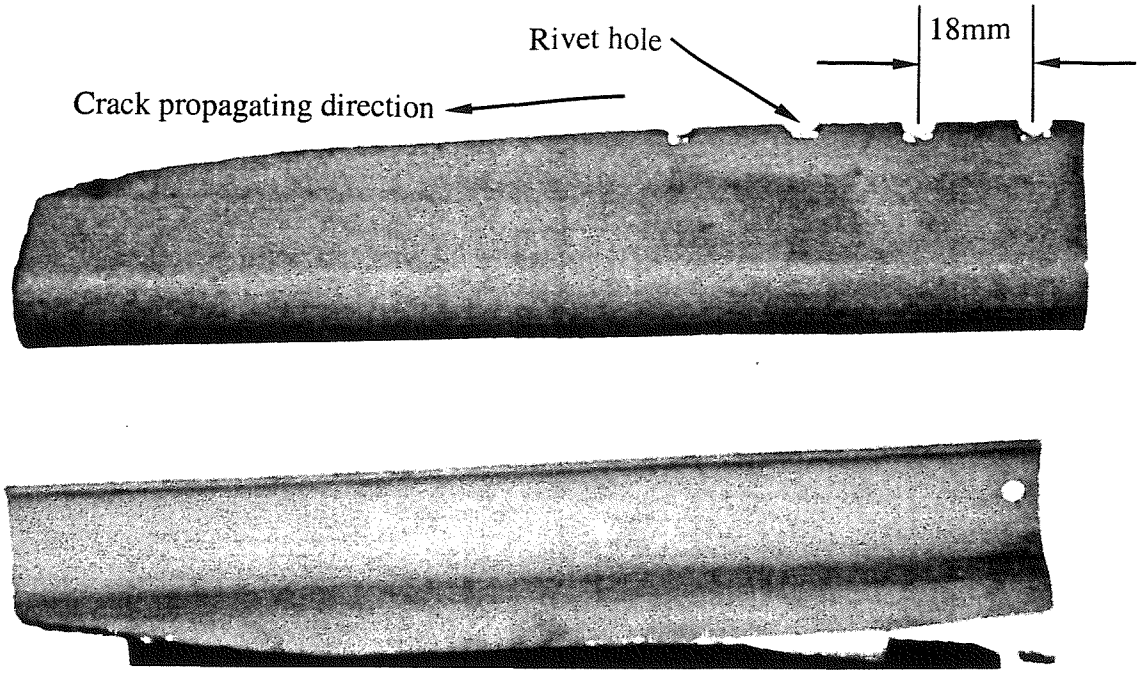

Figure 5.57 End part of stiffener No.3 on bay side B (bottom skin) broken off from the aluminium alloy structure after 50 minutes of acoustic endurance testing (For stringer detail see Appendix D.2)

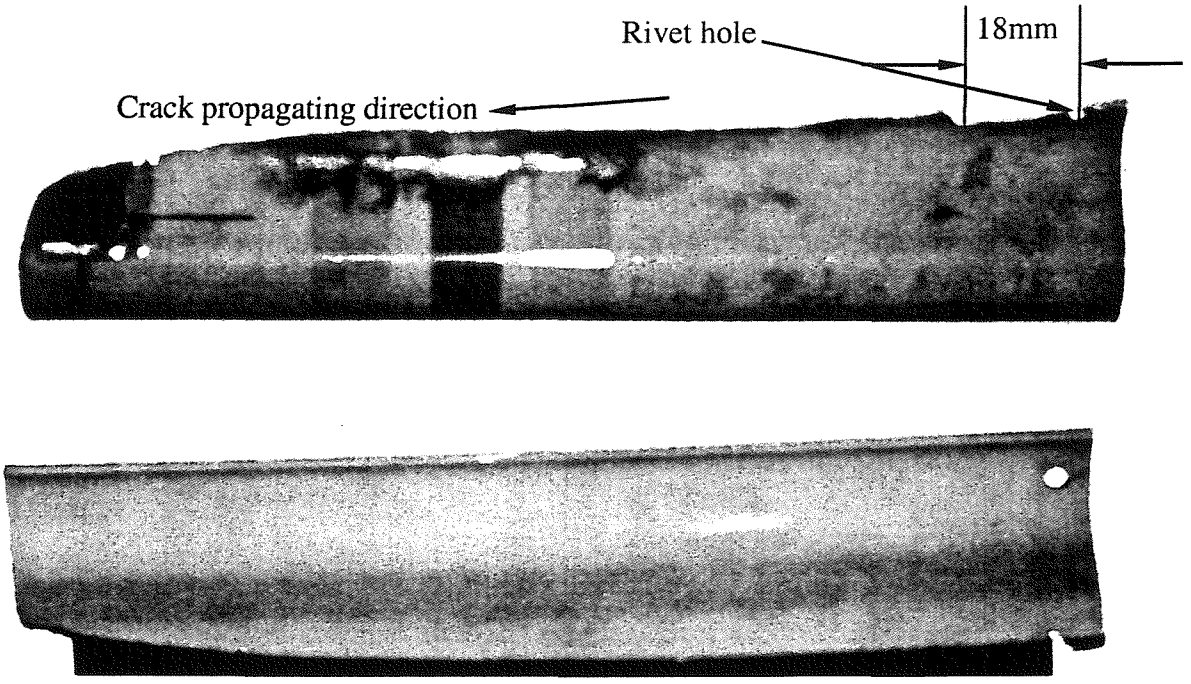

Figure 5.58 End part of stiffener No.3 on bay side A (bottom skin) detached from the aluminium alloy structure after 200 minutes of acoustic endurance testing (For stringer detail see Appendix D.2)

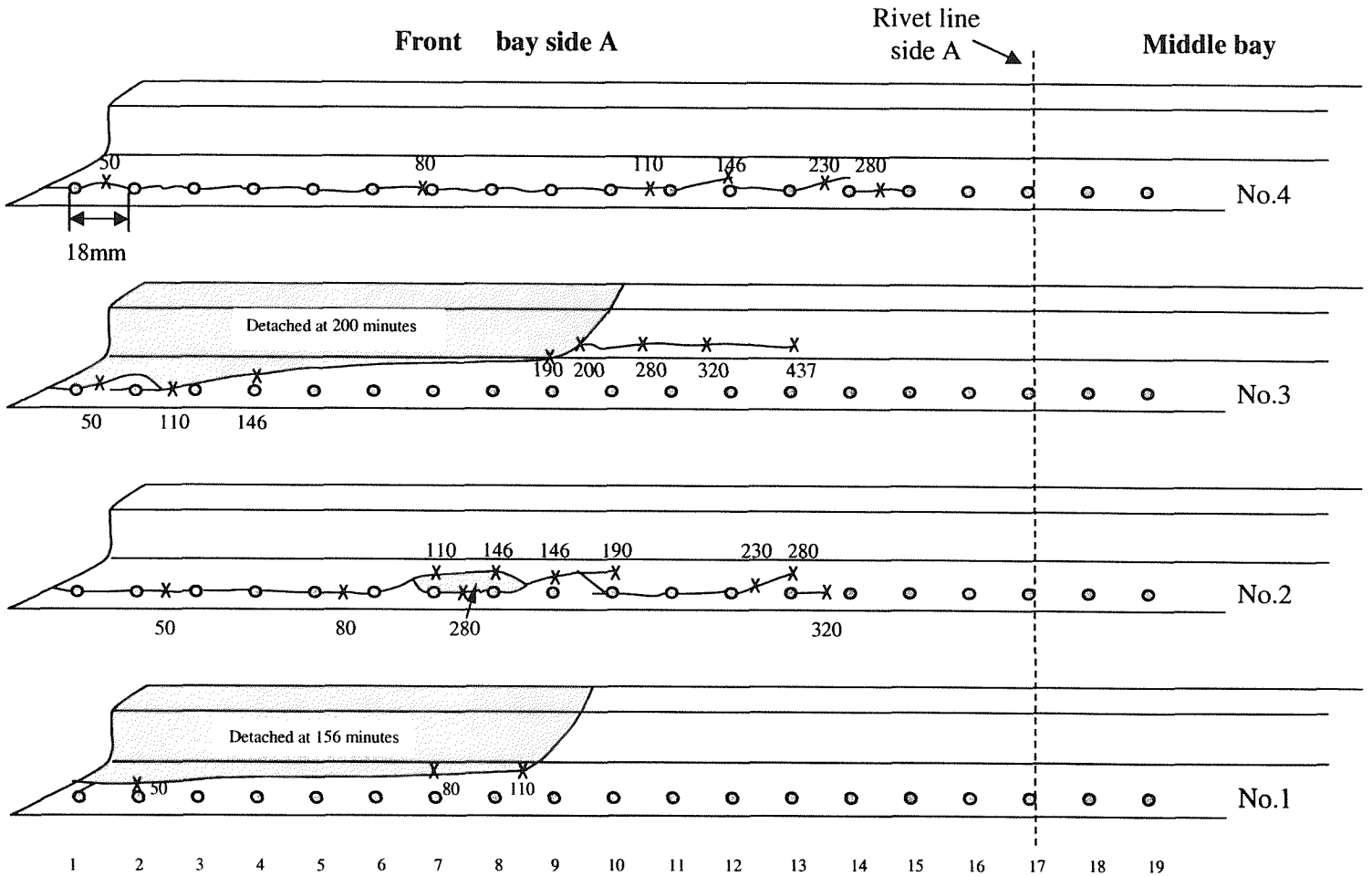

Figure 5.59 Fatigue crack propagation path of the stiffeners on the bottom skin of bay side A of the aluminium alloy structure during acoustic endurance testing

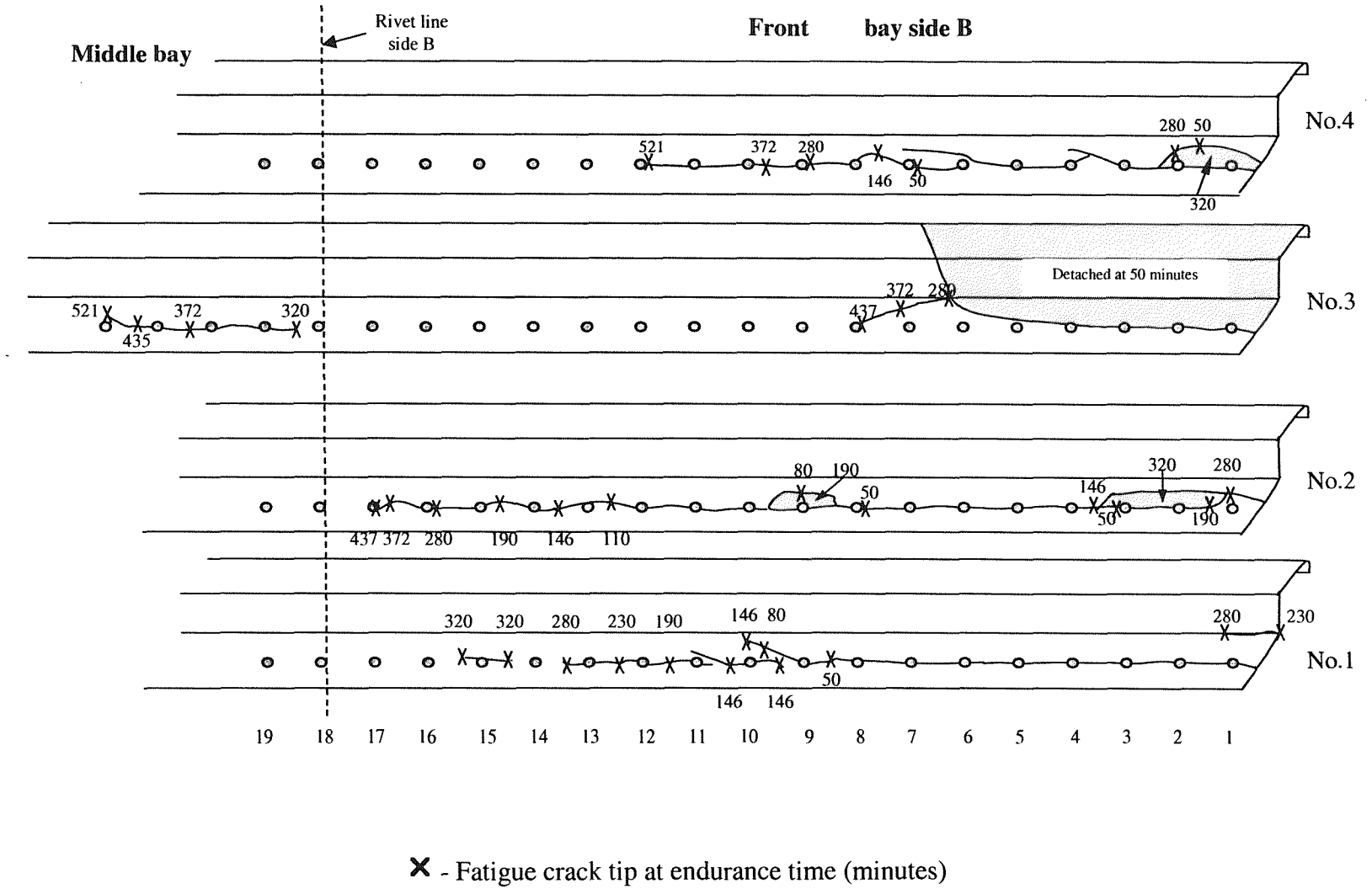

Figure 5.60 Fatigue crack propagation path of the stiffeners on the bottom skin of bay side B and middle bay of aluminium alloy structure during acoustic endurance testing

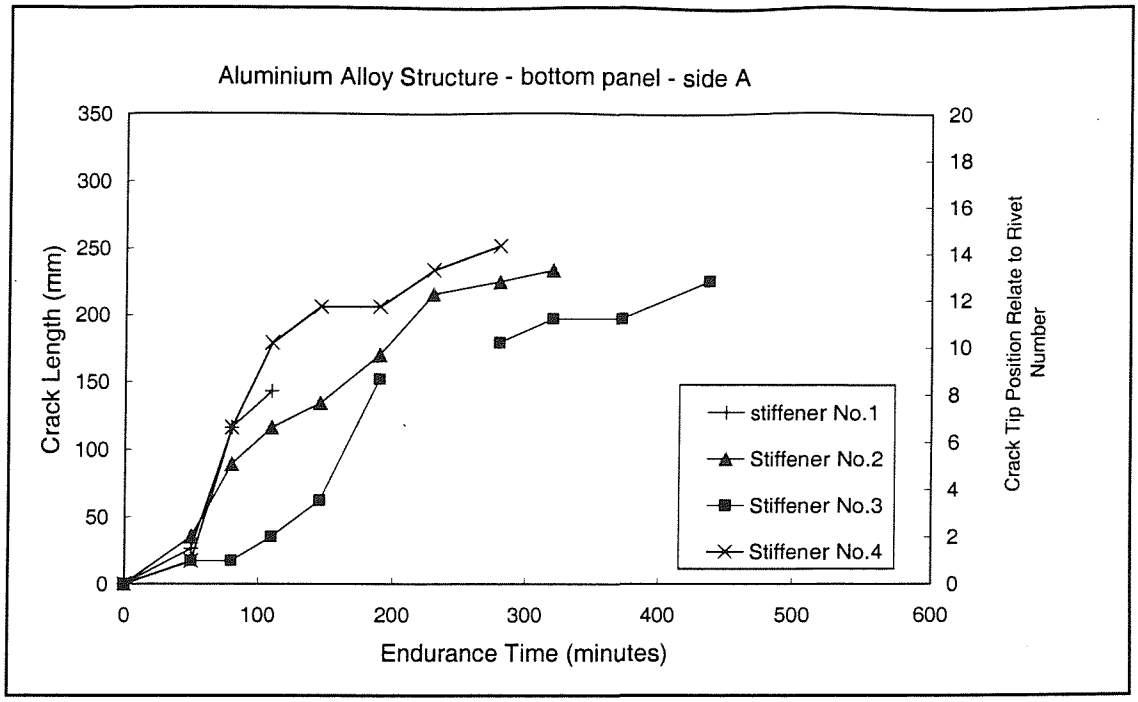

Stiffeners on the bottom skin of bay side A of the aluminium alloy structure

Figure 5.61 Fatigue crack length versus time of endurance testing

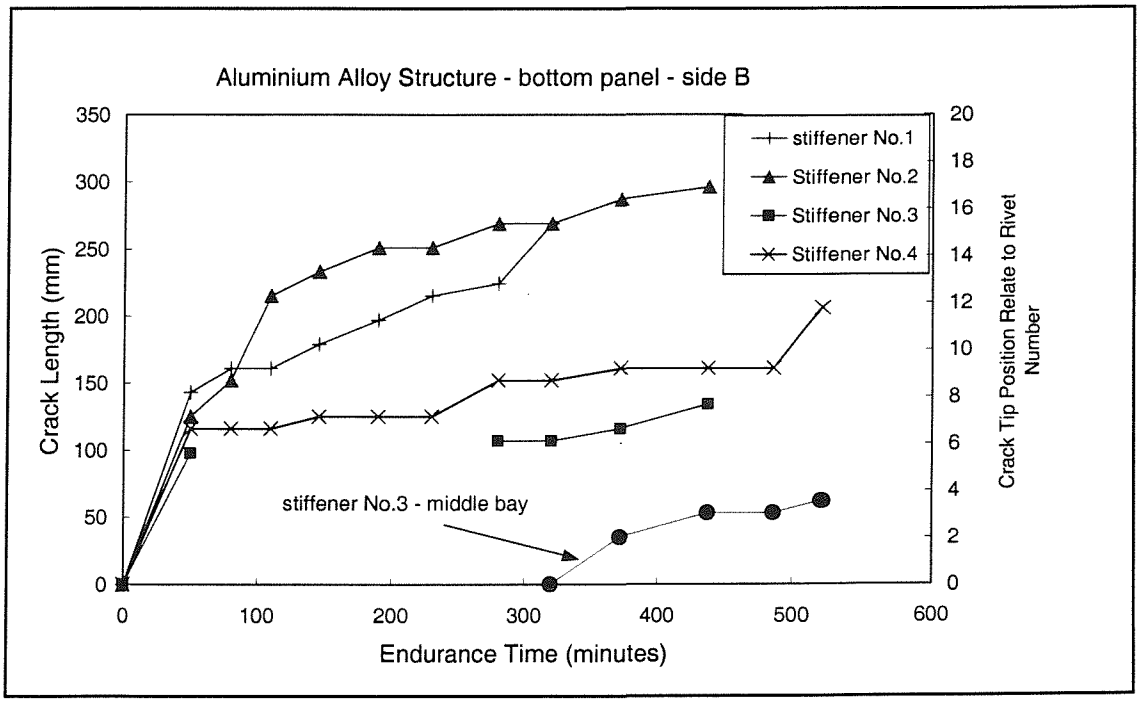

Stiffeners on the bottom skin of middle bay and bay side B of the aluminium alloy structure

Figure 5.62 Fatigue crack length versus time of endurance testing

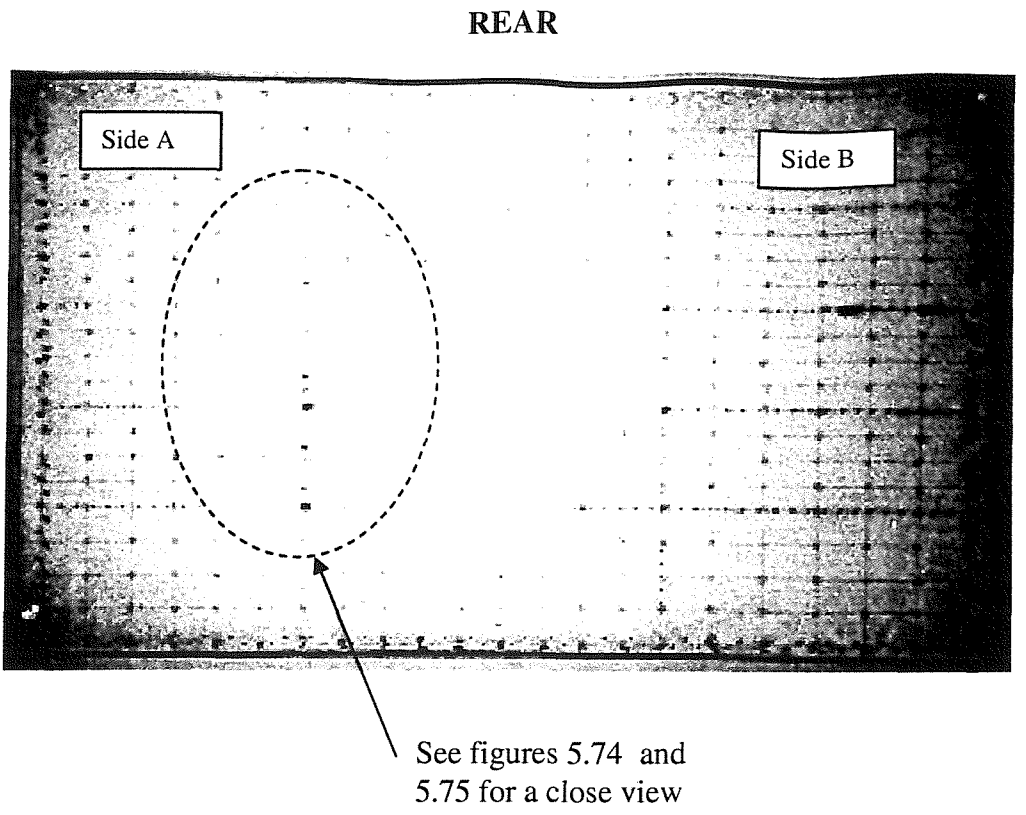

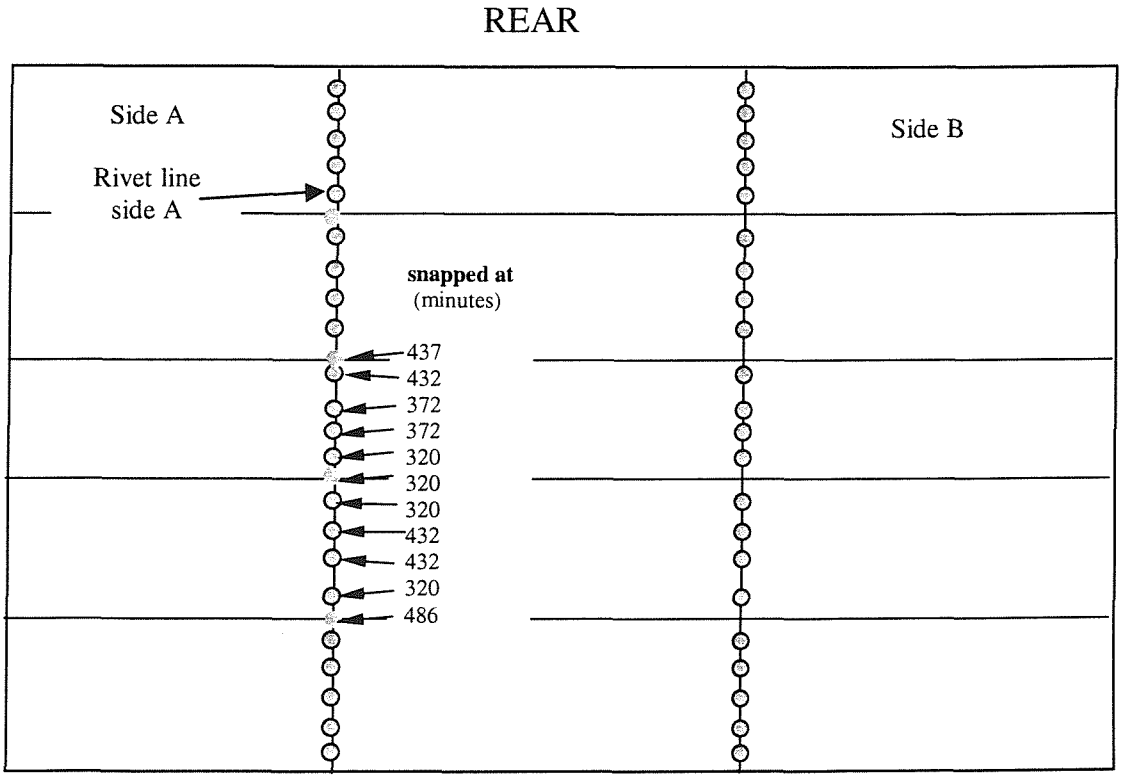

Figure 5.63 Bottom skin of aluminium alloy structure during acoustic endurance testing

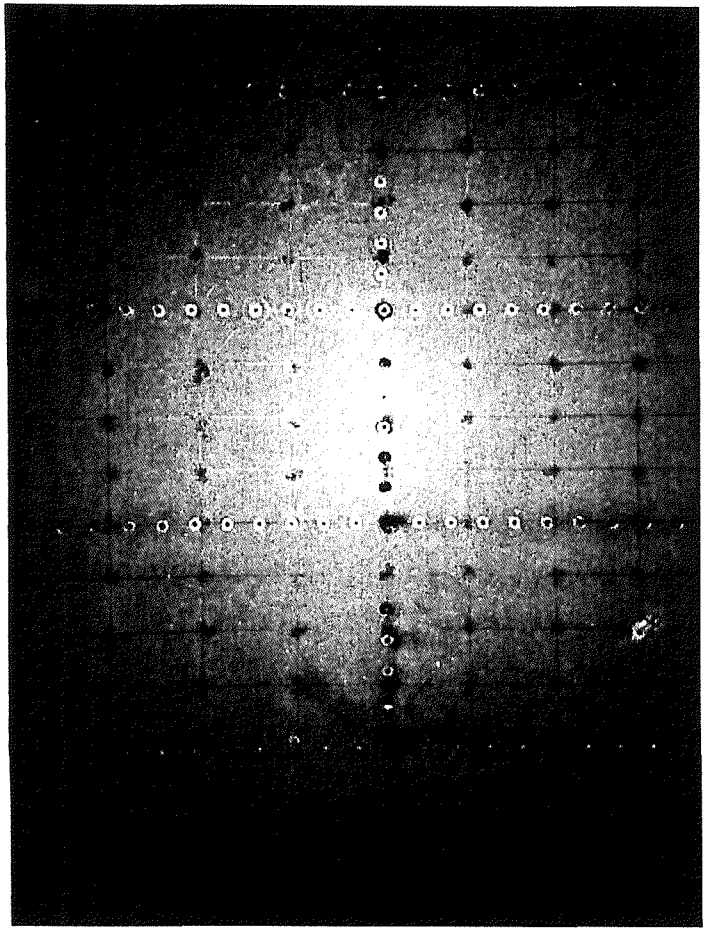

Figure 5.64 Bottom skin of aluminium alloy structure after 320 minutes acoustic endurance testing – close view

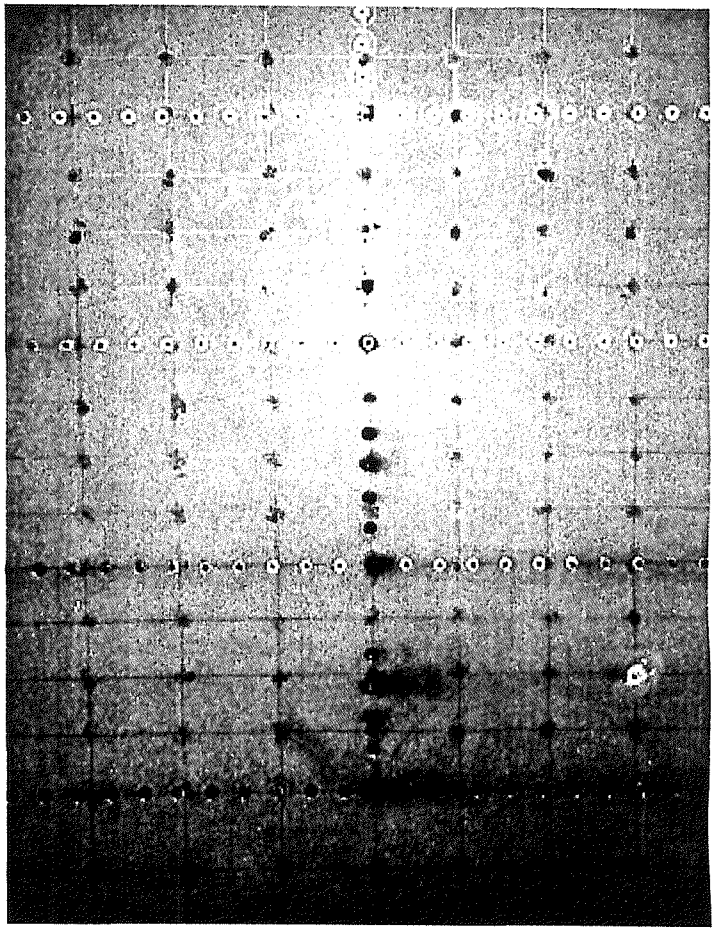

Figure 5.65 Bottom skin of aluminium alloy structure after 437 minutes acoustic endurance testing– close view

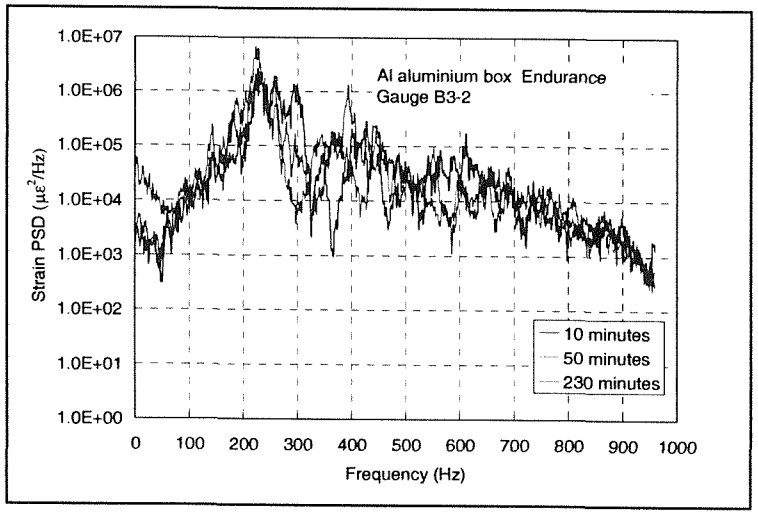

Figure 5.66 Strain spectral density of gauge B3-2 of aluminium alloy structure at various endurance times

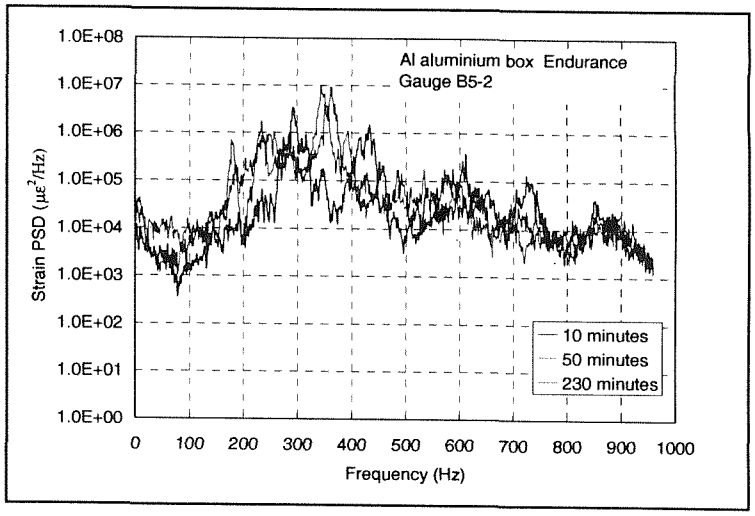

Figure 5.67 Strain spectral density of gauge B5-2 of aluminium alloy structure at various endurance times

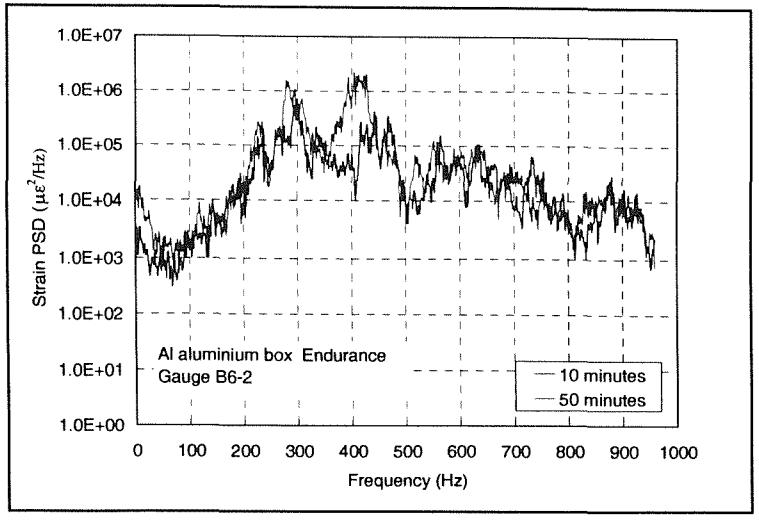

Figure 5.68 Strain spectral density of gauge B6-2 of aluminium alloy structure at various endurance times

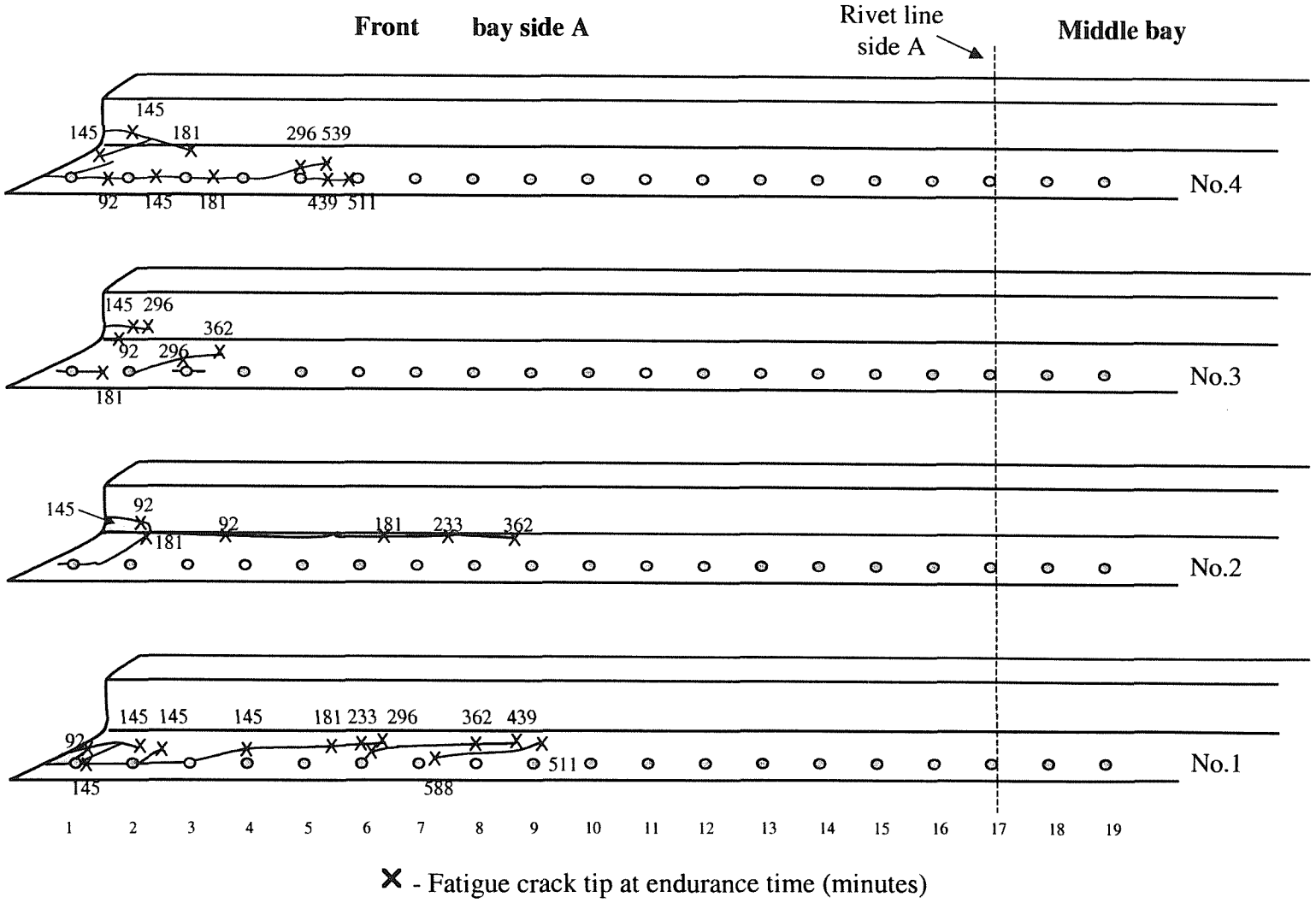

Figure 5.69 Fatigue crack propagation path of the stiffeners on the bottom skin of bay side A of the GLARE structure during acoustic endurance testing

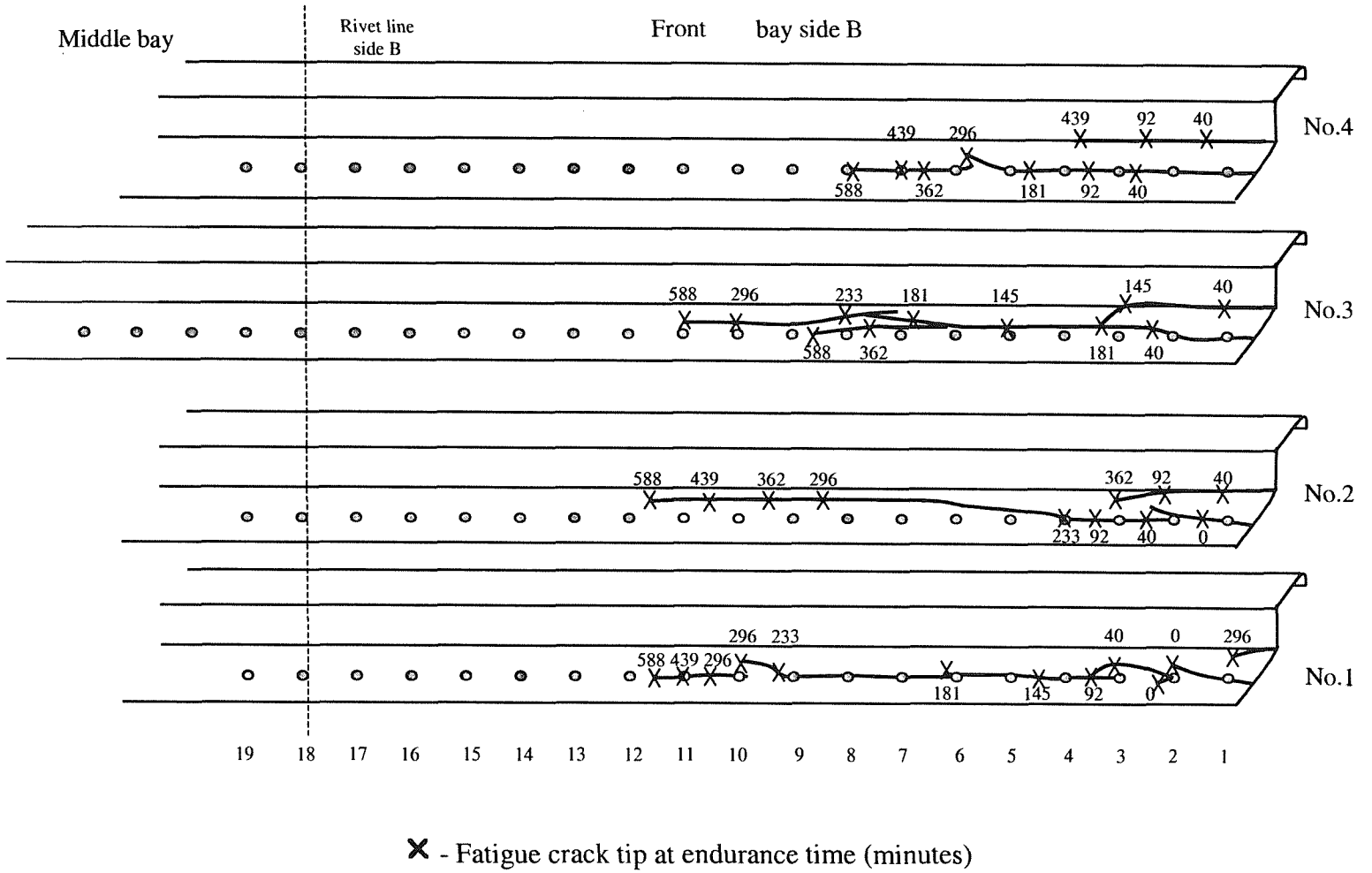

Figure 5.70 Fatigue crack propagation path of the stiffeners on the bottom skin of bay side B of the GLARE structure during acoustic endurance testing

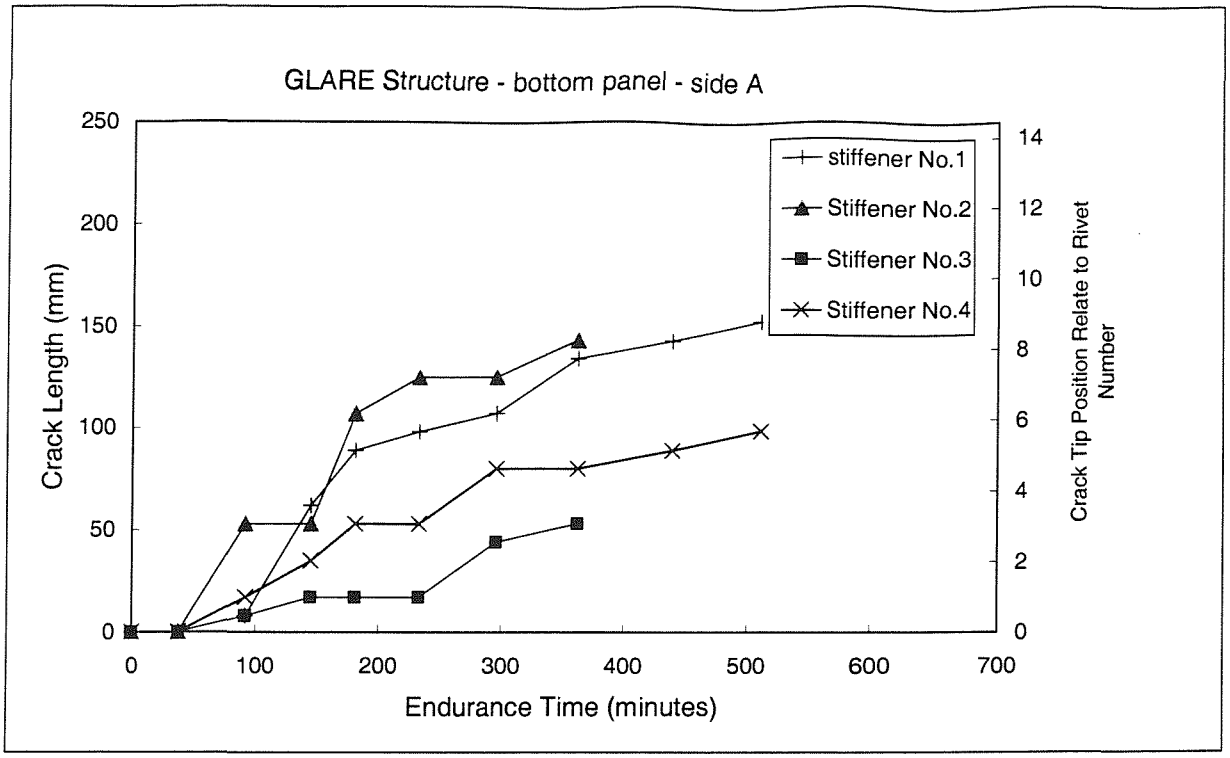

Stiffeners on the bottom skin of bay side A of the GLARE structure

Figure 5.71 Fatigue crack length versus time of endurance testing

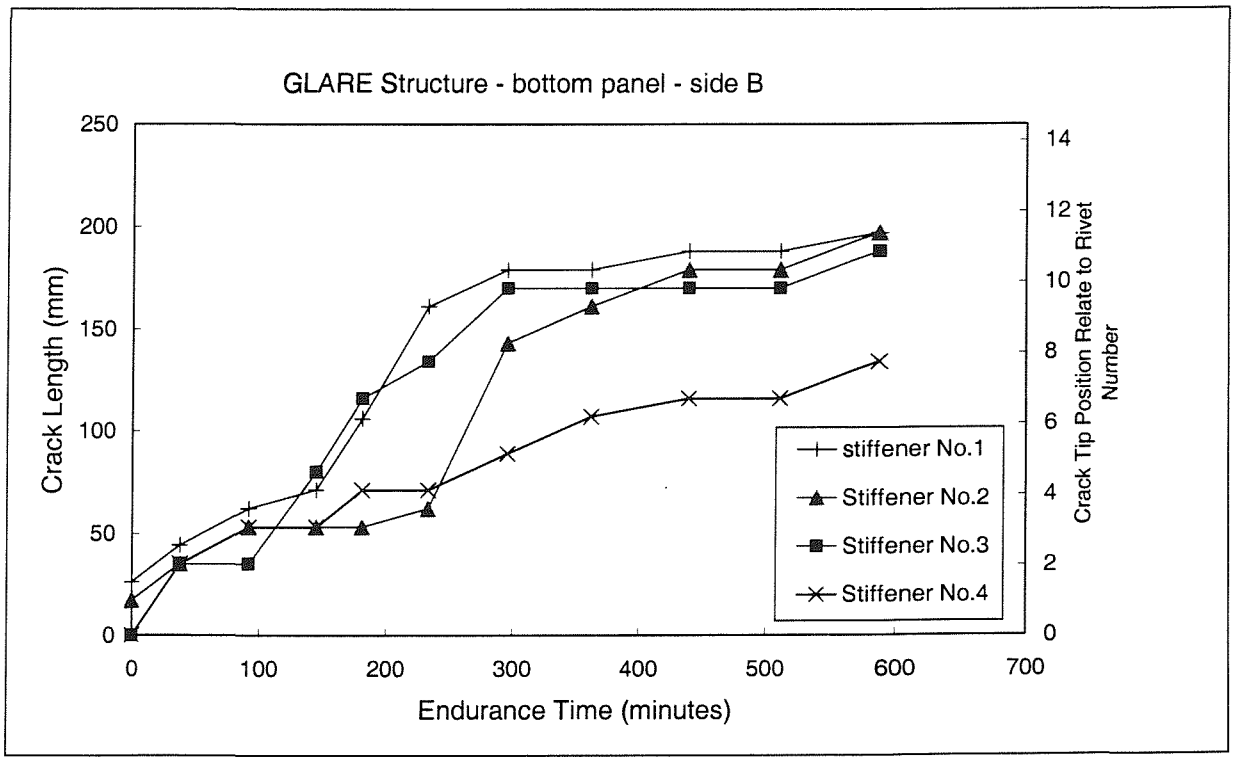

Stiffeners on the bottom panel of bay side B of the GLARE structure

Figure 5.72 Fatigue crack length versus time of endurance testing

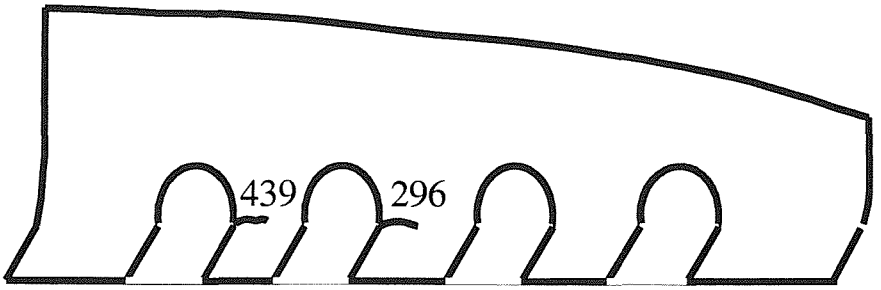

Figure 5.73 Acoustic fatigue cracks found in the inner rib at bay side B of the GLARE structure during endurance testing

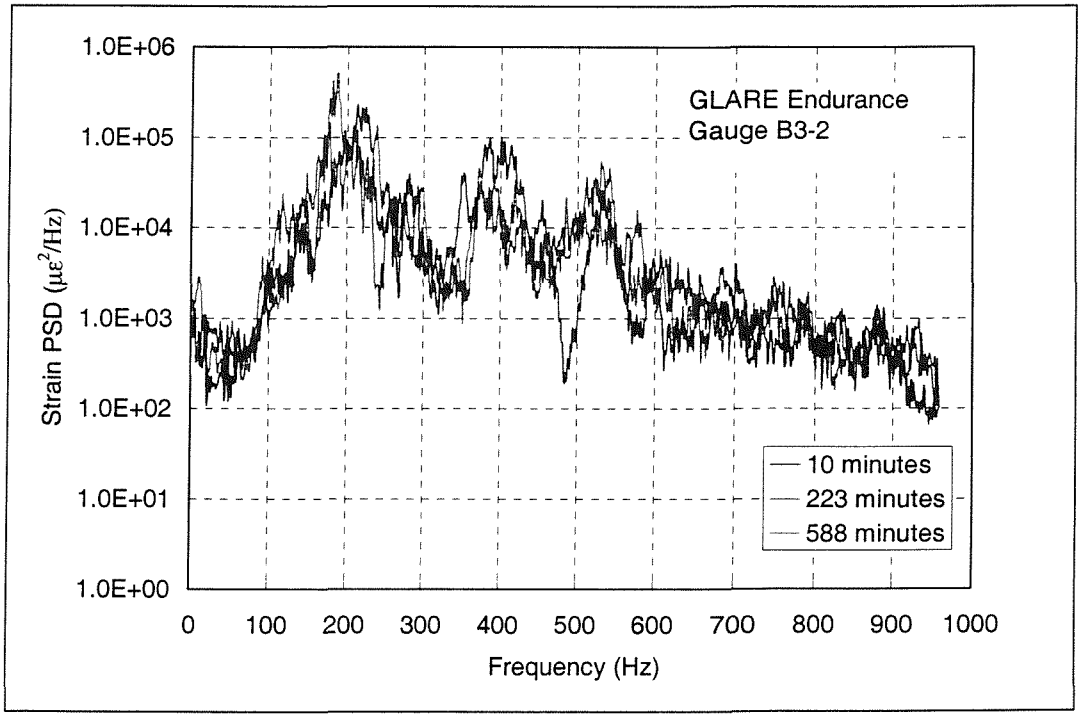

Figure 5.74 Strain spectral density of gauge B3-2 of the GLARE structure at various endurance times

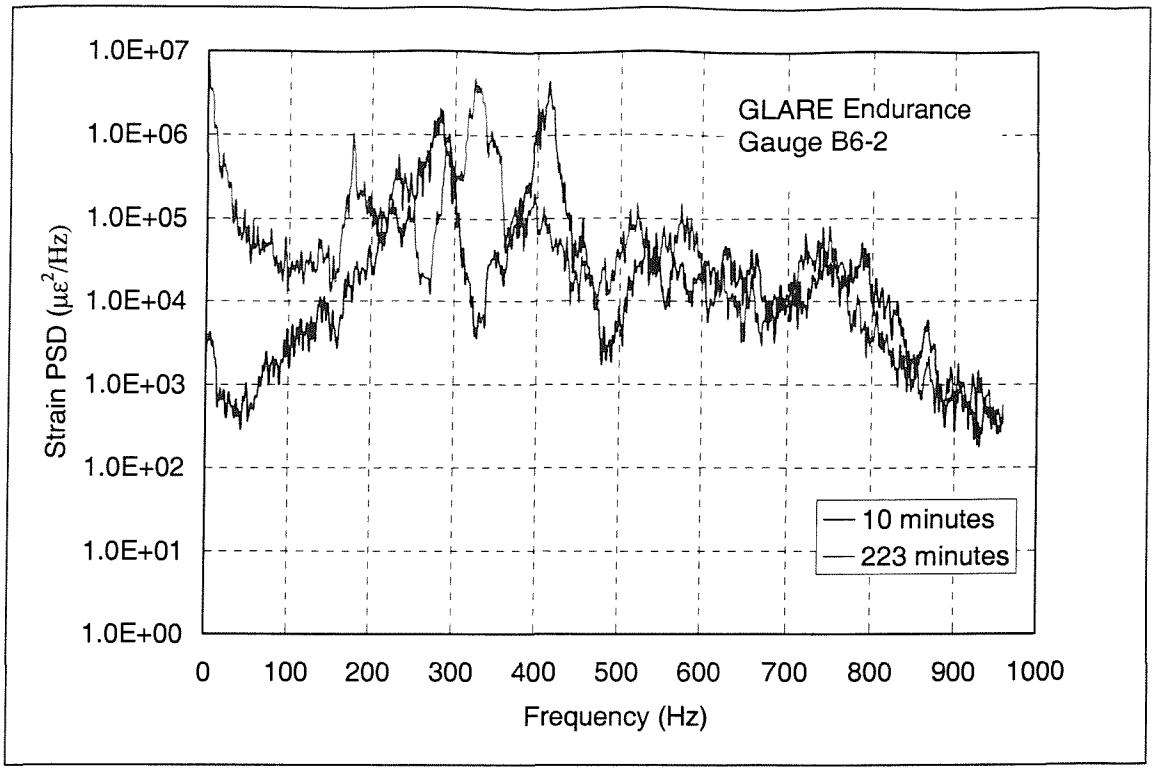

Figure 5.75 Strain spectral density of gauge B6-2 of the GLARE structure at various endurance times

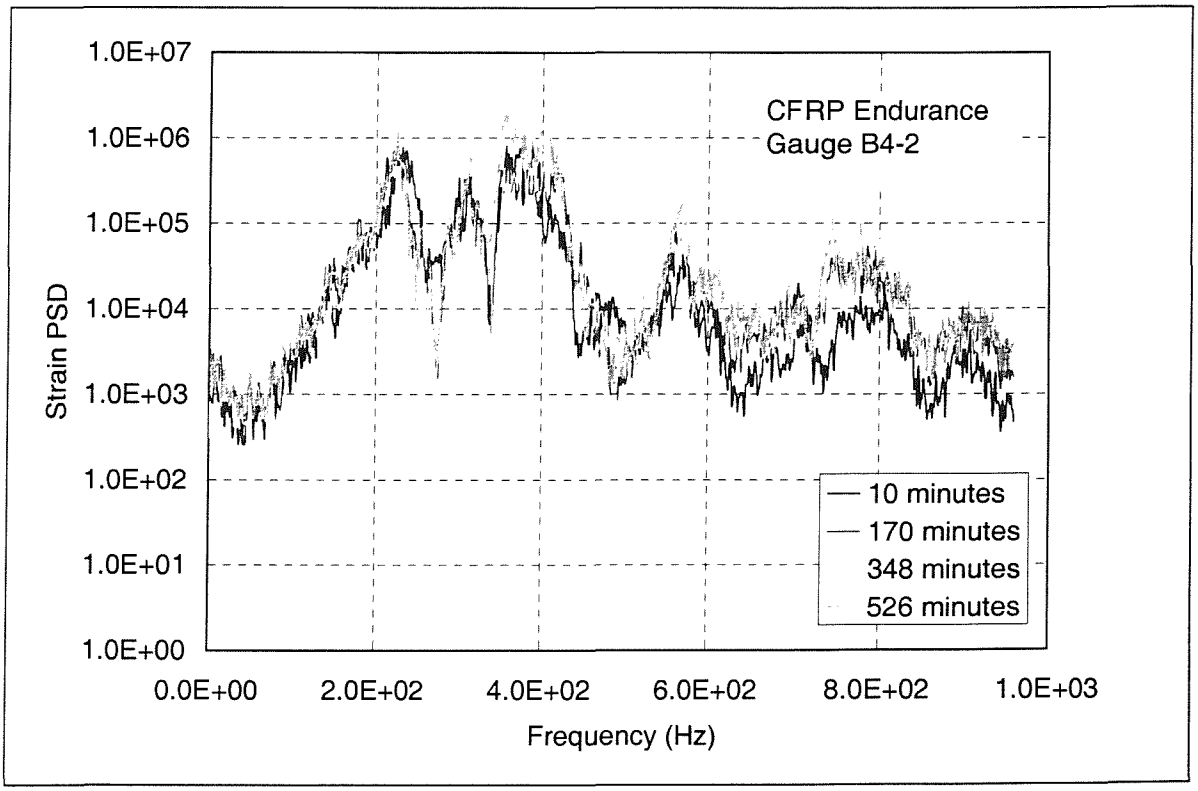

Figure 5.76 Strain spectral density of gauge B4-2 of the CFRP structure at different endurance time

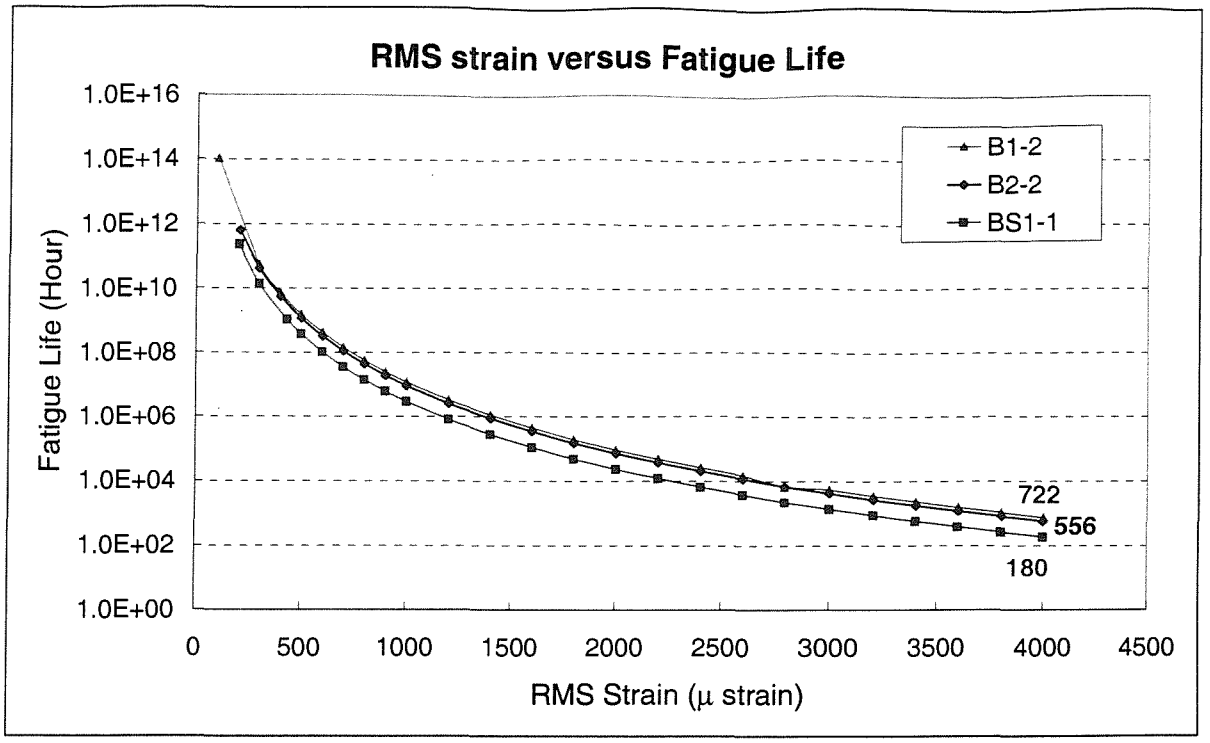

Figure 5.77 Predicted fatigue life of the CFRP at various RMS strain response levels

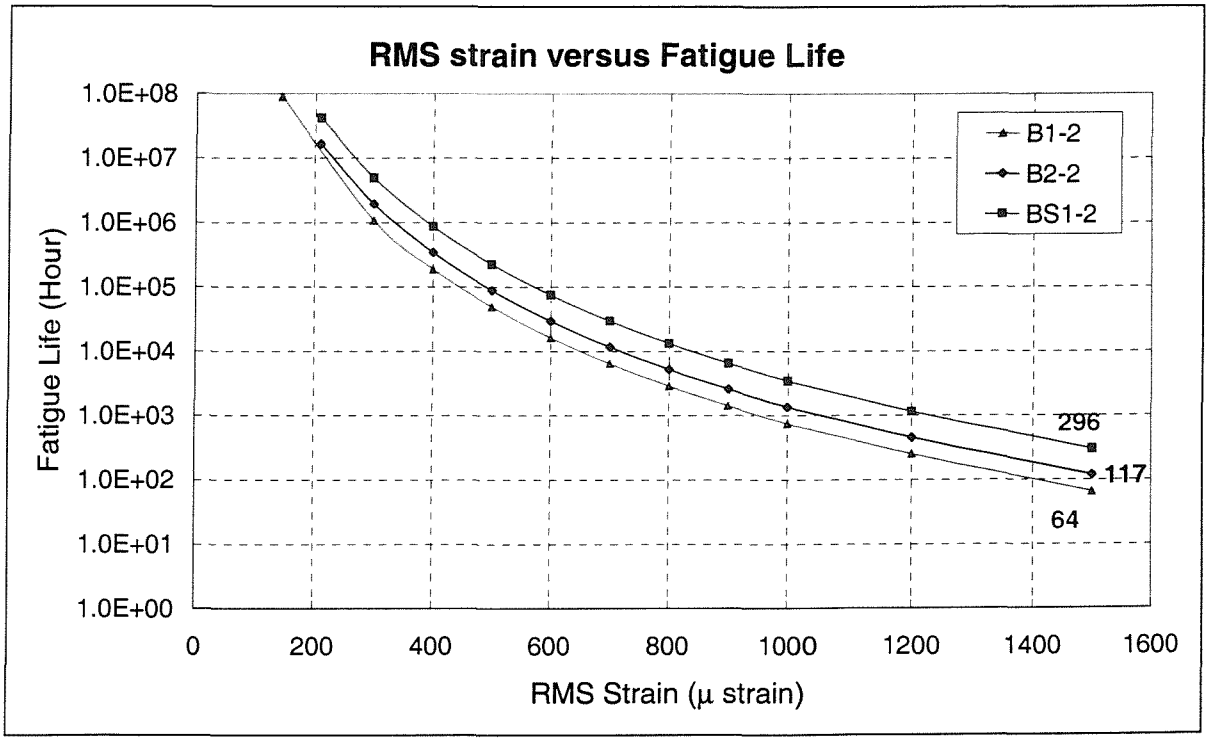

Figure 5.78 Predicted fatigue life of the GLARE at various RMS strain response levels

CHAPTER 6

FINITE ELEMENT ANALYSIS OF COUPON SPECIMENS AND BOX STRUCTURES

6.1 INTRODUCTION

This chapter presents the finite element analyses of CFRP and GLARE coupon specimens, and the CFRP and aluminium alloy box structures. The ANSYS™ FE package was used for the analysis of CFRP coupons, and Msc/Patran and Msc/Nastran for the GLARE coupon, the CFRP and aluminium alloy box structures. Both normal mode and frequency response analyses were carried out. For the response analysis, random excitation was used for prediction of the Power Spectral Density (PSD) distribution and RMS strain of coupons and box structures.

6.2 FINITE ELEMENT ANALYSIS OF CFRP AND GLARE COUPONS

6.2.1 Finite Element Model

In the model construction of CFRP Tee-coupons, ANSYS™ code was used. There are three types of layer elements available for the modelling of composite materials. Two of them are shell elements, SHELL91 and SHELL 99 for modelling composites consisting of up to 16 or 100 layers. Another is the solid element SOLID46, which is an 8-node, 3-D solid element with three degrees of freedom per node (U_x, U_y, U_z) (Figure 6.1). After the initial trial SOLID46 was chosen to model the CFRP Tee-coupon in order to obtain detailed strain

and stress distributions inside the joint region. Each SOLID46 element has 8 layers so the coupon was modelled by two layers of elements stacked above each other to represent the skin panel part. The joint region was modelled using SOLID45. Figure 6.2 shows the FE model of a CFRP Tee-coupon using solid elements. It can be seen that element density was higher in the joint area than in other regions and element size was less than 1mm. There was a total of 1870 elements and 2728 nodes.

For the GLARE Tee-coupon, the FE model was built using Msc/Patran, and the analysis was carried out using Msc/Nastran. The model was built using a shell element with layered properties, which is a 4-node quad element. The skin panel and stringer were connected at the rivet locations. The rivet holes were modelled but rivets were not included in the model. Figure 6.3 shows the finite element model of the GLARE Tee-coupon. The model contained 3970 elements and 4294 nodes.

The material properties used for the analysis were supplied by Airbus and are given in Appendix F.

6.2.2 Finite Element Analysis Results

6.2.2.1 Normal mode analysis

In the finite element modelling, un-damped free vibration analysis is used to determine the natural frequencies and mode shapes of structural components. The equation of motion is expressed as:

$$[M]\{\ddot{u}\}+[K]\{u\}=\{0\} \tag{6.1}$$

where $[M]$ = total mass matrix

For a linear system, free vibration is harmonic:

$$\{u\}=\{\phi\}_i \cos(\omega_i t) \tag{6.2}$$

where $\{\Phi\}$ = eigenvector representing the mode shape at the i^{th} natural frequency.

ω_i = i^{th} circular natural frequency

t = time

thus, the equation of motion becomes:

$$(-\omega_i^2[M]+[K]\{\phi\}=\{0\} \tag{6.3}$$

by solving this equation, up to n values of ω^2 and n eigenvectors $\{\Phi\}$ are determined, where n is the number of degrees of freedom of the FE model.

6.2.2.1.1 Non-constrained free vibration results

In this analysis, the FE models of Tee-coupons were not constrained as in the situation when damping measurements were carried out in Chapter 2. The first six modes are rigid body motions which were ignored.

For the CFRP Tee-coupons, the estimated the first and second natural frequencies are 419 Hz and 971 Hz, and the mode shapes are shown in Figure 6.4. It shows that the first mode is a pure bending mode of the skin plate. The measured average first natural frequency of a CFRP Tee-coupon was 419.6 Hz (see Chapter 2 for the details), agreeing well with the predicted value.

For GLARE coupons, modelling of the connection between skin plate and stringer affects the predictions. In reality, the skin panel and the stringer are connected by rivets. In the FE analysis, if the skin plate and stringer are only connected around the rivet holes, a significant approximation in the modelling, estimated first and second natural frequencies were 276 Hz and 417 Hz. From the measurement results presented in Chapter 2, the first two measured resonance frequencies were 305 and 489 Hz. The FE model gave underestimated resonance frequencies. On the other hand, by assuming that the flange of the stringer and the skin panel are perfectly bonded together, the estimated first two natural frequencies were 325 Hz and 532 Hz, i.e., overestimated. Both sets of FE results showed that the first mode is a skin panel bending mode as shown in Figure 6.5. In practice, when the skin panel deforms upwards, the situation is more like the first assumption concerning constraint at the rivet joints, but when it deforms downwards, it behaves more closely to the second assumption. Therefore it is really a

non-linear system due to behaviour in the region where the skin panel and the flange of the stringer meet. Although contact element may be used to model this situation, results may not be satisfactory because the limitations in combining non-linearity with dynamic in FE analysis.

6.2.2.1.2 Constrained free vibration analyses

For both CFRP and GLARE Tee-coupons, free vibration analyses were carried out for a coupon with tip masses (22. Grams for CFRP and for GLARE), and constrained by the web of the stringer as if mounted on a shaker during the simulated acoustic endurance test.

The predicted first two natural frequencies were 81Hz and 106 Hz for the CFRP coupons, the mode shapes are given in Figure 6.6. The second mode is the skin panel bending mode, i.e., the "Butterfly mode", which is the mode excited in the endurance tests of the specimens. Fatigue tests have shown that the resonance frequencies of the first pure bending mode of the CFRP coupons were between 103 Hz and 108 Hz (Table 2.8). The estimated result therefore agrees quite well with the measured values.

For the GLARE coupons, under the assumption that the skin panel is only connected to the stringer at the rivet points, the first two estimated resonance frequencies are 45 Hz and 80 Hz (mode shapes see Figure 6.7), and 55 Hz and 96 Hz if the skin plate and the flange of the stringer are perfectly bonded. The second mode is the skin plate bending mode. Fatigue tests gave the average resonance frequency of the GLARE coupons as 82 Hz. Again the experimental result is between the two finite element estimations. However, the difference between predicted and measured values is less significant than in the freely supported condition.

6.2.2.2 Dynamic response analysis

ANSYS™ and Msc/Nastran are able to predict the response of a structure to dynamic loading with a given spectrum, both excitation at the support (base) and the nodes are possible. The random vibration of a structure is analysed by means of the Power Spectral Density (PSD) approach. The analysis is based on the free vibration analysis results with a known loading

spectrum to calculate an RMS response value and power spectral density distribution of the displacement, strain and stress in the model. The response PSD is computed from the input PSD with use of transfer functions for single DOF systems $H(\omega)$ and by using modal superposition techniques. This approach is, of course, based upon linear system behaviour. The mode superposition method uses the natural frequencies and mode shapes from the free vibration analysis to characterise the dynamic response of a structure to dynamic loading. Detailed equations are rather complicated and can be obtained from relevant manuals[82, 87] and will not be listed here.

The PSD method was used to estimate the coupon response to the random acceleration excitation of the shaker, i.e., base excitation. In the analysis, the damping loss factor measured in Chapter 2 was used to estimate the coupon response to the acceleration excitation. Acceleration spectral density was defined in the modelling in 1/3 Octave bands with central frequencies of 100 Hz and 80 Hz respectively for the CFRP and GLARE coupons. For the CFRP coupons, two damping loss factors from tests given in Chapter 2 were used in the analysis, i.e., 0.00698 (measured in the freely supported condition, see Table 2.2), and 0.021 (measured in fatigue endurance tests, see Table 2.8) in order to evaluate the effects of damping on the estimation of strain response. Estimated maximum top surface RMS strains are listed in Table 6.1, which shows that damping has a great effect on the estimated strain level. Figure 6.8 gives a comparison of RMS strain levels measured in fatigue tests and estimated using a damping loss factor of 0.021. It shows that estimation underestimated the strain response especially when the excitation level was high. This is probably due to fact that the loss factor used for the estimation was too high, it being possible that damping was strain level dependent.

The RMS strain and stress distributions on the top skin of the CFRP coupons are shown in Figure 6.9. It is clear that the maximum strain and stress occurred at the location where the radius of the joint ended. Transverse stresses on the top surface are shown in Figure 6.10, and the highest stresses were located at the edge, which explains the reason why more damage was seen at the edge from the C-scan picture as shown in Figures 2.32 and 2.33. This type of behaviour had been observed before by Drew[64] who found "edge peeling" to be a damage mechanism in CFRP coupons loaded in flexure in fatigue testing. For the unidirectional filling region, stress distributions are given in Figures 6.11 and 6.12. In Chapter 2 it was concluded

that fatigue damage started at the upper corners of the joint region and then propagated along the interface of the lower 8-layers and the central filling region, and eventually caused the crack in the joint. The stress distributions in Figures 6.11 and 6.12 confirm this observation. The deflected shape of the CFRP Tee-coupon under acceleration excitation is given in Figure 6.13, which shows that the coupon responses in a skin bending mode as expected in a fatigue test. The maximum strain PSD is plotted in Figure 6.14, which is clearly indicative of predominant response in one lightly damped resonance in the frequency range examined.

In the random response analysis of GLARE Tee-coupons, the skin panel and the flange of the stiffener are only connected at the rivet locations in order to obtain more realistic strain and stress distribution at the rivet line where fatigue damage occurred. The damping loss factor (0.030) obtained in the fatigue test was used in the analysis. Estimated RMS strains on the upper surface of the skin panel at the strain gauge locations (Figure 2.25) are compared with measured results as shown in Figure 6.15. It can see that estimated strains are in good agreement with measured data at strain gauge location 2, but strain is underestimated at location 1. The underestimation could be caused by two facts. First, damping could be strain level dependent. Second, non-linear behaviour in a highly strained regionwas not taken into account. Strain distribution at the upper surface of the skin panel is shown in Figure 6.16. It shows that the highest strain is located in rivet hole areas, as could be expected.

In Chapter 2, it was found that the fibre direction of the glass reinforced plastic immediately under the surface aluminium layer was in the direction of the stringer rather than perpendicular to it. This resulted in a lower fatigue life because of the "fibre bridging effect" of the GLARE not being as effective as it should be. A static analysis was carried out to examine the effect of lay up on the strength of coupons. The GRP layers of the skin panel were modelled as two unidirectional layers with fibres perpendicular to each other. Stress and strain results for each layer are compared for the outer layer fibre directions at 0° and 90° as shown in Figure 6.17. For the two lay-ups, the strain distributions are almost the same, but stresses are not comparable. When the fibres in the outer layer are at 0 degrees, the loading is mainly carried by the surface aluminium layer and the composite layer next to it. So when damage occurred in the aluminium layer, the fibres carried the extra load and maintained the strength to a certain level. In the other case, the surface aluminium layer is the main loading carrier, and when it is damaged, because of the lower strength of first GRP layers (Nos. 6 & 2) next to it, fatigue

damage in the surface could develop further and results in loss of strength of the structure and failure.

6.3 FINITE ELEMENT ANALYSIS OF THE BOX STRUCTURES

Finite element analyses of the box structures were carried out to estimate the structural response to high intensity acoustic loading and to compare predicted responses with measured results given in Chapter 5.

6.3.1 Finite Element Model

Msc/Patran was used to prepare finite element models of the box structures. Each model was built using 4-node shell elements. The stiffeners were modelled using shell elements instead of beam elements in order to obtain the detailed strain response of the stringers. Material properties used were provided by Airbus and are given in Appendix F. For aluminium structure, there were 26584 elements and 27065 nodes, and 23343 elements and 21823 nodes for the CFRP structure. There were at least 10 elements between stiffeners in order to obtain accurate mode shape estimations. Figure 6.18 shows the finite element models of aluminium (GLARE) and CFRP structures.

6.3.2 Loading and Boundary Conditions

For the modal analysis the structures were constrained at four sets of 4-node points on the end ribs corresponding to the support positions for the experimental modal analysis. However, during the acoustic endurance tests, the structures were supported by a frame as shown in Figure 5.1, which restricted the deflection of the end ribs. Hence for the random response analysis of the structures to the acoustic loading, the whole of each end rib was constrained to stop translational movements.

For the frequency response analysis, pressure loading with constant amplitude but a varying phase angle of $2\pi fx/V_x$ (x - air flow distance, V_x = 340 ms^{-1} - speed of sound, ref. to Chapter 3 for details) was applied to the skin panel, which represents the acoustic loading experienced by the structures during the acoustic excitation tests described in Chapter 5.

6.3.3 Finite Element Results

Because of the similarity of the aluminium alloy and GLARE structures in construction, only results for aluminium and CFRP structures are given.

For the box structures, normal mode analysis was first carried out to obtain the natural frequencies and mode shapes. Two sets of constraints described above were used for the modal analysis. It was found that the constraints mainly affect the first natural frequency. The first 10 natural frequencies of the aluminium and CFRP box models are listed in Table 6.2. The first mode is the global bending mode of the box structures as shown in Figure 6.19. For the FE model only constrained by two sets of 4-node points on each end rib, the first mode shapes and frequencies are similar to those measured shown in Figure 4.16. It shows that the first mode is the whole structure bending plus deformation of the middle bay of the bottom skin.

The modal analyses of the aluminium alloy and CFRP box structures found far more numerous natural frequencies than resonance frequencies found in the modal tests, see Chapter 4. In the frequency range from 0 to 800 Hz, 169 and 108 modes were predicted for the aluminium alloy and CFRP box structures respectively. These modes are all skin panel modes, the first five mode shapes are given in Figure 6.20 when the end ribs were entirely constrained. To get a clear view, only the top and bottom skin panels are shown in Figure 6.20. The first mode shapes for both structures are similar to those shown in Figure 6.19. At low frequency, i.e., up to the 4^{th} mode for the aluminium alloy structure and 3^{rd} mode for the CFRP box, top and bottom skin panels are weakly coupled. As frequency increased, the two skin panels became strongly coupled.

The responses of the structures to random pressure excitation were calculated by applying random pressure loading of overall sound pressure levels from 140 dB to 160 dB in steps of 5 dB to the bottom skin panel. The pressure loads are considered to have constant amplitude but with varying spatial phase angle, i.e.,

$$P(f, x)=P_0 e^{i 2\pi fx/V} \tag{6.4}$$

This is to simulate the travelling sound wave passing the skin panel of the box structures as described in the Chapter 3. Damping values measured in the modal tests of the box structures given in Chapter 4 were used for the estimation of RMS strain and strain spectral densities at the locations of the strain gauges. Modal tests indicated higher damping loss factor for the first mode, and lower values for rest of the modes. Hence, a damping loss factor of 0.034 (i.e., damping ratio of 1.70%) was used for modes under 300 Hz, and an average damping loss factor of 0.0112 (damping ratio of 0.56%) for rest of the frequency band for the aluminium alloy structure. For the CFRP structure, damping loss factors of 0.05 and 0.023 (damping ratios of 1.15% and 2.5%) were used.

For the aluminium alloy box structure, random pressure load was applied to the bottom skin panel of the box and the RMS strain responses at various strain gauge locations were obtained and are listed in Table 6.3. The measured RMS strain values are also repeated in Table 6.3 for the purpose of comparison. Comparisons of the RMS strains are also plotted in Figures 6.21 and 6.22. From Table 6.3 and Figures 6.21 and 6.22, it can be seen that the estimated strain levels are of the same order and have the similar pattern to those measured. However, for a damping loss factor of 0.0112 (results are noted as estimation 1 in Table 6.3 and Figures 6.21 and 6.22), estimations are far too high compared with measured data for most of the strain gauge locations except at few locations where measured values are higher than those estimated. For example, estimated RMS strain is 210% higher than that measured for the strain gauge B21 at excitation level of 160 dB.

The strain spectral densities at strain gauge locations B12 and BS12 are shown in Figures 6.23(a) and 6.24(a) for the aluminium alloy box with a damping ratio of 0.0112. Estimated and measured PSDs follow the same pattern and agree well in the lower frequency range. In the high frequency range, estimated strains are higher than those measured. This is because lower damping loss factors were used in the frequency range above 300 Hz. It is also noticed that estimated spectral distributions have a peak at 300 Hz, but this did not appear in the measured spectral distribution at excitation level of 160 dB. However, there is a small peak at 300 Hz in measured PSDs at an excitation level of 140 dB. This indicates the change of structural behaviour with increase of excitation level. This change can not be accommodated by finite element analysis because the structural response analysis is based upon linear dynamic theory.

Based on the above results, the same response analyses for the aluminium alloy structure were repeated but with a higher damping loss factor, i.e., constant damping loss factor of 0.034 was used across the frequency range from 0 to 800 Hz. This results in the reduction of response RMS strains in the structure as shown in Figures 6.20 and 6.21 (noted as estimation 2). These results are also listed in Table 6.3. It can be seen that estimates with higher damping gives a better approximation of RMS strains under acoustic loading. The difference between measured and estimated RMS strain values for strain gauge B21 at the excitation level of 160dB was reduced to 56%, for instance. The resultant strain spectral densities are given in Figures 6.23(b) and 6.24(b). The "smearing" effect is obvious across the frequency band especially in the higher frequency region, where strain spectral density curves became more smooth and those separated peaks shown in Figures 6.23(a) and 6.24(a) no longer exist due to high damping being used.

In the acoustic endurance tests of the box structures discussed in Chapter 5, fatigue damage was found at the ends of the stiffeners of both the aluminium alloy and GLARE boxes at an early stage of the endurance tests. This eventually led to the end part of the stiffeners of the aluminium alloy structure breaking away. The response analyses indicated high RMS strains in the lower part of the stringer as shown in Figure 6.25. For a damping loss factor of 0.034, estimated transverse RMS strains are 902μ strain and 949μ strain for sides A and B respectively. This is because tthe ends of the stringers are not constrained for the aluminium and GLARE structures. Under the acoustic loading, the stringer ends could vibrate in the manner of a cantilevered beam, which induced large transverse strains in the stringer. To reduce the strain level at this location, the finite element model of the aluminium box structure was modified by extending the ends of the stringers on the bottom skin and connecting them to the end ribs as shown in Figure 6.26. Normal mode analysis of this modified model showed that the first natural frequency of the box increased from 234 Hz to 240 Hz, which indicates the increase of total stiffness of the structure. Response analysis has revealed that RMS strains in the modified model to the random pressure loading reduced significantly at the ends of the stringers as shown in Figure 6.27. The transverse strains have decreased from 949μ strain to 77μ strain for side A, and from 902μ strain to 129μ strain for side B. Longitudinal strains were also reduced but less significantly. RMS strains at various strain gauge locations in the modified model are listed in Tables 6.4 and 6.5, which show that strain levels are decreased at all the locations except T11, where a 4% increase was found. The maximum reduction of

RMS strain was found, of course, to be in the stringers on the bottom skin panel, e.g., 167% and 98% reductions for the longitudinal and transverse strains at strain gauge BS2 location. For the rest of the strain gauge locations, the decrease of RMS strain levels varies from 3% to 58%. For the aluminium alloy and GLARE boxes when subjected to acoustic endurance excitation. These results indicate that different fatigue behaviours from those observed in Chapter 5 could be seen if the design of the stringers in the test structures was improved according to the findings discussed above.

For the CFRP box structure, the same random response analysis as for the aluminium alloy was also carried out. Measured damping loss factors from modal tests (see Chapter 4) was used, i.e., 0.05 for frequency below 300 Hz and 0.023 for the rest of frequency range. Random pressure loading which represents a travelling wave along the PWT was applied to the bottom skin panel. RMS strain responses to pressure loading from 140 dB to 160 dB in steps of 5 dB at various strain gauge locations were obtained and are listed in Tables 6.6 and 6.7. The experimental data are also listed for the purpose of comparison. For the damping values used, the estimated RMS strain values are much higher than those measured as shown in Figures 6.28 and 6.29; e.g., the difference between measured and estimated strain was 223% at strain gauge location B12, for other locations the difference varies. Strain spectral densities at strain gauge locations B22 and BS21 are shown Figures 6.30(a) and 6.31(a), which show that the estimated values are higher than measured data in the high frequency band. Therefore a higher damping loss factor of 0.05 was used for all frequency bands to calculate the RMS strain response and these results are also listed in Tables 6.6 and 6.7. The results shown that the disagreement between the estimates and experimental data is reduced, for instance, the difference for B12 was reduced to 123%, which is still considerably high, but improvement was apparent. The disagreement between measured and predicted data was found to be greater for the strain locations on the top skin than for the those on the bottom skin. The strain spectral density plots in Figures 6.30(b) and 6.31(b) show that increase of damping loss factor has resulted in the further flattening out of resonance peaks.

6.4 SUMMARY

FE models have been built to estimate the natural frequencies, mode shapes and the structural responses to random excitation of coupon specimens and box type structures.

For the coupon specimen models, the estimates of resonance frequency of CFRP coupons are more accurate compared with measured values than for the GLARE coupons. This is due to the fact that the CFRP model has an integrated stiffener which is easy to model. For the GLARE coupons, the skin panel and stringer are riveted together. How the connection is modelled has great effect on the estimated results. The RMS strain responses of coupons to random excitation were obtained and compared with RMS strains measured during the fatigue tests. Measured damping loss factors were used for the response analyses. It has been found that estimated strains are lower than those measured, especially at the higher excitation levels. The stress and strain distributions of coupon specimens have also been compared with the fatigue damage patterns observed, some similarities between them are apparent.

For the box structures, because of the similarity in construction of the aluminium alloy and GLARE structures, only the finite element analysis results for the aluminium alloy and CFRP structures are presented in this chapter. Both normal mode and response analyses were carried out. A travelling wave with constant pressure amplitude but varying spatial phase angle was applied to the bottom skin panel of the structures. The damping loss factors measured in the modal tests given in Chapter 4 were used and resulted in overestimation of structural responses. By increasing the damping values in the theoretical models, the difference between measurements and estimates narrowed. The estimated strain spectral density distributions are also compared with measured results, good agreement was achieved. It is well known that the damping of modes of a test structure will be much higher when mounted in the PWT because of added acoustic damping due to the fact that the cross section dimension of the tunnel is small relative to the dimension of the test panel. In reference [15], for example, for comparison of predicted and measured dynamic strains, the damping used value was that measured when the plate mounted in the wall of the PWT.

Modification to the end structure of the stringers on the bottom skin of the aluminium alloy box was employed to investigate the structural behaviour under high intensity acoustic

loading. It was found that the RMS strain response in the stringers decreased dramatically when the ends of the stringers were fixed on to the end ribs. This means that the fatigue behaviour of the aluminium alloy and GLARE boxes could be improved significantly if the design of the stringers was modified.

The analyses carried out in this chapter have shown that finite element analysis is a very useful tool in the estimation of the structural response to random acoustic excitation, especially in the design stage. The FE predications can be used to improve the structure design and also served as a guideline to the preparation of experimental work. Good estimation of static and dynamic response of a structure can be achieved by correctly applying the loading, but careful choice of local boundary conditions and modal damping values are also vital.

Table 6.1 Predicted surface bending RMS strains (μ strain) of CFRP Tee-coupons

Tee-coupons under random excitation on fatigue test rig

Damping Loss factor	RMS Acceleration Excitation Level (g=9.81 ms^{-2})				
	3g	5g	6.7g	7.5g	8.75g
	Surface Bending Strain (μ)				
0.0070	1420	2367	3172	3551	4057
0.021	914	1523	2040	2284	2610

Table 6.2 Predicted modal frequencies (Hz) of FE models of the aluminium and CFRP structures with different constraints

Mode no.	Aluminium alloy Structure		CFRP Structure	
	4-node constraints	End rib constraints	4-node constraints	End rib constraints
1	180.8	234.0	191.8	228.2
2	244.1	245.5	250.5	254.5
3	260.5	260.6	252.7	265.8
4	261.6	262.0	270.0	274.8
5	267.3	268.2	280.5	284.9
6	270.8	271.1	283.6	286.9
7	271.9	273.4	303.5	304.2
8	273.3	274.2	304.6	309.9
9	279.8	280.6	316.5	318.4
10	280.7	281.1	318.0	320.7

Table 6.3 Comparison of measured and estimated RMS strains (μ strain) of FE model of the aluminium alloy box when excited on the bottom skin

Estimation 1 - Damping loss factor 0.0340 - below 300 Hz
- Damping loss factor 0.0112 - above 300 Hz
Estimation 2 - Damping loss factor 0.0340

Strain Gauge No.	SPL	140 dB	145 dB	150dB	155 dB	160 dB
B11	Measured	5.4	7.5	12.0	20.5	33.7
	Estimation 1	7.3	12.9	23.0	40.9	72.8
	Estimation 2	4.4	7.8	13.9	24.6	43.8
B12	Measured	13.8	24.7	43.9	77.6	131.2
	Estimation 1	19.2	34.2	60.8	108.1	192.3
	Estimation 2	11.2	19.9	35.3	62.8	111.7
B21	Measured	3.7	6.3	10.8	19.2	34.0
	Estimation 1	10.5	18.7	33.3	59.2	105.3
	Estimation 2	5.3	9.4	16.8	29.9	53.1
B22	Measured	7.6	12.9	23.5	47.1	94.9
	Estimation 1	23.1	41.1	73.2	130.1	231.4
	Estimation 2	13.9	24.7	43.8	78.0	138.7
B31	Measured	3.8	5.0	7.8	13.3	24.0
	Estimation 1	4.6	8.2	14.6	25.9	46.0
	Estimation 2	2.8	5.0	8.8	15.7	27.8
B32	Measured	15.1	29.7	53.7	93.7	156.8
	Estimation 1	16.9	30.1	53.5	95.1	169.2
	Estimation 2	9.9	17.6	31.3	55.7	99.0
B41	Measured	3.8	6.5	11.4	19.8	33.7
	Estimation 1	9.5	16.9	30.0	53.3	94.8
	Estimation 2	4.6	8.3	14.7	26.1	46.4
B42	Measured	20.2	33.4	60.8	104.1	157.0
	Estimation 1	24.5	43.6	77.5	137.8	245.1
	Estimation 2	15.0	26.7	47.5	84.4	150.1
B51	Measured	3.5	5.2	8.8	15.3	26.6
	Estimation 1	9.8	17.4	31.0	55.1	98.0
	Estimation 2	5.0	8.8	15.7	27.9	49.5
B52	Measured	13.1	23.3	42.0	68.8	120.1
	Estimation 1	26.1	46.4	82.5	146.7	260.8
	Estimation 2	17.7	31.5	56.0	99.6	177.0
B61	Measured	2.1	3.8	6.9	12.4	23.1
	Estimation 1	9.4	16.7	29.7	52.9	94.1
	Estimation 2	4.1	7.3	13.1	23.2	41.3
B62	Measured	12.7	25.4	44.4	70.4	109.4
	Estimation 1	17.7	31.5	56.0	99.5	176.9
	Estimation 2	11.0	19.5	34.6	61.6	109.5
BS11	Measured	18.4	34.6	63.5	111.2	175.7
	Estimation 1	11.9	21.2	37.6	66.9	119.0
	Estimation 2	8.5	15.1	26.8	47.6	84.6
BS12	Measured	26.8	51.1	93.5	164.8	266.5
	Estimation 1	27.4	48.8	86.8	154.3	274.5
	Estimation 2	18.5	32.9	58.6	104.1	185.2

Table 6.3 continued

Strain Gauge No.	SPL	140 dB	145 dB	150dB	155 dB	160 dB
BS21	Measured	11.5	24.5	39.3	66.1	107.9
	Estimation 1	11.5	20.5	36.5	64.9	115.3
	Estimation 2	8.6	15.2	27.1	48.2	85.7
BS22	Measured	20.5	43.1	70.0	115.9	185.8
	Estimation 1	28.0	49.8	88.5	157.4	279.8
	Estimation 2	20.0	35.5	63.2	112.4	199.8
T11	Measured	6.7	11.0	15.7	25.5	41.1
	Estimation 1	8.9	15.9	28.2	50.2	89.3
	Estimation 2	4.5	7.9	14.1	25.1	44.6
T12	Measured	4.9	9.7	16.8	37.8	56.5
	Estimation 1	2.7	4.7	8.4	14.9	26.6
	Estimation 2	2.2	4.0	7.1	12.6	22.3
T21	Measured	8.2	8.4	8.9	10.4	13.7
	Estimation 1	4.3	7.6	13.6	24.2	43.0
	Estimation 2	1.6	2.8	4.9	8.7	15.5
T22	Measured	6.4	10.7	15.7	25.5	41.4
	Estimation 1	11.1	19.7	35.0	62.3	110.8
	Estimation 2	4.9	8.8	15.6	27.7	49.2
T61	Measured	7.4	14.2	21.6	29.9	41.2
	Estimation 1	8.1	14.4	25.6	45.6	81.1
	Estimation 2	4.0	7.1	12.6	22.4	39.8
T62	Measured	7.9	9.0	12.5	38.2	78.7
	Estimation 1	3.1	5.4	9.7	17.2	30.5
	Estimation 2	1.3	2.3	4.2	7.4	13.2
T71	Measured	5.7	8.2	12.1	19.4	31.6
	Estimation 1	8.3	14.8	26.4	46.9	83.5
	Estimation 2	3.5	6.2	11.1	19.8	35.1
T72	Measured	5.4	5.5	6.2	9.3	14.7
	Estimation 1	2.3	4.0	7.2	12.7	22.7
	Estimation 2	1.3	2.3	4.0	7.1	12.7
TS21	Measured	10.9	18.9	29.1	42.3	63.0
	Estimation 1	19.5	34.6	61.5	109.4	194.6
	Estimation 2	10.4	18.5	32.9	58.6	104.1
TS22	Measured	6.6	10.3	15.7	22.3	33.4
	Estimation 1	3.1	5.5	9.8	17.4	31.0
	Estimation 2	1.6	2.8	4.9	8.7	15.5

Table 6.4 Comparison of estimated RMS strains (μ strain) on bottom skin panel and stiffeners of original and modified FE models of the aluminium alloy box when excited on the bottom skin

Damping loss factor 0.034

Strain Gauge No.	SPL	140 dB	145 dB	150dB	155 dB	160 dB
B11	Modified	3.4	6.0	10.7	18.9	33.7
	Original	4.4	7.8	13.9	24.6	43.8
B12	Modified	10.7	19.0	33.7	60.0	106.7
	Original	11.2	19.9	35.3	62.8	111.7
B21	Modified	4.9	8.6	15.4	27.3	48.6
	Original	5.3	9.4	16.8	29.9	53.1
B22	Modified	12.7	22.5	40.1	71.3	126.8
	Original	13.9	24.7	43.8	78	138.7
B31	Modified	2.3	4.1	7.3	13.0	23.0
	Original	2.8	5	8.8	15.7	27.8
B32	Modified	7.7	13.6	24.2	43.1	76.6
	Original	9.9	17.6	31.3	55.7	99.0
B41	Modified	3.9	6.9	12.2	21.7	38.6
	Original	4.6	8.3	14.7	26.1	46.4
B42	Modified	12.3	21.8	38.8	68.9	122.6
	Original	15	26.7	47.5	84.4	150.1
B51	Modified	4.5	8.1	14.4	25.5	45.4
	Original	5	8.8	15.7	27.9	49.5
B52	Modified	14.0	24.9	44.3	78.7	140.0
	Original	17.7	31.5	56	99.6	177
B61	Modified	3.4	6.1	10.9	19.4	34.4
	Original	4.1	7.3	13.1	23.2	41.3
B62	Modified	8.57	15.24	27.11	48.21	85.73
	Original	11	19.5	34.6	61.6	109.5
BS11	Modified	5.3	9.5	16.9	30.1	53.5
	Original	8.5	15.1	26.8	47.6	84.6
BS12	Modified	14.6	25.9	46.0	81.9	145.6
	Original	18.5	32.9	58.6	104.1	185.2
BS21	Modified	3.2	5.7	10.2	18.1	32.1
	Original	8.6	15.2	27.1	48.2	85.7
BS22	Modified	10.1	18.0	32.0	56.8	101.1
	Original	20	35.5	63.2	112.4	199.8

Table 6.5 Comparison of estimated RMS strains (μ strain) on top skin panel and stiffeners of original and modified FE models of the aluminium alloy box when excited on the bottom skin

Damping loss factor 0.034

Strain Gauge No.	SPL	140 dB	145 dB	150dB	155 dB	160 dB
T11	Modified	4.7	8.3	14.7	26.2	46.6
	Original	4.5	7.9	14.1	25.1	44.6
T12	Modified	2.2	3.9	6.9	12.2	21.7
	Original	2.2	4	7.1	12.6	22.3
T21	Modified	1.3	2.4	4.2	7.5	13.3
	Original	1.6	2.8	4.9	8.7	15.5
T22	Modified	4.7	8.4	14.9	26.5	47.1
	Original	4.9	8.8	15.6	27.7	49.2
T61	Modified	3.3	5.9	10.5	18.6	33.2
	Original	4	7.1	12.6	22.4	39.8
T62	Modified	1.0	1.9	3.3	5.9	10.4
	Original	1.3	2.3	4.2	7.4	13.2
T71	Modified	2.3	4.1	7.4	13.1	23.3
	Original	3.5	6.2	11.1	19.8	35.1
T72	Modified	1.0	1.7	3.1	5.4	9.7
	Original	1.3	2.3	4	7.1	12.7
TS21	Modified	9.6	17.1	30.5	54.2	96.4
	Original	10.4	18.5	32.9	58.6	104.1
TS22	Modified	1.5	2.7	4.8	8.5	15.1
	Original	1.6	2.8	4.9	8.7	15.5

Table 6.6 Comparison of measured and estimated RMS strains of FE model of CFRP box when excited on the bottom skin

Estimation 1 - Damping loss factor 0.023 - below 300 Hz - 0.050 - above 300 Hz
Estimation 2 - Damping loss factor 0.050
Bottom skin panel and stringers on the bottom skin panel

Strain Gauge No.	SPL	140 dB	145 dB	150dB	155 dB	160 dB
B11	Measured	3.8	4.9	6.7	10.2	18.7
	Estimation 1	4.5	8.0	14.3	25.4	45.1
	Estimation 2	3.2	5.6	10.0	17.8	31.7
B12	Measured	8.5	17.3	28.7	47.3	90.6
	Estimation 1	29.2	52.0	92.5	164.4	292.4
	Estimation 2	20.7	36.8	65.4	116.4	206.9
B21	Measured	2.0	3.4	5.4	8.8	17.2
	Estimation 1	4.6	8.2	14.6	25.9	46.1
	Estimation 2	3.0	5.4	9.5	17.0	30.2
B22	Measured	18.2	37.3	60.5	101.4	184.0
	Estimation 1	26.8	47.7	84.9	151.0	268.4
	Estimation 2	17.7	31.5	56.0	99.6	177.1
B31	Measured	4.0	7.6	12.8	21.3	40.8
	Estimation 1	6.7	12.0	21.3	37.8	67.3
	Estimation 2	4.3	7.7	13.7	24.4	43.3
B32	Measured	10.3	22.9	39.1	65.9	121.5
	Estimation 1	10.1	17.9	31.9	56.6	100.7
	Estimation 2	6.8	12.0	21.4	38.1	67.7
B41	Measured	2.3	3.7	6.4	9.4	18.1
	Estimation 1	3.2	5.6	10.0	17.8	31.7
	Estimation 2	2.1	3.8	6.8	12.1	21.5
B42	Measured	13.2	27.1	44.8	72.7	137.0
	Estimation 1	24.3	43.3	77.0	136.9	243.5
	Estimation 2	17.0	30.2	53.7	95.5	169.9
B51	Measured	2.5	4.6	7.8	12.7	24.5
	Estimation 1	5.4	9.7	17.2	30.6	54.5
	Estimation 2	3.0	5.3	9.4	16.7	29.7
B52	Measured	13.5	29.4	51.1	82.3	156.8
	Estimation 1	31.0	55.2	98.1	174.5	310.2
	Estimation 2	16.4	29.1	51.7	92.0	163.6
B61	Measured	1.9	3.8	5.9	9.2	19.7
	Estimation 1	6.6	11.6	20.7	36.8	65.5
	Estimation 2	4.1	7.3	13.0	23.1	41.1
B62	Measured	12.3	27.7	42.9	68.1	140.6
	Estimation 1	30.8	54.8	97.4	173.2	307.9
	Estimation 2	17.9	31.8	56.6	100.6	178.9
BS11	Measured	33.6	70.9	120.7	201.6	384.9
	Estimation 1	65.7	116.8	207.7	369.4	656.9
	Estimation 2	46.5	82.7	147.0	261.4	464.8
BS12	Measured	9.4	19.9	33.9	56.3	106.7
	Estimation 1	18.3	32.5	57.7	102.7	182.6
	Estimation 2	12.9	23.0	40.9	72.7	129.3
BS21	Measured	32.6	59.2	101.8	163.3	296.4
	Estimation 1	44.5	79.1	140.6	250.1	444.7
	Estimation 2	28.1	49.9	88.7	157.7	280.5
BS22	Measured	9.1	16.4	28.1	45.1	81.7
	Estimation 1	12.3	21.8	38.8	69.0	122.8
	Estimation 2	7.8	13.8	24.5	43.6	77.6

Table 6.7 Comparison of measured and estimated RMS strains of FE model of the CFRP box when excited on the bottom skin

Estimation 1 - Damping loss factor 0.023 - below 300 Hz - 0.050 - above 300 Hz
Estimation 2 - Damping loss factor 0.050

Top skin panel and stringers on the top skin panel

Strain Gauge No.	SPL	140 dB	145 dB	150dB	155 dB	160 dB
T11	Measured	8.7	13.7	22.0	34.5	58.6
	Estimation 1	7.5	13.4	23.8	42.4	75.4
	Estimation 2	4.6	8.3	14.7	26.1	46.4
T12	Measured	6.4	7.0	8.3	11.1	17.7
	Estimation 1	2.0	3.5	6.3	11.2	19.9
	Estimation 2	1.3	2.3	4.1	7.3	12.9
T21	Measured	0.3	0.6	1.4	2.8	7.6
	Estimation 1	9.7	17.3	30.8	54.7	97.3
	Estimation 2	5.9	10.5	18.7	33.3	59.3
T22	Measured	7.8	10.8	16.1	24.1	40.4
	Estimation 1	2.4	4.2	7.5	13.3	23.6
	Estimation 2	1.5	2.7	4.8	8.6	15.3
T61	Measured	2.4	1.4	2.3	3.7	5.5
	Estimation 1	6.5	11.5	20.5	36.5	64.8
	Estimation 2	3.5	6.3	11.1	19.8	35.2
T62	Measured	5.6	5.7	5.7	6.2	8.2
	Estimation 1	1.2	2.1	3.8	6.7	11.9
	Estimation 2	0.7	1.2	2.2	3.9	7.0
T71	Measured	6.1	6.2	6.5	7.2	9.9
	Estimation 1	6.2	11.0	19.5	34.7	61.8
	Estimation 2	3.2	5.7	10.1	17.9	31.9
T72	Measured	8.6	11.7	17.3	25.7	45.5
	Estimation 1	1.1	2.0	3.5	6.3	11.2
	Estimation 2	0.7	1.3	2.3	4.1	7.4
TS21	Measured	8.7	10.9	14.4	19.8	29.6
	Estimation 1	4.6	8.2	14.6	26.0	46.2
	Estimation 2	2.8	4.9	8.7	15.5	27.6
TS22	Measured	17.1	30.3	49.6	74.9	127.2
	Estimation 1	16.6	29.5	52.5	93.4	166.1
	Estimation 2	9.9	17.6	31.3	55.7	99.0

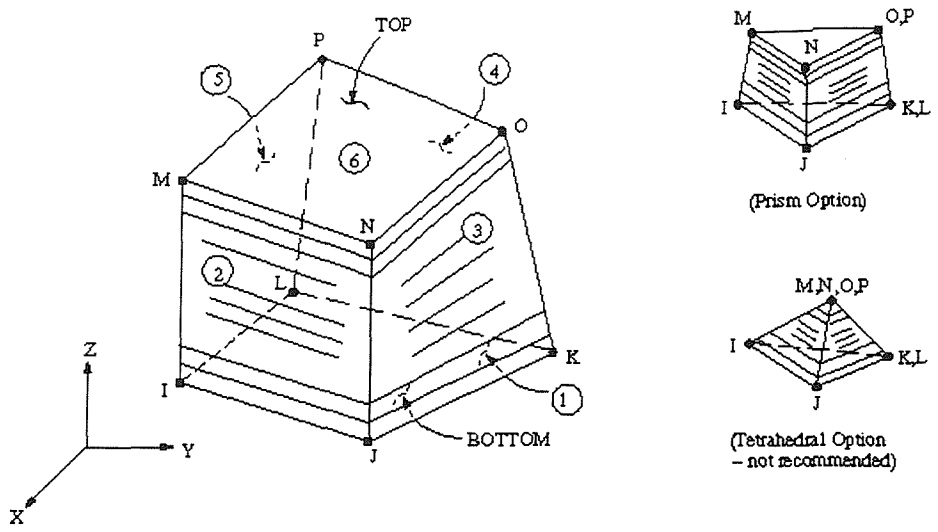

Figure 6.1 SOLID 3-D layered element [86]

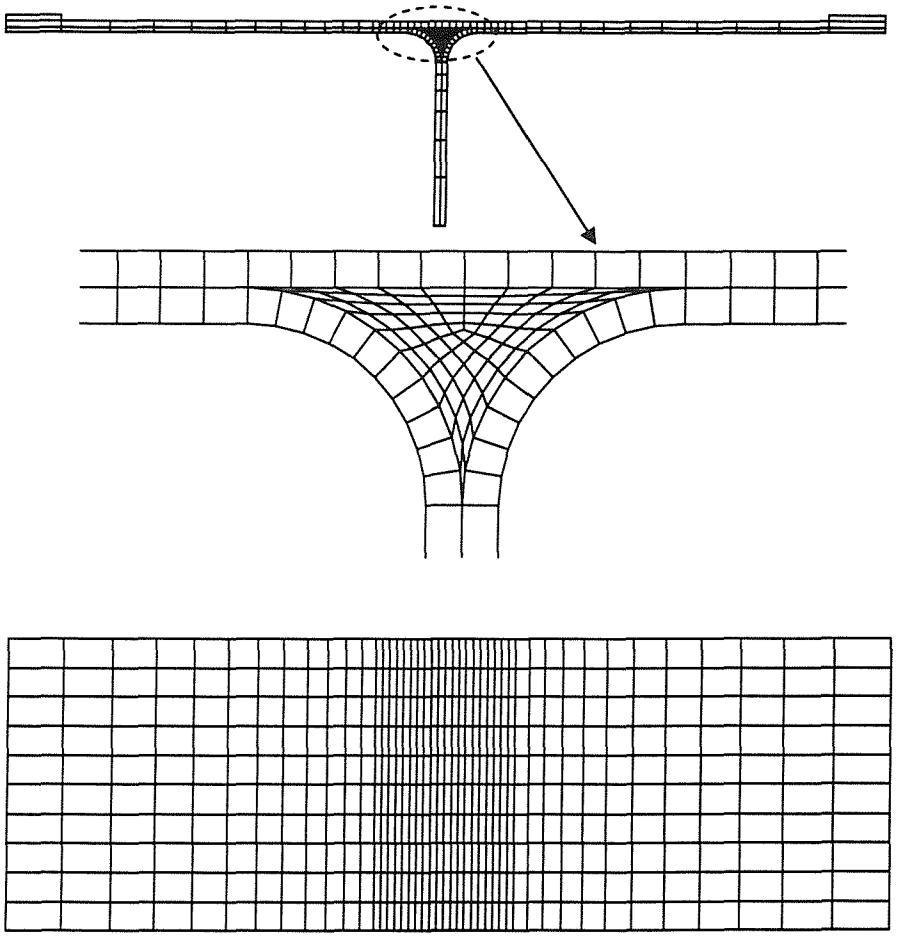

Figure 6.2 FE model of CFRP Tee-coupon with tip masses

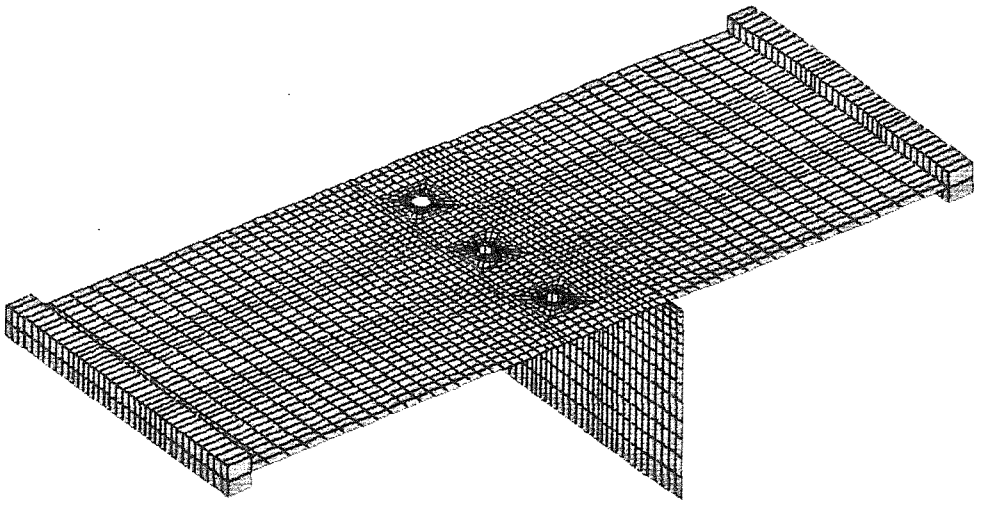

Figure 6.3 FE model of GLARE Tee-coupon with tip masses

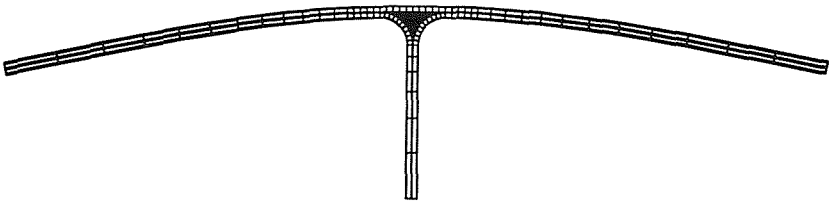

$f_1 = 419$ Hz

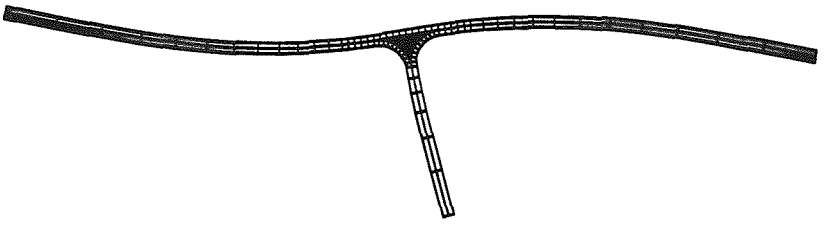

$f_2 = 971$ Hz

Figure 6.4 The first and second mode shapes of FE model of CFRP Tee-coupon (free condition)

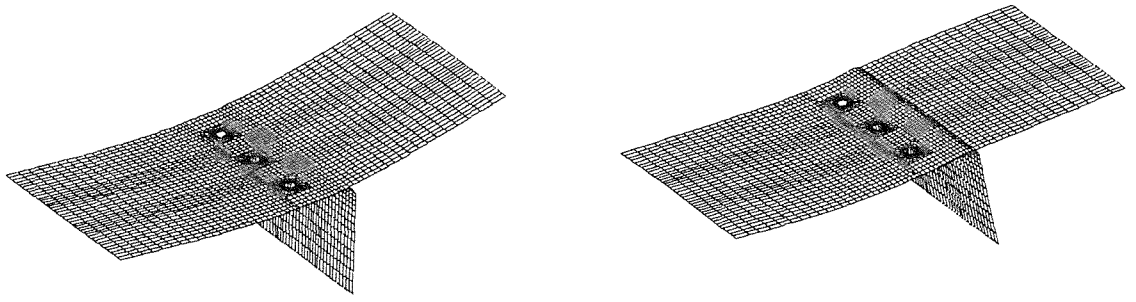

f_1 =276 Hz f_2 = 417 Hz

a) Skin panel and stringer connected at rivet position only

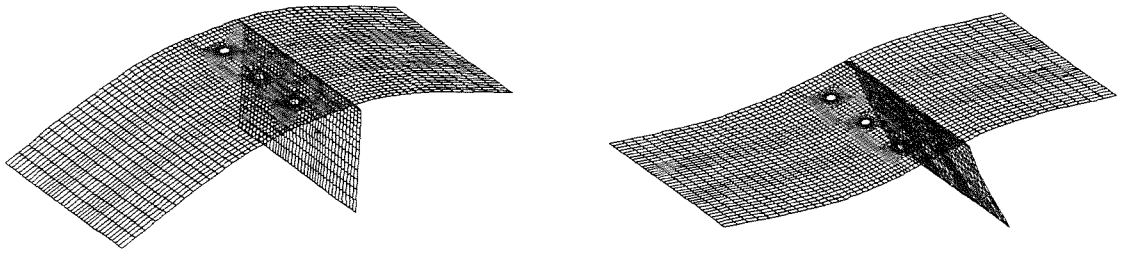

f_1 =325 Hz f_2 = 533 Hz

b) Skin panel and stringer are in perfect bonding

Figure 6.5 The first and second mode shapes of FE model of CFRP Tee-coupon (free condition)

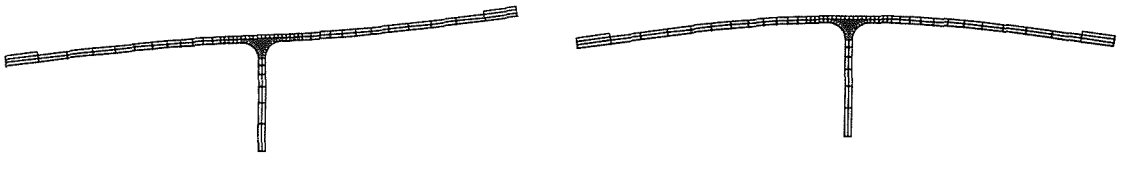

f_1 =81 Hz f_2 = 106 Hz

Figure 6.6 The first and second mode shapes of FE model of CFRP Tee-coupon (constrained by web of stringer)

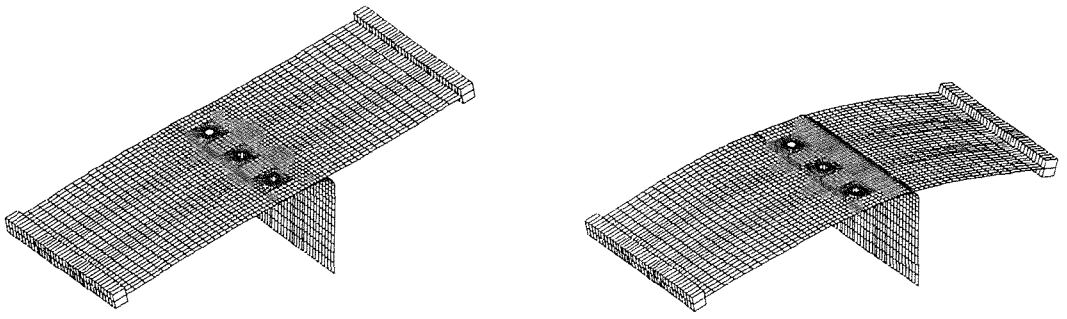

f_1 =45 Hz f_2 = 80 Hz

Skin panel and stringer connected at rivet position only

Figure 6.7 The first and second mode shapes of FE model of GLARE Tee-coupon (constrained by web of stringer)

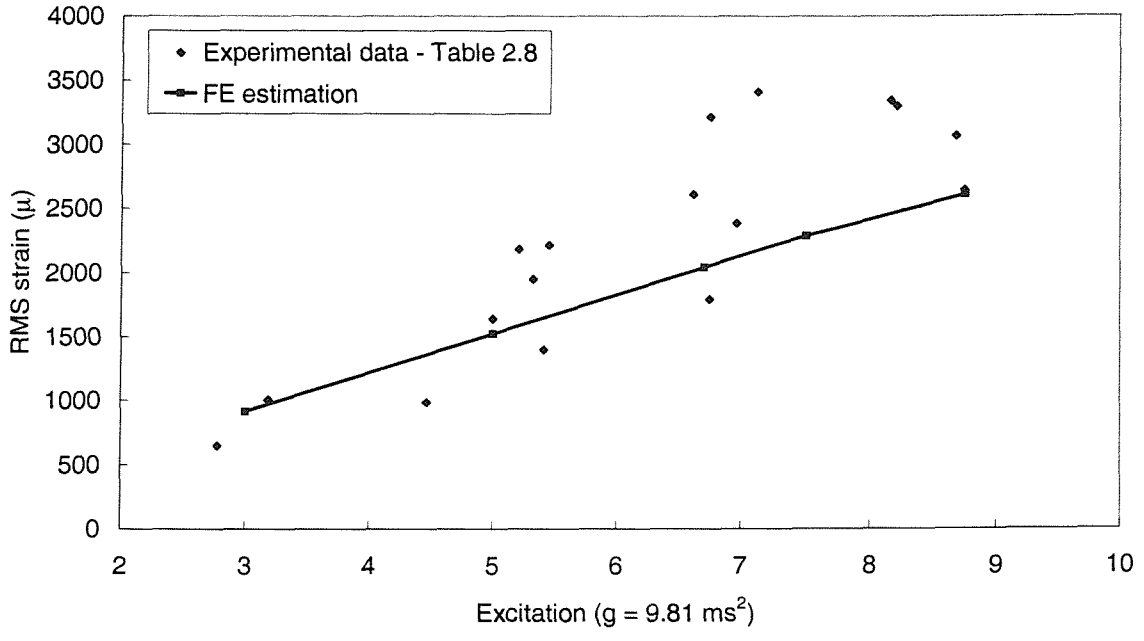

Figure 6.8 Comparison of maximum RMS strain level on the upper surface of the CFRP Tee-coupons (η = 0.021)

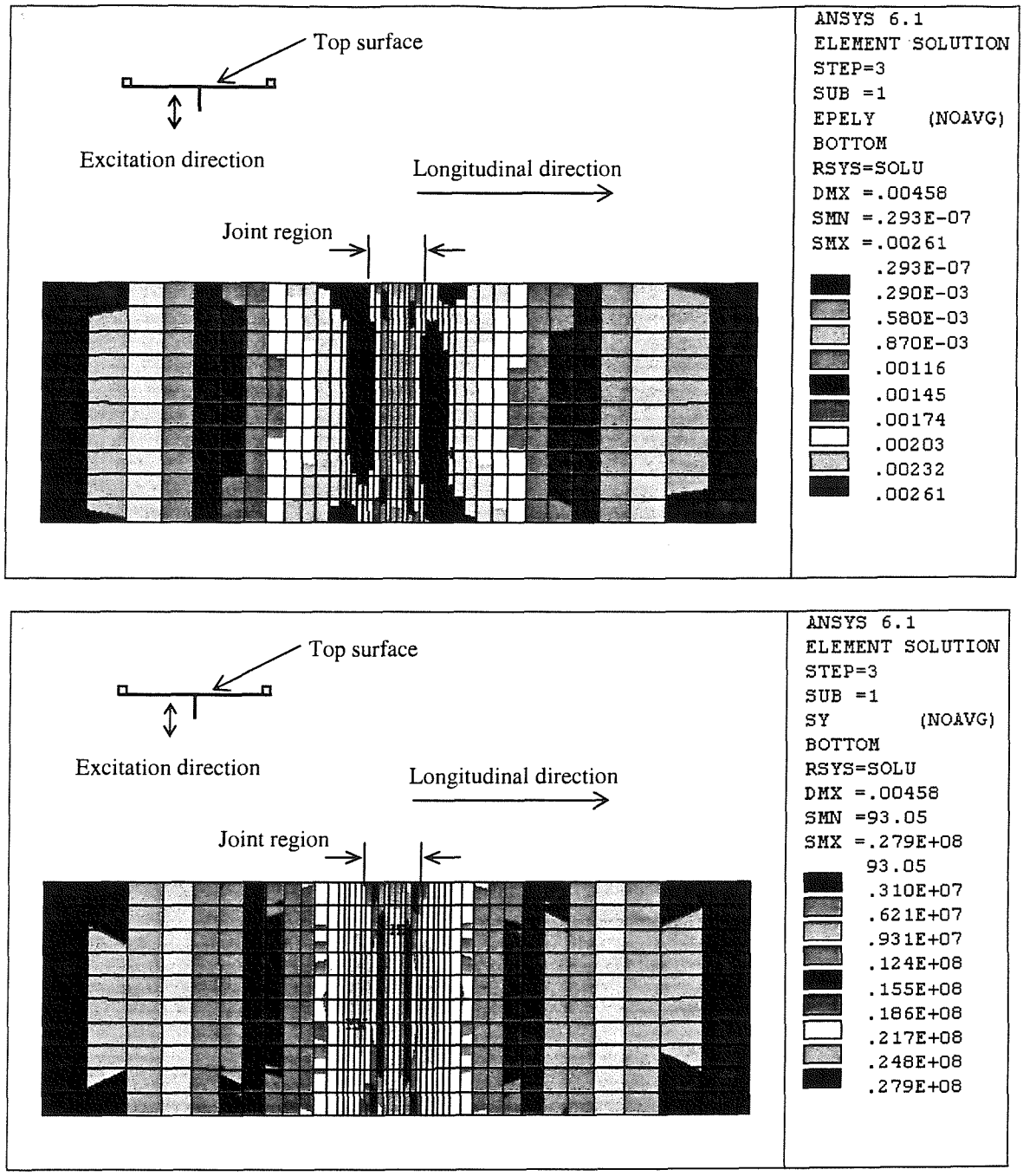

Figure 6.9 Longitudinal strain and stress distribution on the top surface of the CFRP Tee-coupons Under acceleraton excitation of 8.75g (g = 9.81 ms^2)

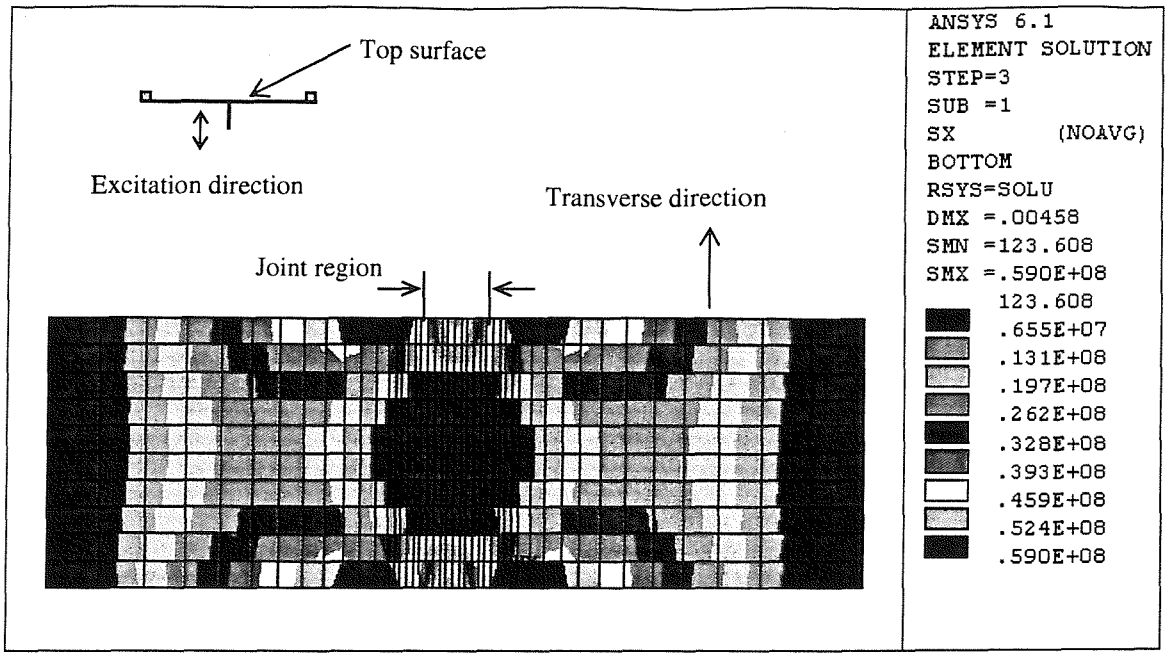

Figure 6.10 Transverse stress distribution on the top surface of the CFRP Tee-coupons under acceleraton excitation of 8.75g (g = 9.81 ms^2)

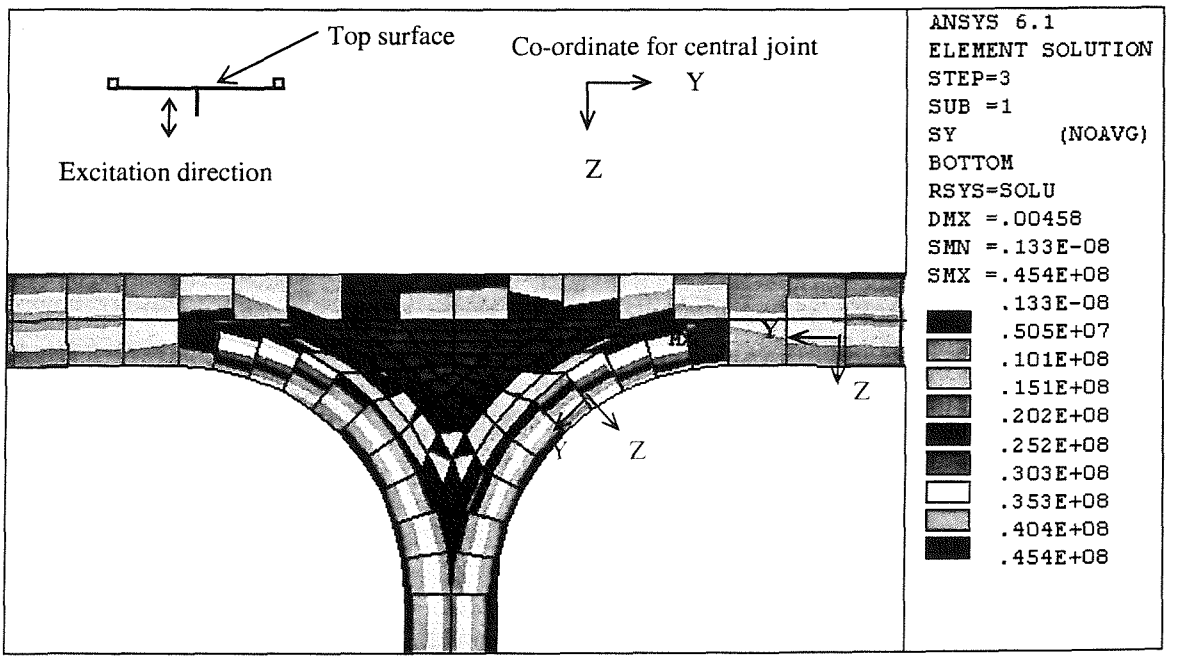

Figure 6.11 Stress Sy in the joint region of skin panel and stringer of the CFRP Tee-coupons under acceleration excitation of 8.75g (g = 9.81 ms^2) (Stresses are shown in element co-ordinates)

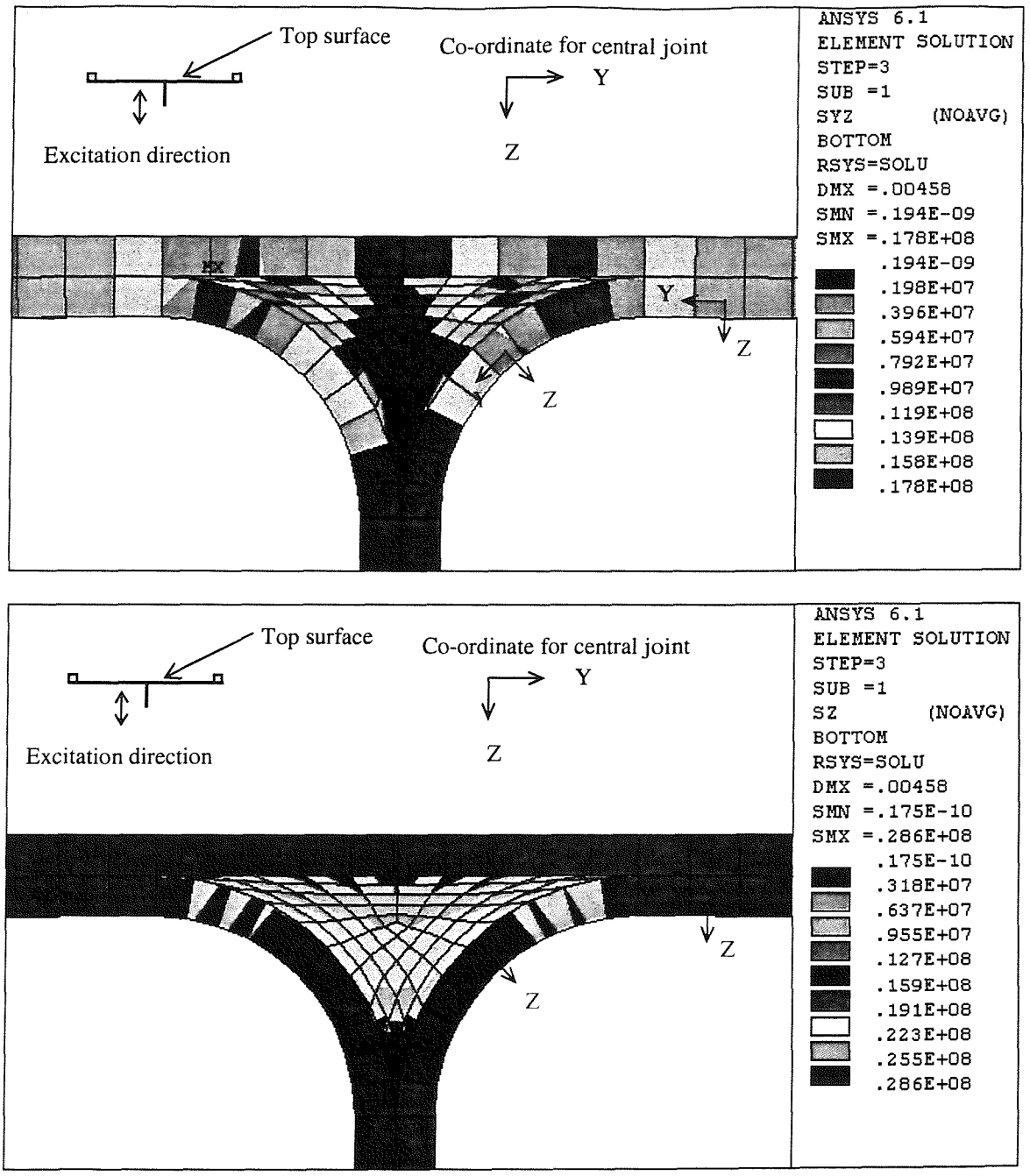

Figure 6.12 Stress Syz and Sz in the joint region of skin panel and stringer of the CFRP Tee-coupons under acceleration excitation of 8.75g (g = 9.81 ms^2) (Stresses are shown in element co-ordinates)

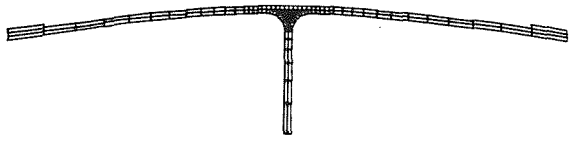

Figure 6.13 Deflection of CFRP Tee-coupon under acceleration excitation

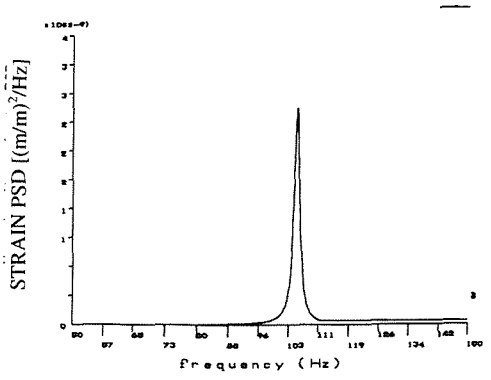

Figure 6.14 Upper surface bending Strain PSD of CFRP Tee-coupon at the maximum strain location

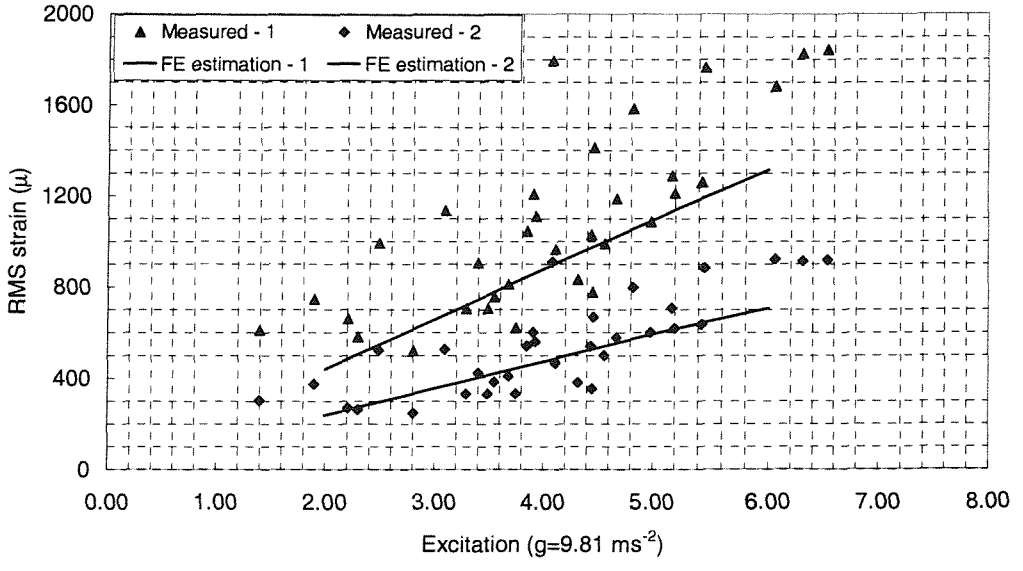

Figure 6.15 Comparison of measured and estimated upper surface RMS strain of GLARE Tee-coupons (η = 0.030)
(1 - strain gauge location 1, 2 strain gauge location 2, see Figure 2.25)

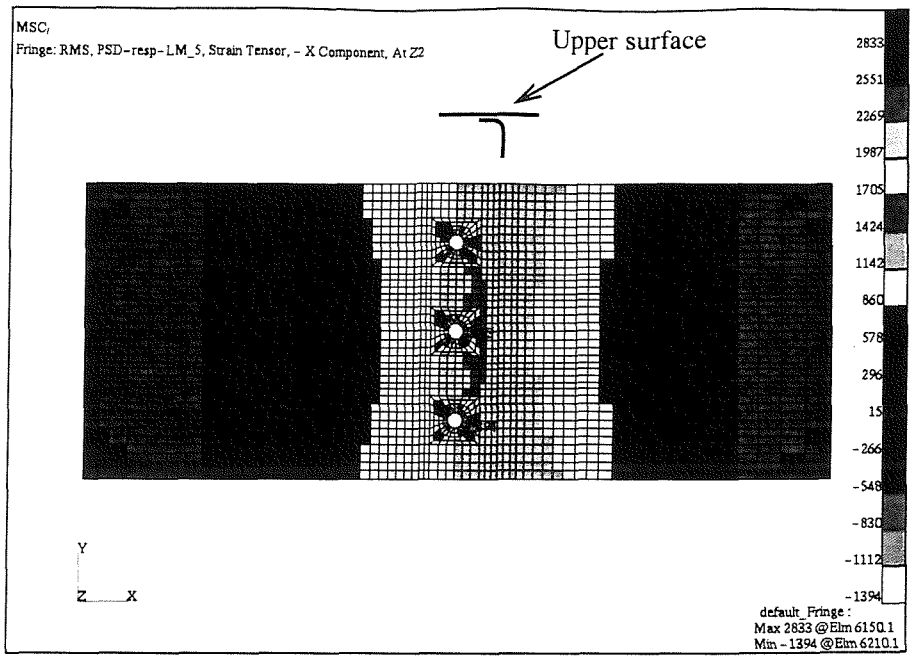

Figure 6.16 RMS strain distribution on the upper surface of GLARE Tee-coupon under acceleration excitation (RMS 6g, g=9.81 ms^{-2})

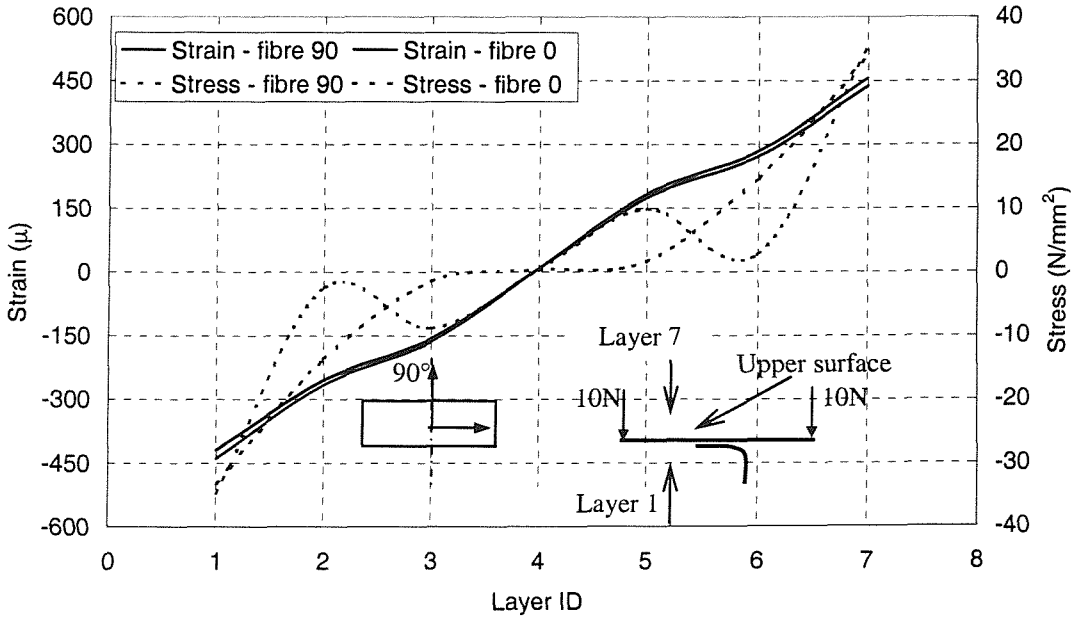

Figure 6.17 Stress and strain distributions along layers under static loading (fibre 0 - GRP lay-up 0°/90°, fibre 90 - GRP lay-up 90°/0°)

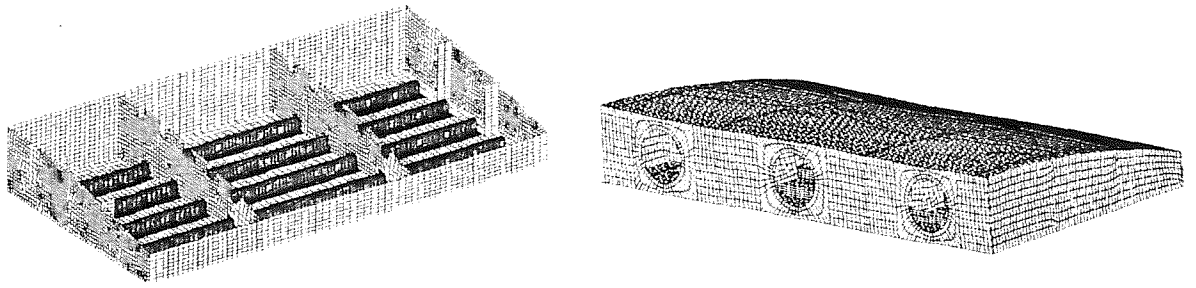

a). Aluminium alloy box without top skin b). CFRP structure

Figure 6.18 Finite element model of the box structures

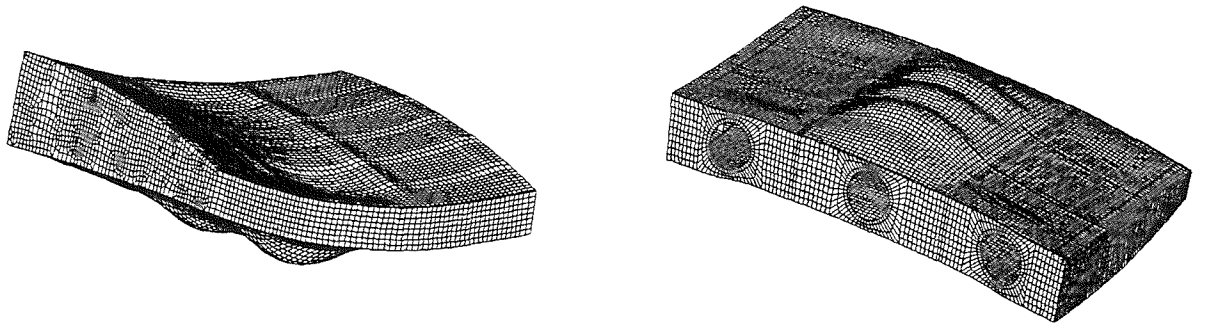

Aluminium alloy box (181Hz) CFRP box (192Hz)

a) Whole structure

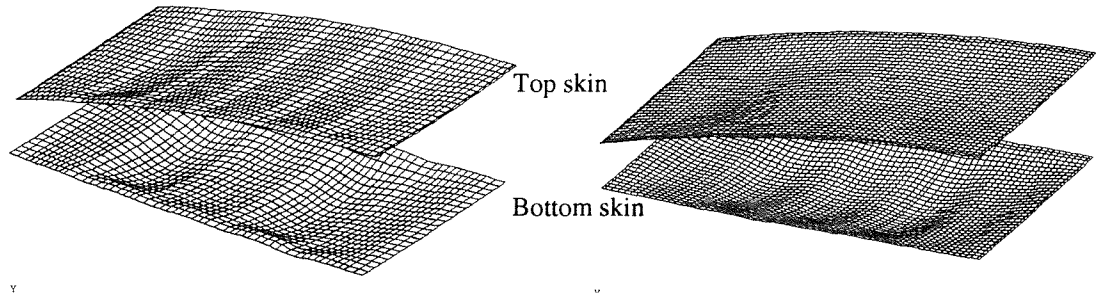

b) Middle bay

Figure 6.19 Mode shapes at the first natural frequency when constrained by two sets of 4-node points on the end ribs

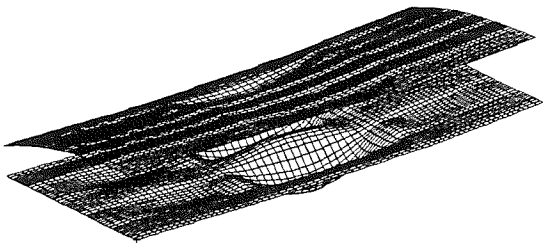

f_1=234.0 Hz

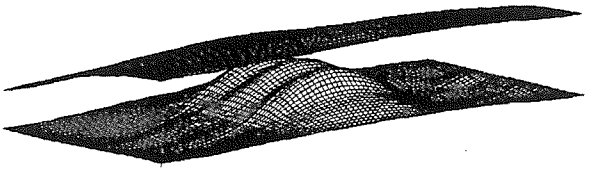

f_1=228.2Hz

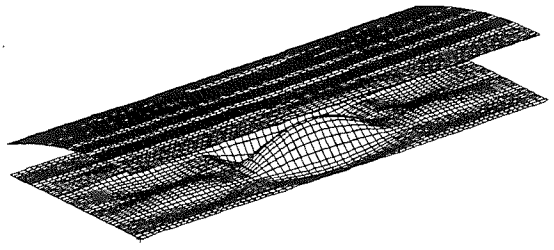

f_2=245.5 Hz

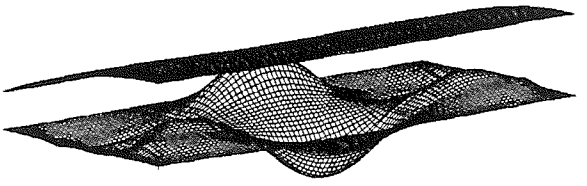

f_2=254.5 Hz

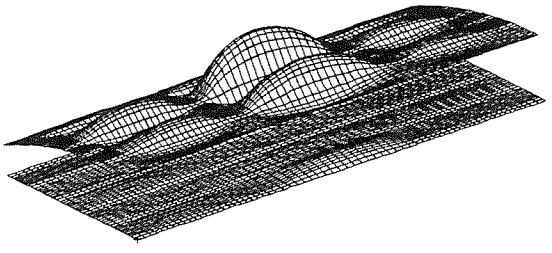

f_3=260.6 Hz

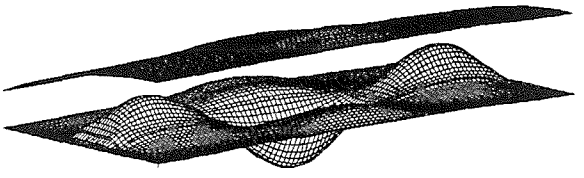

f_3=265.8 Hz

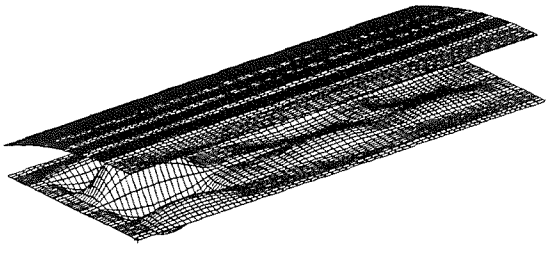

f_4=262.1 Hz

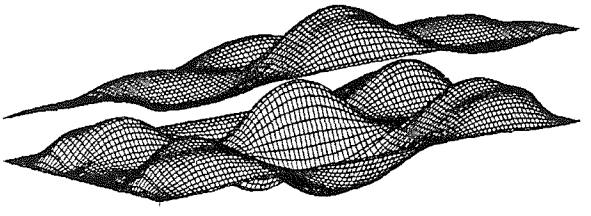

f_4=274.9 Hz

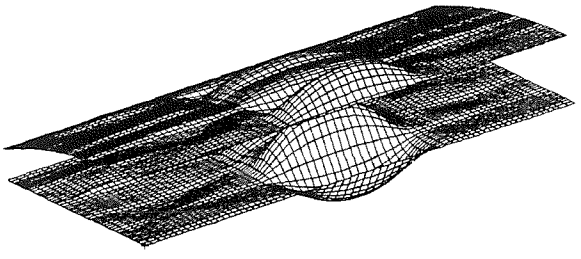

f_5=268.3 Hz

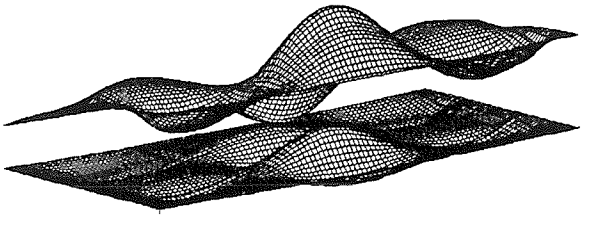

f_5=285.1 Hz

Aluminium alloy box **CFRP box**

Figure 6.20 Mode shapes at various natural frequencies when constrained by two sets of 4-node points on the end ribs

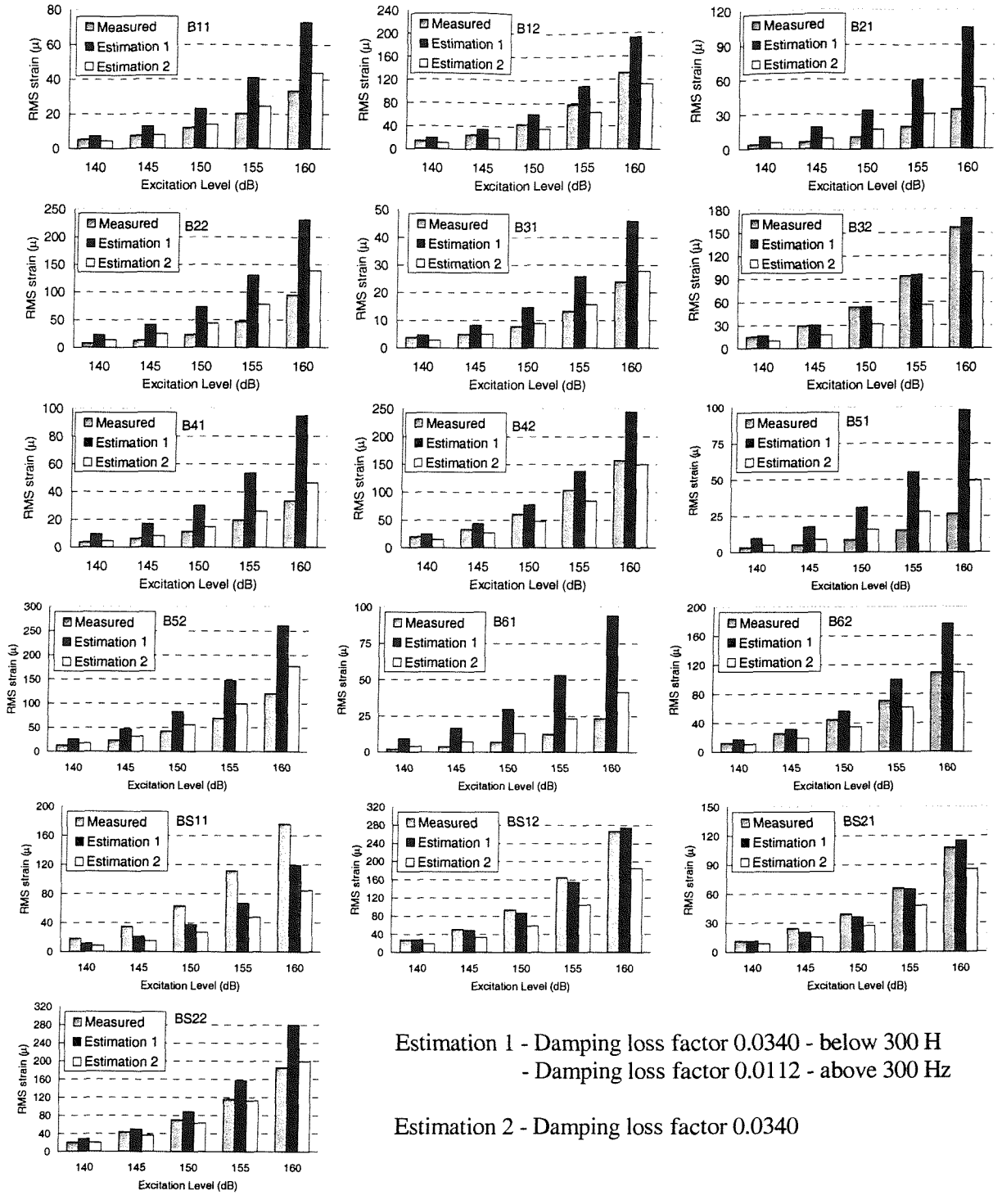

Estimation 1 - Damping loss factor 0.0340 - below 300 H
- Damping loss factor 0.0112 - above 300 Hz

Estimation 2 - Damping loss factor 0.0340

Figure 6.21 Comparison of measured and estimated RMS strains on the bottom skin panel of aluminium structure when excited on bottom skin panel

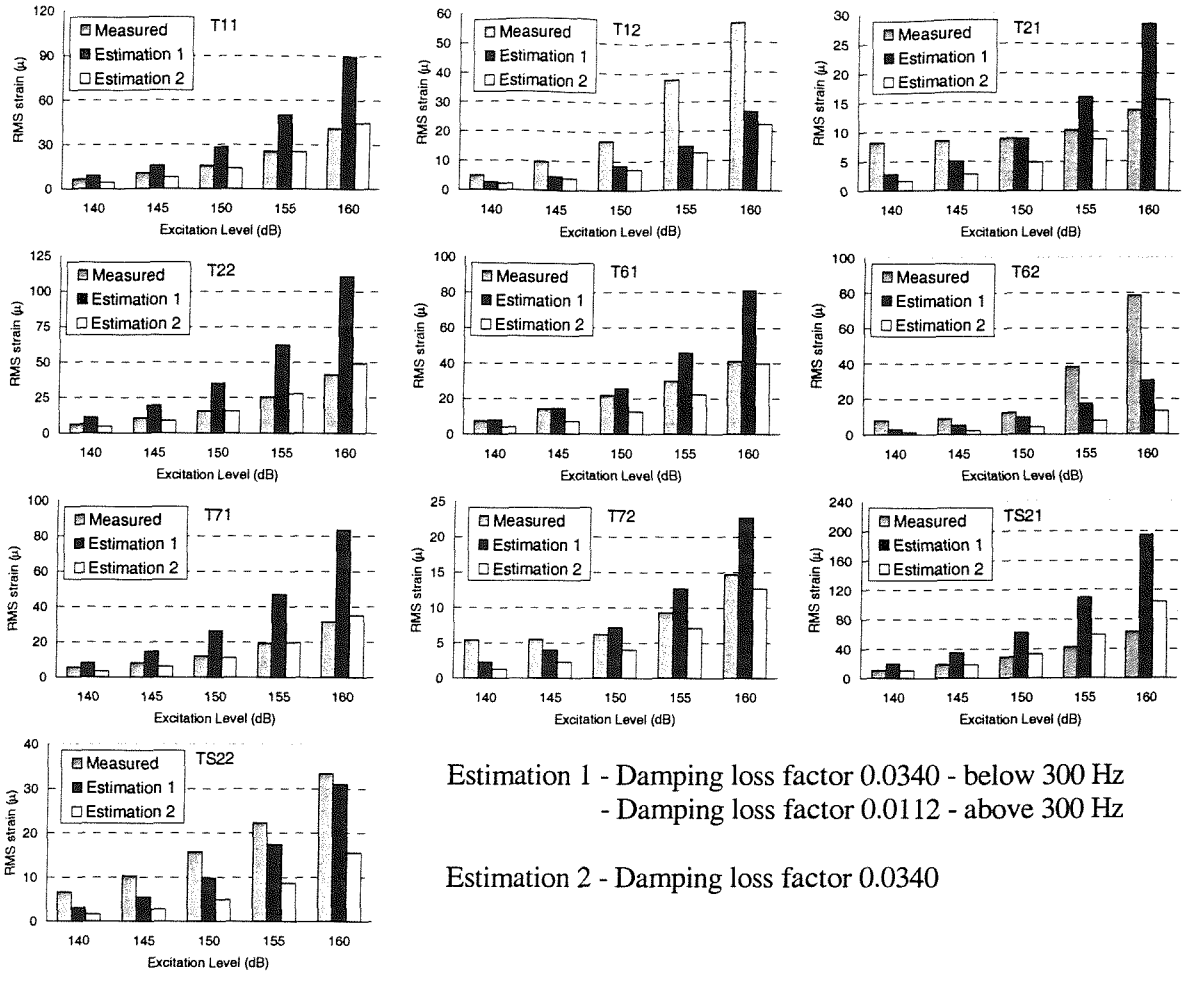

Estimation 1 - Damping loss factor 0.0340 - below 300 Hz
- Damping loss factor 0.0112 - above 300 Hz

Estimation 2 - Damping loss factor 0.0340

Figure 6.22 Comparison of measured and estimated RMS strains on the top skin panel of aluminium structure when excited on bottom skin panel

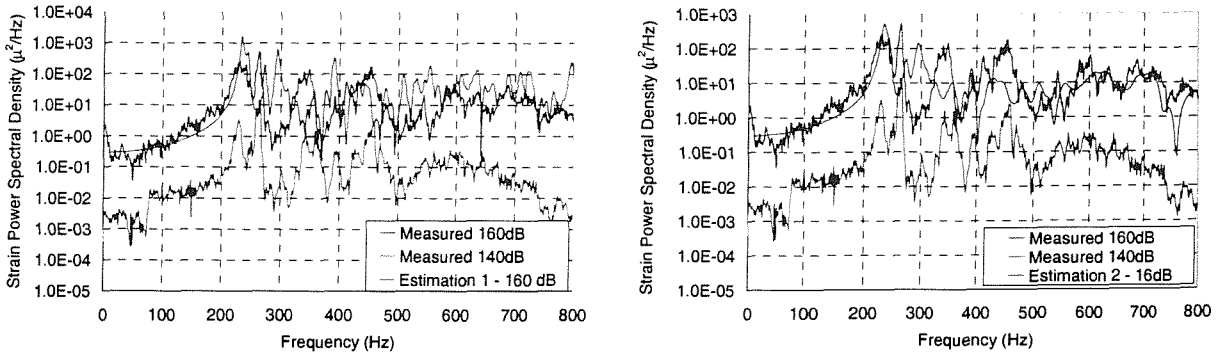

a. Estimation 1
- Damping loss factor 0.0340 - below 300 Hz
- Damping loss factor 0.0112 - above 300 Hz

RMS strain measured =131.2μ
estimated =192.3μ

b. Estimation 2
- Damping loss factor 0.0340

RMS strain measured =131.2μ
estimated =111.7μ

Figure 6.23 Strain power spectral densities at strain gauge location B12 of the aluminium alloy structure excited on bottom skin panel

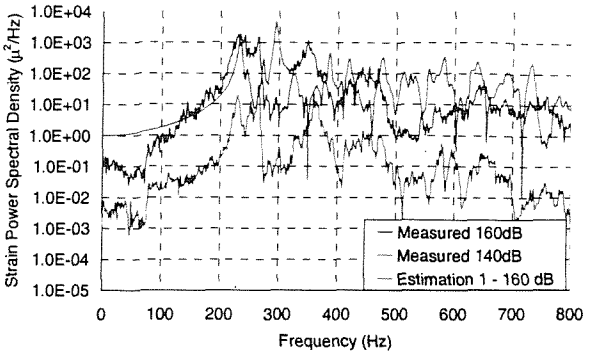

a. Estimation 1
- Damping loss factor 0.0340 - below 300 Hz
- Damping loss factor 0.0112 - above 300 Hz

RMS strain measured =266.5μ
estimated =274.5μ

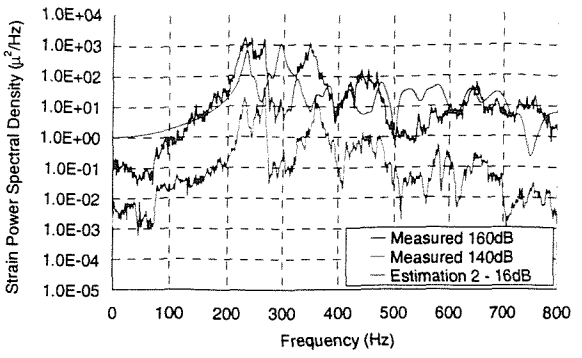

b. Estimation 2
- Damping loss factor 0.0340

RMS strain measured =266.5μ
estimated =185.2μ

Figure 6.24 Strain power spectral densities at strain gauge location BS12 of the aluminium structure excited on bottom skin panel

Damping Loss factor	Side A		Side B	
	L	T	L	T
0.034 (<300Hz) 0.0112 (>300Hz)	95.5	1357.4	77.5	1345.7
0.034	54.7	948.7	64.3	902.1

L - longitudinal T - Transverse

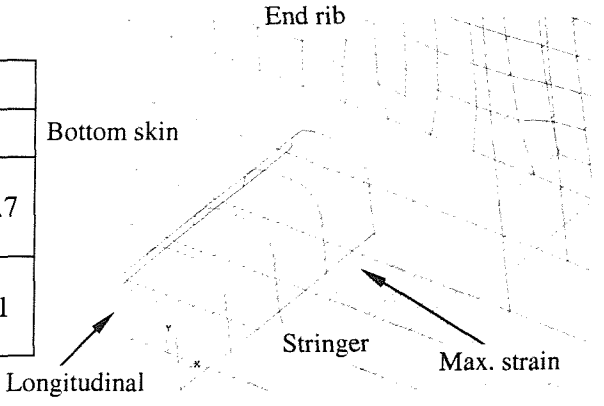

Figure 6.25 Estimated RMS strains (μ strain) at the ends of stringer No. 2 of the bottom panel at excitation level of 160 dB, FE model of aluminium structure

Damping Loss factor	Side A		Side B	
	L	T	L	T
0.034	31.2	76.9	51.0	129.2

L - longitudinal T - Transverse

Figure 6.26 Estimated RMS strains (μ strain) at the ends of stringer No. 2 of the bottom panel at excitation level of 160 dB, FE model of aluminium structure with fixed stringer ends

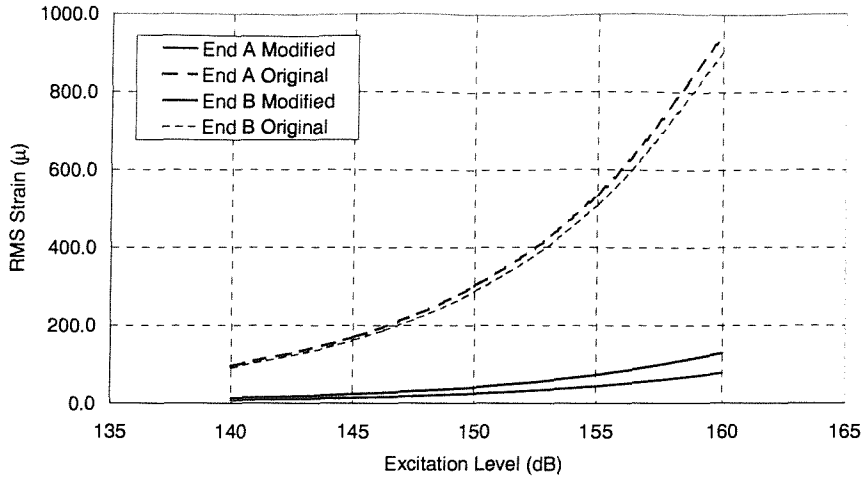

Figure 6.27 Comparison of estimated RMS strains (μ strain) at the ends of stringer No. 2 on the bottom panel of FE models of aluminium structure with free and fixed stringer ends

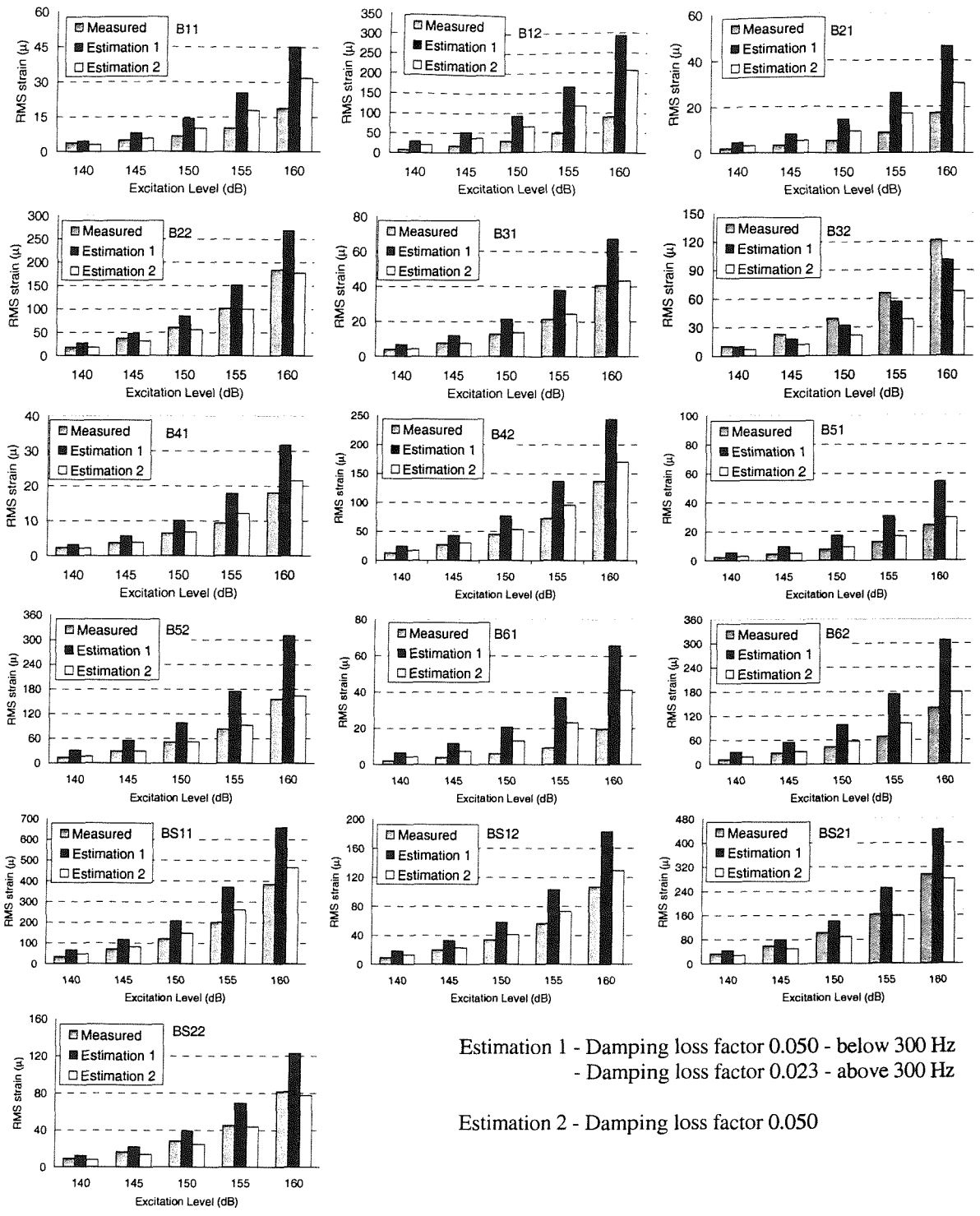

Estimation 1 - Damping loss factor 0.050 - below 300 Hz
- Damping loss factor 0.023 - above 300 Hz

Estimation 2 - Damping loss factor 0.050

Figure 6.28 Comparison of measured and estimated RMS strains on the bottom skin panel of the CFRP structure when excited on bottom skin panel

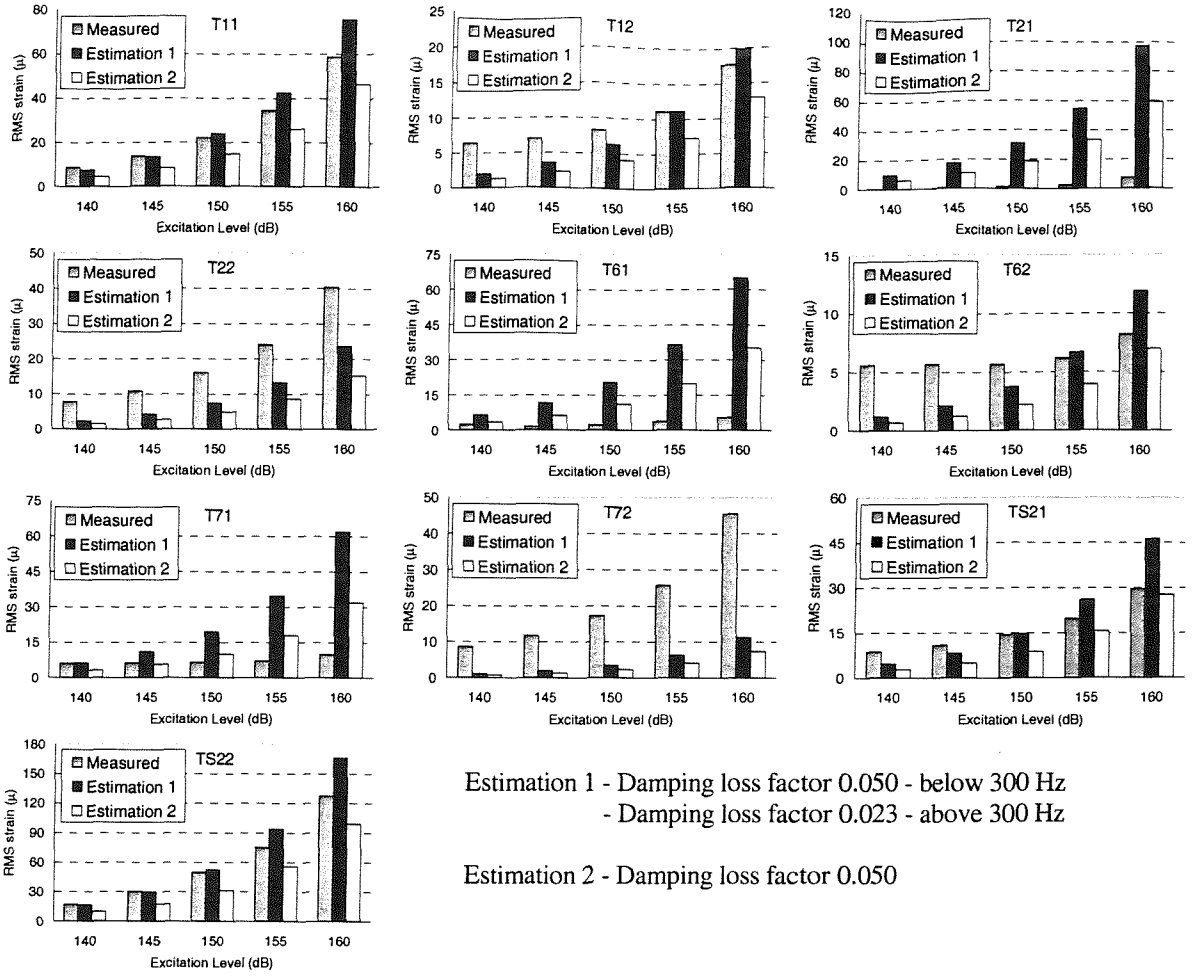

Estimation 1 - Damping loss factor 0.050 - below 300 Hz
- Damping loss factor 0.023 - above 300 Hz

Estimation 2 - Damping loss factor 0.050

Figure 6.29 Comparison of measured and estimated RMS strains on the bottom skin panel of CFRP structure when excited on bottom skin panel

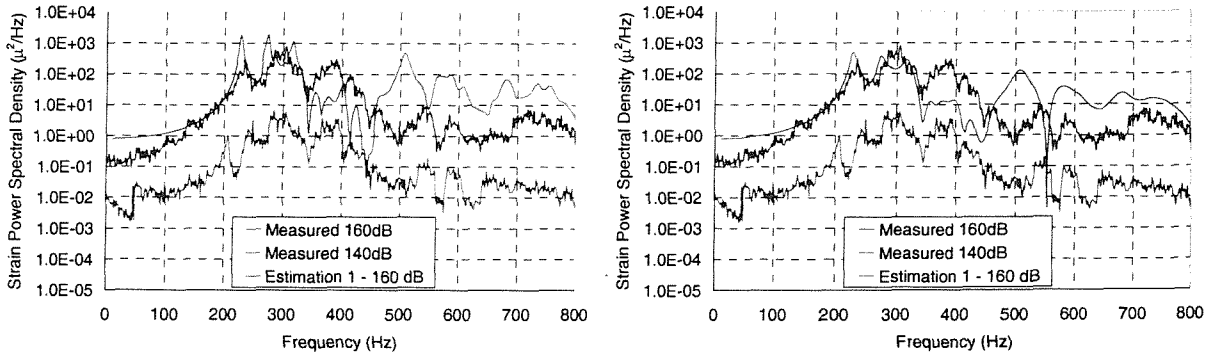

a. Estimation 1
- Damping loss factor 0.023 - below 300 Hz
- Damping loss factor 0.050 - above 300 Hz

RMS strain measured =184.0μ
estimated =268.4μ

b. Estimation 2
- Damping loss factor 0.050

RMS strain measured =184.0μ
estimated =177.1μ

Figure 6.30 Strain spectral densities at strain gauge location B22 of CFRP structure excited on bottom skin panel

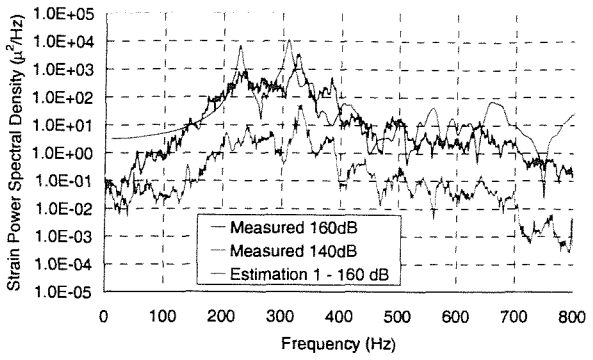

a. Estimation 1
- Damping loss factor 0.023 - below 300 Hz
- Damping loss factor 0.050 - above 300 Hz

RMS strain measured =296.4μ
estimated =444.7μ

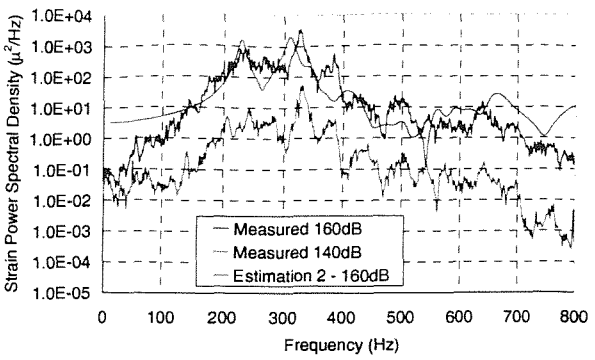

b. Estimation 2
- Damping loss factor 0.050

RMS strain measured =296.4μ
estimated =280.5μ

Figure 6.31 Strain spectral densities at strain gauge location BS21 of CFRP structure excited on bottom skin panel

CHAPTER 7

GENERAL CONCLUSIONS

7.1 INTRODUCTION

Although the acoustic fatigue problem in aircraft was addressed as early as the late 1950s, there is still a gap between theoretical analysis methods for dynamic response prediction and experimental data. This has been further complicated by increased demands for the use of composites and the development of high speed and large capacity aircraft. For wing-mounted flaps on aircraft, which are deployed behind engines, there is a particular need to develop guidelines for the design of acoustic fatigue resistant structures.

In modern wing design, leading and trailing edge devices are used to change the lift capacity of aircraft. One of the trailing edge devices is take-off and landing flaps, which are used to supply high lift at relatively low speed when they are deployed. Because all Airbus aircraft have wing mounted engines, the flaps experience very high sound pressure loading when they are deployed. The highest sound pressure level measured on the flaps of an Airbus aircraft was 155 dB. This level of excitation could result in acoustic fatigue damage of the flaps, unless they are sufficiently robust to resist high intensity pressure loading.

Box-type structures are those constructed of relatively thin stringer stiffened skins on a skeletal structure comprising a number of span-wise spars and fairly regularly spaced chordwise ribs. Besides flaps, there are other components of an aircraft structure which are also box-type in nature, such as wings, ailerons, fins and rudders. Although the direct subject of this study was flap structures, the results are applicable to all box-type structures.

The experimental work carried out involved three simplified flap-like, box-type structures made of three different materials, aluminium alloy, CFRP and GLARE, and a number of test coupons of these materials in different forms. Two types of tests were carried out on the box-type structures. First, the test structures were subjected to modal testing in order to identify basic structural properties, such as resonance frequencies, mode shapes and structural damping which is especially of importance in theoretical modelling. Secondly, the box structures were excited by high intensity acoustic loading by means of a Progressive Wave Tube (PWT), which facilitated investigation of the dynamic response of the structures to this type of excitation.

In the acoustic fatigue study of aircraft structures, estimation of the fatigue life of a component under acoustic loading is one of the important tasks. In the project, a number of test coupons were tested under simulated acoustic loading to generate S-N (strain versus number of cycles to failure) data for the composite materials (CFRP and GLARE) from which box-type structures were made.

7.2 BACKGROUND

In an attempt to summarize the state-of-art and developments in the study of acoustic fatigue in the aircraft industry, a review was presented in Chapter 1 based on the literature published on the topic. There are three factors which generally influence fatigue life estimation of aircraft structures. These are the nature of the acoustic loading, structural response analysis technique and the methods used for fatigue life estimation. Acoustic loading data, which are suitable for use in structural response analysis, are still very poor at present. So the uniform loading distribution is used for most analyses. Due to the random characteristics of acoustic loading, estimation of the structural response is very complicated. In theoretical analysis, some assumptions are used to simplify the problem, which has resulted in methods used in the ESDU Data Sheets. To cope with new problems created by composites and high pressure/temperature loading, new developments in theoretical and experimental research have occurred. Improvement of computer power has permitted the development of numerical methods. One of the most often used numerical methods is Finite Element Analysis. The factors which affect the accuracy of use of the FEA are the modelling of acoustic loading, modelling of reinforcements, more accurate representation of boundary conditions, damping

effects, mesh size, large deflection effects, etc. By the proper use of the method and consideration of these factors, the FEM can model structures with any shape and boundary conditions and defined acoustic loading. Non-linearity of structural response occurs in practice due to the high level pressure loading which drives the panel responses to large amplitudes. Some methods have been developed to analyse nonlinear behaviour of panels, but have not yet reached at a state of generally satisfactory application.

On the other hand, experimental work plays an important role in aircraft structure research and development. Coupon testing provides fatigue data for design and research purposes. Also, reverberation chamber and progressive wave tube (PWT) facilities are used for acoustic fatigue testing. The PWT is a very useful facility in which high sound pressure levels can be used, so that structures can be tested in an environment similar to actual flight conditions.

Although much work has been done to increase understanding of acoustic fatigue behaviour, more research is needed to develop improved design techniques which will be based upon improved knowledge of the behaviour of complicated structures composed of new materials. This is vital if full advantage is to be taken of new forms of construction in the aerospace industries.

7.3 COMPOSITE MATERIALS

The use of composite materials in aircraft structures has increased rapidly in the last 15 to 20 years. More and more composite components are gradually replacing aluminium alloy ones and the composites are moving from secondary structures to primary structures. Comparing with aluminium alloy conventionally used as aircraft material, the main attraction of composites is that they have low weight, high strength and stiffness, which are of importance in the development of large and high speed aircraft.

In this study, the acoustic fatigue behaviour of two types of composites were investigated, they are Carbon Fibre Reinforced Plastics (CFRP) and GLAssfibre REinforced aluminium laminates (GLARE). CFRP has been used in aircraft structures for many years and GLARE is relatively new form of hybrid material. To have a good understand to the characteristics and fatigue behaviour of the composites, a brief introduction to CFRP and GLARE was also given

in Chapter 1. The damage mechanisms and fatigue resistance of these two composites were discussed. Over the years, extensive studies have been carried out in on the dynamic behaviour and damage mechanism of CFRP material. The damage mechanisms of CFRP are in several categories, namely, matrix cracking, matrix yielding, interfacial debonding and delamination and fibre breakage or fibre pull out, etc. One or several of these damage modes could be present in CFRP before failure. The fatigue of composites is defined as the progression of the damage rather than the initiation of a crack as in metals. The presence of damage in composites has a great influence on their dynamic properties, such as stiffness, damping and natural frequency. Stiffness, and hence natural frequency, are reduced as the damage develops, which are parameters associated with fatigue and are used as criteria to define fatigue failure in the composites.

GLARE is a Fibre Metal Laminates consisting of alternating thin metal alloy sheets and unidirectional or cross-ply layers of fibre composites. Research has shown that the fibre-metal hybrid material has fatigue resistance superior to that of aluminium alloy. Crack growth rates in the fibre-metal material are much lower than those in aluminium alloys due to a mechanism called **'the fibre bridging' effect'**, i.e., a crack initiated in a metal layer is bridged by the fibres. When a crack is initiated in a metal layer, the fibres in the composite layers impose restraint on further opening at the crack tip. At the same time, unbroken fibres in the cracked area still carry the load through the crack. However, most previous studies have been based on in-plane loading; more research is needed to assess the fatigue behaviour of GLARE in flexure.

7.4 EXPERIMENTAL STUDIES

The demands for high capacity and high speed aircraft have resulted in the increased use of composite materials in aircraft structures. In this research project, flap-like box structures constructed from CFRP and GLARE, together with a conventional aircraft construction material, aluminum alloy, were investigated. Experimental studies on composite coupons were also carried out.

7.4.1 Coupon Specimen Investigation

Coupon testing is an important part of research on the acoustic fatigue of aircraft structures. Typical coupon specimens used were Tee-coupons and beam-coupons made of CFRP and GLARE materials. Coupons were designed and manufactured according to the requirements stated in ESDU data sheets No.84027 and No.72015. Two types of measurement were carried out on coupon specimens, damping measurements and simulated acoustic endurance tests

7.4.1.1 Damping measurement of the coupon specimens

Damping plays an important role in the structural response level to dynamic loading. In theoretical analysis, the accuracy of damping values used has great influence on predicted dynamic strains. Damping measurement had the objective of providing damping values of the CFRP and GLARE composites. Measurements were carried out for CFRP Tee-coupons, CFRP Tee-beam coupons, GLARE Tee-coupons and GLARE plain beams. Results have shown that the CFRP Tee-coupons had the highest average loss factor of 0.0070 among those coupons tested. The average loss factor of the GLARE Tee-coupons was 0.0038 which was 46% lower than that of CFRP coupons. The results show that the beam specimens tended to have lower damping values than Tee-coupons. The loss factor of the CFRP Tee-beams was 0.0044 and was 36% of that of the CFRP Tee-coupons. For GLARE, the beams had a loss factor of 0.0016, which is 43% lower than that of GLARE Tee-coupons. Although the GLARE coupons had a lower loss factor compared with CFRP ones, it is still higher than that of aluminium alloy due to the presence of glass fibre composite layers. During the fatigue tests of the coupons, the damping values were also measured. The average damping loss factors were measured to be 0.021 and 0.030 for the CFRP and GLARE coupons respectively in the condition of the fatigue tests. These values are much higher than those measured in free supported conditions, which are the combination of material damping, the damping due to acoustic radiation and joint friction, etc.

7.4.1.2 Fatigue tests of the CFRP and GLARE Tee-coupons

In research on the acoustic fatigue of aircraft components, one of the main test methods, for obtaining basic structural fatigue data, is the endurance testing of structural coupons subjected to simulated random loading. In the tests, specimens are excited using narrow band

acceleration excitation to produce random response as a simulation of the response of an aircraft structural panel to acoustic loading in a resonant mode. The purpose of the tests was to establish fatigue data, i.e. S (RMS strain/stress) versus N (number of cycles to failure) curves valid for random excitations of materials used in aircraft components. Detailed tests have been carried out and some conclusions were drawn.

For the CFRP Tee-coupons, fatigue damage forms observed were delamination of the skin plate and de-bonding and cracking of the joint filling. Once damage occurred, resonance frequency decreased rapidly due to the loss of stiffness. Fatigue data (RMS strain versus Number of cycles to failure) were produced for the CFRP Tee-coupons under investigation using a 2% decrease in resonance frequency or the occurrence of detectable /visible damage as the criteria for "failure".

For the GLARE coupons, the damage mechanism observed was fatigue cracking along the rivet line. Once damage occurred, the coupon resonance frequency decreased rapidly due to loss of stiffness. The 'fibre bridging effect', which could have been the most distinguishing factor in the fatigue resistance of the GLARE, was not very apparent. This may well be due to the lay-ups of the composite layers in the specimens tested in this project, for which the fibres in the layers next to the outer aluminium layer were parallel to the fatigue crack rather than perpendicular to it. The conclusions from the fatigue testing of GLARE coupons have highlighted the possible problem regard the use of GLARE for areas under flexural loading, but it is not a definite and general conclusion concerning GLARE structures. GLARE is a relatively new composite, there are not enough experimental data, especially for the GLARE coupons under flexural loading conditions, available to precisely characterise its fatigue behaviour.

7.4.2 Box-Type Structure Tests

The test specimens used were the three flap-like box-type structures designed and manufactured by British Aerospace Airbus Ltd. These are representatives of aircraft flaps and were constructed from three different materials, aluminium alloy, CFRP composite and GLARE laminates. These boxes consist of one flat (bottom) and one curved (top) stringer stiffened skin panel together with front and rear spars and inner ribs which divide the structures into three bays. Boxes were built in the same way with the same external

dimensions, The aluminium alloy and GLARE structures were of almost exactly the same dimensions with Z-shaped stiffeners, which were connected to the skins by rivets. The CFRP structure was slightly different in the dimensions of the three bays from the other two structures and had integral stiffeners (I-shaped). The skin panels, ribs and spars were all connected by riveting.

To understand the dynamic characteristics of the three structures described above. Two types of experimental studies were carried out: Experimental modal analysis and acoustic endurance tests

7.4.2.1 Experimental modal tests

Tests were carried out on the box-type structures to identify the basic structural properties, such as mode shapes, resonance frequencies and damping values. The objective was to provide modal data, which could be used to verify theoretical models for the prediction of response to random acoustic loading, incorporating measured damping data. Results show that stiffened skin panels behave like an un-stiffened panel at low frequency where the stiffeners are mainly subjected to bending deformation, i.e., global modes dominate. At high frequency, each bay between stiffeners vibrates essentially as a simply supported plate, i.e., localised modes dominate, and the stiffeners are mainly in torsion.

The modal damping ratios were obtained, which showed that the CFRP box structure had the highest damping ratios and the aluminium alloy structure had the lowest damping values among the three box structures. Typical damping ratios for the CFRP, GLARE and aluminium alloy structures are 1.14%, 0.71% and 0.55% respectively. These values are much higher than those obtained from coupon tests mentioned above.

7.4.2.2 Acoustic excitation tests

Acoustic excitation was carried by means of the Progressive Wave Tube (PWT). To simulate the acoustic loading on aircraft components, the PWT is designed to produce a high intensity sound pressure field in the test section where a test structure is mounted in an opening in the wall. The tube is driven by a siren via a horn and can produce an overall Sound Pressure Level up to 163 dB at the test section. First, a series of sound measurements were carried out to characterise the acoustic pressure field at the test section of the PWT. It was found that the

sound pressure field has an approximately uniform spectral density in the frequency band from 80 Hz to 600 Hz. Sound pressure level is controllable in the range of 135 dB to 163 dB. The sound pressure field is uniformly distributed in amplitude around the test section but spatial phase change occurs in the direction along the axis of the PWT. The phase difference can be written as $2\pi fx/V$ ($V = 341 ms^{-1}$ is the speed of sound in the PWT along its axial direction). Three structures were excited on their flat and curved skin panels from 140 dB to 160 dB (or higher) in steps of 5 dB with random acoustic loading of bandwidth from 80 Hz to 800 Hz. The responses of the structures to the acoustic loading were measured by a number of strain gauges. These gauges were installed inside the structures at various locations of interest.

The CFRP structure had the highest strain response to the acoustic loading compared with other two structures. The strain response levels of Aluminium alloy and Glare structures were similar but with some differences. Stiffeners of all three structures showed high strain levels. For the stiffeners of the aluminium alloy and GLARE structures, maximum strain was in the transverse direction to the length of the stiffeners, which indicates that the stiffeners responded mainly in torsion during acoustic excitation. For the CFRP structure, the maximum strain on a stiffener was in the longitudinal direction along the length of the stiffener, which means that stiffeners were mainly undergoing bending deformation during acoustic excitation.

Non-linear relationships between excitation levels and RMS response strains at various locations of the test structures were observed, especially for the aluminium alloy and GLARE boxes. When the structures were excited on one skin panel, the other skin panel and inner ribs all showed relatively high strain response, which indicates coupling of the top and bottom skins. The bottom skin showed higher response level when excitation was on the top skin than top skin when excitation was on the bottom skin panel. Of three boxes, the maximum responses of the bottom skin panels were 61%, 122% and 125% of the maximum strain values found on the top skin panels for aluminium alloy, GLARE and CFRP structures respectively. For excitation on the top skin panels, the ratio of the highest strains between top and bottom skin panels were 50%, 28% and 32%, which were lower compared with those for bottom excitation cases, but still were not negligible. The response levels of inner ribs for three boxes were of similar level and were also relatively high. These emphasis the coupling effect of various components of box structures.

As the excitation level increased, strain energy redistributed in the frequency band of interest, i.e., the response of higher frequency modes enhanced, and their contribution the total strain therefore became more significant. This phenomenon was seen in all three test structures, but was more evident for the GLARE and aluminium alloy structures, especially when the boxes were excited on their flat skin panels. For example, when excited on the bottom skin of the aluminium alloy box, for strain response of the bottom skin, the first two resonance peaks between 200 Hz to 300 Hz were account for the 58% of total strain measured at 140dB, but reduced to 45% at 160dB. The difference in the resonance frequencies were found when panels were directly or indirectly excited. When the bottom skin of the GLARE box was directly excited, the response peak at one measuring location on the bottom skin was about 430 Hz, but only a 400 Hz peak in the same location was seen when the top skin was excited. It indicates that higher response level could lead to non-linear response. As excitation increased, adjacent individual frequency peaks tended to coalesce to form broad peaks. Results for the CFRP box showed less peaky resonance peaks due to high damping. These behaviours, such as peak broadening, resonance frequency shifting and strain energy redistribution, of the test structures are indication of the existence of non-linear dynamic behaviour. Statistical characteristics of strain responses were also investigated, very low levels of non-Gaussian behaviour were found at higher excitation levels.

After all the strain measurements had been completed, the three structures were subjected to acoustic fatigue endurance tests. The random excitation was applied to the bottom skin panel at an overall sound pressure level of 161dB with bandwidth from 80 Hz to 800 Hz. The structures were inspected at intervals during endurance tests using an endoscope to trace the propagation of fatigue cracks. Total endurance times for the three structures were 521 (aluminium alloy), 588 (GLARE) and 536 (CFRP) minutes respectively.

For both aluminium alloy and GLARE structures, acoustic fatigue cracks were found after a short time. Fatigue crack growth rates and paths were recorded. Most of the cracks were found in the two side bays of these two structures. Rivet snap was another damage mechanism observed. But no visible fatigue damage was seen in the CFRP structure.

It can be concluded that the CFRP structure had superior fatigue resistance compared with the GLARE and aluminium alloy structures. No visible fatigue damage found in the CFRP structure apart from a few original rivets snapping during the endurance tests. For the

aluminium alloy and GLARE structures, fatigue cracks located in the stiffeners of both side bays started at an early stage of the endurance tests. Due to the existence of glass fibre composites, the growth rates of fatigue cracks in the GLARE structure were lower than those in the aluminium alloy structure. Some rivets connecting the inner ribs and bottom skin panel of the aluminium alloy structure failed. This behaviour did not occur in the GLARE structure. For both aluminium alloy and GLARE structures, longer fatigue cracks occurred in the "down stream" bay.

Types of acoustic fatigue failures in the aluminium alloy and GLARE structures have been recorded. Crack propagation rate data are also presented. From the endurance testing carried out, it appears that for the box-type structures of the form used in this work, the CFRP structure was the most acoustic fatigue resistant followed by the GLARE structure, the aluminium alloy structure being the least fatigue resistant. It must be noted, however, that only visual inspections were carried out during the tests, no NDT examinations were made for the CFRP structure.

7.5 FATIGUE LIFE PREDICTION OF BOX STRUCTURES

Fatigue life prediction formulae based Miner's accumulation theory and fatigue data of CFRP and GLARE from the coupon tests has been derived, which uses a broadband approach and took into account the frequency distribution of the strain responses. It was found that fatigue life of the boxes was very sensitive to the change of response level, and frequency distribution of strain spectral density has strong influence on the fatigue life. These formulae could give a good indication of the fatigue life at the joint line of skin and stiffener. In the situation of lack of fatigue data in other locations of the test structures, these formulae could also be used to give a quick estimation of fatigue. At the design stage, these formulae can be used with predicted response spectra to predict the fatigue life and serve as a initial design guide. However, it should be noted that an unrealistic fatigue life could be produced due to the lack of valid fatigue limit data in the S-N curves when these formulae are used to estimate the fatigue life of a structure with very low response levels.

7.6 FINITE ELEMENT ANALYSIS OF COUPONS AND BOX STRUCTURES

Finite element analysis was used to predict the natural frequencies, mode shapes and response to the acoustic loading of both coupon specimens and box structures.

7.6.1 Finite Element Analysis of the Coupon Specimens

The finite element analysis of CFRP and GLARE coupons was carried out in two ways. First it was used to predict the natural frequencies and response to simulated acoustic loading. The results were used together with the preliminary test results can set up the fatigue tests procedures. The experimental data then were used to verify and improve the predictions. It was found that finite element analysis of the coupons can give relatively accurate estimation of the resonance frequencies, especially the for the CFRP coupons. For the GLARE coupons, connection between the skin panel and stringer has great effect on the estimation. In the prediction of RMS strain to random exaction, finite element prediction can have good agreement with measurements provided that suitable damping values are used. The stress and strain distributions obtained from finite element analysis can provide clear explanations of fatigue damage mechanisms.

7.6.2 Finite Element Analysis of Box Structures

For the box structures, because of the similarity of the aluminium and GLARE structures, only the finite element analysis results for aluminium and CFRP structures are presented in this thesis. Both normal mode and response analyses were carried out. A travelling wave with constant pressure amplitude but varying phase angle was applied to the bottom skin panel of the structures. The damping ratios measured by modal tests were used and resulted in overestimation of structural response. By increasing the damping value, the difference between measurements and estimation reduced. The estimated strain spectral density distributions were also compared with measured results, good agreement was achieved. This is because that it is has been proved that damping of modes of test structures when mounted in a PWT will be higher.

The analyses carried out in this thesis have shown that the finite element method is a very useful tool in the estimation of structural response to random excitation. Good predictions can be made by correctly applying the loading, the boundary conditions and damping.

7.7 SUGGESTIONS FOR FURTHER WORK

The comprehensive experimental and finite element studies carried out in this research have given detailed information on the dynamic characteristics of box type structures as representative of aircraft flaps. These results combined with the fatigue data obtained from coupon tests can be used to estimate the fatigue life of this type of structure. It has been shown that CFRP is the best choice as the most acoustic fatigue resistant material. GLARE has shown limited advantage over aluminium alloy in the type of structure examined in relation to acoustic fatigue. Findings and conclusions drawn from this project have formed a good foundation for further research to be carried out in the understanding of structural behavior of box structures especially those of composite materials. Further studies need to be carried out towards the development of a practical guide for use by industry. Below are some suggestions for further developments

1. Experimental studies on the GLARE coupon specimens and box structure have found that the fatigue resistance of the GLARE material was not as high as expected. The failure observed during the acoustic endurance tests pointed to the unfavourable lay-up in the composite layer, which results in failure of the "bridging effect" of the glass fibres. Further detailed study should be carried to confirm this finding

2. Further fatigue testing needs to be performed on glare coupons under bending loading. In most published literature, the fibre bridging effect was found to be effective when the specimens are under in-plane loading.

3. The fatigue damage found in the aluminium and GLARE box structures was in the ends of stringers. This was due to the poor design of the stringers, which were free at their ends, this was not very representative of the practical case. Finite element analysis has shown that by constraining the stringer ends, strain level in the structure decreased dramatically. The fatigue results from the GLARE and aluminium alloy boxes emphases that good structural design is of importance in the fatigue resistance

of box-type structures. A further study could be carried out on modified structures.

4. Finite element analysis has proved to be useful and can produce reliable estimates of structural response to a certain degree. The results, however, are dependent on the assumptions made concerning boundary conditions, loading and damping. Hence the development of a database, which provides the input for the finite element analysis, based on experimental results would be useful.

5. To accurately monitor the initiation and development of fatigue damage, a reliable and practical method or equipment are needed. In the investigation of the box structures, damage was only recorded when it became visible. Coupon tests have shown that the damage in the CFRP coupons occurred mainly in the joint region of the top 8 and bottom layers which formed the stringer. No method was available for ascertaining if damage initiated in the CFRP box unless it propagated into the surface. This will affect the accuracy of fatigue life estimation.

6. To reflect the multi-mode response nature of box-type structures, a fatigue life prediction method, which takes into account the contributions from not only the amplitude distributions but also frequency composition of the structural response, needs to be developed.

REFERENCES

[1] Kirkby W T, et al, 'Design Against Fatigue - Current Trends', *Aeronautical Journal of the Royal Aeronautical Society*, Vol. 84, No. 829, pp1-12, January 1980.

[2] Liebowitz H, 'Fracture mechanics of aircraft structures', AGARDograph No.176, 1974.

[3] Green P D, 'Current and Future Problems in Structural Acoustic Fatigue', AGARD-CP-549, September 1994, p1-1.

[4] Richards E J and Mead D J, Noise and Acoustic Fatigue in Aeronautics, John Wiley & Sons Ltd, 1968.

[5] ESDU Engineering Data: Acoustic Fatigue Series

Volume 1	General
	Endurance under acoustic loading
Volume 2	Loading actions
	Damping
Volume 3	Stress/Strain response of plate structures
Volume 4	Natural frequencies of plate structures
Volume 5	Natural frequencies of shell structures
Volume 6	Natural frequencies of sandwich panels and box structures.

[6] Rudder F F and Plumblee H E, 'Sonic Fatigue Guide for Military Aircraft', AFFDL TR-74-112, February 1975.

[7] Mixson J S, 'Overview of Acoustic Fatigue activities at NASA Langley Research Centre', Proceedings of the third international conference on recent advances in structural dynamics, pp573-591, July 1988.

[8] Clarkson B L, 'Review of Sonic Fatigue Technology', NASA Contractor Report 4587, April 1994.

[9] Vaicaitis R, 'Nonlinear Response and Sonic Fatigue of National Aerospace Space Plane Surface Panels', *Journal of Aircraft*, Vol.31, No.1, January - February 1994.

[10] Thompson A G R, 'The estimation of near field sound pressure levels due to jet noise in acoustic fatigue design', AGARDograph 162, 1972.

[11] Willis C M, Schoenster JA and Mixson JS, 'Acoustic loads on upper-surface-blown powered-lift systems', *Journal of Aircraft*, Vol.15, 1978.

[12] Miles J W, 'On structural fatigue under random loading', *Journal of the Aeronautical Sciences*, 21:753-762,1954.

[13] Powell A, 'On the fatigue failure of structures due to vibrations excited random pressure fields', *The Journal of the Acoustical Society of America*, 30(12):1130-1135, 1958.

[14] Clarkson B L, 'Stresses in skin panels subjected to random acoustic loading', *The Aeronautical Journal of the Royal aeronautical Society*, 72:1000-1010, 1968.

[15] White R G, 'Developments in the acoustic fatigue design process for composite aircraft structures', *Composite Structures*, Vol. 16, pp171-192, 1990.

[16] Holehouse I, Sonic fatigue design techniques for advanced composite aeroplane structures, Ph.D Thesis, ISVR, University of Southampton, 1983.

[17] Holehouse I, 'Sonic fatigue design method for the response of CFRP stiffened-skin panels', Proceedings of the second international conference on recent advances in structural dynamics, pp787-798, April 1984.

[18] Holehouse I, 'Sonic fatigue of diffusion-bonded titanium sandwich structure', AGARD CP-113, September 1972.

[19] Robinson J, 'Element evaluation - a set of assessment points and standard tests', Finite Element Methods in the Commercial Environment, Robinson and Associates, Wimborne 1978.

[20] Lindberg G M, 'Accurate finite element modelling of flat and curved stiffened panels', AGARD CP-113, Sept. 1972.

[21] Climent H and Casalengua J, 'Application of the PSD technique to acoustic fatigue stress calculations in complex substructures', AGARD CP-549, Sept. 1994.

[22] Green P D and Killey A, 'Time domain dynamic finite element modelling in acoustic fatigue design', Proceedings of 6th International Conference on Recent Advances in Structural Dynamics, pp1007-1026, July 1997.

[23] Tougard D, BRITE-EURAM Programme: ACOUFAT acoustic fatigue and related damage tolerance of advanced composite and metallic structures', AGARD-CP-549, Sept. 1994.

[24] Koenig K, 'Limits of representative acoustic fatigue prediction', 17th Symposiums of International Conference on Aeronautical Fatigue, ICAF 93, 9-11 June 1993, pp127-145.

[25] Newman J C, Jr, 'Fracture analysis of stiffened panels under biaxial loading with widespread cracking', AGARD-CP-568, Dec.1995.

[26] Gordon R W, 'Modelling a local structural area using artificial boundary stiffness', AIAA paper 94-1470-CP, 1994.

[27] Hwang C and Pi W S, 'Nonlinear acoustic response analysis of plates using the finite element method', *AIAA Journal*, Vol.10, pp276-281, 1972.

[28] Mei C and Chiang C K, 'A finite element large deflection random response analysis of beams and plates subjected to acoustic loading', AIAA-88-65-6, 1988.

[29] Wolfe H F, An experimental investigation of nonlinear behaviour of beams and plates excited to high levels of dynamic response, Ph.D thesis, University of Southampton, 1995.

[30] Lorch D R, 'Ultra high bypass aircraft sonic fatigue', *The Journal of Environmental Sciences*, pp26-34, July/August, 1989.

[31] Lin Y K, 'Free vibrations of continuous skin-stringer panels', *Journal of Applied Mechanics*, 1960.

[32] Blevins R D, Formulas for natural frequency and mode shape, Robert E Krieger Publishing Company, Malabar, Florida, 1979.

[33] Mei C and Wolfe H F, 'On large deflection analysis in acoustic fatigue design', Random Vibration - Status and recent developments (Editor: Elishakoff I), Elsevier, pp279 -302, 1986.

[34] Ibrahim S R and Mikulcik E C, 'A method for the direct identification of vibration parameters form the free response', *The Shock and Vibration Bulletin*, 1977.

[35] White R G, 'Effects of non-linearity due to large deflections in the resonance testing of structures', *Journal of Sound and Vibration*, 16(2), pp255-267, 1971.

[36] Benamar R, al et, 'The effects of large vibration amplitudes on the mode shapes and natural frequencies of thin elastic structures. Part I: Simply supported and clamped-clamped beams', *Journal of Sound and Vibration*, 149(2), pp179-195, 1991.

[37] Benamar R, al et, 'The effects of large vibration amplitudes on the mode shapes and natural frequencies of thin elastic structures. Part II: Fully clamped rectangular isotropic plates', *Journal of Sound and Vibration*, 164(2), pp295-316, 1993.

[38] White R G, 'A comparison of some statistical properties of the responses of aluminium alloy and CFRP plates to acoustic excitation', *Composites*, October, pp-251-258, 1978.

[39] Wolfe H F and White R G, 'Nonlinear dynamic response of aircraft structures to acoustic excitation', AGARD-CP-549, 1994.

[40] Mei C and Wentz K R, 'Large-amplitude random response of angle-ply laminated composite plates', *AIAA Journal*, Vol.20, pp1450-1458, 1992.

[41] Mei C and Prasad C B, 'Effects of non-linear damping on random response of beams to acoustic loading', *Journal of Sound and Vibration*, Vol.117, No.1, pp173-186, 1987.

[42] Mei C and Prasad C B, 'Response of symmetric rectangular composite laminates with non-linear damping subjected to acoustic loading', AIAA paper 86-1933.

[43] Locke J, ' Nonlinear random response of angle-ply laminates with static and thermal preloads', *AIAA Journal*, Vol.29, No.9, pp1480-1487, 1991.

[44] Robinson J and Mei C, 'The influence of non-linear damping on the random response of panels by time domain simulation', AIAA paper 89-1104, 1989.

[45] Koenig K, ' Acoustic fatigue testing on different materials and skin-stringer elements', presented at a symposium on 'impact of acoustic loads on Aircraft structure' held in Lillehammer, Norway, May 1994.

[46] Louwers M, 'Overview of existing test facilities for acoustic fatigue in aeronautics', Internoise'93, pp1773-1176.

[47] Roussos L A and Brewer T, 'Effect of boundary conditions on dynamic strain response of rectangular panels', AIAA paper 87-0935-CP, 1987.

[48] Bennouna M M and White R G, 'The effects of large vibration amplitudes on the dynamic strain response of a clamped-clamped beam with consideration of fatigue life', *Journal of Sound and Vibration*, Vol.96, No.3, pp281-308, 1984.

[49] Sun J Q and Miles R N, 'Acoustic fatigue life prediction for non-linear structures', *Journal of Sound and Vibration*, Vol. 150, No.3, pp531-535, 1991.

[50] Blevins R, 'An approximate method for sonic fatigue analysis of plates and shells', *Journal of Sound and Vibration*, Vol.129, No.1, pp51-71, 1989

[51] Winterstein S R, 'Nor-Normal responses and fatigue damage', *Journal of Engineering Mechanics*, Vol.111, No.10, pp1291-1295, 1985.

[52] Winterstein S R, 'Nonlinear vibration models for extremes and fatigue', *Journal of Engineering Mechanics*, Vol.114, No.10, pp1772--1790, 1988.

[53] Jensen J J, 'Fatigue damage due to non-Gaussian responses', *Journal of Engineering Mechanics*, Vol.116, No.1, pp240-246, 1990.

[54] Kutt T V and Bienick M P, 'Cumulative damage and fatigue life prediction', *AIAA Journal*, Vol.26, No.2, pp213-219, 1988.

[55] Lowson M V, 'Future Use Of Advanced Materials', Proceedings of the Royal Aeronautical Society Conference on Aerospace Applications of Advanced Materials, March 1989.

[56] Hartmut M, 'The Potential Sales Volume of the European Commercial Aircraft Industry, Emphasising the technological Aspects', Proceedings of the 13th international european chapter conference of the society for the advancement of material and processing engineering, Hamburg, Germany, May 1992.

[57] Middleston D H (editor), Composite Materials In Aircraft Structures, Harlow: Longman Scientific & Technical, 1990.

[58] Leslie N Phillips, Design with Advanced Composite materials, The Design Council, Springe-Verlag, 1989.

[59] Abdin E M Y, Dynamic Properties of Some Carbon Fibre Reinforced Plastics, Ph.D Thesis, ISVR, University of Southampton, October 1982.

[60] Curtis, P T, 'CRAG Test Methods for the Measurement of the Engineering Properties of Fibre Reinforced Plastics', Technical Report 88012, Royal Aerospace Establishment, February 1988.

[61] White, R G, 'Some Measurements of the Dynamic Properties of Mixed Carbon Fibre Reinforced Plastic Beams and Plates', *Aeronautical Journal of the Royal Aeronautical Society*, pp318-325, July 1975.

[62] Reifsinder K, 'Fatigue Behaviour of Composite Materials', *International Journal of Fracture*, Vol.16, No.6, pp563-583, 1980.

[63] Curtis P T and Dorey D, 'Fatigue of Composite Materials', Fatigue of Engineering Materials and Structures, Vol.II, Proceedings of the Institution of Mechanical Engineers, 1986-9, pp297-306.

[64] Drew R C, An Investigation into Damage Initiation and Propagation in Carbon Fibre Reinforced Plastics, Ph.D thesis, University of Southampton, 1989.

[65] Giavotto V, et al, 'Consideration of the Early Fatigue Damage, on Damage Accumulation and on Delamination Mechanism for Composite Material Structures', The Proceedings of the 14th Symposium of the International Committee on Aeronautical Fatigue, 8-12 June 1987, Ottawa, Canada.

[66] Mayer R M, 'Design of Composite Structures Against Fatigue - Application to Wind Turbine Blades', MEP, 1996.

[67] Galea S C P, Effects of Temperature on Acoustically Induced Strains and Damage Propagation in CFRP Plates, Ph.D thesis, University of Southampton, 1989.

[68] Sumsion H T and Williams D P, 'Effects of Environment of the Fatigue of Graphite-Epoxy Composites', Fatigue of Composite Materials, ASTI SAP 569, American Society for Testing and Materials, 1975, pp226-247.

[69] Barnard P M and Young J B, 'Cumulative Fatigue and Life Prediction of Fibre Composites: Final Report, Part I: Literature Review', Cranfield College of Aeronautics, November 1986.

[70] Elangovan P T, al et, 'Acoustic Fatigue Behaviour of GLARE Composites', Symposium on 'Impact of Acoustic Loads on Aircraft Structures,' Lillehammer, Norway, May 1994, p17.

[71] Roebroeks G H J J, 'Fibre-Metal Laminates, Recent Developments and Applications', *International Journal of Fatigue*, Vol.16 No.1, 1994, pp33-42.

[72] Young J B, el al, 'Crack Growth and Residual Strength Characteristics of Two Grades of Glass-Reinforced Aluminium 'GLARE'', *Composites Structures* 27 (1994), pp457-469.

[73] Customer Data Information Sheet 1.000, Structural Laminates Company, 26 January 1994.

[74] Schijve J, 'Fatigue of Aircraft Materials of Aircraft Structures', *Journal of Fatigue*, Vol.16, No.1, 1994, pp21-32.

[75] Verbruggen M L C E and Gunnink J W, 'Metal Laminates - A Family of Advanced Materials', SAMPE European Chapter 1990, pp455-465.

[76] Schijve J, 'Predictions on Fatigue', *JSME International Journal*, Series I, Vol.34, No.3, 1991, pp269-280.

[77] Davenport S B, Fatigue Response of Fibre Reinforced Aluminium-lithium Laminates, Ph.D Thesis, University of Southampton, 1995.

[78] Vlot A D, 'Low and high velocity impact loading of fibre/metal laminates, carbon/peek and monolithic aluminium 2024-T3', SAMPE European Chapter 1992, pp347-360.

[79] Ohrloff N and Horst P, 'Feasibility study of the application of Glare materials in wide body aircraft fuselages', SAMPE European Chapter 1992, pp131-142.

[80] Chow L C and Cummins R J, 'Airbus Aircraft Acoustic Fatigue Certification', *Acoustics Bulletin*, pp5-10, November/December 1994.

[81] ANSYS users manuals, vision 5.3, Swason Analysis Systems, Inc.(SASI)..

[82] White R G and Walker J G, Noise and Vibration, Ellis Horwood Ltd, 1982.

[83] B&K, Acoustic Noise Measurements, DK-2850 DAERUM, DENMARK, January 1979.

[84] Steinwolf A and White R G, 'Probability Density Functions of Acoustically Induced Strains in Experiments with Composite Plates', *AIAA Journal*, Vol.35, No.12, December 1997.

[85] Ewins D J, Modal Testing – theory and practice, Research Studies Press, Herfordshire, England, 1984.

[86] 6-2. 'STAR – Structural Measurement Systems', 510 Cottonwood Drive, Milpitas, CA 95035, January 1990.

[87] 'ANSYS Theory Reference', 000656. Seventh Edition. SAS IP©.

[88] Sitton G, 'MSC/NASTRAN Basic Dynamic Analysis User's Guide', The MacNeal-Schwendler Corporation. January 1998.

[89] Newland D E, An Introduction to Random Vibrations and Spectral Analysis, Second Edition, Longman Group Limited, 1984.

[90] Xiao Y and White R G, 'Development of Design Techniques for the Avoidance of Acoustic Fatigue of Box-Type Aircraft Structures, Final Report - Part 7: *Acoustic Endurance of The Flap-Like Box Structures*', Department of Aeronautics and Astronautics, University of Southampton, January 1999.

[91] Cunningham P R, 'Response Prediction of Acoustically-Excited Composite Honeycomb Sandwich Structures with Double Curvature', Ph.D Thesis, Department of Aeronautics and Astronautics, School of Engineering Sciences, University of Southampton, May 2001.

[92] Adams R D, 'Effect of Fibre Orientation and Laminate Geometry on the Dynamic Properties of CFRP', Journal of Composite Materials, Vol. 7, P402, October 1973.

[93] Ni R G and Adams R D, 'The damping and Dynamic Moduli of Symmetric Laminated Composite Beams – Theoretical and Experimental Results', Journal of Composite Materials, Vol. 18, P104, March 1984.

[94] Lin D X, Ni R G and Adams R D, 'Prediction and Measurement of the Vibrational Damping Parameters of Carbon and Glass Fibre-Reinforced Plastics Plates', Journal of Composite Materials, Vol. 18, P132, March 1984.

[95] Beranek Leo L, Noise and Vibration Control, McGraw-Hill Book Company, 1971.

[96] Adams R D, 'The Damping Characteristics of Certain Steels, Cast Irons and Other Metals', Journal of Sound and Vibration, 23(2), pp199-216, 1972.

APPENDIX A PRELIMINARY TESTS

A.1 PRELIMINARY TESTS OF CFRP TEE-COUPONS

A.1.1 Static Test Results

According to Finite Element predictions which showed that the maximum surface bending strain in Tee-coupons would be located at the joint line area, five strain gauges were attached to the upper surface of the skin plate of one of the CFRP Tee-coupons. The positions of the strain gauges are shown in Figure A.1. TML normal foil strain gauges with a gauge length of 5mm, gauge resistance of 120Ω, gauge factor of 2.16 and temperature compensation factor of 23 were used. The test specimens were clamped on the stringer and static loading, which produces tensile or compressive bending strain in the coupon surface, was applied by means of standard weights, The forces applied to the specimens were calculated. Test results for the upper surface strains of CFRP Tee-coupons are plotted in Figure A.2 and are also listed in Table A.1. Results indicated that the maximum strain occurred in the region where the joint radius ends for CFRP Tee-coupons, and along the lines where stringer and skin plate meet (Gauges No. 2 and 4). Strain gauge locations for fatigue tests were therefore chosen as shown in Figure 2.24. Further static bending tests producing tension in the upper surface were carried out on several coupons and results are shown in Figure A.3 and also in Table A.2. All coupons tested showed very similar static bending behaviour. One of the coupons was also loaded to a high strain level to check its linearity. Figure A.4 and Table A.3 show results. Results show that strain/load characteristics of the coupons followed a linear relationship within the range investigated.

A.1.2 Dynamic Evaluation Test

This part of the test programme was carried out to determine suitable shaker excitation and coupon response levels. Because of the low density and high stiffness of CFRP materials, the coupons tested had very low weights (29.5 grams) but were very stiff. The initial shaker excitation tests showed that coupons had very low strain response levels. To increase the

strain, the tip mass loading method was used and various weights were applied. Table A.4 shows the effect of tip mass on the resonance frequency and RMS strain response of CFRP Tee-coupons to random loading. It can be seen that the addition of tip masses reduced coupon resonance frequencies and increased strain response by about 10 times to 100μ strain for RMS acceleration excitation of 1.34g (1 g = 9.81 ms^{-2}). Comparing with some fatigue data illustrated in an ESDU data sheet[5] for similar materials, this strain level is not high enough to cause fatigue damage of CFRP Tee-coupons. Because it is not practical to increase tip mass much beyond the values used in Table A.4, increase of excitation level was the solution to the testing problem.

The initial intention was to test four coupons simultaneously on the shaker. But due to the weight of the fixture which limited shaker vibration output level, it was not possible to produce high enough excitation levels to coupons during fatigue testing. To solve this problem, a simple fixture was made to test only one coupon at a time as shown in Figures 2.22 and 2.23. This increased the shaker excitation level by 300%. Table A.5 gives a comparison of RMS acceleration excitation applied to a coupon for the same input power to the shaker from the power amplifier for two fixtures.

Following the initial tests, a tip mass of 24.72 grams was used at each end of the CFRP coupon skin plate which reduced the resonance frequency of the coupons from about 323 Hz to 108 Hz. Five RMS acceleration shaker excitation levels were chosen as fatigue test inputs: 3.0, 5.0, 6.7, 7.50 and 8.75g which were expected to produce coupon surface RMS strain levels in the range of 1000 to 3000μ strain for CFRP Tee-coupons.

A.2 PRELIMINARY TESTS OF GLARE TEE-COUPONS

A.2.1 Static Tests Results

To determine the location of the maximum strain of GLARE Tee-coupons in the test configuration, four strain gauges were attached to the upper surface of the skin plate of a GLARE Tee-coupon. The positions of the strain gauges are shown in Figure A.5. The same kind of strain gauge and loading method as for the CFRP coupons were used. Test results for the upper surface strains of the GLARE Tee-coupon are plotted in Figure A.6(a) and are also listed in Table A.6. Results indicate that the maximum strain occurred in the region along the

lines where stringer and skin plate meet (Gauges Nos. 2 and 4). Strain gauge locations for fatigue tests were therefore chosen as shown in Figure 2.25. Further static bending tests, which produced tensile bending strain in the upper surface, were carried out on several coupons (Gauge locations as shown in Figure 2.25). Results are shown in Figure A.6(b) and also listed in Table A.7. All coupons tested showed very similar static bending behaviour. One of the coupons was also loaded to a high strain level to check its linearity. Figure A.7 and Table A.8 give the results of the linearity check on a GLARE Tee-coupon.

A.2.2 Dynamic Evaluation Tests

The same method as descried in section A.2 was used, and the tip mass of 24.3 grams was chosen.

Table A.1. Static bending test results for CFRP Tee- coupon

Upper surface of skin plate (μ strain)

Gauge No.	1	2	3	4	5
Force (N)	Tension				
0.49	10	25	21	48	20
0.98	23	52	40	74	50
1.47	34	80	58	96	70
1.96	47	110	77	120	98
2.45	57	132	99	142	123
	Compression				
0.49	27	79	62	36	55
0.98	31	99	82	57	74
1.47	40	120	108	80	92
1.96	50	150	130	101	116
2.45	60	170	151	128	136

Table A.2 Static test data for CFRP Tee-coupons

Tension (μ strain)

Coupon No.	Force (N)				
	0.49	0.98	1.47	1.96	2.45
1	26	50	69	90	111
2	21	42	63	86	110
3	25	51	77	104	130
4	25	50	73	98	126
6	22	48	70	93	115
9	30	60	88	115	141
10	22	47	66	85	108
11	27	55	84	110	140

Table A.3 Static linearity check of CFRP Tee-coupon

	μ Strain			μ Strain	
Force (N)	Gauge 1	Gauge 2	Force (N)	Gauge 1	Gauge 2
0.49	21	20	21.58	1120	1000
0.98	58	60	23.54	1250	1100
1.96	118	110	25.51	1300	1200
2.94	141	136	27.47	1420	1250
3.92	191	178	29.43	1510	1360
4.90	280	238	31.39	1610	1440
5.89	330	280	33.35	1710	1510
6.87	380	320	35.32	1860	1600
7.85	420	370	37.28	1940	1700
8.83	500	440	39.24	2000	1800
9.81	540	450	41.20	2100	1950
11.77	640	600	43.16	2200	2000
13.73	740	710	45.13	2280	2100
15.70	840	800	47.09	2400	2200
17.66	960	900			
19.62	1020	910			

Table A.4 Effect of tip mass loading
(RMS acceleration excitation = 1.34g)

Mass weight	Resonance frequency	RMS μ Strain	
(grams)	(Hz)	Gauge 1	Gauge 2
0	323.1	9.31	10.39
11.35	153.3	36.77	45.61
24.72	108.8	67.43	74.24
36.10	85.7	100.95	112.00

Table A.5 Shaker excitation levels (g=9.81ms^{-2}) for two fixtures

Power amplifier reading	4-coupon fixture	1- coupon fixture
3	1.09g	3.12g
4	1.87g	5.0g
5	2.57g	7.43g
6	3.65g	11.2g

Table A.6 Static bending test results for GLARE Tee- coupon No. 33

Tension in upper surface (μ strain)

Force (N)	Strain Gauge No.			
	1	2	3	4
0.49	15	18	15	19
0.98	32	40	27	39
1.47	45	61	42	56
1.96	63	80	60	77
2.45	78	100	75	98
2.94	90	120	89	116
3.43	106	139	105	137
3.92	120	157	121	154
4.41	134	177	137	175
4.91	147	195	150	192
5.40	162	215	166	213
5.89	173	234	180	230

Table A.7 Static bending test data for GLARE coupons

Tension in upper surface (μ strain)

Coupon No.	Strain Gauge	Force (N)					
		0.98	1.96	2.94	3.92	4.91	6.02
3	Gauge 2	24	54	80	106	136	164
	Gauge 1	42	86	130	176	218	262
6	Gauge 2	28	59	82	108	139	168
	Gauge 1	44	86	128	176	218	262
34	Gauge 2	33	67	101	131	159	191
	Gauge 1	50	97	140	188	236	291

Table A.8 Static linearity check of GLARE Tee-coupon No. 33

Tension in upper surface (μ strain)

	Strain (μ)				Strain (μ)		
(N)	Gauge 1	Gauge 2	Gauge 4	(N)	Gauge 1	Gauge 2	Gauge 4
0.98	25	39	40	14.71	470	630	620
1.96	57	80	80	15.70	500	670	680
2.94	86	120	120	16.68	530	710	720
3.92	117	160	160	17.66	560	750	765
4.91	148	200	200	18.64	600	795	805
5.89	170	250	240	19.62	610	835	850
6.87	200	280	280	20.60	650	870	900
7.85	230	320	320	21.58	680	940	910
8.83	260	370	370	22.56	700	950	990
9.81	300	410	410	23.54	730	1000	1030
10.80	330	460	450	24.52	800	1050	1080
11.78	360	500	500	25.50	810	1090	1120
12.75	400	530	540	26.48	840	1125	1160
13.73	430	580	590				

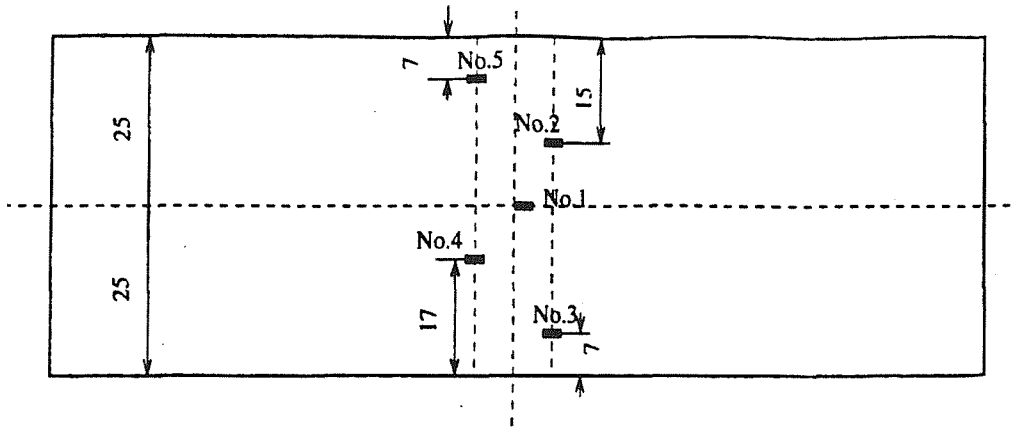

Figure A.1 Strain gauge locations for static bending tests of CFRP Tee-coupons

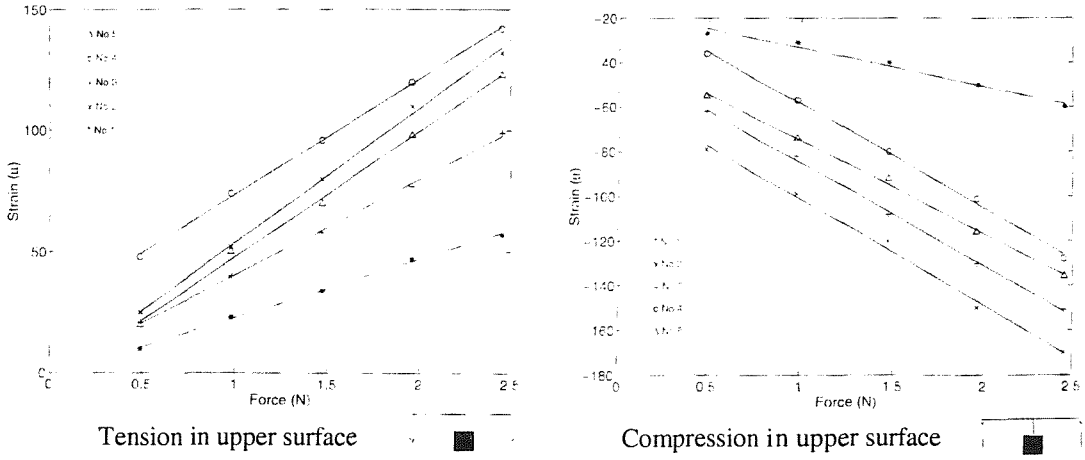

Figure A.2 Static bending test of CFRP Tee-coupon
(Gauge positions as shown in Figure A.1)

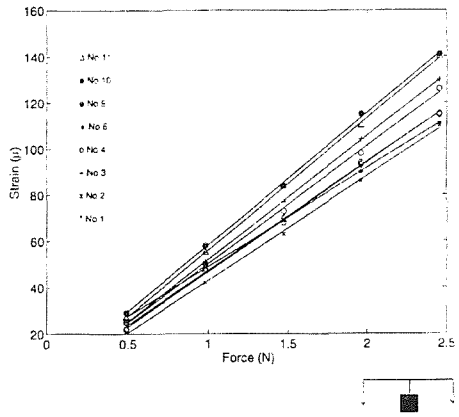

Figure A.3 Static bending tests for different the CFRP coupons
(Gauge position as shown in Figure 2.24)

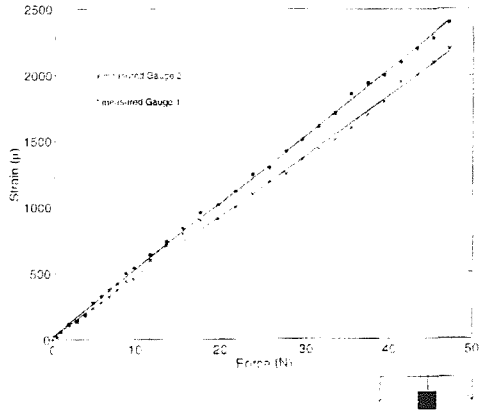

Figure A.4 Static bending tests for linearity check
(Gauge position as shown in Figure 2.24)

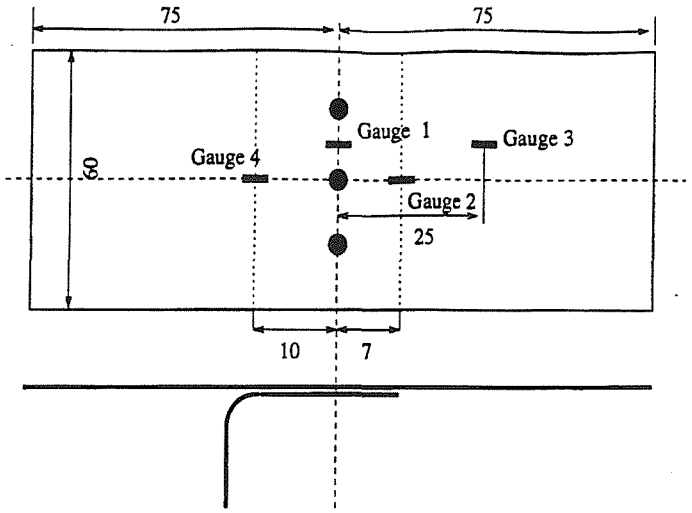

Figure A.5 Strain gauge locations for static bending test to determine maximum strain location on coupon upper surface

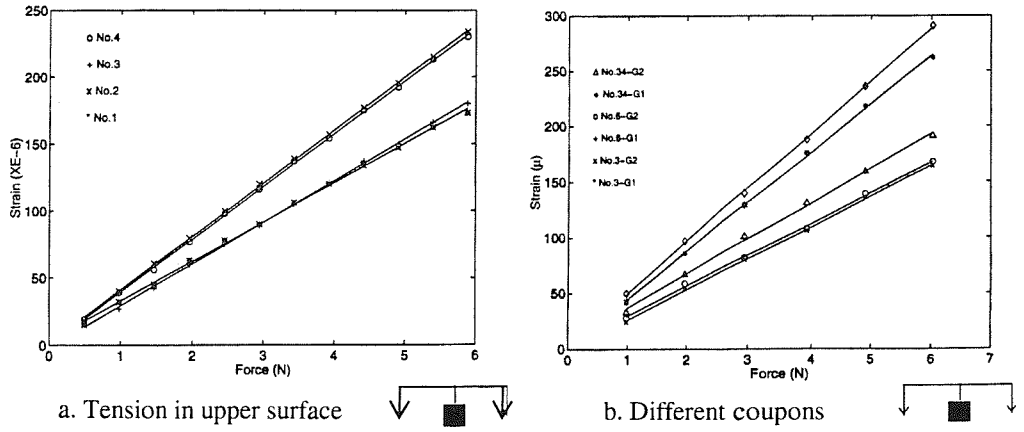

a. Tension in upper surface b. Different coupons

Figure A.6 Static bending test of GLARE coupons

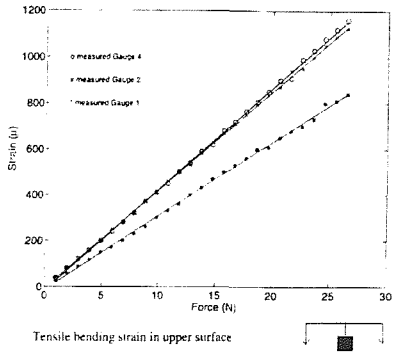

Figure 4B 8 Static bending tests of a coupon for linearity check (Gauge position as shown in Figure 4B 4)

Figure A.7 Static linearity check of GLARE Tee-coupons

APPENDIX B STATISTICAL PARAMETERS AND PROBABILITY DISTRIBUTIONS OF SOUND PRESSURE SIGNALS

Table B.1 Statistical parameters of sound pressure signals at point 1 of test section of the PWT

Ref.Mic (dB)	Reference Microphone				
	μ	rms	σ	λ	γ
135	-9.73E-03	5.41E-01	5.41E-01	1.48E-02	3.11E+00
140	-7.64E-03	2.69E+00	2.69E+00	-2.22E-02	4.46E+00
145	-8.17E-03	1.49E+00	1.49E+00	-1.68E-01	5.58E+00
150	-9.90E-03	2.98E+00	2.98E+00	7.44E-02	4.01E+00
155	-9.45E-03	1.68E+00	1.68E+00	3.13E-01	4.08E+00
160	-8.33E-03	3.04E+00	3.04E+00	4.71E-01	3.41E+00
	Panel Micropone at point 1				
135	-3.60E-03	1.28E-01	1.28E-01	-4.27E-02	3.00E+00
140	-3.95E-03	6.37E-01	6.37E-01	1.11E-01	4.38E+00
145	-3.38E-03	3.41E-01	3.41E-01	1.70E-01	5.05E+00
150	-3.32E-03	7.37E-01	7.37E-01	1.95E-01	3.77E+00
155	-3.26E-03	1.20E+00	1.20E+00	6.39E-02	3.69E+00
160	-3.88E-03	7.57E-01	7.57E-01	-7.81E-02	3.74E+00

Table B.2 Statistical parameters of sound pressure signals at point 3 of test section of the PWT

Ref.Mic (dB)	Reference Microphone				
	μ	rms	σ	λ	γ
135	-1.02E-02	6.77E-01	6.77E-01	8.44E-02	2.54E+00
140	-1.10E-02	2.56E+00	2.56E+00	-1.96E-02	3.96E+00
145	-1.07E-02	1.49E+00	1.49E+00	2.17E-02	4.08E+00
150	-8.68E-03	3.27E+00	3.27E+00	1.08E-01	3.51E+00
155	-1.09E-02	1.80E+00	1.80E+00	2.47E-01	3.46E+00
160	-6.13E-03	2.99E+00	2.99E+00	3.71E-01	3.16E+00
	Panel Micropone at point 3				
135	-4.40E-03	8.66E-02	8.67E-02	-2.82E-02	3.03E+00
140	-4.66E-03	5.61E-01	5.61E-01	2.63E-02	4.23E+00
145	-4.58E-03	3.32E-01	3.32E-01	1.35E-02	4.19E+00
150	-4.67E-03	7.41E-01	7.41E-01	1.06E-01	3.72E+00
155	-4.44E-03	3.65E-01	3.65E-01	1.47E-01	3.47E+00
160	-4.74E-03	8.06E-01	8.06E-01	-9.76E-02	4.29E+00

Table B.3 Statistical parameters of sound pressure signals at point 4 of test section of the PWT

Ref.Mic (dB)	Reference Microphone				
	μ	rms	σ	λ	γ
135	-1.01E-02	5.61E-01	5.62E-01	5.68E-02	3.12E+00
140	-1.15E-02	2.92E+00	2.92E+00	9.53E-02	3.61E+00
145	-8.06E-03	1.80E+00	1.80E+00	-9.72E-02	4.06E+00
150	-8.47E-03	3.04E+00	3.04E+00	1.54E-01	3.74E+00
155	-8.08E-03	1.64E+00	1.64E+00	2.86E-01	3.79E+00
160	-9.71E-03	2.97E+00	2.97E+00	3.86E-01	3.31E+00
	Panel Micropone at point 4				
135	-4.01E-03	1.37E-01	1.37E-01	2.99E-02	3.06E+00
140	-4.31E-03	5.88E-01	5.88E-01	7.74E-02	4.10E+00
145	-4.00E-03	4.07E-01	4.07E-01	7.14E-02	3.68E+00
150	-3.93E-03	7.63E-01	7.63E-01	5.99E-02	3.43E+00
155	-3.97E-03	4.12E-01	4.12E-01	2.94E-02	3.37E+00
160	-4.33E-03	7.78E-01	7.78E-01	-5.36E-02	2.89E+00

Table .4 Statistical parameters of sound pressure signals at point 5 of the test section of the PWT

Ref.Mic (dB)	Reference Microphone				
	μ	rms	σ	λ	γ
135	-8.94E-03	1.30E+00	1.30E+00	-1.11E-01	6.97E+00
140	-8.75E-03	2.71E+00	2.71E+00	2.38E-02	4.69E+00
145	-7.00E-03	1.60E+00	1.60E+00	7.47E-02	5.33E+00
150	-1.05E-02	3.10E+00	3.10E+00	1.37E-01	4.14E+00
155	-8.67E-03	1.76E+00	1.76E+00	3.95E-01	3.85E+00
160	-7.03E-03	3.08E+00	3.08E+00	4.33E-01	3.28E+00
	Panel Micropone at point 5				
135	-4.00E-03	1.27E-01	1.28E-01	1.46E-02	3.04E+00
140	-4.05E-03	5.91E-01	5.91E-01	3.81E-02	4.62E+00
145	-3.98E-03	4.60E-01	4.60E-01	3.01E-02	4.43E+00
150	-4.44E-03	8.85E-01	8.85E-01	3.96E-02	3.78E+00
155	-4.40E-03	5.56E-01	5.56E-01	-4.60E-02	3.20E+00
160	-4.06E-03	1.03E+00	1.03E+00	-1.57E-02	2.70E+00

Table B.5 Statistical parameters of sound pressure signals at point 6 of test section of the PWT

Ref.Mic (dB)	Reference Microphone				
	μ	rms	σ	λ	γ
135	-9.18E-03	4.81E-01	4.81E-01	4.05E-02	3.49E+00
140	-1.12E-02	2.48E+00	2.48E+00	-4.21E-02	5.45E+00
145	-9.24E-03	1.78E+00	1.78E+00	2.45E-01	4.45E+00
150	-7.42E-03	2.79E+00	2.79E+00	2.26E-01	3.93E+00
155	-9.53E-03	1.71E+00	1.71E+00	3.60E-01	3.35E+00
160	-8.27E-03	2.05E+00	2.05E+00	4.55E-01	3.15E+00
	Panel Micropone at point 6				
135	-3.64E-03	1.98E-01	1.98E-01	1.86E-02	3.02E+00
140	-3.69E-03	1.17E+00	1.17E+00	1.27E-02	5.44E+00
145	-3.47E-03	8.01E-01	8.01E-01	-2.51E-02	4.31E+00
150	-3.69E-03	3.72E-01	3.72E-01	3.18E-02	3.70E+00
155	-3.21E-03	7.48E-01	7.48E-01	-3.76E-02	3.32E+00
160	-3.89E-03	9.41E-01	9.41E-01	-6.20E-02	3.10E+00

Table B.6 Statistical parameters of sound pressure signals at point 7 of test section of the PWT

Ref.Mic (dB)	Reference Microphone				
	μ	rms	σ	λ	γ
135	-1.05E-02	5.39E-01	5.39E-01	2.20E-01	3.72E+00
140	-1.18E-02	2.40E+00	2.40E+00	1.17E-02	3.56E+00
145	-1.15E-02	1.81E+00	1.81E+00	1.25E-02	3.73E+00
150	-1.23E-02	2.93E+00	2.93E+00	7.88E-02	3.52E+00
155	-1.15E-02	1.53E+00	1.53E+00	2.58E-01	3.71E+00
160	-1.25E-02	3.30E+00	3.30E+00	4.94E-01	3.31E+00
	Panel Micropone at point 7				
135	-4.39E-03	1.32E-01	1.32E-01	-5.05E-02	3.00E+00
140	-4.54E-03	5.37E-01	5.37E-01	-4.00E-02	4.31E+00
145	-4.29E-03	4.01E-01	4.01E-01	1.69E-02	4.56E+00
150	-4.25E-03	7.05E-01	7.05E-01	5.33E-02	3.98E+00
155	-4.30E-03	3.47E-01	3.47E-01	-2.54E-02	3.43E+00
160	-4.77E-03	8.98E-01	8.98E-01	2.05E-01	3.93E+00

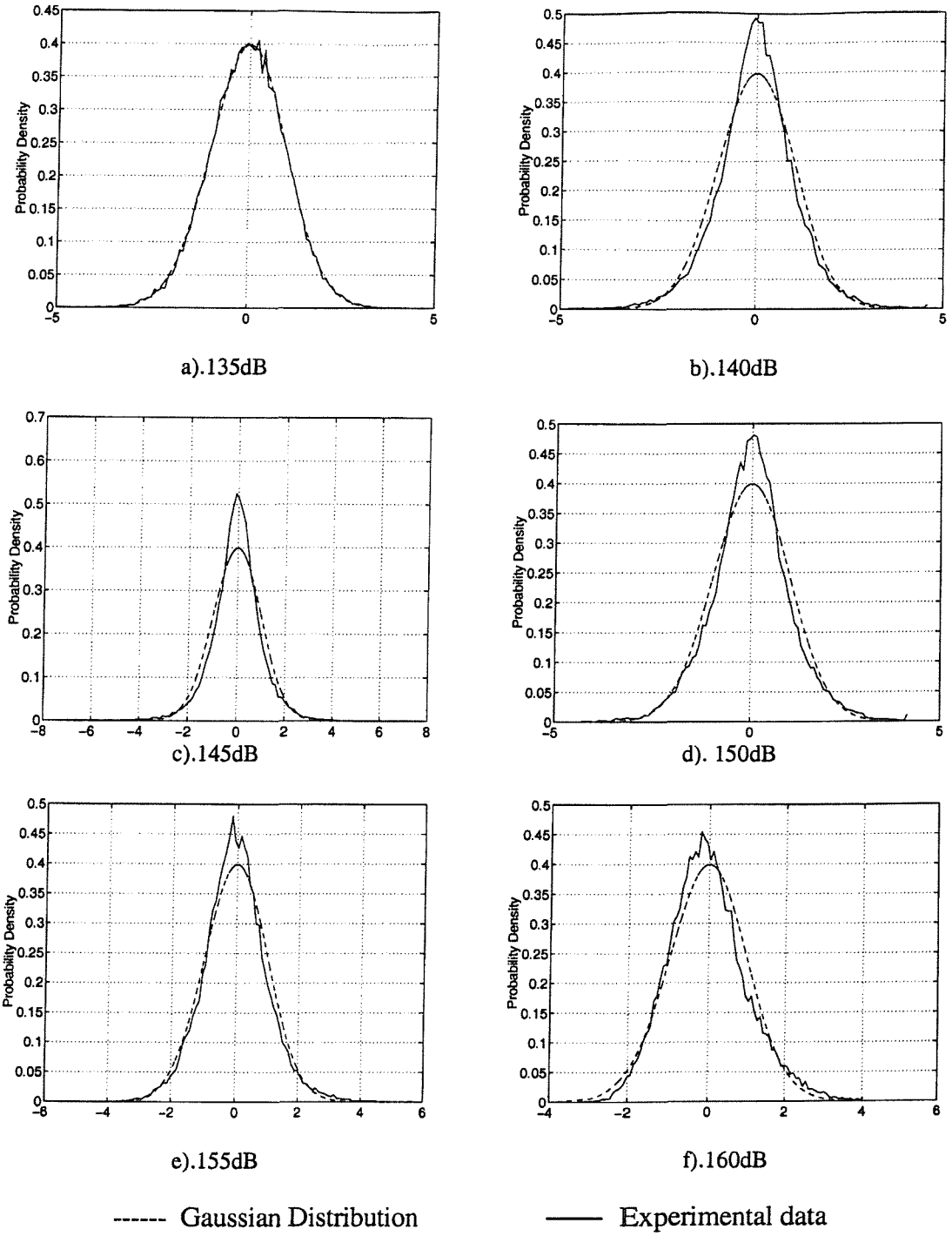

Figure B.1 Probability distribution of sound pressure signal measured by reference microphone

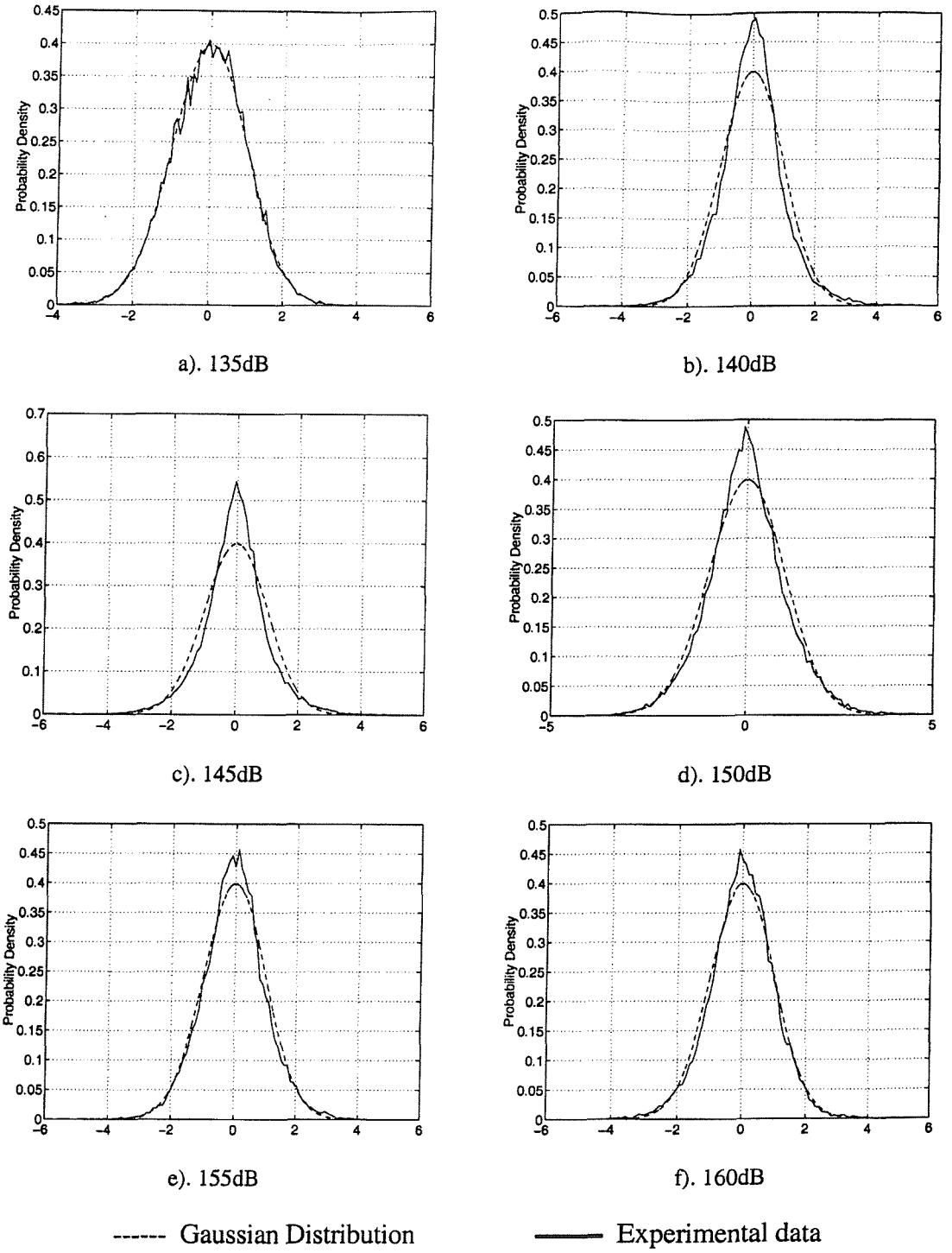

Figure B.2 Probability distribution of sound pressure signal measured by panel microphone at point 1

APPENDIX C CALIBRATION AND TRANSFER FUNCTIONS OF THE FLAP-LIKE BOX STRUCTURES

C.1 CALIBRATION RESULTS OF TRANSDUCERS FOR THE EXPERIMENTAL MODAL ANALYSIS OF BOX STRUCTURES

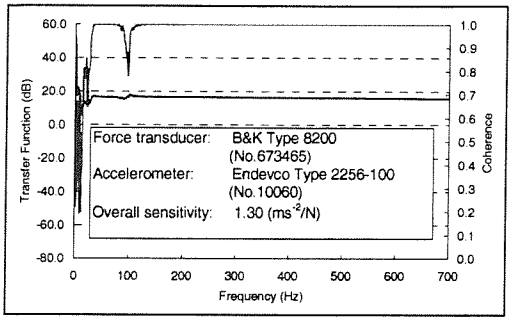

Figure C.1

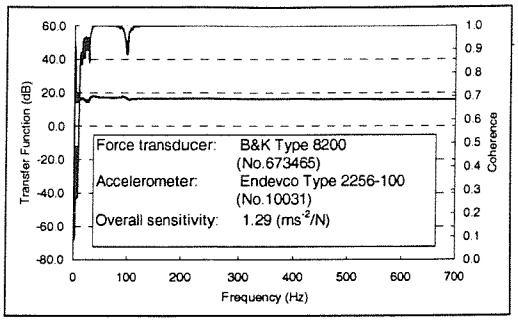

Figure C.2

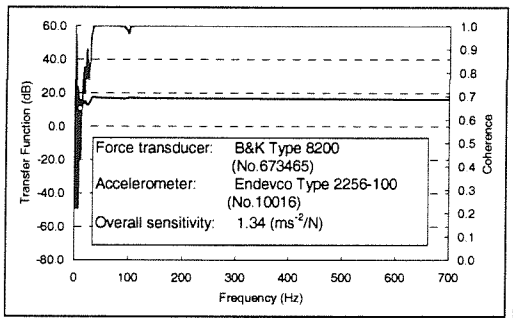

Figure C.3

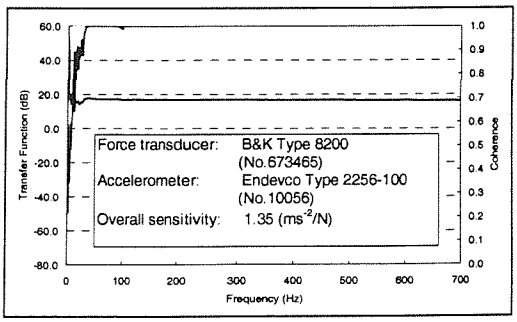

Figure C.4

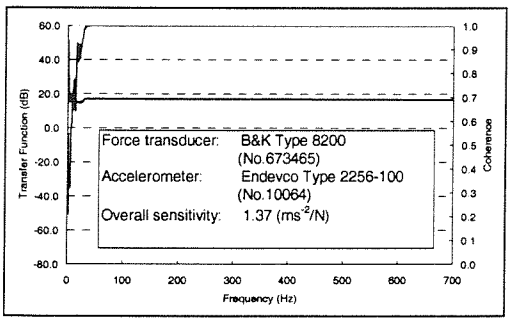

Figure C.5

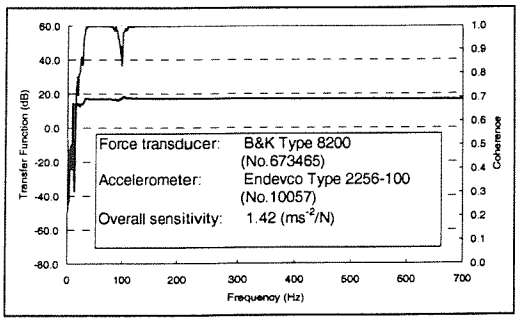

Figure C.6

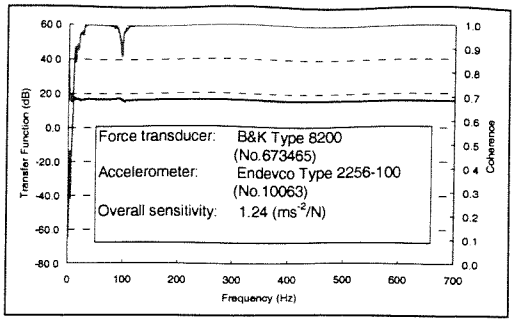

Figure C.7

C.2 TRANSFER FUNCTION PLOTS FOR THE EXPERIMENTAL MODAL ANALYSIS OF BOX STRUCTURES

C.2.1 Aluminium Structure - Excited at Curved Panel

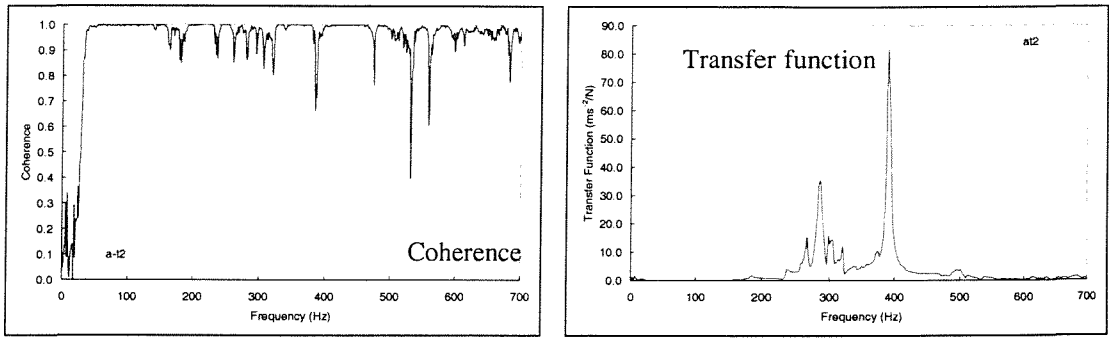

FigureC.8 Measuring point T2

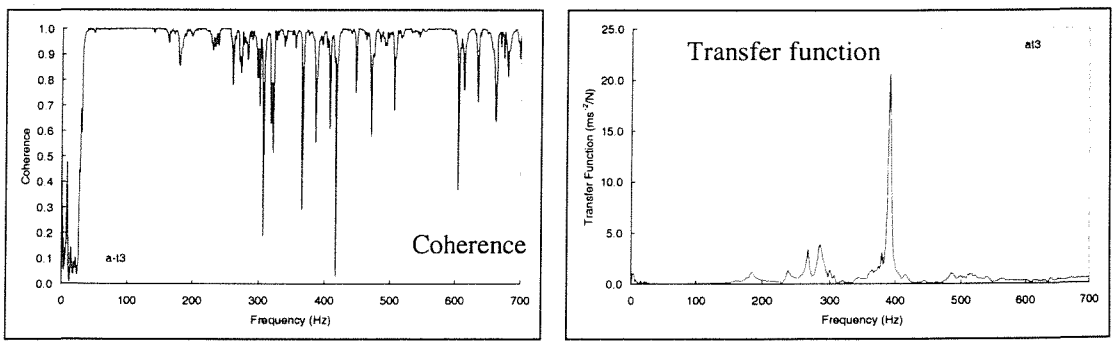

Figure C.9 Measuring point T3

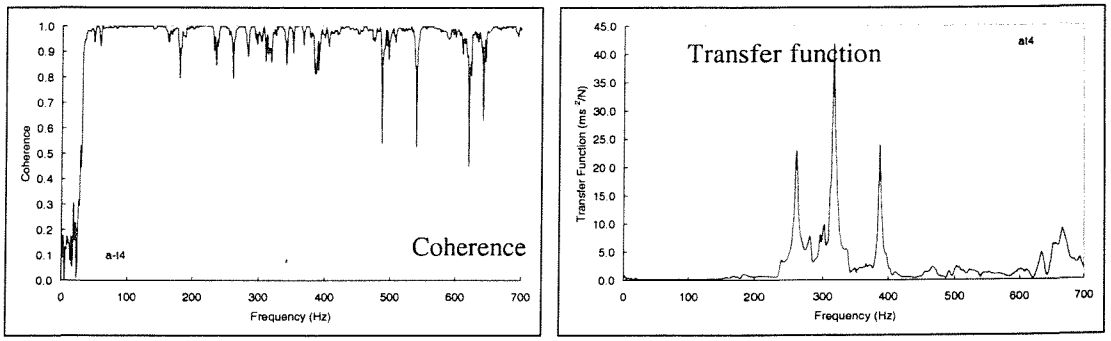

Figure C.10 Measuring point T4

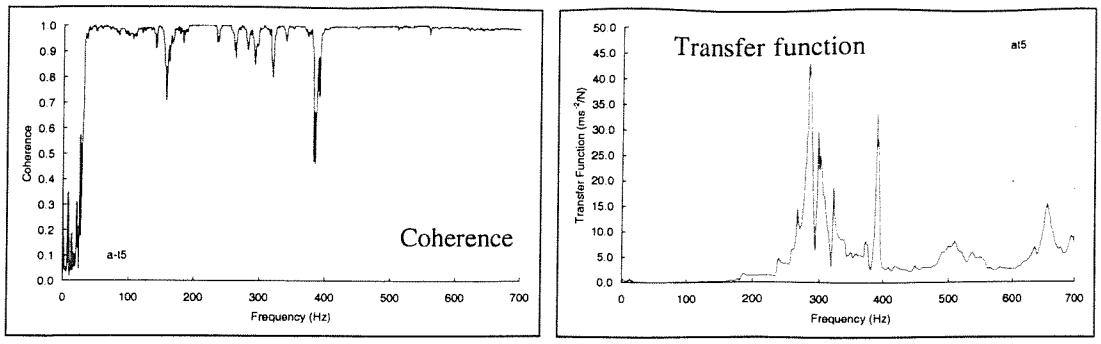

Figure C.11 Measuring point T5

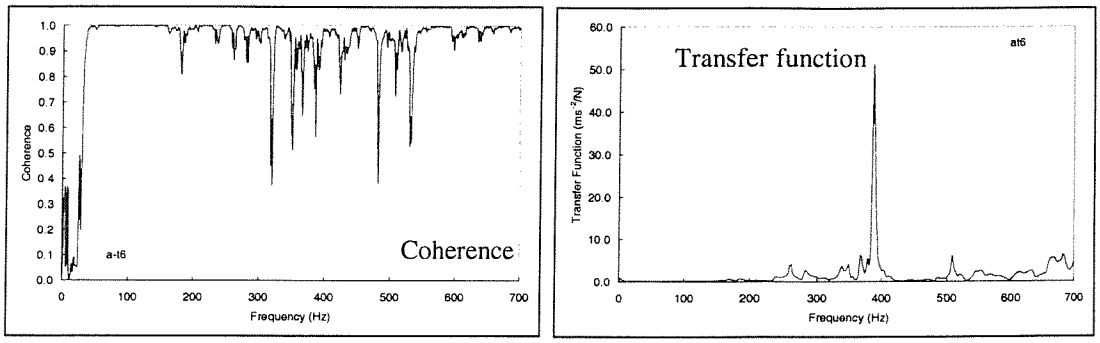

Figure C.12 measuring point T6

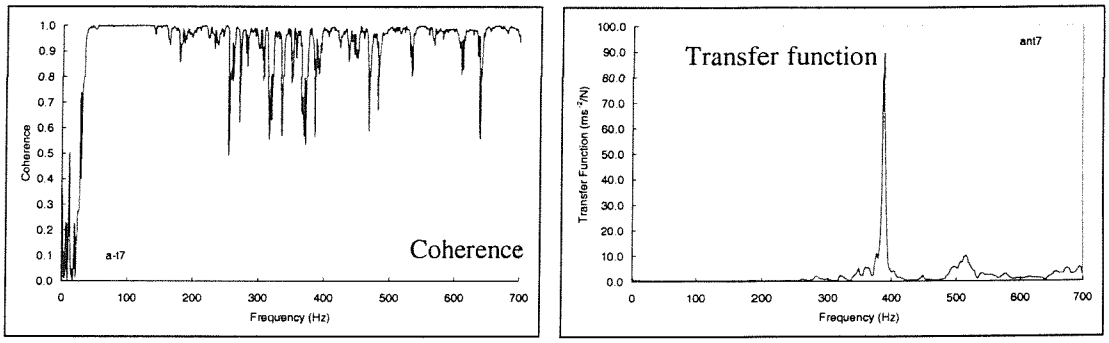

Figure C.13 measuring point T7

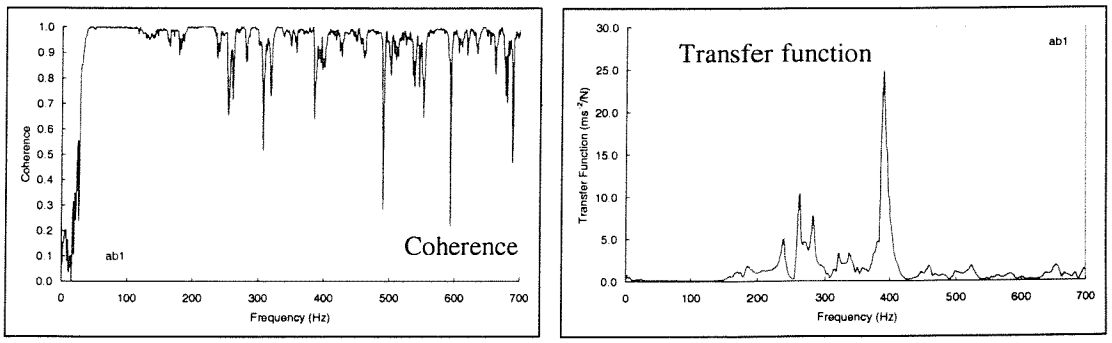

Figure C.14 Measuring point B1

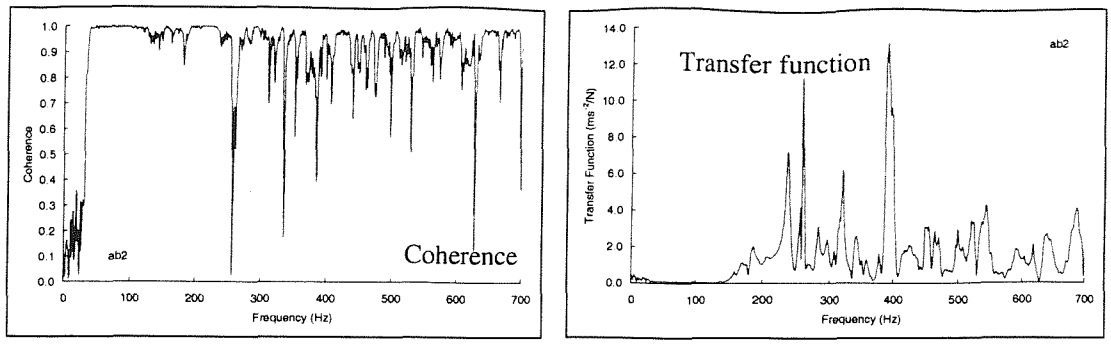

Figure C.15 Measuring point B2

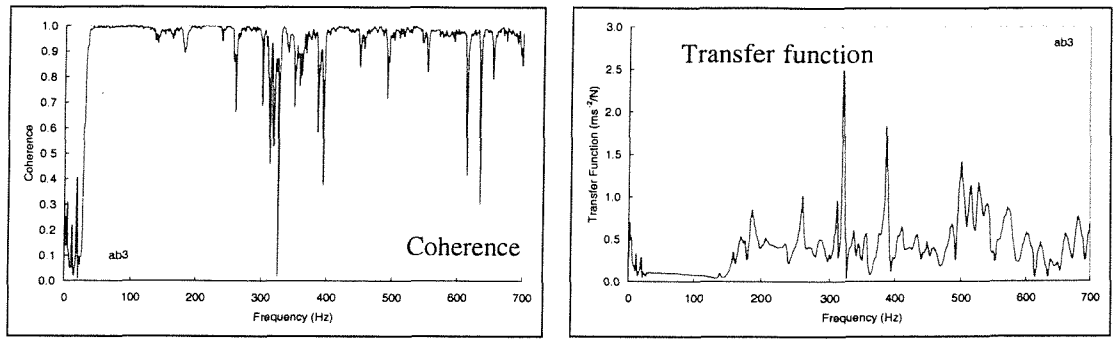

Figure C.16 Measuring point B3

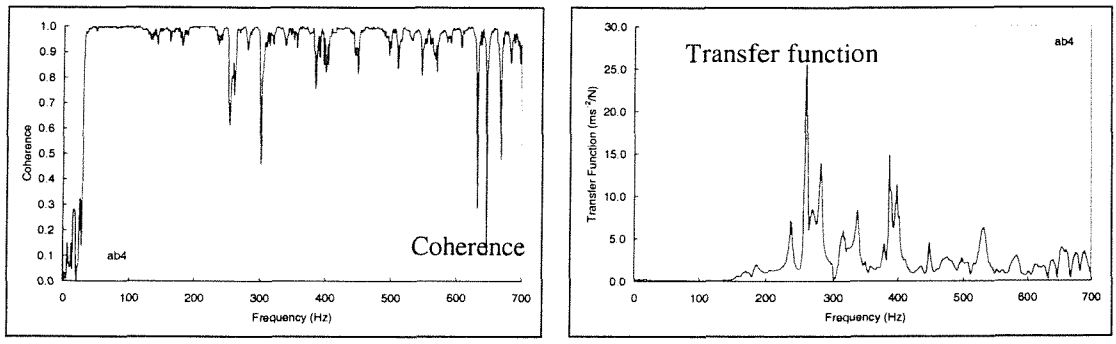

Figure C.17 Measuring point B4

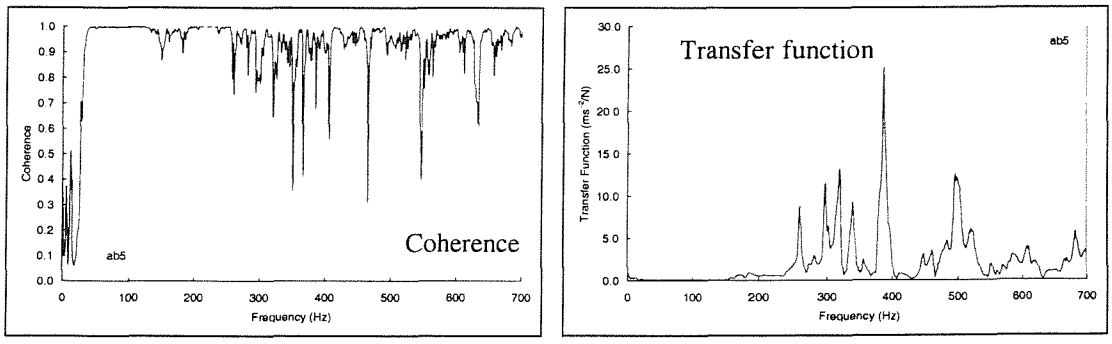

Figure C.18 Measuring point B5

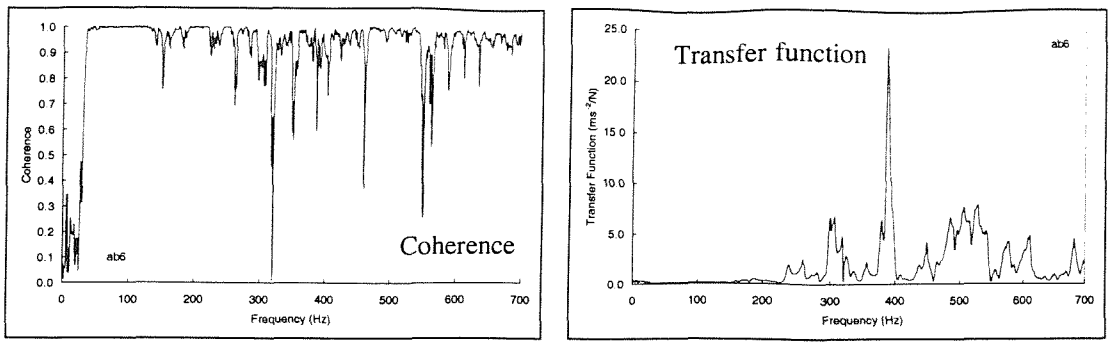

Figure C.19 Measuring point B6

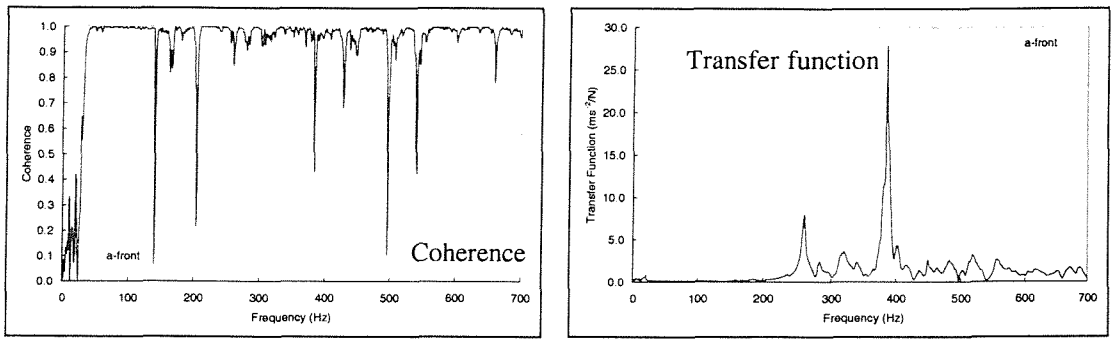

Figure C.20 Measuring point - middle of the front spar

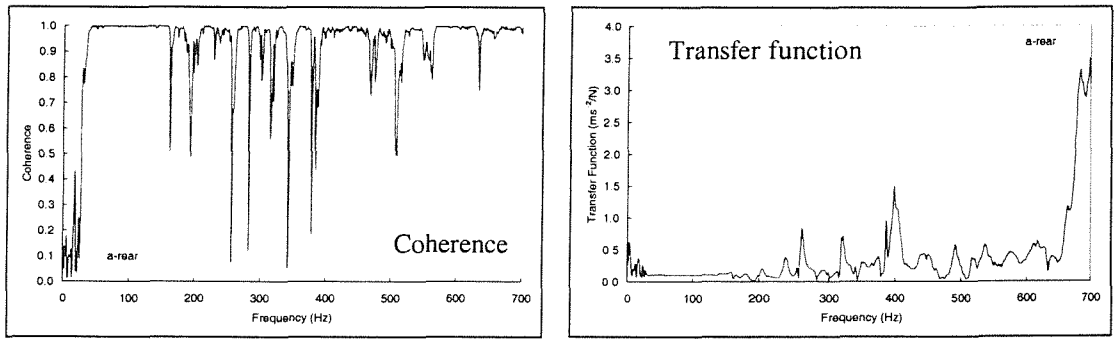

Figure C.21 Measuring point - middle of the rear spar

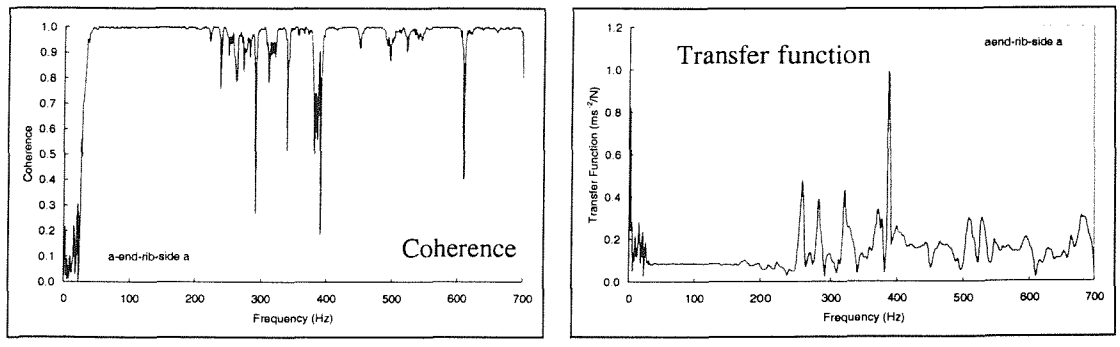

Figure C.22 Measuring point - middle of the side A end rib

C.2.2 GLARE Structure - Excited at Curved Panel

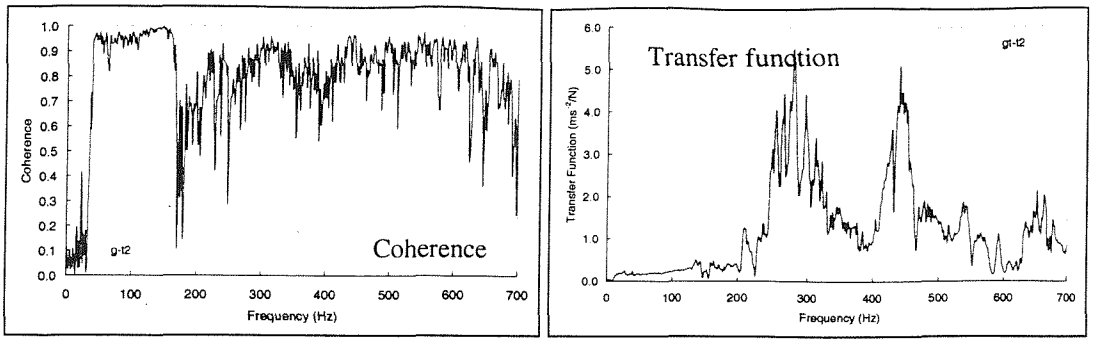

Figure C.23 Measuring point T2

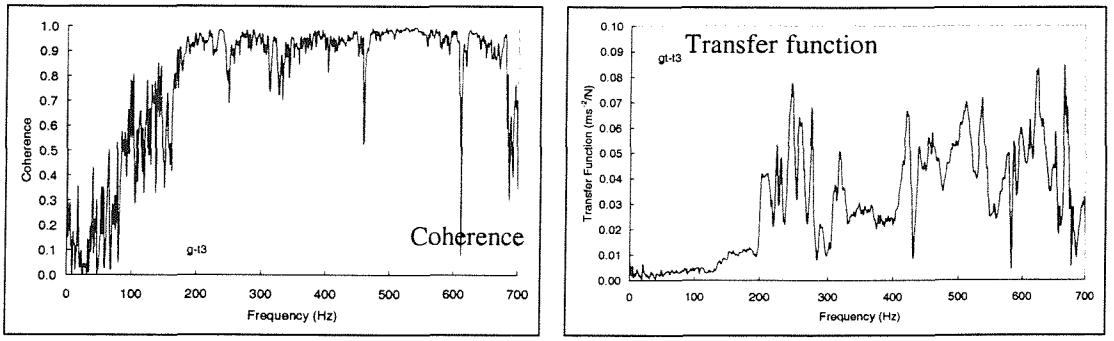

Figure C.24 Measuring point T3

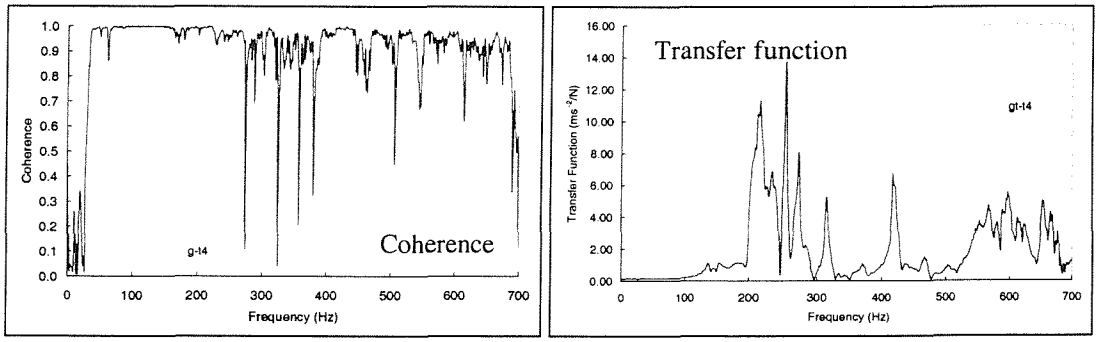

Figure C.25 Measuring point T4

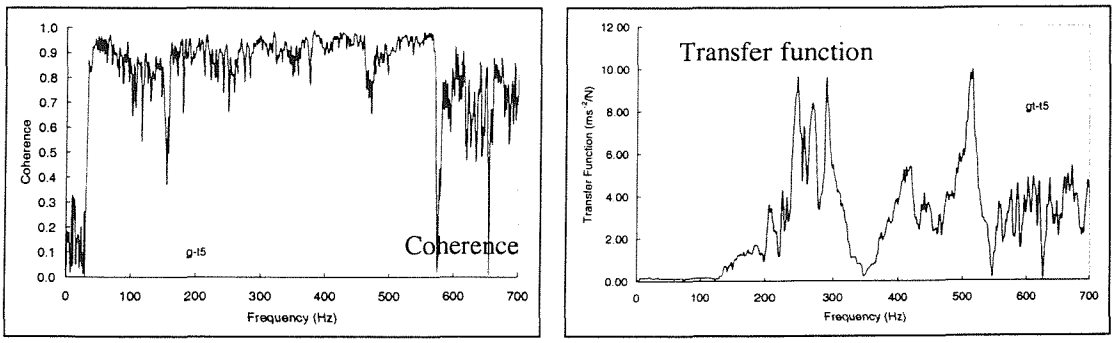

Figure C.26 Measuring point T5

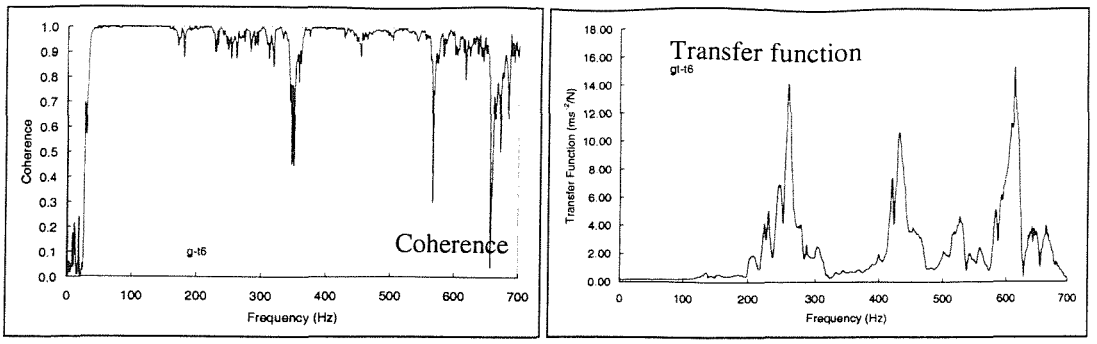

Figure C.27 Measuring point T6

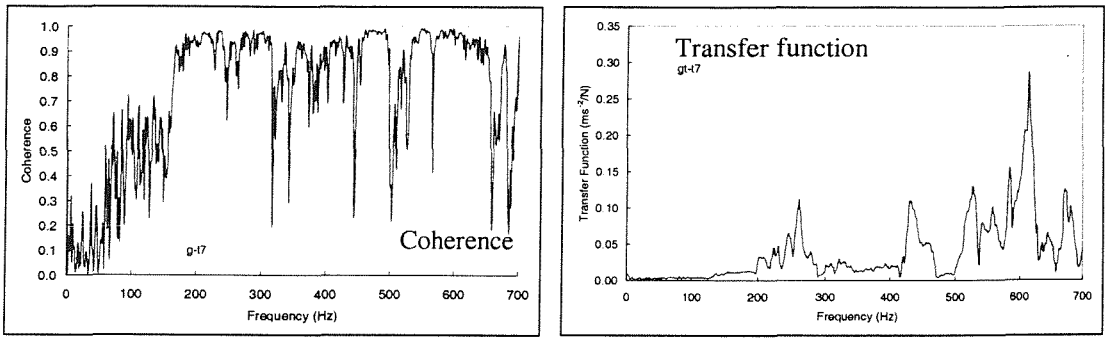

Figure C.28 Measuring point T7

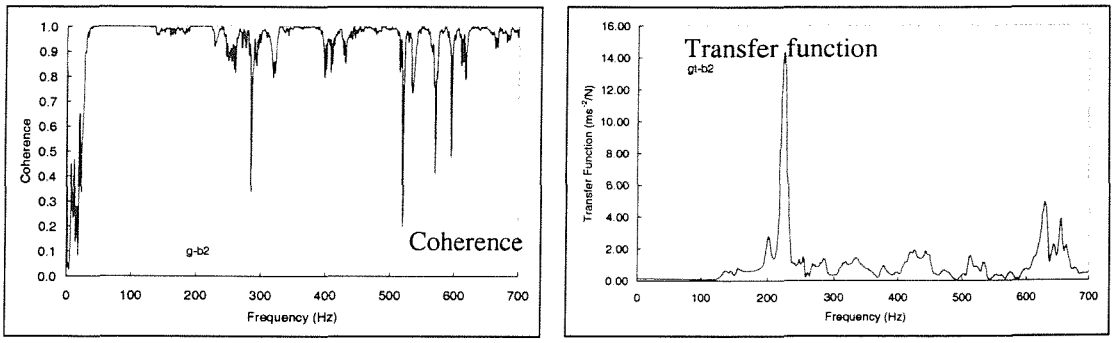

Figure C.29 Measuring point B2

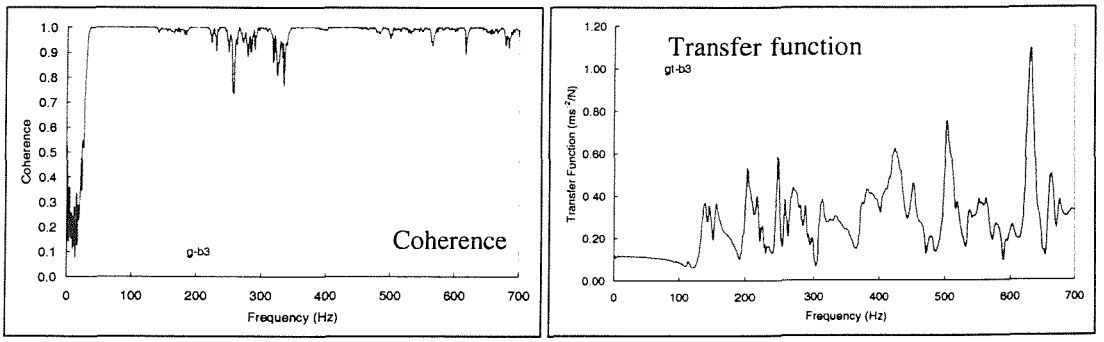

Figure C.30 Measuring point B3

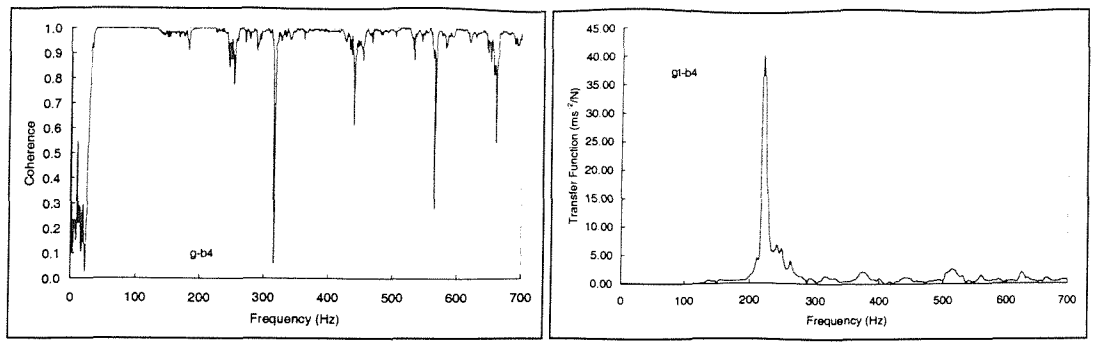

Figure C.31 Measuring point B4

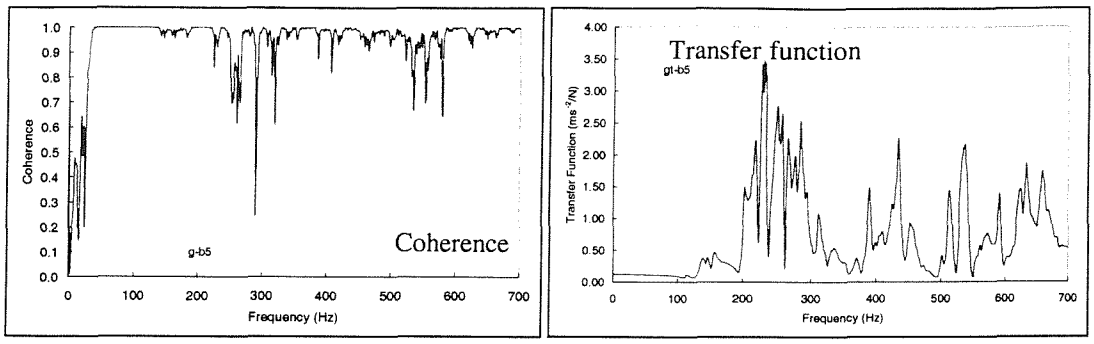

Figure C.32 Measuring point B5

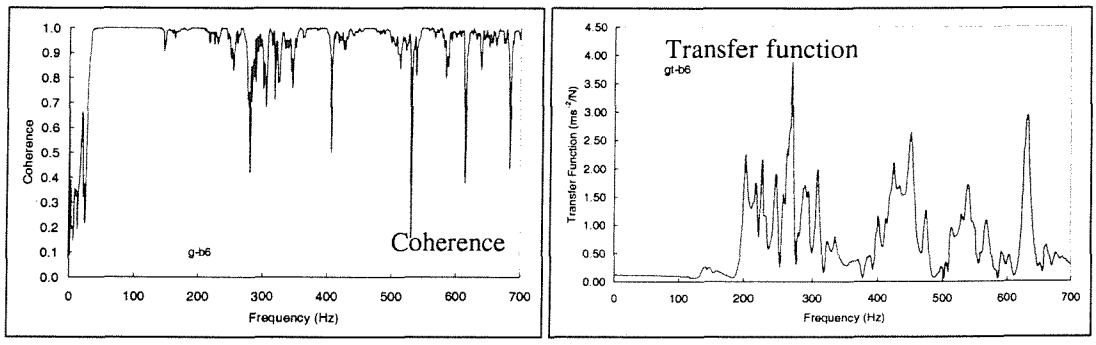

Figure C.33 Measuring point B6

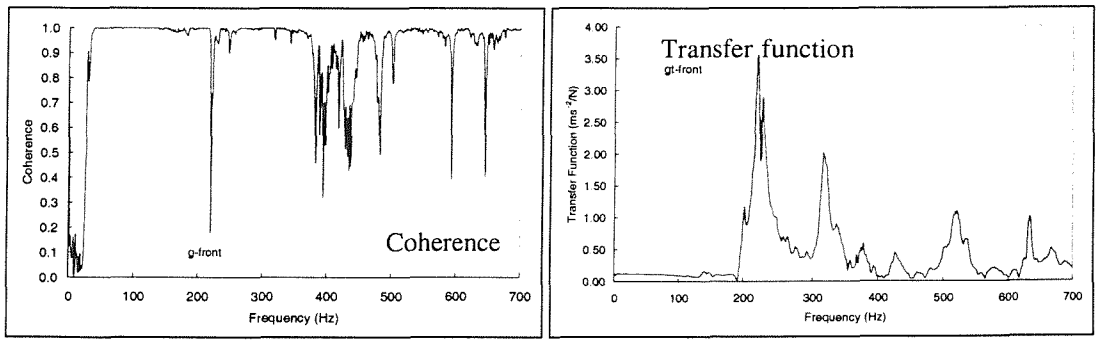

Figure C.34 Measuring point - middle of the front spar

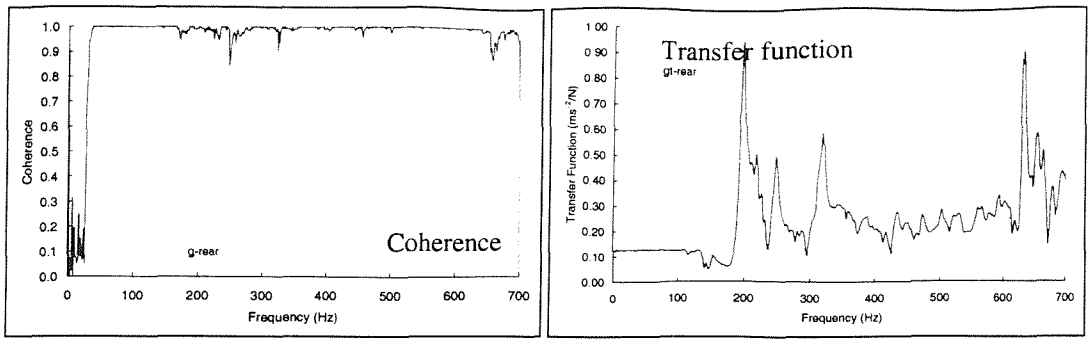

Figure C.35 Measuring point - middle of the rear spar

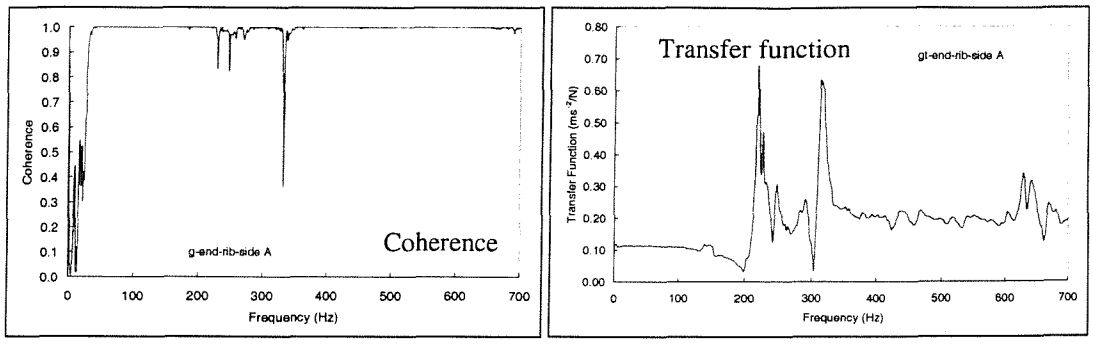

Figure C.36 Measuring point - middle of the end rib at side A

C.2.3 CFRP Structure - Excited at Curved Panel

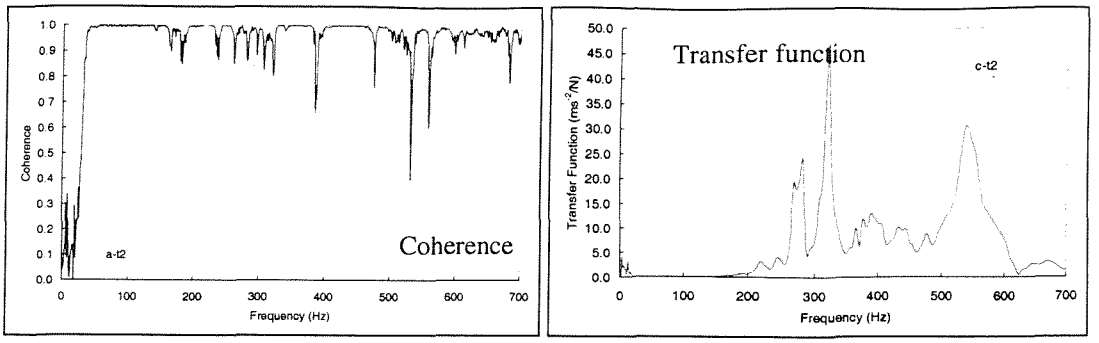

Figure C.37 Measuring point - T2

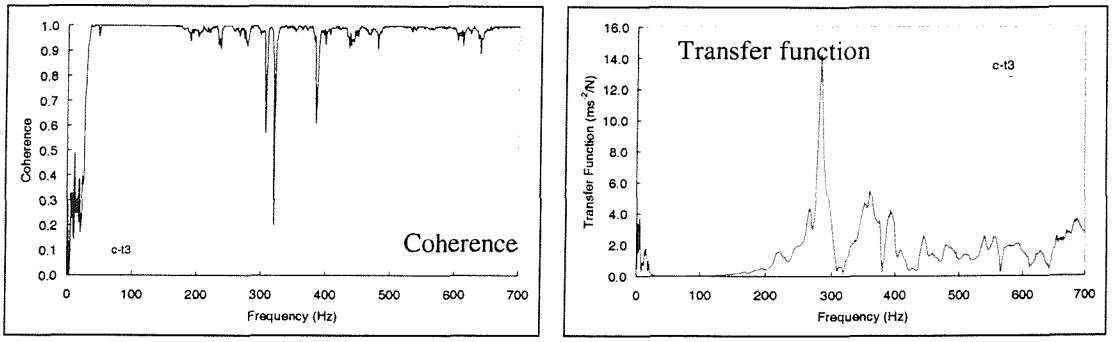

Figure C.38 Measuring point - T3

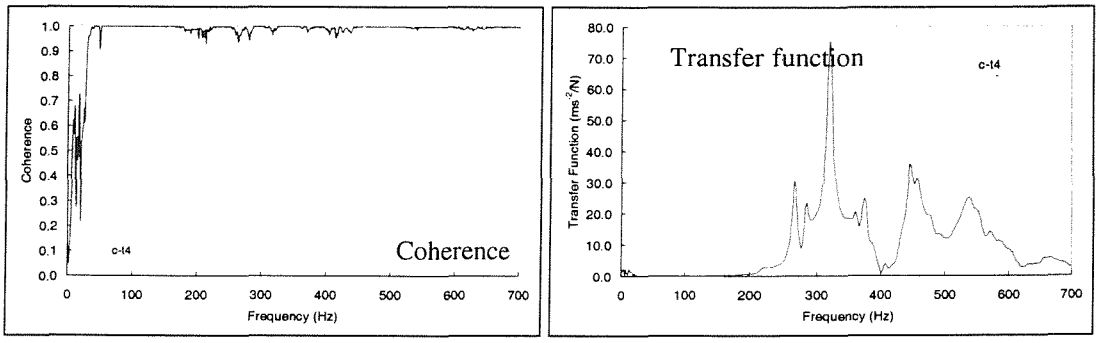

Figure C.39 Measuring point - T4

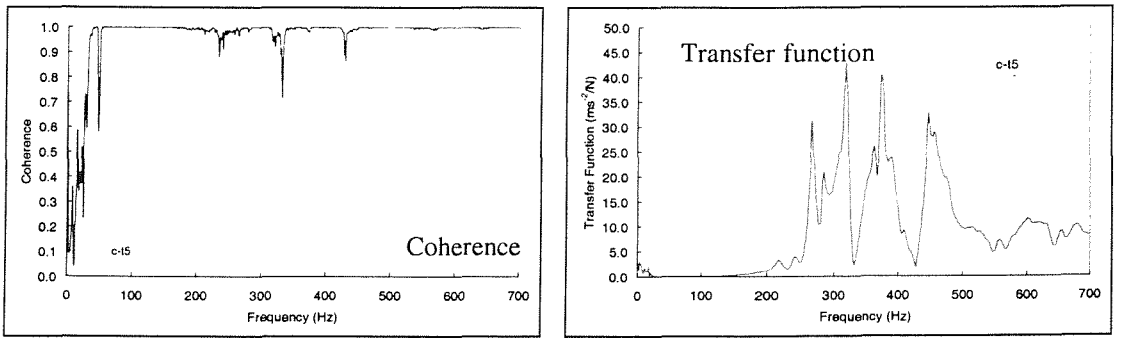

Figure C.40 Measuring point - T5

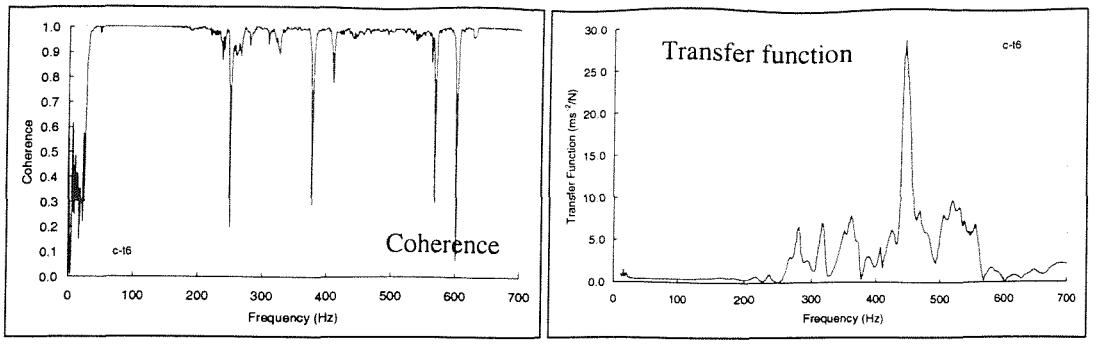

Figure C.41 Measuring point - T6

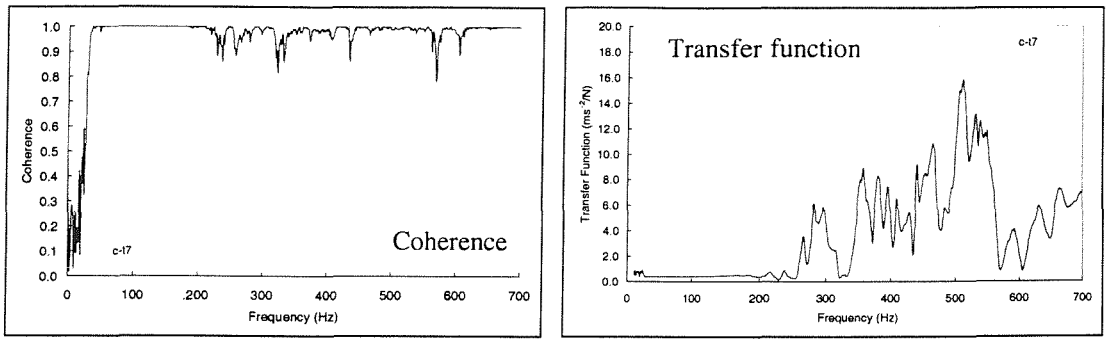

Figure C.42 Measuring point - T7

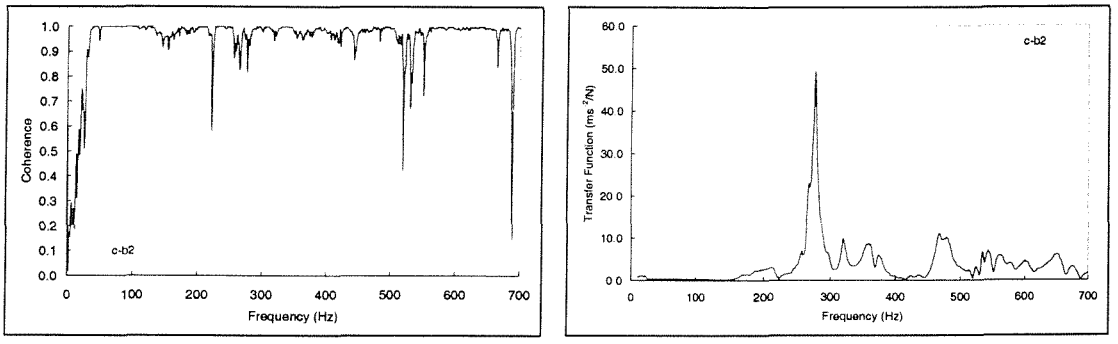

Figure C.43 Measuring point - B2

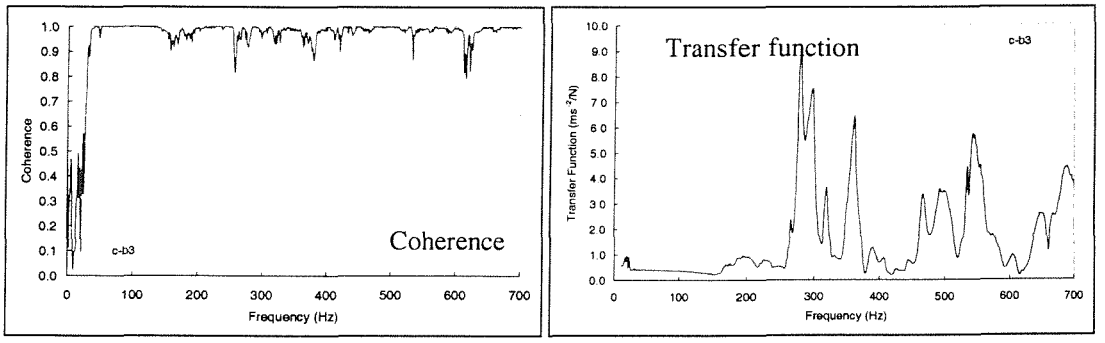

Figure C.44 Measuring point - B3

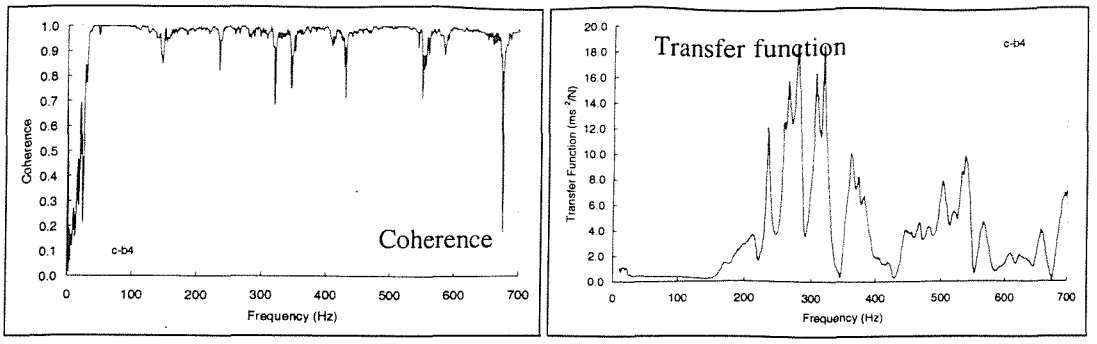

Figure C.45 Measuring point - B4

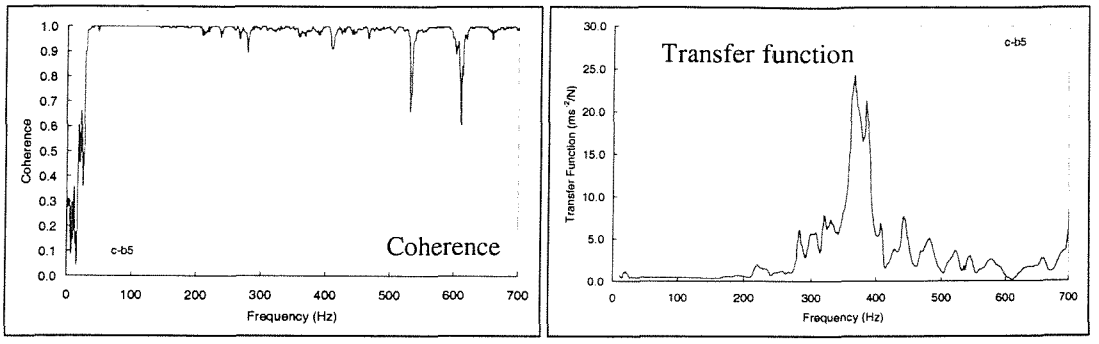

Figure C.46 Measuring point - B5

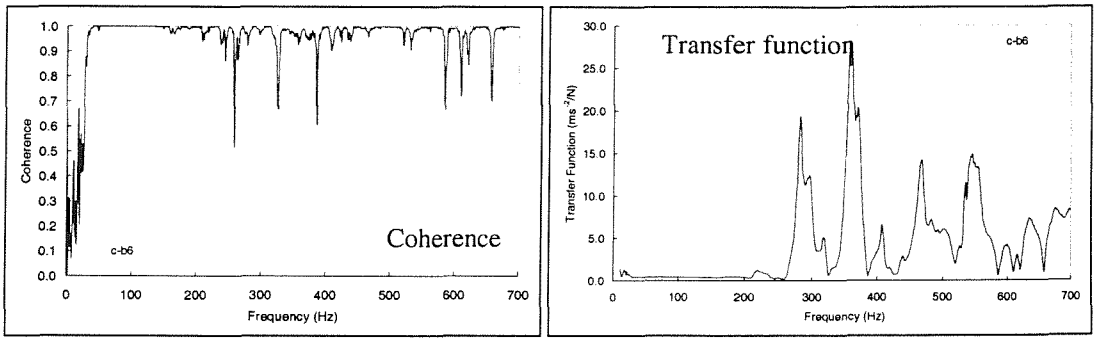

Figure C.47 Measuring point - B6

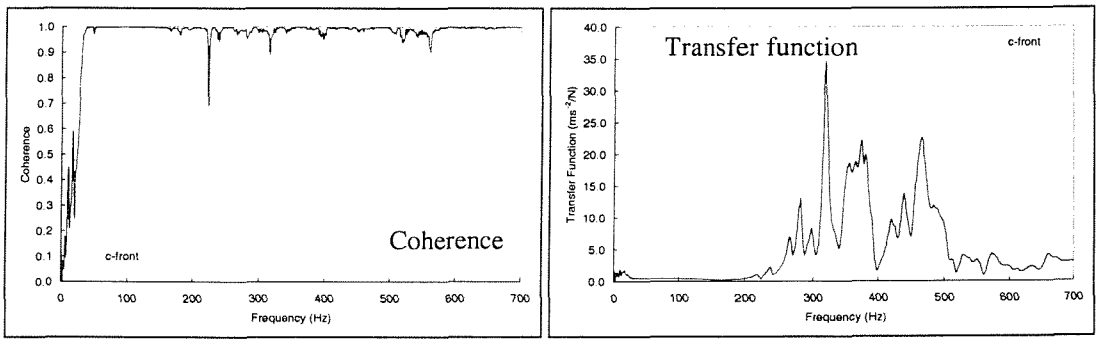

Figure C.48 Measuring point - middle of the front spar

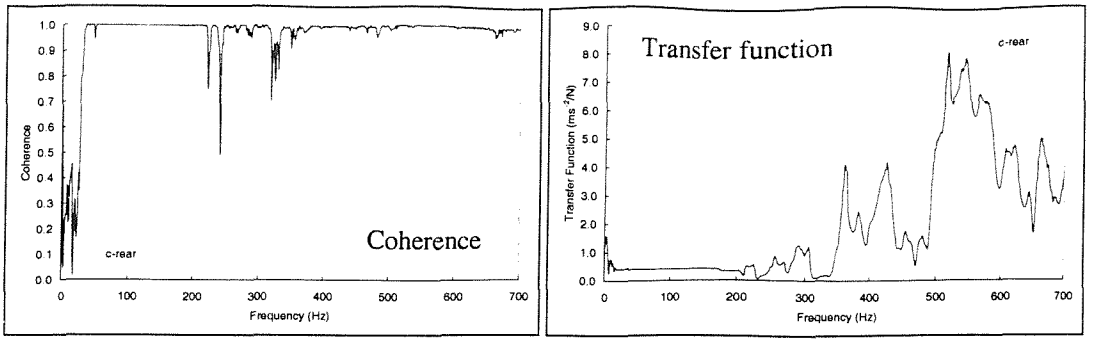

Figure C.49 Measuring point - middle of rear spar

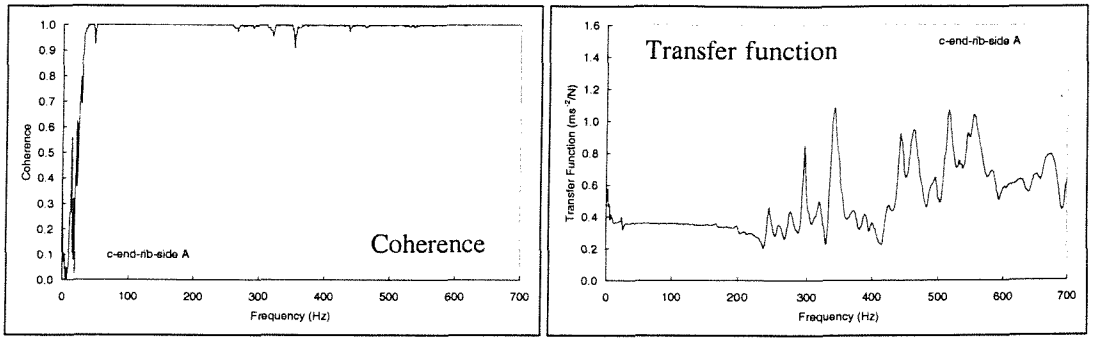

Figure C.50 Measuring point - middle of the end rib on side A

C.2.4 Mode Shapes of Box Structures

C.2.4.1 Aluminium box - flat skin panel

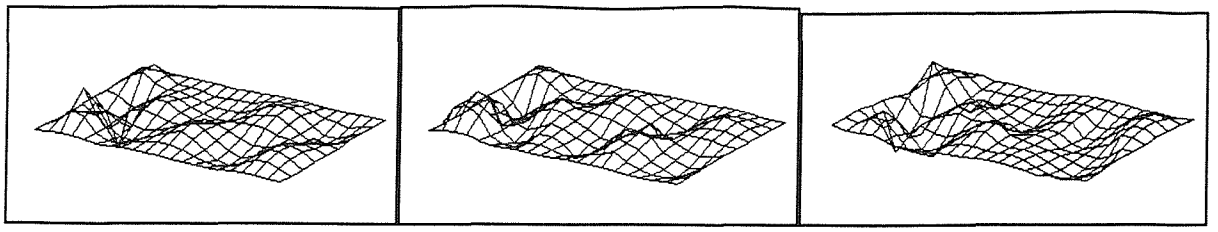

f_9=518.4 Hz f_{10}=530.4 Hz f_{11}=565.2 Hz

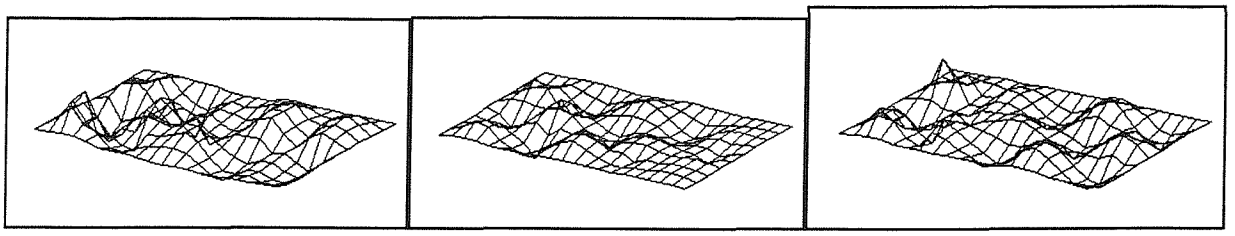

f_{12}=584.4 Hz f_{13}=628.8 Hz f_{14}=661.2 Hz

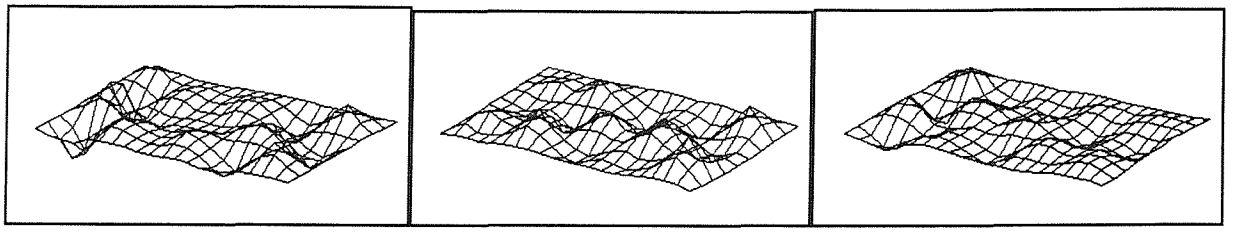

f_{15}=676.8 Hz f_{16}=694.8 Hz f_{17}=728.4 Hz

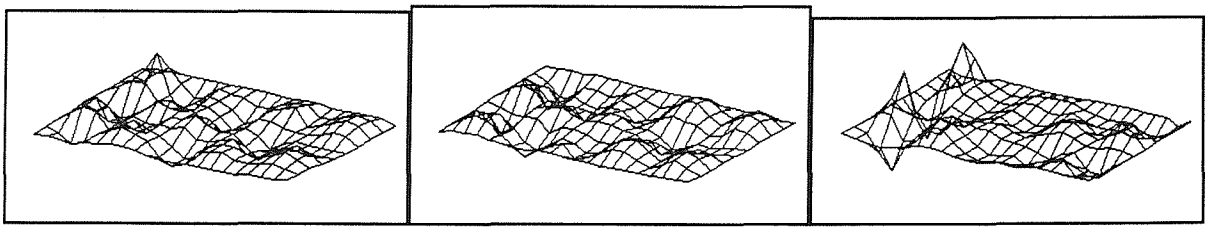

f_{18}=756.0 Hz f_{19}=769.2 Hz f_{20}=814.8 Hz

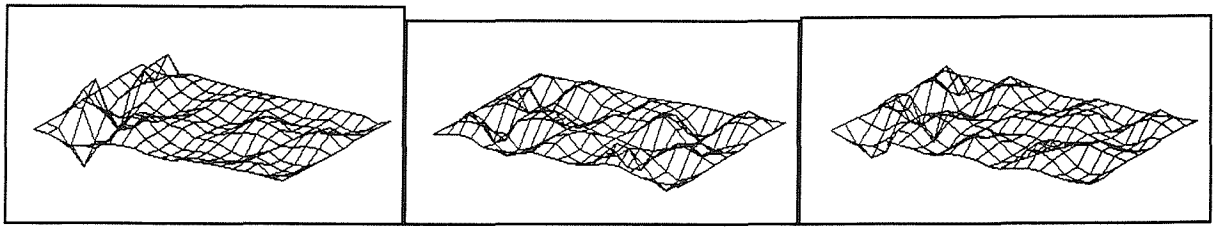

f_{21}=818.4 Hz f_{22}=865.2 Hz f_{23}=894.0 Hz

C.2.4.2 Aluminium box - curved skin panel

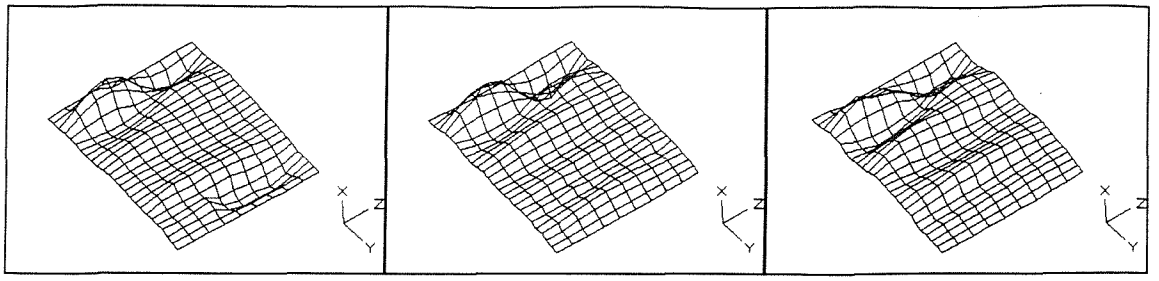

f_9=395.4 Hz f_{10}=457.2 Hz f_{11}=498.0 Hz

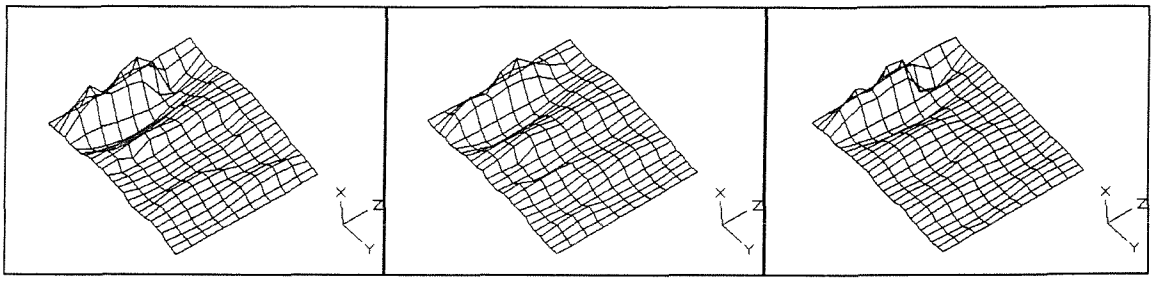

f_{12}=520.8 Hz f_{13}=546.0 Hz f_{14}=573.6 Hz

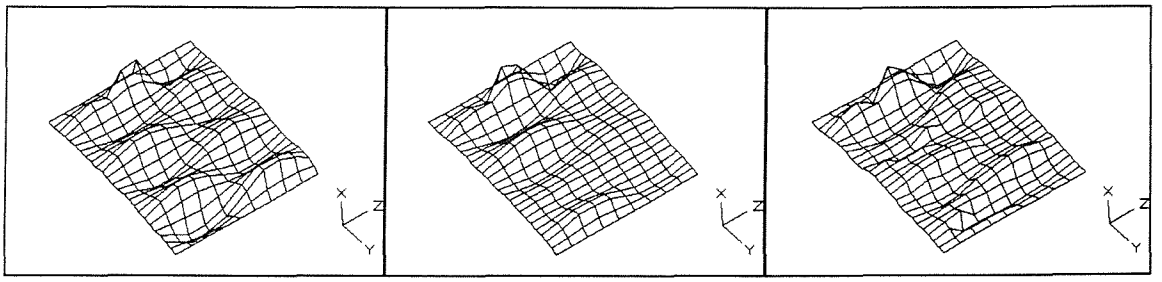

f_{15}=633.6 Hz f_{16}=657.6 Hz f_{17}=681.6 Hz

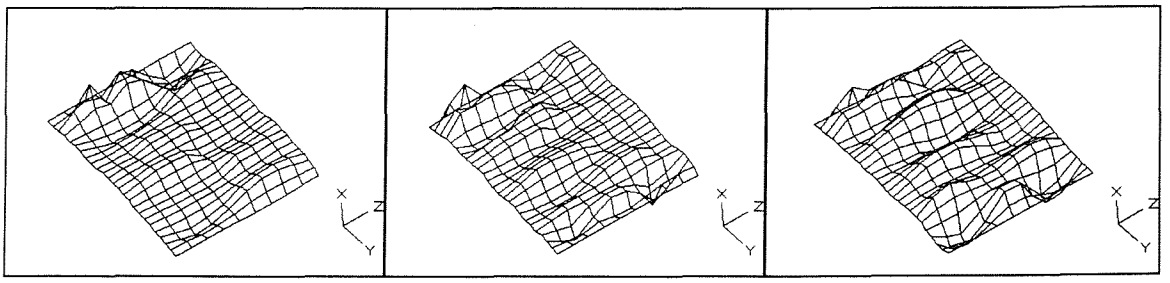

f_{18}=694.8 Hz f_{19}=807.6 Hz f_{20}=819.6 Hz

C.2.4.3 GLARE box - flat skin panel

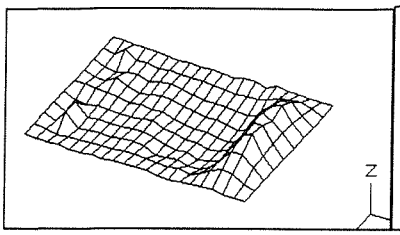

f_9=318.1 Hz

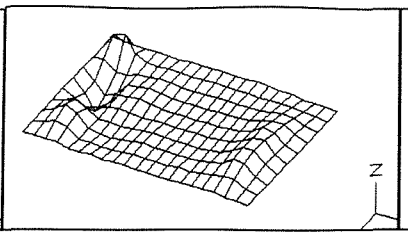

f_{10}=348.0 Hz

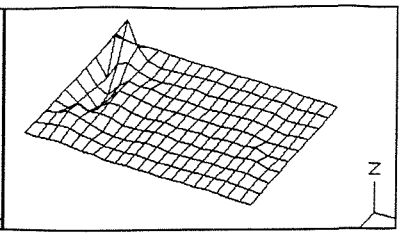

f_{11}=368.4 Hz

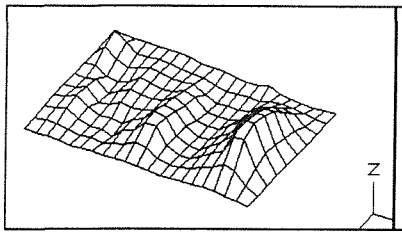

f_{12}=383.3 Hz

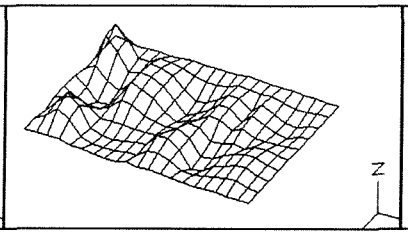

f_{13}=410.4 Hz

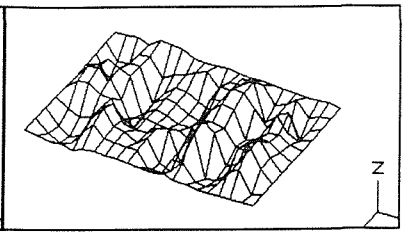

f_{14}=412.8 Hz

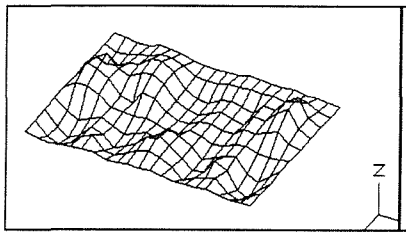

f_{15}=442.8 Hz

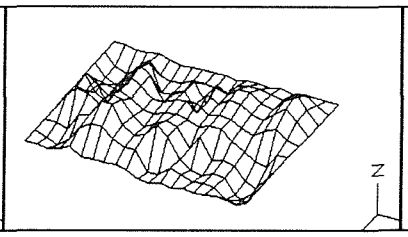

f_{16}=462.0 Hz

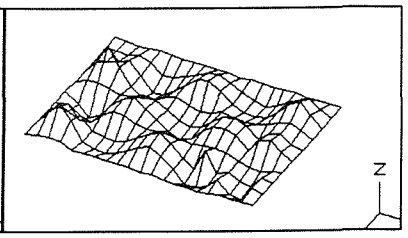

f_{17}=541.2 Hz

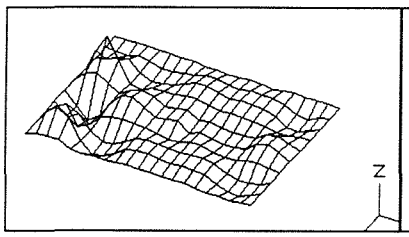

f_{18}=567.6 Hz

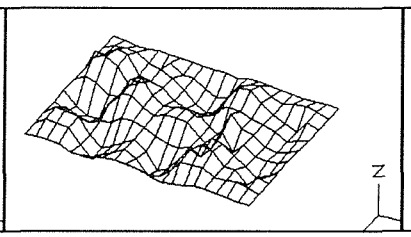

f_{19}=596.4 Hz

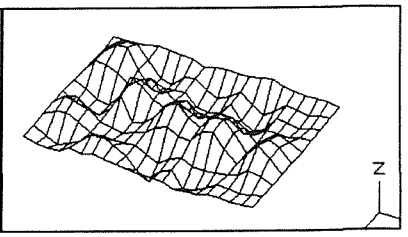

f_{20}=637.2 Hz

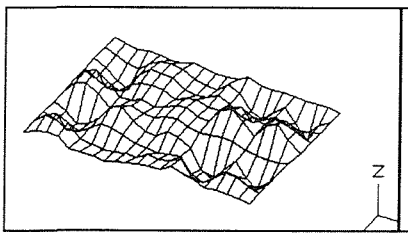

f_{21}=678.0 Hz

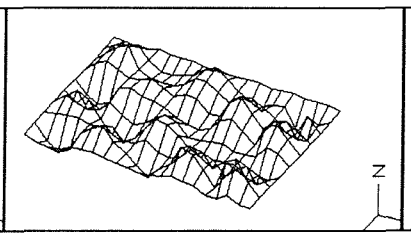

f_{22}=686.4 Hz

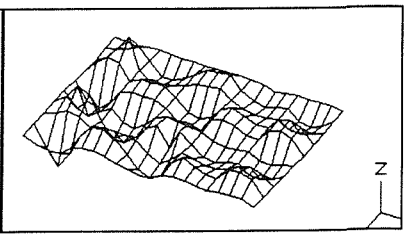

f_{23}=727.2 Hz

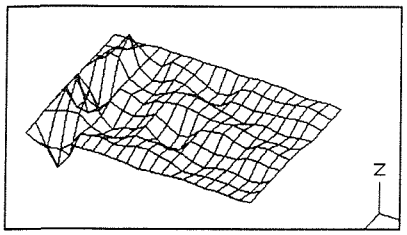

f_{24}=740.4 Hz

C.2.4.4 CFRP box - flat skin panel

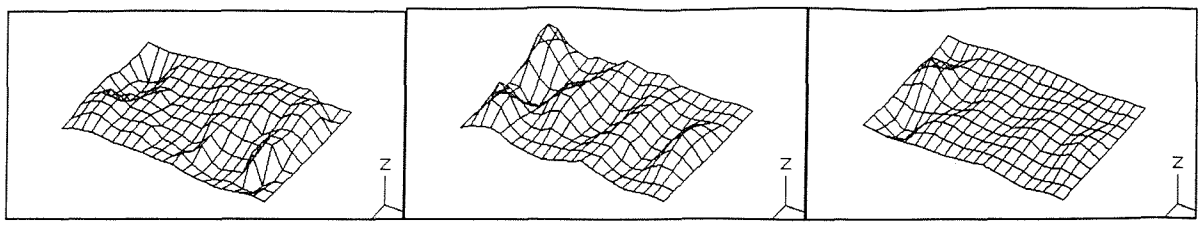

f_9=541.2 Hz f_{10}=613.2 Hz f_{11}=638.4 Hz

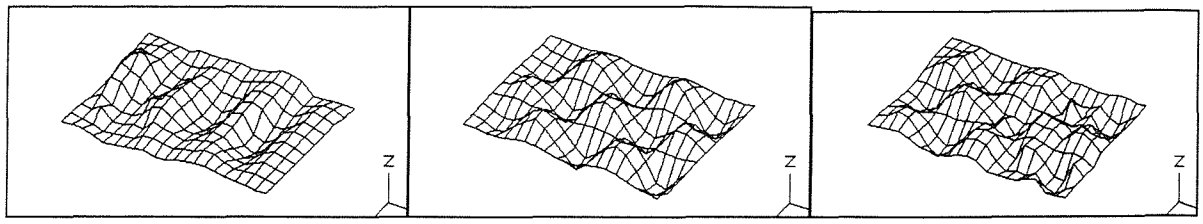

f_{12}=652.8 Hz f_{13}=699.6 Hz f_{14}=740.4 Hz

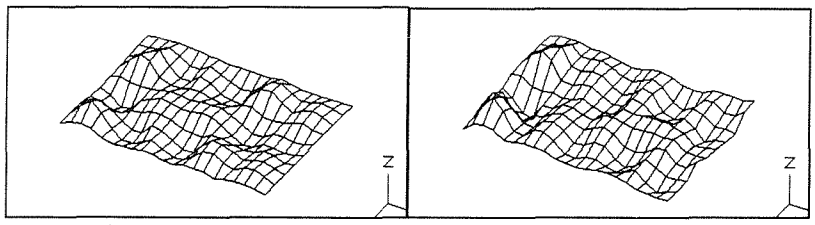

f_{15}=825.6 Hz f_{16}=872.4 Hz

C.2.4.5 CFRP box - curved skin panel

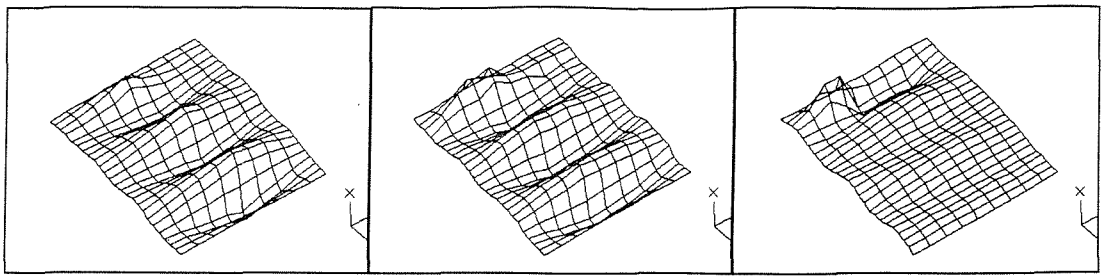

f_9=433.2 Hz f_{10}=459.6 Hz f_{11}=477.2 Hz

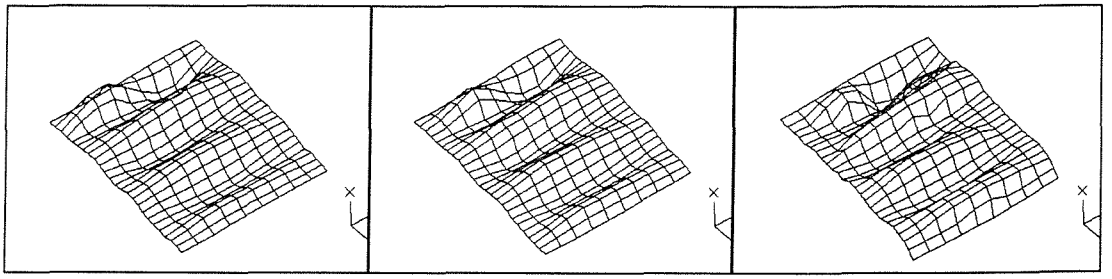

f_{12}=493.2 Hz f_{13}=540.0 Hz f_{14}=568.8 Hz

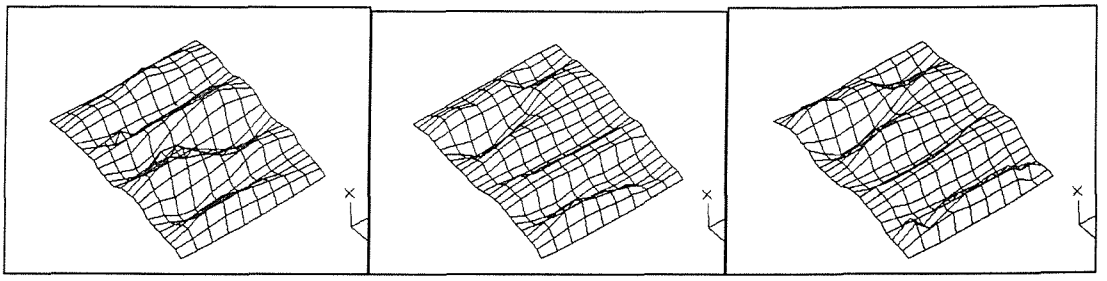

f_{15}=579.6 Hz f_{16}=616.8 Hz f_{17}=658.8 Hz

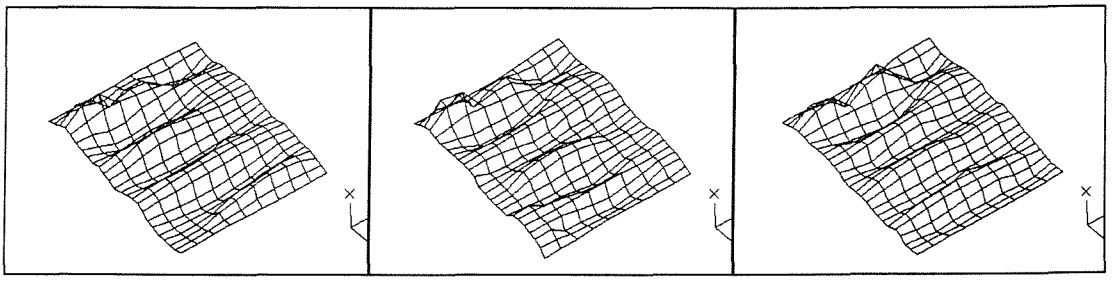

f_{18}=724.8 Hz f_{19}=788.4 Hz f_{20}=849.6 Hz

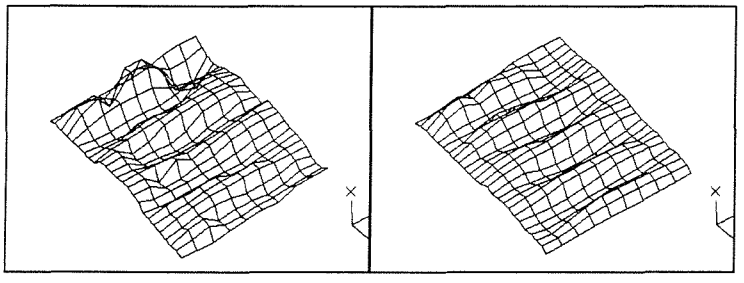

f_{21}=877.2 Hz f_{22}=930.0 Hz

APPENDIX D CONSTRUCTION DETAILS OF THE BOX STRUCTURES

D.1 ALUMINIUM ALLOY STRUCTURE

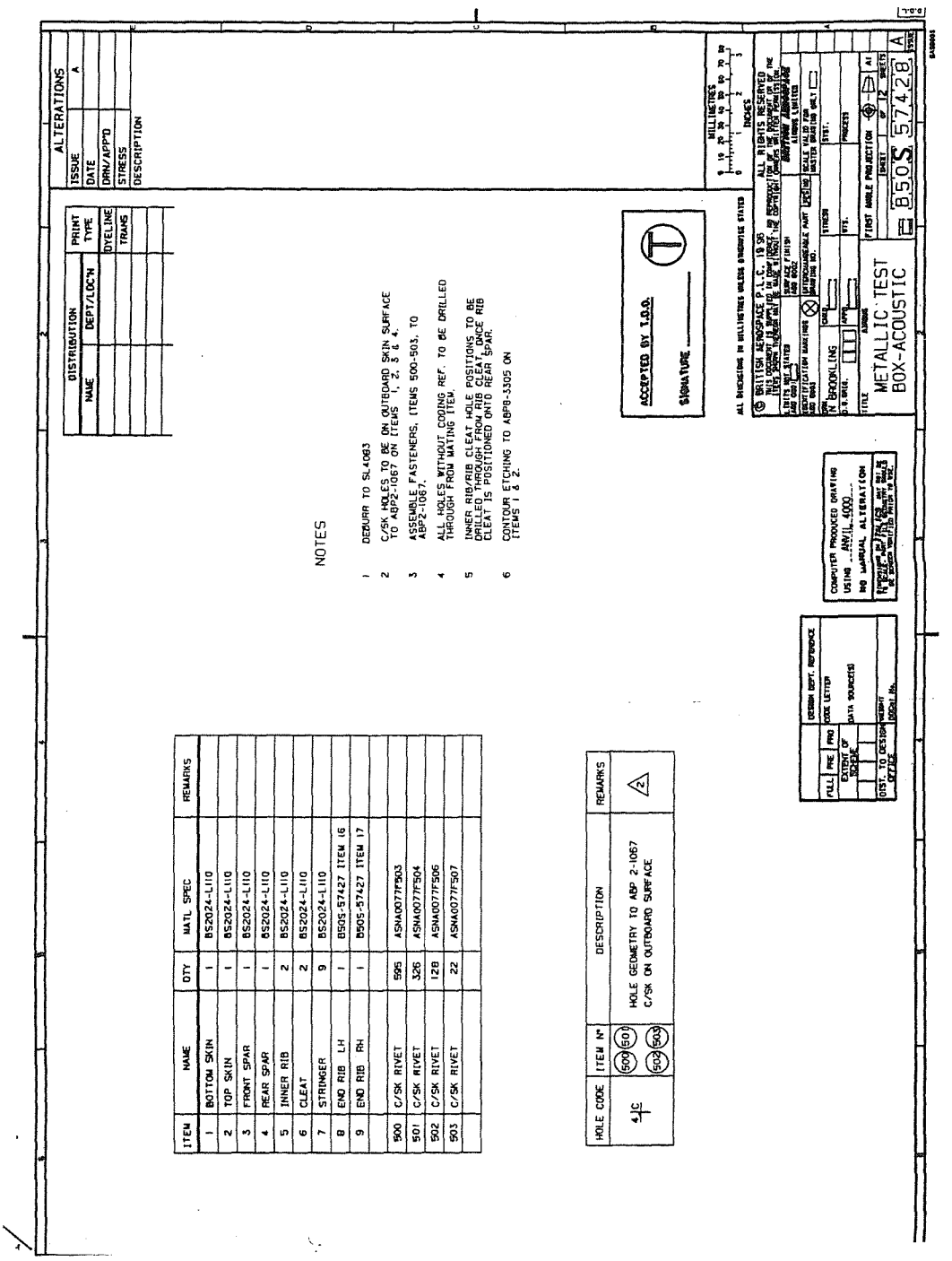

D.2 GLARE STRUCTURE

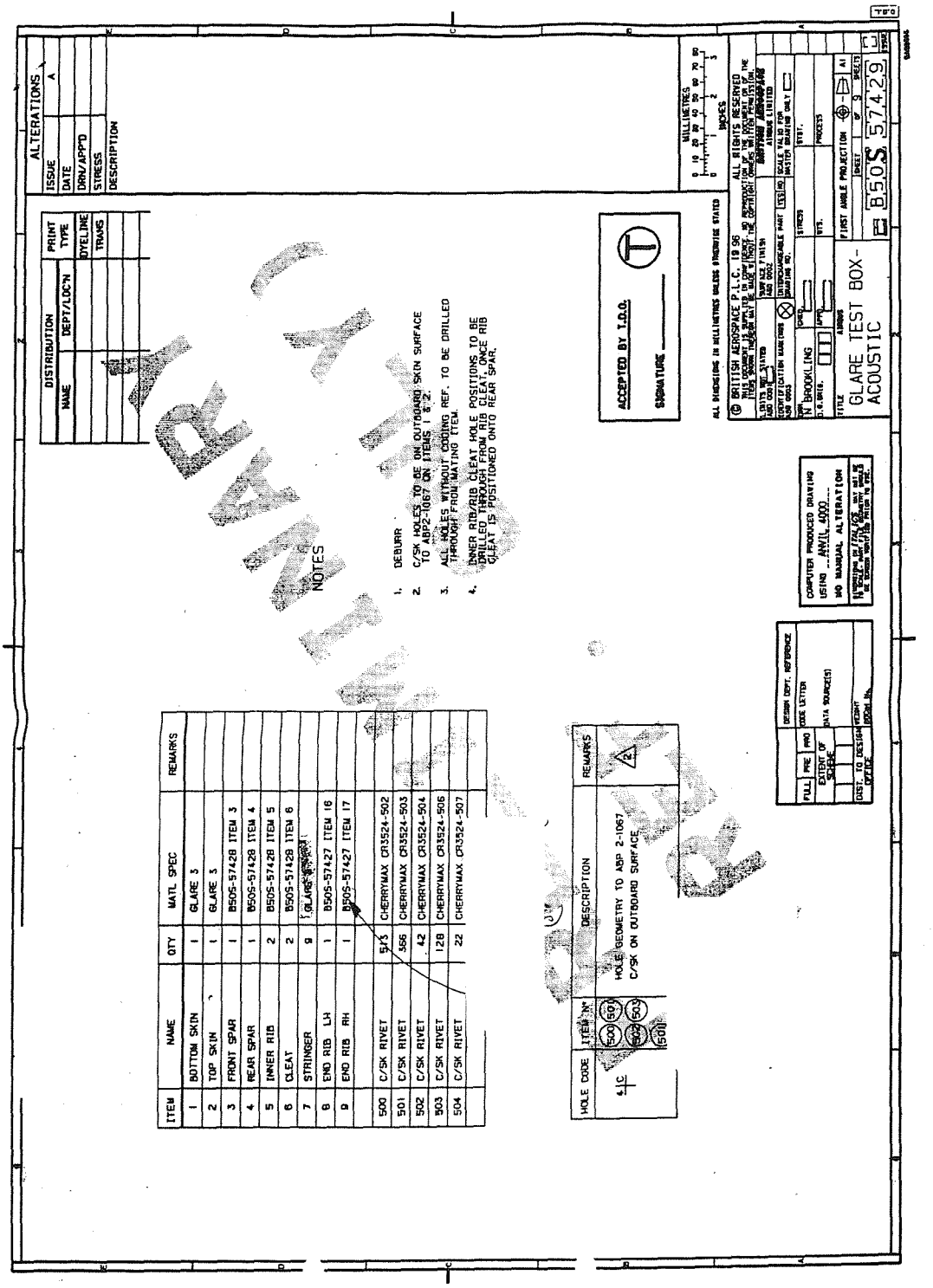

28-AUG-1996 11:17 FROM M47 / S81 TO 901703593058 P.01

BRITISH AEROSPACE AIRBUS

Fax Transmission
Filton

From: Richard Pedwell
Development Engineer
Manufacturing Development

Tel: (0117) 936 4527

Fax: (0117) 936 4883

Ref: RP / FAX / 022

British Aerospace Airbus Ltd
New Filton House
Filton
Bristol
BS99 7AR
ENGLAND

To: Ms. Y. XIAO

Company: University of Southampton

Date: August 28th 1996

Fax: 01703 593058

Pages (including this one): 1

Information For Glare Acoustic Fatigue Box

Component	Material	Configuration	Aluminium alloy sheet thickness	Prepreg layer thickness	Prepreg Orientation
Stringers	Glare 2	3/2	0.3 mm	0.25 mm	Unidirectional (0°)
Top Skin	Glare 3	3/2	0.3 mm	0.25 mm	Cross-ply (0°/ 90°)
Bottom Skin	Glare 3	3/2	0.3 mm	0.25 mm	Cross-ply (0°/ 90°)

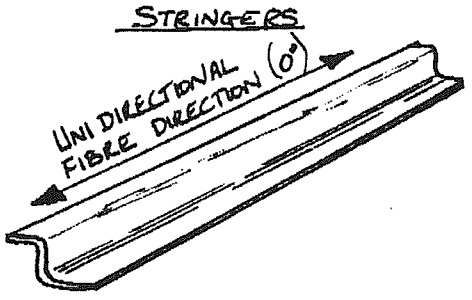

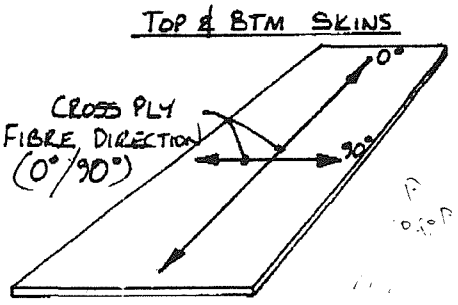

I hope that this answers your question.

Regards,

RP Pedwell

Richard Pedwell

TOTAL P.01

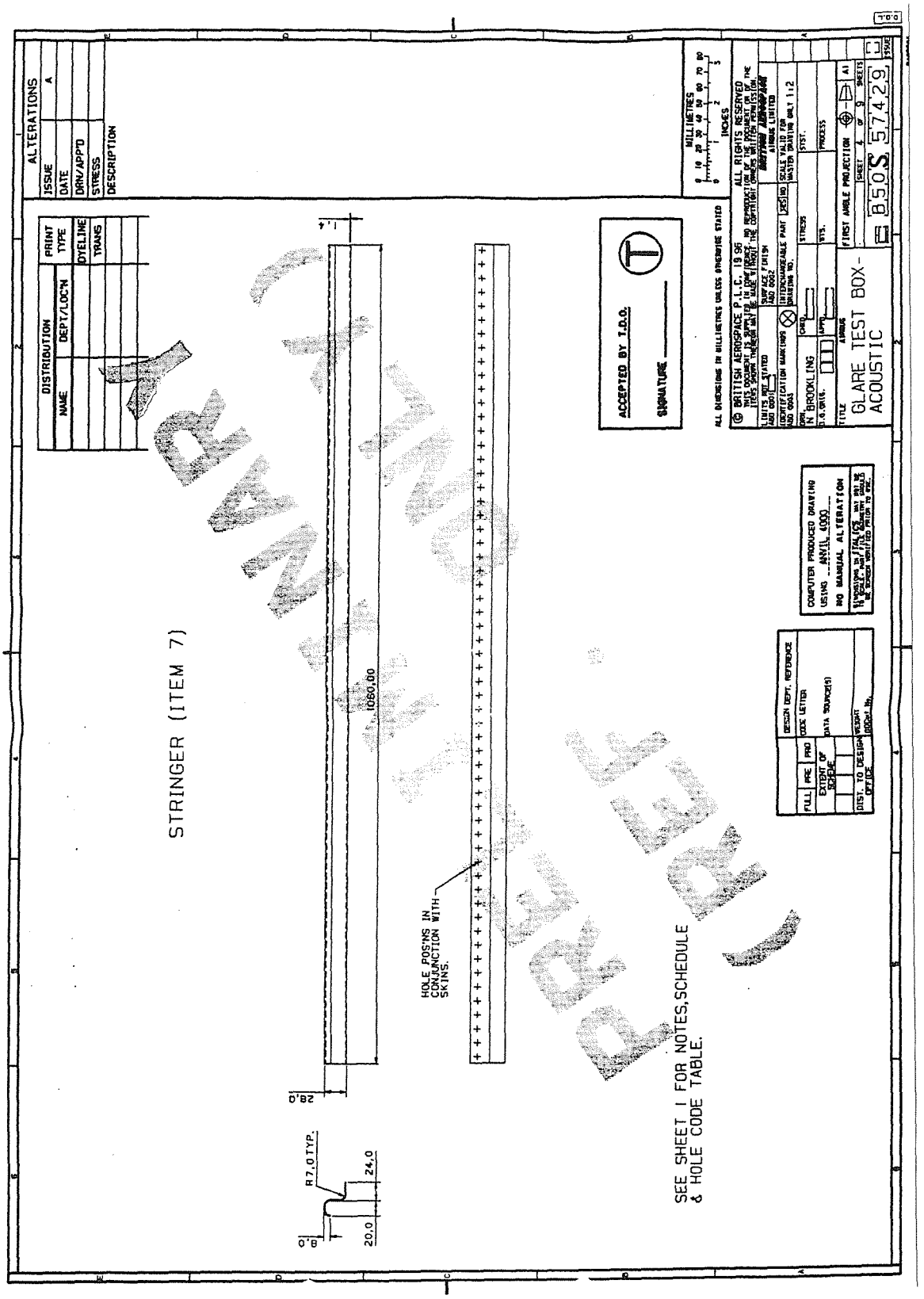
STRINGER (ITEM 7)
1080.00
28.0
HOLE POS'NS IN CONJUNCTION WITH SKINS.
R7.0 TYP.
24.0
20.0
8.0
SEE SHEET 1 FOR NOTES, SCHEDULE & HOLE CODE TABLE.
ALTERATIONS
ISSUE
DATE
DRN/APP'D
STRESS
DESCRIPTION
DISTRIBUTION
NAME
DEPT/LOC'N
PRINT TYPE
DYELINE
TRANS
ACCEPTED BY T.D.O.
SIGNATURE
MILLIMETRES
INCHES
© BRITISH AEROSPACE P.L.C. 1996
ALL RIGHTS RESERVED
DRN.
N BROOKLING
D.O.(W)16.
TITLE
GLARE TEST BOX-ACOUSTIC
FIRST ANGLE PROJECTION
SHEET 4 OF 9 SHEETS
ISSUE
B50S 57429
COMPUTER PRODUCED DRAWING
USING ANVIL 4000
NO MANUAL ALTERATION
DESIGN DEPT. REFERENCE
CODE LETTER
DATA SOURCE(S)
WEIGHT
FULL
PRE
PRO
EXTENT OF SCHEME
DIST. TO DESIGN OFFICE

29/10/1996 15:55 01179365903 STRUCTURES ENGINEERS PAGE 01

BRITISH AEROSPACE AIRBUS

Fax Transmission

Filton

From: L. C. CHOW
STRUCTURES TECH, B45
TECHNICAL CENTRE

British Aerospace Airbus Ltd
New Filton House
Filton
Bristol BS99 7AR

To: Ms. Ying Xiao
Research Assistant

Tel: 0117-363210
Fax: 0117-9365903

Company: Southampton University

Date: 29 October 1996

Fax: 01703-593058

Pages: (including this one)1

Re: Glare Test Coupons (phosphoric acid anodised)

I have requested my colleague to manufacture 28 off the following T coupons for you . I am not sure whether the delivered stringers will be in L shape or Z shape. If it is in Z shape, you may have to cut it in order to clamp the coupon for testing. Please note that the centre line of the fasteners are in the centre of the coupons. When you do your testing of the Glare (chromatic acid anodised) coupons, you should cut to the same format. The dimensions of the coupons (to be sent) are as follows:

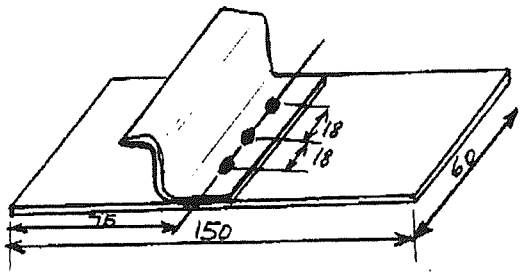

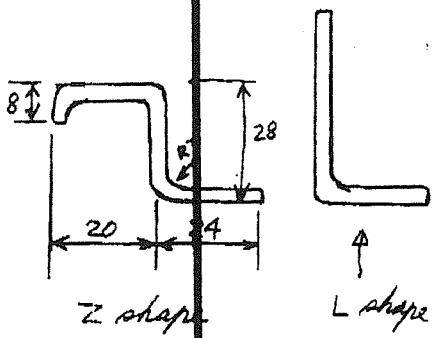

Best Regards,

D.3 CFRP STRUCTURE

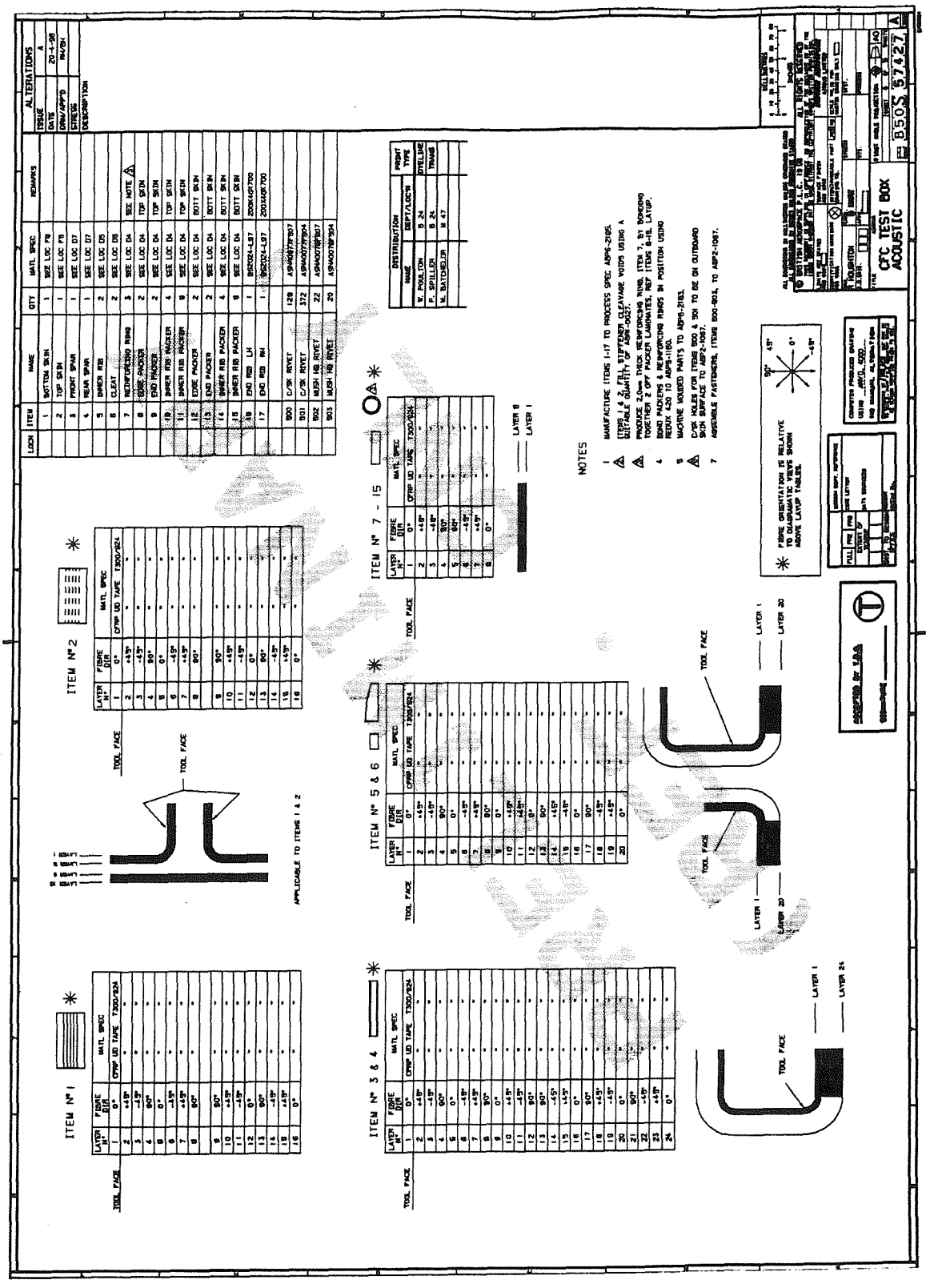

APPENDIX E CALIBRATION OF STRAIN MEASURING AMPLIFIERS AND CFRP STRUCTURE REPAIR REPORT

E.1 CALIBRATION OF STRAIN MEASURING AMPLIFIERS

An aluminium alloy cantilever beam was used to calibrate the strain gauge amplifiers.

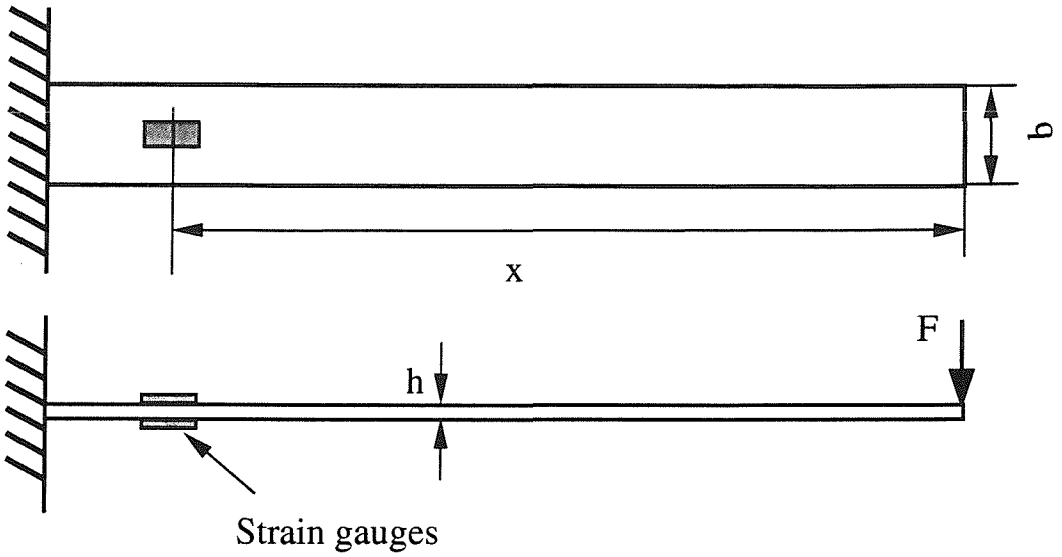

Strain of the beam at the location of the gauges was calculated using following formula:

$$\varepsilon = \pm \frac{6Fx}{Ebh^2}$$

where x = 260mm

b = 25.6mm

h = 4.88mm

E = 65MPa

F = 4.91, 7.36 & 9.81N

Table E.1 Calibrations of the strain amplifiers

EXTERNAL CALIBRATION:						
STRAIN ON THE CALIBRATION BEAM: 193.1με (4.91N), 289.6με (7.36N), 386.2 με (9.81N)						
MEASURING AMPLIFIER: MM 2100						
INTERNAL CALIBRATION: FACTOR 945.3με /2V						
	4.91N		7.36N		9.81N	
CHANNEL No.	METER (V)	STRAIN (με)	METER (V)	STRAIN (με)	METER (V)	STRAIN (με)
1	0.406	191.90	0.608	287.37	0.810	382.85
2	0.402	190.01	0.604	285.48	0.806	380.96
3	0.404	190.95	0.610	288.32	0.813	384.26
4	0.402	190.01	0.606	286.43	0.808	381.90
5	0.401	189.53	0.603	285.01	0.805	380.48
6	0.401	189.53	0.606	286.43	0.808	381.90
7	0.405	191.42	0.609	287.84	0.812	383.79
8	0.399	188.59	0.605	285.95	0.807	381.43
9	0.401	189.53	0.606	286.43	0.809	382.37
10	0.400	189.06	0.604	285.48	0.809	382.37

EXTERNAL CALIBRATION:						
STRAIN ON THE CALIBRATION BEAM: 193.1με (4.91N), 289.6με (7.36N), 386.2 με (9.81N)						
MEASURING AMPLIFIER: MM2310						
INTERNAL CALIBRATION: FACTOR 188.6με /0.4V						
	4.91N		7.36N		9.81N	
CHANNEL No.	METER (V)	STRAIN (με)	METER (V)	STRAIN (με)	METER (V)	STRAIN (με)
1	0.401	189.07	0.605	285.26	0.810	381.92
2	0.403	190.01	0.607	286.20	0.811	382.39
3	0.403	190.01	0.607	286.20	0.812	382.86
4	0.406	191.43	0.609	287.14	0.821	387.10
5	0.405	190.96	0.610	287.62	0.814	383.80
6	0.402	189.54	0.605	285.26	0.811	382.39
7	0.406	191.43	0.608	286.67	0.813	383.33
8	0.395	186.24	0.597	281.49	0.800	377.20
9	0.407	191.90	0.612	288.56	0.819	386.16
10	0.403	190.01	0.609	287.14	0.807	380.50

EXTERNAL CALIBRATION:								
STRAIN ON THE CALIBRATION BEAM: 193.1με (4.91N), 289.6με (7.36N), 386.2 με (9.81N)								
MEASURING AMPLIFIER: YEW 3126								
	INTERNAL CAL.	4.91N		7.36N		9.81N		
CHANNEL No.	READING (V) FOR 200με	METER (V)	STRAIN (με)	METER (V)	STRAIN (με)	METER (V)	STRAIN (με)	
1	0.814	0.772	189.68	1.150	282.56	1.515	372.24	
2	0.800	0.785	196.25	1.168	292.00	1.537	384.25	
3	0.797	0.757	189.96	1.132	284.07	1.497	375.66	
4	0.792	0.759	191.67	1.134	286.36	1.495	377.53	
5	0.794	0.744	187.41	1.111	279.85	1.474	371.28	
6	0.824	0.749	181.80	1.113	270.15	1.487	360.92	
7	0.790	0.752	190.38	1.118	283.04	1.505	381.01	
8	0.815	0.782	191.90	1.164	285.70	1.555	381.71	
9	0.823	0.777	188.94	1.157	281.22	1.562	379.82	
10	0.852	0.806	189.08	1.237	290.26	1.646	386.38	

E.2 CFRP STRUCTURE REPAIR REPORT

ACOUSTIC BOX REPAIR
M I S B47/07/0150

COMPONENT NO
B47/05/1311

INVESTIGATION.
The acoustic box was returned to Filton having failed early during test on receipt it appeared that the rivets had snapped.
Retrieve drawings **B50S54727 ISS A SHEETS 1 TO 5**
Retrieve process spec **ABP 2-1067**

1) **IDENTIFY** rivets used ,As the ones fitted do not appear to be what is called up on Drawing
RESULT The fitted rivets are alloy, length is correct diameter is correct
THE CALL UP IS FOR MONEL RIVET NOT ALLOY
The Alloy rivet used is not structural and should be removed in accordance with ABP –1067
Hole examined and recorded.
Result
Hole size has not been affected by insertion of the soft rivet
Holes are still within acceptable limits **NO ACTION REQUIRED TO REPAIR.**

2)PLAN OF ACTION.
Procure correct rivets determine lead times
Lead time Two weeks for Counter sink Six for musheads.
DUE TO LONG LEAD TIME AND MIN ORDER QTY OF MUSHEAD RIVETS ONLY REPLACE COUNTERSINKS
ORDER 500-4s 200-7s
DONE

REPAIR
Drill out rivets.
Complete repair using issued drawings and ABP-2-1067
Record all materials used

RIVETS:- ASNA77F504 MMR 0765
RIVETS:- ASNA77F507 MMR 0769
SEALANT BATCH NO:- MMR 0770 F069050
OPERATOR:-

ENGINEERS SIGN OFF

NAME

SIG:
DATE:-

APPENDIX F CFRP AND GLARE PROPERTIES

F.1 MATERIAL PROPERTIES OF THE CFRP UD TAPE T300/924

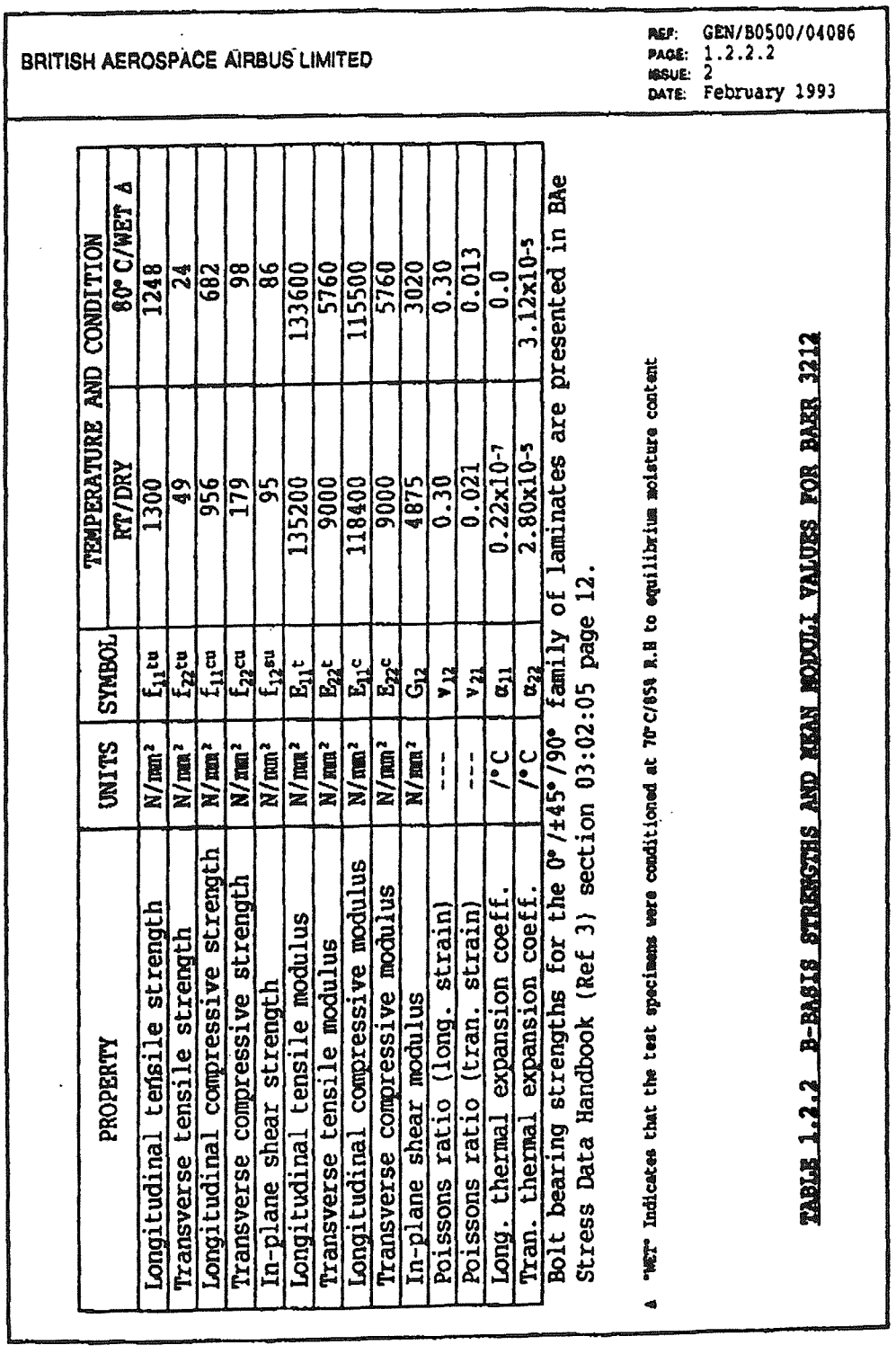

BRITISH AEROSPACE AIRBUS LIMITED

REF: GEN/B0500/04086
PAGE: 1.2.2.2
ISSUE: 2
DATE: February 1993

PROPERTY	UNITS	SYMBOL	TEMPERATURE AND CONDITION	
			RT/DRY	80° C/WET Δ
Longitudinal tensile strength	N/mm²	f_{11}^{tu}	1300	1248
Transverse tensile strength	N/mm²	f_{22}^{tu}	49	24
Longitudinal compressive strength	N/mm²	f_{11}^{cu}	956	682
Transverse compressive strength	N/mm²	f_{22}^{cu}	179	98
In-plane shear strength	N/mm²	f_{12}^{su}	95	86
Longitudinal tensile modulus	N/mm²	E_{11}^{t}	135200	133600
Transverse tensile modulus	N/mm²	E_{22}^{t}	9000	5760
Longitudinal compressive modulus	N/mm²	E_{11}^{c}	118400	115500
Transverse compressive modulus	N/mm²	E_{22}^{c}	9000	5760
In-plane shear modulus	N/mm²	G_{12}	4875	3020
Poissons ratio (long. strain)	---	ν_{12}	0.30	0.30
Poissons ratio (tran. strain)	---	ν_{21}	0.021	0.013
Long. thermal expansion coeff.	/°C	α_{11}	0.22×10^{-7}	0.0
Tran. thermal expansion coeff.	/°C	α_{22}	2.80×10^{-5}	3.12×10^{-5}

Bolt bearing strengths for the 0°/±45°/90° family of laminates are presented in BAe Stress Data Handbook (Ref 3) section 03:02:05 page 12.

Δ "WET" Indicates that the test specimens were conditioned at 70°C/85% R.H to equilibrium moisture content

TABLE 1.2.2 B-BASIS STRENGTHS AND MEAN MODULI VALUES FOR BAER 3212

F.2 MATERIAL PROPERTIES OF THE GLARE CONSTITUENTS

F.2.1 Aluminium T2024

Customer data information sheet

No.: 2.300

Page: 1/2

Subject: Properties of FML Constituents -- Aluminum 2024-T3 Bare/Clad

Test method: Modified ASTM D3039-76

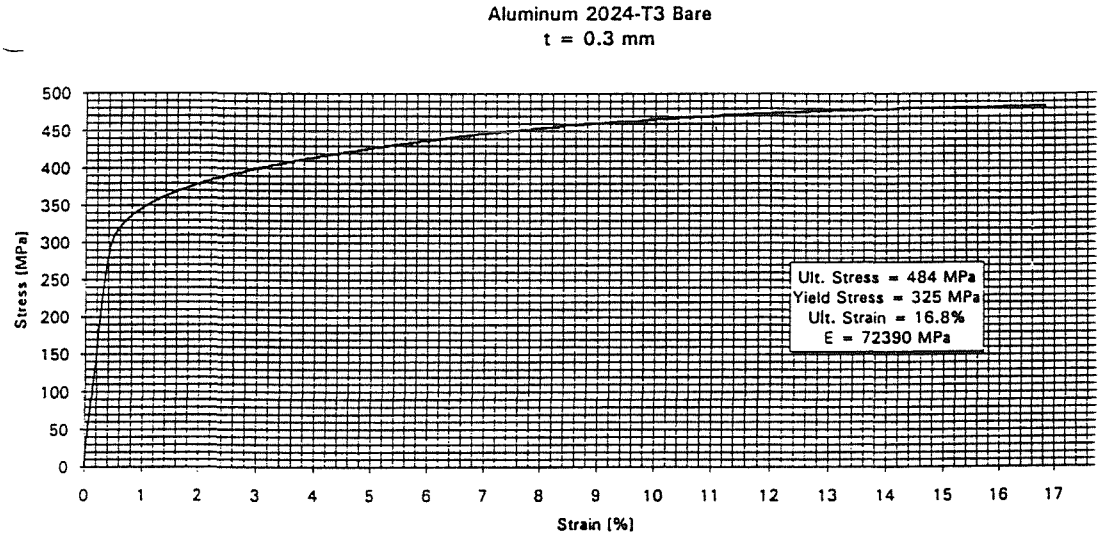

Typical tensile stress-strain curve for 0.3 mm aluminum 2024-T3 bare at room temperature.

compiled	A. Mattousch		issue date	2-9-'93
checked	G. Roebroeks		issue number	1
	B. van Wimersma Greidanus		No. of pages	2
	M. Verbruggen		reference	idis 2.300
authorized	J.W. Gunnink			

F.2.2 Glass Fibre Composite

Customer data information sheet No.: 2.200

Page: 1/1

Subject: Properties of FML Constituents -- Prepregs

Test method: The prepreg properties are calculated with the classic laminate theory using the fiber and adhesive properties given in data sheet 2.100.

		UD Aramid Prepreg	UD Glass Prepreg	0/90 Glass Prepreg
E1	(MPa)	59871	53980	31700
E2	(MPa)	3793	9412	31700
G12	(MPa)	1199	5548	5548
v12		0.344	0.33	0.098
v21		0.022	0.0575	0.098
α1	(1/°C)	-0.8E-6	6.1E-6	9.1E-6
α2	(1/°C)	68.3E-6	26.2E-6	9.1E-6
Density	(g/cm^3)	1.32	2.0	2.0

supersedes cdis 011

compiled	A. Mattousch		issue date	12-10-'93
checked	G. Roebroeks		issue number	1
	B. van Wimersma Greidanus		No. of pages	1
	M. Verbruggen		reference	idis 2.200
authorized	J.W. Gunnink			

F.2.3 Fibres & Adhesive

Customer data information sheet No.: 2.100

Page: 1/1

Subject: Properties of FML Constituents -- Fibers & Adhesive

		Aramid Fibers	Glass Fibers	AF163-2
E1	(MPa)	124000	88000	1850
E2	(MPa)	6700	88000	1850
G12	(MPa)	2463	33100	695
v12		0.36	0.33	0.33
v21		0.019	0.33	0.33
α1	(1/°C)	-2.0E-6	5.2E-6	75.0E-6
α2	(1/°C)	50.0E-6	5.2E-6	75.0E-6

supersedes cdis 011

compiled	A. Mattousch		issue date	12-10-'93
checked	G. Roebroeks		issue number	1
	B. van Wimersma Greidanus		No. of pages	1
	M. Verbruggen		reference	idis 2.100
authorized	J.W. Gunnink			

F.2.4 Material Properties of GLARE Laminates

Customer data information sheet **No.: 1.000**

Page: 1/1

Subject: Typical mechanical properties of fiber metal laminates
(3/2 lay-up; Aluminum layer thickness 0.3 mm)

			GLARE				ARALL		Aluminum
			1	2	3	4	2	3	2024-T3
Tensile ultimate strength	MPa	L	1282	1074	717	930	717	765	455
		LT	352	317	700	592	317	352	448
Tensile yield strength	MPa	L	545	360	305	352	365	565	359
		LT	338	228	283	255	228	296	324
Tensile modulus	GPa	L	64	65	58	57	66	68	72
		LT	49	50	58	50	53	49	72
Ultimate strain	%	L	4.1	4.5	4.5	4.5	2.5	1.8	19
		LT	7.7	10.8	4.5	4.5	12.7	6.4	19
Compression yield strength	MPa	L		415	310	365	255	317	303
		LT		236	310	285	234	331	345
Compression moduius	GPa	L		67	59	60	65	66	74
		LT		52	59	54	53	50	74
Shear yield	MPa	L					110	159	207
		LT					110	159	207
Bearing ultimate strength (e/D = 1.5)	MPa	L		566	644		545	579	758
		LT		619	644		593	634	758
Bearing ultimate strength (e/D = 2.0)	MPa	L	834	727	819	662	634	669	945
		LT		757	819		621	655	945
Bearing yield strength (e/D = 1.5)	MPa	L		440	445		393	476	538
		LT		410	445		393	483	538
Bearing yield strength (e/D = 2.0)	MPa	L	710	574	573	517	469	552	648
		LT		493	573		455	531	648
Blunt notch strength (1)	MPa	L	793	765	496	593	441	545	414
		LT	352	283	496	414	276	352	414
Sharp notch strength (2)	MPa	L	669	558	393	476	331	331	372
		LT	228	228	393	331	248	248	372
Density	g/cm^3		2.49	2.48	2.48	2.40	2.31	2.33	2.77

(1) Net residual strength, Open hole specimen: w = 100 mm, D = 25 mm
(2) Net residual strength, Center crack specimen: w = 100 mm, 2a(0) = 25 mm

Supersedes cdis 012

compiled	A.C. Mattousch		issue date	26-1-'94
checked	G. Roebroeks		issue number	1
	B. van Wimersma		No. of pages	1
	M. Verbruggen	p/o	reference	idis 1.000
authorized	J.W. Gunnink			

APPENDIX G PC BASED FREQUENCY COUNTER

A comparator circuit converted the received signal to TTL pulses. These were fed to a Computer Boards DAS16/330 Data Acquisition Card inside the PC. This featured a 8254 down counter which counted these pulses over a number of seconds, so that the program could calculate the resonant frequency of the sample.

While the resonant frequency stayed close to its original value, the system stored a collection of data samples at a low repeat rate.
If the resonant frequency changed, indicating a fracture, the system acquired data at an increased repeat rate.

This arrangement greatly reduced the amount of data to be processed, but retained the information that was of interest.

APPENDIX H PERMISSION – ESDU 84027

----- Original Message -----

From: Cyrus Chinoy **To:** y.xiao@breathemail.net **Cc:** Dave Mitchell **Sent:** Wednesday, October 16, 2002 9:31 AM **Subject:** RE: ESDU 84027 Amendment A (Issue 1)

Dear Ms Xiao,

I am pleased to say that we at ESDU should be perfectly happy for you to use the figures from ESDU 84027 in your thesis.

Wishing you success in your effort towards your doctorate,

Yours sincerely,

Cyrus Chinoy

C B Chinoy

Head of Aircraft Noise and Structural Dynamics

ESDU International plc